V. 123, NO. 2
MARCH 2026

# ACI MATERIALS JOURNAL

A JOURNAL OF THE AMERICAN CONCRETE INSTITUTE

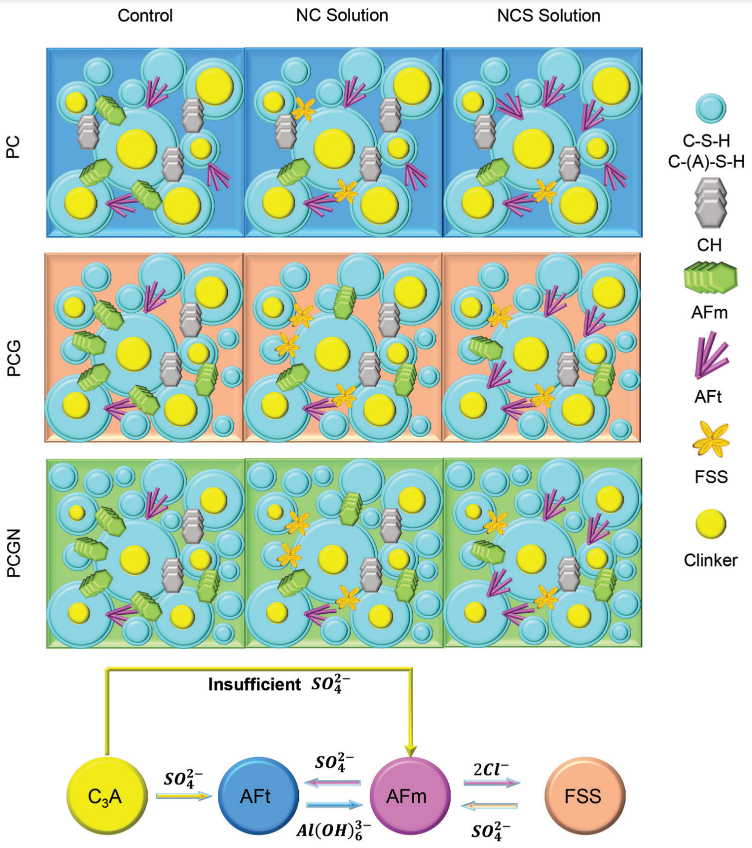

American Concrete Institute

# CONTENTS

**Editorial Board**
Shiho Kawashima, Editor-in-Chief,
*Columbia University*
Liberato Ferrara,
*Polytechnic University of Milan*
Raissa Ferron,
*The University of Texas at Austin*
O. Burkan Isgor,
*Oregon State University*
Prannoy Suraneni,
*University of Miami*

**Board of Direction**

**President**
Maria Juenger

**Vice Presidents**
Scott M. Anderson
Matthew R. Sherman

**Directors**
Michael Ahern
Corina-Maria Aldea
Oscar R. Antommattei
Peter Barlow
Arturo Gaytan Covarrubias
James H. Hanson
Carol Hayek
Werner K. Hellmer
Mary Beth Diesz Hueste
Kimberly Waggle Kramer
Enrique Pasquel
Xiomara Sapón-Roldán

**Past President Board Members**
Charles K. Nmai
Antonio Nanni
Michael J. Paul

**Executive Vice President**
Frederick H. Grubbe

**Staff**
*Publisher*
John C. Glumb

*Senior Managing Director of Technical Operations*
Michael L. Tholen

*Engineers*
Will J. Gold
Matthew R. Senecal
Michael L. Tholen
Gregory M. Zeisler

*Managing Editor*
Lauren E. Mentz

*Associate Editor*
Kimberly K. Olesky

*Editors*
Erin N. Azzopardi
Lauren C. Brown
Kaitlyn J. Dobberteen
Tiesha Elam
Angela R. Noelker
Kelli R. Slayden

PRINTED WITH SOY INK®

## ACI Materials Journal

**March 2026, V. 123, No. 2**

A JOURNAL OF THE AMERICAN CONCRETE INSTITUTE
AN INTERNATIONAL TECHNICAL SOCIETY

*Contents continued on next page*

*ACI Materials Journal*
© 2026 American Concrete Institute. All rights reserved.

This material may not be reproduced or copied, in whole or in part, in any form or by any means, including making copies by any photo process, or by electronic or mechanical device, printed, written, graphic, or oral, or recording for sound or visual reproduction for use in any knowledge or retrieval system or device, without the written consent of ACI. This material may not be used by data mining, robots, screen scraping, or similar data gathering and extraction tools such as artificial intelligence ("AI") for purposes of developing or training a machine learning or AI model, conducting computer analysis or creating derivatives of this material, without the written consent of ACI.

American Concrete Institute®, ACI®, Always Advancing®, *ACI Structural Journal*®, and *ACI Materials Journal*® are registered trademarks of American Concrete Institute.

The *ACI Materials Journal* (ISSN 0889-325x) is published bimonthly by the American Concrete Institute. Publication office: 38800 Country Club Drive, Farmington Hills, MI 48331. Periodicals postage paid at Farmington, MI, and at additional mailing offices. Subscription rates: $229 per year, payable in advance. POSTMASTER: Send address changes to: *ACI Materials Journal*, 38800 Country Club Drive, Farmington Hills, MI 48331.

Canadian GST: R 1226213149.

Direct correspondence to 38800 Country Club Drive, Farmington Hills, MI 48331. Telephone: +1.248.848.3700.
**Website: http://www.concrete.org.**

# CONTENTS

# MEETINGS

## APRIL-MAY 2026

**29-1—Structures Congress 2026**, Boston, MA, www.structurescongress.org

## MAY 2026

**4-6—*Engineering News-Record* (*ENR*) FutureTech**, San Francisco, CA, www.enr.com/future-tech

**4-7—2026 PTI Convention**, Long Beach, CA, www.post-tensioning.org/events/conventions/registration.aspx?step=EventChoice_0

**12-14—2nd International Conference on Iron-Sulfide Reactions in Concrete (ICISR 2026)**, Mystic, CT, https://crumblingconcrete.engr.uconn.edu/icisr-2026

**12-15—15th International Conference "Modern Building Materials, Structures and Techniques,"** Vilnius, Lithuania, https://conferences.vilniustech.lt/index.php/MBMST

**13-14—2026 CCT/TxDOT Concrete Conference**, Austin, TX, https://web.cvent.com/event/8d854390-cd43-43d4-b4d2-e7433683c5f6/summary

**18-20—Building Innovation Conference 2026**, McLean, VA, www.buildinginnovation.org

**18-21—The International Conference on the Environmental and Technical Implications of Construction with Alternative Materials (WASCON 2026)**, Fukuoka, Japan, https://wascon2026.jp

**18-22—32nd International Conference on Structural Failures (ICSF 2026)**, Międzyzdroje, Poland, www.awarie.zut.edu.pl/en

## JUNE 2026

**9-10—3rd Global CemCCUS Conference, Exhibition and Awards 2026**, Hamburg, Germany, www.globalcement.com/conferences/cemccus

## ACI CONCRETE CONVENTION: FUTURE DATES

**2026**—Oct. 11-14, Hilton Atlanta, Atlanta, GA
**2027**—Mar. 21-24, Caesars Palace Las Vegas, Las Vegas, NV
**2027**—Oct. 24-27, Caribe Royale Orlando, Orlando, FL
**2028**—Apr. 2-5, Seattle Convention Center & Sheraton Grand Seattle, Seattle, WA

**For additional information, contact:**
Event Services, ACI
38800 Country Club Drive
Farmington Hills, MI 48331
Telephone: +1.248.848.3795
email: conventions@concrete.org

**ON FRONT COVER: 123-M23**, p. 128, Fig. 13—Ground-granulated blast-furnace slag (GGBFS)-nanosilica (NS) or sulfate affecting chloride ingress of GGBFS-NS cement composites within chloride-rich environment.

Papers appearing in the *ACI Materials Journal* are reviewed according to the Institute's Publication Policy by individual experts in the subject area of the papers.

## Contributions to *ACI Materials Journal*

The *ACI Materials Journal* is an open forum on concrete technology and papers related to this field are always welcome. All material submitted for possible publication must meet the requirements of the "American Concrete Institute Publication Policy" and "Author Guidelines and Submission Procedures." Prospective authors should request a copy of the Policy and Guidelines from ACI or visit ACI's website at **www.concrete.org** prior to submitting contributions.

Papers reporting research must include a statement indicating the significance of the research.

The Institute reserves the right to return, without review, contributions not meeting the requirements of the Publication Policy.

All materials conforming to the Policy requirements will be reviewed for editorial quality and technical content, and every effort will be made to put all acceptable papers into the information channel. However, potentially good papers may be returned to authors when it is not possible to publish them in a reasonable time.

### Discussion

All technical material appearing in the *ACI Materials Journal* may be discussed. If the discussion is received within four months of the paper's print publication, it will appear in the issue dated ten months from this journal's date. Discussion material received after specified dates will be considered individually for publication or private response. ACI Standards published in ACI Journals for public comment have discussion due dates printed with the Standard. Discussion should be complete and ready for publication, including finished, reproducible illustrations. Discussion must be confined to the scope of the paper and meet the ACI Publication Policy.

Follow the style of the current issue. Discussions should not exceed 1800-word equivalents (illustrations and tables count as 300 words each). References should be complete. Do not repeat references cited in original paper; cite them by original number. Numbering of additional references, figures, tables, and equations should follow sequentially from the original manuscript throughout the discussion. The discusser must indicate the month, year, volume number, issue number, authors' names, and manuscript number of the original manuscript. Closures responding to a single discussion should not exceed 1800-word equivalents in length, and to multiple discussions, approximately one half of the combined lengths of all discussions. Closures are published together with the discussions.

Discuss the paper, not some new or outside work on the same subject. Use references wherever possible instead of repeating available information.

Discussion offered for publication should offer some benefit to the general reader. Discussion which does not meet this requirement will be returned or referred to the author for private reply.

**Send manuscripts to:**
**http://mc.manuscriptcentral.com/aci**

**Send discussions to:**
**Journals.manuscripts@concrete.org**

ACI MATERIALS JOURNAL TECHNICAL PAPER

Title No. 123-M13

# Benchtop Tests to Predict Service Life of Concrete Exposed to Microbially Induced Concrete Corrosion

by Feyza Nur Sahan, Ali Riza Erbektas, W. Jason Weiss, and O. Burkan Isgor

*Service life modeling of microbially induced concrete corrosion (MICC) is essential for assessing structural durability, optimizing maintenance, and minimizing risks in wastewater environments. ASTM C1904-20 is a recently developed biogenic benchtop method for assessing MICC that is safe, accelerated, and practical compared to conventional laboratory tests. The objective of this study is to use the benchtop test to predict the service life of concrete exposed to MICC in sewer pipes. This correlation is based on Pomeroy's model, which relates the field $H_2S$ concentrations, wastewater flow conditions, pipe and flow geometry, and the properties of the concrete. A demonstration study is provided to show how the ASTM C1904 data could be used to predict the performance of different types of concrete and antimicrobial products in realistic exposure scenarios. The projected corrosion rates in field conditions reflected the delayed and reduced corrosion rates for mixtures with antimicrobial treatment.*

**Keywords:** biodeterioration; biogenic acidification; biogenic benchtop test; microbial attack; microbially induced corrosion of concrete (MICC); Pomeroy's model; service life model; sewer.

## INTRODUCTION

Concrete is a commonly used construction material for wastewater infrastructure.[1] These structures are subject to deterioration due to chemical, physical, mechanical, and biological mechanisms.[2] While approximately 10% of concrete deterioration in wastewater systems has been attributed to microbial effects,[3] microbial corrosion may reduce service life from an expected 75 to 100 years to as low as 10 years.[4,5] Microbially induced corrosion of concrete (MICC) is a multi-stage acid attack caused by bacteria activity within wastewater[6] with enormous financial, environmental, and social/health costs. The Environmental Protection Agency (EPA) estimates that $271 billion is required within the next 25 years for the United States to maintain the existing wastewater infrastructure.[7]

MICC consists of three fundamental stages.[6,8,9] Stage 1 involves abiotic acidification of the concrete surface to pH levels that would allow bacterial survival (9 to $10 < \text{pH} < 12.5$), which could be caused by the carbonation of the concrete surface[8,10] or calcium leaching from concrete when concrete is exposed to moisture.[11] Stages 2 and 3 require sulfate-reducing bacteria (SRB) such as *Desulfovibrio desulfuricans*[12,13] and sulfur-oxidizing bacteria (SOB) such as *Halothiobacillus neapolitanus*[14] that can metabolize various sulfur-containing organic and inorganic compounds and ions in wastewater.[15] SRB reduces the sulfate ions to sulfides to generate aqueous hydrogen sulfide ($H_2S$).[16] Aqueous $H_2S$ is released into the airspace above wastewater as a gas and condenses into the moisture layer on concrete surfaces. Stage 2 involves the attachment of SOB to form biofilms on the concrete surface, which reduces the pH further (4 to $6 < \text{pH} < 9$ to 10). The SOB produce biogenic sulfuric acid ($H_2SO_4$) through the oxidation of sulfur-containing substrates such as $H_2S$, thiosulfate, and elemental sulfur.[2,17] During this stage, colonization by neutrophilic SOB (NSOB) begins; these microorganisms oxidize $H_2S$ and other reduced sulfur compounds, leading to the formation of biogenic $H_2SO_4$. As the pH further decreases, acidophilic SOB (ASOB) becomes dominant, producing additional $H_2SO_4$, which plays a primary role in the biodeterioration of sewer infrastructure. Stage 3 involves severe sulfuric acid attack on concrete ($\text{pH} < 4$).[18,19] At this stage, ASOB dominates the microbial community, and concentrated $H_2SO_4$ generation is observed. The biogenic sulfuric acid produced by both NSOB and ASOB reacts with concrete, accelerating chemical degradation and structural deterioration.

Biogenic $H_2SO_4$ acid reacts with major hydration products of concrete, specifically calcium hydroxide ($Ca(OH)_2$) and calcium-silicate-hydrate (C-S-H) phases. These reactions lead to the formation of ettringite ($3CaO{\cdot}Al_2O_3{\cdot}3CaSO_4{\cdot}32H_2O$) and gypsum ($CaSO_4$). The reactions that result in gypsum and ettringite cause approximately 124% and 227% expansion in volume, respectively.[20] These expansive reactions, as shown here,[21,22] are key mechanisms driving concrete degradation[14,17,23]

$$H_2SO_4 + Ca(OH)_2 \rightarrow CaSO_4 + 2H_2O \tag{1}$$

$$H_2SO_4 + CaO{\cdot}SiO_2{\cdot}2H_2O \rightarrow CaSO_4 + H_2O + Si(OH)_2 \tag{2}$$

$$3CaSO_4 + 3CaO{\cdot}Al_2O_3{\cdot}6H_2O + 26H_2O \rightarrow 3CaO{\cdot}Al_2O_3{\cdot}3CaSO_4{\cdot}32H_2O \tag{3}$$

The test methods to evaluate the resistance of concrete to MICC can be categorized into three main groups: laboratory-based chemical acidification tests,[6,24] laboratory-based biogenic acidification tests,[6,18,25-27] and in-place field tests.[28-30] Laboratory-based chemical acidification tests are acid immersion tests, such as the ASTM C1898-20 test,[24] that are designed to be economical and practical. However,

---

*ACI Materials Journal*, V. 123, No. 2, March 2026.
MS No. M-2023-224.R2, doi: 10.14359/51749321, received August 25, 2025, and reviewed under Institute publication policies. Pertinent discussion including author's closure, if any, will be published ten months from this journal's date if the discussion is received within four months of the paper's print publication.

these methods do not take the bacterial activity into account and do not realistically simulate MICC conditions.[12,28,31-35] Laboratory-based biogenic acidification tests can be grouped under chamber and benchtop tests. In both approaches, the acidification of the exposure media is achieved by bacterial activity and intended to simulate all three stages of MICC. The chamber tests emulate field conditions in controlled breeding chambers, where $H_2S$ is produced by bacterial activity and acidification is caused by the conversion of $H_2S$ to sulfuric acid.[10,18,26,31,36] Besides the safety concerns associated with $H_2S$ use, these tests are cumbersome, time-intensive, and error-prone.[6] These concerns are mitigated by benchtop biogenic acidification tests, where biogenic acidification is achieved by SOB, which can convert elemental sulfur or thiosulfate to sulfuric acid without the use of $H_2S$.[23,27,37] Recently, a benchtop biogenic acidification test was standardized as ASTM C1904-20.[25] The last assessment approach involves in-place field tests, which usually entail placing concrete samples in sewers, monitoring sewer conditions, and assessing sewer conditions and their deterioration regularly over extended periods (months to years). Although field experiments provide more realistic exposure conditions, they are time-consuming, expensive, and impractical.

The development of the standardized benchtop biogenic acidification test, ASTM C1904-20,[25] provides significant opportunities to simplify MICC assessment, especially with respect to the evaluation of the effectiveness of mitigative actions, such as the use of antimicrobial products and proportioning concrete mixtures for increased acid resistance. However, so far, no research has been done on using the results of ASTM C1904-20 to make service life predictions for concrete exposed to real-life exposure conditions. The objective of this study is to develop a service life model for concrete exposed to MICC by using accelerated benchtop biogenic acidification testing. In this study, this test method will be correlated with the field conditions to predict the service life of real sewer systems. The developed approach is based on the hypothesis that Pomeroy's model (PM) for MICC can be used as an underlying theory that can link the "accelerated" biogenic test to the field conditions.

## RESEARCH SIGNIFICANCE

This study provides an approach to use the results of ASTM C1904-20 to make service life predictions for concrete exposed to real-life exposure conditions. The standardized benchtop biogenic acidification test (ASTM C1904-20) is correlated with the field conditions to predict the service life of real sewer systems. The developed approach is based on the hypothesis that PM for MICC can be used as an underlying theory that can link the "accelerated" biogenic test to the field conditions.

## BACKGROUND

### Pomeroy's model (PM)

Pomeroy[38-40] developed an empirical formula to predict sulfide generation and corrosion rates in sewer systems. This formula was developed using studies of the Los Angeles County wastewater collection system in the 1970s. The corrosion rate of concrete $cr_{PM}$ (mm/yr) exposed to $H_2S$ containing sewer environments as a thickness loss using[38,41,42]

$$cr_{PM} = 11.5k\text{Ø}_{sw}\frac{1}{A} \tag{4}$$

where 11.5 is the empirical factor; $k$ is a correction factor relative to the climate and depends on engineering judgment; $\text{Ø}_{sw}$ is the average flux of $H_2S$ to the surface of concrete ($g/m^2 \cdot h$); and $A$ is the alkalinity factor for the cementitious system.

Acid that forms on the concrete surface due to biogenic activities of SOB might not react completely with the cementitious products, and some of this acid might flow back to the sewer stream. The factor $k$ accounts for the amount of acid remaining on the concrete surface. A factor of $k = 1$ implies that all acid remains on the concrete surface; $k = 0$ is the extreme case when all acid returns to the sewer stream. For typical sewers under moderate climates, $k = 0.8$ has been reported to be a reasonable estimate, but $k$ could be as low as 0.3 in some systems.[38,43,44]

The parameter $A$ is a measure of alkalinity of the cementitious system[45]

$$A = 1.786\frac{c\,[\text{CaO}]_{cem} + a\,[\text{CaO}]_{agg}}{d} \tag{5}$$

where $c$ is the cement content (kg cement per $m^3$ of concrete); $[\text{CaO}]_{cem}$ is the CaO content of the cement (kg/kg of cement); $a$ is the aggregate content (kg aggregate per $m^3$ of concrete); $[\text{CaO}]_{agg}$ is the CaO content of the aggregate (kg/kg of aggregate); and $d$ is the density of concrete ($kg/m^3$). The constant factor 1.786 represents the ratio of molar masses of $CaCO_3$ (100 g/mol) and CaO (56 g/mol).

### Accelerated benchtop biogenic acidification test (ASTM C1904)

ASTM C1904-20 is an accelerated benchtop biogenic acidification test to assess the effects of antimicrobial additives and different cementitious materials during the biogenic acidification process. The standard provides three test methods: 1) Test Method A assesses the efficacy of antimicrobial admixtures in delaying or preventing biogenic acidification in a nutrient-rich simulated wastewater exposure solution; 2) Test Method B assesses the effectiveness of antimicrobial admixtures in a prescribed cementitious system (Option B1) or assesses the performance of different cementitious systems (Option B2) in delaying or preventing MICC in Stage 2 of MICC; and 3) Test Method C assesses the suitability of cementitious systems in delaying or preventing MICC in Stage 3 of MICC. In this paper, Option B of ASTM C1904-20 is used as the basis for developing the service life prediction model for concrete resisting MICC because it is designed for simulating Stage 2 of MICC, which typically corresponds to the operational conditions in sewers (4 to 6 < pH < 9 to 10). Option A is designed for antimicrobial effectiveness in simulated wastewater (not cementitious systems), and Option C is designed for the investigation of MICC under Stage 3 conditions (pH < 4), which lead to rapid deterioration and are not covered by the proposed service life model.

Test Method B uses active *Halothiobacillus neapolitanus* bacteria (ATCC 23641) to inoculate paste or mortar disk samples (diameter = 50.8 mm) that are 2.65 ± 0.15 mm thick. The selection of *H. neapolitanus* is based on its well-established sulfur-oxidizing metabolic pathway and its proven applicability in controlled laboratory investigations simulating MICC. *H. neapolitanus* is a biosafety level 1, aerobic NSOB, which can thrive within a pH range of 8.0 to 3.5, enabling Stage 2 simulation of MICC. Besides, it can use thiosulfate as nutrient source and produces $H_2SO_4$, the primary metabolic by-product. These characteristics make *H. neapolitanus* a safe, practical, and effective organism for evaluating acidification potential and material degradation mechanisms.

Two different cells are used during the test: one for the inoculated specimens exposed and acidified with bacteria, and one for the control specimens without any exposure to bacteria. The pH, calcium-ion concentrations, and sulfate-ion concentrations of the exposure solutions are monitored at regular time intervals for the duration of the test (typically less than 60 days). As per ASTM C1904 recommendations, the pH and free calcium-ion concentration of the exposure solution are monitored daily, whereas the sulfate-ion concentration is assessed every 3 days or more frequently, as needed. The nutrient exposure solution was refreshed upon the pH reaching a value of 4 to simulate Stage 2 of MICC; this procedure was repeated at least three cycles based on ASTM C1904 recommendations. At the end of the exposure period, the control and inoculated samples are tested for flexural strength using ball-on-three-balls (B3B) testing[46] to determine the strength loss and corresponding corrosion rate. Figure 1 illustrates the B3B setup and parameters. The B3B flexural strength, $\sigma_{max}$ (MPa), is calculated as[47]

$$\sigma_{max} = f\left(\frac{d}{R}, \frac{R_a}{R}, v\right)\frac{F}{d^2} \tag{6}$$

where $F$ (N) is the peak load; $d$ (mm) is the sample thickness measured after the test; $R$ (mm) is the radius of the disk sample; $R_a$ (mm) is the radius of the support; $v$ is Poisson's ratio; and the function of $f$ is a parameter based on $t/R$, $R_a/R$, and $v$[47]

$$f\left(\frac{d}{R}, \frac{R_a}{R}, v\right) = c_0 + \frac{c_1 + c_2\frac{d}{R} + c_3\left(\frac{d}{R}\right)^2 + c_4\left(\frac{d}{R}\right)^3}{1 + c_5\frac{d}{R}} \times \left(1 + c_6\frac{R_a}{R}\right) \tag{7}$$

The coefficients $c_0$ to $c_6$ are a set of constants based on Poisson's ratio, which can be found in the literature.[48]

The effective thickness loss, $d_{loss}$ (mm), can be calculated by assuming that the strength of the undeteriorated thickness of the sample does not change during MICC such that

$$\sigma_c = \sigma_a \tag{8}$$

$$f_c\frac{F_c}{d_c^2} = f_a\frac{F_a}{d_a^2} \tag{9}$$

$$d_a = d_c\sqrt{\frac{F_a}{F_c}\frac{f_a}{f_c}} \tag{10}$$

$$d_{loss} = d_c - d_a \tag{11}$$

where the indexes $c$ and $a$ indicate control and acid-exposed samples, respectively.

This thickness loss occurs on both sides of the samples; therefore, the corrosion rate per side is half $d_{loss}$, assuming both sides corrode at the same rate. Therefore, the corrosion rate from the ASTM C1904 $cr_{1904}$ test can be calculated from

$$cr_{1904} = \frac{d_{loss}}{2} \times \frac{365}{t} \tag{12}$$

where $t$ is the duration of the test in days.

## PROPOSED CORRELATION BETWEEN ASTM C1904 AND FIELD EXPOSURE

To use the results of the ASTM C1904 test for service life prediction purposes, a correlation needs to be established between the MICC of concrete exposed to a real sewer in the field and ASTM C1904 test results performed on the corresponding paste or mortar mixture. The developed approach in this study is based on the hypothesis that PM for MICC can be used as an underlying theory that can link the "accelerated" biogenic test to the field conditions. The role of each individual parameter affecting MICC is considered separately and discussed in the following sections.

### Alkalinity of cementitious system

The alkalinity of the cementitious system plays a crucial role in the corrosion rate such that high alkalinity provides more substances to react with biogenically generated sulfuric acid, thereby reducing the corrosion rate.[12,38,40] Although cement type, pozzolanic materials, and mixture designs are not directly related to the corrosion rate calculation in PM, the alkalinity of the mixture is a fundamental variable, as shown in Eq. (4). ASTM C1904 biogenic acidification testing is designed for cement paste or mortar samples; therefore, the two approaches need to be correlated. The alkalinity factor, $A$, typically decreases with the increasing aggregate content or decreasing paste content. For example, typical paste might have $A$ = 0.8 to 0.9, while concrete might have $A$ = 0.2 to 0.3. It should be noted that Eq. (4) considers the CaO content of cement and aggregates; however, this equation was originally developed for ordinary portland cement (OPC) systems. The incorporation of supplementary cementitious materials (SCMs) and fillers such as limestone would influence the alkalinity of the cementitious system in addition to the microstructure of the matrix. In addition, the aggregate type, particularly whether it is siliceous (for example, sand) or calcareous (for example, limestone), can affect the degradation mechanism, as certain aggregates may exhibit sacrificial behavior,[49,50] partially contributing to neutralization by undergoing dissolution themselves. Underlying assumptions in the use of the alkalinity factor for corrosion rate prediction include homogeneous distribution of the

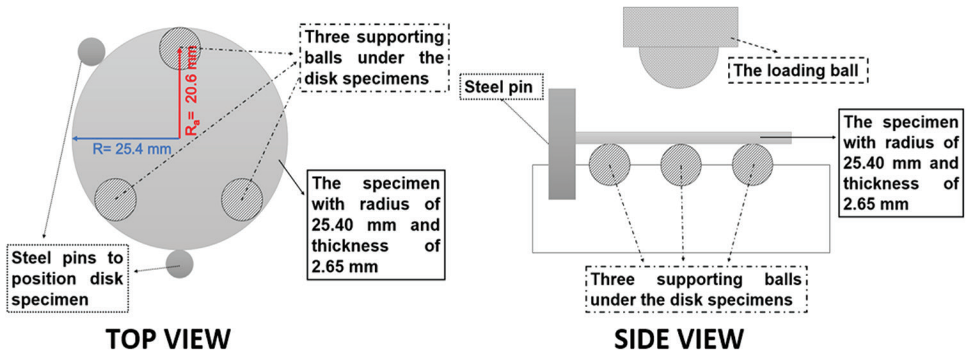

*Fig. 1—Ball-on-three-balls (B3B) test setup adapted from Zaw.*[46]

cement matrix, neutralization capacity of aggregates, and exclusion of change in the microstructure. Due to the inverse relation of alkalinity and corrosion rate, MICC would occur at a higher rate compared to cement paste or mortar. Therefore, when interpreting the corrosion rates obtained from the ASTM C1904 test, a correction factor needs to be employed to correlate the corrosion rate from the ASTM C1904 test to the field conditions. This correction factor can be assumed to be the ratio between the alkalinities of concrete (used in the field) and the paste or mortar (tested in ASTM C1904), and can be written as

$$C_A = \frac{A_{sw}}{A_{1904}} \qquad (13)$$

where $A_{sw}$ is the alkalinity of the concrete used in the field; and $A_{1904}$ is the alkalinity of the paste or mortar sample used in the ASTM C1904 test.

## $H_2S$ concentration

In a real sewer environment, the MICC is mainly caused by the biogenic acidification of $H_2S$ by SOB.[51-53] In the ASTM C1904 test, the biogenic acidification is caused by SOB converting other forms of sulfur sources (for example, thiosulfate, $S_2O_3^{2-}$). Therefore, to correlate the two exposure environments, the two exposure conditions need to be represented in the same unit of exposure. Because PM is based on $H_2S$ exposure, in this work, the correlation between the two environments is done using the measured (or assumed) $H_2S$ exposure in the field and the equivalent $H_2S$ content in the ASTM C1904 test. Ignoring other factors would affect the kinetics of conversion of sulfur species to sulfuric acid by different types of SOB; it is assumed that one unit of thiosulfate ($S_2O_3^{2-}$) produces the same effect as two units of $H_2S$, based on the sulfur content of these species (based on the number of sulfur atoms per mole). With this assumption, the equivalent $H_2S$ concentration in the ASTM C1904 test, $Ø_{1904}$ ($g/m^2{\cdot}h$), can be calculated using

$$Ø_{1904} = \frac{1}{2}\frac{W_{H_2S}}{S_A t} \qquad (14)$$

where $S_A$ ($m^2$) is the exposed surface area of each ASTM C1904 sample; $t$ is the test duration; and $W_{H_2S}$ (g) is the equivalent mass of $H_2S$ in the nutrient medium solution of the ASTM C1904 test

$$W_{H_2S} = C_{H_2S} V_{solution} \qquad (15)$$

where $C_{H2S}$ (g/L) is the equivalent concentration of $H_2S$ in the ASTM C1904 test cell; and $V_{solution}$ (L) is the volume of the solution in the ASTM C1904 test cell.

The thiosulfate concentration in the ASTM C1904 test is typically approximately 0.06 M; therefore, the equivalent $H_2S$ exposure would correspond to 0.12 M, which corresponds to 0.284 $g/m^2{\cdot}h$ per sample tested in ASTM C1904, assuming that test cell volume, $V_{solution}$, is 0.4 L and test duration, $t$, is 42 days. This equivalent $H_2S$ content might be significantly higher than the typical exposure conditions found in sewer environments ($Ø_{sw}$),[1,28] which is the main reason the ASTM C1904 test provides accelerated conditions for MICC. The correlation factor can be written as

$$C_Ø = \frac{Ø_{sw}}{Ø_{1904}} \qquad (16)$$

## *k*-factor

The *k*-factor accounts for how much of the acid that forms on the concrete surface remains on the concrete surface. A factor of $k = 1$ implies that all acid remains on the concrete surface, and $k = 0$ is the extreme case when all acid returns to the sewer stream. In ASTM C1904 testing, specimens are completely immersed in the biogenic acidified exposure solution. As specimens are exposed to the acid during the testing, it can be assumed that the *k*-factor is high in the ASTM C1904 test (~1) at all times, which represents accelerated conditions compared to field exposure, where *k* values would typically be less than 1 and as low as 0.3.[38-40] Therefore, a correlation factor, $C_k$, could be introduced between the field and ASTM C1904 conditions such that

$$C_k = \frac{k_{sw}}{k_{1904}} \qquad (17)$$

where $k_{sw}$ is the *k*-factor of the concrete used in the field; and $k_{1904}$ is the *k*-factor of the paste or mortar sample used in the ASTM C1904 test.

## Sewer flow conditions

The Pomeroy equation, Eq. (4), was initially developed without considering the following: 1) corrosion in a typical sewer occurs at a higher rate at the crown than other concrete surfaces; and 2) the increased turbulence of the sewer flow

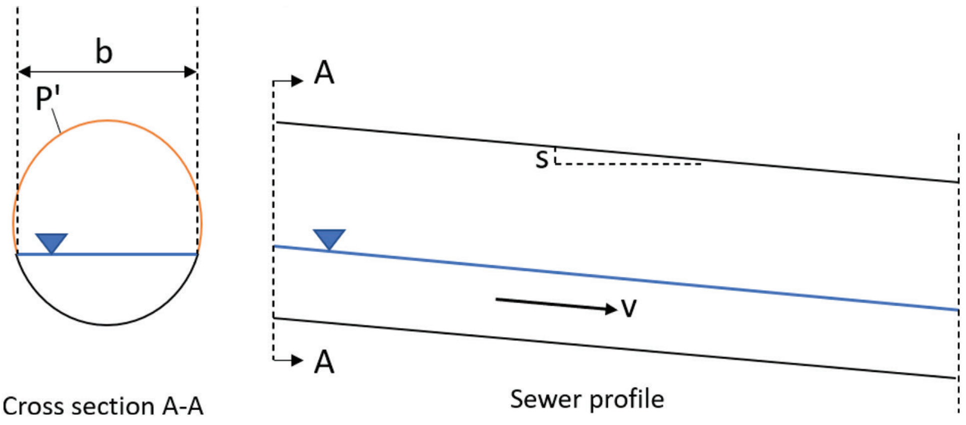

*Fig. 2—Typical sewer profile and cross section defining variables in Eq. (19).*

increases the corrosion rate. For example, in a typical sewer, the corrosion rate might be 1.5 to 2.0 times higher in the crown than in other parts of the sewer surface.[54,55] The turbulence of the flow can increase the corrosion rate up to 2.5 for typical turbulent flow and as much as 10 times for high turbulent flow.[54,55] To account for these effects, two additional factors were introduced to PM such that[55]

$$cr_{sw} = 11.5k\O_{sw}\frac{1}{A}(\mathrm{CCF})(\mathrm{TCF}) \tag{18}$$

where $cr_{sw}$ (mm/yr) is the corrosion rate in the field; CCF is the crown corrosion factor; and TCF is the turbulence corrosion factor. The values of CCF and TCF depend on the flow stream conditions in the sewer; additional guidance on these factors is provided in the EPA report.[40] Because the ASTM C1904 test is performed in stagnant fluid immersion, these factors are not included in corrosion rate calculations.

In Eq. (18), the average flux of $H_2S$ (expressed as sulfide) at the air-wall interface, in g/m$^2$·h, can be simplified for typical sewer conditions without high turbulence or high velocity by[44]

$$\O_{sw} = 0.7(sv)^{0.375}J[DS]C_T\frac{b}{P'} \tag{19}$$

where $s$ is the slope of the sewer (m/m); $v$ is the stream velocity (m/s); $J$ is the pH-dependent factor for proportion of $H_2S$; $DS$ is dissolved sulfide concentration (mg/L); $C_T$ is the temperature factor; $b$ is surface width of the stream (m); and $P'$ is exposed perimeter (m). The $J$-factor is a variable depending on the pH of the sewer solution and can be found in the literature.[38] The properties of the sewer geometry and flow conditions are shown in Fig. 2.

PM considers the temperature coefficient ($C_T$) as equal to unity at 20°C. However, the temperature in the field conditions is a variable that influences the release of $H_2S_{(aq)}$ to the gas phase. Figure 3 illustrates equilibrium concentrations of gaseous $H_2S$ (ppm) in a closed system as a function of temperature and $H_2S$ concentration in solution. An increase in temperature increases the $H_2S_{(g)}$ concentration, and this might affect the corrosion rate significantly for higher $H_2S$. Hence, the temperature coefficient ($C_T$) is computed by following for a known $H_2S$ concentration

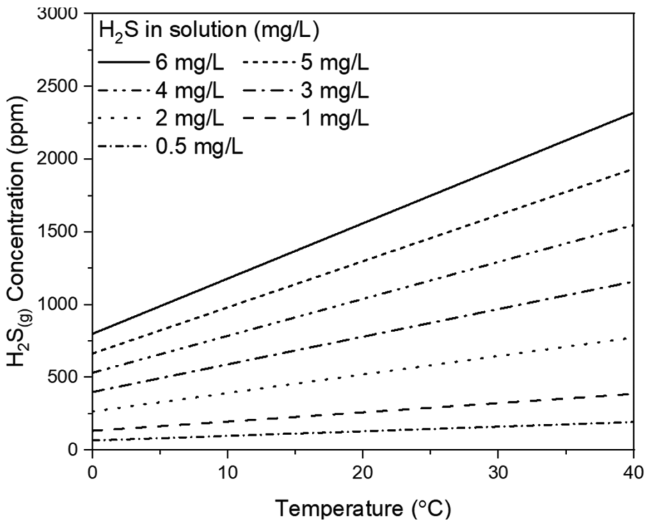

*Fig. 3—Concentrations of gaseous $H_2S$ in closed system as function of temperature and $H_2S$ concentration in solution.[19,44]*

$$C_T = \frac{(H_2S_{(g)})_T}{(H_2S_{(g)})_{20°C}} \tag{20}$$

## Role of antimicrobial product leaching during ASTM C1904 testing

Antimicrobial treatment is one of the common methods to prevent or delay MICC, and ASTM C1904 (Option B) is developed to evaluate the efficiency of different mixtures and antimicrobial products. It has been observed in some ASTM C1904 tests that the antimicrobial admixture might leach out of the paste or mortar sample into the exposure solution and delay its acidification because the increased antimicrobial content in the solution reduces the bacterial activity. Figure 4(a) illustrates such a test where the pH of the solution remains high for the first 30 to 40 days of the testing period. As shown, the delay of pH reduction is longer for the samples with higher antimicrobial dosage. This leaching effect is an artifact of the test setup because the samples are immersed in the exposure solution (unlike the field conditions) and the volume of the exposure solution is rather small (~0.4 L), which exacerbates the effect of the antimicrobial admixture leaching. Therefore, when correlating the corrosion rate obtained from the ASTM C1904 test to the

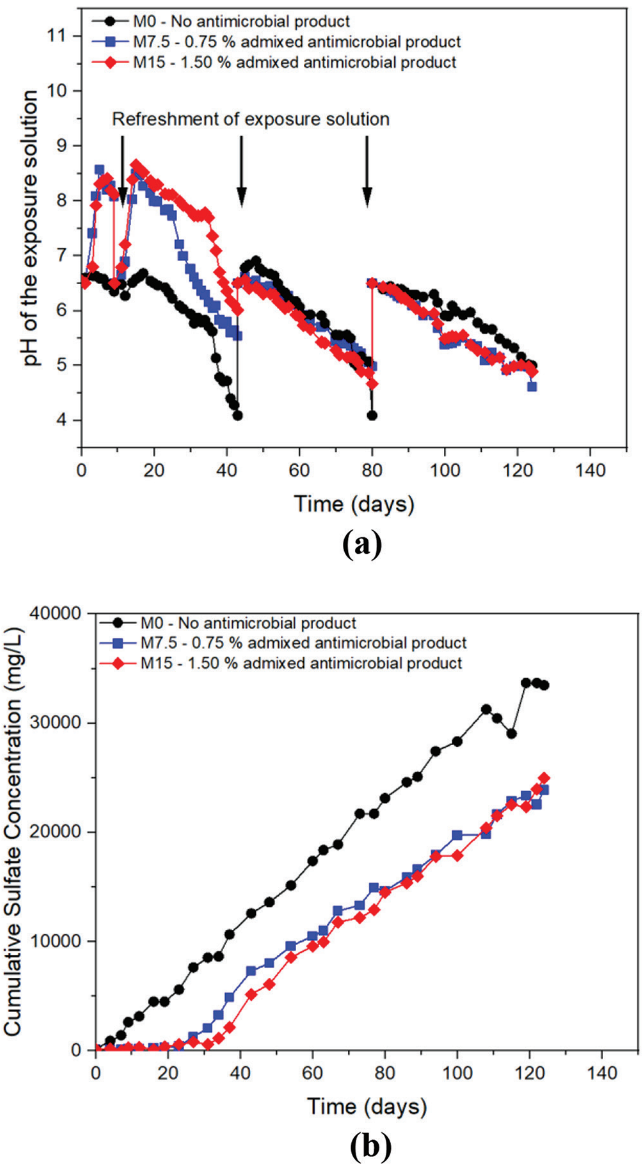

Fig. 4—*Example ASTM C1904 data demonstrating: (a) pH; and (b) sulfate concentration change in exposure solution.*

corrosion rate under the field conditions, the delay in deterioration needs to be considered.

Because this delay is time-dependent, a time-dependent factor is needed. It can be seen in Fig. 4(b) that the cumulative sulfate measurements, which are required to be reported in ASTM C1904 testing, provide a time-dependent quantification. During the leaching period (30 to 40 days from the start of the testing), the sulfate concentration in the exposure solution remains low, which indicates that paste or mortar samples in the cell are not deteriorating and corrosion rates are low. Therefore, collected sulfate measurements in the exposure solution will be used to describe a delay factor by using the rate of the sulfate formation.

The time-dependent delay factor, $C_d(t)$, can be written as

$$C_d(t) = \left\{ \begin{array}{ll} \frac{s_1}{s_2} & \text{time} < t_d \\ \frac{s_2}{s_2} = 1 & \text{time} > t_d \end{array} \right\} \quad (21)$$

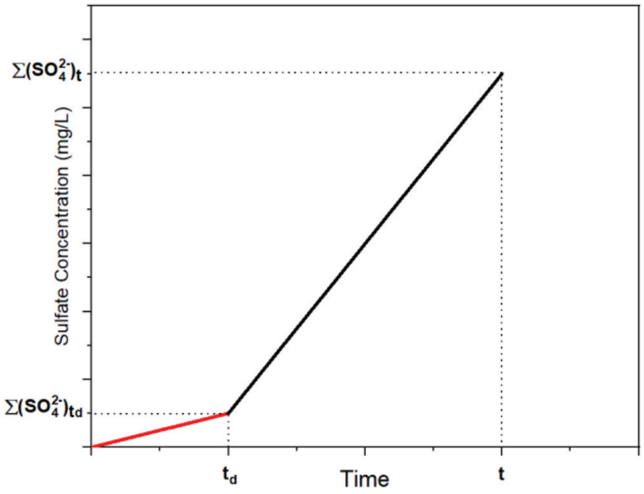

Fig. 5—*Representation of cumulative sulfate concentration versus time with delayed effect of antimicrobial additive.*

where $s_1$ and $s_2$ are the slopes in the cumulative sulfate measurements, as shown in Fig. 5; $t_d$ (days) is the delay time; $t$ (days) is the duration of the ASTM C1904 test; and $T_d$ (days) is the expected delay time in the field, which are related with one another as follows

$$\frac{t}{T} = \frac{C_k \times C_\varnothing}{C_A} \quad (22)$$

$$\frac{t_d}{t} = \frac{T_d}{T} \quad (23)$$

The slope $s_1$ represents the slope during the delay, and $s_2$ illustrates the slope during the steady state and can be written in terms of cumulative sulfate concentrations as follows

$$s_1 = \frac{\sum[SO_4^{2-}]_{t_d} - \sum[SO_4^{2-}]_0}{t - t_0} \quad (24)$$

$$s_2 = \frac{\sum[SO_4^{2-}]_t - \sum[SO_4^{2-}]_{t_d}}{t - t_d} \quad (25)$$

## Summary: corrosion rate correlation

As the environmental and laboratory conditions are examined and correlated with several factors in this study, the corrosion rate obtained from the ASTM C1904 testing can be converted to field conditions as follows

$$cr_{sw}(t) = cr_{1904} \frac{C_k C_\varnothing}{C_A} C_d(t) \quad (26)$$

Here, $cr_{1904}$ is calculated using the total test duration from Eq. (14). A more accurate calculation for $cr_{1904}$ can be made if the variable $t$ in Eq. (14) is replaced with the duration of the test after the antimicrobial leaching delay. This delay period ($t_d$) can be obtained from cumulative sulfate measurements in ASTM C1904 testing.

## DEMONSTRATION STUDY

### Application of PM to ASTM C1904 and biogenic chamber tests

As PM is used to relate ASTM C1904 to field conditions, it is useful to show that PM can predict corrosion rates of these two cases with reasonable accuracy. Unfortunately, there are not many field test data available with adequate controls and sufficient details for their proper use in PM; therefore, in this study, biogenic chamber tests from the literature are used. These tests are intended to simulate field conditions, and they use $H_2S$ gas and SOB to induce MICC; therefore, they could be used to generate data as surrogate validation data. Even though biogenic chamber tests involve a high degree of variability, they are the closest version of laboratory tests that can simulate field conditions.

Selected specimens from four sets of biogenic chamber test data were used by considering the use of antimicrobial products, the alkalinity factor, and $H_2S$ concentration. Because these tests involve a significant amount of detail, only basic background is provided here, and the readers are referred to cited references for additional information. The first study was conducted by House[18] and involved testing of 12 different concrete mixtures at an average $H_2S$ concentration of ~100 ppm for up to 360 days. The second study was conducted by Ding[26] and involved the testing of 13 different concrete mixtures at an average $H_2S$ concentration of ~150 ppm for up to 360 days. The third study was conducted by De Belie et al.[12] and involved the testing of eight different concrete mixtures at an average $H_2S$ concentration of ~250 ppm for up to four cycles of 17 days. The fourth study was performed by Gutiérrez-Padilla et al.[56] and involved testing of 13 different concrete mixtures at an $H_2S$ concentration of ~300 to 600 ppm for up to 215 days.

**Table 1—Mixture proportions of paste specimens tested with ASTM 1904 testing**

| Mixture ID | P0 | P15 | P15C | P15T |
|---|---|---|---|---|
| Admixed antimicrobial, % of cement | 0.00 | 1.50 | 1.50 | 1.50 |
| Colloidal silica, % of cement | 0.00 | 0.00 | 9.10 | 0.00 |
| Topical antimicrobial | No | No | No | Yes |
| Water-cement ratio (*w*/*c*) | 0.42 | 0.42 | 0.42 | 0.42 |
| Cement, kg/m$^3$ | 1356 | 1356 | 1356 | 1356 |
| Water, kg/m$^3$ | 569 | 569 | 569 | 569 |
| Aggregates, kg/m$^3$ | — | — | — | — |
| $[CaO]_{cem}$, kg/kg | 0.62 | 0.62 | 0.62 | 0.62 |
| $[CaO]_{agg}$, kg/kg | — | — | — | — |
| Density, kg/m$^3$ | 1926 | 1926 | 1926 | 1926 |
| Alkalinity *A* | 0.78 | 0.78 | 0.78 | 0.78 |

In addition to the chamber test, the ability of PM to predict the ASTM C1904 corrosion rates was also investigated. As stated before, PM is based on $H_2S$ exposure; therefore, to predict corrosion rates from the ASTM C1904 test, thiosulfate content should be converted to an equivalent $H_2S$ content. Although other factors would affect the kinetics of conversion of sulfur species to sulfuric acid by different types of SOB, it is assumed that one unit of thiosulfate ($S_2O_3^{2-}$) produces the same effect as two units of $H_2S$, based on the sulfur content of these species. This assumption is tested in this investigation by using PM to predict the corrosion rates of samples tested in ASTM C1904 testing. For the comparison of ASTM C1904 testing and PM, two different mixtures were chosen. Because PM is only applicable to the conditions without any antimicrobial treatment, the cement paste mixture (P0) in Table 1 and the mortar mixture (M0) in Table 2 without any antimicrobial treatment were considered for the comparison of experimental and computational results.

### Relating ASTM C1904 test results to field conditions

This investigation demonstrates the process of relating ASTM C1904 test results to a hypothetical field exposure site. One set of paste and one set of mortar samples were tested following ASTM C1904-20. The mixture details of the paste and mortar samples are provided in Tables 1 and 2, respectively.

In the paste mixtures shown in Table 1, P0 is the control mixture without any antimicrobial treatment, while P15, P15C, and P15T contain an admixed antimicrobial additive with a dosage of 1.5% of cement weight. Additionally,

**Table 2—Mixture proportions of mortar specimens tested with ASTM 1904 testing**

| Mixture ID | M0 | MT | M7.5 | M7.5T | M15 | M15T |
|---|---|---|---|---|---|---|
| Admixed antimicrobial, % of cement | 0.00 | 0.00 | 0.75 | 0.75 | 1.50 | 1.50 |
| Colloidal silica, % of cement | 0.00 | 0.00 | 1.50 | 1.50 | 3.00 | 3.00 |
| Topical antimicrobial | No | Yes | No | Yes | No | Yes |
| *w*/*c* | 0.42 | 0.42 | 0.42 | 0.42 | 0.42 | 0.42 |
| Cement, kg/m$^3$ | 720 | 720 | 720 | 720 | 720 | 720 |
| Water, kg/m$^3$ | 302 | 302 | 302 | 302 | 302 | 302 |
| Aggregates, kg/m$^3$ | 1400 | 1400 | 1400 | 1400 | 1400 | 1400 |
| $[CaO]_{cem}$, kg/kg | 0.67 | 0.67 | 0.67 | 0.67 | 0.67 | 0.67 |
| $[CaO]_{agg}$, kg/kg | 0.10 | 0.10 | 0.10 | 0.10 | 0.10 | 0.10 |
| Density, kg/m$^3$ | 2120 | 2120 | 2120 | 2120 | 2120 | 2120 |
| Alkalinity *A* | 0.52 | 0.52 | 0.52 | 0.52 | 0.52 | 0.52 |

### Table 3—Mixture proportions of concrete used for sewer pipe in field

| Mixture ID | S0 |
|---|---|
| *w*/*c* | 0.40 |
| Cement, kg/m$^3$ | 360.00 |
| Water, kg/m$^3$ | 144.00 |
| Aggregates 1, kg/m$^3$ | 700.00 |
| Aggregates 2, kg/m$^3$ | 1380.00 |
| $[CaO]_{cem}$, kg/kg | 0.60 |
| $[CaO]_{agg1}$, kg/kg | 0.05 |
| $[CaO]_{agg2}$, kg/kg | 0.00 |
| Density, kg/m$^3$ | 2440 |
| Alkalinity *A* | 0.18 |

the P15C mixture contains a liquid cement matrix densifying additive containing colloidal silica, and antimicrobial topical treatment was applied for P15T specimens by using a water-repellent sealer containing silane, siloxane, and silane quaternary ammonium chloride with a dosage of approximately 13.4 mL/m$^2$, as per the manufacturer's instructions.

In the mortar mixtures shown in Table 2, M0 is the control mixture without any antimicrobial treatment, while M7.5 and M7.5T contain an admixed antimicrobial with a dosage of 0.75% of cement weight as well as a liquid cement matrix densifying additive containing colloidal silica at a dosage of 1.5% of cement weight. Mixtures M15 and M15T have the same admixed antimicrobial with a dosage of 1.5% of cement weight and a liquid cement matrix densifying additive containing colloidal silica at a dosage of 3.0% of cement weight. Additionally, MT, M7.5T, and M15T mixtures are topically treated with another antimicrobial product with a dosage of 203.7 mL/m$^2$, as per the manufacturer's instructions.

The hypothetical mixture design of the concrete in the field where the service life predictions are made for the samples described in Tables 1 and 2 is summarized in Table 3. The ASTM C1904 data were used to predict the performance of concrete in the sewer, and the mixture details are given in Table 3. The mixture S0 represents the concrete used for the sewer pipe in the field. This mixture design aligns with commonly used mixtures in practice; siliceous aggregates were considered to eliminate the neutralization effect of aggregates. The alkalinity factor is computed by considering this mixture. Then, the effect of alkalinity is considered by using the correlation factor between alkalinity of concrete in the sewer pipe in Table 3 and alkalinity of cement paste and mortar from the ASTM C1904 test in Tables 1 and 2, respectively.

Field conditions for the demonstration example, as determined using ASTM C1904 testing, are given in Table 4. The sewer characteristics, which influence the average flux of $H_2S$ ($Ø_{sw}$) and the corrosion rate in the sewer ($cr_{sw}$), were used for the calculations in the proposed service life modeling. Several sewer characteristics are used from the real field measurements in the literature. The pH of the wastewater is assumed to change during a year, following the annual data used by Aleksić et al.[57] As pH is time-dependent, the pH-dependent factor (*J*) in PM also becomes a time-dependent variable. In the modeling, the annual sulfide amount in the wastewater is taken from Pomeroy.[38] The elevation of the water level varying during a year is obtained by using the flow rate[58] in the sewer pipe. Hence, the surface width of the stream (*b*) and exposed perimeter ($P'$) is computed based on the water elevation, which plays a crucial role in the average flux of $H_2S$. The effect of the temperature on corrosion rate is considered by using the seasonal temperature data from the study of Wells and Melchers.[59] By using the mixture proportions of concrete in the field in Table 3 and the sewer characteristics in Table 4, the information required for the correlation factors is obtained.

### Table 4—Hypothetical sewer characteristics in field

| Characteristics | Value | Reference |
|---|---|---|
| Turbulence corrosion factor (TCF) | 1 | — |
| Crown corrosion factor (CCF) | 2 | — |
| Acid reaction factor (*k*) | 0.95 | — |
| pH of liquid | * | (Fig. A1)[57] |
| Dissolved sulfide concentration (DS), mg/L | * | (Fig. A2)[38] |
| Flow rate, m | * | (Fig. A3)[58] |
| Temperature (*T*), °C | * | (Fig. A4)[59] |
| Stream velocity (*v*), m/s | 1.07 | — |
| Slope of sewer (*s*), % | 0.10 | — |
| Alkalinity factor (*A*) | 0.18 | — |

*These characteristics are not constant; these values are time-dependent and vary over a year.

## RESULTS AND DISCUSSION

### Application of PM to ASTM C1904 and biogenic chamber tests

Figure 6 illustrates corrosion rates calculated by using PM for both the biogenic chamber tests (used as a surrogate for field exposure) and ASTM C1904 versus the corrosion rates measured experimentally. As can be seen from Fig. 6, PM predicts both cases well, mostly within the 25% error lines. The difference in corrosion rate predictions may be attributed to several factors, including variability in testing conditions such as chamber design and environmental conditions, the transport properties of the cementitious system, which are not accounted for in PM, and the specific characteristics of the aggregates.[49,50,60] De Belie et al.[12] proposed a degradation prediction method based on alkalinity and water absorption, with water absorption used as a measure of concrete porosity. Because porosity directly influences the microstructure, it governs the transport of aggressive agents such as sulfates and microorganisms, thereby influencing the rate of degradation. Although laboratory testing conditions may show variability in experimental corrosion rate, the experimental and computational corrosion rates by using PM were comparable, despite many varying parameters such as $H_2S$, chamber design, and mixture design. Therefore, it is reasonable to assume that PM can be used to relate ASTM C1904 testing to field conditions.

## Relating ASTM C1904 test results to field conditions

*ASTM C1904 results*—Figures 7 and 8 present the pH, calcium-ion content, and sulfate-ion content in the exposure during the ASTM C1904 testing of the paste and mortar specimens, respectively. Table 5 provides the corrosion rates, as reported by ASTM C1904 for the paste and mortar specimens. The corrosion rate for the P0 cement paste mixture without antimicrobial treatment was 4.63 mm/yr, while mortar mixture M0 without antimicrobial treatment had a corrosion rate of 1.65 mm/yr. The difference in corrosion rates may be attributed to the change in matrix type (paste versus mortar), differences in alkalinity, and microstructural variations. Kiliswa et al.[61] studied the corrosion rates of OPC- and calcium-aluminate cement (CAC)-based concrete at the Virginia experimental sewer. OPC-based concrete mixtures showed increasing biogenic corrosion rates with higher cement content (1.12 mm/yr at 16% and 1.57 mm/yr at 23%), whereas CAC-based mixtures showed the opposite trend, with corrosion rates decreasing to 0.60 mm/yr at 16% and 0.35 mm/yr at 23% CAC. The study highlighted the effect of mixture design, such as cement content and type, on corrosion rates. The corrosion rate of the M0 mixture (1.65 mm/yr) with 29% cement content was comparable to the corrosion rate of the OPC mixture (1.57 mm/yr) with 23% cement content as reported by Kiliswa et al.[61] As can

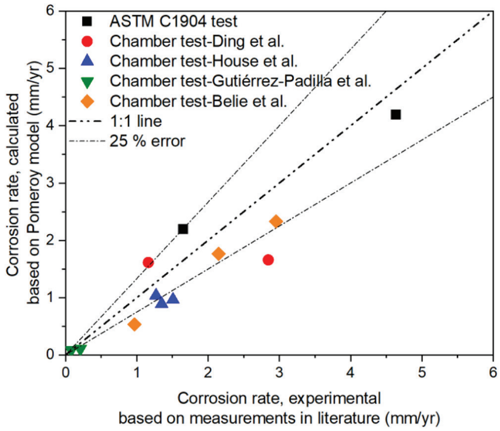

*Fig. 6—Corrosion rates calculated by using PM versus corrosion rates measured from biological chamber and ASTM C1904 testing.*

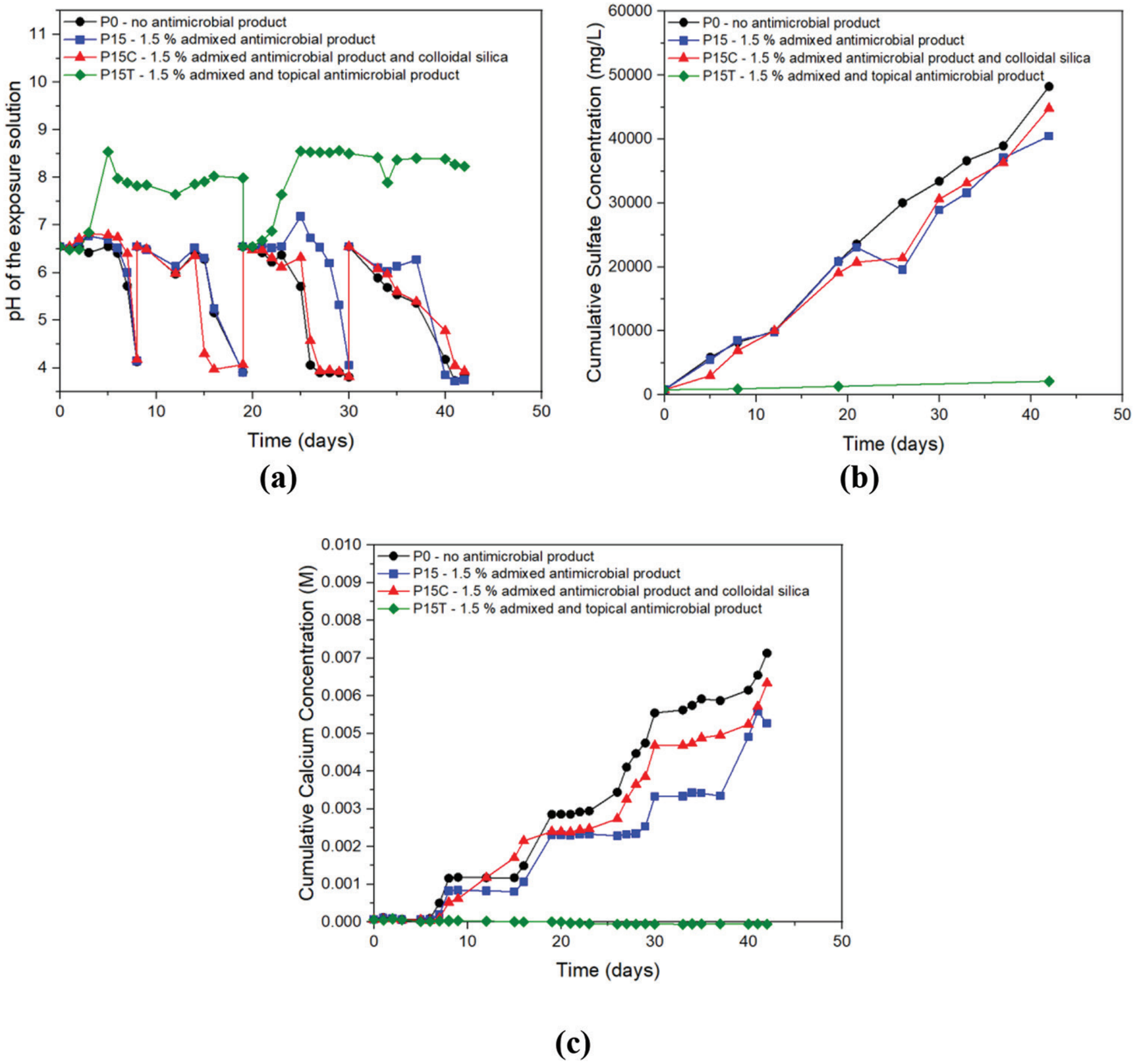

(a)

(b)

(c)

*Fig. 7—Measurements of exposure solution during ASTM C1904 testing of cement paste specimens for: (a) pH; (b) cumulative calcium-ion content; and (c) cumulative sulfate-ion content.*

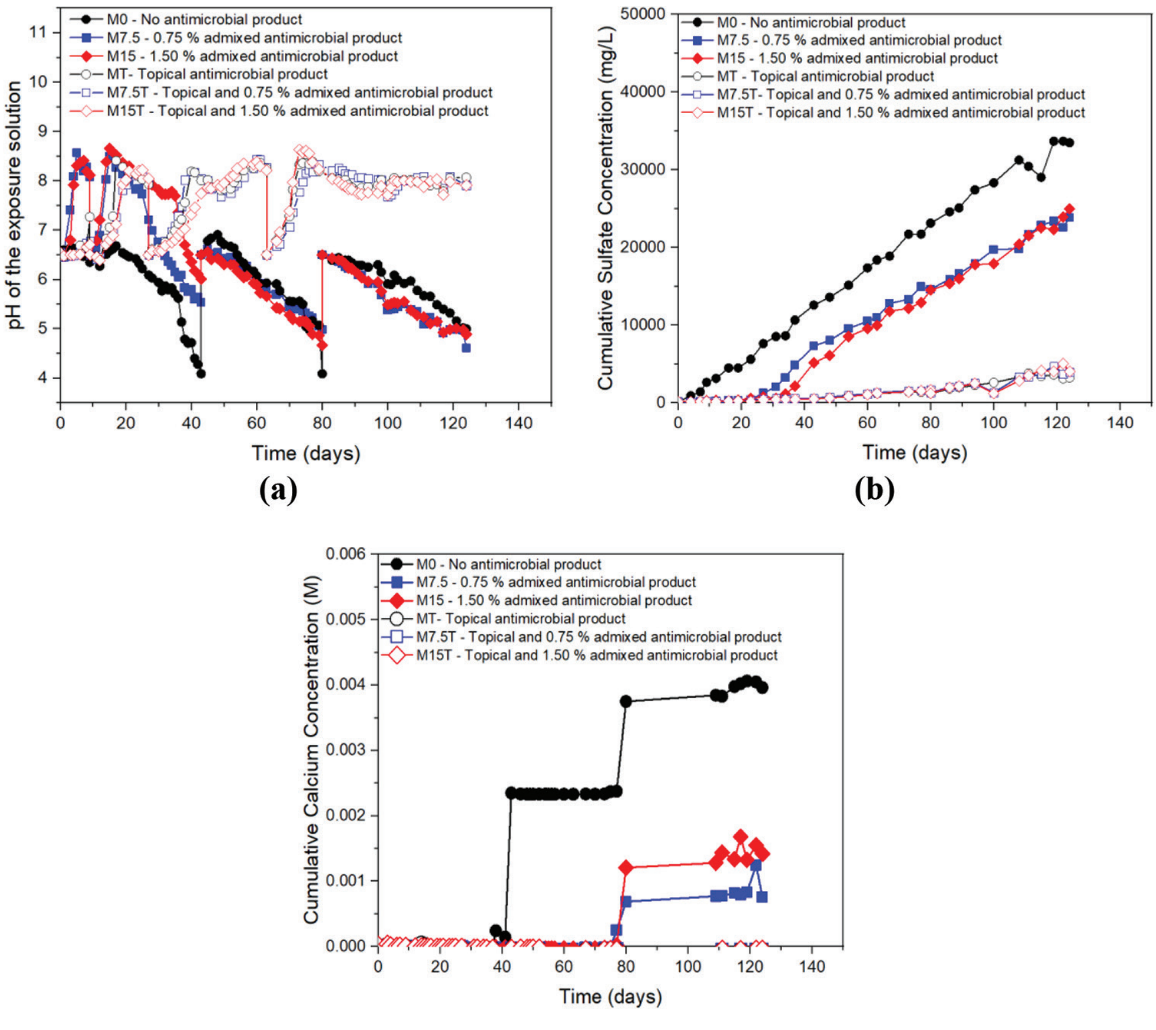

(a)

(b)

(c)

*Fig. 8—Measurements of exposure solution during ASTM C1904 testing of mortar specimens for: (a) pH; (b) cumulative calcium-ion content; and (c) cumulative sulfate-ion content.*

**Table 5—Experimental corrosion rates for cement paste and mortar mixtures**

| Mixture ID | P0 | P15 | P15C | P15T | M0 | MT | M7.5 | M7.5T | M15 | M15T |
|---|---|---|---|---|---|---|---|---|---|---|
| $d_{loss}$, mm | 1.07 | 0.90 | 0.54 | –0.02 | 1.12 | –0.03 | 0.24 | 0.08 | 0.36 | –0.15 |
| Strength reduction, % | 63.27 | 56.28 | 37.27 | N/A | 57.87 | –2.10 | 16.16 | 5.34 | 24.02 | –11.02 |
| Corrosion rate ($cr_{1904}$), mm/yr | 4.63 | 3.93 | 2.34 | 0.05 | 1.65 | 0.00 | 0.35 | 0.12 | 0.53 | 0.00 |

Note: N/A is not available.

be seen in Fig. 7(a), P15T showed the best performance against biogenic attack, as the pH remained above 7 and had low cumulative sulfate- and calcium-ion concentrations, as seen in Fig. 7(b) and (c), respectively. The other three mixtures (P0, P15, and P15C) followed similar trends for pH and cumulative sulfate- and calcium-ion concentrations. However, slight decreases were observed in cumulative sulfate- and calcium-ion concentrations for P15 and P15C mixtures compared to P0.

Figure 8 shows the pH of exposure solution, cumulative sulfate concentration, and cumulative calcium concentration of mortar specimens exposed to the biogenic attack during ASTM C1904 testing. A rapid and early decline in pH indicates increased susceptibility to MICC. The M0 mixture without antimicrobial product was most susceptible, while mixtures with admixed antimicrobial (M7.5 and M15) showed delayed pH decrease. Consistent with the pH trend, the M0 mixture displayed the greatest concentrations of both sulfate and calcium, indicators of degradation. The high pH in Fig. 8(a) and low ion concentration in Fig. 8(b) and (c) can be interpreted as the mixtures with topical treatment (MT, M7.5T, and M15T) show better resistance. Figure 8 and Table 5 show that the corrosion rates of the M7.5 and M15 mixtures were lower than that of M0 due to some resistance with initial pH increase, delayed and decreased sulfate concentration, and lower calcium concentration.

*Projected corrosion rates in field*—Following the methodology explained, the correlation factors were calculated

**Table 6—Correlation factors relating ASTM C1904 to field data**

| | P0 | P15 | P15C | P15T | M0 | MT | M7.5 | M7.5T | M15 | M15T |
|---|---|---|---|---|---|---|---|---|---|---|
| $C_k$ | 0.95 | 0.95 | 0.95 | 0.95 | 0.95 | 0.95 | 0.95 | 0.95 | 0.95 | 0.95 |
| $C_A$ | 0.231 | 0.231 | 0.231 | 0.231 | 0.343 | 0.343 | 0.343 | 0.343 | 0.343 | 0.343 |
| $C_\phi$ | * | * | * | * | * | * | * | * | * | * |
| $C_d(t)$ | 1.0 | † | † | † | 1.0 | ‡ | ‡ | ‡ | ‡ | ‡ |

*This factor is calculated using Eq. (16) data using field data presented in Table 4.

†This factor is calculated using Eq. (21) using data presented in Fig. 7(b).

‡This factor is calculated using Eq. (21) using data presented in Fig. 8(b).

for all samples investigated in this study. Table 6 provides the correlation factors for $C_k$, $C_\phi$, $C_A$, and $C_d(t)$ for the paste and mortar specimens to link to the concrete mixture and field conditions described in Tables 3 and 4, respectively. It should be noted that the realistic, variable field conditions, such as the pH of the solution, temperature, and the wastewater depth, presented in Table 4 influence the correlation factor for $H_2S$ concentration ($C_\phi$). The correlation factor for $H_2S$ concentration is computed for a year.

Using these correlation factors, corrosion rates in the defined hypothetical field exposure were calculated using Eq. (26). Table 5 provides information about the average corrosion rate calculated with constant parameters. However, the parameters, such as a decrease in pH during the attack and the impact of the antimicrobial treatment, could modify the corrosion rate. Figure 9 shows the experimental corrosion rate and corrosion depth obtained for cement paste mixtures described in Table 1 from ASTM C1904 testing, and the projected corrosion rate and corrosion depth for the concrete described in Table 3 by using the corresponding cement paste mixtures from the ASTM C1904 testing. Figure 7 shows that there was no delayed effect of the antimicrobials for the cement paste mixtures by observing pH, sulfate, and calcium measurements. Figure 9(a) shows the corrosion rates (mm/yr) for the cement paste mixtures obtained from ASTM C1904 testing. As shown in Fig. 9(a), the P0 mixture, without any antimicrobial treatment, exhibited the highest corrosion rate. In contrast, the P15T mixture exhibited complete resistance, while the admixed antimicrobial mixtures (P15 and P15C) demonstrated improved resistance, with significantly lower corrosion rates than P0. When the ASTM C1904 testing results were correlated to field conditions, the resistance of the antimicrobial mixtures was reflected in field conditions. The projected corrosion rates are shown in Fig. 9(b), where the corrosion rate is represented for a year based on the annual hypothetical field conditions given in Table 4. These rates are repeated by assuming the same conditions for subsequent years. For given hypothetical conditions, the highest corrosion rates are seen in spring. The increase in the temperature encourages bacterial activity and increases the $H_2S_{(g)}$ concentration in the sewer, as seen in Fig. 3. Despite the higher dissolved sulfide content and the temperature (refer to Fig. A2 and A4 in the Appendix*) in the summer, the effect of the low wastewater depth and high pH observed in the summer (refer to Fig. A1 and A3) decreases the corrosion rates significantly by influencing the average flux of $H_2S$ ($Ø_{sw}$).

For the given field conditions, the combined effect of the sewer geometry and environmental conditions resulted in the highest corrosion rate in the spring. While sewer geometry and environmental conditions influence corrosion rates under field conditions throughout the year, as considered in this study, the corrosion rate may also vary depending on the progression of the MICC. Wells and Melchers[62] exposed concrete coupons in a sewer system in Perth by monitoring $H_2S$ concentration, relative humidity, and temperature. Their research findings supported the three-stage model of MICC proposed by Islander et al.[19]; the corrosion rate at Stage 3 exposure was found to be 11 mm/yr. They stated that the less aggressive conditions might extend the duration of Stages 1 and 2, which results in lower corrosion rates. This study focuses on projecting the Option B method (Stage 2) of ASTM C1904 on field conditions. Further research could further refine this model by incorporating the influence of pH dynamics. The corrosion depth for cement paste mixtures from ASTM C1904 testing and the projected corrosion depth for concrete are given in Fig. 9(c) and (d), respectively.

Figure 10 illustrates the experimental and projected corrosion rates and corrosion depths from ASTM testing of mortar mixtures. As shown in Fig. 8, the M7.5 and M15 mixtures with admixed antimicrobials showed a delayed effect in deterioration. This delay is considered by following the method described in the section "Role of antimicrobial product leaching during ASTM C1904 testing." The mixtures M7.5 and M15 showed approximately 23- and 34-days delay for 124 days of ASTM C1904 testing, as shown in Fig. 10(a). The projected delay corresponds approximately to 0.7 and 1.0 years in the field for the sewer described, as shown in Fig. 10(b). In Fig. 10(b), the corrosion rate is represented for 3 years based on the annual hypothetical field conditions given in Table 4. The corrosion rates observed after the delayed effect, which corresponds to the third year, are repeated by assuming the same conditions for subsequent years. Figures 10(c) and (d) show the corrosion depth of mortar for ASTM testing and the projected corrosion depth of the concrete for field exposure, respectively. Although the performance of the paste and mortar from ASTM C1904 is projected for the same field conditions, the projected corrosion rate for mortar specimens, as seen in Fig. 10(b), is approximately 30% lower than the projected corrosion rate for cement paste specimens, as seen Fig. 9(b). Figure A5 illustrates the relationship between corrosion depth of M0 over

---

*The Appendix is available at **www.concrete.org/publications** in PDF format, appended to the online version of the published paper. It is also available in hard copy from ACI headquarters for a fee equal to the cost of reproduction plus handling at the time of the request.

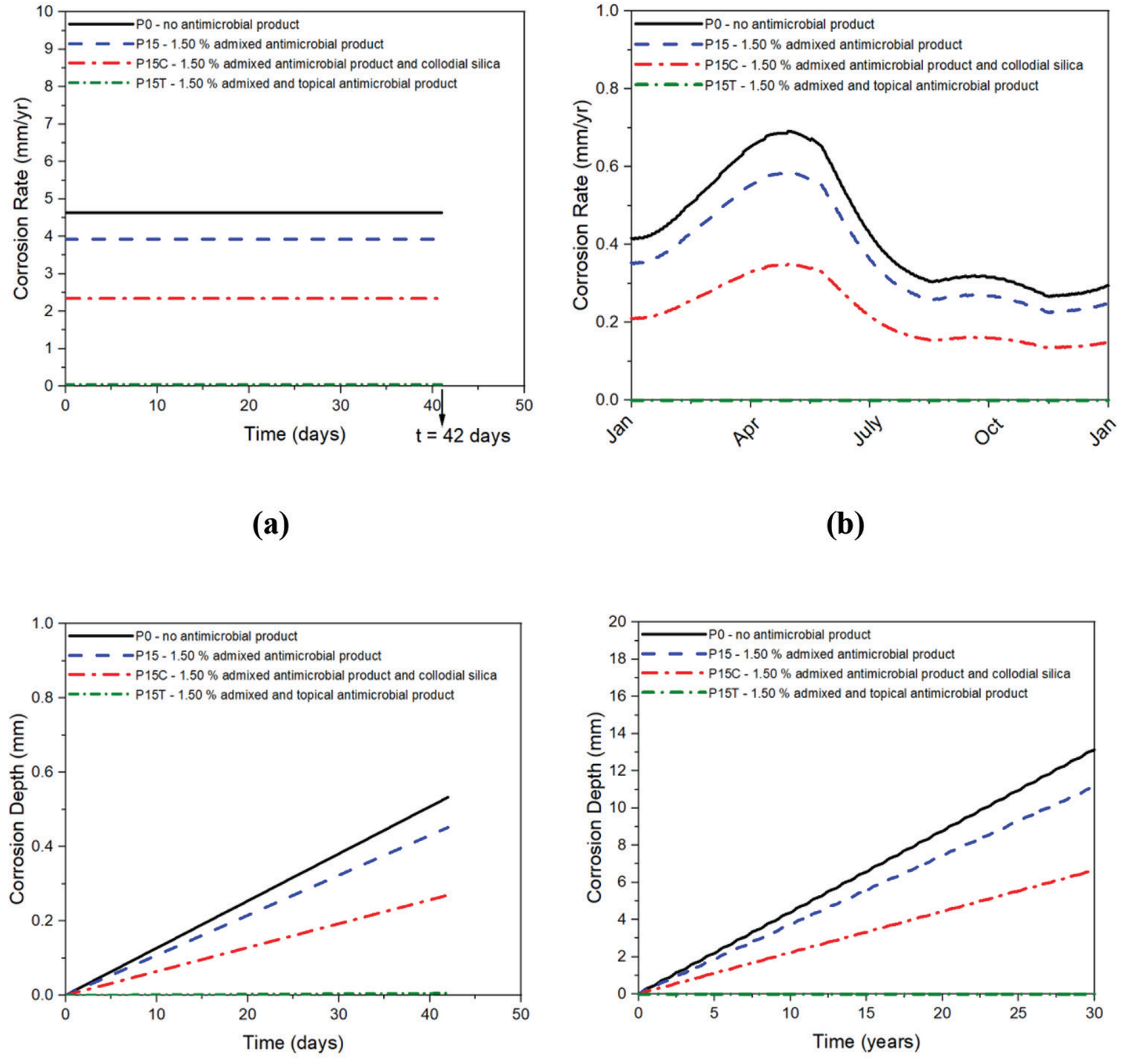

(a)

(b)

(c)

(d)

*Fig. 9—Results for cement paste specimens: (a) corrosion rates in ASTM C1904 testing; (b) projected corrosion rates expected for concrete in sewer; (c) corrosion depth versus time (days) in ASTM C1904 testing; and (d) projected corrosion depth versus time (years) expected for concrete in sewer.*

30 years and two correlation factors, which depend on the alkalinity and *k*-factor. In Fig. A5(a), the corrosion depth is shown to increase with decreasing alkalinity in sewer conditions, suggesting that mixtures with lower alkalinity exhibit reduced resistance MICC due to diminished acid-neutralization capacity. In Fig. A5(b), a linear relationship is observed between corrosion depth and $k_{sw}$, suggesting that higher $k_{sw}$ values lead to increased corrosion depth. As the *k*-factor is based on engineering judgment and reflects the dynamics of acid exposure at the concrete surface, Fig. A5(b) highlights the crucial role of accurately estimating this parameter in estimating corrosion depth in sewers. Although the alkalinity and *k*-factor in PM are significant factors, these might not be the only factors influencing the corrosion rates. The other mixture and durability factors, such as porosity, the matrix (paste/mortar), and hydration products, might affect corrosion rates.

## CONCLUSIONS

The purpose of this study was to develop a service life model to predict the performance of concrete exposed to microbially induced corrosion of concrete (MICC) in sewer structures by using a benchtop acidification test. The proposed service life modeling aims to provide a correlation between field conditions and ASTM C1904 testing by using Pomeroy's model (PM). For this purpose, correlation factors between ASTM C1904 testing and field exposure were introduced to eliminate differences of exposure conditions of the laboratory testing and the field, mixture composition, and design. The feasibility of using PM to predict the performance of laboratory testing was validated by comparing corrosion rates for different mixtures and exposure conditions with experimental results.

The proposed service life model allows prediction of the performance of the ASTM C1904 testing in the field for

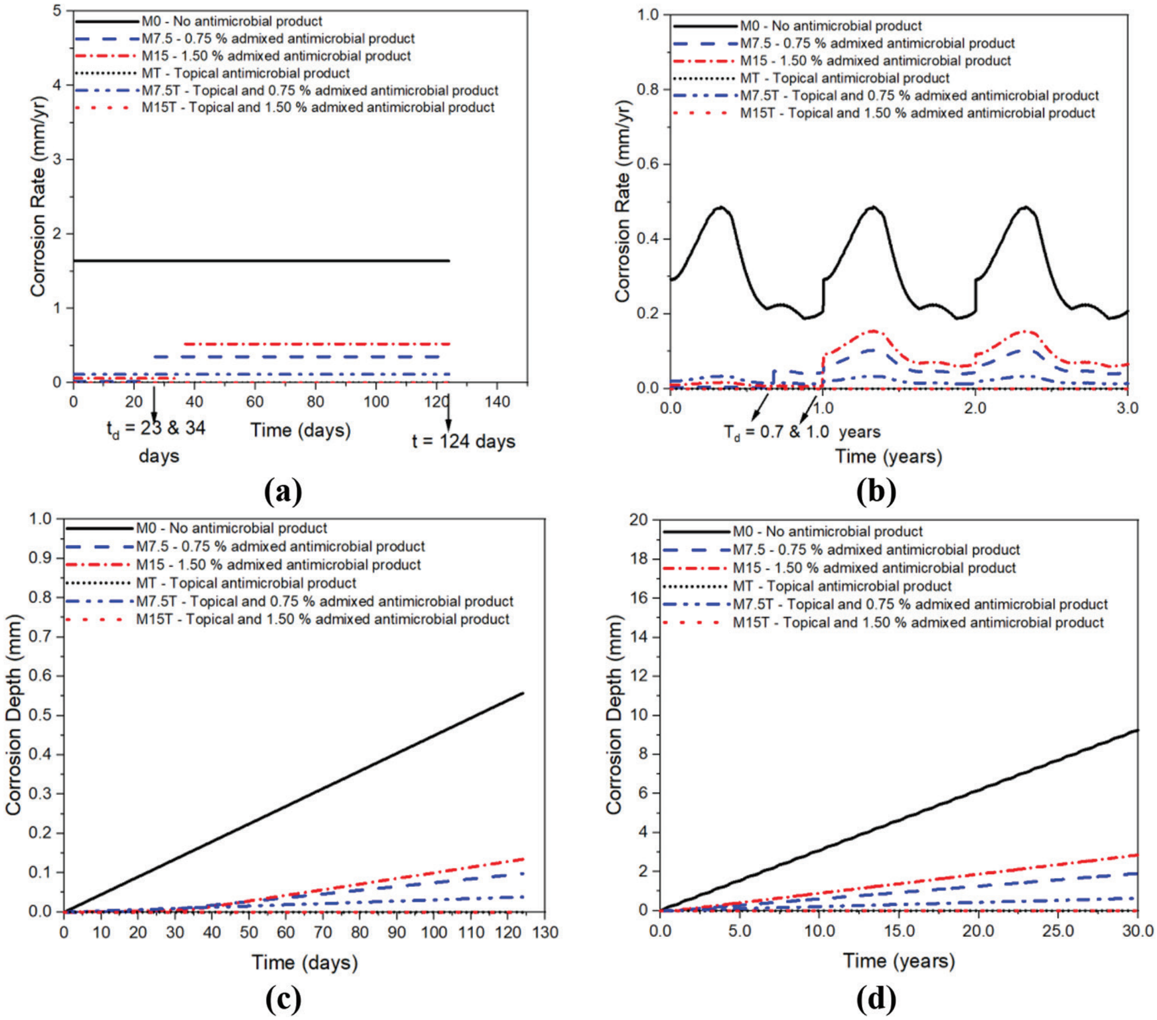

(a)

(b)

(c)

(d)

Fig. 10—Results for mortar specimens: (a) corrosion rates in ASTM C1904 testing; (b) projected corrosion rates expected for concrete in sewer; (c) corrosion depth versus time (days) in ASTM C1904 testing; and (d) projected corrosion depth versus time (years) expected for concrete in sewer.

different mixture designs and considers acute or delayed effects of antimicrobial products. Ten paste and mortar mixtures were assessed under hypothetical field conditions. Corrosion depth in the field during service can be predicted by using the proposed approach, which allows for predicting long-term structural performance, optimizing maintenance strategies, and reducing the economic and safety risks associated with premature deterioration in wastewater infrastructure.

The model can also consider the effect of antimicrobial treatments and capture the lower corrosion rates and a delayed onset of corrosion when they are used. For the same field conditions, the difference of the projected corrosion rates between the cement paste and mortar from ASTM C1904 might be because of other mixture and durability parameters that are not included in PM. While some parameters, such as *k*-factor and alkalinity, are included in the proposed model, more investigation might be conducted on determining those values. Besides, the effect of other parameters, such as porosity, the matrix (paste/mortar), hydration products, and various antimicrobial treatments, on the corrosion rates might be investigated as future work. Further validation of the proposed approach is recommended using real sewer data. For this, controlled field experiments need to be conducted.

## AUTHOR BIOS

*ACI member* **Feyza Nur Sahan** *is a PhD Student at Oregon State University, Corvallis, OR. Her research interests include microbially induced corrosion of concrete, acid attack, and thermodynamic modeling of cementitious systems.*

**Ali Riza Erbektas** *received his BS from Gazi University, Ankara, Turkey, and his MS from Oregon State University. His research interests include microbially induced corrosion of concrete.*

**W. Jason Weiss**, *FACI, is the Miles Lowell and Margaret Watt Edwards Distinguished Chair in Engineering in the School of Civil and Construction Engineering at Oregon State University. He is the former Editor-in-Chief of the* ACI Materials Journal *and is a member of the ACI Technical Activities Committee.*

**O. Burkan Isgor**, *FACI, is the Eric H.I. and Janice Hoffman Professor in Civil and Construction Engineering at Oregon State University. He is past Chair and a current member of ACI Committee 222, Corrosion of Metals in Concrete, and a member of ACI Committees 236, Material Science of Concrete, and 365, Service Life Prediction.*

## ACKNOWLEDGMENTS

The authors acknowledge the funding provided by Concrete Sealants, Inc., to support this project.

# REFERENCES

1. Wu, M.; Wang, T.; Wu, K.; and Kan, L., "Microbiologically Induced Corrosion of Concrete in Sewer Structures: A Review of the Mechanisms and Phenomena," *Construction and Building Materials*, V. 239, 2020, Article No. 117813. doi: 10.1016/j.conbuildmat.2019.117813

2. Wang, D.; Guan, F.; Feng, C.; Mathivanan, K.; Zhang, R.; and Sand, W., "Review on Microbially Influenced Concrete Corrosion," *Microorganisms*, V. 11, No. 8, 2023, Article No. 2076. doi: 10.3390/microorganisms11082076

3. Kaempfer, W., and Berndt, M., "Estimation of Service Life of Concrete Pipes in Sewer Networks," *Durability of Building Materials and Components 8: Service Life and Asset Management: Proceedings of the Eighth International Conference on Durability of Building Materials and Components*, M. A. Lacasse and D. J. Vanier, eds., Vancouver, BC, Canada, V. 1, 1999, pp. 36-45.

4. Wu, L.; Hu, C.; and Liu, W. V., "The Sustainability of Concrete in Sewer Tunnel—A Narrative Review of Acid Corrosion in the City of Edmonton, Canada," *Sustainability*, V. 10, No. 2, 2018, Article No. 517. doi: 10.3390/su10020517

5. Jensen, H. S.; Nielsen, A. H.; Lens, P.; Hvitved-Jacobsen, T.; and Vollertsen, J., "Hydrogen Sulphide Removal from Corroding Concrete: Comparison Between Surface Removal Rates and Biomass Activity," *Environmental Technology*, V. 30, No. 12, 2009, pp. 1291-1296. doi: 10.1080/09593330902894356

6. ASTM C1894-22 "Standard Guide for Microbially Induced Corrosion of Concrete Products," ASTM International, West Conshohocken, PA, 2022, 8 pp.

7. EPA, "Clean Watersheds Needs Survey 2012: Report to Congress," Report No. EPA-830-R-15005, U.S. Environmental Protection Agency, Washington, DC, 2016, 41 pp.

8. Yuan, H.; Dangla, P.; Chatellier, P.; and Chaussadent, T., "Degradation Modeling of Concrete Submitted to Biogenic Acid Attack," *Cement and Concrete Research*, V. 70, 2015, pp. 29-38. doi: 10.1016/j.cemconres.2015.01.002

9. Grengg, C.; Mittermayr, F.; Ukrainczyk, N.; Koraimann, G.; Kienesberger, S.; and Dietzel, M., "Advances in Concrete Materials for Sewer Systems Affected by Microbial Induced Concrete Corrosion: A Review," *Water Research*, V. 134, 2018, pp. 341-352. doi: 10.1016/j.watres.2018.01.043

10. Joseph, A. P.; Keller, J.; Bustamante, H.; and Bond, P. L., "Surface Neutralization and $H_2S$ Oxidation at Early Stages of Sewer Corrosion: Influence of Temperature, Relative Humidity and $H_2S$ Concentration," *Water Research*, V. 46, No. 13, 2012, pp. 4235-4245. doi: 10.1016/j.watres.2012.05.011

11. Wei, S.; Jiang, Z.; Liu, H.; Zhou, D.; and Sanchez-Silva, M., "Microbiologically Induced Deterioration of Concrete: A Review," *Brazilian Journal of Microbiology*, V. 44, No. 4, 2013, pp. 1001-1007. doi: 10.1590/S1517-83822014005000006

12. De Belie, N.; Monteny, J.; Beeldens, A.; Vincke, E.; Van Gemert, D.; and Verstraete, W., "Experimental Research and Prediction of the Effect of Chemical and Biogenic Sulfuric Acid on Different Types of Commercially Produced Concrete Sewer Pipes," *Cement and Concrete Research*, V. 34, No. 12, 2004, pp. 2223-2236. doi: 10.1016/j.cemconres.2004.02.015

13. Kaushal, V.; Najafi, M.; Love, J.; and Qasim, S. R., "Microbiologically Induced Deterioration and Protection of Concrete in Municipal Sewerage System: Technical Review," *Journal of Pipeline Systems Engineering and Practice*, ASCE, V. 11, No. 1, 2020, p. 03119002. doi: 10.1061/(ASCE)PS.1949-1204.0000424

14. Chaudhari, B.; Panda, B.; Šavija, B.; and Chandra Paul, S., "Microbiologically Induced Concrete Corrosion: A Concise Review of Assessment Methods, Effects, and Corrosion-Resistant Coating Materials," *Materials*, V. 15, No. 12, 2022, Article No. 4279. doi: 10.3390/ma15124279

15. Sun, X., "Improving the Understanding of Concrete Sewer Corrosion Through Investigations of the Gaseous Hydrogen Sulfide Uptake and Transformation Processes in the Corrosion Layer," PhD thesis, School of Chemical Engineering, The University of Queensland, Brisbane, QLD, Australia, 2015.

16. Aboulela, A.; Peyre Lavigne, M.; Buvignier, A.; Fourré, M.; Schiettekatte, M.; Pons, T.; Patapy, C.; Robin, O.; Bounouba, M.; Paul, E.; and Bertron, A., "Laboratory Test to Evaluate the Resistance of Cementitious Materials to Biodeterioration in Sewer Network Conditions," *Materials*, V. 14, No. 3, 2021, Article No. 686. doi: 10.3390/ma14030686

17. Roberts, D.; Nica, D.; Zuo, G.; and Davis, J., "Quantifying Microbially Induced Deterioration of Concrete: Initial Studies," *International Biodeterioration and Biodegradation*, V. 49, No. 4, 2002, pp. 227-234. doi: 10.1016/S0964-8305(02)00049-5

18. House, M. W., "Using Biological and Physico-Chemical Test Methods to Assess the Role of Concrete Mixture Design in Resistance to Microbially Induced Corrosion," master's thesis, Purdue University, West Lafayette, IN, 2013.

19. Islander, R. L.; Devinny, J. S.; Mansfeld, F.; Postyn, A.; and Shih, H., "Microbial Ecology of Crown Corrosion in Sewers," *Journal of Environmental Engineering*, ASCE, V. 117, No. 6, 1991, pp. 751-770. doi: 10.1061/(ASCE)0733-9372(1991)117:6(751)

20. Idriss, A.; Negi, S.; Jofriet, J.; and Hayward, G., "Effect of Hydrogen Sulphide Emissions on Cement Mortar Specimens," *Canadian Biosystems Engineering*, V. 43, No. 5, 2001, pp. 523-528.

21. Wu, L.; Huang, G.; and Liu, W. V., "Methods to Evaluate Resistance of Cement-Based Materials Against Microbially Induced Corrosion: A State-of-the-Art Review," *Cement and Concrete Composites*, V. 123, 2021, Article No. 104208. doi: 10.1016/j.cemconcomp.2021.104208

22. Chen, X.; Liu, X.; Luo, H.; Long, L.; and Liu, C., "Microscopic Damage to Limestone under Acidic Conditions: Phenomena and Mechanisms," *Sustainability*, V. 14, No. 18, 2022, Article No. 11771. doi: 10.3390/su141811771

23. Erbektas, A. R.; Isgor, O. B.; and Weiss, W. J., "An Accelerated Testing Protocol for Assessing Microbially Induced Concrete Deterioration During the Bacterial Attachment Phase," *Cement and Concrete Composites*, V. 104, 2019, Article No. 103339. doi: 10.1016/j.cemconcomp.2019.103339

24. ASTM C1898-20, "Standard Test Methods for Determining the Chemical Resistance of Concrete Products to Acid Attack," ASTM International, West Conshohocken, PA, 2020, 4 pp.

25. ASTM C1904-20, "Standard Test Methods for Determination of the Effects of Biogenic Acidification on Concrete Antimicrobial Additives and/or Concrete Products," ASTM International, West Conshohocken, PA, 2020, 14 pp.

26. Ding, L., "Assessing the Performance of Antimicrobial Concrete Admixtures in Concrete Subjected to Microbially Induced Corrosion," master's thesis, Purdue University, West Lafayette, IN, 2015.

27. Peyre Lavigne, M.; Bertron, A.; Auer, L.; Hernandez-Raquet, G.; Foussard, J.-N.; Escadeillas, G.; Cockx, A.; and Paul, E., "An Innovative Approach to Reproduce the Biodeterioration of Industrial Cementitious Products in a Sewer Environment. Part I: Test Design," *Cement and Concrete Research*, V. 73, 2015, pp. 246-256. doi: 10.1016/j.cemconres.2014.10.025

28. Monteny, J.; Vincke, E.; Beeldens, A.; De Belie, N.; Taerwe, L.; Van Gemert, D.; and Verstraete, W., "Chemical, Microbiological, and In Situ Test Methods for Biogenic Sulfuric Acid Corrosion of Concrete," *Cement and Concrete Research*, V. 30, No. 4, 2000, pp. 623-634. doi: 10.1016/S0008-8846(00)00219-2

29. Grengg, C.; Mittermayr, F.; Baldermann, A.; Böttcher, M. E.; Leis, A.; Koraimann, G.; Grunert, P.; and Dietzel, M., "Microbiologically Induced Concrete Corrosion: A Case Study from a Combined Sewer Network," *Cement and Concrete Research*, V. 77, 2015, pp. 16-25. doi: 10.1016/j.cemconres.2015.06.011

30. Mori, T.; Nonaka, T.; Tazaki, K.; Koga, M.; Hikosaka, Y.; and Noda, S., "Interactions of Nutrients, Moisture and Ph on Microbial Corrosion of Concrete Sewer Pipes," *Water Research*, V. 26, No. 1, 1992, pp. 29-37. doi: 10.1016/0043-1354(92)90107-F

31. Ehrich, S.; Helard, L.; Letourneux, R.; Willocq, J.; and Bock, E., "Biogenic and Chemical Sulfuric Acid Corrosion of Mortars," *Journal of Materials in Civil Engineering*, ASCE, V. 11, No. 4, 1999, pp. 340-344. doi: 10.1061/(ASCE)0899-1561(1999)11:4(340)

32. Erbektas, A. R.; Isgor, O. B.; and Weiss, W. J., "Comparison of Chemical and Biogenic Acid Attack on Concrete," *ACI Materials Journal*, V. 117, No. 1, Jan. 2020, pp. 255-264.

33. Huber, B.; Hilbig, H.; Drewes, J. E.; and Müller, E., "Evaluation of Concrete Corrosion After Short-And Long-Term Exposure to Chemically and Microbially Generated Sulfuric Acid," *Cement and Concrete Research*, V. 94, 2017, pp. 36-48. doi: 10.1016/j.cemconres.2017.01.005

34. Huber, B.; Hilbig, H.; Mago, M. M.; Drewes, J. E.; and Müller, E., "Comparative Analysis of Biogenic and Chemical Sulfuric Acid Attack on Hardened Cement Paste Using Laser Ablation-ICP-MS," *Cement and Concrete Research*, V. 87, 2016, pp. 14-21. doi: 10.1016/j.cemconres.2016.05.003

35. Monteny, J.; De Belie, N.; Vincke, E.; Verstraete, W.; and Taerwe, L., "Chemical and Microbiological Tests to Simulate Sulfuric Acid Corrosion of Polymer-Modified Concrete," *Cement and Concrete Research*, V. 31, No. 9, 2001, pp. 1359-1365. doi: 10.1016/S0008-8846(01)00565-8

36. Sand, W., and Bock, E., "Concrete Corrosion in the Hamburg Sewer System," *Environmental Technology*, V. 5, No. 12, 1984, pp. 517-528.

37. Yousefi, A.; Allahverdi, A.; and Hejazi, P., "Accelerated Biodegradation of Cured Cement Paste by *Thiobacillus* Species Under Simulation Condition," *International Biodeterioration and Biodegradation*, V. 86, 2014, pp. 317-326. doi: 10.1016/j.ibiod.2013.10.008

38. Pomeroy, R. D., "Process Design Manual for Sulfide Control in Sanitary Sewerage Systems," U.S. Environmental Protection Agency, Technology Transfer, Washington, DC, 1974.

39. Pomeroy, R. D., and Parkhurst, J. D., "The Forecasting of Sulfide Build-Up Rates in Sewers," *Proceedings of the 8th International Conference on Water Pollution Research*, S. H. Jenkins, ed., Sydney, NSW, Australia, 1978, pp. 621-628.

40. EPA, "Hydrogen Sulfide Corrosion in Wastewater Collection and Treatment Systems: Report to Congress," U.S. Environmental Protection Agency, Office of Water, Washington, DC, 1991, 8 pp.

41. Morton, R. L.; Yanko, W. A.; Graham, D. W.; and Arnold, R. G., "Relationships Between Metal Concentrations and Crown Corrosion in Los Angeles County Sewers," *Research Journal of the Water Pollution Control Federation*, V. 63, 1991, pp. 789-798.

42. Nielsen, P. H., and Hvitved-Jacobsen, T., "Effect of Sulfate and Organic Matter on the Hydrogen Sulfide Formation in Biofilms of Filled Sanitary Sewers," *Journal (Water Pollution Control Federation)*, V. 60, No. 5, 1988, pp. 627-634.

43. Pomeroy, R. D., "The Problem of Hydrogen Sulphide in Sewers," Clay Pipe Development Association Ltd., London, UK, 1990.

44. EPA, "Odor and Corrosion Control in Sanitary Sewerage Systems and Treatment Plants: Design Manual," Center for Environmental Research Information, U.S. Environmental Protection Agency, Cincinnati, OH, 1985, 142 pp.

45. Björk, F., and Eriksson, C. A., "Measurement of Alkalinity in Concrete by a Simple Procedure, to Investigate Transport of Alkaline Material from the Concrete Slab to a Self-Levelling Screed," *Construction and Building Materials*, V. 16, No. 8, 2002, pp. 535-542. doi: 10.1016/S0950-0618(02)00035-1

46. Zaw, M., "Automated Chemical Acidification Testing of Cementitious Materials," master's thesis, Oregon State University, Corvallis, OR, 2021.

47. Fu, T., and Weiss, W. J., "The Ball-on-Three-Ball (B3B) Test-Application to Cement Paste and Mortar," *Advances in Civil Engineering Materials*, V. 9, No. 1, 2020, pp. 128-142. doi: 10.1520/ACEM20180070

48. Börger, A.; Supancic, P.; and Danzer, R., "The Ball on Three Balls Test for Strength Testing of Brittle Discs: Part II: Analysis of Possible Errors in the Strength Determination," *Journal of the European Ceramic Society*, V. 24, No. 10-11, 2004, pp. 2917-2928. doi: 10.1016/j.jeurceramsoc.2003.10.035

49. Chang, Z.-T.; Song, X.-J.; Munn, R.; and Marosszeky, M., "Using Limestone Aggregates and Different Cements for Enhancing Resistance of Concrete to Sulphuric Acid Attack," *Cement and Concrete Research*, V. 35, No. 8, 2005, pp. 1486-1494. doi: 10.1016/j.cemconres.2005.03.006

50. Fernandes, I.; Pericão, M.; Hagelia, P.; Noronha, F.; Ribeiro, M.; and Maia, J., "Identification of Acid Attack on Concrete of a Sewage System," *Materials and Structures*, V. 45, No. 3, 2012, pp. 337-350. doi: 10.1617/s11527-011-9769-y

51. Puthenpurayil, J. A.; Bond, P.; and Keller, J., "Examination of Concrete Corrosion Using a Laboratory Experimental Set Up Simulating Sewer Conditions," *Proceedings of the 6th IWA Specialist Conference on Sewer Processes and Networks*, Gold Coast, QLD, Australia, 2010.

52. Wells, P., and Melchers, R. E., "Microbial Corrosion of Sewer Pipe in Australia-Initial Field Results," *Proceedings of the 18th International Corrosion Congress 2011*, Perth, WA, Australia, 2011.

53. Jiang, G.; Keller, J.; and Bond, P. L., "Determining the Long-Term Effects of $H_2S$ Concentration, Relative Humidity and Air Temperature on Concrete Sewer Corrosion," *Water Research*, V. 65, 2014, pp. 157-169. doi: 10.1016/j.watres.2014.07.026

54. Bakera, A. T.; Alexander, M. G.; and Beushausen, H., "Corrosion Prediction Models for Biogenic Acid Attack Concrete in Sewers," *Proceedings of the Young Concrete Researchers, Engineers and Technologist Symposium (YCRETS)*, J. Kanjee, ed., 2021, pp. 175-185.

55. Bowker, R.; Audibert, G.; Shah, H.; and Webster, N., "Detection, Control, and Correction of Hydrogen Sulfide Corrosion in Existing Wastewater Systems," Office of Wastewater Enforcement and Compliance, U.S. Environmental Protection Agency, Washington, DC, 1992, 162 pp.

56. Gutiérrez-Padilla, M. G. D.; Bielefeldt, A.; Ovtchinnikov, S.; Hernandez, M.; and Silverstein, J., "Biogenic Sulfuric Acid Attack on Different Types of Commercially Produced Concrete Sewer Pipes," *Cement and Concrete Research*, V. 40, No. 2, 2010, pp. 293-301. doi: 10.1016/j.cemconres.2009.10.002

57. Aleksić, A. D.; Gordić, D. R.; Šušteršič, V. M.; and Babić, M. J., "Application of Fat Trap for the Wastewater Treatment in Margarine Production," *Desalination and Water Treatment*, V. 57, No. 8, 2016, pp. 3466-3472. doi: 10.1080/19443994.2014.986529

58. City of McMinnville, "Water Reclamation Facilities Plan," McMinnville, OR, 2009.

59. Wells, T., and Melchers, R., "Modelling Concrete Deterioration in Sewers Using Theory and Field Observations," *Cement and Concrete Research*, V. 77, 2015, pp. 82-96. doi: 10.1016/j.cemconres.2015.07.003

60. Jariyathitipong, P.; Hosotani, K.; Fujii, T.; and Ayano, T., "Sulfuric Acid Resistance of Concrete with Blast Furnace Slag Fine Aggregate," *Journal of Civil Engineering and Architecture*, V. 8, No. 11, 2014, pp. 1403-1413. doi: 10.17265/1934-7359/2014.11.007

61. Kiliswa, M. W.; Scrivener, K. L.; and Alexander, M. G., "The Corrosion Rate and Microstructure of Portland Cement and Calcium Aluminate Cement-Based Concrete Mixtures in Outfall Sewers: A Comparative Study," *Cement and Concrete Research*, V. 124, 2019, Article No. 105818. doi: 10.1016/j.cemconres.2019.105818

62. Wells, T., and Melchers, R., "An Observation-Based Model for Corrosion of Concrete Sewers Under Aggressive Conditions," *Cement and Concrete Research*, V. 61-62, 2014, pp. 1-10. doi: 10.1016/j.cemconres.2014.03.013

## NOTES:

ACI MATERIALS JOURNAL TECHNICAL PAPER

Title No. 123-M14

# Effect of Limestone on Electrical Properties of Cementitious Systems

by W. Jason Weiss, O. Burkan Isgor, and Keshav Bharadwaj

*The composition of ordinary portland cement (OPC) changed in North America with the addition of ground limestone in 2004 (since the adoption of ASTM C150-04a), which reacts to form carboaluminate hydration products. This paper discusses the potential influence of limestone addition on the porosity, pore connectivity, formation factor, and electrical properties of cementitious systems. The carboaluminate reaction products can result in a system with limestone that has an equivalent water-powder ratio (*w/p*) approximately 0.07 lower than the system without limestone (occurring at the minimum porosity). When reactive alumina is added to the system, a greater amount of limestone reacts, and a reduction in porosity occurs. The carboaluminate phases impact the transport properties of mixtures to a greater extent for mixtures with moderately low* w/p *and aluminous supplementary cementitious materials (SCMs). This has implications for standards and specifications, which are based on historical research and testing using cements that do not contain limestone and therefore would have a higher porosity and lower formation factor than cements manufactured in the United States after approximately 2004 at the same* w/p*.*

**Keywords:** durability; electrical resistivity; formation factor; limestone; porosity; portland-limestone cement (PLC).

## BACKGROUND AND INTRODUCTION

Historically, hydraulic cement (that is, ordinary portland cement [OPC]) primarily consisted of clinker, a source of sulfate, and grinding aids.[1] Over time, the incorporation of finely graded limestone has become more common in the United States.[2,3] In 2004, ASTM C150 was changed to permit the addition of up to 5% limestone. In 2012, ASTM C595 was changed to allow Type IL cements containing up to 15% limestone, also called portland-limestone cement (PLC). These changes in cement composition have been made largely to reduce the global warming potential (GWP) associated with cement production and use by reducing the clinker content in the cement.[3,4] Reducing GWP is an admirable goal; however, it is also important to understand and contextualize how these changes in cement composition impact the knowledge of cement and concrete data on which many of the codes and specifications are based.

Several studies have summarized the results of cementitious materials made using cement with limestone additions.[2,3,5-8] Matschei et al.[6,7] demonstrated that the addition of limestone results in hydration products (carboaluminates) that initially decrease porosity before dilution leads to an increase in porosity until the original porosity is attained at approximately 15% limestone addition.[7,9] Lothenbach et al.[10] and De Weerdt et al.[11,12] observed that limestone promoted the formation of mono- and hemicarboaluminate as opposed to monosulfoaluminate, which helped to stabilize ettringite, reducing porosity. Porosity is often related to compressive strength.[13-17] Some common relationships between compressive strength and porosity are those of Feldman and Sereda,[17] Feret's law,[14] Abrams' law,[13] and Powers and Brownyard's gel-space ratio.[18] These relations are well ingrained in popular approaches available in the literature to predict strength; for example, tools such as CEMHYD3D and HYDCEM use Powers and Brownyard's gel-space ratio to predict strength.[19,20] Figure 1 provides an example of how porosity and compressive strength are impacted with limestone replacement of clinker (after Matschei et al.[7]). If clinker is replaced with reactive alumina, it can be noticed that the porosity can be further reduced,[9,21] and a similar trend in compressive strength is predicted based on the gel-space ratio.

While the formation of aluminate-based reaction products can reduce overall porosity, other properties of limestone, such as fineness, also play an important role in the pore structure and fresh properties. Cost et al.[22] and Bentz et al.[23] studied the role of limestone fineness on the setting and strength development. Finer limestones typically result in faster setting, less bleed, and more rapid strength development. ASTM C595 Type IL cement is typically 20% finer than the parent ASTM C150 cement to counteract slow strength development.[24] Bucher et al.[25,26] demonstrated that coarser limestones had less shrinkage at the same limestone replacement level, presumably due to lower capillary stress. This also led to a reduced potential for cracking; however, the 28-day strength may be lower than that of the parent material for coarse limestone. Many commercial ASTM C595 cements have been more finely ground and tested to demonstrate a similar shrinkage and cracking potential to the parent ASTM C150 cement.[27] Sellevold et al.[28] showed that the fineness of additives was critical for promoting nucleation reactions. It was surmised that fine limestone that nucleated reaction products would refine the connectivity of the pore structure.[2] The influence of nucleation and increased space for hydration products has been discussed as a potential reason for increased clinker reaction at early ages.[5,29] Brookbanks[30] showed that an increased limestone fineness

---

*ACI Materials Journal*, V. 123, No. 2, March 2026.
MS No. M-2023-277.R1, doi: 10.14359/51749381, received May 30, 2025, and reviewed under Institute publication policies. Pertinent discussion including author's closure, if any, will be published ten months from this journal's date if the discussion is received within four months of the paper's print publication.

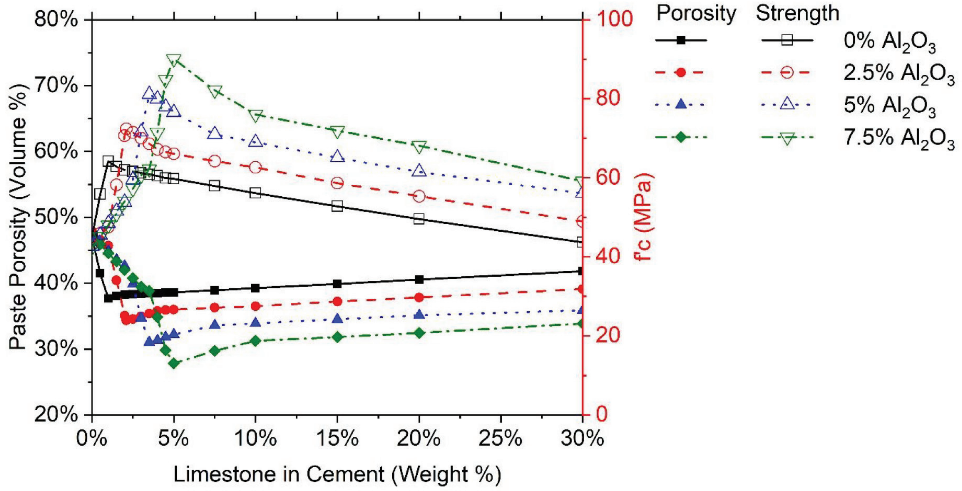

*Fig. 1—Illustration of porosity and compressive strength when cement systems are replaced with limestone and combination of limestone and reactive alumina.*

results in a reduction in bleeding rate in fresh concrete. This may also influence finishing operations.

Other researchers have examined the influence of limestone replacement of clinker on transport properties, and the results can appear contradictory and confusing. For example, Schmidt[31,32] reported that limestone addition reduced the porosity of the system. Moir and Kelham[33] found that the addition of limestone increased permeability, though the limestone was generally coarse. Tsivilis et al.[34] reported reduced water permeability with limestone addition, despite similar porosity. Tezuka et al.[35] measured the diffusion coefficient of cement paste with 0, 5, 10, and 15% limestone replacement and reported that the system containing 5% limestone had the lowest diffusivity, and the 15% system had the highest diffusivity. Barrett et al.[36,37] reported that the chloride diffusion coefficient for PLC concrete may increase from 2 to 30% when compared to conventional OPC with similar clinker composition; however, fly ash + limestone showed a dramatic reduction due to a reduction in connectivity. They also showed that the resistivity of the PLC mixtures is generally within ±25% of that of their OPC counterparts but had a dependency on the water-powder ratio (*w*/*p*). Muni et al.[38] reported increases in the resistivity of concrete with limestone and clay additions. Garcia et al.[39] reported that the addition of limestone decreases the electrical resistivity of a concrete mixture, implying that it might also increase its permeability; however, they reported that supplementary cementitious materials (SCMs) could be used with PLC to overcome any detrimental effects of limestone addition. Choudhary et al.[40] reported the porosity of PLC to be approximately 2 to 6% higher than the porosity of commercial OPC mortar (with 2 to 3% interground limestone); however, the resistivity of the PLC was generally statistically similar to the OPC system with similar clinker composition. Furthermore, Choudhary et al.[40] reported that the resistivity in SCM systems with limestone was two to four times greater than in the systems without SCMs.[40,41] As mentioned, the literature findings appear to show that the addition of limestone may increase or decrease porosity and transport properties, which appears to be due to the baseline cement used, the mixture proportions, and the proportion of limestone replacement.

In this work, numerical simulations were performed to examine four separate topics. Specifically, the study examined: 1) how the replacement clinker with limestone impacted the expected reaction products; 2) how the reaction products that form alter the porosity of systems with the same *w*/*p*; 3) how limestone and reactive alumina are synergistic and, when used together, further reduce porosity; and 4) how the reaction products impact the pore connectivity and the formation factor. Examples are provided to compare the analytical results with experimental measurements. The impacts of these findings are discussed as they relate to experimental interpretation, as well as specification and standard development.

## Background on modeling transport properties

This paper hypothesizes that some of the contradictory and confusing reports related to the role of limestone in the electrical resistivity and formation factor can be explained using computational modeling concepts, such as those used by Matschei et al.[7] and Bharadwaj et al.[9,42] for porosity and strength. While compressive strength is related to porosity using the gel-space relationship (Fig. 1), electrical properties such as resistivity or formation factor are related to porosity in a more complex manner, as they involve both the volume of pores and the connectivity of the pore space.[43] For instance, the formation factor ($F$) of a porous medium is defined as the inverse product of the total porosity ($\phi$) and the pore connectivity ($\beta$), as shown in Eq. (1)[43,44]

$$F = \frac{1}{\phi\beta} \tag{1}$$

The total porosity is defined as the total volume of voids in the system. The pore connectivity is a mathematical quantity used to describe the tortuosity and interconnectedness of the pore structure in the system.[45-48] The pore connectivity calculations have been described in previous work[45-47] and are modeled using a series model consisting of the connectivity of the capillary pores ($\beta_{cap}$) and the connectivity of the gel pores ($\beta_{gel}$) using Eq. (2)

$$\beta_{paste} = \beta_{gel} + \beta_{cap} \tag{2}$$

The formation factor can also be calculated as the ratio of the bulk resistivity of the concrete ($\rho_{bulk}$) to the resistivity of the pore solution filling the pores ($\rho_{ps}$), shown in Eq. (3)[43,44,49-52]

$$F = \frac{\rho_{bulk}}{\rho_{ps}} \tag{3}$$

The resistivity of concrete is often used in practice because it is determined by a relatively simple experimental procedure that measures resistance and corrects for geometry (ASTM C1876, AASHTO T 358, and AASHTO T 402).

## RESEARCH SIGNIFICANCE

Modern cement uses ground limestone, which impacts electrical and transport properties such as the formation factor. Low limestone replacement volumes result in the formation of carboaluminate phases, which reduce porosity and connectivity and increase electrical resistivity and the formation factor. As the limestone replacement volumes increase, dilution becomes more prevalent, which increases porosity and connectivity, resulting in a reduction in electrical resistivity. This is significant because historical research and testing (systems without limestone addition from which most specifications and codes are based) would have a higher porosity, lower pore connectivity, and lower formation factor than cements manufactured in the United States after approximately 2004 at the same *w*/*p*. Further, historical cements are less impacted by SCMs containing reactive alumina. Consideration of ground limestone in specification changes moving forward may be prudent.

## COMPUTATIONAL METHODOLOGY

This paper uses a computational tool that couples thermodynamics,[53-57] kinetics,[58,59] and pore partitioning models[45-47] for cementitious systems. The computational tool (previously described in the literature[45-47,60,61]) is able to use the cement chemistry, SCM chemistry, SCM reactivity,[62,63] volumes of each material, and water content to predict the volumes of reaction products, pore solution chemistry, pore solution volume, and information about porosity. The details of the tool are available in previously published literature cited previously and are not repeated here for brevity. Briefly, the cement chemistry, SCM chemistry, and reactivity (DOR*, as measured using the pozzolanic reactivity test [PRT[64]]) are inputs to the modified Parrot-Killoh kinetic model.[65] The kinetic model provides the amounts of individual cement and SCM phases that react as a function of time, which is then input into the GEMS3K thermodynamic modeling tool.[56,57] In this work, the GEMS3K v3.5.0 software is used in conjunction with the default PSI/Nagra database and the Cemdata v18.01 thermodynamic database.[66] The outputs of GEMS are processed through a pore partitioning model[67,68] to predict the porosity and pore volumes. The calculated total porosity can further be subdivided into four types of pores: gel, capillary, chemical shrinkage, and entrained air.[46,47]

While porosity is relatively well understood, the computational tool describes how the relative change in the types of pores impacts pore connectivity. Previous work[46,47] described the formation factor using a series approach, with the first term approximating the connectivity of the gel pores and the second term accounting for the connectivity of the capillary pores. In the previous work, when the capillary porosity decreased below 18%, it was assumed to be disconnected,[69,70] which is in line with the observations of capillary discontinuity observed by Powers et al.[71] The relative proportion of the gel to capillary pores in a system is related to the pore connectivity. As such, the impact of altering the relative proportions of pore sizes can be discussed here, using a system with 30% porosity as an example. If the system is composed of capillary pores, the formation factor is quite low (approximately 3). However, as the proportion of the gel pores increases to 10% of the total porosity, the formation factor increases by more than 10 times, to a value of 36. If 50% of the pores are gel pores, the formation factor is approximately 135, and if all the pores are gel pores, the formation factor exceeds 200.[51,72,73] This clearly illustrates that the connectivity of the pores is crucial. It should be noted that in this work, the chemical shrinkage and air voids are not considered to be fluid-filled or conductive (that is, the sealed condition).

The chemistry of the base cement (herein, the base cement refers to cement before limestone addition and is referred to as cement through the remainder of the paper) used throughout the majority of the paper is from Bharadwaj et al.[42]: $C_3S$ = 69.09%, $C_2S$ = 5.08%, $C_3A$ = 6.61%, $C_4AF$ = 6.94%, $Na_2O$ = 0.21%, $K_2O$ = 0.48, MgO = 1.43%, and $SO_3$ = 2.55%. The cement had a specific gravity of 3.15 and a fineness of 375 $m^2/kg$. The reactive alumina studied was 100% $Al_2O_3$ with a maximum degree of reactivity (DOR*) of 100%, a specific gravity of 3.94, and a fineness of 450 $m^2/kg$.[42] The limestone was 100% $CaCO_3$, with a specific gravity of 2.71 and a fineness of 450 $m^2/kg$. An additional cement was simulated to compare with the results of the Barrett et al.[36,37] study with a chemistry of[36]: $C_3S$ = 42.42%, $C_2S$ = 34.08%, $C_3A$ = 3.28%, $C_4AF$ = 12.38%, and $SO_3$ = 1.15%, a specific gravity of 3.16, and a fineness of 376 $m^2/kg$. The systems had a *w*/*p* of 0.40 with limestone replacements of 0, 1.15, 4.31, and 13.31% by mass.

The final portion of this paper discusses two concepts using computational simulations. The first item discussed refers to the comparison of historical ASTM C150 cements (that is, ASTM C150 OPC prior to 2004, before limestone addition) and modern ASTM C150 (OPC) and ASTM C595/EN 197-5 (PLC) cements. The second item performs simulations to discuss the role of *w*/*p* when OPC and PLC mixtures are compared.

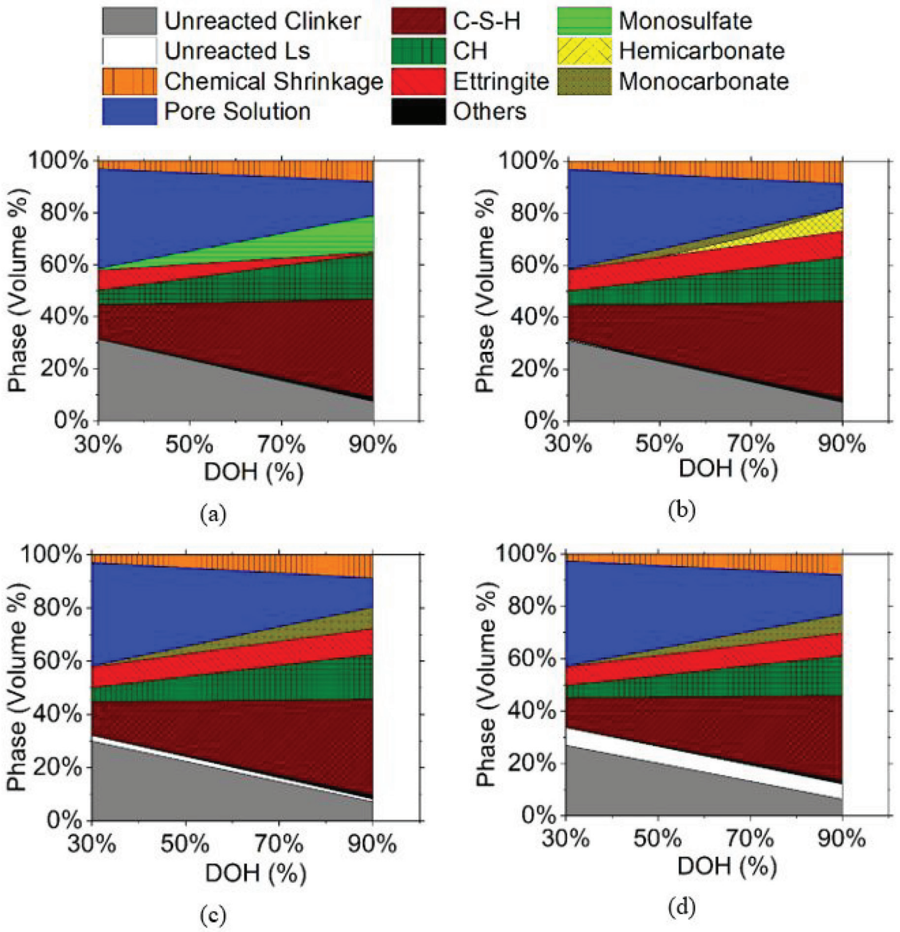

(a) (b) (c) (d)

*Fig. 2—Plots of unreacted and reacted phases of paste with* w/p *of 0.40 containing: (a) 0%; (b) 1.15%; (c) 4.31%; and (d) 13.31% ground limestone.*

## RESULTS AND DISCUSSION OF SIMULATIONS

### Limestone replacement level and reaction products

A series of simulations was performed to illustrate the reaction products that form when a portion of the clinker in cement is replaced with ground limestone. The simulations were performed for degrees of hydration (DOH) ranging from 30 to 90% (approximately 1 day to 20 years). Figure 2 illustrates the unreacted phases (cement, limestone, other minor fractions such as brucite and goethite, and pore solution), the chemical shrinkage (volume reduction due to reaction), and the hydrated phases (calcium-silicate-hydrate [C-S-H], calcium hydroxide [CH], ettringite, monosulfate, and hemicarbonate, and monocarbonate). As the DOH increased, the clinker and water (that is, the pore solution) were consumed, and hydration products were formed. In general, the volume of reaction products increases with an increase in the DOH. The C-S-H and CH increased with DOH. The cumulative volume of ettringite, monosulfate, hemicarbonate, and monocarbonate increased with DOH; however, the relative proportions of each varied. When limestone was not present in the system (Fig. 2(a)), ettringite formed at a low DOH and converted to monosulfate as the DOH increased. No monosulfate and hemicarbonate formed in the system without limestone. At low limestone levels (Fig. 2(b))—that is, limestone < 1.15%), ettringite formed and monocarbonate formed instead of monosulfate. As the DOH increased, the monocarbonate gave way to hemicarbonate formation. At higher limestone contents (Fig. 2(c) and (d)), ettringite and monocarbonate formed, and unreacted limestone remained. The conditions for the formation of each of these phases are outlined in Georget et al.[74] and Matschei et al.[75]

### Reaction products and resulting porosity

Figure 3(a) illustrates the phases that form at 75% DOH (that is, an approximate age of 90 days for a *w/p* of 0.40) as a function of the limestone content. First, it can be noted that as the limestone content increased, the volume of unreacted cement clinker decreased (as cement clinker was replaced with limestone); however, the volume of unreacted limestone increased. This is not surprising, as only a portion of the limestone is soluble and able to react. The predicted chemical shrinkage showed a small increase as the limestone increased from 0 to 0.86% (for this system at the DOH studied), due to the formation of monocarbonate, ettringite, and hemicarbonate phases. Note that the critical limestone content for minimum porosity ($LS_{cr}$) varied with the DOH of the system studied (for example, $LS_{cr}$ = 1.51% at a 90% DOH and $LS_{cr}$ = 0.86% at a 75% DOH). The simulations predict that the $LS_{cr}$ is the limestone content at which maximum ettringite and hemicarbonate formation occur. As the limestone content increases (for example, to levels

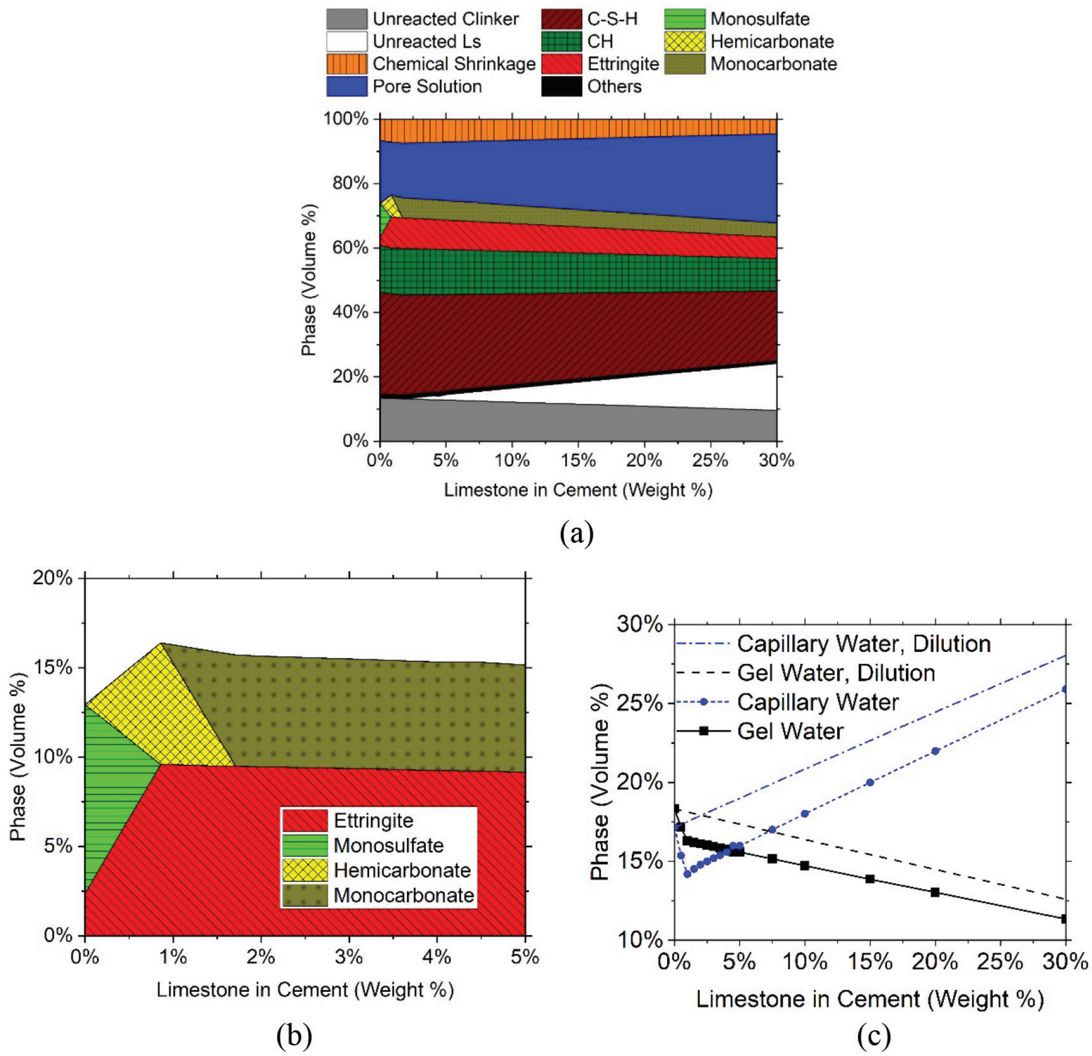

(a)

(b)

(c)

*Fig. 3—Plots of paste with* w/p *of 0.40 at 75% DOH: (a) phase composition; (b) detailed look at volume of ettringite, monosulfate, hemicarbonate, and monocarbonate; and (c) gel and capillary pores. (Note: Black dashed line and blue dash-dot line are visual guides to show influence of simple dilution without limestone reactions; full-color PDF available at www.concrete.org.)*

greater than $LS_{cr}$ = 0.86%), the chemical shrinkage then decreases as less clinker has reacted, forming fewer reaction products (Note: there is less unreacted clinker, but this is due to the powder having less clinker and more limestone as the limestone increases).

It should also be noted that in general, the resistivity of the pore solution of the PLC system is approximately 0.20 Ω·m for the 0% limestone system and increases to 0.26 Ω·m for the 30% limestone due to the dilution of the alkali content of the clinker and an increase in the volume of the pore solution.

Figure 3(b) focuses on the primary difference in the volume-specific reaction products (ettringite, monosulfate, hemicarbonate, and monocarbonate). For systems without limestone, both ettringite and monosulfate formed. However, as limestone was added, the monosulfate was replaced by the formation of an increased volume of ettringite and hemicarbonate. Hemicarbonate has a greater volume than monosulfate. The changes in the products that form, however, can result in a change in the pore volume, with these phases representing approximately 13% of the paste when there is no limestone replacement, 17% of the phases at 0.86% limestone replacement, and 11% of the paste when 30% limestone replacement occurs. The volume of phases in Fig. 3(b) (as well as early-age reactions) is sensitive to the volume of sulfate in the system. The volume of the products increases with sulfate concentration, with a reacted phase volume of ~13%, 17%, and 19% for 1, 2.6, and 3.5% $SO_3$, respectively.

Figure 3(c) illustrates the volume fraction of the associated gel water and capillary water of this system. As the limestone increased, the gel water initially decreased due to the water in the structure of the carbonate and ettringite phases.[67,68,76] At the same time, the capillary porosity decreased due to the increase in the volume of the phases, as shown in Fig. 3(a). At higher concentrations of limestone, the gel porosity decreased due to a reduction in the volume of gel present.

Figure 4 illustrates the porosity for systems with different *w/p* (at the same DOH: 75%), and, as one would anticipate, the porosity increased with an increase in the *w/p*. For comparison, porosity is also plotted for systems where 0.86% of the clinker was replaced with limestone. When limestone was added, the porosity was lower for the same *w/p* due to the formation of the hemicarbonate and monocarbonate products discussed in the previous section. Considering equivalent porosity, a system without limestone has an equivalent *w/p* that is approximately 0.07 greater than the system with 0.86% limestone. This is important as the *w/p* is often thought of as an indirect measure of the porosity, strength, or durability of a system.[15,16] As one may expect, at lower *w/p* (typically <0.30), the difference between these lines diminishes as the capillary pores begin to fill completely, leaving only gel pores in the system. In the following section of the paper, the addition of reactive alumina is discussed, where this reduction in porosity is even greater.

## Synergistic combination of limestone and reactive alumina

The previous section focused on systems consisting of water, cement, and limestone. This section will describe the impacts of adding SCMs that contain reactive alumina. Previous research has shown that limestone and alumina behave synergistically,[9,12,77-79] and this work attempts to quantify their potential impact on transport. As a reminder, the alumina used in the simulations was 100% reactive; however, in practice, this may include SCMs such as calcined clay, slag, or fly ash, all with varying DOR* and other chemical compounds. Figure 5(a) illustrates when 2.5% reactive alumina is added to the system, and Fig. 5(b) illustrates when the reactive alumina is increased to 7.5%. A few observations can be made. First, the addition of reactive alumina causes a greater limestone reaction. Second, a greater volume of hemicarbonate and monocarbonate forms, resulting in a substantial reduction in porosity. Third, the limestone that corresponds to the lowest porosity increases from 0.86% to nearly 5%. Finally, the amount of CH that remains in the system decreases due to the pozzolanic reaction of the $Al_2O_3$, until nearly no CH remains in the 7.5% alumina system. Note that when CH is available in the system, the $Al_2O_3$ reacts to form ettringite and carboaluminates, and when CH is depleted, the $Al_2O_3$ reacts to form strätlingite; both these reactions reduce the porosity. The reduction in porosity is illustrated in Fig. 1. It may be noted that the choice of replacement of 15% clinker with limestone in PLC systems is to match the compressive strength at 0% limestone, similar to what is shown by Matschei et al.[6,7] and Bharadwaj et al.[9]

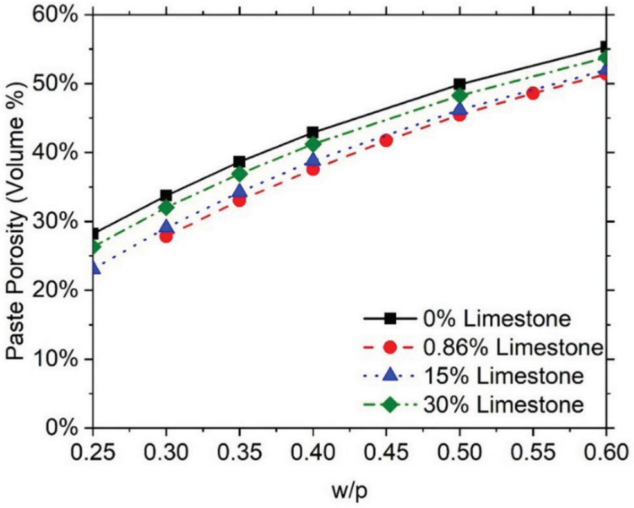

*Fig. 4—Plot of porosity and* w/p *of systems without limestone, and with 0.86, 15, and 30% limestone (75% DOH).*

## Reaction products, pore connectivity, and formation factor

While plots like Fig. 1 relating porosity and compressive strength have been used, Fig. 6 illustrates a similar plot comparing the porosity, pore connectivity, and formation factor. Similar to the way the gel-space ratio was used for compressive strength, the connectivity estimate proposed by Bharadwaj et al.[46] is used here as described earlier. First, porosity decreases with limestone and limestone + alumina, as discussed earlier. Second, a decrease in connectivity occurs due to the greater proportion of gel porosity in the total porosity. The formation factor (and resistivity) is inversely proportional to the product of porosity and connectivity, which magnifies the effects that the limestone and limestone + alumina may have on transport. This

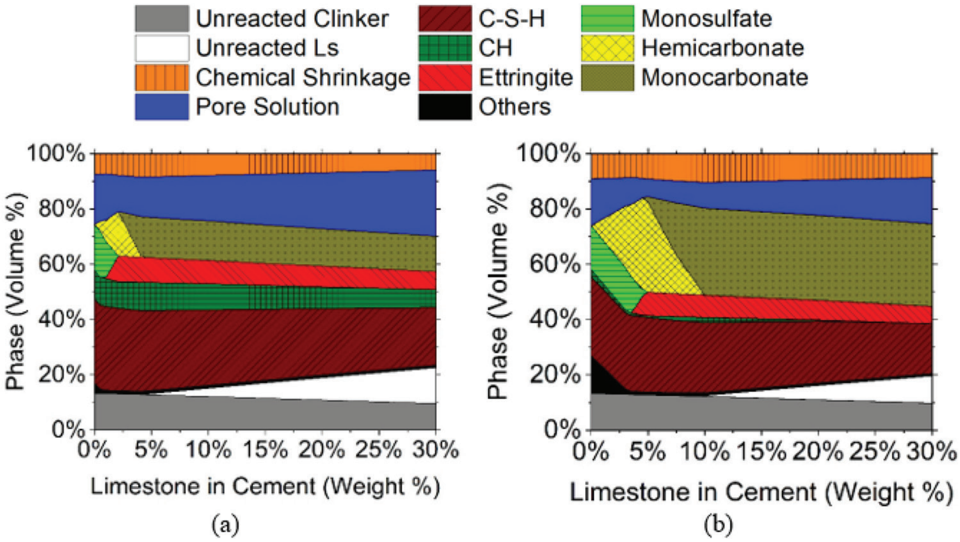

*Fig. 5—Plots of unreacted and reacted phases of paste with* w/p *of 0.40 containing: (a) 2.5%; and (b) 7.5% reactive limestone at degree of hydration of 75%. (Reminder: 0% is shown in Fig. 3(a).)*

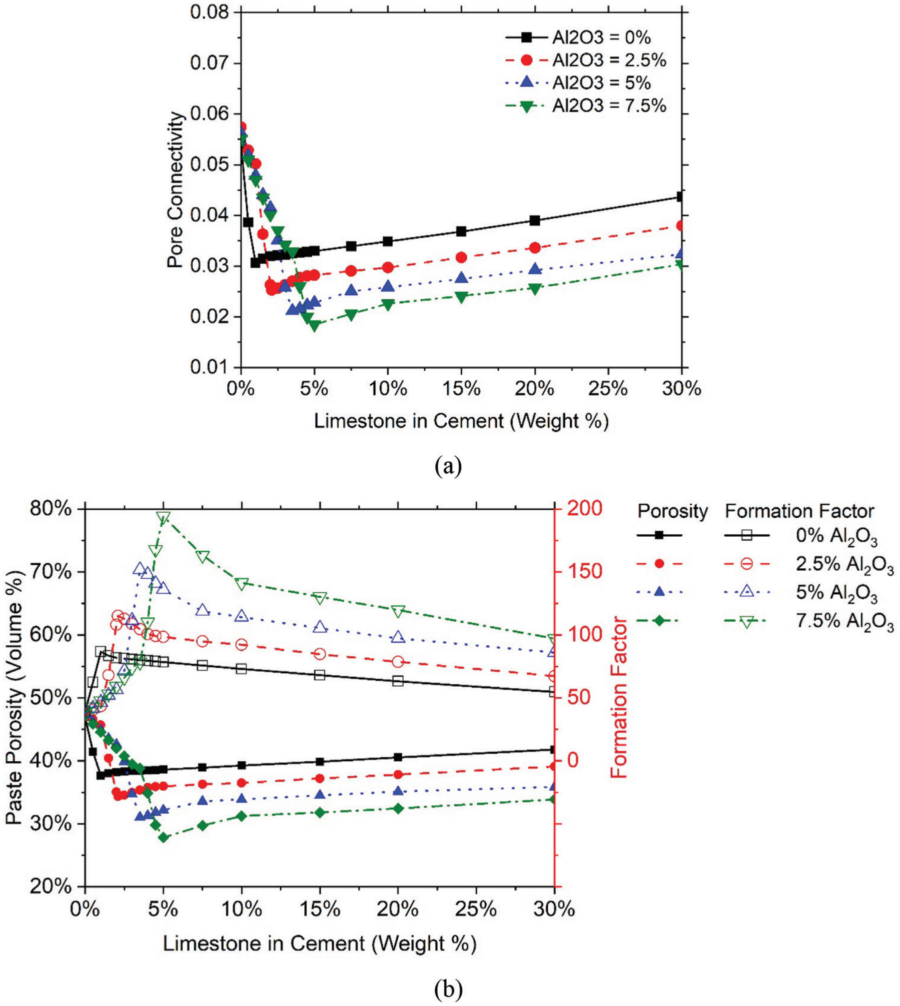

(a)

(b)

*Fig. 6—Plot of formation factor (open symbols) and porosity (closed symbols).*

is consistent with findings that pore refinement of SCMs results in a two- to six-times increase in the resistivity.[40,42,46]

## Comparing historical OPC, modern OPC, and PLC

The pioneering work by Feret,[14] Abrams,[13] and Powers and Brownyard[18,80] was performed on systems without limestone. Those studies, and others of the time, form the basis of many of the standards, specifications, and rules of thumb in the construction industry.[15] Brouwers[81,82] extended some of the calculations in the Powers and Brownyard model to ideal systems containing $C_3A + CaCO_3$; however, it does not appear that his work directly impacted specifications. This work suggests that the baseline values associated with these *w*/*p* may have inadvertently shifted when limestone was initially added to cement in 2004[83] (for example, Fig. 4). While the addition of limestone to ASTM C150 cements after 2004 was nearly always conservative (that is, higher compressive strength), the impact that this change may have had is important to understand. For example, when the *w*/*p* was introduced to mixture design procedures and code limits, this predominately corresponds to cement without limestone.[84-89] When limestone was added, the overall performance may have improved for the same *w*/*p* due to the porosity reductions.

Figure 7 illustrates one example of the measured bulk resistivity for one cementitious system (made using the cement illustrated earlier in the paper, where the OPC had a limestone content of 2.02% and the PLC had a limestone content of 8.42%). Note that because the resistivity of the pore solution was relatively constant, as described earlier ($\rho_{ps}$ = 0.20 Ω·m), the bulk resistivity was used in this plot (instead of the formation factor). First, the cement used for the simulations shown in Fig. 6[36] was based on commercially produced OPC and PLC (that is, the sulfate and grind may also have changed). To start, the OPC shown has a formation factor that is approximately 70 to 85% greater than what would be expected from this same clinker if it did not contain limestone. This implies that prior to 2004, the formation factor of a historical OPC concrete would have been lower. Second, the formation factor of concrete made with the PLC (13% limestone; $F = 97$ at a $w/p = 0.42$) is 35% higher than the formation factor of the concrete without limestone ($F = 68$ at a $w/p = 0.42$). Third, the low-*w*/*p* mixtures are more dramatically impacted by the limestone, as they have a relatively smaller capillary pore volume. It is often popular to perform tests comparing the performance of the ASTM C150 OPC (as produced today) and the ASTM C595 PLC; however, it may be prudent to examine this practice carefully because, as pointed out earlier, the values of the

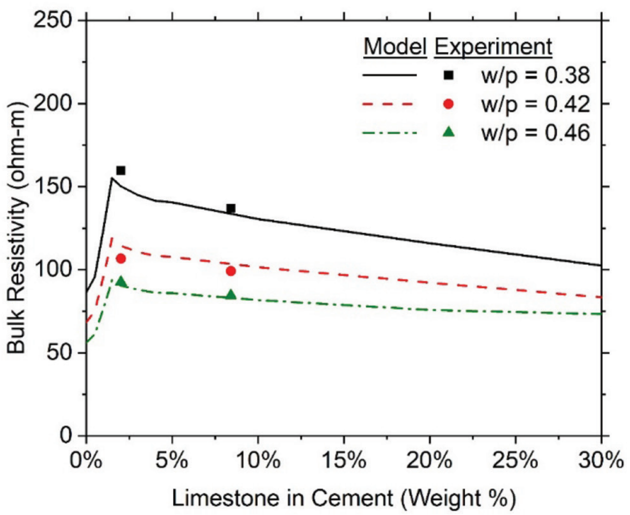

*Fig. 7—Illustration of change in apparent formation factor as function of limestone content.*

OPC may have changed over time and the reference value may be very sensitive to the amount of limestone used for the OPC cement. The formation factor at 1.15% limestone is 120 (at a *w*/*p* = 0.42, approximately 76% greater than the 0% limestone), primarily due to the change in connectivity, as the change in porosity would only account for a 15% increase. Note that the discussion in this paper is limited in scope to the PLCs produced in the United States, as the focus is on ASTM standards and U.S. specifications; however, the concepts in this paper may be applied to the PLCs produced in other regions as well.

### Comparing OPC and PLC: role of *w/p* and SCMs

Figure 8 provides a plot of the formation factor as a function of limestone and *w*/*p* for three systems, with Fig. 8(a) and (b) having 0% alumina, and Fig. 8(c) having 5% alumina. Increasing the *w*/*p* results in a reduction in the formation factor (for example, a system with a higher diffusion coefficient or permeability coefficient). Increasing the limestone results in an increase in the formation factor at low limestone levels, which decreases at higher limestone concentrations due to the carboaluminates, as previously discussed. It is, however, interesting to note that the benefit of limestone addition changes as the *w*/*p* changes. At very low *w*/*p*, the capillary porosity can be minimized, leading to conduction primarily through the gel pores, which results in a somewhat constant formation factor with limestone addition (for example, ~300 to 350). This is especially clear for systems with reactive alumina (Fig. 8(b)). An increase in the *w*/*p* can increase the volume of capillary pores; however, this depends on the limestone replacement level. As such, the formation factors remain relatively high for systems with limestones between 1 and 4%, for example (due to the relatively low volume of capillary pores in the system). When the *w*/*p* is raised to values above 0.45 or 0.50, the relative impact of the limestone addition is reduced (as a greater number of the pores are capillary pores). The impact of these changes increases with the addition of the reactive alumina phase, as discussed earlier in this paper.

The practical implications of this observation can be discussed by examining results from the Barrett et al.[36,37] study. First, it was reported that the relative resistivity ratio (RRR, resistivity of the PLC/OPC, which is very similar to a relative formation factor) was ±20% for a *w*/*p* of 0.38 at 91 days. As mentioned earlier, the RRR is highly dependent on the limestone concentration of the OPCs, which was generally between 0.5 and 2.9% using thermogravimetric analysis (TGA). The systems that had a relatively lower PLC performance (RRR of 0.8) had limestone additions of 2.0 and 0.9% in the OPC system, while the systems that showed relatively higher PLC performance (RRR of approximately 1.2) had lower limestone additions (0.5% in the OPC), which would have a lower formation factor. As the *w*/*p* increased to 0.42, the RRR was between 0.8 and 1.05, and a further increase in the *w*/*p* to 0.46 resulted in an RRR of 0.8 for all mixtures (one mixture was higher). This confirms that the initial limestone level of the OPC impacts the results. Further, it shows that at lower *w*/*p*, the carboaluminate phases may be more impactful in reducing the capillary porosity and formation factor. The mixtures containing fly ash showed little improvement for the water-cementitious materials ratio (*w*/*cm*) of 0.38 (presumably due to the system consisting of a greater gel volume); however, a dramatic increase in the RRR was observed for the *w*/*cm* of 0.42, and a lesser increase in the RRR was observed for the *w*/*cm* of 0.46. Again, this speaks to the refinement of the resulting pore structure. Research on systems with SCMs by Barrett et al.,[36,37] Ramanathan et al.,[90] and Choudhary et al.[40,41] all demonstrated that the use of SCMs resulted in a two- to six-times improvement in resistivity.

While these studies use the model to approximate previous experiments, it would be beneficial to conduct studies using clinker in which the limestone and alumina sources are intentionally and systematically varied and the resulting hydration phases are monitored. Further, while this paper used previously established calculations of connectivity based on SCM addition and pore refinement, this approach should be further validated based on the sulfate and carboaluminate phases described herein.

## SUMMARY AND CONCLUSIONS

Limestone is being increasingly used as a replacement for clinker in cementitious binders. This paper employs a thermodynamics-based model to assess the impact of limestone replacement of clinker on porosity. The presence of limestone promotes the formation of ettringite, hemicarbonate, and monocarbonate, which reduce porosity at low limestone replacement levels. For example, a paste with a water-powder ratio (*w*/*p*) of 0.40 has 43% porosity for 0% limestone and 36% porosity for 1.15% limestone (a 7% reduction in porosity). As the limestone replacement level is further increased, the reduction in porosity is offset by dilution, resulting in an increase in porosity. For example, an increase of approximately 0.2% porosity is observed per percent of limestone added due to dilution. The reductions in porosity are accompanied by changes in pore connectivity and an increase in the formation factor (or resistivity). This implies that adding limestone would be expected to impact transport more than it does strength. The combination of

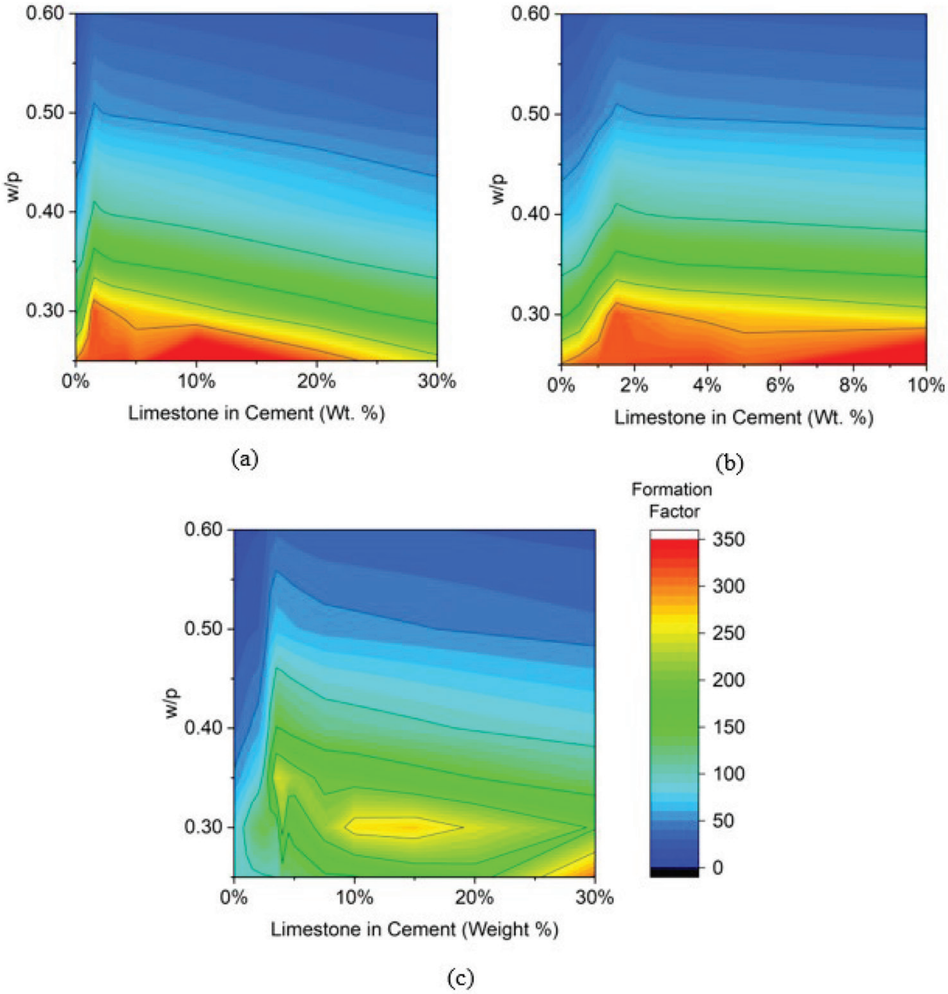

*Fig. 8—Formation factor as function of* w/p *and limestone replacement level: (a) PLC paste; (b) PLC paste (same as (a), x-axis zoomed to 10% limestone content); and (c) PLC + 5% $Al_2O_3$ paste.*

limestone and reactive alumina is synergistic (that is, limestone and alumina react), resulting in greater volumes of hemicarbonate and monocarbonate. This synergistic effect further reduces the porosity at low limestone levels and reduces the pore connectivity as the relative proportion of gel pores increases.

Examples are provided to compare the analytical results with experimental measurements. It is suggested that, because prior to 2004, the ordinary portland cement (OPC) in North America did not contain limestone, the baseline performance associated with OPC (*w*/*p* or resistivity) may have inadvertently changed as limestone was added to OPC. This can result in ASTM C150 cement produced after 2004 demonstrating improved performance as compared to the same cement produced before limestone addition. This needs to be carefully considered when comparing the results of modern cement to historical cement (systems from before 2004). Further, the use of a relative resistivity ratio (RRR; for example, the resistivity of the portland-limestone cement [PLC] to the resistivity of the OPC) may be complicated by the fact that the volume of limestone in the OPC varies. Further, the OPC made after 2004 may not represent values that are consistent with historical cements prior to 2004.

Finally, it is suggested that the relative performance of a PLC (as determined using factors such as the RRR) can be influenced by the *w*/*p* of the baseline mixture. This has implications for concrete producers and standardization bodies. Very low *w*/*p* have a formation factor that is dominated by conduction through the gel pores, and as such, the PLC does not substantially impact the performance. Moderate *w*/*p* may be more impacted by limestone addition due to changes in the relatively small volume of capillary pores with the ettringite, hemicarbonate, and monocarbonate phases that change connectivity (and formation factor or resistivity). Higher-*w*/*p* mixtures demonstrate some impact of limestone on the porosity and connectivity, but it is lower than in moderate-*w*/*p* mixtures due to the proportionally higher capillary pore volume and higher connectivity.

## AUTHOR BIOS

**W. Jason Weiss**, *FACI, is the Miles Lowell and Margaret Watt Edwards Distinguished Chair in Engineering in the School of Civil and Construction Engineering at Oregon State University, Corvallis, OR. He is a member of the ACI Technical Activities Committee (TAC).*

**O. Burkan Isgor**, *FACI, is a Professor in the School of Civil and Construction Engineering at Oregon State University. His research interests include corrosion of steel in concrete, service life modeling of concrete, and thermodynamic and reactive-transport modeling of cementitious systems.*

*ACI member* **Keshav Bharadwaj** *is an Assistant Professor in the Department of Civil Engineering at the Indian Institute of Science, Bangalore, Bengaluru, Karnataka, India. He was previously a postdoctoral scholar at Oregon State University. His research interests include thermodynamic modeling, reactivity, and transport in cementitious systems.*

## ACKNOWLEDGMENTS

The authors wish to express their gratitude and sincere appreciation to the California Department of Transportation and the University Transportation Center for Durable and Resilient Transportation Infrastructure (Grant No. 69A3552348339) for supporting this work.

## REFERENCES

1. Rogue, R. H., and Lerch, W., "Hydration of Portland Cement Compounds," *Industrial & Engineering Chemistry*, V. 26, No. 8, 1934, pp. 837-847. doi: 10.1021/ie50296a007

2. Hawkins, P.; Tennis, P.; and Detwiler, R., "The Use of Limestone in Portland Cement: A State-of-the-Art Review," Engineering Bulletin 227, American Cement Association, Washington, DC, 2005, 41 pp.

3. Tennis, P. D.; Thomas, M. D. A.; and Weiss, W. J., "State-of-the-Art Report on Use of Limestone in Cements at Levels of up to 15%," PCA R&D SN3148, American Cement Association, Washington, DC, 2011, 78 pp.

4. ACA, "Reducing Carbon at the Cement Plant," American Cement Association, Washington, DC, 2023.

5. Nadelman, E. I., and Kurtis, K. E., "Application of Powers' Model to Modern Portland and Portland Limestone Cement Pastes," *Journal of the American Ceramic Society*, V. 100, No. 9, Sept. 2017, pp. 4219-4231. doi: 10.1111/jace.14913

6. Matschei, T.; Lothenbach, B.; and Glasser, F. P., "The Role of Calcium Carbonate in Cement Hydration," *Cement and Concrete Research*, V. 37, No. 4, Apr. 2007, pp. 551-558. doi: 10.1016/j.cemconres.2006.10.013

7. Matschei, T.; Herfort, D.; Lothenbach, B.; and Glasser, F. P., "Relationships of Cement Paste Mineralogy to Porosity and Mechanical Properties," *Proceedings of MHM 2007: International Conference on Modelling of Heterogeneous Materials with Applications in Construction and Biomedical Engineering*, M. Jirásek, Z. Bittnar, and H. Mang, eds., Prague, Czech Republic, June 2007, pp 262-263.

8. Panesar, D. K., and Zhang, R., "Performance Comparison of Cement Replacing Materials in Concrete: Limestone Fillers and Supplementary Cementing Materials – A Review," *Construction and Building Materials*, V. 251, Aug. 2020, Article No. 118866. doi: 10.1016/j.conbuildmat.2020.118866

9. Bharadwaj, K.; Isgor, O. B.; and Weiss, W. J., "Supplementary Cementitious Materials in Portland-Limestone Cements," *ACI Materials Journal*, V. 119, No. 2, Mar. 2022, pp. 141-154. doi: 10.14359/51734356

10. Lothenbach, B.; Le Saout, G.; Gallucci, E.; and Scrivener, K., "Influence of Limestone on the Hydration of Portland Cements," *Cement and Concrete Research*, V. 38, No. 6, June 2008, pp. 848-860. doi: 10.1016/j.cemconres.2008.01.002

11. De Weerdt, K.; Haha, M. B.; Le Saout, G.; Kjellsen, K. O.; Justnes, H.; and Lothenbach, B., "Hydration Mechanisms of Ternary Portland Cements Containing Limestone Powder and Fly Ash," *Cement and Concrete Research*, V. 41, No. 3, Mar. 2011, pp. 279-291. doi: 10.1016/j.cemconres.2010.11.014

12. De Weerdt, K.; Kjellsen, K. O.; Sellevold, E.; and Justnes, H., "Synergy Between Fly Ash and Limestone Powder in Ternary Cements," *Cement and Concrete Composites*, V. 33, No. 1, Jan. 2011, pp. 30-38. doi: 10.1016/j.cemconcomp.2010.09.006

13. Abrams, D. A., "Design of Concrete Mixtures," Bulletin 1, Structural Materials Research Laboratory, Lewis Institute, Chicago, IL, May 1919, 20 pp.

14. Feret, M., "On the Compactness of Hydraulic Mortars," Annales des Ponts et Chaussées, Mémoires et Documents, V. 4, Série 7, Semestre 2, 1892, pp. 5-164. (in French)

15. Mindess, S.; Young, J. F.; and Darwin, D., *Concrete*, second edition, Pearson Education, Inc., Upper Saddle River, NJ, 2003, 644 pp.

16. Mehta, P. K., and Monteiro, P. J. M., *Concrete: Microstructure, Properties, and Materials*, third edition, McGraw-Hill Professional, New Delhi, India, 2006, 675 pp.

17. Feldman, R. F., and Sereda, P. J., "Written Discussion of 'Structures and Physical Properties of Cement Paste' by George J. Verbeck and Richard H. Helmuth (Portland Cement Association, Skokie, Ill, U.S.A.)," *Proceedings of the 5th International Symposium on the Chemistry of Cement*, Tokyo, Japan, 1968, pp. 36-44.

18. Powers, T. C., "Structure and Physical Properties of Hardened Portland Cement Paste," *Journal of the American Ceramic Society*, V. 41, No. 1, Jan. 1958, pp. 1-6. doi: 10.1111/j.1151-2916.1958.tb13494.x

19. Bentz, D. P., "Modeling the Influence of Limestone Filler on Cement Hydration Using CEMHYD3D," *Cement and Concrete Composites*, V. 28, No. 2, Feb. 2006, pp. 124-129. doi: 10.1016/j.cemconcomp.2005.10.006

20. Holmes, N.; Kelliher, D.; and Tyrer, M., "Simulating Cement Hydration Using HYDCEM," *Construction and Building Materials*, V. 239, Apr. 2020, Article No. 117811. doi: 10.1016/j.conbuildmat.2019.117811

21. Chiker, T., and Aggoun, S., "Limestone Powder and Silica Fume Performance on Slag-Blended PLC Plain and Self-Consolidating Mortars Properties," *Archives of Civil and Mechanical Engineering*, V. 24, No. 1, Feb. 2024, Article No. 26. doi: 10.1007/s43452-023-00805-5

22. Cost, V. T.; Howard, I. L.; and Shannon, J., "Improving Concrete Sustainability and Performance with Use of Portland–Limestone Cement Synergies," *Transportation Research Record: Journal of the Transportation Research Board*, V. 2342, No. 1, Jan. 2013, pp. 26-34. doi: 10.3141/2342-04

23. Bentz, D. P.; Sato, T.; de la Varga, I.; and Weiss, W. J., "Fine Limestone Additions to Regulate Setting in High Volume Fly Ash Mixtures," *Cement and Concrete Composites*, V. 34, No. 1, Jan. 2012, pp. 11-17. doi: 10.1016/j.cemconcomp.2011.09.004

24. Tennis, P. D., "Chemical and Physical Characteristics of US Hydraulic Cements: 2014," PCA R&D SN3284, American Cement Association, Washington, DC, 2016, 32 pp.

25. Bucher, B.; Radlinska, A.; and Weiss, J., "Preliminary Comments on Shrinkage and Shrinkage Cracking Behavior of Cement Systems that Contain Limestone," NRMCA Concrete Technology Forum: Focus on Sustainable Development, Denver, CO, May 2008, 8 pp.

26. Bucher, B. E., "Shrinkage and Shrinkage Cracking Behavior of Cement Systems Containing Ground Limestone, Fly Ash, and Lightweight Synthetic Particles," master's thesis, Purdue University, West Lafayette, IN, 2009.

27. Barrett, T.; Sun, H.; Villani, C.; Barcelo, L.; and Weiss, J., "Early-Age Shrinkage Behavior of Portland Limestone Cement," *Concrete International*, V. 36, No. 2, Feb. 2014, pp. 51-57.

28. Sellevold, E. J.; Bager, D. H.; Klitgaard Jensen, E.; and Knudsen, T., "Silica Fume Cement Paste—Hydration and Pore Structure," 1982, pp. 19-50.

29. De la Varga, I.; Castro, J.; Bentz, D. P.; Zunino, F.; and Weiss, J., "Evaluating the Hydration of High Volume Fly Ash Mixtures Using Chemically Inert Fillers," *Construction and Building Materials*, V. 161, Feb. 2018, pp. 221-228. doi: 10.1016/j.conbuildmat.2017.11.132

30. Brookbanks, P., "Properties of Fresh Concrete," *Performance of Limestone-Filled Cements: Proceedings of a Seminar of the Joint BRE/BCA/Cement Industry Working Party, Held at the Building Research Establishment, Garston, on 28 November 1989*, Building Research Establishment, Garston, Watford, UK, 1993.

31. Schmidt, M., "Cement with Interground Additives - Capabilities and Environmental Relief, Part 1," *ZKG International, Edition B*, V. 45, No. 2, 1992, pp. 64-69.

32. Schmidt, M., "Cement with Interground Additives – Capabilities and Environmental Relief, Part 2," *ZKG International, Edition B*, V. 45, No. 6, 1992, pp. 296-301.

33. Moir, G., and Kelham, S., "Durability 1," *Performance of Limestone-Filled Cements: Proceedings of a Seminar of the Joint BRE/BCA/Cement Industry Working Party, Held at the Building Research Establishment, Garston, on 28 November 1989*, Building Research Establishment, Garston, Watford, UK, 1993.

34. Tsivilis, S.; Voglis, N.; and Photou, J., "A Study of the Intergrinding of Clinker and Limestone," *Minerals Engineering*, V. 12, No. 7, July 1999, pp. 837-840. doi: 10.1016/S0892-6875(99)00068-0

35. Tezuka, Y.; Gomes, D. Jr.; Martins, J. M.; and Djanikian, J. G., "Durability Aspects of Cements with High Limestone Filler Content," *Proceedings of the 9th International Congress on the Chemistry of Cement*, New Delhi, India, 1992, pp. 53-59.

36. Barrett, T. J., "Performance of Portland Limestone Cements: Cements Designed to Be More Sustainable That Include up to 15% Limestone Addition," master's thesis, Purdue University, West Lafayette, IN, 2013.

37. Barrett, T. J.; Sun, H.; Nantung, T.; and Weiss, W. J., "Performance of Portland Limestone Cements," *Transportation Research Record: Journal of the Transportation Research Board*, V. 2441, No. 1, Jan. 2014, pp. 112-120. doi: 10.3141/2441-15

38. Muni, H.; Dhandapani, Y.; Vignesh, K.; and Santhanam, M., "Anomalous Early Increase in Concrete Resistivity with Calcined Clay Binders," *Calcined Clays for Sustainable Concrete: Proceedings of the 3rd International Conference on Calcined Clays for Sustainable Concrete*, S. Bishnoi, ed., Springer, Singapore, 2020, pp. 749-757.

39. Garcia, J. E.; Tiburzi, N. B.; Folliard, K. J.; and Drimalas, T., "Mechanical Properties and Electrical Resistivity of Portland Limestone Cement Concrete Systems Containing Greater than 15% Limestone and Supplementary Cementitious Materials," *Cement*, V. 8, June 2022, Article No. 100026. doi: 10.1016/j.cement.2022.100026

40. Choudhary, A.; Ghantous, R. M.; Bharadwaj, K.; Opdahl, O. H.; Isgor, O. B.; and Weiss, W. J., "Electrical and Transport Properties of Cement Mortar Made Using Portland Limestone Cement," *Advances in Civil Engineering Materials*, V. 11, No. 1, 2022, pp. 263-279. doi: 10.1520/ACEM20210119

41. Choudhary, A., "The Pozzolanic Reactivity Test and the Properties of Portland Limestone Cement," PhD thesis, Oregon State University, Corvallis, OR, 2021.

42. Bharadwaj, K.; Chopperla, K. S. T.; Choudhary, A.; Glosser, D.; Ghantous, R. M.; Vasudevan, G. D.; Ideker, J. H.; Isgor, O. B.; Trejo, D.; and Weiss, W. J., "CALTRANS: Impact of the Use of Portland-Limestone Cement on Concrete Performance as Plain or Reinforced Material: Final Report," Oregon State University, Corvallis, OR, 2021, 320 pp.

43. Qiao, C.; Moradllo, M. K.; Hall, H.; Ley, M. T.; and Weiss, W. J., "Electrical Resistivity and Formation Factor of Air-Entrained Concrete," *ACI Materials Journal*, V. 116, No. 3, May 2019, pp. 85-93.

44. Archie, G. E., "The Electrical Resistivity Log as an Aid in Determining Some Reservoir Characteristics," *Transactions of the AIME*, V. 146, No. 1, Dec. 1942, pp. 54-62.

45. Bharadwaj, K., "Towards the Development of Performance-Based Concrete Mixtures Made with Modern Cementitious Materials Using Thermodynamic Modeling," PhD dissertation, Oregon State University, Corvallis, OR, 2022, 327 pp.

46. Bharadwaj, K.; Ghantous, R. M.; Sahan, F.; Isgor, O. B.; and Weiss, W. J., "Predicting Pore Volume, Compressive Strength, Pore Connectivity, and Formation Factor in Cementitious Pastes Containing Fly Ash," *Cement and Concrete Composites*, V. 122, Sept. 2021, Article No. 104113. doi: 10.1016/j.cemconcomp.2021.104113

47. Bharadwaj, K.; Glosser, D.; Moradllo, M. K.; Isgor, O. B.; and Weiss, W. J., "Toward the Prediction of Pore Volumes and Freeze-Thaw Performance of Concrete Using Thermodynamic Modelling," *Cement and Concrete Research*, V. 124, Oct. 2019, Article No. 105820. doi: 10.1016/j.cemconres.2019.105820

48. Matyka, M.; Khalili, A.; and Koza, Z., "Tortuosity-Porosity Relation in Porous Media Flow," *Physical Review E*, V. 78, No. 2, Aug. 2008, Article No. 026306. doi: 10.1103/PhysRevE.78.026306

49. Garboczi, E. J., "Permeability, Diffusivity, and Microstructural Parameters: A Critical Review," *Cement and Concrete Research*, V. 20, No. 4, July 1990, pp. 591-601. doi: 10.1016/0008-8846(90)90101-3

50. Snyder, K. A., "The Relationship Between the Formation Factor and the Diffusion Coefficient of Porous Materials Saturated with Concentrated Electrolytes: Theoretical and Experimental Considerations," *Concrete Science and Engineering*, V. 3, No. 12, Dec. 2001, pp. 216-224.

51. Christensen, B. J.; Coverdale, T.; Olson, R. A.; Ford, S. J.; Garboczi, E. J.; Jennings, H. M.; and Mason, T. O., "Impedance Spectroscopy of Hydrating Cement-Based Materials: Measurement, Interpretation, and Application," *Journal of the American Ceramic Society*, V. 77, No. 11, Nov. 1994, pp. 2789-2804. doi: 10.1111/j.1151-2916.1994.tb04507.x

52. Whittington, H. W.; McCarter, J.; and Forde, M. C., "The Conduction of Electricity Through Concrete," *Magazine of Concrete Research*, V. 33, No. 114, Mar. 1981, pp. 48-60. doi: 10.1680/macr.1981.33.114.48

53. Lothenbach, B.; Matschei, T.; Möschner, G.; and Glasser, F. P., "Thermodynamic Modelling of the Effect of Temperature on the Hydration and Porosity of Portland Cement," *Cement and Concrete Research*, V. 38, No. 1, Jan. 2008, pp. 1-18. doi: 10.1016/j.cemconres.2007.08.017

54. Lothenbach, B., and Winnefeld, F., "Thermodynamic Modelling of the Hydration of Portland Cement," *Cement and Concrete Research*, V. 36, No. 2, Feb. 2006, pp. 209-226. doi: 10.1016/j.cemconres.2005.03.001

55. Lothenbach, B., and Zajac, M., "Application of Thermodynamic Modelling to Hydrated Cements," *Cement and Concrete Research*, V. 123, Sept. 2019, Article No. 105779. doi: 10.1016/j.cemconres.2019.105779

56. Kulik, D. A.; Wagner, T.; Dmytrieva, S. V.; Kosakowski, G.; Hingerl, F. F.; Chudnenko, K. V.; and Berner, U. R., "GEM-Selektor Geochemical Modeling Package: Revised Algorithm and GEMS3K Numerical Kernel for Coupled Simulation Codes," *Computational Geosciences*, V. 17, No. 1, Feb. 2013, pp. 1-24. doi: 10.1007/s10596-012-9310-6

57. Wagner, T.; Kulik, D. A.; Hingerl, F. F.; and Dmytrieva, S. V., "GEM-Selektor Geochemical Modeling Package: TSolMod Library and Data Interface for Multicomponent Phase Models," *The Canadian Mineralogist*, V. 50, No. 5, Oct. 2012, pp. 1173-1195. doi: 10.3749/canmin.50.5.1173

58. Parrot, L. J., and Killoh, D. C., "Prediction of Cement Hydration," *Proceedings of the British Ceramic Society*, V. 35, 1984, pp. 41-53.

59. Glosser, D.; Isgor, O. B.; and Weiss, W. J., "Non-Equilibrium Thermodynamic Modeling Framework for Ordinary Portland Cement/Supplementary Cementitious Material Systems," *ACI Materials Journal*, V. 117, No. 6, Nov. 2020, pp. 111-123.

60. Isgor, O. B.; Ideker, J.; Trejo, D.; Weiss, J.; Bharadwaj, K.; Choudhary, A.; Chopperla, K. S. T.; Glosser, D.; and Vasudevan, G., "Performance-Based Mixture Proportioning of Concrete Incorporating Off-Spec Fly Ash: Mixture Proportioning Method Development and Validation," Electric Power Research Institute (EPRI), Inc., Palo Alto, CA, 2020, 78 pp.

61. Isgor, O. B., and Weiss, W. J., "Correction to: A Nearly Self-Sufficient Framework for Modelling Reactive-Transport Processes in Concrete," *Materials and Structures*, V. 52, No. 6, Dec. 2019, Article No. 130. doi: 10.1617/s11527-019-1422-1

62. Bharadwaj, K.; Isgor, O. B.; and Weiss, W. J., "Pozzolanic Reactivity of Supplementary Cementitious Materials," *ACI Materials Journal*, V. 120, No. 4, July 2023, pp. 63-76.

63. Glosser, D.; Choudhary, A.; Isgor, O. B.; and Weiss, W. J., "Investigation of Reactivity of Fly Ash and Its Effect on Mixture Properties," *ACI Materials Journal*, V. 116, No. 4, July 2019, pp. 193-200.

64. Bharadwaj, K.; Isgor, O. B.; and Weiss, W. J., "A Simplified Approach to Determine the Pozzolanic Reactivity of Commercial Supplementary Cementitious Materials," *Concrete International*, V. 44, No. 1, Jan. 2022, pp. 27-32.

65. Glosser, D.; Suraneni, P.; Isgor, O. B.; and Weiss, W. J., "Estimating Reaction Kinetics of Cementitious Pastes Containing Fly Ash," *Cement and Concrete Composites*, V. 112, Sept. 2020, Article No. 103655. doi: 10.1016/j.cemconcomp.2020.103655

66. Lothenbach, B.; Kulik, D. A.; Matschei, T.; Balonis, M.; Baquerizo, L.; Dilnesa, B.; Miron, G. D.; and Myers, R. J., "Cemdata18: A Chemical Thermodynamic Database for Hydrated Portland Cements and Alkali-Activated Materials," *Cement and Concrete Research*, V. 115, Jan. 2019, pp. 472-506. doi: 10.1016/j.cemconres.2018.04.018

67. Glosser, D.; Azad, V. J.; Suraneni, P.; Isgor, O. B.; and Weiss, W. J., "Extension of Powers-Brownyard Model to Pastes Containing Supplementary Cementitious Materials," *ACI Materials Journal*, V. 116, No. 5, Sept. 2019, pp. 205-216. doi: 10.14359/51714466

68. Azad, V. J.; Suraneni, P.; Isgor, O. B.; and Weiss, W. J., "Interpreting the Pore Structure of Hydrating Cement Phases Through a Synergistic Use of the Powers-Brownyard Model, Hydration Kinetics, and Thermodynamic Calculations," *Advances in Civil Engineering Materials*, V. 6, No. 1, Jan. 2017, pp. 1-17. doi: 10.1520/ACEM20160038

69. Bentz, D. P., and Garboczi, E. J., "Percolation of Phases in a Three-Dimensional Cement Paste Microstructural Model," *Cement and Concrete Research*, V. 21, No. 2-3, Mar.-May 1991, pp. 325-344. doi: 10.1016/0008-8846(91)90014-9

70. Sant, G.; Bentz, D.; and Weiss, J., "Capillary Porosity Depercolation in Cement-Based Materials: Measurement Techniques and Factors Which Influence Their Interpretation," *Cement and Concrete Research*, V. 41, No. 8, Aug. 2011, pp. 854-864. doi: 10.1016/j.cemconres.2011.04.006

71. Powers, T. C.; Copeland, L. E.; and Mann, H. M., "Capillary Continuity or Discontinuity in Cement Pastes," *Journal of the PCA Research and Development Laboratories*, V. 1, No. 2, May 1959, pp. 38-48.

72. Garboczi, E. J., and Bentz, D. P., "Computer Simulation of the Diffusivity of Cement-Based Materials," *Journal of Materials Science*, V. 27, No. 8, Apr. 1992, pp. 2083-2092. doi: 10.1007/BF01117921

73. Zhang, J., and Li, Z., "Application of GEM Equation in Microstructure Characterization of Cement-Based Materials," *Journal of Materials in Civil Engineering*, ASCE, V. 21, No. 11, Nov. 2009, pp. 648-656. doi: 10.1061/(ASCE)0899-1561(2009)21:11(648)

74. Georget, F.; Lothenbach, B.; Wilson, W.; Zunino, F.; and Scrivener, K. L., "Stability of Hemicarbonate Under Cement Paste-Like Conditions," *Cement and Concrete Research*, V. 153, Mar. 2022, Article No. 106692. doi: 10.1016/j.cemconres.2021.106692

75. Matschei, T.; Lothenbach, B.; and Glasser, F. P., "The AFm Phase in Portland Cement," *Cement and Concrete Research*, V. 37, No. 2, Feb. 2007, pp. 118-130. doi: 10.1016/j.cemconres.2006.10.010

76. Weiss, W. J.; Isgor, O. B.; Ideker, J. H.; Bharadwaj, K.; Ghantous, R. M.; Rajabipour, F.; Gomez, E.; Kaladharan, G.; Lan, Y.-C.; Juenger, M. C. G.; Katz, L.; Zhu, T.; Zavattieri, P.; Wang, Y.; and Innis, A., "Development of Thermodynamic and Kinetic Simulation Tools and Testing Procedures for Enhanced Durability of Concrete Containing Industrial By-Products," Oregon State University, Corvallis, OR, 2022.

77. Avet, F., and Scrivener, K., "Investigation of the Calcined Kaolinite Content on the Hydration of Limestone Calcined Clay Cement ($LC^3$)," *Cement and Concrete Research*, V. 107, May 2018, pp. 124-135. doi: 10.1016/j.cemconres.2018.02.016

78. Scrivener, K.; Martirena, F.; Bishnoi, S.; and Maity, S., "Calcined Clay Limestone Cements ($LC^3$)," *Cement and Concrete Research*, V. 114, Dec. 2018, pp. 49-56. doi: 10.1016/j.cemconres.2017.08.017

79. Sharma, M.; Bishnoi, S.; Martirena, F.; and Scrivener, K., "Limestone Calcined Clay Cement and Concrete: A State-of-the-Art Review," *Cement and Concrete Research*, V. 149, Nov. 2021, Article No. 106564. doi: 10.1016/j.cemconres.2021.106564

80. Powers, T. C., and Brownyard, T. L., "Studies of the Physical Properties of Hardened Portland Cement Paste," *ACI Journal Proceedings*, V. 43, No. 9, Titles 43-5a to 43-5g, Dec. 1946, pp. 101-992.

81. Brouwers, H. J. H., "The Work of Powers and Brownyard Revisited: Part 1," *Cement and Concrete Research*, V. 34, No. 9, Sept. 2004, pp. 1697-1716. doi: 10.1016/j.cemconres.2004.05.031

82. Brouwers, H. J. H., "The Work of Powers and Brownyard Revisited: Part 2," *Cement and Concrete Research*, V. 35, No. 10, Oct. 2005, pp. 1922-1936. doi: 10.1016/j.cemconres.2005.04.009

83. ASTM C150-04ae1, "Standard Specification for Portland Cement," ASTM International, West Conshohocken, PA, 2004, 8 pp.

84. ACI Committee 211, "Standard Practice for Selecting Proportions for Normal, Heavyweight, and Mass Concrete (ACI 211.1-91) (Reapproved 2009)," American Concrete Institute, Farmington Hills, MI, 1991, 38 pp.

85. Hover, K. C., "Concrete Mixture Proportioning with Water-Reducing Admixtures to Enhance Durability: A Quantitative Model," *Cement and Concrete Composites*, V. 20, No. 2-3, 1998, pp. 113-119. doi: 10.1016/S0958-9465(98)00002-X

86. Hover, K. C., "Concrete Design: Part II. Proportioning Water, Cement, and Air," *Civil Engineering News*, V. 10, No. 9, 1998, pp. 56-59.

87. Hover, K., "Graphical Approach to Mixture Proportioning by ACI 211.1-91," *Concrete International*, V. 17, No. 9, Sept. 1995, pp. 49-53.

88. Ozyildirim, C., and Halstead, W. J., "Optimum Mixture Proportions for Concretes Containing Fly Ash and Silica Fume," Report No. FHWA/VA-91-R21, Virginia Transportation Research Council, Charlottesville, VA, June 1991, 30 pp.

89. ACI Committee 318, "Building Code Requirements for Structural Concrete (ACI 318-08) and Commentary (ACI 318R-08)," American Concrete Institute, Farmington Hills, MI, 2008, 473 pp.

90. Ramanathan, S.; Kasaniya, M.; Tuen, M.; Thomas, M. D. A.; and Suraneni, P., "Linking Reactivity Test Outputs to Properties of Cementitious Pastes Made with Supplementary Cementitious Materials," *Cement and Concrete Composites*, V. 114, Nov. 2020, Article No. 103742. doi: 10.1016/j.cemconcomp.2020.103742

ACI MATERIALS JOURNAL TECHNICAL PAPER

Title No. 123-M15

# Rheology of Superabsorbent Polymer-Modified Magnesia for Three-Dimensional Printing

by Ala Eddin Douba, Jan Olek, and Kendra A. Erk

*This work investigated the rheological properties of pastes made from magnesia cement modified with superabsorbent polymers (SAPs), with the aim to uncover the mechanisms governing their interactions. The findings highlighted the significant improvement in static yield stress brought about by the addition of SAP, with minimal impact on dynamic flow properties. Furthermore, the incorporation of small quantities of methylcellulose was observed to amplify SAP's absorption capacity during the initial stages of hydration. This study also revealed that SAP's absorption behavior does not impede the rate at which hydration products form. In addition, the value of the critical strain can be used as a rheological indicator of SAP's degree of absorption. Overall, this investigation indicated that the incorporation of SAP was highly advantageous with respect to enhancing the rheological characteristics of magnesia cement, particularly with respect to facilitating its use in three-dimensional (3-D) printing applications.*

**Keywords:** magnesia cement; rheology; superabsorbent polymers (SAPs); three-dimensional (3-D) printing.

## INTRODUCTION

Magnesia (MgO), which has traditionally constituted 1 to 6% of typical ordinary portland cement (OPC) mixtures over the past 150 years, has not been used as the main binding material due to its weak mechanical properties and expansive hydration reaction.[1-3] However, recent interest has grown in using 100% MgO as a replacement for OPC due to the increasing demand for more sustainable cement alternatives with lower carbon footprints.[1,4,5] While cement production generates ~0.78 to 0.83 $CO_2$ tons/cement tons, MgO production through magnesite calcination generates 1.1 $CO_2$ tons/MgO tons despite the latter's lower calcination temperature.[6,7] Despite this higher initial $CO_2$ emission, MgO offers significantly higher carbon sequestration potential. The carbonation of MgO forms magnesium carbonates, which increases the material's mechanical strength and can reduce $CO_2$ emissions by up to 70% compared to OPC, making MgO an attractive option for reducing the environmental impact of concrete production.[8] Furthermore, recent research suggests that MgO can be harvested from reject brine water using carbon-neutral processes such as electrochemical harvesting through anion-exchange membranes (AEMs) and cation-exchange membranes (CEMs), making MgO a possible concrete replacement with a negative carbon footprint.[5,9,10]

The hydration of MgO produces brucite ($Mg(OH)_2$), which only has a few MPa of compressive strength until undergoing a carbonation reaction, forming the physically stronger one or more forms of hydrated magnesium carbonates.[1,6] Unlike OPC, both the hydration and carbonation reactions of MgO are expansive. Achieving 100% carbonation of dense, large structural MgO concrete members may result in cracking and poor mechanical performance. However, prior research has shown that MgO in porous members, such as masonry blocks, can achieve high mechanical strength more rapidly.[8] For example, Unluer and Al-Tabbaa[6] demonstrated that a 10% substitution of OPC with MgO in cement mixtures used to produce porous blocks resulted in more than double the compressive strength of plain cement blocks.[6] Recently, interest has grown in the use of three-dimensional (3-D) printing to enable the use of more sustainable binders such as MgO.[8] Khalil et al.[11] showed that magnesia cements are printable using combinations of light-burned MgO and magnesium acetate, achieving a compressive strength of 31 MPa (~4500 psi). In contrast, Panda et al.[12] used a mixture of MgO, silica fume, and high-range water-reducing admixture (HRWRA) to enable 3-D printing and achieved a compressive strength of 44 MPa (6381 psi). Douba et al.[13,14] also demonstrated that 3-D printing of pastes with only MgO as the binder can achieve similarly high compressive strength.

In general, 3-D printing concrete requires a careful balance between contrasting properties that originate in the material's rheological characteristics. Specifically, it is crucial to balance pumpability, extrudability, buildability, and shape stability. Pumpability is directly influenced by dynamic yield stress and viscosity, with higher values generally leading to worse pumpability.[15-17] On the other hand, higher viscosity has been linked to improved extrudability and increased resistance to bleeding.[18] Most admixtures that increase static yield stress and structuration rate, which are key properties that enhance buildability and shape stability, also tend to increase dynamic yield stress and viscosity.[19-21] Nanoclays (NCs) have been shown to uniquely satisfy the complex rheological demands of 3-D printing by increasing static yield stress without significantly increasing viscosity, particularly at moderately low weight percentages.[22-24] Douba et al.[13,14] demonstrated that the unique combination of methylcellulose (MC) and NC can meet this complex rheological demand in MgO cements. Other researchers similarly highlighted the efficacy of NC to improve the structuration of MgO paste and achieved a compressive strength of 38 MPa

---

*ACI Materials Journal*, V. 123, No. 2, March 2026.

MS No. M-2024-109.R2, doi: 10.14359/51749254, received August 27, 2025, and reviewed under Institute publication policies. Pertinent discussion including author's closure, if any, will be published ten months from this journal's date if the discussion is received within four months of the paper's print publication.

(~5500 psi).[25] However, unlike in the case of 3-D-printed OPC mixtures, where the static yield stress effectively prevents collapse during the printing up to the start of hardening, in the case of 3-D-printed MgO, the static yield stress plays a pivotal role in resisting the collapse even after the start of hardening, primarily due to the very low (<3 MPa [435 psi]) compressive strength of the hardened brucite.[13]

To increase the compressive strength of brucite, it is necessary to carbonate it through the formation of carbonic acid ($H_2CO_3$) in pore solution and the leaching of $Mg^{2+}$ ions from the dissolution of brucite, as described by Ruan and Unluer.[26] Achieving full carbonation requires sufficient water to ensure complete hydration. For instance, Unluer and Al-Tabbaa[27] demonstrated that increased MgO hydration leads to greater conversion of MgO into hydrated magnesium carbonates, which in turn results in higher compressive strength in porous masonry blocks containing MgO. On the other hand, significantly overdosing the water content can slow down carbonation, as $CO_2$ diffusion in water is much slower than in air, by $10^4$ to $10^5$.[27,28] Because the 3-D-printing process produces filaments with high surface area and layered interfaces, water evaporation is exacerbated during the early stages of hydration.[29-31] This could result in the removal of water necessary for full hydration or the formation of carbonic acid. This effect was confirmed in a prior study, which showed that despite achieving compressive strengths up to 60 MPa (~8700 psi), some unhydrated MgO remained even after 28 days of carbon incubation.[13] On the other hand, the increased water evaporation increases porosity, thus allowing for greater carbon penetration and overall strength gain, as reported in the previous study on 3-D-printed MgO pastes[13] or cast MgO with air-entraining admixtures.[32]

Superabsorbent polymers (SAPs) are covalently crosslinked chains of polymer hydrogels that swell when in contact with aqueous solution, leading to their absorption.[33] Their absorption/desorption mechanism can be attributed to the osmotic pressure gradient generated by the chemical charge differential across the hydrogel-fluid interface, resulting in fluid diffusion into the hydrogel along with other solution ions until electroneutrality is established.[34-36] In cement systems, SAPs have been shown to absorb and retain water for up to 20 hours from the onset of hydration.[37] Consequently, SAPs are highly appealing additives in MgO systems, serving two primary functions. First, SAPs can retain water during the early stages of hydration, when 3-D-printed MgO experiences greater water evaporation, and later release it to maximize hydration and carbon sequestration. Second, the macropores (approximately 100 μm) left by de-swollen SAPs[38] may help prevent expansive cracking by providing space for the formation of brucite and carbonated phases.

The absorption behavior of a hydrogel is influenced by various factors, such as the composition of the absorbent, particle size, size distribution, crosslinking agent, and the surface area.[33,37] In OPC-based systems, the changes in the pore solution's ionic concentration have been identified as one of the key factors controlling the absorption/desorption kinetics of SAP.[38-40] The rheology of MgO modified with SAP has not been previously studied, but similar effects to those observed in portland cement systems are expected. Previous literature on cement and geopolymers containing SAP showed enhanced static yield stress (measured through shear rheology, buildability, or flow tests), higher thixotropy rate, improved mechanical performance, and reduced shrinkage cracking.[40-47] Oh et al.[44] showed that increasing the SAP dosage increased the static yield stress and thixotropy rate up to 1 wt. % of SAP and attributed such increases to changes in interparticle friction, solid volume fraction, and particle-size distribution. Their results also suggested that increasing the SAP dosage begins shifting the cement paste's behavior from shear thinning to shear thickening.[44] Similar results were reported by Ma et al.,[47] who also showed that the effects of SAP on cement rheology are dependent on SAP particle size and content.

The hydration kinetics of MgO follow dissolution-precipitation models based on boundary nucleation and growth, mirroring the behavior observed in OPC.[2,48,49] Therefore, this study characterizes the rheology of MgO paste with SAP, using the structuration principles described by Roussel et al.[50] for portland cement pastes. While the primary focus is on SAP, the inclusion of NC and MC was necessary to enable successful 3-D printing, as these additives have been shown in previous studies to improve rheology for 3-D-printing applications.[13,25,51,52] The focus of this investigation is on MgO systems with high water-binder ratios (*w*/*b*) of 1.1 and 1.3. Previous studies have shown that unhydrated MgO remained at a *w*/*b* of 1.1 after 28 days of carbon incubation, but higher *w*/*b* likely increased porosity due to greater water evaporation.[13] Therefore, this research aims to understand how SAP can function as an internal curing agent, increasing the amount of brucite ($Mg(OH)_2$) available for carbonation without compromising the desirable properties of high *w*/*b* or decreasing static yield stress.

## RESEARCH SIGNIFICANCE

This research investigates the effects of incorporating SAP on the rheology of magnesia cement for 3-D-printing applications. While SAP has been studied in cement, the impact of the *w*/*b* and pH on the osmotic gradient pressure of the pore solution and, consequently, on the sorption mechanisms of SAP has not been fully explored. Therefore, this study focuses on the rheological impact of SAP incorporation and monitors changes in rheological properties over prolonged resting times, aiming to maintain high printability performance while preserving the hydration benefits of SAP.

## EXPERIMENTAL PROCEDURE

### Materials

A high-reactivity MgO was sourced from a producer of magnesium oxide; this product is a high-purity, light-burned magnesium oxide (MgO > 98%). Its chemical and physical properties are shown in Table 1. The SAP used in this study was a commercial product obtained from a manufacturer of water-soluble polymers. It is a crosslinked copolymer of acrylamide and potassium acrylate, with an anionic polyacrylamide-based structure that enables the absorption and retention of large amounts of water. The maximum (dry) size

**Table 1—Chemical and physical properties of MgO used in this study**

| Chemical composition, % | | | | | | | |
|---|---|---|---|---|---|---|---|
| MgO | CaO | $SiO_2$ | $Fe_2O_3$ | $Al_2O_3$ | Cl | $SO_3$ | Loss on ignition (LOI) |
| 98.2 | 0.8 | 0.35 | 0.15 | 0.10 | 0.35 | 0.05 | 1.7% |

| Physical properties | | | | |
|---|---|---|---|---|
| Loose bulk density, g/cm$^3$ | Median particle size, μm | Surface area, m$^2$/g | Activity, seconds | % passing 325 mesh |
| 0.35 | 3-8 | 20 to 30 | 18 | 99 |

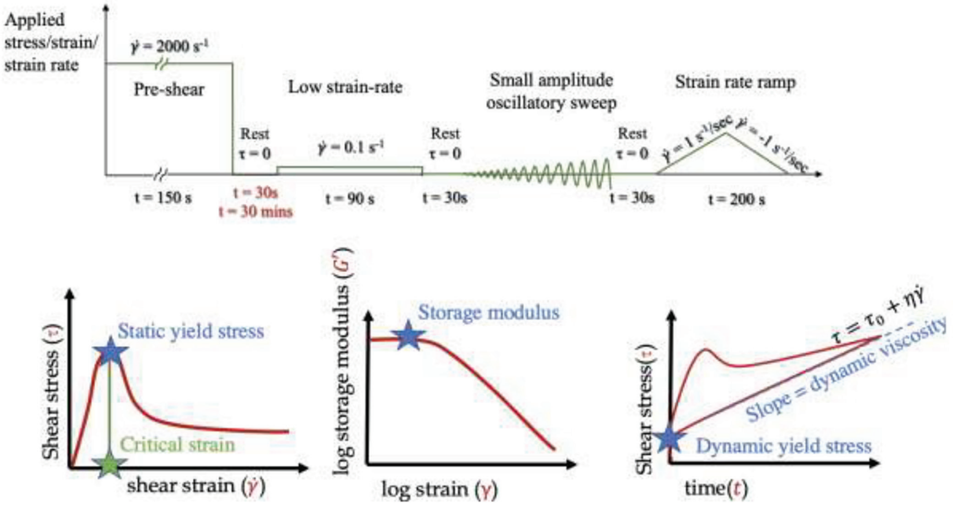

*Fig. 1—Rheological protocol used to characterize static yield stress, critical strain, storage modulus, dynamic viscosity, and dynamic yield stress of MgO pastes.*

of SAP particles was 300 μm (0.0118 in.). NC was used to increase the mixture's static yield stress, stiffness, and print stability.[52] The particles of that material were 1.5 to 2 μm ($5.9 \times 10^{-5}$ to $7.87 \times 10^{-5}$ in.) long, and their average diameter was 30 nm ($1.18 \times 10^{-6}$). They were dispersed in water using a magnetic stirrer. MC of a low molecular weight (14,000 g/mol) and a methyl degree of substitution (DS) between 1.5 and 1.9 was additionally used for its capacity to mitigate water segregation effects during printing. The MC was premixed as powder with the MgO prior to being exposed to water. All additives (NC, MC, and SAP) were added as mass replacement of MgO.

## Rheological protocol

The experiments were conducted using a stress-controlled rheometer equipped with a 24 mm (0.945 in.) diameter, four-blade vane placed inside a 28.91 mm (1.138 in.) inner diameter cup, creating a 2.45 mm gap (0.0965 in.). Pastes were mixed by adding solution (NC dispersed in deionized [DI] water) to dry powder, then mixing with a handheld mixer at 350 rpm for 1 minute. The paste was then loaded into the cup, which was subsequently placed in the rheometer operating at a controlled temperature of 25°C (77°F). The rheological procedure, as depicted in Fig. 1, commenced approximately 5 to 6 minutes after the initial contact between water and MgO. Each paste was subjected to pre-shearing at a strain rate of 2000 s$^{-1}$ for 150 seconds, followed by a stress-controlled resting period of either 30 seconds or 30 minutes. After the rest period, a low strain rate of 0.1 s$^{-1}$ was applied to measure the static yield stress while collecting the stress-strain response of the paste. The static yield stress was determined as the peak stress during this stage, whereas the colloidal critical strain, henceforth referred to as the critical strain, represents the strain corresponding to the static yield stress. This stage was followed by another 30-second stress-controlled rest period, which, in turn, was followed by a small-amplitude oscillatory sweep (between $1 \times 10^{-5}$ and 0.1 strain at 1 Hz) to measure the storage modulus. The nature of the storage modulus of MgO pastes is similar to that observed in OPC pastes and is a measure of the rigid interactions caused by the formation of new hydration products.[50] Afterward, an additional 30-second stress-controlled rest period was implemented, succeeded by a stress rate ramp ranging from 0 to 100 s$^{-1}$ and returning to 0 (over a time period of 200 seconds). This step aimed to quantify the dynamic properties by fitting the downward part of the experimental curve (between the strain rates of 20 and 100 s$^{-1}$) to a Bingham model. A minimum of three, and up to eight, samples were prepared for each admixture combination to ensure statistical significance of the results.

## Absorption tests

SAP's absorption capacity was measured using the teabag test, as reported by Zhong et al.[53] and Snoeck et al.,[54] who recommended standardized approaches for testing sorption by SAPs prior to their implementation in cement-based materials. To perform the test, a measured ~0.1 g (~0.0353 oz.) of dry SAP powder was placed inside a dry teabag and immersed in either DI water, 3 wt. % NC solution, or 3 wt. %

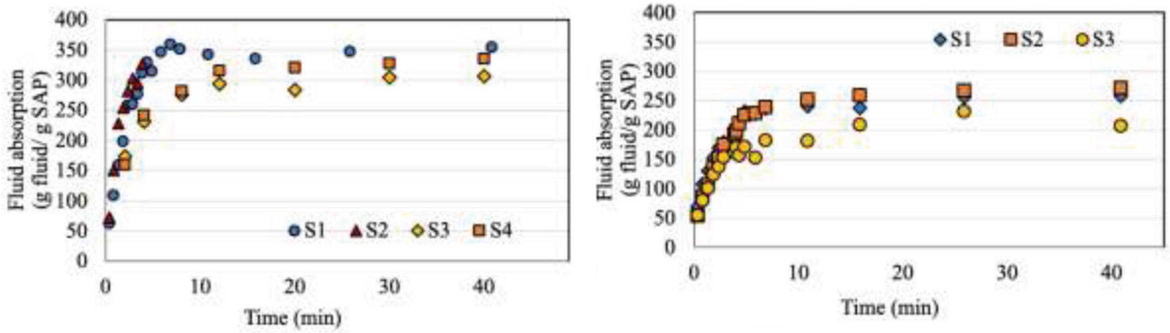

(a) DI-water

(b) 3 wt.% NC solution in DI water

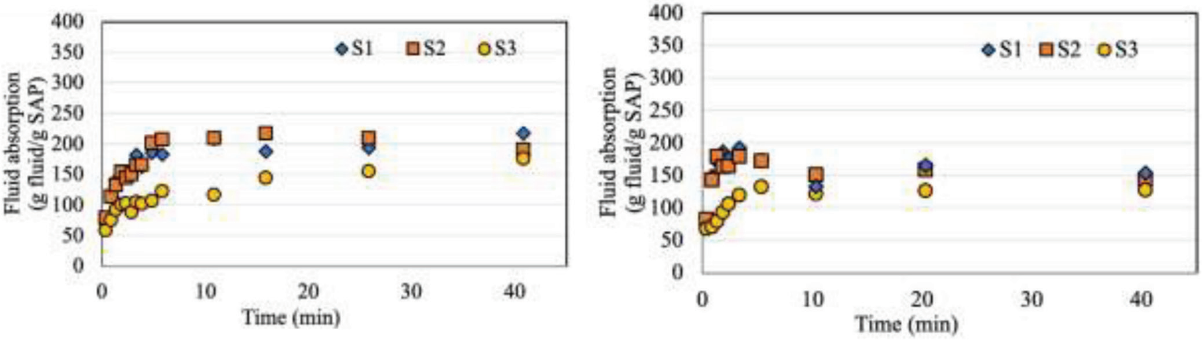

(c) 3 wt.% NC with 1 wt.% MC solution in DI water

(d) 3 wt.% NC and 1 wt.% MC in synthetic pore solution

*Fig. 2—Absorption test results of SAP in different solutions, where S1, S2, S3, and S4 denote sample numbers.*

NC with 1 wt. % MC solution prepared with either DI water or synthetic pore solution. The teabag remained immersed in the solution for a recorded period and then was placed on top of an 11 μm filter paper under vacuum pressure to dry the teabag. The total mass was recorded over time, and the total absorbed water mass was calculated by subtracting the masses of dry SAP particles and the dry teabag. Three tests were conducted for each solution to ensure statistical significance of the results. The synthetic pore solution was produced by mixing MgO with DI water at 5 *w*/*b*, allowing the mixture to rest for 30 minutes before filtering the solution through filter paper with a pore size of 11 μm ($4.33 \times 10^{-4}$). The acquired solution was then placed in an airtight container for a minimum of 72 hours to allow for residual particle sedimentation before extracting the synthetic pore solution. Because MC is not dispersible at room temperature in DI water without the presence of secondary positively charged particles, an MC solution was used instead. This solution was made by heating DI water to 70 to 80°C (158 to 176°F), dispersing MC powder using a magnetic stirring process, and lowering the temperature to ~5°C (41°F) with continuous magnetic stirring. The NC was dispersed with the MC powder in the same step to create a hybrid mixture (solution) containing 3 wt. % NC and 1 wt. % MC. The solution was stirred for a minimum of 24 hours at room temperature prior to being used in the test and agitated by magnetic stirring during the absorption test to minimize possible sedimentation of NC particles. The synthetic pore solution containing NC and MC was prepared by mixing an equal amount of synthetic pore solution with 6 wt. % NC and 2 wt. % MC solutions to yield an overall 3 wt. % NC and 1 wt. % MC dosage in the synthetic pore solution.

## RESULTS

### Absorption test

The absorption test results are shown in Fig. 2 for SAP in DI water, 3 wt. % NC in DI water, 3 wt. % NC with 1 wt. % MC solution in DI water, and 3 wt. % NC with 1 wt. % MC solution in synthetic pore solution. The results show that the average maximum absorption capacity of the SAP used in this study, when exposed solely to DI water, was ~320 g fluid/g SAP and that it was reached within approximately 10 minutes. The average maximum absorption capacity of the same SAP was reduced by approximately 20% in a solution of DI water with 3 wt. % NC, by approximately 37% in the solution of DI water with 3 wt. % NC plus 1 wt. % MC, and by approximately 55% in a synthetic pore solution. Nevertheless, the time required to reach maximum absorption capacity remained consistent across all solutions: approximately 10 minutes. This indicates that the rate of absorption was not significantly affected by the type of solution. The results demonstrate that the presence of both NC and MC impacted SAP absorption, with a more pronounced effect observed in the synthetic pore solution compared to DI water. Specifically, in the synthetic pore solution (Fig. 2(d)), the absorption capacity of SAP was lower than in DI water with both NC and MC Fig. 2(c). This reduction in absorption is attributed to the higher ionic concentration in the synthetic

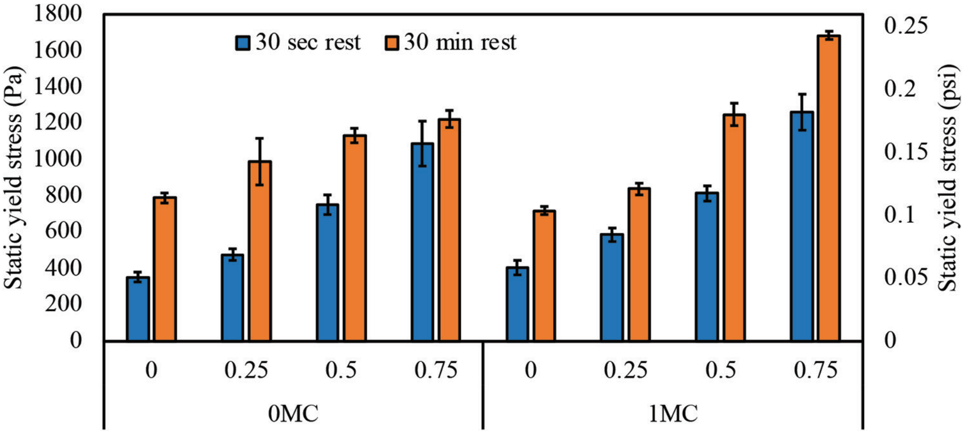

*Fig. 3—Static yield stress results of MgO pastes at 1.3* w/b.

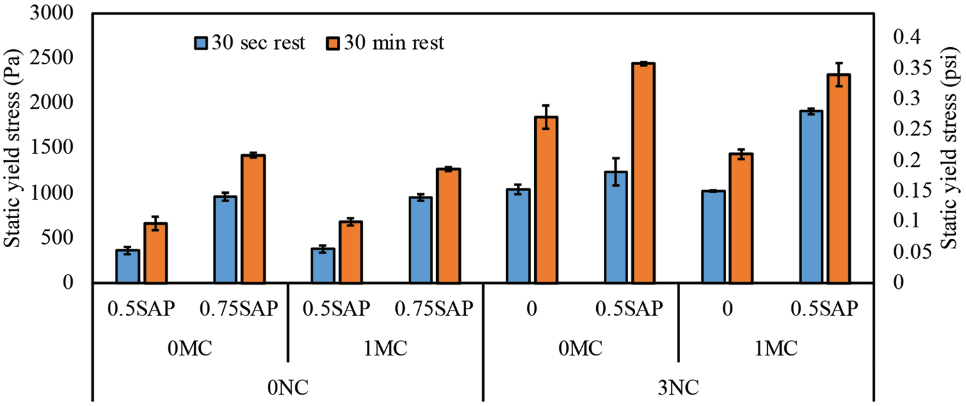

*Fig. 4—Static yield stress results of MgO pastes at 1.1* w/b.

pore solution, particularly the presence of $Mg^{2+}$ ions, which affect the osmotic pressure gradient.

## Static yield stress

The static yield stress results for MgO pastes prepared at 1.3 and 1.1 *w*/*b* are shown in Fig. 3 and 4, respectively. Mixtures with low SAP and NC content were excluded from consideration at both *w*/*b* due to their high water content, which led to segregation, resulting in particle sedimentation when the paste was left at rest. Additionally, in this investigation, mixtures incorporating 1 wt. % SAP were also excluded from analysis due to the observed occurrence of shear banding and shear localization. This behavior was attributed to the limited availability of free water within the mixture, resulting in wall slip phenomena, as depicted in Fig. 5. The results showed that the addition of SAP increased the static yield stress of MgO proportionally to the SAP content. The static yield stress peaked at approximately 200% at a 0.75 wt. % SAP dosage.

The mixing and rheological protocols used in this study captured the static yield stress at ~10 and 40 minutes of water and binder interaction, where SAP particles were likely swollen. This reduced free water and subsequently simulated a higher solid volume fraction, thus increasing the static yield stress. As MgO dissolution commenced and continued during sample preparation, pre-shear, and rest periods, the ionic concentration of pore solution also changed, altering the maximum SAP absorption levels. Extending the resting time to 30 minutes raised the ionic concentration of the pore solution, which likely increased the osmotic pressure gradient, causing SAP to release some water. However, the increase in available water did not completely overcome the increase in structuration, and the static yield stress continued to grow. As a result, the percentage increase in static yield stress with SAP addition was lower at the longer resting time of 30 minutes compared to 30 seconds, as shown in Fig. 6.

The effect of resting time on static yield stress varied with SAP addition and was also influenced by the presence of MC. Without MC, increasing SAP's concentration resulted in a decrease in static yield stress growth from 124 to 13%, as observed in Fig. 7, for 0 and 0.75 wt. % SAP, respectively. Nevertheless, the initial increase in static yield stress due to the SAP addition remained prevalent, indicating that SAP is effective as an admixture to increase the static yield stress of hydrating binders. Similar increases in static yield stress with an increase in the SAP dosage and resting time have been reported by Oh et al.,[44] albeit to a lesser extent. This difference in magnitude can possibly be attributed to the variation in the *w*/*b*, considering that the MgO employed in this experiment uses approximately three to four times the quantity of water.

Even though Fig. 6 shows mixtures with and without MC with a similar percentage increase in static yield stress compared to their respective references at 30 seconds of rest, the mixtures containing MC showed higher static yield stress at the longer rest period of 30 minutes, as shown in

*Fig. 5—Images of four-blade vane retrieved from cup subsequent to executing rheological protocol on pastes containing high admixture dosages: (a) wall slip observed in paste containing 3 wt. % NC with 1.0 wt. % SAP at 1.1* w/b*; and (b) localized shear banding in paste containing 3 wt. % NC along with 1 wt. % SAP at 30 minutes of resting time at 1.3* w/b.

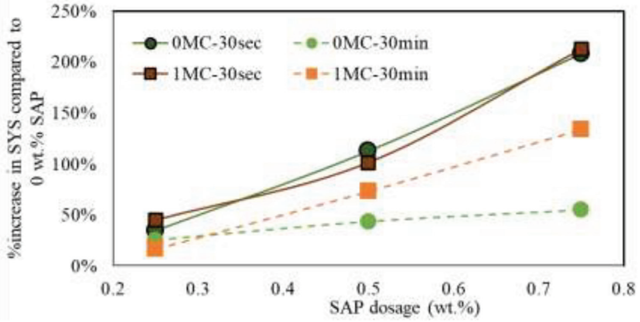

*Fig. 6—Percentage change in static yield stress with SAP addition compared to mixtures without SAP in pastes prepared at 1.3* w/b.

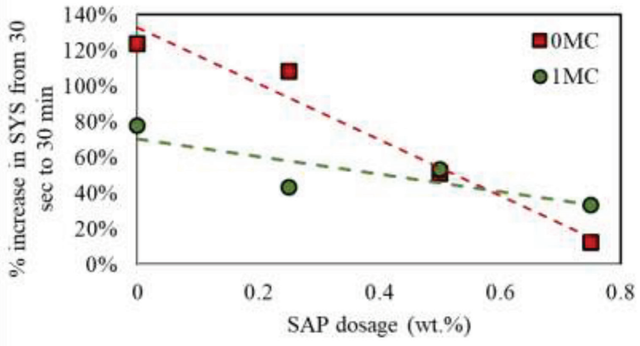

*Fig. 7—Percentage change in static yield stress with increased resting time from 30 seconds to 30 minutes.*

Fig. 3. This was attributed to the adsorption mechanism of MC on MgO grains, which caused a delay in hydration, as has been previously observed in cement and other geopolymers.[51,55,56] The dissolution of MgO generates $MgOH^+$ on the surface of MgO particles while releasing $OH^-$ into the pore solution, as indicated by Eq. (1).[2,3,57,58] Despite MC possessing a zeta potential close to zero and lacking charged groups,[59] its adsorption onto the positively charged particles such as $MgOH^+$ is primarily influenced by its anionic nature. Similar observations have been documented concerning cement.[60] Consequently, it is hypothesized that such mechanisms have led to a decrease in the amount of $Mg^{2+}$ ions released into the pore water, as denoted by Eq. (2) and (3), which potentially either increased the maximum absorption levels of SAP in the matrix or slowed down its desorption compared to mixtures without MC. As a result, the mixture containing 0.75 wt. % SAP reached a static yield stress of 1260 Pa (0.18 psi) when mixed with 1 wt. % MC, compared to 1090 Pa (0.16 psi) when mixed without.

$$MgO_{(solid)} + H_2O_{(liquid)} \rightarrow MgOH^+_{(surface)} + OH^-_{(aqueous)} \quad (1)$$

$$MgOH^+_{(surface)} + OH^-_{(aqueous)} \rightarrow (MgOH^+{\cdot}OH^-)_{(surface)} \quad (2)$$

$$(MgOH^+{\cdot}OH^-)_{(surface)} \rightarrow Mg^{2+}_{(aqueous)} + 2OH^-_{(aqueous)} \quad (3)$$

$$Mg^{2+}_{(aqueous)} + 2OH^-_{(aqueous)} \rightarrow Mg(OH)_{2(solid)} \quad (4)$$

## Stress-strain behavior

The median stress-strain behavior of all tested pastes at 1.3 *w*/*b* is shown in Fig. 8 and 9 for mixtures without and with 1 wt. % MC, respectively. Consequently, the average critical strains denoting the strain at the peak stress are summarized in Fig. 10. The stress-strain of 1 wt. % SAP is included here, showing the formation of shear bands as confirmed visually in Fig. 5. The addition of MC to the 3 wt. % NC resulted in an increase in the critical strain from 0.5 to 1.9%, in agreement with previous findings in cement pastes.[51] Increasing SAP dosage overall corresponded to an increase in critical strain in agreement with measurements reported in the literature,[46,61] indicating a softening of the colloidal network. Furthermore, there was a notable broadening of the peaks surrounding the static yield stress observed after 30 seconds of resting time, which subsequently narrowed down after 30 minutes of resting time. These characteristics more accurately represent the behavior of soft materials. The SAP particles used in this study were notably larger than MgO particles, approximately six to eight times larger in their dry state. When considering that SAP particles can grow up to twice their size,[62] swollen SAP can be 12 to 16 times the size of MgO particles. As a result, the displacement exerted by SAP particles can be approximated to be between six and 16 times that of the MgO matrix when neglecting stiffness effects. In addition, SAP's absorption creates compliant soft elastic particles with relatively low elastic modulus (in the range of 15 to 50 kPa [2.18 to 7.25 psi]), which soften with greater SAP absorption levels.[33,63,64] On the other hand, the bulk elastic modulus of MgO pastes containing NC and MC can be approximated to be 30 to 120 kPa (4.35 to 17.4 psi) based on the shear modulus measurements reported in Douba

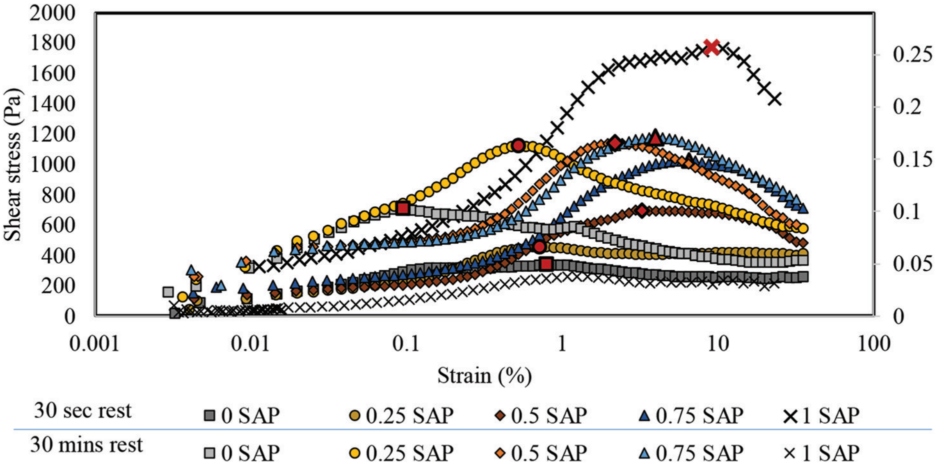

*Fig. 8—Stress-strain behavior of MgO without MC at 1.3* w/b *under low strain rate to initiate flow, with peak stresses denoted by red markers (full-color PDF can be accessed at www.concrete.org).*

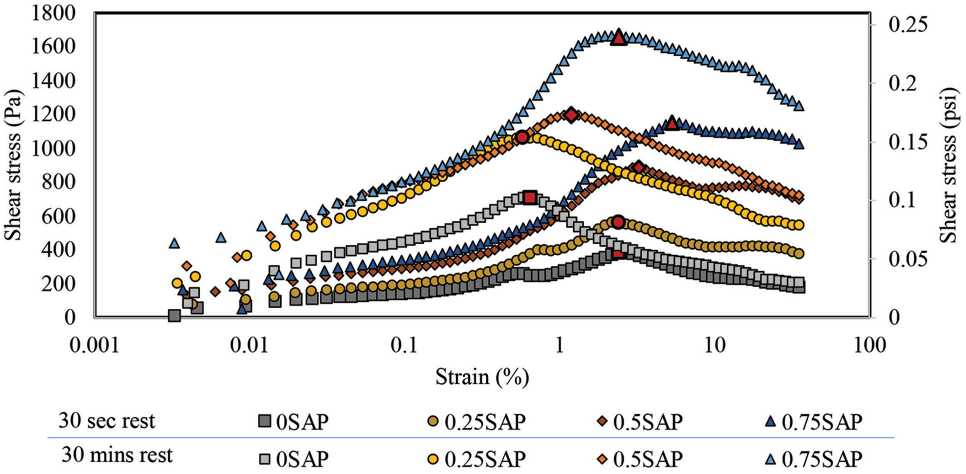

*Fig. 9—Stress-strain behavior of MgO with 1 wt. % MC at 1.3* w/b *under low strain rate to initiate flow, with peak stresses denoted by red markers (full-color PDF can be accessed at www.concrete.org).*

et al.[13] and assuming a Poisson's ratio of 0.5 for fluids. Therefore, the significantly high critical strains observed in Fig. 10, alongside the widening of the static yield stress peaks observed in Fig. 8 and 9, are most likely attributed to SAP rather than the MgO matrix. Greater strains were similarly attributed to the presence of soft elastic polymer particles in hardened cement by Wang et al.[65]

MC is a coiled polymer with a low molecular weight of 14,000 g/mol, and it is approximately 25 to 80 nm ($9.82 \times 10^{-7}$ to $3.15 \times 10^{-6}$) in size.[66] Prior work on MC in cementitious systems including gypsum has suggested dosage dependency of its water retention mechanism, shifting from water sorption below the critical overlap concentration (COC) to swelling and physical pore plugging at or above COC.[67-71] Therefore, at more than 1.6 DS, MC can be considered a nanoscale hydrophilic polymer particle due to its high water retention.[72-74] MC is expected to adsorb on MgO's surface, as has been observed for cement[37,42,43] in decoiled, coiled, or agglomerated states. Likewise, it is anticipated that NC particles will adhere to the surface of MgO owing to their extensive negative charge along their length, a phenomenon previously observed in cement.[75] Hence, the microstructure representation of MgO incorporating MC, NC, and SAP is depicted in Fig. 11, illustrating their respective size-scale ranges. This visualization supports the assertion that the observed behavior of soft materials is attributable to the influence of SAP.

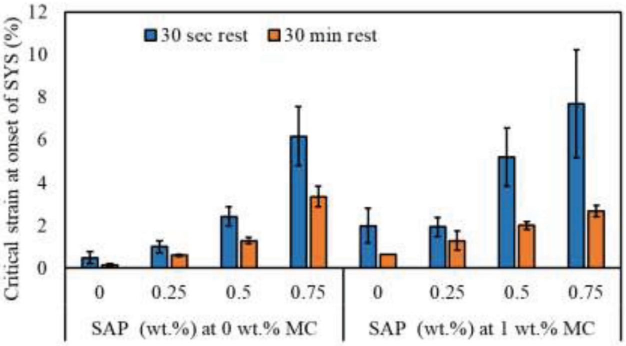

*Fig. 10—Critical strain results for MgO pastes correlating to results shown in Fig. 3.*

The dual-peak behavior observed in Fig. 8 for paste with 1 wt. % SAP after a 30-second resting time was reproduced by increasing MC dosage to 3 wt. % while decreasing the SAP dosage to 0.5 wt. %, as shown in Fig. 12. In both

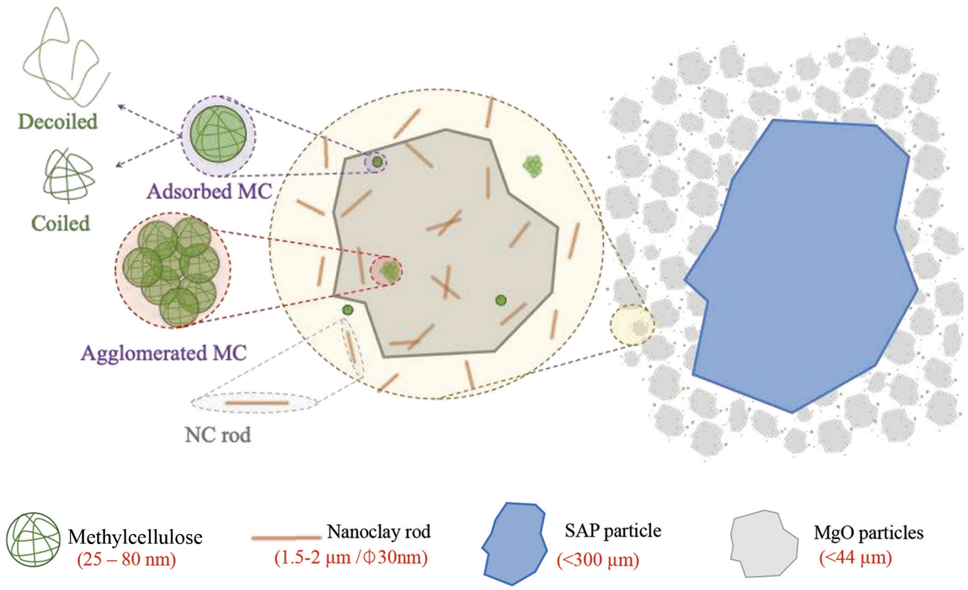

*Fig. 11—Schematic depicting suggested microstructure map of MgO containing NC, MC, and SAP during initial stages of hydration at rest.*

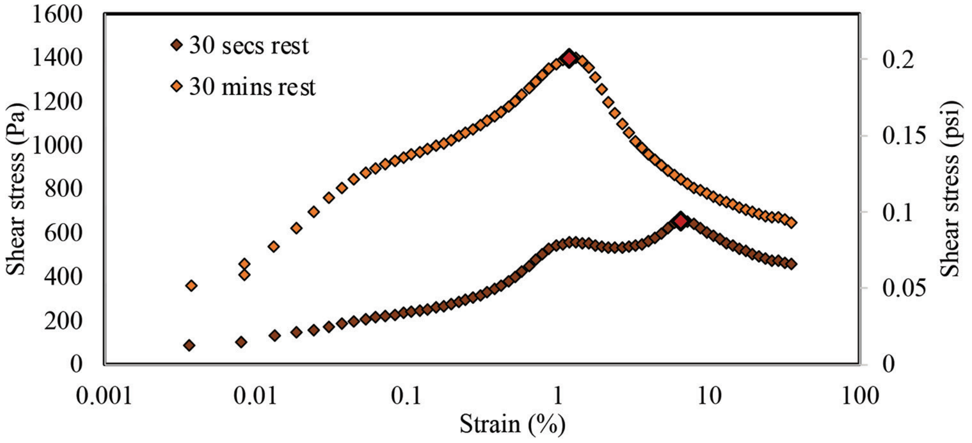

*Fig. 12—Stress-strain behavior of pastes at 1.3* w/b *containing 3 wt. % MC and 0.5 wt. % SAP.*

Fig. 8 and 9, the second peak diminishes as the structuration time increases, aligning with a decrease in critical strains. Comparing pastes containing 0.5 wt. % SAP at 0, 1, and 3 wt. % MC in Fig. 8, 9, and 12, respectively, the critical strain increases from 2.4% at 0 wt. % MC to 5.2 and 8.0% at 1 and 3 wt. % at the short resting time. The critical strain decreases from those values at the longer resting time to 1.3%, 2.0%, and 1.3% for 0, 1, and 3 wt. % MC, respectively. A similar decrease in the critical strain at longer resting times was also reported in cement paste.[61] Based on the previously hypothesized attribution of high critical strains to different levels of absorptions of SAP, it is further hypothesized that the critical strain can be used as a rheological probe into SAP's absorption level. It is also worth noting that the double-peak and wide-peak behavior observed in all stress-strain curves containing SAP may require updating the definition of static yield stress. Specifically, further investigation is required to verify whether the highest peak stress, the first peak, or the inflection point is what signifies the collapse of the colloidal network, causing static instability and likely flow.

## Storage modulus

The results of storage modulus measurements of MgO pastes with 1.3 *w*/*b* are shown in Fig. 13. All measurements are at least one order of magnitude lower than those reported for OPC cement pastes at 0.1 MPa (14.5 psi) at a *w*/*b* of 0.4 and 0.2 MPa (29 psi) at a *w*/*b* of 0.34.[50,52] This correlates to the significantly weaker binding strength of brucite compared to OPC hydration products such as calcium-silicate-hydrate (C-S-H). The addition of SAP had little effect on the storage modulus compared to the reference mixture without MC at both short and long structuration times. Because SAP's absorption is a function of the osmotic pressure gradient generated by the pore solution's ionic concentration, SAP does not hinder the formation of rigid interactions driven by hydration product nucleation or rigidification during early hydration. The addition of MC without SAP led to a decrease in storage modulus, in agreement with the dissolution delay caused by MC.[51,55,56] Conversely,the addition of SAP into MgO mixtures containing MC led to an increase in storage modulus with increasing SAP dosage. This countered the previously observed decrease associated

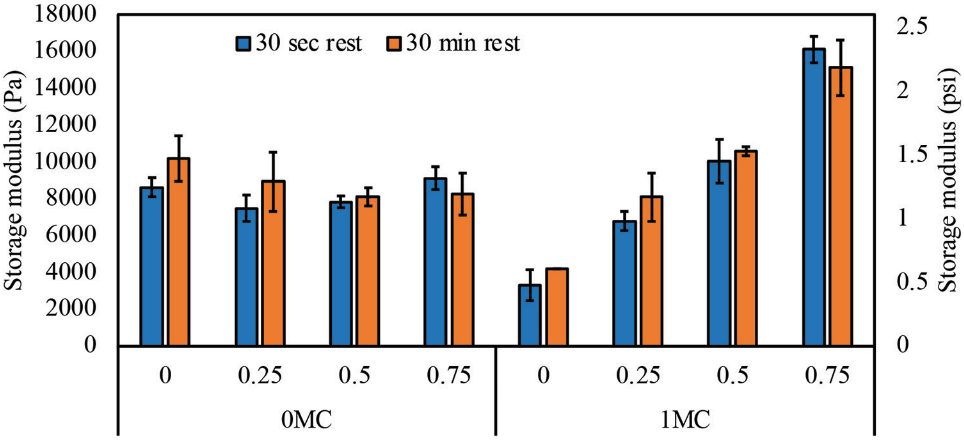

*Fig. 13—Storage modulus results of SAP-MgO pastes at 1.3* w/b.

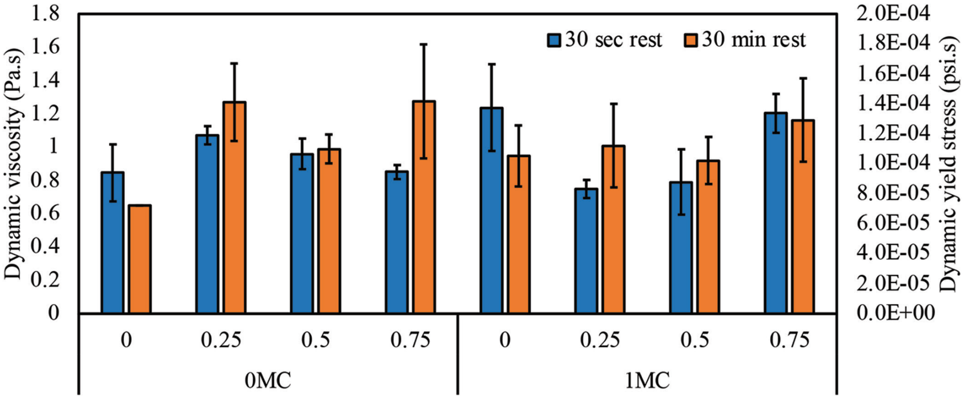

*Fig. 14—Dynamic viscosity results of MgO pastes at 1.3* w/b.

with MC, particularly evident at approximately 0.25 wt. % SAP dosage. Moreover, the mixtures containing MC exhibited a higher storage modulus at 0.5 and 0.75 wt. % of SAP compared to those without MC. It is important to note that no significant increase in storage modulus was observed with increased structuration time for all mixtures. That is, the effects of SAP absorption or desorption during the prolonged structuration time showed no significant impact on MgO's hydration, measured as storage modulus evolution (rigidification). The rise in storage modulus observed in mixtures containing MC (illustrated in Fig. 13) is notable during early hydration stages, plateauing thereafter with no discernible further increase over longer hydration periods. This suggests that the storage modulus augmentation due to SAP addition in mixtures containing MC likely took place within the initial 10 minutes of sample preparation and the pre-shear period. The delay in dissolution due to MC's addition retards hydration, corresponding to a decrease in storage modulus, which contradicts the reported results.[51,55,56] Thus, the addition of MC did not directly cause the observed increase in storage modulus. As it appears improbable that the observed rise in storage modulus with increasing SAP content in the presence of MC was directly caused by either SAP or MC, this increase may not solely indicate heightened rigid interactions. This emphasizes the need for further investigation into its origins and its correlation to the development of the rigid network.

## Dynamic viscosity and yield stress

The dynamic viscosity and yield stress were calculated by fitting a Bingham model to the slope of the downward curve of a strain rate ramp based on Fig. 1, and the results are shown in Fig. 14 and 15, respectively. Overall, the results showed that despite the reduction in free water with SAP addition, the dynamic viscosity was not significantly altered and stayed at sufficiently low values in the range of 0.6 to 1.4 Pa·s ($8.7 \times 10^{-5}$ to $1.2 \times 10^{-4}$ psi·s). Furthermore, increasing the structuration time did not lead to significant changes in the values of dynamic viscosity, except for an increase observed in the mixture with 0.75 wt. % SAP without MC. Likewise, the inclusion of SAP in mixtures without MC demonstrated minimal alterations in the dynamic yield stress, except for the mixture containing 0.75 wt. % SAP. However, the introduction of MC resulted in a decrease in dynamic yield stress. No significant difference in dynamic yield stress was observed with increasing the structuration time for all mixtures without MC, whereas some increase was observed for mixtures with MC. The dynamic yield stress generally measures the ability of particles to rearrange nearest neighbors according to the shear-induced particle migration process,[76,77] where larger particles migrate to lower shear rate regions and smaller particles accumulate in higher shear regions.[77] Thus, an increase in dynamic yield stress resembles greater resistance to particle migration. However, because the examined MgO pastes were highly concentrated suspensions with significant shear history prior to measuring

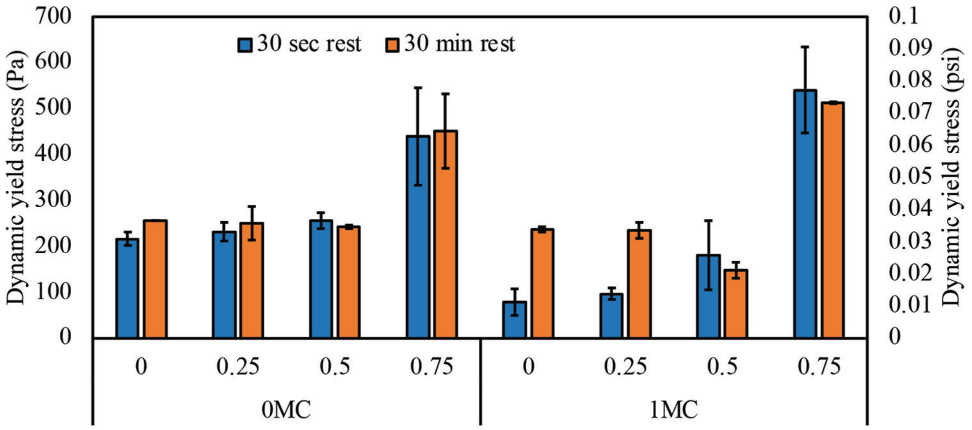

*Fig. 15—Dynamic yield stress of MgO pastes at 1.3* w/b.

dynamic properties, particles were less likely to have been free to migrate or have previously locally migrated during prior steps. Therefore, further inquiry is needed to describe the origins of the increase in dynamic yield stress for these cases.

## CONCLUSIONS

The focus of this study was to investigate the effects of the addition of superabsorbent polymers (SAPs) on the rheology of magnesia (MgO) pastes, with the goal of gaining a comprehensive understanding of the origins of these effects and how they may enhance MgO's suitability for extrusion-based three-dimensional (3-D) printing applications. The pastes investigated contained varying percentages of SAP (0.25, 0.5, 0.75, and 1% by weight of MgO), along with 3 wt. % of nanoclay (NC), and were prepared with either 1 wt. % of methylcellulose (MC) or without MC. The analysis included assessment of static yield stress, critical strain, storage modulus, dynamic viscosity, and dynamic yield stress. The outcomes of this investigation yield the following key conclusions:

- The incorporation of SAP resulted in a notable increase in static yield stress, which was directly proportional to the amount of SAP added. A particularly significant increase in static yield stress was observed during extended structuration periods when MC was included in the mixture. This increase was primarily attributed to MC's retarding influence on MgO, which likely reduced the osmotic pressure gradient, either enhancing SAP absorption or prolonging its absorption over time.
- Increasing the resting time—that is, structuration time—led to a decrease in the rate of structuration of MgO mixtures, with the decline being proportional to the amount of SAP added. This effect was mainly due to the substantial increase in static yield stress during the early stages of hydration.
- Critical strain increased, and the stress peaks widened in proportion to the amount of SAP added. However, increasing structuration time reduced these effects, suggesting that SAP desorption occurred over time. Additionally, at similar SAP dosages, mixtures containing MC exhibited higher critical strains compared to those without MC, supporting the idea that MC enhances SAP absorption. Overall, the results indicated that critical strain could serve as a rheological probing tool to indirectly measure the relative absorption capacity of SAP during hydration.
- The addition of SAP without MC showed no significant changes to the storage modulus, suggesting that the decrease in interstitial water did not alter the hydration kinetics. However, the combined addition of SAP and MC led to an increase in storage modulus with increasing SAP content.
- The addition of SAP did not have significant effects on dynamic viscosity or dynamic yield stress, except for the dosage of 0.75 wt. % SAP. At this dosage, a notable increase in dynamic yield stress was observed, regardless of the presence of MC.
- Overall, the findings imply that incorporating SAP offers advantages in improving the rheological properties of MgO, particularly in extrusion-based 3-D printing. Furthermore, the synergistic effects observed when combining SAP with a viscosity-modifying admixture, such as MC, highlight additional positive enhancements in the material's rheology.

## AUTHOR BIOS

*ACI member* **Ala Eddin Douba** *is the Lillian Gilbreth Postdoctoral Fellow in Materials Engineering at Purdue University, West Lafayette, IN. He received his BS from the American University of Sharjah, Sharjah, UAE; his MS from The University of New Mexico, Albuquerque, NM; and his PhD from Columbia University, New York, NY, all in civil engineering. His research interests include cement rheology, nanomaterials and polymeric admixtures, magnesia cement, and three-dimensional (3-D) printing of concrete.*

**Jan Olek**, *FACI, is the James H. and Carol H. Cure Professor in Civil Engineering at Purdue University. He received his BS from Cracow University of Technology, Kraków, Poland; his MS from The University of Texas at Austin, Austin, TX; and his PhD from Purdue University, all in civil engineering. He is past Chair of ACI Committee 552, Cementitious Grouting, and a member of several other ACI committees. His research interests include mixture proportioning, characterization and use of supplementary cementitious materials, durability of concrete, and 3-D printing of concrete.*

**Kendra A. Erk** *is an Associate Professor in materials engineering at Purdue University. She received her BS from Purdue University and her PhD from Northwestern University, Evanston, IL. Her research interests include the structure, properties, and performance of soft materials used in health-care, personal care, energy, concrete, and advanced material applications.*

# ACKNOWLEDGMENTS

The authors gratefully acknowledge the support of the Lillian Gilbreth Postdoctoral Fellowship at Purdue University. Additionally, the authors would like to acknowledge the contributions of Active Minerals International, LLC, for their donation of nanoclays, and Premier Magnesia, LLC, for their donation of reactive magnesia cement. The MgO was sourced from Martin Marietta Magnesia Specialties, and the SAP was from SNF Floerger.

# REFERENCES

1. Walling, S. A., and Provis, J. L., "Magnesia-Based Cements: A Journey of 150 Years, and Cements for the Future?" *Chemical Reviews*, V. 116, No. 7, Apr. 2016, pp. 4170-4204. doi: 10.1021/acs.chemrev.5b00463

2. Zhang, J., "Recent Advance of MgO Expansive Agent in Cement and Concrete," *Journal of Building Engineering*, V. 45, Jan. 2022, Article No. 103633. doi: 10.1016/j.jobe.2021.103633

3. Amaral, L. F.; Oliveira, I. R.; Salomão, R.; Frollini, E.; and Pandolfelli, V. C., "Temperature and Common-Ion Effect on Magnesium Oxide (MgO) Hydration," *Ceramics International*, V. 36, No. 3, Apr. 2010, pp. 1047-1054. doi: 10.1016/j.ceramint.2009.12.009

4. Unluer, C., "Carbon Dioxide Sequestration in Magnesium-Based Binders," *Carbon Dioxide Sequestration in Cementitious Construction Materials*, F. Pacheco-Torgal, C. Shi, and A. Palomo Sanchez, eds., Woodhead Publishing, Sawston, UK, 2018, pp. 129-173. doi: 10.1016/B978-0-08-102444-7.00007-1

5. Badjatya, P.; Akca, A. H.; Fraga Alvarez, D. V.; Chang, B.; Ma, S.; Pang, X.; Wang, E.; van Hinsberg, Q.; Esposito, D. V.; and Kawashima, S., "Carbon-Negative Cement Manufacturing From Seawater-Derived Magnesium Feedstocks," *PNAS*, V. 119, No. 34, Aug. 2022, Article No. e2114680119.

6. Unluer, C., and Al-Tabbaa, A., "Impact of Hydrated Magnesium Carbonate Additives on the Carbonation of Reactive MgO Cements," *Cement and Concrete Research*, V. 54, Dec. 2013, pp. 87-97. doi: 10.1016/j.cemconres.2013.08.009

7. Ruan, S., and Unluer, C., "Comparative Life Cycle Assessment of Reactive MgO and Portland Cement Production," *Journal of Cleaner Production*, V. 137, Nov. 2016, pp. 258-273. doi: 10.1016/j.jclepro.2016.07.071

8. Peng, Y., and Unluer, C., "Development of Alternative Cementitious Binders for 3D Printing Applications: A Critical Review of Progress, Advantages and Challenges," *Composites Part B: Engineering*, V. 252, Mar. 2023, Article No. 110492. doi: 10.1016/j.compositesb.2022.110492

9. Singh, I.; Hay, R.; and Celik, K., "Recovery and Direct Carbonation of Brucite from Desalination Reject Brine for Use as a Construction Material," *Cement and Concrete Research*, V. 152, Feb. 2022, Article No. 106673. doi: 10.1016/j.cemconres.2021.106673

10. Dong, H.; Unluer, C.; Yang, E.-H.; and Al-Tabbaa, A., "Recovery of Reactive MgO from Reject Brine via the Addition of NaOH," *Desalination*, V. 429, Mar. 2018, pp. 88-95. doi: 10.1016/j.desal.2017.12.021

11. Khalil, A.; Wang, X.; and Celik, K., "3D Printable Magnesium Oxide Concrete: Towards Sustainable Modern Architecture," *Additive Manufacturing*, V. 33, May 2020, Article No. 101145. doi: 10.1016/j.addma.2020.101145

12. Panda, B.; Sonat, C.; Yang, E.-H.; Tan, M. J.; and Unluer, C., "Use of Magnesium-Silicate-Hydrate (M-S-H) Cement Mixes in 3D Printing Applications," *Cement and Concrete Composites*, V. 117, Mar. 2021, Article No. 103901. doi: 10.1016/j.cemconcomp.2020.103901

13. Douba, A. E.; Badjatya, P.; and Kawashima, S., "Enhancing Carbonation and Strength of MgO Cement Through 3D Printing," *Construction and Building Materials*, V. 328, Apr. 2022, Article No. 126867. doi: 10.1016/j.conbuildmat.2022.126867

14. Douba, A. E.; Badjatya, P.; and Kawashima, S., "Influence of Infill Pattern on Reactive MgO Printed Structures," *Third RILEM International Conference on Concrete and Digital Fabrication: Digital Concrete 2022*, R. Buswell, A. Blanco, S. Cavalaro, and P. Kinnell, eds., Springer, Cham, Switzerland, 2022, pp. 167-172.

15. Jiao, D.; Shi, C.; Yuan, Q.; An, X.; Liu, Y.; and Li, H., "Effect of Constituents on Rheological Properties of Fresh Concrete—A Review," *Cement and Concrete Composites*, V. 83, Oct. 2017, pp. 146-159. doi: 10.1016/j.cemconcomp.2017.07.016

16. Qian, Y., and Kawashima, S., "Use of Creep Recovery Protocol to Measure Static Yield Stress and Structural Rebuilding of Fresh Cement Pastes," *Cement and Concrete Research*, V. 90, Dec. 2016, pp. 73-79. doi: 10.1016/j.cemconres.2016.09.005

17. Qian, Y.; Ma, S.; Kawashima, S.; and De Schutter, G., "Rheological Characterization of the Viscoelastic Solid-Like Properties of Fresh Cement Pastes with Nanoclay Addition," *Theoretical and Applied Fracture Mechanics*, V. 103, Oct. 2019, Article No. 102262. doi: 10.1016/j.tafmec.2019.102262

18. Yang, L.; Jia, H.; Jiao, H.; Dong, M.; and Yang, T., "The Mechanism of Viscosity-Enhancing Admixture in Backfill Slurry and the Evolution of Its Rheological Properties," *Minerals*, V. 13, No. 8, Aug. 2023, Article No. 1045. doi: 10.3390/min13081045

19. Ma, S., and Kawashima, S., "A Rheological Approach to Study the Early-Age Hydration of Oil Well Cement: Effect of Temperature, Pressure and Nanoclay," *Construction and Building Materials*, V. 215, Aug. 2019, pp. 119-127. doi: 10.1016/j.conbuildmat.2019.04.177

20. Ma, S.; Qian, Y.; and Kawashima, S., "Experimental and Modeling Study on the Non-Linear Structural Build-Up of Fresh Cement Pastes Incorporating Viscosity Modifying Admixtures," *Cement and Concrete Research*, V. 108, June 2018, pp. 1-9. doi: 10.1016/j.cemconres.2018.02.022

21. Liu, Y.; Han, J.; Li, M.; and Yan, P., "Effect of a Nanoscale Viscosity Modifier on Rheological Properties of Cement Pastes and Mechanical Properties of Mortars," *Construction and Building Materials*, V. 190, Nov. 2018, pp. 255-264. doi: 10.1016/j.conbuildmat.2018.09.110

22. Sonebi, M.; Dedenis, M.; Amziane, S.; Abdalqader, A.; and Perrot, A., "Effect of Red Mud, Nanoclay, and Natural Fiber on Fresh and Rheological Properties of Three-Dimensional Concrete Printing," *ACI Materials Journal*, V. 118, No. 6, Nov. 2021, pp. 97-110. doi: 10.14359/51733108

23. Irshidat, M. R.; and Al-Saleh, M. H., "Influence of Nanoclay on the Properties and Morphology of Cement Mortar," *KSCE Journal of Civil Engineering*, V. 22, No. 10, Oct. 2018, pp. 4056-4063. doi: 10.1007/s12205-018-1642-x

24. Panda, B.; Ruan, S.; Unluer, C.; and Tan, M. J., "Investigation of the Properties of Alkali-Activated Slag Mixes Involving the Use of Nanoclay and Nucleation Seeds for 3D Printing," *Composites Part B: Engineering*, V. 186, Apr. 2020, Article No. 107826. doi: 10.1016/j.compositesb.2020.107826

25. Chu, S. H.; Yang, E. H.; and Unluer, C., "Development of Nanofiber Reinforced Magnesia-Based Composites for 3D Printing," *Construction and Building Materials*, V. 366, Feb. 2023, Article No. 130270. doi: 10.1016/j.conbuildmat.2022.130270

26. Ruan, S., and Unluer, C., "Influence of Mix Design on the Carbonation, Mechanical Properties and Microstructure of Reactive MgO Cement-Based Concrete," *Cement and Concrete Composites*, V. 80, July 2017, pp. 104-114. doi: 10.1016/j.cemconcomp.2017.03.004

27. Unluer, C., and Al-Tabbaa, A., "Enhancing the Carbonation of MgO Cement Porous Blocks Through Improved Curing Conditions," *Cement and Concrete Research*, V. 59, May 2014, pp. 55-65. doi: 10.1016/j.cemconres.2014.02.005

28. Richardson, M. G., *Carbonation of Reinforced Concrete: Its Causes and Management*, Citis Ltd., Dublin, Ireland, 1988, 205 pp.

29. Shahmirzadi, M. R.; Gholampour, A.; Kashani, A.; and Ngo, T. D., "Shrinkage Behavior of Cementitious 3D Printing Materials: Effect of Temperature and Relative Humidity," *Cement and Concrete Composites*, V. 124, Nov. 2021, Article No. 104238. doi: 10.1016/j.cemconcomp.2021.104238

30. Moelich, G. M.; Kruger, J.; and Combrinck, R., "Plastic Shrinkage Cracking in 3D Printed Concrete," *Composites Part B: Engineering*, V. 200, Nov. 2020, Article No. 108313. doi: 10.1016/j.compositesb.2020.108313

31. Nerella, V. N.; Hempel, S.; and Mechtcherine, V., "Effects of Layer-Interface Properties on Mechanical Performance of Concrete Elements Produced by Extrusion-Based 3D-Printing," *Construction and Building Materials*, V. 205, Apr. 2019, pp. 586-601. doi: 10.1016/j.conbuildmat.2019.01.235

32. Ruan, S., and Unluer, C., "Effect of Air Entrainment on the Performance of Reactive MgO and PC Mixes," *Construction and Building Materials*, V. 142, July 2017, pp. 221-232. doi: 10.1016/j.conbuildmat.2017.03.068

33. Zhu, Q.; Barney, C. W.; and Erk, K. A., "Effect of Ionic Crosslinking on the Swelling and Mechanical Response of Model Superabsorbent Polymer Hydrogels for Internally Cured Concrete," *Materials and Structures*, V. 48, No. 7, July 2015, pp. 2261-2276. doi: 10.1617/s11527-014-0308-5

34. Wall, F. T., "*Principles of Polymer Chemistry*. Paul J. Flory. Cornell Univ. Press, Ithaca, New York, 1953. 688 pp. Illus. $8.50," *Science*, V. 119, No. 3095, Apr. 1954, pp. 555-556. doi: 10.1126/science.119.3095.555.b

35. Horkay, F.; Tasaki, I.; and Basser, P. J., "Osmotic Swelling of Polyacrylate Hydrogels in Physiological Salt Solutions," *Biomacromolecules*, V. 1, No. 1, Mar. 2000, pp. 84-90. doi: 10.1021/bm9905031

36. Horkay, F.; Tasaki, I.; and Basser, P. J., "Effect of Monovalent–Divalent Cation Exchange on the Swelling of Polyacrylate Hydrogels in Physiological Salt Solutions," *Biomacromolecules*, V. 2, No. 1, Mar. 2001, pp. 195-199. doi: 10.1021/bm0056153

37. Schröfl, C.; Erk, K. A.; Siriwatwechakul, W.; Wyrzykowski, M.; and Snoeck, D., "Recent Progress in Superabsorbent Polymers for Concrete," *Cement and Concrete Research*, V. 151, Jan. 2022, Article No. 106648. doi: 10.1016/j.cemconres.2021.106648

38. Bose, B.; Davis, C. R.; and Erk, K. A., “Microstructural Refinement of Cement Paste Internally Cured by Polyacrylamide Composite Hydrogel Particles Containing Silica Fume and Nanosilica,” *Cement and Concrete Research*, V. 143, May 2021, Article No. 106400. doi: 10.1016/j.cemconres.2021.106400

39. Zhang, W.; Wang, P.; Liu, S.; Chen, J.; Chen, R.; He, X.; Ma, G.; and Lei, Z., “Factors Affecting the Properties of Superabsorbent Polymer Hydrogels and Methods to Improve Their Performance: A Review,” *Journal of Materials Science*, V. 56, No. 29, Oct. 2021, pp. 16223-16242. doi: 10.1007/s10853-021-06306-1

40. Adams, C. J.; Bose, B.; Olek, J.; and Erk, K. A., “Evaluation of Mix Design Strategies to Optimize Flow and Strength of Mortar Internally Cured with Superabsorbent Polymers,” *Construction and Building Materials*, V. 324, Mar. 2022, Article No. 126664. doi: 10.1016/j.conbuildmat.2022.126664

41. Aghaee, K.; Sposito, R.; and Khayat, K. H., “Synergistic Effect of Shrinkage Mitigating Materials on Rheological Properties of Flowable and Thixotropic Cement Paste,” *Cement and Concrete Composites*, V. 133, Oct. 2022, Article No. 104686. doi: 10.1016/j.cemconcomp.2022.104686

42. Inozemtcev, A. S.; Korolev, E. V.; and Duong, T. Q., “Lightweight Concrete for 3D-Printing with Internal Curing Agent for Portland Cement Hydration,” *Magazine of Civil Engineering*, V. 109, No. 1, Feb. 2022, Article No. 10915. doi: 10.34910/MCE.109.15

43. Melichar, J.; Žižková, N.; Brožovský, J.; Mészárosová, L.; and Hermann, R., “Study of the Interaction of Cement-Based Materials for 3D Printing with Fly Ash and Superabsorbent Polymers,” *Buildings*, V. 12, No. 11, Nov. 2022, Article No. 2008. doi: 10.3390/buildings12112008

44. Oh, S.; Hong, G.; and Choi, S., “Determining the Effect of Superabsorbent Polymers, Macrofibers, and Resting Time on the Rheological Properties of Cement Mortar Using Analysis of Variance (ANOVA): A 3D Printing Perspective,” *Journal of Building Engineering*, V. 75, Sept. 2023, Article No. 106967. doi: 10.1016/j.jobe.2023.106967

45. Fu, C.; Ye, H.; Lei, A.; Yang, G.; and Wan, P., “Effect of Novel Superabsorbent Polymer Composites on the Fresh and Hardened Properties of Alkali-Activated Slag,” *Construction and Building Materials*, V. 232, Jan. 2020, Article No. 117225. doi: 10.1016/j.conbuildmat.2019.117225

46. Sujitha, V. S.; Ramesh, B.; and Xavier, J. R., “Effect of Superabsorbent Polymer Hydrogels in the Advancement of Cementitious Materials—A Review,” *Journal of Polymers and the Environment*, V. 31, No. 7, July 2023, pp. 2761-2778. doi: 10.1007/s10924-023-02782-5

47. Ma, X.; Yuan, Q.; Liu, J.; and Shi, C., “Effect of Water Absorption of SAP on the Rheological Properties of Cement-Based Materials with Ultra-Low w/b Ratio,” *Construction and Building Materials*, V. 195, Jan. 2019, pp. 66-74. doi: 10.1016/j.conbuildmat.2018.11.050

48. Thomas, J. J.; Musso, S.; and Prestini, I., “Kinetics and Activation Energy of Magnesium Oxide Hydration,” *Journal of the American Ceramic Society*, V. 97, No. 1, Jan. 2014, pp. 275-282. doi: 10.1111/jace.12661

49. Liu, J. P.; Wang, Y. J.; Tian, Q.; and Zhang, S. Z., “Modeling Hydration Process of Magnesia Based on Nucleation and Growth Theory: The Isothermal Calorimetry Study,” *Thermochimica Acta*, V. 550, Dec. 2012, pp. 27-32. doi: 10.1016/j.tca.2012.09.033

50. Roussel, N.; Ovarlez, G.; Garrault, S.; and Brumaud, C., “The Origins of Thixotropy of Fresh Cement Pastes,” *Cement and Concrete Research*, V. 42, No. 1, Jan. 2012, pp. 148-157. doi: 10.1016/j.cemconres.2011.09.004

51. Douba, A. E., and Kawashima, S., “Use of Nanoclays and Methylcellulose to Tailor Rheology for Three-Dimensional Concrete Printing,” *ACI Materials Journal*, V. 118, No. 6, Nov. 2021, pp. 275-289. doi: 10.14359/51733129

52. Douba, A. E.; Ma, S.; and Kawashima, S., “Rheology of Fresh Cement Pastes Modified with Nanoclay-Coated Cements,” *Cement and Concrete Composites*, V. 125, Jan. 2022, Article No. 104301. doi: 10.1016/j.cemconcomp.2021.104301

53. Zhong, P.; Wang, J.; Wang, X.; Liu, J.; Li, Z.; and Zhou, Y., “Comparison of Different Approaches for Testing Sorption by a Superabsorbent Polymer to be Used in Cement-Based Materials,” *Materials*, V. 13, No. 21, Nov. 2020, Article No. 5015. doi: 10.3390/ma13215015

54. Snoeck, D.; Schröfl, C.; and Mechtcherine, V., “Recommendation of RILEM TC 260-RSC: Testing Sorption by Superabsorbent Polymers (SAP) Prior to Implementation in Cement-Based Materials,” *Materials and Structures*, V. 51, No. 5, Oct. 2018, Article No. 116. doi: 10.1617/s11527-018-1242-8

55. Khayat, K. H., “Viscosity-Enhancing Admixtures for Cement-Based Materials — An Overview,” *Cement and Concrete Composites*, V. 20, No. 2-3, 1998, pp. 171-188. doi: 10.1016/S0958-9465(98)80006-1

56. Betioli, A. M.; Gleize, P. J. P.; Silva, D. A.; John, V. M.; and Pileggi, R. G., “Effect of HMEC on the Consolidation of Cement Pastes: Isothermal Calorimetry *versus* Oscillatory Rheometry,” *Cement and Concrete Research*, V. 39, No. 5, May 2009, pp. 440-445. doi: 10.1016/j.cemconres.2009.02.002

57. Aphane, M. E.; van der Merwe, E. M.; and Strydom, C. A., “Influence of Hydration Time on the Hydration of MgO in Water and in a Magnesium Acetate Solution,” *Journal of Thermal Analysis and Calorimetry*, V. 96, No. 3, June 2009, pp. 987-992. doi: 10.1007/s10973-008-9095-y

58. Fruhwirth, O.; Herzog, G. W.; Hollerer, I.; and Rachetti, A., “Dissolution and Hydration Kinetics of MgO,” *Surface Technology*, V. 24, No. 3, Mar. 1985, pp. 301-317. doi: 10.1016/0376-4583(85)90080-9

59. Espinal-Ruiz, M.; Parada-Alfonso, F.; Restrepo-Sánchez, L.-P.; Narváez-Cuenca, C.-E.; McClements, D. J., “Impact of Dietary Fibers [Methyl Cellulose, Chitosan, and Pectin] on Digestion of Lipids Under Simulated Gastrointestinal Conditions,” *Food & Function*, V. 5, No. 12, Dec. 2014, pp. 3083-3095.

60. Tanguler-Bayramtan, M.; Alam, B.; Sucu, M.; Delibas, T.; and Yaman, I. O., “Cement and Hydroxyethyl Methyl Cellulose Interaction: The Performance of Cement-Based Adhesives,” *Materials and Structures*, V. 55, No. 3, Apr. 2022, Article No. 91. doi: 10.1617/s11527-022-01937-5

61. Ma, S.; Huang, C.; Baah, P.; Nantung, T.; and Lu, N., “The Influence of Water-to-Cement Ratio and Superabsorbent Polymers (SAPs) on Solid-Like Behaviors of Fresh Cement Pastes,” *Construction and Building Materials*, V. 275, Mar. 2021, Article No. 122160. doi: 10.1016/j.conbuildmat.2020.122160

62. Davis, C. R.; Kelly, S. L.; and Erk, K. A., “Comparing Laser Diffraction and Optical Microscopy for Characterizing Superabsorbent Polymer Particle Morphology, Size, and Swelling Capacity,” *Journal of Applied Polymer Science*, V. 135, No. 14, Apr. 2018, Article No. 46055. doi: 10.1002/app.46055

63. Bashir, S.; Hina, M.; Iqbal, J.; Rajpar, A. H.; Mujtaba, M. A.; Alghamdi, N. A.; Wageh, S.; Ramesh, K.; and Ramesh, S., “Fundamental Concepts of Hydrogels: Synthesis, Properties, and Their Applications,” *Polymers*, V. 12, No. 11, Nov. 2020, Article No. 2702. doi: 10.3390/polym12112702

64. Davis, C. R.; Bose, B.; Alcaraz, A. M.; Martinez, C. J.; and Erk, K. A., “Altering the Crosslinking Density of Polyacrylamide Hydrogels to Increase Swelling Capacity and Promote Calcium Hydroxide Growth in Cement Voids,” *3rd International Conference on the Application of Superabsorbent Polymers (SAP) and Other New Admixtures Towards Smart Concrete*, W. P. Boshoff, R. Combrinck, V. Mechtcherine, and M. Wyrzykowski, eds., Springer, Cham, Switzerland, 2020, pp. 20-28. doi: 10.1007/978-3-030-33342-3_3

65. Wang, X.; Xu, M.; Qin, Y.; Song, J.; Chen, R.; and Yin, Z., “The Effect of Polymer Elastic Particles Modified with Nano-Silica on the Mechanical Properties of Oil Well Cement-Based Composite Materials,” *Polymers*, V. 15, No. 14, July 2023, Article No. 3130. doi: 10.3390/polym15143130

66. Funami, T.; Kataoka, Y.; Hiroe, M.; Asai, I.; Takahashi, R.; and Nishinari, K., “Thermal Aggregation of Methylcellulose with Different Molecular Weights,” *Food Hydrocolloids*, V. 21, No. 1, Jan. 2007, pp. 46-58. doi: 10.1016/j.foodhyd.2006.01.008

67. Bülichen, D.; Kainz, J.; and Plank, J., “Working Mechanism of Methyl Hydroxyethyl Cellulose (MHEC) as Water Retention Agent,” *Cement and Concrete Research*, V. 42, No. 7, July 2012, pp. 953-959. doi: 10.1016/j.cemconres.2012.03.016

68. Yammamuro, H.; Izumi, T.; and Mizunuma, T., “Study of Non-Adsorptive Viscosity Agents Applied to Self-Compacting Concrete,” *Fifth CANMET/ACI International Conference on Superplasticizers and Other Chemical Admixtures in Concrete*, SP-173, V. M. Malhotra, ed., American Concrete Institute, Farmington Hills, MI, 1997, pp. 427-444.

69. Jenni, A.; Herwegh, M.; Zurbriggen, R.; Aberle, T.; and Holzer, L., “Quantitative Microstructure Analysis of Polymer-Modified Mortars,” *Journal of Microscopy*, V. 212, No. 2, Nov. 2003, pp. 186-196. doi: 10.1046/j.1365-2818.2003.01230.x

70. Desbrieres, J., “Cement Cake Properties in Static Filtration. On the Role of Fluid Loss Control Additives on the Cake Porosity,” *Cement and Concrete Research*, V. 23, No. 6, Nov. 1993, pp. 1431-1442. doi: 10.1016/0008-8846(93)90080-S

71. Desbrieres, J., “Cement Cake Properties in Static Filtration. Influence of Polymeric Additives on Cement Filter Cake Permeability,” *Cement and Concrete Research*, V. 23, No. 2, Mar. 1993, pp. 347-358. doi: 10.1016/0008-8846(93)90100-N

72. Nasatto, P. L.; Pignon, F.; Silveira, J. L. M.; Duarte, M. E. R.; Noseda, M. D.; and Rinaudo, M., “Methylcellulose, a Cellulose Derivative with Original Physical Properties and Extended Applications,” *Polymers*, V. 7, No. 5, May 2015, pp. 777-803. doi: 10.3390/polym7050777

73. Nokhodchi, A.; Ford, J. L.; and Rubinstein, M. H., “Studies on the Interaction Between Water and (Hydroxypropyl)Methylcellulose,” *Journal of Pharmaceutical Sciences*, V. 86, No. 5, May 1997, pp. 608-615. doi: 10.1021/js960279a

74. Katzhendler, I.; Mäder, K.; and Friedman, M., “Structure and Hydration Properties of Hydroxypropyl Methylcellulose Matrices Containing

Naproxen and Naproxen Sodium," *International Journal of Pharmaceutics*, V. 200, No. 2, May 2000, pp. 161-179. doi: 10.1016/S0378-5173(00)00360-4

75. Douba, A. E.; Hou, P.; and Kawashima, S., "Hydration and Mechanical Properties of High Content Nano-Coated Cements with Nano-Silica, Clay and Calcium Carbonate," *Cement and Concrete Research*, V. 168, June 2023, Article No. 107132. doi: 10.1016/j.cemconres.2023.107132

76. Jiang, T., and Zukoski, C. F., "Dynamic Localization and Shear-Induced Hopping of Particles: A Way to Understand the Rheology of Dense Colloidal Dispersions," *Journal of Rheology*, V. 58, No. 5, Sept. 2014, pp. 1277-1299.

77. Eslami Pirharati, M.; Krauss, H.-W.; Schilde, C.; and Lowke, D., "Effect of Different Shear Rates on Particle Microstructure of Cementitious Materials in a Wide Gap Vane-in-cup Rheometer," *Materials*, V. 13, No. 9, May 2020, Article No. 2035. doi: 10.3390/ma13092035

## NOTES:

ACI MATERIALS JOURNAL TECHNICAL PAPER

Title No. 123-M16

# Optimized Fiber-Reinforced Slag Concrete for Freezing-and-Thawing Resilience

by A. B. Dahar, F. T. Al Rikabi, I. Khoury, S. Ahmed, H. H. Hussein, and S. Sargand

*This paper presents findings from an experimental study focused on the performance of concrete composed entirely of 100% slag aggregate, enhanced with polypropylene (PP) fibers, subjected to severe freezing-and-thawing cycling between –60°C and +60°C. The research employed varying fiber lengths of 19.01, 38.1, and 57.15 mm and dosages of 3, 6, and 9 kg/m$^3$. Findings indicate that the incorporation of fibers contributes to the overall resilience of the slag aggregate concrete under freezing-and-thawing conditions. To evaluate freezing-and-thawing resistance, the coefficient of thermal expansion (CTE) was determined using the Ohio CTE method and AASHTO TP 60-00. Additionally, dynamic modulus, mass loss, and flexural strength were assessed. X-ray fluorescence (XRF) analysis was performed on slag aggregates to characterize their chemical composition. Findings indicate that the incorporation of fibers, particularly at a dosage of 9 kg/m$^3$ and a length of 57.15 mm, enhances the resilience of the slag aggregate concrete under 300 freezing-and-thawing cycles, as specified in ASTM C666/C666M-15, leading to improved flexural strength and reduced mass loss (less than 7%). However, some fiber-reinforced concrete samples experienced up to a 26.776% decrease in flexural strength after freezing-and-thawing cycles. Additionally, 38.1 mm fibers at varying dosages effectively mitigated the adverse effects of freezing-and-thawing cycles on the concrete's thermal expansion. In contrast, concrete without fibers lost over 40% of its mass. This contribution is particularly significant given the scarcity of data on the performance of concrete entirely made up of slag aggregate and mixed with PP fibers of different lengths in extreme weather environments.*

**Keywords:** dynamic modulus; electric arc furnace (EAF) steel slag; flexural strength; freezing-and-thawing durability; polypropylene (PP) fibers; slag concrete; X-ray fluorescence (XRF) analysis.

## INTRODUCTION

The building sector greatly influences environmental degradation through significant resource use and waste production (Ahmed and Lim 2021). Steel slag, a by-product of steel manufacturing, offers a more sustainable alternative for concrete production (Mekonen et al. 2024). Despite an annual production of roughly 270 million tons of slag worldwide in 2020, its application is minimal, especially in less developed nations (USGS 2022; Guo et al. 2018). Van Ho and Huynh (2023) underlined the advantages of incorporating 100% slag into concrete. Moreover, adding polypropylene (PP) fibers can improve concrete's mechanical characteristics and, potentially, its thermal behavior and resistance to freezing and thawing (Buratti and Mazzotti 2015; ACI Committee 544 2010). However, detailed investigations into the combined use of slag and fibers are essential.

The addition of PP fibers into concrete enhances key mechanical properties, such as flexural strength and elasticity. The success of these improvements relies on the fibers' size, shape, arrangement, and type (Kuder and Shah 2010; Çavdar 2012). Concrete with PP fibers, used in amounts between 2.4 and 10.7 kg/m$^3$, shows particular promise in concrete pipes by reducing steel reinforcement needs and enhancing load distribution to the soil (Deng et al. 2022; Peyvandi et al. 2014). However, the impact of PP fibers on the coefficient of thermal expansion (CTE) of concrete remains unclear, with notable differences from that of traditional concrete, indicating a need for further examination, particularly under environmental stressors such as freezing-and-thawing cycles (Latifi et al. 2022; ACI Committee 209 1992; Buratti and Mazzotti 2015).

Daily temperature fluctuations, particularly during freezing-and-thawing cycles, exert stress on concrete structures, causing surface cracks that can lead to corrosion and concrete deterioration. ACI 544.5R-10 (ACI Committee 544 2010) mentions the scarcity of detailed research on the impact of freezing-and-thawing cycles on synthetic fiber-reinforced concrete. Although some studies, such as those by Yun and Rokugo (2012) and Richardson et al. (2012), indicate that fibers can enhance durability, these often concentrate on low fiber dosages and fail to adhere to ASTM C666/C666M-15 (2015) standards, leaving the concrete's resistance to harsh freezing-and-thawing conditions largely unexplored. Research on how these cycles influence other mechanical properties remains limited.

## OBJECTIVE

This study investigates the impact of 3, 6, and 9 kg/m$^3$ PP fibers with lengths of 19.01, 38.11, and 57.15 mm on the dynamic modulus of elasticity, flexural strength, and CTE of fiber-reinforced concrete using 100% slag aggregate. The research, conducted over 300 freezing-and-thawing cycles according to ASTM C666/C666M-15, aims to understand how fiber-reinforced concrete performs under extreme weather conditions. The CTE measurements were taken in a dry state, with temperature variations from –60 to +60°C, to mimic the wide range of temperatures that concrete structures face in the United States.

---

*ACI Materials Journal*, V. 123, No. 2, March 2026.

MS No. M-2024-310.R3, doi: 10.14359/51749255, received August 18, 2025, and reviewed under Institute publication policies. Pertinent discussion including author's closure, if any, will be published ten months from this journal's date if the discussion is received within four months of the paper's print publication.

## INFLUENCE OF TEMPERATURE ON CONCRETE MATERIALS

Highlighting the critical role of temperature changes, AASHTO (1989) points out that such variations can induce both longitudinal and lateral stresses. These stresses may lead to cracking and can adversely affect the material's long-term functionality. Choubane and Tia (1992) categorize temperature effects into three types: uniform, linear, and nonlinear. The nonlinear component represents the remaining variation after subtracting the uniform and linear effects. This nonlinear temperature gradient plays a role in the development of thermal stress, which is closely associated with changes in the CTE. As noted in ACI 209R-92 (ACI Committee 209 1992), the typical CTE range for normal-strength concrete is between $8.5 \times 10^{-6}$ and $11.7 \times 10^{-6}$/°C, a metric that fluctuates based on the aggregate's nature, composition, and moisture level, essentially reflecting the average thermal expansion of the concrete's constituents. Nonetheless, the nuanced effects of varying fiber types and dosages on concrete's CTE have yet to be fully explored.

Historical methodologies for measuring the CTE of concrete include ASTM C531-00(2012) (2012), CRD-C 39-81 (U.S. Army Corps of Engineers 1981), AASHTO TP 60-00 (2007), and FHWA Protocol P63 (Simpson et al. 2007), each presenting particular challenges, especially concerning the temperature range and state of the concrete samples (whether oven-dried, saturated, or air-dried). Specifically, ASTM C531-00(2012) mandates oven-dry conditions for CTE testing within a 23 to 99°C range. Conversely, CRD-C 39-81 and similar protocols require saturated specimens, showcasing a limited temperature scope. According to ACI 209R-92, lower CTE values are observed in both saturated and oven-dry states, compared with air-dry conditions. All these indicate a need to adjust the thermal expansion values from saturated samples to be compared with expected moisture conditions. However, a wide range of air temperatures, from –34.4 to 43.3°C, is included in these established methods. To accurately reflect the conditions concrete structures face outdoors, it is crucial to measure the CTE of air-dried concrete across the full temperature range, addressing this methodological gap.

## RESEARCH SIGNIFICANCE

This study significantly advances the understanding of the performance of 100% slag aggregate concrete reinforced with PP fibers under extreme freezing-and-thawing conditions. By providing comprehensive experimental data from three varying fiber lengths and three dosages, this research thoroughly investigates the influence of these parameters on the mechanical and thermal properties of concrete. This robust data set will serve as a foundation for the future development of constitutive models tailored specifically for fiber-reinforced slag concrete, addressing a critical gap in knowledge, as existing models for normal aggregate concrete with fibers (Buratti and Mazzotti 2015; Çavdar 2012) may not fully capture the unique behavior of slag-based composites under extreme temperature variations. The findings are expected to enhance the design of durable and sustainable concrete structures in harsh environments.

### Table 1—Composition and physical attributes of EAF slag aggregate

| Properties | EAF slag aggregate |
|---|---|
| Size, mm | 4 to 20 |
| Specific gravity | 3.11 |
| Water absorption, % | 8.55 |
| Los Angeles abrasion loss, % | 15 |
| Proportion after primary crushing, % | 73 |
| Expansion average (ASTM D4792-00) | 0.24% |
| Chemical composition | EAF steel slag, % |
| CaO | 34.18 |
| $Fe_2O_3$ | 29.13 |
| $Al_2O_3$ | 9.1 |
| $SiO_2$ | 17.42 |
| MgO | 4.24 |
| $K_2O$ | 0.52 |
| $SO_3$ | 0.27 |
| $TiO_2$ | 0.57 |
| Cl | <0.01 |
| Loss on ignition | — |
| MnO | 3.65 |
| $P_2O_5$ | 0.55 |
| $Na_2O$ | 0.13 |

## MATERIAL AND PROPERTIES

### EAF slag and PP fibers

The steel slag used in this study was procured from an electric arc furnace (EAF) located in Ohio. The slag underwent a standardized treatment process (Manso et al. 2004) involving fragmentation, crushing, sorting, magnetic separation, and preparation for subsequent use. Stability tests, conducted according to ASTM D4792-00 (2000), demonstrated that the slag's expansion upon water immersion at 70°C for 1 week was less than 1%, conforming to the ASTM D2940-03 (2003) standard for aggregate expansion, which is less than 0.5%. Chemical analysis, consistent with Fares et al. (2021), indicated the slag's suitability for structural concrete due to its elevated $Fe_2O_3$ content and density exceeding that of limestone. The X-ray fluorescence (XRF) analysis results, presented in Table 1, further confirm the slag's chemical adequacy. However, according to the Spanish standard (EHE-08 [2008]), the slag could also have a tendency for water absorption beyond the necessary limit, which could weaken the strength and workability of concrete.

Figure 1(a) illustrates the twisted bundle monofilament PP fibers, characterized by a uniform diameter of 40 μm and lengths of 19.01, 38.1, and 57.15 mm. These fibers, with aspect ratios from 475 to 1429, were incorporated to examine their effects on hardened-state cracking, flexural strength, thermal expansion, and freezing-and-thawing durability, with the goal of improving overall concrete performance. Figure 1(b) illustrates the slag aggregate and sand used in the concrete mixtures.

Table 2 summarizes the PP fibers' specifications, including their specific gravity, length, diameter, Young's modulus, tensile strength, CTE, and excellent chemical resistance. The aim of using these materials is to assess their combined effect on the durability and structural integrity of concrete mixtures, concentrating on the essential physical and chemical properties needed for structural purposes.

## SPECIMEN PREPARATION

In this study, specimens were fabricated in prism shapes with specified dimensions of 75 x 100 x 405 mm to test flexural strength, dynamic modulus of elasticity, and the effects of freezing-and-thawing cycles on mass, according to ASTM C215-14 (2014), ASTM C666/C666M-15, and ASTM C1609/C1609M-12 (2012) protocols. To assess the CTE, two distinct specimen sizes were used: concrete discs measuring 150 mm in diameter and 38 mm in thickness for the Ohio CTE test, and concrete cylinders with a diameter of 100 mm and a height of 200 mm for the AASHTO TP 60-00 standard. For each unique mixture formulation and test type, three replicate samples were prepared and tested, resulting in a total of 135 specimens for the entire experimental program. At a fiber dosage of 9 kg/m$^3$, the concrete mixture showed mildly reduced workability, with slightly increased stiffness and occasional light fiber clustering during mixing, which was addressed with slightly longer mixing durations to ensure uniform dispersion. Table 3 shows the slag aggregate concrete mixture design specifications for the varied fiber dosages used in this study. Al Rikabi et al. (2018) documented improved freezing-and-thawing durability with a 49°C, 6-hour steam-curing cycle; consequently, that regimen was applied here after a 3-day casting period.

### Table 2—Characteristics of PP fibers

| | |
|---|---|
| Specific gravity | 0.92* |
| Length, mm | 19.01, 38.1, and 57.15* |
| Diameter, μm | 40* |
| Young's modulus, N/mm$^2$ | 4050* |
| Tensile strength, N/mm$^2$ | 586* |
| CTE, $10^{-6}$/°C | 70 to 100* |
| Chemical resistance | Excellent* |

*Properties were provided by manufacturer.

## EXPERIMENTAL DESIGN

### Coefficient of thermal expansion

The CTE of the concrete samples was determined using the Ohio CTE method, adhering to AASHTO TP 60-00 guidelines and incorporating methods suggested by Akentuna et al. (2017) and Kim et al. (2015). Figure 2(a) illustrates the Ohio CTE device schematic, and Fig. 2(b) shows a specimen mounted within the chamber. Prior to testing, the apparatus was meticulously calibrated using a nickel-iron alloy cross square, and the measurement device was validated with 6061 aluminum and stainless steel discs, following the procedures described in Akentuna et al. (2017) and Kim et al. (2015). To mitigate the effects of moisture, the samples were initially dried at 60°C for 48 hours. Subsequently, they were acclimatized at –60°C for 1 hour in a chamber, gradually warmed over 6 hours to –60°C, and maintained at this temperature for an additional hour. Data on deformation and temperature were collected at 1-minute intervals.

Additionally, the AASHTO TP 60-00 method was employed for CTE determination, as depicted in Fig. 3. In this setup, calibration was performed using a 304 stainless steel cylinder, and concrete specimens were preconditioned in a water tank for 48 hours. The length of each specimen was measured thrice, and the values were averaged. For the test, specimens were placed with a linear variable

### Table 3—Slag aggregate concrete mixture design specifications with varied fiber dosages

| Fiber dosage, kg/m$^3$ | Fiber lengths, mm | Coarse aggregate, kg | Fine aggregate, kg | Cement, kg | Air-entraining admixture, L/m$^3$ | Water, kg | *w/c* |
|---|---|---|---|---|---|---|---|
| 3.0 | 19.01, 38.1, and 57.15 | 576 | 863 | 307 | 1.2 | 98 | 0.32 |
| 6.0 | 19.01, 38.1, and 57.15 | 576 | 863 | 307 | 1.2 | 98 | 0.32 |
| 9.0 | 19.01, 38.1, and 57.15 | 576 | 863 | 307 | 1.2 | 98 | 0.32 |

Note: *w/c* is water-cement ratio.

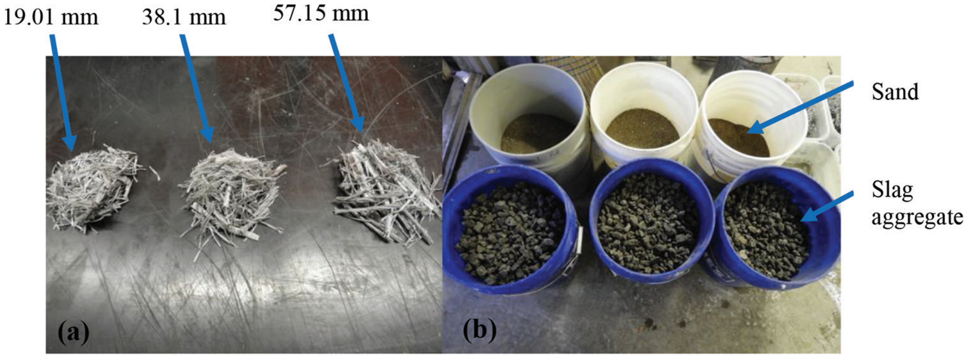

*Fig. 1—(a) Fibers of 19.01, 38.1, and 57.15 mm in length; and (b) slag aggregate and sand in separate containers.*

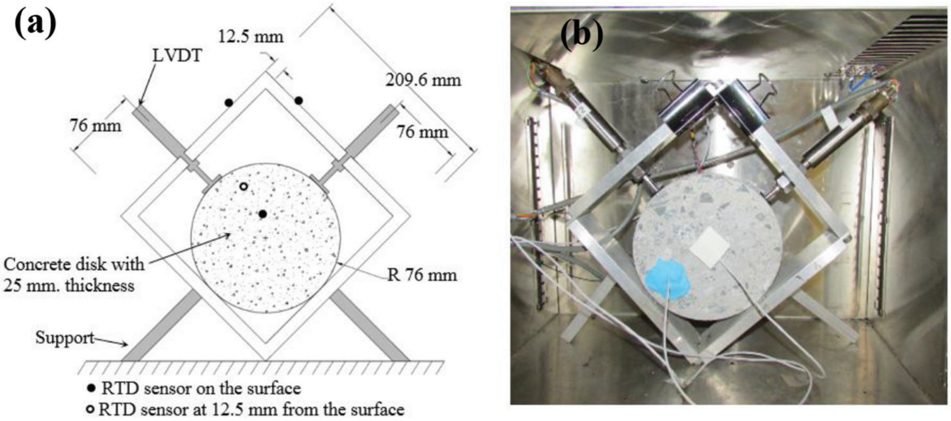

*Fig. 2—Ohio CTE device: (a) device schematic; and (b) specimen mounted in chamber. (Note: RTD is resistance temperature detector.)*

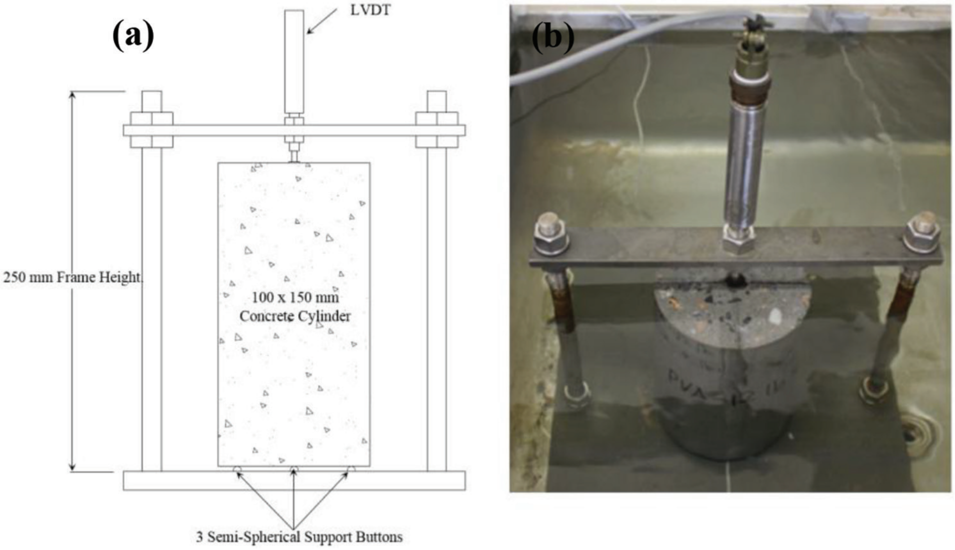

*Fig. 3—AASHTO CTE test setup: (a) measurement schematic; and (b) specimen arrangement.*

differential transformer (LVDT) at the center, within a frame, in a temperature-controlled bath for saturation. The protocol began at 10°C for 1.5 hours, increased to 50°C over 2 hours, and sustained at 50°C for an additional 1.5 hours.

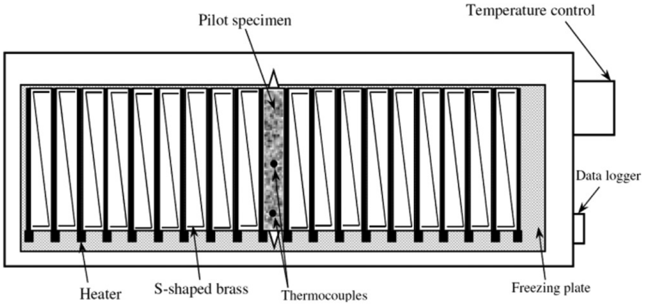

*Fig. 4—Schematic of freezing-and-thawing cabinet.*

## Flexural strength

Flexural properties were assessed by determining the peak tensile strength, midpoint deflection, and load-deflection characteristics following the guidelines of ASTM C78/C78M-15 (2015) and ASTM C1609/C1609M-12. The experiment used a displacement speed of 0.1 mm/min. An LVDT positioned on the loading plate was used to record deflection at the beam's center.

## Freezing-and-thawing cycles

The freezing-and-thawing experiment was conducted in accordance with ASTM C666/C666M-15 Procedure A. Each cycle spanned 4 to 5 hours, with temperature fluctuations between 4 and –18°C. The methodology used a freezing-and-thawing cabinet for cyclic freezing and thawing of specimens, as shown in Fig. 4. The configuration employed stainless steel prism molds for the experiments, including one specifically for the reference sample, all of which were positioned within a dedicated chamber. This setup included a lamp to maintain conditions and thermometers for accurate temperature adjustments and observations. To maintain a consistent temperature difference of no more than 10°C between the outer layer and the inner part of the specimen, two thermocouples were thoughtfully placed. Additionally, to ensure optimal water circulation and minimize thermal transfer from the specimen to its mold base, which was in immediate contact with the equipment's cooling element, S-shaped brass wires were placed beneath each specimen.

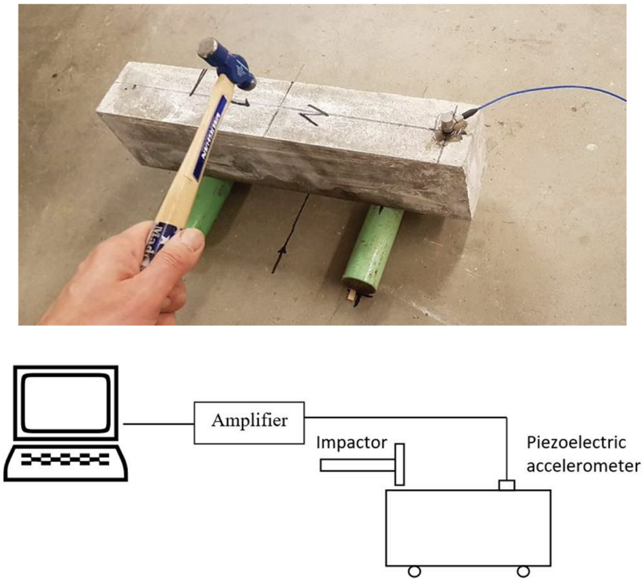

*Fig. 5—Setup for dynamic modulus testing experiments.*

The research aimed to assess the resilience of fiber-reinforced concrete under freezing-and-thawing scenarios by examining changes in mass, dynamic modulus of elasticity, and bending strength. Following the guidelines of ASTM C666/C666M-15, changes in mass and dynamic modulus of elasticity were noted after each set of 30 cycles, whereas tests to determine bending strength were conducted after the completion of 100, 200, and 300 cycles. Before undergoing tests, the specimens were soaked in water for a fortnight, and mass recordings were performed to a precision level of 0.001 kg, in accordance with ASTM C666/C666M-15.

## Dynamic modulus of elasticity

The dynamic modulus of elasticity was measured in accordance with ASTM C215-14, including sample weighing and fundamental transverse frequency determination. As shown in Fig. 5, each specimen was placed on a specialized base with a 25 mm overhang at one end. A piezoelectric accelerometer, covering a frequency range of 100 Hz to 100 kHz, was affixed to the prism and connected to a high-speed data acquisition system capable of sampling at 65,000 samples per second. Specimens were vibrated with a 23 g hammer, and their fundamental transverse frequency was pinpointed through Fourier series analysis. The dynamic modulus of elasticity was then calculated using Eq. (1), as provided in ASTM C215-14

$$E = 0.9464(L^3T/bt^3)Mn^2 \qquad (1)$$

where $L$ is the length in meters (m); $T$ is the adjustment factor; $t$ and $b$ are the cross-sectional area in meters (m); $M$ is the mass in kilograms (kg); and $n$ is the fundamental transverse frequency in hertz (Hz).

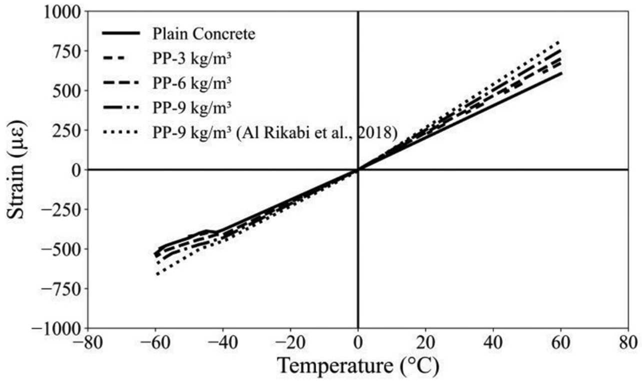

*Fig. 6—Thermal strain versus temperature.*

## RESULTS AND DISCUSSION

### Impact of incorporating fiber on mechanical characteristics of concrete

*Coefficient of thermal expansion*—The examination of the impact of fiber addition on the mechanical properties of concrete, specifically focusing on the CTE, was conducted using the Ohio method across a temperature range from –60 to 60°C. Figure 6 shows the thermal strain versus temperature. The analysis revealed a distinct linear correlation between thermal strain and fiber content, especially noticeable between –40 and 60°C. The integration of PP fibers noticeably affects thermal strain outcomes. The thermal strain across various fiber dosages and lengths was recorded from 606 to 709 με at 60°C and 530 to 572 με at –60°C. Notably, the inclusion of 9 kg/m$^3$ of fiber with a length of 57.05 mm resulted in an increase in thermal strain of approximately 17% at 60°C and approximately 7.92% at –60°C compared to plain concrete. The analysis across temperatures from –60 to 60°C showed that both the length and dosage of fibers had an influence on thermal strain. Al Rikabi (2018) also found that 9 kg/m$^3$ of PP fibers increased thermal strain in normal aggregate concrete to approximately 815 με at 60°C and –661 με at –60°C. These values align with the current study's findings of 753 με at 60°C and –600 με at –60°C, confirming the strong influence of fiber dosage on thermal expansion.

Table 4 displays the results from the analysis of the CTE carried out through the Ohio method, containing data for various dosages over the full temperature range from –60 to 60°C, including separate figures for the lower (–60 to 0°C) and upper (0 to 60°C) halves of the spectrum. Consequently, it may be critical to consider the impact of CTE on fiber-reinforced slag aggregate concrete in structural design. This analysis becomes particularly relevant when comparing CTE values obtained through the Ohio method with those from the AASHTO TP 60-00 method. The observed discrepancy in CTE values between oven-dried samples (Ohio) and water-saturated samples (AASHTO) corroborates findings from AASHTO TP 60-00 and Neville (1995), indicating the profound effect of moisture on CTE values. Consequently, adjustments based on the estimated saturation level of concrete are recommended for practical applications.

Table 5 demonstrates that CTE values derived from the Ohio method exceed those obtained from the AASHTO method, evidencing an 8.77% increase for plain concrete

**Table 4—Pre-freezing-and-thawing CTE of fiber-reinforced concrete using Ohio method**

| Fiber dosage, kg/m$^3$ | Fiber length, mm | CTE | | | | | |
|---|---|---|---|---|---|---|---|
| | | Temperature from –60 to 60°C, $10^{-6}$/°C | Coefficient of variation, % | Temperature from –60 to 0°C, $10^{-6}$/°C | Coefficient of variation, % | Temperature from 0 to 60°C, $10^{-6}$/°C | Coefficient of variation, % |
| 0 | — | 10.411 | 2.94 | 9.9 | 7.038 | 11.2 | 6.448 |
| 3 | 19.01 | 10.989 | 7.52 | 10.1 | 5.506 | 13.3 | 3.235 |
| 6 | 19.01 | 11.37 | 2.7 | 7.53 | 6.874 | 13.3 | 6.07 |
| 9 | 19.01 | 11.236 | 1.46 | 10.44 | 3.0 | 12.29 | 2.317 |
| 3 | 38.1 | 11.504 | 0.82 | 10.09 | 5.277 | 13.54 | 2.388 |
| 6 | 38.1 | 12.391 | 3.01 | 9.21 | 1.802 | 12.67 | 2.441 |
| 9 | 38.1 | 12.964 | 2.55 | 9.39 | 3.061 | 12.63 | 4.677 |
| 3 | 57.15 | 13.133 | 0.51 | 8.87 | 3.297 | 13.24 | 3.791 |
| 6 | 57.15 | 13.324 | 3.21 | 8.33 | 8.478 | 12.36 | 7.437 |
| 9 | 57.15 | 13.55 | 4.7 | 10.27 | 1.772 | 12.89 | 2.438 |

**Table 5—Comparison of CTE results: Ohio CTE device versus AASHTO TP 60-00**

| Fiber dosage, kg/m$^3$ | Fiber length, mm | CTE temperature from 10 to 50°C | | Reduction in CTE due to saturation, % |
|---|---|---|---|---|
| | | Ohio CTE device (dry), $10^{-6}$/°C | AASHTO TP 60-00 (saturated), $10^{-6}$/°C | |
| 0 | — | 11.18 | 10.2 | 8.77 |
| 3 | 19.01 | 11.27 | 10.39 | 7.81 |
| 6 | 19.01 | 11.5 | 10.55 | 8.26 |
| 9 | 19.01 | 11.65 | 10.7 | 8.15 |
| 3 | 38.1 | 12.23 | 10.99 | 10.14 |
| 6 | 38.1 | 12.57 | 11.19 | 10.98 |
| 9 | 38.1 | 12.78 | 11.31 | 11.50 |
| 3 | 57.15 | 13.25 | 11.59 | 12.53 |
| 6 | 57.15 | 13.51 | 11.79 | 12.73 |
| 9 | 57.15 | 13.76 | 11.98 | 12.94 |

**Table 6—Modulus of elasticity variations in concrete prisms by fiber dosage and length**

| Fiber dosage, kg/m$^3$ | Fiber length, mm | Dynamic modulus, MPa | Coefficient of variation, % |
|---|---|---|---|
| 0 | — | 31,171 | 1.179 |
| 3 | 19.01 | 31,673.58 | 5.731 |
| 6 | 19.01 | 31,888.27 | 5.06 |
| 9 | 19.01 | 32,157.64 | 3.811 |
| 3 | 38.1 | 31,212.63 | 5.641 |
| 6 | 38.1 | 32,893.95 | 2.38 |
| 9 | 38.1 | 33,433.67 | 3.183 |
| 3 | 57.15 | 33,664.91 | 1.649 |
| 6 | 57.15 | 34,288.33 | 3.918 |
| 9 | 57.15 | 34,978.24 | 0.403 |

and a 12.94% increase for concrete reinforced with 9 kg/m$^3$ of PP. These insights stress the necessity to account for the severe air-dry conditions a concrete structure may face and the importance of evaluating the thermal effects on fiber-reinforced slag aggregate concrete across an extensive temperature range to ensure accurate design and maintain structural integrity.

*Dynamic modulus of elasticity*—Table 6 shows the initial dynamic modulus of elasticity measurements for the samples before they were subjected to freezing-and-thawing cycles, following the specifications of ASTM C215-14. The addition of PP fibers to the slag aggregate concrete mixture is likely to result in an improved modulus of elasticity, indicative of a potential enhancement over conventional concrete. This improvement stems from the fibers' reinforcement capabilities, enhancing the concrete's rigidity and its ability to withstand structural stresses. The recorded dynamic modulus readings show a trend of increasing dynamic modulus with the incorporation of fibers, ranging from a low of approximately 31,171 MPa in fiberless samples to a high of 34,978.24 MPa in samples supplemented with 9 kg/m$^3$ of fibers and fiber lengths of 57.15 mm. This inclusion of fibers seems to not only enhance the concrete's stiffness but also its adaptability, suggesting the potential for fiber-reinforced slag aggregate concrete structures to offer better resistance against shape changes. Such durability is key to managing distortions more effectively before they lead to a failure in the structure. These results align with the findings

**Table 7—Flexural properties of slag aggregate concrete with PP fiber reinforcement**

| Fiber dosage, kg/m$^3$ | Fiber length, mm | Flexural strength, MPa | Coefficient of variation, % |
|---|---|---|---|
| 0 | — | 3.72 | 1.179 |
| 3 | 19.01 | 5.01 | 5.731 |
| 6 | 19.01 | 5.49 | 5.06 |
| 9 | 19.01 | 5.68 | 3.811 |
| 3 | 38.1 | 5.63 | 5.641 |
| 6 | 38.1 | 6.31 | 2.38 |
| 9 | 38.1 | 6.60 | 3.183 |
| 3 | 57.15 | 6.58 | 1.649 |
| 6 | 57.15 | 6.98 | 3.918 |
| 9 | 57.15 | 7.45 | 0.403 |

of Ren et al. (2018), who found that fibers tend to increase the dynamic modulus of elasticity, highlighting their role in improving mechanical performance.

*Flexural strength analysis*—Table 7 shows the flexural strength of slag aggregate concrete reinforced with PP fiber at various fiber dosages and lengths. The findings underscore a direct correlation between the addition of fibers—both in length and dosage—and an enhancement in flexural strength. This outcome is anticipated, considering fibers serve to counteract the inherent brittleness of plain concrete by effectively interlinking across both larger and finer cracks within the concrete matrix. This action enhances the material's ability to withstand bending forces (Banthia and Sappakittipakorn 2007). The flexural strength spans from a low of roughly 3.72 MPa in samples devoid of fibers, climbing to a peak of approximately 7.45 MPa in specimens that benefit from the inclusion of fibers at a rate of 9 kg/m$^3$ and with a fiber length measuring 57.15 mm. Table 2 details the physical properties of PP fibers, highlighting their extensive surface area, which is conducive to bonding and contributes to the observed increase in flexural strength. The reinforced concrete specimens, incorporating PP fibers, exhibit enhanced load-bearing capacity and improved post-cracking performance compared to those made with plain slag aggregate concrete. Figure 7 illustrates the superior performance of fiber-reinforced specimens at a serviceability deflection of 3 mm (conforming to ASTM C1609/C1609M-12), where PP fibers maintained a strong bond with the concrete matrix, preventing the splitting observed in unreinforced specimens at this deflection.

## Influence of freezing-and-thawing cycles on mechanical properties of fiber-reinforced concrete

Freezing-and-thawing cycles in concrete can lead to microcrack formation, compromising the concrete's structural integrity and material properties by disrupting the bond between its components. PP fibers were incorporated to enhance the concrete's cohesion and counteract these detrimental effects.

*Coefficient of thermal expansion*—The effect of freezing-and-thawing cycles on the CTE for both fiber-reinforced and plain concrete was monitored over 100-cycle increments, as depicted in Fig. 8. After 200 cycles, plain concrete exhibited a 21.23% decrease in the CTE, and beyond 300 cycles, the degradation was so severe that CTE measurements were not feasible. The formation of microcracks from the freezing-and-thawing process compromises the concrete's cohesion, leading to a diminished CTE.

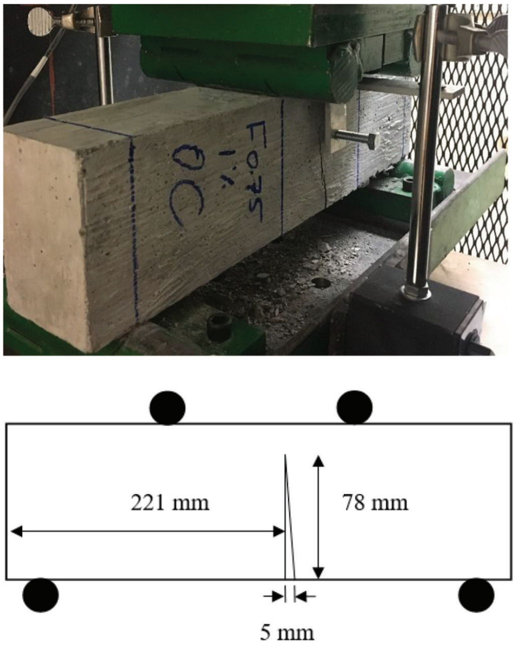

*Fig. 7—Crack width in PP fiber-enhanced slag aggregate concrete with 9 kg/m$^3$ and 19.01 mm fibers at 3 mm deflection.*

Figure 8(a) outlines the variations in the CTE for concrete samples reinforced with 19.01 mm PP fibers over 300 freezing-and-thawing cycles. Notably, at the 300-cycle mark, reductions in CTE of 27.14, 31.5, and 20.7% were observed for fiber dosages of 3, 6, and 9 kg/m$^3$, respectively. Conversely, Fig. 8(b) examines samples with 38.1 mm fibers, where an increase in CTE was recorded at 200 cycles, showing reductions of 0.20, 4.01, and 5.91% for the same fiber dosages. Figure 8(c) further explores samples with 57.15 mm fibers and shows a pronounced increase in the CTE at 300 cycles, with gains of 14.78, 15.66, and 16.58% for fiber dosages of 3, 6, and 9 kg/m$^3$, respectively.

The observed change in the CTE for fiber-reinforced concrete following 300 freezing-and-thawing cycles suggests that the fibers play a crucial role in bridging microcracks, thereby enhancing the material's capacity to undergo thermal expansion and contraction. This is notably illustrated in Fig. 8. The findings imply that among the PP fiber lengths tested (19.01, 38.1, and 57.15 mm), a fiber length of 38.1 mm at 3, 6, and 9 kg/m$^3$ consistently yielded the minimal increase in CTE, indicating its efficiency in mitigating the adverse effects of freezing-and-thawing cycles on concrete's thermal expansion properties.

Al Rikabi et al. (2018) also studied the impact of freezing-and-thawing cycles on plain and fiber-reinforced normal aggregate concrete, as depicted in Fig. 8(c). Their findings showed a 99.78% reduction in CTE for plain concrete to

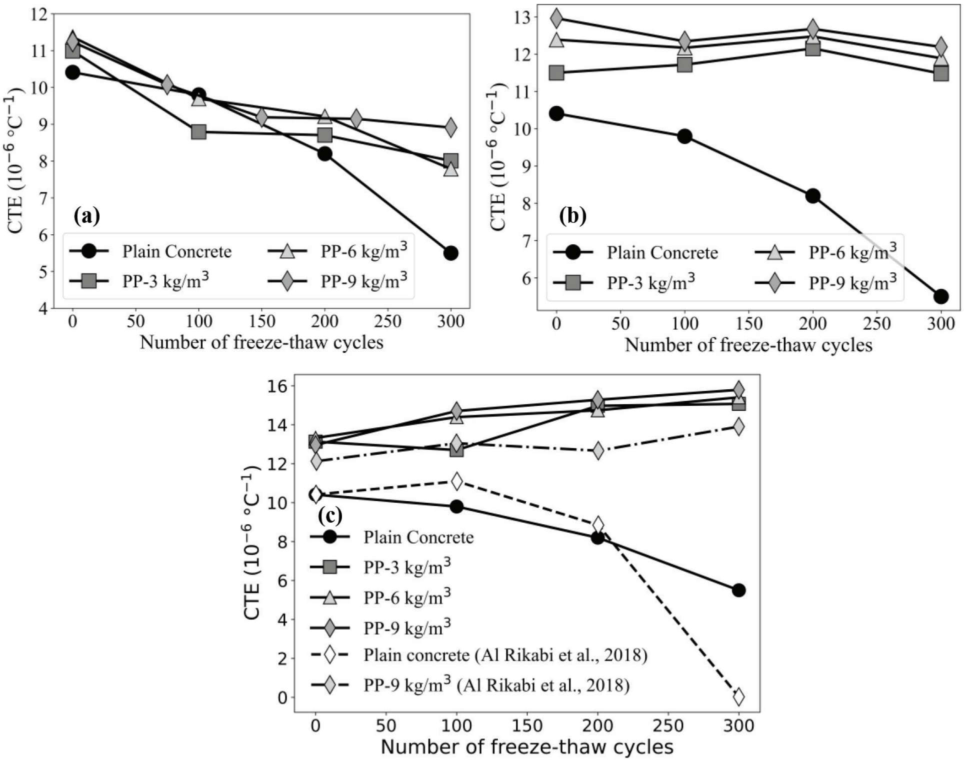

*Fig. 8—Impact of freezing-and-thawing cycles on CTE for slag aggregate concrete reinforced with PP fibers at lengths of: (a) 19.01 mm; (b) 38.1 mm; and (c) 57.15 mm.*

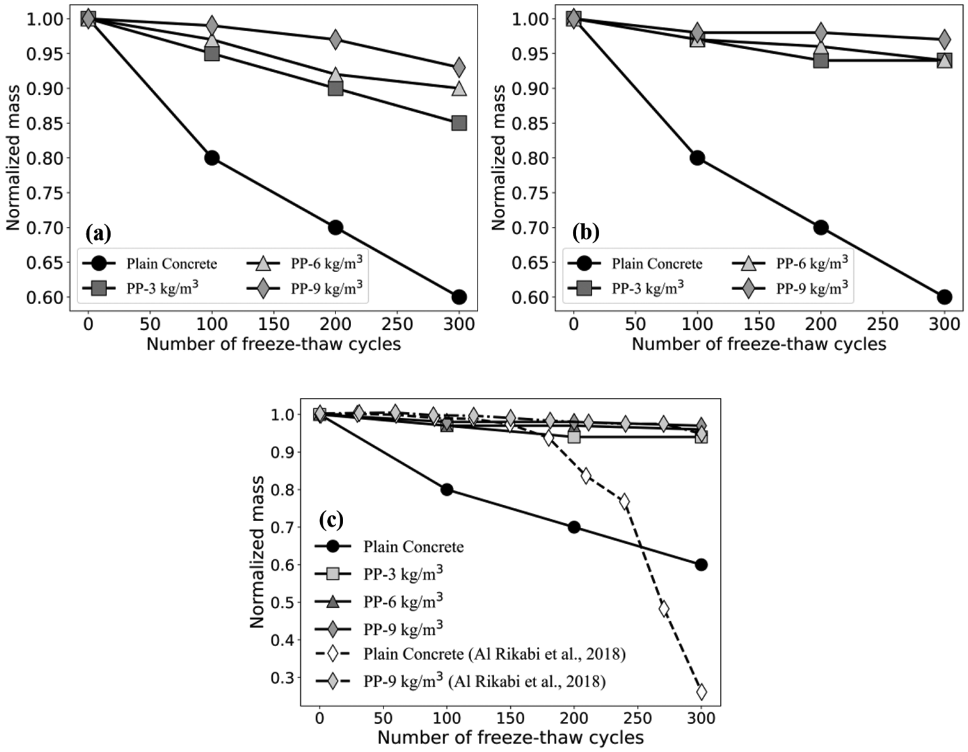

*Fig. 9—Mass change percentage in concrete prisms with different PP fiber lengths after 300 freezing-and-thawing cycles: (a) 19.01 mm; (b) 38.1 mm; and (c) 57.15 mm.*

approximately 0.0225 × $10^{-6}$/°C after 300 cycles, whereas this study observed a 47.16% reduction in CTE for plain concrete to 5.5 × $10^{-6}$/°C after 300 cycles. For fiber-reinforced normal aggregate concrete with 9 kg/m$^3$ PP fibers, Al Rikabi et al. (2018) observed a CTE increase to 13.907 × $10^{-6}$/°C, aligning with the current study's findings of an increase to 15.7964 × $10^{-6}$/°C, showing a 21.7% increase.

*Mass reduction*—Figure 9 illustrates the mass change in concrete prisms after enduring 300 freezing-and-thawing cycles, presented as a percentage of their initial mass.

**Table 8—Dynamic modulus variations in PP fiber-reinforced slag aggregate concrete under freezing-and-thawing cycles**

| Fiber dosage, kg/m$^3$ | Fiber length, mm | Dynamic modulus at 100 cycles, MPa | Coefficient of variation, % | Dynamic modulus at 200 cycles, MPa | Coefficient of variation, % | Dynamic modulus at 300 cycles, MPa | Coefficient of variation, % |
|---|---|---|---|---|---|---|---|
| 3 | 19.01 | 30,406.637 | 1.498 | 30,141.013 | 1.232 | 26,916.598 | 3.33 |
| 6 | 19.01 | 30,931.622 | 3.803 | 30,458.576 | 3.465 | 28,128.194 | 0.849 |
| 9 | 19.01 | 31,836.064 | 1.661 | 30,920.873 | 2.771 | 29,234.106 | 0.791 |
| 3 | 38.1 | 30,276.251 | 2.928 | 30,059.995 | 2.404 | 27,039.568 | 3.727 |
| 6 | 38.1 | 32,236.071 | 2.395 | 32,084.803 | 2.832 | 29,441.292 | 4.734 |
| 9 | 38.1 | 33,099.333 | 2.104 | 32,394.663 | 3.427 | 31,185.103 | 3.781 |
| 3 | 57.15 | 32,654.963 | 0.624 | 32,527.108 | 0.382 | 30,685.712 | 1.217 |
| 6 | 57.15 | 33,945.447 | 0.814 | 33,665.639 | 3.88 | 32,084.209 | 2.099 |
| 9 | 57.15 | 34,978.447 | 3.781 | 33,951.486 | 1.413 | 33,706.305 | 3.176 |

Specimens reinforced with 19.01 mm PP fibers experienced mass reductions of 16.1, 10.32, and 7.43% for fiber dosages of 3, 6, and 9 kg/m$^3$, respectively. Similarly, specimens with 38.1 mm PP fibers underwent mass decreases of 6.59, 6.48, and 4.17% for the same fiber dosages. For specimens enhanced with 57.15 mm PP fibers, the observed mass losses after 300 freezing-and-thawing cycles were 6.18, 4.29, and 3.51% for fiber dosages of 3, 6, and 9 kg/m$^3$, respectively. Al Rikabi et al. (2018) found a more severe mass reduction in plain concrete to 0.2614 (normalized mass) after 300 cycles, compared to 0.60 in the current study, as depicted in Fig. 9(c). For fiber-reinforced concrete with 9 kg/m$^3$ PP fibers, the mass reduction to 0.948 aligns with the current study's finding of 0.9649, confirming the effectiveness of PP fibers in mitigating freezing-and-thawing damage and enhancing durability.

Figure 10 illustrates how PP fibers in slag aggregate concrete mitigate freezing-and-thawing damage by reducing voids and efflorescence, thus enhancing durability and minimizing mass loss. The mass loss in plain concrete specimens is attributed to the volumetric expansion of water upon freezing within the concrete's porous structure, as discussed by Grübl and Sotkin (1980) and Korhonen (2002). This expansion can exert pressure that exceeds the concrete's tensile strength, leading to the initiation and progressive widening of microcracks through successive freezing-and-thawing cycles. Such deterioration results in compromised structural integrity and reduced mass of the specimens. The incorporation of PP fibers into the concrete matrix serves as a countermeasure to this degradation. By interlinking across the developing cracks, the fibers enhance the concrete's resilience against freezing-and-thawing-induced damage, thus preserving its mass and overall durability more effectively. In field applications such as pavements and bridge decks, this reduction in mass loss is critical, as it directly correlates with surface scaling, material disintegration, and the eventual need for costly repairs or premature replacement due to durability failure under cyclic environmental loading (Abou Sleiman et al. 2019).

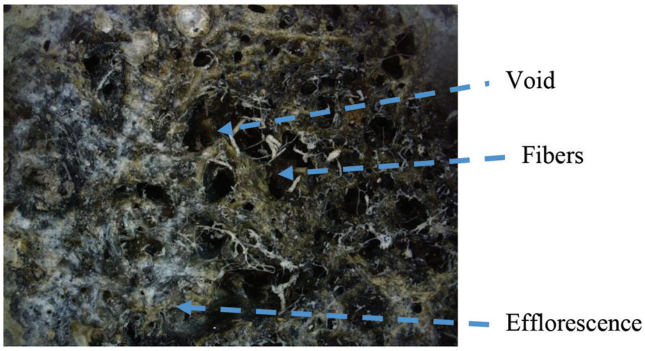

*Fig. 10—Microscopic view of voids, efflorescence, and PP fibers in concrete post-freezing-and-thawing testing.*

*Dynamic modulus of elasticity*—Table 8 highlights the impact of freezing-and-thawing cycles on the dynamic modulus of elasticity in concrete samples. After 200 cycles, assessing this modulus in plain concrete became challenging due to degradation. Concrete prisms reinforced with 19.01 mm PP fibers exhibited reductions in dynamic modulus of 15.02, 11.79, and 9.09% for fiber dosages of 3, 6, and 9 kg/m$^3$, respectively, following 300 cycles. Contrary to previous studies that attributed a decrease in dynamic modulus to the use of PP fibers, linking it to an increased surface area within the mortar matrix that could compromise mixture workability (Karahan and Atiş 2011; Salih and Al-Azaawee 2008; Raghavan et al. 1998; Yao and Zhong 2007), findings with slag aggregate PP concrete demonstrate an increase in dynamic modulus. This suggests that the slag aggregates may mitigate the workability issues and enhance the composite action between PP fibers and the concrete matrix, leading to improved mechanical properties. Furthermore, Bagherzadeh et al. (2012) found that fiber addition could reduce bleeding and segregation, potentially improving durability through a more supportive matrix. However, the increase in porosity and water absorption might compromise freezing-and-thawing durability due to higher water-filled air-void content, which, upon freezing, could exceed the concrete's tensile strength and initiate microcracks (Neville and Brooks 1993), particularly at higher fiber overlaps, thus adversely impacting the dynamic modulus of elasticity. After 300 cycles, concrete samples with PP fibers exhibited varying degrees of resistance to deterioration, depending on fiber length and dosage. The samples with 19.01 mm fibers

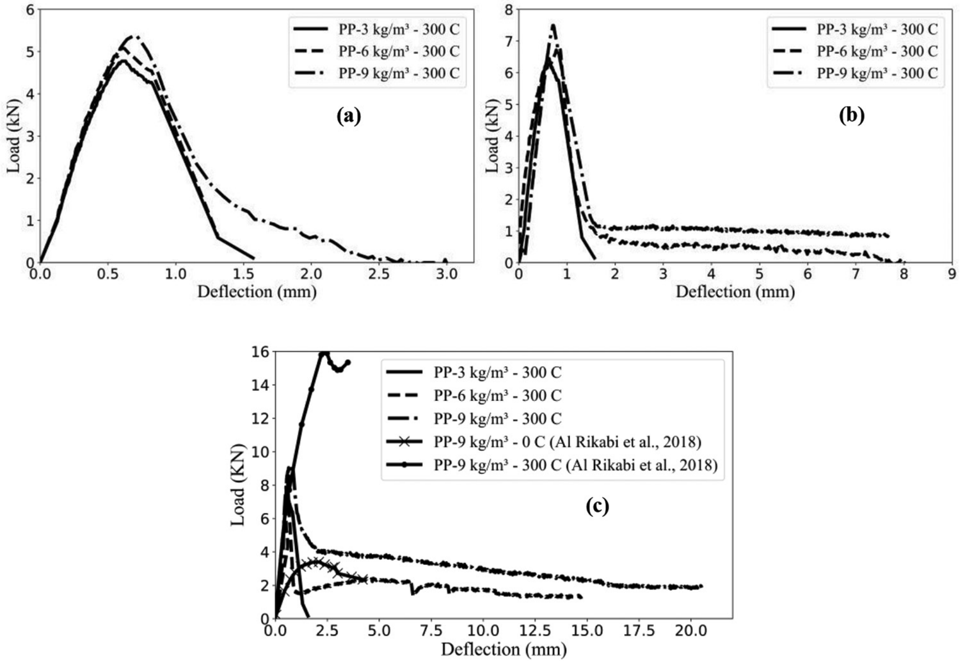

*Fig. 11—Load-deflection behavior of prisms reinforced with PP fibers at various dosages following 300 freezing-and-thawing cycles: (a) 19.01 mm; (b) 38.1 mm; and (c) 57.15 mm.*

at a dosage of 3 kg/m$^3$ showed the least resistance, while the most substantial increase in dynamic modulus was evident in samples with 57.15 mm fibers at a dosage of 9 kg/m$^3$. This contrast highlights the influence of fiber length and dosage on the structural integrity of concrete under stress. The resilience, attributed to fiber bridging, effectively counteracts the material's vulnerabilities, with the combination of 57.15 mm fibers at 9 kg/m$^3$ showing the most pronounced ability to maintain structural integrity. These findings underscore the critical role of specific lengths and dosages of PP fibers in enhancing concrete's resistance to degradation over 300 cycles.

*Flexural strength*—Figure 11 shows the effectiveness of PP fibers in maintaining the flexural strength of concrete through freezing-and-thawing cycles. Specimens reinforced with PP fibers displayed measurable decreases in flexural strength after 300 cycles: fibers measuring 19.01 mm saw reductions of 22.95, 26.776, and 22.34% across dosages of 3, 6, and 9 kg/m$^3$, respectively; 38.1 mm fibers experienced decreases of 7.28, 12.84, and 9.24%; and 57.15 mm fibers had drops of 12, 0.72, and 0.80% for the same dosages. Notably, increasing the PP fiber length from 19.01 to 57.15 mm substantially reduced the loss in flexural strength after 300 freezing-and-thawing cycles, particularly at higher dosages (6 and 9 kg/m$^3$). This suggests a critical fiber length threshold for effective microcrack interconnection, with the impact being more pronounced at higher fiber contents. Figure 11(c) contrasts Al Rikabi et al. (2018), who found an increase in strength without deflection for 57 mm fibers at 9 kg/m$^3$ after 300 cycles at 16 kN. The normal concrete strength increased from 7 to 16 kN, representing a 128.6% increase.

This study's results align with Richardson's (2012) findings, indicating that a low dosage of fibers (6 kg/m$^3$) leads to decreased strength in concrete after numerous freezing-and-thawing cycles. This effect arises from fibers increasing air voids and reducing capillarity within the concrete, thus diminishing water penetration and potentially enhancing resistance to freezing-and-thawing damage. However, Richardson et al. (2012) observed that an air content exceeding 12% reduces durability, attributed to the elevated air content and stress from water expansion in voids upon freezing, which is prevalent at high fiber dosages. This highlights the necessity of balancing fiber dosage to optimize freezing-and-thawing durability while avoiding excessive air incorporation.

## CONCLUSIONS

This research explored the effects of incorporating synthetic polypropylene (PP) fibers into slag aggregate concrete, with a focus on changes in mechanical properties before and after exposure to freezing-and-thawing cycles. The main conclusions drawn from the study are as follows:

1. Concrete samples reinforced with PP fibers exhibited increased coefficient of thermal expansion (CTE) values compared to non-reinforced concrete. The highest CTE was measured in samples containing the maximum dosage of 9 kg/m$^3$ and a fiber length of 57.15 mm.

2. The dynamic modulus of elasticity was consistently higher in fiber-reinforced specimens than in plain concrete and continued to increase with both dosage and fiber length, reaching a maximum at a dosage of 9 kg/m$^3$ and a fiber length of 57.15 mm.

3. PP fiber inclusion enhanced the concrete's flexural strength, with the most substantial enhancement observed at a fiber dosage of 9 kg/m$^3$ and a fiber length of 57.15 mm.

4. After 300 freezing-and-thawing cycles, PP fiber reinforcement effectively mitigated adverse effects on concrete's thermal expansion. A fiber length of 38.1 mm at dosages of

3, 6, and 9 kg/m$^3$ consistently showed the smallest increase in CTE.

5. While plain concrete samples underwent over 40% mass loss after 300 cycles, fiber-reinforced samples experienced less than a 7% loss, particularly at dosages of 3, 6, and 9 kg/m$^3$ and with fiber lengths of 38.1 and 57.15 mm.

6. Despite an overall enhancement in properties, fiber-reinforced concrete's flexural strength decreased after undergoing 300 freezing-and-thawing cycles, with the most considerable decline of 26.776% observed in samples with 3 kg/m$^3$ and 19.01 mm PP fibers.

7. A fiber dosage of 9 kg/m$^3$ provided the best performance among the dosages tested, offering balanced improvements across flexural strength and dynamic modulus of elasticity, besides maintaining structural integrity under freezing-and-thawing conditions.

These findings are specific to the PP fiber-reinforced slag aggregate concrete tested, considering the mixture designs and dosages employed. The optimal dosages identified are based on the tested ranges, and further investigations could refine these recommendations. Additional studies incorporating various synthetic fiber types and concrete mixture formulations are essential for a comprehensive understanding of the behavior of synthetic fiber-reinforced slag aggregate concrete. Although no supplementary characterization techniques—such as X-ray diffraction (XRD), mercury intrusion porosimetry (MIP), or thermogravimetric analysis (TGA)—were performed in this study, their inclusion in future work is recommended to better understand the microstructural changes and durability mechanisms involved.

## AUTHOR BIOS

**Abdul Basit Dahar** *is a PhD Candidate in the Department of Civil Engineering at Ohio University, Athens, OH. He also works as a Structural Engineer at DeSimone Consulting Engineering in Chicago, IL. His research interests include reinforced structures at ambient and high temperatures, finite element analysis of reinforced concrete (RC) structures, post-earthquake fire, seismic analysis and retrofitting of RC and masonry structures, and durability of thermomechanically treated steel bars.*

**Fouad T. Al Rikabi** *is a Project Engineer at AECOM. He received his PhD in civil engineering from Ohio University. His research interests include ultra-high-performance concrete for adjacent box-beam bridges, fiber-reinforced concrete pipes and structural elements, bridge performance and durability under various loading conditions, advanced numerical modeling, and finite element analysis.*

**Issam Khoury** *is an Associate Professor in the Department of Civil Engineering at Ohio University, where he received his PhD in civil engineering. He has served as a research engineer for the Ohio Research Institute for Transportation and the Environment (ORITE) since 1993 and has been involved in instrumentation and research projects for the Ohio Department of Transportation, New York State Department of Transportation, and the Federal Highway Administration. His research interests include structural instrumentation and data collection, concrete pavement performance and testing, and geotechnical data collection and analysis.*

**Safiya Ahmed** *is a Design Engineer at E.L. Robinson Engineering. She received her PhD in civil engineering from Ohio University. Her research interests include bridge design, transportation infrastructure, and advanced computational modeling of concrete structures.*

**Husam H. Hussein** *is a Principal Analyst and Project Manager at Gannett Fleming TranSystems (GFT). He received his PhD in civil engineering from Ohio University. His research interests include ultra-high-performance concrete, fiber-reinforced concrete, bridge engineering and structural performance, advanced numerical modeling and analysis, strengthening, and durability of structural systems.*

**Shad Sargand** *has served as the Russ Professor of Civil Engineering at Ohio University since 1990, and has led the Ohio Strategic Highway Research Program National Test Road on U.S. Route 23 in Delaware County, OH, since 1995. He received his PhD from the Virginia Polytechnic Institute and State University (Virginia Tech), Blacksburg, VA. His research interests include rigid and flexible pavements, finite element methods, soil-structure interaction, and pipes and conduits.*

## REFERENCES

AASHTO, 1989, "AASHTO Guide Specifications: Thermal Effects in Concrete Bridge Superstructures," American Association of State Highway and Transportation Officials, Washington, DC.

AASHTO TP 60-00 (2007), 2007, "Standard Method of Test for Coefficient of Thermal Expansion of Hydraulic Cement Concrete," American Association of State Highway and Transportation Officials, Washington, DC.

Abou Sleiman, C. N.; Shi, X.; and Zollinger, D. G., 2019, "An Approach to Characterize the Wearability of Concrete Pavement Surface Treatments," *Transportation Research Record: Journal of the Transportation Research Board*, V. 2673, No. 1, Jan., pp. 230-239. doi: 10.1177/0361198118821668

ACI Committee 209, 1992, "Prediction of Creep, Shrinkage, and Temperature Effects in Concrete Structures (ACI 209R-92) (Reapproved 2008)," American Concrete Institute, Farmington Hills, MI, 47 pp.

ACI Committee 544, 2010, "Report on the Physical Properties and Durability of Fiber-Reinforced Concrete (ACI 544.5R-10) (Reapproved 2023)," American Concrete Institute, Farmington Hills, MI, 31 pp.

Ahmed, W., and Lim, C. W., 2021, "Production of Sustainable and Structural Fiber Reinforced Recycled Aggregate Concrete with Improved Fracture Properties: A Review," *Journal of Cleaner Production*, V. 279, Jan., Article No. 123832. doi: 10.1016/j.jclepro.2020.123832

Akentuna, M.; Kim, S. S.; Nazzal, M.; and Abbas, A. R., 2017, "Asphalt Mixture CTE Measurement and the Determination of Factors Affecting CTE," *Journal of Materials in Civil Engineering*, ASCE, V. 29, No. 6, June, p. 04017010. doi: 10.1061/(ASCE)MT.1943-5533.0001840

Al Rikabi, F. T.; Sargand, S. M.; Khoury, I.; and Hussein, H. H., 2018, "Material Properties of Synthetic Fiber–Reinforced Concrete under Freeze-Thaw Conditions," *Journal of Materials in Civil Engineering*, ASCE, V. 30, No. 6, June, p. 04018090. doi: 10.1061/(ASCE)MT.1943-5533.0002297

ASTM C78/C78M-15, 2015, "Standard Test Method for Flexural Strength of Concrete (Using Simple Beam with Third-Point Loading)," ASTM International, West Conshohocken, PA, 4 pp.

ASTM C215-14, 2014, "Standard Test Method for Fundamental Transverse, Longitudinal, and Torsional Resonant Frequencies of Concrete Specimens," ASTM International, West Conshohocken, PA, 7 pp.

ASTM C531-00(2012), 2012, "Standard Test Method for Linear Shrinkage and Coefficient of Thermal Expansion of Chemical-Resistant Mortars, Grouts, Monolithic Surfacings, and Polymer Concretes," ASTM International, West Conshohocken, PA, 3 pp.

ASTM C666/C666M-15, 2015, "Standard Test Method for Resistance of Concrete to Rapid Freezing and Thawing," ASTM International, West Conshohocken, PA, 7 pp.

ASTM C1609/C1609M-12, 2012, "Standard Test Method for Flexural Performance of Fiber-Reinforced Concrete (Using Beam with Third-Point Loading)," ASTM International, West Conshohocken, PA, 9 pp.

ASTM D2940-03, 2003, "Standard Specification for Graded Aggregate Material For Bases or Subbases for Highways or Airports," ASTM International, West Conshohocken, PA, 2 pp.

ASTM D4792-00, 2000, "Standard Test Method for Potential Expansion of Aggregates from Hydration Reactions," ASTM International, West Conshohocken, PA, 2 pp.

Bagherzadeh, R.; Pakravan, H. R.; Sadeghi, A.-H.; Latifi, M.; and Merati, A. A., 2012, "An Investigation on Adding Polypropylene Fibers to Reinforce Lightweight Cement Composites (LWC)," *Journal of Engineered Fibers and Fabrics*, V. 7, No. 4, Dec., pp. 13-21.

Banthia, N., and Sappakittipakorn, M., 2007, "Toughness Enhancement in Steel Fiber Reinforced Concrete Through Fiber Hybridization," *Cement and Concrete Research*, V. 37, No. 9, Sept., pp. 1366-1372. doi: 10.1016/j.cemconres.2007.05.005

Buratti, N., and Mazzotti, C., 2015, "Experimental Tests on the Effect of Temperature on the Long-Term Behaviour of Macrosynthetic Fibre Reinforced Concretes," *Construction and Building Materials*, V. 95, Oct., pp. 133-142. doi: 10.1016/j.conbuildmat.2015.07.073

Çavdar, A., 2012, "A Study on the Effects of High Temperature on Mechanical Properties of Fiber Reinforced Cementitious Composites," *Composites Part B: Engineering*, V. 43, No. 5, July, pp. 2452-2463. doi: 10.1016/j.compositesb.2011.10.005

Choubane, B., and Tia, M., 1992, "Nonlinear Temperature Gradient Effect on Maximum Warping Stresses in Rigid Pavements," *Transportation*

*Research Record: Journal of the Transportation Research Board*, V. 1370, No. 1, pp. 11-19.

CRD-C 39-81, 1981, "Test Method for Coefficient of Linear Thermal Expansion of Concrete," U.S. Army Corps of Engineers, Washington, DC, 2 pp.

Deng, Z.; Liu, X.; Chen, P.; de la Fuente, A.; Zhou, X.; Liang, N.; Han, Y.; and Du, L., 2022, "Basalt-Polypropylene Fiber Reinforced Concrete for Durable and Sustainable Pipe Production. Part 1: Experimental Program," *Structural Concrete*, V. 23, No. 1, Feb., pp. 311-327. doi: 10.1002/suco.202000759

EHE-08, 2008, "Instrucción de Hormigón Estructural: Con Comentarios de los Miembros de la Comisión Permanente del Hormigón," Ministerio de Fomento, Secretaría General Técnica, Madrid, Spain, 704 pp.

Fares, A. I.; Sohel, K. M. A.; Al-Jabri, K.; and Al-Mamun, A., 2021, "Characteristics of Ferrochrome Slag Aggregate and Its Uses as a Green Material in Concrete – A Review," *Construction and Building Materials*, V. 294, Aug., Article No. 123552. doi: 10.1016/j.conbuildmat.2021.123552

Grübl, P., and Sotkin, A., 1980, "Rapid Ice Formation in Hardened Cement Paste, Mortar and Concrete due to Supercooling," *Cement and Concrete Research*, V. 10, No. 3, May, pp. 333-345. doi: 10.1016/0008-8846(80)90109-X

Guo, J.; Bao, Y.; and Wang, M., 2018, "Steel Slag in China: Treatment, Recycling, and Management," *Waste Management*, V. 78, Aug., pp. 318-330. doi: 10.1016/j.wasman.2018.04.045

Karahan, O., and Atiş, C. D., 2011, "The Durability Properties of Polypropylene Fiber Reinforced Fly Ash Concrete," *Materials & Design*, V. 32, No. 2, Feb., pp. 1044-1049. doi: 10.1016/j.matdes.2010.07.011

Kim, S.-S.; Nazzal, M.; Abbas, A. R.; Akentuna, M.; and Arefin, M. S., 2015, "Evaluation of Low Temperature Cracking Resistance of WMA," Report No. FHWA/OH-2015/11, Ohio Department of Transportation, Office of Statewide Planning & Research, Columbus, OH, 121 pp.

Korhonen, C., 2002, "Effect of High Doses of Chemical Admixtures on the Freeze–Thaw Durability of Portland Cement Concrete," Technical Report ERDC/CRREL TR-02-5, Cold Regions Research and Engineering Laboratory, U.S. Army Corps of Engineers Engineer Research and Development Center, Hanover, NH, 38 pp.

Kuder, K. G., and Shah, S. P., 2010, "Processing of High-Performance Fiber-Reinforced Cement-Based Composites," *Construction and Building Materials*, V. 24, No. 2, Feb., pp. 181-186. doi: 10.1016/j.conbuildmat.2007.06.018

Latifi, M. R.; Biricik, Ö.; and Mardani Aghabaglou, A., 2022, "Effect of the Addition of Polypropylene Fiber on Concrete Properties," *Journal of Adhesion Science and Technology*, V. 36, No. 4, pp. 345-369. doi: 10.1080/01694243.2021.1922221

Manso, J. M.; Gonzalez, J. J.; and Polanco, J. A., 2004, "Electric Arc Furnace Slag in Concrete," *Journal of Materials in Civil Engineering*, ASCE, V. 16, No. 6, Dec., pp. 639-645. doi: 10.1061/(ASCE)0899-1561(2004)16:6(639)

Mekonen, T. B.; Alene, T. E.; Alem, Y. A.; and Nebiyu, W. M., 2024, "Influence of Steel Slag as a Partial Replacement of Aggregate on Performance of Reinforced Concrete Beam," *International Journal of Concrete Structures and Materials*, V. 18, No. 1, Dec., Article No. 56. doi: 10.1186/s40069-024-00698-5

Neville, A. M., 1995, *Properties of Concrete*, fourth edition, John Wiley & Sons, Inc., New York, 844 pp.

Neville, A. M., and Brooks, J. J., 1993, *Concrete Technology*, Longman Scientific and Technical, Harlow, Essex, UK, 460 pp.

Peyvandi, A.; Soroushian, P.; and Jahangirnejad, S., 2014, "Structural Design Methodologies for Concrete Pipes with Steel and Synthetic Fiber Reinforcement," *ACI Structural Journal*, V. 111, No. 1, Jan.-Feb., pp. 83-92.

Raghavan, D.; Huynh, H.; and Ferraris, C. F., 1998, "Workability, Mechanical Properties, and Chemical Stability of a Recycled Tyre Rubber-Filled Cementitious Composite," *Journal of Materials Science*, V. 33, No. 7, Apr., pp. 1745-1752. doi: 10.1023/A:1004372414475

Ren, G. M.; Wu, H.; Fang, Q.; and Liu, J. Z., 2018, "Effects of Steel Fiber Content and Type on Dynamic Compressive Mechanical Properties of UHPCC," *Construction and Building Materials*, V. 164, Mar., pp. 29-43. doi: 10.1016/j.conbuildmat.2017.12.203

Richardson, A. E.; Coventry, K. A.; and Wilkinson, S., 2012, "Freeze/Thaw Durability of Concrete with Synthetic Fibre Additions," *Cold Regions Science and Technology*, V. 83-84, Dec., pp. 49-56. doi: 10.1016/j.coldregions.2012.06.006

Salih, S. A., and Al-Azaawee, M. E., 2008, "Effect of Polypropylene Fibers on Properties of Mortar Containing Crushed Bricks as Aggregate," *Engineering and Technology Journal*, V. 26, No. 12, Dec., pp. 1508-1523. doi: 10.30684/etj.26.12.6

Simpson, A. L.; Schmalzer, P. N.; and Rada, G. R., 2007, "Long Term Pavement Performance Project Laboratory Materials Testing and Handling Guide," Publication No. FHWA-HRT-07-052, Office of Infrastructure Research and Development, Federal Highway Administration, McLean, VA, 589 pp.

USGS, 2022, "Mineral Commodity Summaries: Iron and Steel Slag," National Minerals Information Center, U.S. Geological Survey, Reston, VA, 2 pp.

Van Ho, Q., and Huynh, T.-P., 2023, "A Comprehensive Investigation on the Impacts of Steel Slag Aggregate on Characteristics of High-Performance Concrete Incorporating Industrial By-Products," *Journal of Building Engineering*, V. 80, Dec., Article No. 107982. doi: 10.1016/j.jobe.2023.107982

Yao, W., and Zhong, W., 2007, "Effect of Polypropylene Fibers on the Long-Term Tensile Strength of Concrete," *Journal of Wuhan University of Technology-Materials Science Edition*, V. 22, No. 1, Feb., pp. 52-55. doi: 10.1007/s11595-005-1052-z

Yun, H.-D., and Rokugo, K., 2012, "Freeze-Thaw Influence on the Flexural Properties of Ductile Fiber-Reinforced Cementitious Composites (DFRCCs) for Durable Infrastructures," *Cold Regions Science and Technology*, V. 78, July, pp. 82-88. doi: 10.1016/j.coldregions.2012.02.002

ACI MATERIALS JOURNAL TECHNICAL PAPER

Title No. 123-M17

# Application of Artificial Intelligence for Accurate Chloride Permeability Predictions in Concrete Structures

by Mohamad Kharseh and Fayez Moutassem

*The durability of reinforced concrete is often compromised by chloride penetration, leading to corrosion of reinforcing steel and reduced structural strength. To improve the sustainability and longevity of concrete structures, it is crucial to model and predict chloride permeability (CP) accurately, thereby minimizing the time and resources required for extensive experimental testing.*

*This paper presents a proof-of-concept study applying artificial neural networks (ANNs) to predict CP in concrete structures. The model was trained on a small but carefully controlled experimental data set of 10 concrete mixtures, considering four key parameters: water-cementitious materials ratio, silica fume content, cementitious materials content, and air content. Despite the limited data set size, which constrains generalizability and statistical robustness, the ANN captured nonlinear relationships among the input parameters and CP. The comparison between experimental and simulated CP values showed reasonable agreement, with errors ranging between –242 and 420 coulombs. These results establish the trustworthiness and reliability of the proposed model, providing a valuable tool for predicting CP and informing the design of durable and sustainable concrete structures.*

**Keywords:** artificial neural networks (ANNs); chloride permeability; concrete structures; durability; sustainability.

## INTRODUCTION AND BACKGROUND

Reinforced concrete structures face significant challenges in harsh environments, particularly at the foundation level, where durability is crucial. One of the primary causes of environmental degradation is chloride penetration, which leads to the corrosion of reinforcing steel and a substantial reduction in the strength and serviceability of concrete structures. This degradation often necessitates premature repairs or even replacement of the entire structure. Conversely, preventing such deterioration enhances concrete durability and contributes to sustainability by reducing the negative environmental impact associated with the production and lifecycle of concrete. Campos Silva et al.[1] emphasized that increasing the economic lifecycle of concrete structures leads to reduced material use and a lower carbon dioxide ($CO_2$) footprint in concrete production.

Efficient reduction of concrete deterioration resulting from chloride penetration requires using durable and impermeable concrete that can effectively prevent or slow down the ingress of chlorides to the level of the reinforcing steel. Capillary absorption, hydrostatic pressure, and diffusion are the primary transport mechanisms through which chloride ions penetrate concrete. Diffusion, in particular, is the primary method by which chlorides reach the level of steel reinforcement. However, the process of chloride-ion diffusion into concrete is slow and impractical to determine directly within a timeframe suitable for quality control measures. Therefore, it is essential to determine the chloride-ion penetration characteristics of different concretes through design to ensure adequate quality control.

The pore structure is affected by the rate at which chloride ions penetrate concrete, which is, in turn, affected by the concrete mixture and its age. The key variables that influence the pore structure include the water-cement ratio ($w/c$), degree of cement hydration, air content, and the inclusion of supplementary cementing materials.[2] It is widely recognized that an increase in the $w/c$ results in more voids and consequently reduces the strength and durability of the concrete. The degree of cement hydration primarily depends on the concrete's age, the type and proportions of cement paste, and the curing process. Proper curing ensures adequate water availability for cement hydration, and the age of the concrete is directly proportional to the level of hydration and the development of the pore structure. Concrete mixtures containing supplementary cementitious materials, such as fly ash and slag, exhibit slower reactivity and require an extended hydration period.[3] Furthermore, research has demonstrated that the packing density of aggregates in concrete significantly influences its hardened properties.[4,5] By optimizing the proportions and gradation of aggregates, denser packing, resulting in several benefits, can be achieved. These include enhanced concrete strength, reduced porosity, and minimized voids due to a reduction in both the amount and size of voids. This improvement leads to a more robust and durable concrete structure.

Over the years, numerous test methods have been developed to predict the amount of chloride-ion penetration into concrete. The rapid chloride permeability test (RCPT) is widely adopted in ASTM and AASHTO standards. ASTM C1202/C1202M-22[6] shows that a water-saturated concrete specimen is subjected to a 60 V applied DC voltage for 6 hours, with a 3.0% NaCl solution in one reservoir and a 0.3 M NaOH solution in the other. The total charge passed is determined and used to assess the quality of the concrete according to specific criteria. When a higher current passes at a specific voltage, it indicates a lower quality of concrete. Table 1 presents the RCPT ratings based on ASTM C1202/C1202M. To ensure quality control before concrete casting,

---

*ACI Materials Journal*, V. 123, No. 2, March 2026.

MS No. M-2024-343.R4, doi: 10.14359/51749256, received August 20, 2025, and reviewed under Institute publication policies. Pertinent discussion including author's closure, if any, will be published ten months from this journal's date if the discussion is received within four months of the paper's print publication.

**Table 1—RCPT ratings according to ASTM C1202**

| Charge passed, coulombs | Chloride-ion permeability |
|---|---|
| >4000 | High |
| 2000 to 4000 | Moderate |
| 1000 to 2000 | Low |
| 100 to 1000 | Very low |
| <100 | Negligible |

accurate prediction of chloride-ion permeability is essential. However, existing predictive models for chloride permeability in concrete have limitations. Many models are incomplete, lacking important parameters, or overly complex, requiring extensive experimental testing or statistical calibration involving many constants. Previous studies have linked these parameters with compressive strength and concrete durability, making this study a valuable contribution to the existing body of research.[7]

Artificial intelligence (AI) has emerged as a promising computational approach in civil engineering research and practical applications, particularly in modeling and predicting complex behaviors in concrete materials. AI refers to a broad field of computer science that aims to simulate human intelligence in machines through techniques such as expert systems, fuzzy logic, genetic algorithms, and machine learning. Within this field, artificial neural networks (ANNs) are a specialized subset of machine learning inspired by the structure and functioning of the human brain. ANNs are particularly effective at modeling complex, nonlinear relationships in engineering applications. In this study, the term AI is used to reflect the overarching methodology, while the specific predictive tool applied is the ANN model. This distinction is noted here to avoid confusion and to clarify that the focus of this research is on the application of ANNs within the broader context of AI-based techniques in concrete durability prediction.

Among the various AI tools, ANNs are particularly powerful and advanced computational models inspired by the structure and functioning of the human central nervous system, with interconnected artificial neurons. ANN is a powerful tool for developing models that capture intricate relationships between input variables and output parameters. In concrete research, ANN has been extensively used to predict important properties, particularly the compressive strength, which is a reliable indicator of concrete quality.

ANN has demonstrated its effectiveness in modeling the compressive strength of various types of concrete. Studies have successfully employed ANN to predict the compressive strength of self-consolidating concrete,[8-13] high-performance concrete,[14,15] rubberized concrete,[16] ferrocement concrete,[17] recycled aggregate concrete,[18,19] nano-silica concrete,[20] fiber-reinforced polymer (FRP) confined concrete,[21] metakaolin and silica fume concrete,[22] and high-strength concrete.[23]

In addition to concrete properties, ANN has found wide applications in modeling compressive strength using nondestructive testing data. For instance, a previous study used nondestructive methods such as ultrasonic pulse velocity (UPV), sclerometric, and pullout tests to evaluate concrete properties.[24] By integrating ANN into the analysis, they successfully predicted the compressive strength of concrete based on the results of these nondestructive tests. The researchers trained and tested five different network architectures, demonstrating that incorporating nondestructive testing data into ANN enables accurate identification of compressive strength for similar types of concrete. Another study compared the prediction of concrete compressive strength using ANN and multiple regression analysis, using weight and UPV as input variables for both methods.[25] The results revealed that the ANN model outperformed multiple regression analysis regarding accuracy, offering an alternative approach for assessing compressive strength without resorting to destructive testing. By establishing this relationship, the study provided an alternative to the empirical relationships provided by manufacturers, thus enhancing the understanding and prediction of concrete compressive strength.

Through their ability to capture complex relationships and leverage nondestructive testing data, ANN models offer significant advantages in predicting concrete properties and compressive strength. They provide valuable insights into concrete behavior, enabling improved quality control and assessment without the need for destructive testing methods. Recent advancements in machine learning have significantly enhanced the prediction of chloride permeability in concrete. For instance, Güneyisi et al.[26] developed an ANN model to estimate the chloride permeability of concrete containing ground-granulated blast-furnace slag (GGBS), illustrating the role of mixture composition and age in influencing durability. Huang et al.[27] introduced a hybrid model that combined extreme learning machine (ELM) and random forest (RF), optimized using a whale optimization algorithm, to predict the chloride permeability coefficient of rubberized concrete. Their results demonstrated that integrating optimization techniques with machine learning models can improve prediction performance. Similarly, Li et al.[28] developed ensemble models, including an inverse variance-based model, an ANN-based model, and a tree-based model using the RF regression algorithm, to predict the chloride migration coefficient (CMC) of concrete. Their study highlighted that ensemble models outperform single models such as ANN and support vector regression (SVR) in predicting CMC, with the combined RF and ANN model showing the highest accuracy. While these studies offer strong predictive capabilities, they often use diverse or specialized materials. In contrast, this research focuses on a core set of practical mixture design parameters—water-cementitious materials ratio (*w*/*cm*), silica fume content, cement content, and air content—allowing for a more accessible and design-phase-friendly model for engineers.

This paper aims to address these limitations by formulating a fundamental chloride permeability predictive model that is representative and relatively easy to apply. The proposed model considers essential design variables—namely, *w*/*cm*, cementitious materials content, air content, and silica fume (microsilica) content. Silica fume was selected as the sole supplementary cementitious material in the experimental program due to its rapid pozzolanic reactivity and

**Table 2—Concrete mixtures design composition and experimental testing results**

| Mixture No. | *w/c* | Maximum aggregate size, mm (in.) | Water content, kg/m$^3$ (lb/ft$^3$) | Cement content, kg/m$^3$ (lb/ft$^3$) | CA, kg/m$^3$ (lb/ft$^3$) | FA, kg/m$^3$ (lb/ft$^3$) | Silica fume, % | Air content, % | Slump, mm (in.) | 28-day $f_c'$, MPa (psi) | CP, coulombs |
|---|---|---|---|---|---|---|---|---|---|---|---|
| 1 | 0.30 | 19 (0.75) | 150 (9.36) | 500 (31.21) | 960 (59.93) | 852 (53.19) | 0 | 2.2 | 80 (3.15) | 97.0 (14,068.66) | 840 |
| 2 | 0.30 | 19 (0.75) | 150 (9.36) | 425 (26.53) | 960 (59.93) | 827 (51.63) | 15 | 2.1 | 90 (3.54) | 97.9 (14,199.19) | 155 |
| 3 | 0.40 | 19 (0.75) | 150 (9.36) | 375 (23.41) | 960 (59.93) | 960 (59.93) | 0 | 1.5 | 75 (2.95) | 72.1 (10,457.22) | 1236 |
| 4 | 0.40 | 19 (0.75) | 150 (9.36) | 319 (19.91) | 960 (59.93) | 940 (58.68) | 15 | 1.4 | 95 (3.74) | 88.3 (12,806.83) | 214 |
| 5 | 0.40 | 19 (0.75) | 150 (9.36) | 375 (23.41) | 960 (59.93) | 852 (53.19) | 0 | 6.4 | 90 (3.54) | 45.6 (6613.72) | 1230 |
| 6 | 0.40 | 19 (0.75) | 150 (9.36) | 319 (19.91) | 960 (59.93) | 832 (51.94) | 15 | 8.0 | 90 (3.54) | 45.4 (6584.71) | 725 |
| 7 | 0.40 | 19 (0.75) | 184 (11.49) | 460 (28.72) | 960 (59.93) | 687 (42.89) | 0 | 3.5 | 65 (2.56) | 55.8 (8093.11) | 2400 |
| 8 | 0.40 | 19 (0.75) | 184 (11.49) | 391 (24.41) | 960 (59.93) | 663 (41.39) | 15 | 3.8 | 25 (0.98) | 62.3 (9035.85) | 979 |
| 9 | 0.40 | 19 (0.75) | 205 (12.80) | 513 (32.03) | 960 (59.93) | 693 (43.26) | 0 | 2.2 | 90 (3.54) | 55.8 (8093.11) | 1920 |
| 10 | 0.40 | 19 (0.75) | 205 (12.80) | 436 (27.22) | 960 (59.93) | 667 (41.64) | 15 | 2.6 | 40 (1.57) | 62.0 (8992.34) | 1459 |

well-established role in reducing chloride permeability. By accurately assessing and predicting chloride permeability, the model enables optimization of concrete mixtures for enhanced durability and sustainability. The findings will support engineers in predicting concrete performance characteristics at the design stage or through nondestructive evaluation during later stages of construction.

## RESEARCH SIGNIFICANCE

This research significantly enhances the durability and sustainability of reinforced concrete structures by addressing the critical issue of chloride-induced corrosion. Traditional methods for assessing chloride permeability (CP) are time-consuming and costly, making them impractical for routine use. The development of an ANN model to predict CP offers a more efficient and accurate solution. By incorporating key mixture design variables, the ANN model provides a reliable tool for optimizing concrete mixtures, improving their resistance to chloride penetration.

The successful application of ANN in this context demonstrates its potential to revolutionize quality control processes in civil engineering, leading to longer-lasting structures with reduced maintenance needs. This research not only advances the field of AI in concrete technology but also contributes to creating more sustainable infrastructure by minimizing material consumption and extending the service life of concrete structures.

## METHODOLOGY

### Experimental program design, data collection, and experimental testing

An experimental program was developed to assess the precision and accuracy of the proposed ANN model in predicting CP measurements on concrete cylinders after 28 days. The program was designed to analyze the impact of traditional design variables on the CP values when proportioning concrete mixtures. The selected design variables included the *w*/*cm*, silica fume content, cementitious materials content, and air content.

A total of 10 concrete mixtures were designed following the ACI 211 guidelines, as presented in Table 2, encompassing the specified ranges of variables. The designed concrete mixtures correspond to compressive strength grades ranging from approximately 45 to 98 MPa (6526.70 to 14,213.70 psi), covering both conventional and high-performance applications. Slump values were targeted between 25 and 100 mm (0.98 and 3.94 in.) to reflect a workability range suitable for structural concrete. The experimental procedure was carried out consistently for all concrete mixtures and involved several steps, including mixing, placing, consolidating, curing, and testing. A Type I portland cement with a specific gravity of 3.15 was used. Densified silica fume powder with a specific gravity of 2.25 was used for half of the concrete mixtures. The densified silica fume used in this study had a silicon dioxide ($SiO_2$) content exceeding 96%, in compliance with ASTM C1240-20,[29] ensuring high pozzolanic reactivity and material quality. The coarse aggregate (CA) used in concrete is crushed limestone with a maximum aggregate size of 19 mm (0.75 in.), whereas the fine aggregate (FA) is well-graded sand. The specific gravity, absorption percent, and bulk density for the CA are 2.68, 1.2%, and 1600 kg/m$^3$ (99.88 lb/ft$^3$), respectively. The fineness modulus, specific gravity, absorption percent, and bulk density for the FA are 2.82, 2.67, 2.5%, and 1800 kg/m$^3$ (112.37 lb/ft$^3$), respectively. Values of specific gravity, absorption percent, and bulk density for CA and FA were

Fig. 1—RCPT testing setup.

determined following ASTM C127-15[30] and ASTM C128-15,[31] respectively. The particle size distributions of CA and FA and the fineness modulus of FA were measured and were found to conform to the ASTM C136/C136M-19[32] specification requirements. A high-range water reducer meeting the requirements of ASTM C494/C494M-19[33] was used in mixtures 1 to 5 to improve the workability of fresh concrete. The dosage ranged between 0.8 and 1.2% by weight of cementitious materials, selected based on trial mixtures to achieve the desired slump values without increasing the *w*/*cm*. This contributed to better flowability, improved compaction, and a denser concrete matrix, ultimately enhancing durability. In addition, an air-entraining admixture meeting the requirements of ASTM C260/C260M-10a[34] was used in mixtures 5 to 8. The testing results for each mixture, as shown in Table 2, include the actual air content (%), the amount of slump (mm), the compressive strength of concrete at 28 days (MPa), and the chloride ion permeability (coulombs).

To prepare for the RCPT test following ASTM C1202/C1202M, concrete specimens were cast into cylinders (100 mm [3.94 in.] diameter x 200 mm [7.87 in.] height) and moist-cured at 23 ± 2°C (73.4 ± 3.6°F) for 28 days. After curing, each specimen was cut into 50 mm (1.97 in.) thick discs using a water-cooled diamond saw. The cut surfaces were rinsed and cleaned to remove debris. Specimens were then vacuum-saturated by placing them in a vacuum chamber for 3 hours followed by immersion in de-aerated water for 1 hour under atmospheric pressure. For RCPT testing (Fig. 1), each specimen was mounted in a two-cell acrylic setup, with one side filled with a 3.0% NaCl solution and the other with a 0.3 N NaOH solution. A constant 60 V DC voltage was applied across the specimen for a duration of 6 hours. The total charge passed (in coulombs) was recorded at hourly intervals using a data-acquisition system and integrated to determine the chloride ion permeability. The classification of chloride permeability was interpreted in accordance with ASTM C1202/C1202M thresholds.

The last column in Table 2 presents the experimental results obtained from the CP testing of the concrete cylinders prepared from the designed mixtures. These results form the basis for training and validating the ANN model, enabling the comparison and evaluation of the model's accuracy and performance in predicting CP.

Valuable data on CP and its relationship with the selected design variables were obtained by meticulously designing and conducting the experimental program. This data set serves as the foundation for training the ANN model, enabling accurate predictions of CP in concrete structures based on the input parameters.

## ANN model development

The development of the ANN model aimed to establish a robust and reliable relationship between the input design variables and the corresponding CP values. A systematic approach was followed to achieve this, encompassing various key steps. Figure 2 illustrates the model architecture employed in this study, designed to effectively capture the intricate connections between the input variables and the predicted CP values.

The ANN model consisted of an input layer with four neurons, each representing one of the following design variables: *w*/*cm*, silica fume content, cementitious materials content, and air content. These variables play a vital role in influencing the CP of concrete structures. A one-neuron hidden layer was incorporated to capture the complexity of these interactions, enabling the model to learn and identify underlying patterns within the data. Finally, the output layer consisted of a single neuron providing the predicted CP value.

The development of the ANN model involved meticulous considerations, such as selecting an appropriate network architecture, determining suitable weight optimization algorithms, and evaluating performance metrics to ensure accurate predictions of CP. For weight optimization, the Levenberg-Marquardt (LM) algorithm was employed. This algorithm iteratively adjusted the network weights through gradient descent, aiming to minimize the mean squared error, which served as the cost function. The choice of the tansig transfer function for the neurons in the input layer allowed for the modeling of nonlinear relationships using hyperbolic tangent functions. In contrast, the purelin transfer function, representing a linear function, was selected for the neuron in the output layer, facilitating the direct mapping of inputs to outputs, as illustrated in Fig. 2.

The collected data set of concrete mixtures and their corresponding measured CP values, presented in Table 2, was used to train the ANN model. The data set was divided into three subsets to ensure robustness: 70% for training, 15% for validation, and 15% for testing. During training, the ANN received the input parameters for each training instance, processed the signals through the network, and generated the predicted CP values. The network weights were then updated

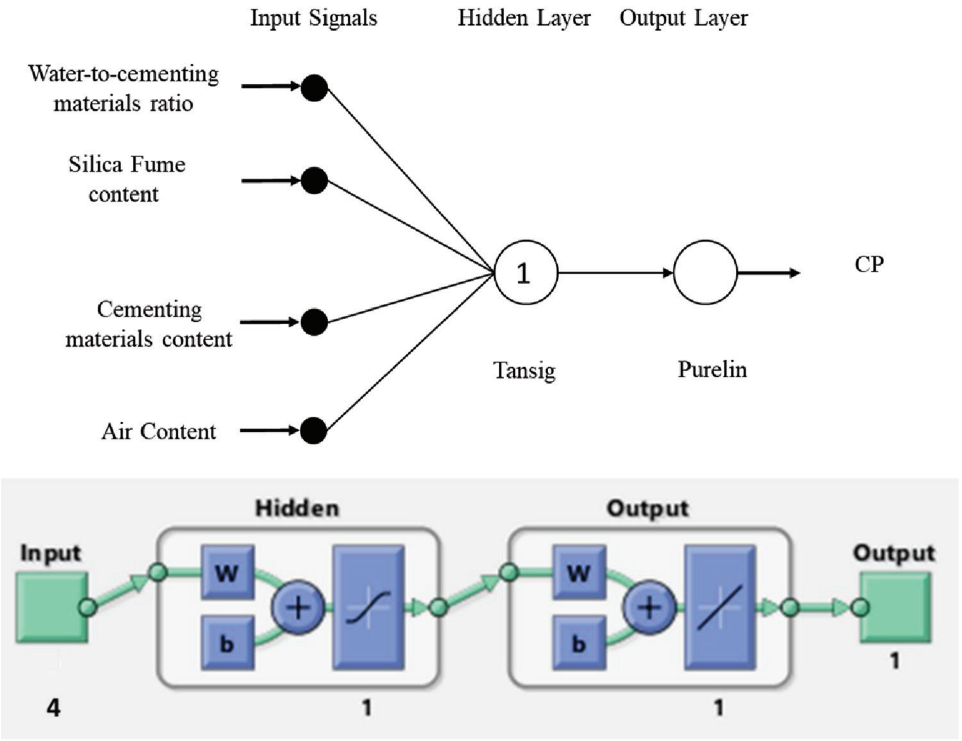

*Fig. 2—Architecture of neural network used in current study.*

using the difference between the predicted and measured CP values, employing the back-propagation algorithm. Various metrics, such as error and coefficient of determination ($R^2$), were employed to evaluate the model's performance. These metrics provided valuable insights into the accuracy and reliability of the ANN model in accurately predicting CP for concrete structures.

This well-defined and carefully crafted approach tailored the ANN model to accurately predict CP in concrete structures, providing valuable insights for designing and optimizing durable and sustainable concrete mixtures.

## RESULTS AND DISCUSSION

### Comparison of experimental and simulated CP values

To enhance the practical relevance of the findings, the CP values for all tested mixtures were compared with the rating ranges specified in ASTM C1202. According to Table 1, the CP values span from "Very low" to "High" permeability categories. For example, mixtures 2 and 6 fall within the "Very low" category (<1000 coulombs), while mixtures such as 7 and 9 exhibit "High" permeability (>4000 coulombs). Correspondingly, the measured 28-day compressive strength of these mixtures ranges from approximately 45 to 98 MPa (6526.70 to 14,213.70 psi), as shown in Table 2. Although strength was not used as an input or output in the ANN model, this variation highlights how concrete with similar strength grades may exhibit significantly different durability levels depending on mixture design, particularly silica fume content and air content. This reinforces the importance of CP as an independent design consideration and demonstrates the model's utility in predicting durability-related performance beyond compressive strength alone.

The comparison between the measured experimental CP values and the simulated values generated by the ANN model revealed a remarkable level of agreement. The analysis demonstrated that the proposed model fits the experimental data well without discerning patterns or outliers. As shown in Fig. 3, the error between the experimental CP values and the ANN model's simulated values varies between –242 and 420 coulombs. This high level of accuracy in predicting CP indicates the reliability and trustworthiness of the developed model.

To further evaluate the performance of the ANN model, standard regression performance metrics were computed. These include:

- Mean absolute error (MAE): Measures the average magnitude of the errors.
- Root mean square error (RMSE): Gives higher weight to large errors.
- Coefficient of determination ($R^2$): Indicates the proportion of the variance in the dependent variable predictable from the independent variables (that is, the average and overall deviation between the predicted and experimental CP values).

The performance metrics for the prediction of CP are shown in Table 3 and Fig. 4. These results indicate that the ANN model provides acceptable prediction performance for CP.

### Limitations of data set and data splitting

While the results presented indicate that the ANN model reproduced the experimental data with good agreement, it is important to acknowledge the limitations imposed by the small data set ($n$ = 10). The decision to split this data set into 70% training (seven samples), 15% validation (one

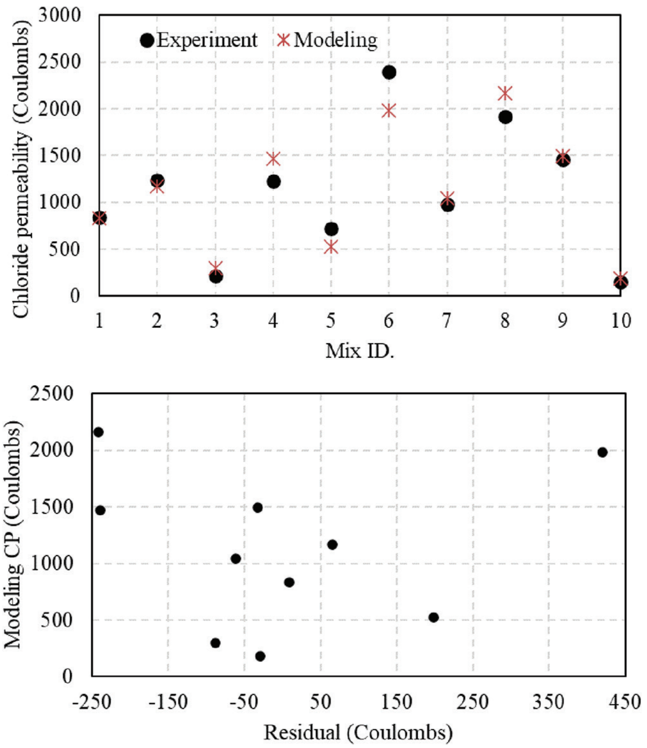

*Fig. 3—Comparison between experimental results and results obtained from ANN model.*

to two samples), and 15% testing (one to two samples) is recognized as statistically weak, because such small subsets cannot provide meaningful variance estimates or robust evaluation of predictive accuracy. As a result, the reported MAE, RMSE, and $R^2$ values should be interpreted with caution. The present analysis therefore represents an exploratory proof-of-concept study demonstrating that ANN techniques can capture non-linear trends in chloride permeability when influenced by *w/c*, silica fume content, and air content. The model outcomes highlight potential, but they are not presented as fully generalizable or validated predictive tools at this stage.

## Mathematical equation for CP

This study distinguishes itself from existing work by focusing on simplicity, applicability, and model transparency. For instance, Güneyisi et al.[26] used ANN to model CP in GGBS-modified concrete, while Huang et al.[27] combined ELM and RF with whale optimization to predict chloride transport in rubber concrete. Li et al.[28] developed ensemble models integrating ANN and RF regression algorithms to predict the chloride migration coefficient of concrete, demonstrating that such ensemble models outperform single models in predictive accuracy. However, many of these models incorporate specialized or diverse materials and do not provide clear mathematical formulation. In contrast, the ANN model developed in this study was trained using controlled experimental data and a limited yet practical set of mixture design parameters. The use of AI in the study led to an explicit mathematical representation of the trained ANN as follows. The feedforward ANN model maps input features $X = [x_1, x_2, ..., x_n]$ to an output $\hat{y}$ (predicted compressive strength) using multiple hidden layers

$$h_j = f\left(\sum_{i=1}^{n} w_i x_i + b_i\right)$$

$$\hat{y} = f_{out}\left(\sum_{j=1}^{m} w_j h_j + b\right)$$

where $h_j$ is the activation of the *j*-th hidden node; $w_i$ and $w_j$ are weights; $b_i$ and $b$ are biases; $f$ is the activation function (in this study tansig); and $f_{out}$ is the output layer function (in this study linear).

This created a precise mathematical equation that strongly links CP to concrete characteristics, including *w/cm*, silica fume content, cementitious materials content, and air content

$$\mathrm{CP} = 22.6938 + \frac{2323.0828}{e^{0.1306 \cdot \mathrm{SF} - 0.1074 \cdot \mathrm{Air\ content} - 0.0175 \cdot \mathrm{Cementitious} - 28.6467 w/c \boxplus 18.2043} + 1}$$

where SF is silica fume content in %; air content is in %; cementitious materials content is in kg/m$^3$; and *w/c* is dimensionless.

The derived equation provides a practical and efficient means of estimating CP in concrete, offering potential applications for concrete properties in various fields. This positions this work as a streamlined, interpretable, and reliable tool for early-stage durability assessment.

## CONCLUSIONS AND FUTURE WORK

The application of artificial intelligence, specifically artificial neural networks (ANNs), has demonstrated its potential in accurately predicting chloride permeability (CP) in concrete structures. By modeling the complex relationships between input design variables and CP values, the proposed ANN model offers a valuable tool for designing concrete mixtures that meet durability requirements, ultimately

### Table 3—Performance metrics for prediction of CP

| Metric | Value |
|---|---|
| MAE | 0.0 |
| RMSE | 187.1 |
| $R^2$ score | 92.1% |

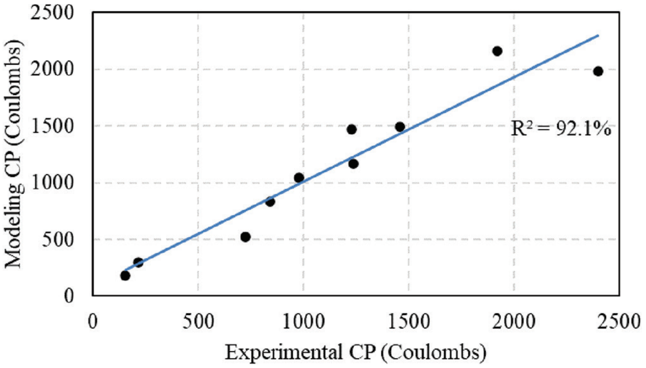

*Fig. 4—Model validation.*

improving the sustainability and longevity of concrete structures.

Through an experimental program and data collection, the developed ANN model successfully simulates CP based on four key parameters: water-cementitious materials ratio (*w*/*cm*), silica fume content, cementitious materials content, and air content. The comparison between the measured experimental CP and the simulated values generated by the ANN model showed an excellent match, with the error values varying between –242 and 420 coulombs. This confirms the reliability and accuracy of the proposed model in determining CP.

Incorporating ANN in predicting CP opens up new possibilities for quality control and design optimization in concrete construction. By using the ANN model, engineers and designers can assess and adjust concrete mixtures to meet specific durability requirements, ensuring long-term performance and reducing the need for premature repairs or replacements. This, in turn, reduces the environmental impact associated with concrete production and improves overall sustainability.

Furthermore, the ANN model provides a valuable alternative to traditional methods of predicting CP, which can be time-consuming, complex, or require extensive experimental testing. The ANN model's ability to capture the intricate relationships between input variables and CP values allows for more efficient and accurate predictions, facilitating better decision-making in concrete construction projects. While this study focused on predicting chloride permeability at 28 days using mixtures with silica fume, future research should consider evaluating long-term performance at 91 days and beyond, and include additional supplementary cementitious materials such as fly ash and slag to broaden the model's applicability and reliability over time. Additionally, future studies should consider incorporating alkali-aggregate reactivity (AAR) testing, particularly when assessing long-term durability in environments susceptible to freezing-and-thawing cycles, as reactive aggregates may lead to microcracking, increased permeability, and reduced structural lifespan. The current ANN model was developed using concrete mixtures containing silica fume at replacement levels of 0% and 15%, as outlined in Table 2. Its performance for lower dosages (for example, 5% or 10%) has not been assessed and should be addressed in future research to extend the model's practical relevance.

Although the study used a relatively small data set of 10 mixtures, all were prepared under controlled experimental conditions to ensure high data quality and consistency. This data set size, however, is far below the scale typically recommended for training ANNs, and consequently, the statistical power of the analysis is limited. In particular, the train/validation/test split (7/1/2 samples) is not statistically robust, as the validation and test subsets are too small to provide reliable estimates of model variance or predictive performance. For this reason, the current model should be considered an initial feasibility study rather than a finalized predictive framework.

To address these limitations, future work will focus on:

- Expanding the data set substantially by including additional mixtures with a wider range of supplementary cementitious materials (for example, fly ash and slag) and longer curing periods (91 days and beyond).
- Implementing *k*-fold cross-validation rather than single-split validation, which will enable more reliable assessment of model performance with limited data.
- Comparing ANN performance with simpler baseline models such as multiple linear regression and decision trees, to assess whether ANN provides added value given the data set size.
- Conducting hyperparameter tuning and regularization studies once larger data sets are available to prevent overfitting and improve model robustness.

## AUTHOR BIOS

**Mohamad Kharseh** *is a Faculty Member in the Department of Mechanical and Industrial Engineering at the American University of Ras Al Khaimah, Ras Al Khaimah, UAE. He received his PhD in renewable energy from Luleå University of Technology, Luleå, Sweden, in 2011. His research interests include sustainability and energy consumption systems in buildings and optimizing renewable energy projects to reduce greenhouse emissions using different approaches.*

**Fayez Moutassem** *is the Chair of the Department of Civil and Infrastructure Engineering at the American University of Ras Al Khaimah. He received his MS from Texas A&M University, College Station, TX, and his PhD in civil engineering from McMaster University, Hamilton, ON, Canada. His research interests include concrete structures and materials including precast and prestressed members, sustainability in design and construction, green buildings, quality control, and in the properties of structural concrete using special materials.*

## ACKNOWLEDGMENTS

The authors would like to thank Mohammed Bin Rashid for Smart Learning Program (MBRSLP) for funding Project No. MBRSLP/05/23, as well as the American University of Ras Al Khaimah for providing the resources and time needed that help shape the development of the proposed models, the analysis, and the writing of the paper.

## STATEMENTS AND DECLARATIONS

On behalf of all authors, the corresponding author states that there is no conflict of interest.

## REFERENCES

1. Campos Silva, H.; Garces Terradillos, P.; Zornoza, E.; Mendoza-Rangel, J. M.; Castro-Borges, P.; and Juarez Alvarado, C. A., "Improving Sustainability through Corrosion Resistance of Reinforced Concrete by Using a Manufactured Blended Cement and Fly Ash," *Sustainability*, V. 10, No. 6, 2018, p. 2004. doi: 10.3390/su10062004

2. McGrath, P., "Development of Test Methods for Predicting Chloride Penetration into High Performance Concrete," PhD thesis, Department of Civil Engineering, University of Toronto, Toronto, ON, Canada, 1996.

3. Bamforth, P. B., "Improving the Durability of Concrete using Mineral Admixtures," *Concrete Durability in the Arabian Gulf*, 1995, pp. 1-26.

4. De Larrard, F., *Concrete Mixture Proportioning*, first edition, CRC Press, Boca Raton, FL, 1999.

5. Chidiac, S. E.; Moutassem, F.; and Mahmoodzadeh, F., "Compressive Strength Model for Concrete," *Magazine of Concrete Research*, V. 65, No. 9, 2013, pp. 557-572. doi: 10.1680/macr.12.00167

6. ASTM C1202/C1202M-22, "Standard Test Method for Electrical Indication of Concrete's Ability to Resist Chloride Ion Penetration," ASTM International, West Conshohocken, PA, 2022, 8 pp.

7. Güçlüer, K., "Investigation of the Effects of Aggregate Textural Properties on Compressive Strength (CS) and Ultrasonic Pulse Velocity (UPV) of Concrete," *Journal of Building Engineering*, V. 27, 2020, p. 100949. doi: 10.1016/j.jobe.2019.100949

8. Aggarwal, Y., and Aggarwal, P., "Prediction of Compressive Strength of SCC Containing Bottom Ash Using Artificial Neural Networks," *International Journal of Mathematics and Computer Science*, V. 5, No. 5, 2011, pp. 762-767.

9. Suryadi, A.; Qomariah, Q.; and Sarosa, M., "An Artificial Neural Networks Model for Compressive Strength of Self-Compacting Concrete," *Applied Mechanics and Materials*, V. 845, 2016, pp. 226-230. doi: 10.4028/www.scientific.net/AMM.845.226

10. Uysal, M., and Tanyildizi, H., "Predicting the Core Compressive Strength of Self-Compacting Concrete (SCC) Mixtures with Mineral Additives Using Artificial Neural Network," *Construction and Building Materials*, V. 25, No. 11, 2011, pp. 4105-4111. doi: 10.1016/j.conbuildmat.2010.11.108

11. Raheman, A., and Modani, P. O., "Prediction of Properties of Self Compacting Concrete Using Artificial Neural Network," *International Journal of Engineering Research and Applications*, V. 3, No. 4, 2013, pp. 333-339.

12. Moutassem, F., and Kharseh, M., "Artificial Neural Network Model for Concrete Strength Predictions Based on Ultrasonic Pulse Velocity Measurement," *ACI Materials Journal*, V. 121, No. 4, July 2024, pp. 61-68.

13. Moutassem, F., and Kharseh, M., "Sustainability-Driven Model for Predicting Compressive Strength in Concrete Structures," *Cogent Engineering*, V. 11, No. 1, 2024, p. 2374947. doi: 10.1080/23311916.2024.2374947

14. Yeh, I.-C., "Modeling of Strength of High-Performance Concrete Using Artificial Neural Networks," *Cement and Concrete Research*, V. 28, No. 12, 1998, pp. 1797-1808. doi: 10.1016/S0008-8846(98)00165-3

15. Muthupriya, P.; Subramanian, K.; and Vishnuram, B. G., "Prediction of Compressive Strength and Durability of High Performance Concrete by Artificial Neural Networks," *International Journal of Optimization in Civil Engineering*, V. 1, No. 1, 2011, pp. 189-209.

16. Abdollahzadeh, A.; Masoudnia, R.; and Aghababaei, S., "Predict Strength of Rubberized Concrete Using Artificial Neural Network," *WSEAS Transactions on Computers*, V. 10, No. 2, 2011, pp. 31-40.

17. Khan, S. U.; Ayub, T.; and Rafeeqi, S. F. A., "Prediction of Compressive Strength of Plain Concrete Confined with Ferrocement using Artificial Neural Network (ANN) and Comparison with Existing Mathematical Models," *American Journal of Civil Engineering and Architecture*, V. 1, No. 1, 2013, pp. 7-14. doi: 10.12691/ajcea-1-1-2

18. Duan, Z. H.; Kou, S. C.; and Poon, C. S., "Prediction of Compressive Strength of Recycled Aggregate Concrete Using Artificial Neural Networks," *Construction and Building Materials*, V. 40, 2013, pp. 1200-1206. doi: 10.1016/j.conbuildmat.2012.04.063

19. Deshpande, N.; Londhe, S.; and Kulkarni, S., "Modeling Compressive Strength of Recycled Aggregate Concrete by Artificial Neural Network, Model Tree and Non-Linear Regression," *International Journal of Sustainable Built Environment*, V. 3, No. 2, 2014, pp. 187-198. doi: 10.1016/j.ijsbe.2014.12.002

20. Gupta, S., "Using Artificial Neural Network to Predict the Compressive Strength of Concrete Containing Nano-Silica," *Civil Engineering and Architecture*, V. 1, No. 3, 2013, pp. 96-102. doi: 10.13189/cea.2013.010306

21. Naderpour, H.; Kheyroddin, A.; and Amiri, G. G., "Prediction of FRP-Confined Compressive Strength of Concrete Using Artificial Neural Networks," *Composite Structures*, V. 92, No. 12, 2010, pp. 2817-2829. doi: 10.1016/j.compstruct.2010.04.008

22. Sarıdemir, M., "Prediction of Compressive Strength of Concretes Containing Metakaolin and Silica Fume by Artificial Neural Networks," *Advances in Engineering Software*, V. 40, No. 5, 2009, pp. 350-355. doi: 10.1016/j.advengsoft.2008.05.002

23. Öztaş, A.; Pala, M.; Özbay, E.; Kanca, E.; Çağlar, N.; and Bhatti, M. A., "Predicting the Compressive Strength and Slump of High Strength Concrete Using Neural Network," *Construction and Building Materials*, V. 20, No. 9, 2006, pp. 769-775. doi: 10.1016/j.conbuildmat.2005.01.054

24. Hoła, J., and Schabowicz, K., "Application of Artificial Neural Networks to Determine Concrete Compressive Strength Based on Non-Destructive Tests," *Journal of Civil Engineering and Management*, V. 11, No. 1, 2005, pp. 23-32. doi: 10.3846/13923730.2005.9636329

25. Lande, P. S., and Gadewar, A. S., "Application of Artificial Neural Networks in Prediction of Compressive Strength of Concrete by Using Ultrasonic Pulse Velocities," *IOSR Journal of Mechanical and Civil Engineering*, V. 3, No. 1, 2012, pp. 34-42. doi: 10.9790/1684-0313442

26. Güneyisi, E.; Gesoğlu, M.; Özturan, T.; and Özbay, E., "Estimation of Chloride Permeability of Concretes by Empirical Modeling: Considering Effects of Cement Type, Curing Condition and Age," *Construction and Building Materials*, V. 23, No. 1, 2009, pp. 469-481. doi: 10.1016/j.conbuildmat.2007.10.022

27. Huang, X.; Wang, S.; Lu, T.; Li, H.; Wu, K.; and Deng, W., "Chloride Permeability Coefficient Prediction of Rubber Concrete Based on the Improved Machine Learning Technique: Modelling and Performance Evaluation," *Polymers*, V. 15, No. 2, 2023, p. 308. doi: 10.3390/polym15020308

28. Li, L.; Su, L.; Guo, B.; Cai, R.; Wang, X.; and Zhang, T., "Prediction and Prevention of Concrete Chloride Penetration: Machine Learning and MICP Techniques," *Frontiers in Materials*, V. 11, 2024, p. 1445547. doi: 10.3389/fmats.2024.1445547

29. ASTM C1240-20, "Standard Specification for Silica Fume Used in Cementitious Mixtures," ASTM International, West Conshohocken, PA, 2020, 7 pp.

30. ASTM C127-15, "Standard Test Method for Relative Density (Specific Gravity) and Absorption of Coarse Aggregate," ASTM International, West Conshohocken, PA, 2015, 6 pp.

31. ASTM C128-15, "Standard Test Method for Relative Density (Specific Gravity) and Absorption of Fine Aggregate," ASTM International, West Conshohocken, PA, 2015, 6 pp.

32. ASTM C136/C136M-19, "Standard Test Method for Sieve Analysis of Fine and Coarse Aggregates," ASTM International, West Conshohocken, PA, 2019, 5 pp.

33. ASTM C494/C494M-19, "Standard Specification for Chemical Admixtures for Concrete," ASTM International, West Conshohocken, PA, 2019, 15 pp.

34. ASTM C260/C260M-10a, "Standard Specification for Air-Entraining Admixtures for Concrete," ASTM International, West Conshohocken, PA, 2010, 4 pp.

ACI MATERIALS JOURNAL TECHNICAL PAPER

Title No. 123-M18

# Comparison of Plane-Strain and Three-Dimensional Analysis of Reinforced Concrete Subjected to Nonuniform Corrosion

by Aditi Chauhan, Yogesh M. Desai, Sauvik Banerjee, and Umesh Kumar Sharma

*Analysis of reinforced concrete (RC) damage under nonuniform corrosion has mostly been performed by adopting the two-dimensional (2-D) plane-strain assumption to reduce computational efforts compared with three-dimensional (3-D) models. This paper aims to compare results obtained from the 2-D plane-strain formulation with 3-D analysis in the context of nonuniform corrosion, highlighting differences and similarities to gain valuable insights into the structural response and damage prediction. The findings indicate that both the 2-D and 3-D models yield reasonably similar damage patterns, with minor discrepancies in crack orientation, and predict comparable hairline crack widths on the concrete surface. During initial corrosion stages, both models exhibit similar stress and strain distributions. However, as corrosion progresses, distinct variations in stress and strain patterns emerge. Interestingly, despite these differences, the extent of damage converges as corrosion advances, suggesting a critical stage beyond which the RC response remains consistent regardless of the modeling approach. The study emphasizes stress and strain variations over time for accurate RC behavior representation.*

**Keywords:** corrosion-induced damage; finite element (FE); plane strain; reinforced concrete (RC); three-dimensional (3-D) model.

## INTRODUCTION

Reinforced concrete (RC) damage under chloride-induced corrosion is a major durability concern. Localized corrosion of steel is a characteristic of chloride-induced corrosion, which can adversely impact the structural behavior of RC structures. The dissolution of iron in specific chloride-rich areas gives rise to a nonuniform generation of corrosion by-products, which accumulate locally and result in concrete cracking. Thorough evaluation of RC damage under nonuniform corrosion has been a topic of research in recent times. To model complex and realistic behavior of concrete deterioration caused by nonuniform corrosion, researchers have adhered to advantageous numerical models. The nonuniform corrosion-induced cracking of RC has been modeled as a plane-strain two-dimensional (2-D) problem in the literature.[1-7] These models have been able to predict damage in RC well, by capturing the nonuniformity of corrosion around the steel circumference. For example, Cheng et al.[4] implemented numerical simulation of nonuniform corrosion using the concrete damaged plasticity (CDP) model and predicted cracking propagation in RC. Zhang et al.[7] obtained the crack propagation process of cover concrete under nonuniform corrosion as a function of concrete cover, reinforcing bar diameter, and bar spacing. They simulated damage using the CDP model in Abaqus. Similar work was carried out by Molina et al.,[5] who simulated concrete damage under corrosion using the smeared-crack modeling approach. Chauhan and Sharma[2] obtained crack patterns in RC under nonuniform corrosion by including the effect of climatic relative humidity and temperature. In addition to the aforementioned models, there are plane-strain numerical models in the literature that predict damage/crack in RC under nonuniform corrosion as a discrete entity, thereby enabling prediction of not only crack patterns but also crack widths directly from the model. For example, Yang et al.[6] were able to determine crack patterns and obtain accurate surface crack width values in RC using cohesive zone modeling under nonuniform corrosion. Similar work was carried out by Chauhan and Sharma[1] to predict not only the crack patterns but also crack widths in RC subject to nonuniform corrosion. They also considered the effect of climatic temperature and relative humidity variations on the crack patterns and crack widths in the model.

Clearly, many advancements have been made to simulate nonuniform corrosion in 2-D, which has proven to be a computationally efficient way to capture damage in RC. However, a typical 2-D analysis assumes uniform chloride-induced corrosion along the entire length of the steel bar, which does not reflect real scenarios. In a real scenario, chloride-induced corrosion is nonuniform along a reinforcing bar's length, dependent on concrete microstructure, local steel environment, and other factors. To capture the nonuniformity of chloride-induced corrosion along the bar length, it is imperative to carry out three-dimensional (3-D) numerical modeling. Owing to the highly complex nature of heterogeneous concrete, 3-D modeling of chloride-induced corrosion is a challenging task. However, there are 3-D models developed in the past considering different pit shapes[8-10] and different anode-cathode combinations[11-16] along the reinforcing bar length to simulate nonuniformity of chloride-induced corrosion longitudinally. These models are well established and validated with different experimental[16-18] and field test[19] results.

---

*ACI Materials Journal*, V. 123, No. 2, March 2026.

MS No. M-2024-360.R3, doi: 10.14359/51749322, received September 16, 2025, and reviewed under Institute publication policies. Pertinent discussion including author's closure, if any, will be published ten months from this journal's date if the discussion is received within four months of the paper's print publication.

It is clear from the previous discussion that numerical modeling techniques to simulate damage under nonuniform corrosion have been performed by the researchers separately in 2-D and 3-D.

However, one important aspect missing is the comparison between the 2-D and 3-D models, and this study aims to compare the damage obtained from 2-D and 3-D models. The aim is to investigate corrosion damage in areas where anodes are present, particularly where rust expansion occurs and disregarding the extent of damage at the anode-cathode junction along the reinforcing bar length. It has been observed by the authors in their previous 3-D numerical nonuniform corrosion model[16] that concrete sustains more damage near the anode locations as compared to the anode-cathode junction. This observation therefore justifies comparing 2-D and 3-D models, assuming uniform corrosion along the reinforcing bar length—that is, only anodes are present along the length of the steel bar. The present work extends the authors' 2-D nonuniform corrosion model, as presented in Chauhan and Sharma,[1,2] to evaluate and compare the damage in RC structures. A 3-D finite element (FE) analysis is conducted to assess the applicability and accuracy of the 2-D plane-strain model. An additional effect of climatic variations in relative humidity and temperature on corrosion loading is also considered in the study as a true representation of corrosion in RC under real climate conditions.

## RESEARCH SIGNIFICANCE

Chloride-induced corrosion of RC poses a serious threat to infrastructure durability. Extensive research efforts are focused on understanding and mitigating this damage, with experimental studies, field investigations, and numerical simulation forming the core methodologies employed worldwide. While experimental and field investigations are often labor-intensive and time-consuming, numerical simulation offers a more efficient alternative. Accurate estimation, however, necessitates comprehensive 3-D simulations of the corrosion in RC. Despite their accuracy, these 3-D models are resource-intensive and costly. As a result, 2-D models are frequently used for simulation. However, the literature lacks a comprehensive comparison of 2-D and 3-D models to evaluate the adequacy of 2-D simulations in predicting damage to RC subject to chloride-induced corrosion. This study aims to fill this gap by presenting a comparative analysis of 3-D and 2-D models for damage prediction.

## NONUNIFORM CORROSION MODELING

Corrosion of steel in concrete under chloride ingress is nonuniform in nature, which means the steel is attacked unevenly inside the concrete. This nonuniform corrosion arises from varying rates at which chlorides, moisture, and oxygen permeate the concrete from different directions. Consequently, the occurrence of uniform and widespread corrosion of the reinforcement is relatively uncommon. To address the nonuniform corrosion phenomenon, a numerical approach is presented within this section. This approach is designed to simulate and model the nonuniform corrosion process, and it holds applicability for both the 2-D and 3-D models presented in this study. Chloride ingress and its dispersion surrounding the steel bar as a function of concrete microenvironment was modeled in 2-D by the authors in their previous work.[1] This established approach, as illustrated in Fig. 1, will be adopted once again in the present study. Equation numbers are the same as used in the figure. Chloride ingress in the concrete cover is modeled using Fick's law of diffusion

$$\frac{\partial C_{fc}}{\partial t} = D_c'\left(\frac{\partial^2 C_{fc}}{\partial x^2} + \frac{\partial^2 C_{fc}}{\partial y^2}\right) \tag{1}$$

Moisture transport

$$\frac{\partial w_e}{\partial t} = \frac{\partial w_e}{\partial h}\frac{\partial h}{\partial t} = D_h\left(\frac{\partial^2 h}{\partial x^2} + \frac{\partial^2 h}{\partial y^2}\right) \tag{2}$$

and heat transfer

$$\rho_c c_q \frac{\partial T}{\partial t} = \lambda\left(\frac{\partial^2 T}{\partial x^2} + \frac{\partial^2 T}{\partial y^2}\right) \tag{3}$$

inside concrete cover are also undertaken along with chloride ingress, as shown in Fig. 1. Out of the total chlorides, unbound—that is, free—chlorides primarily initiate corrosion of steel in concrete. Therefore, once these unbound chloride ions ($C_{fc}$) attain the threshold value on the steel bar, they disrupt the steel passive layer, which triggers the formation of electrochemical cells. The specific points where the chloride-ion concentration exceeds the threshold yield anodic sites, while the rest of the passive surface gives rise to cathodic sites. Once the locations of these anodes and cathodes are identified, the potential of the corrosion mechanism is determined through the application of Laplace's equation

$$\frac{\partial^2 \phi}{\partial x^2} + \frac{\partial^2 \phi}{\partial y^2} = 0 \tag{4}$$

on the steel surface, as illustrated in Fig. 1. This phenomenon is driven by variations in moisture content, oxygen concentration, and temperature, as shown in the figure. Upon deriving potential values across the steel surface, it becomes possible to calculate anodic ($i_a$) current density

$$i_a = i_{oa}\exp\left(2.303\,\frac{\phi - \phi_a^0}{\beta_a}\right) \tag{5}$$

and cathodic ($i_c$) current density

$$i_c = \frac{C_{o_2}}{C_{o_2}^s}\, i_{0c}\exp\left(2.303\,\frac{\phi_c^0 - \phi}{\beta_c}\right) \tag{6}$$

These parameters are subsequently used to comprehensively assess the rate of corrosion ($i_{corr}$) as given by

$$i_{corr} = i_{mac,anode} + i_{mic,anode} \tag{7}$$

where

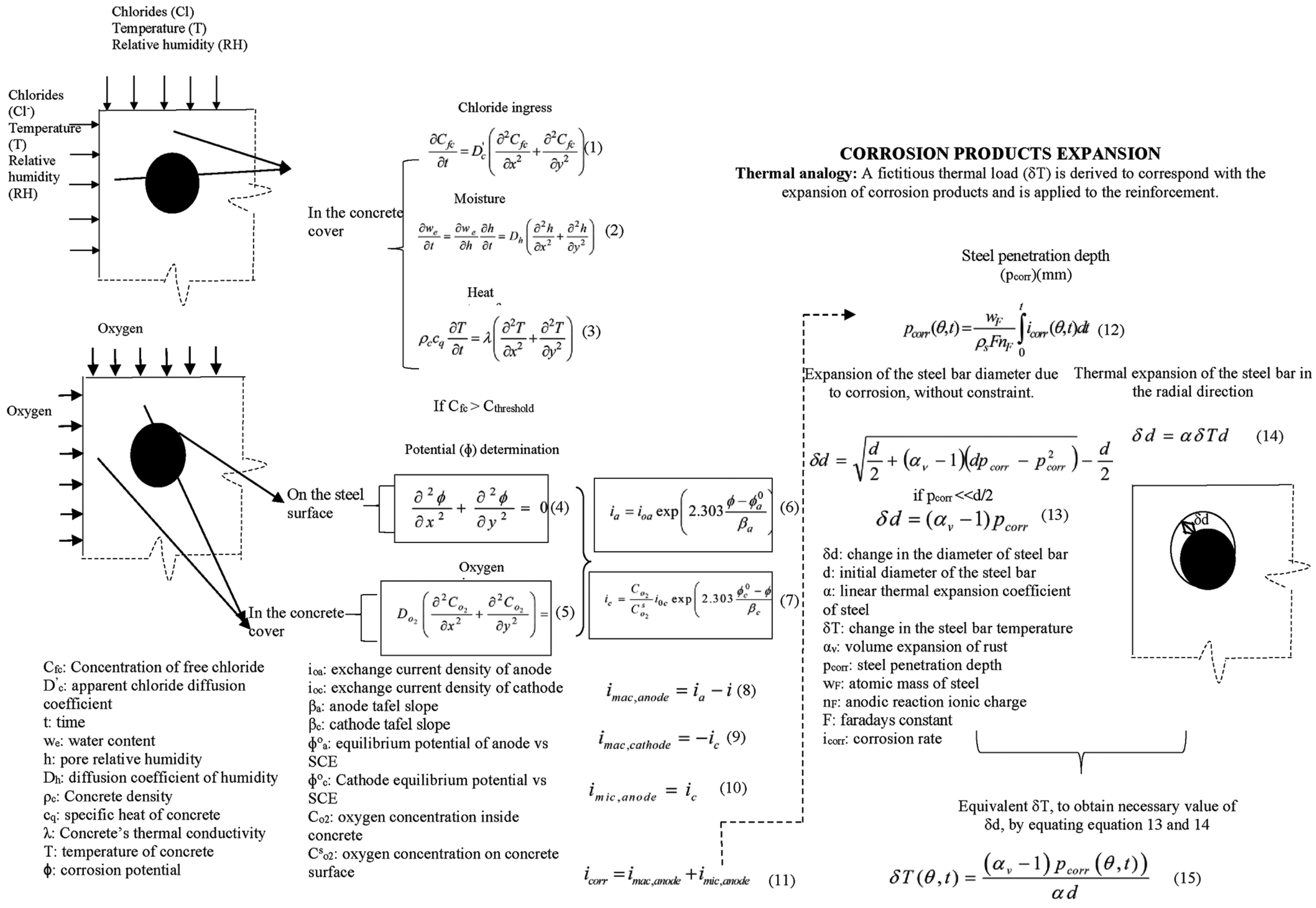

*Fig. 1—Flowchart showing corrosion initiation and propagation under nonuniform corrosion.*

$$i_{mac,anode} = i_a - i_c \tag{8}$$

$$i_{mac,cathode} = -i_c \tag{9}$$

$$i_{mic,anode} = i_c \tag{10}$$

The formation of anodes and cathodes as a function of relative humidity and temperature, and determination of corrosion rate is explained in Chauhan and Sharma.[1] Rust formed at the location of anodes grows with time, dependent on corrosion rate, and cracks the concrete, which is weak in tension. To model the damage initiation and damage propagation in RC subject to nonuniform corrosion, expansion of the corrosion products needs to be determined. Corrosion rate is used to determine the steel penetration depth ($p_{corr}$) using Faraday's law, as given by

$$p_{corr}(\theta,t) = \frac{w_F}{\rho_s F n_F}\int_0^t i_{corr}(\theta,t)\,dt \tag{11}$$

Once these parameters are established, the expansion of rust is simulated using the concept of thermal analogy.[3,17] The methodology to obtain the value of rust expansion from the corrosion rate values, as a function of space and time using thermal analogy, is given in the flowchart in Fig. 1. Thermal analogy relies on determining the expansion of steel that corresponds to the expansion of corrosion products, achieved by equating the radial expansion of a steel bar due to thermal loading

$$\delta d = \alpha \delta T d \tag{12}$$

with the expansion caused by corrosion

$$\delta d = \sqrt{\frac{d}{2} + (\alpha_v - 1)(dp_{corr} - p_{corr}^2)} - \frac{d}{2} \tag{13}$$

in reference to Yang et al.[20] To achieve the required value of $\delta d$, the coefficient of thermal expansion $\alpha$ is assumed and equivalent $\delta T$ is obtained. The steel expansion is simulated using the achieved thermal distribution

$$\delta T(\theta,t) = \frac{(\alpha_v - 1)p_{corr}(\theta,t)}{\alpha d} \tag{14}$$

that is applied as a function of space ($\theta$) and time ($t$). This approach effectively models nonuniform corrosion within both the 2-D and 3-D models.

## CONCRETE DAMAGE MODEL

Once the rust expansion under nonuniform corrosion is known, it is applied as corrosion loading onto the RC and damage in concrete is determined. Numerical simulation of damage caused by nonuniform corrosion in concrete is performed by using the CDP constitutive model in Abaqus.

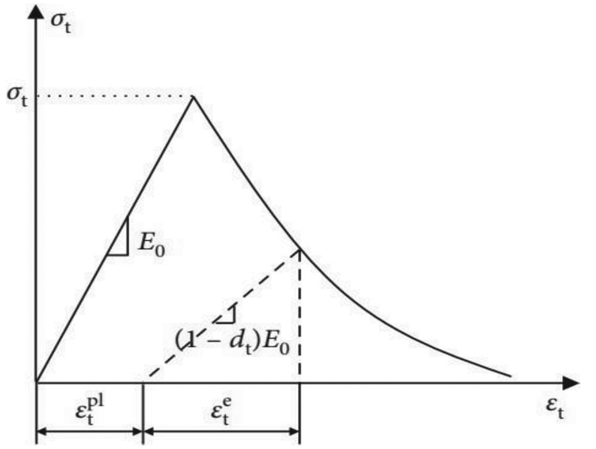

*Fig. 2—Response of concrete under uniaxial tension from Abaqus.*

This model captures the irreversible damage to the concrete that occurs by the fracturing process. The model assumes two distinct failure mechanisms of concrete: concrete crushing and tensile cracking. Within the model reduction, the material stiffness attributed to microcracking is addressed by plastic straining in both tension and compression. Upon the attainment of maximum principal strain, concrete exhibits tension-softening behavior. It is postulated that the vector perpendicular to the crack plane aligns parallel to the direction of the maximum principal plastic strain.[4] Once cracking initiates, stiffness reduces from $E_0$ to $(1–dt)E_0$. This is depicted in Fig. 2, which illustrates the stress and strain behavior under uniaxial tension. The damage is represented through DAMAGET (*dt*), a tensile damage variable and plastic strain ($\varepsilon_t^{pl}$) under tension.[7] The evolution of plastic strains under tension is characterized by the following equation

$$\sigma_t = (1 - d_t)E_0(\varepsilon_t - \varepsilon_t^{pl}) \tag{15}$$

where $\sigma_t$ is the tensile stress in concrete; and $\varepsilon_t$ is the total strain in concrete.

To implement the damage (cracking) mechanism within Abaqus using the plasticity model, it is imperative to define precise material properties and parameters related to crack initiation and progression. Linear approximation simplifies incorporating crack opening laws into the model. Despite making the material response slightly stiffer with linear softening behavior, it often provides accurate results across different scenarios. In the current model, linear softening is used based on the approach outlined by Hillerborg[21] and shown in Fig. 3.

This model represents the post-cracking behavior of concrete by including softening effects. To implement the cracking mechanism properties such as fracture energy, the tensile strength and evolution of the damage parameter need to be defined in the Abaqus model. One limitation of the CDP model is its restricted applicability in predicting crack width values only up to a certain limit, typically limited to hairline crack widths. This limitation arises because the model calculates crack-opening displacements based on decreased stress values at the damaged location, which in turn relies on the input stress-strain model. As the CDP model primarily relies on stress-based criteria to predict cracking, it may not accurately capture the behavior of concrete beyond the hairline crack regime. In situations where larger crack widths or more significant damage occurs, accuracy may diminish, leading to less-reliable predictions.

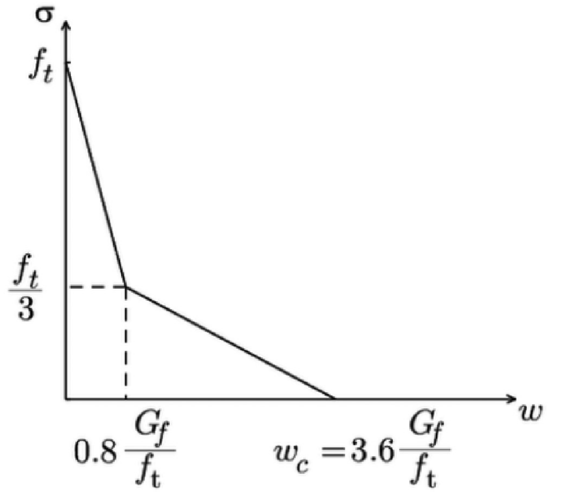

*Fig. 3—Tension-softening model given by Hillerborg.[21]*

## VALIDATION

The proposed concrete damage model has been validated against accelerated corrosion tests conducted by the authors. To simulate the corrosion process, alternate wetting-and-drying cycles were employed in combination with an externally applied impressed voltage. The RC specimen, consisting of three reinforcing steel bars (anodes), is shown in Fig. 4 and is similar to the specimen used in the authors' earlier study.[1] A stainless-steel rod of 10 mm diameter, serving as the cathode, was positioned below the middle steel bar. The specimen was exposed to a 3.5% chloride concentration solution from the top and side faces, while an impressed voltage of 10 V direct current (DC) was applied only during the wet cycles and switched off during the dry cycles. The experimental setup, including electrical connections and the wetting arrangement, is illustrated in Fig. 4. Throughout the test, the full length of the reinforcing bars was exposed to chloride ingress, and current densities were obtained directly from the DC supply. The concrete surface was monitored for crack initiation using a crack microscope with the least count of 0.05 mm, and crack propagation was subsequently recorded on a weekly basis using a crack comparator. For the numerical simulation, certain conservative assumptions were adopted. It is assumed that all corrosion products contribute directly to expansive pressure on the surrounding concrete. Accordingly, crack initiation and propagation were modeled under the assumption that no rust penetrates the pore structure or existing cracks. For validation, an elliptical distribution of corrosion products was assumed for nonuniform corrosion rust expansion, following Jin et al.[22] and Yang et al.[20] Current densities for each reinforcing bar were calculated as the ratio of the current values from the DC supply to the exposed bar surface area, as a

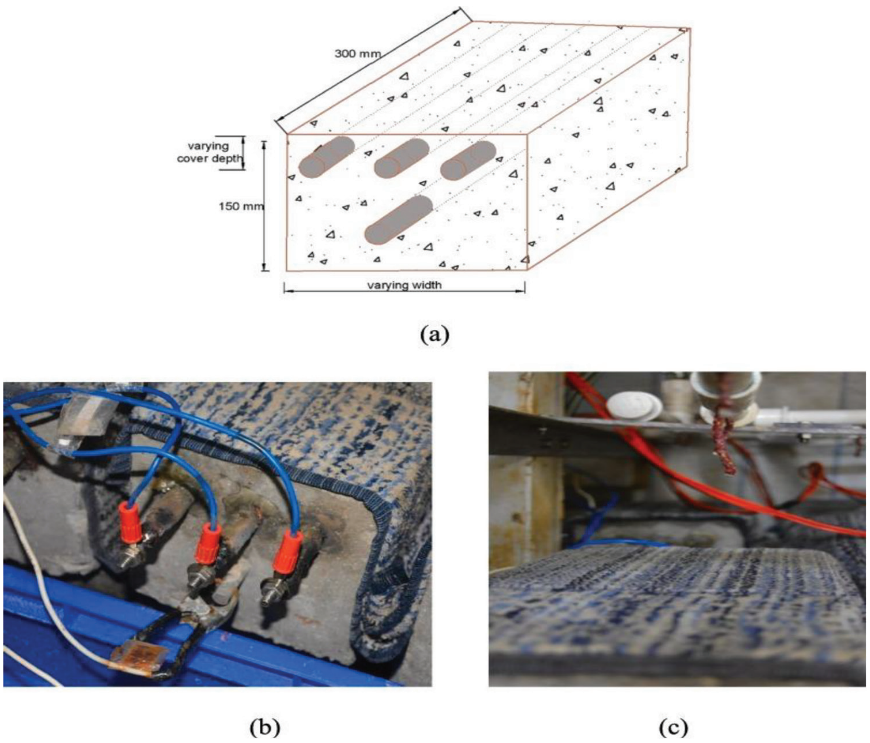

*Fig. 4—Experimental setup to carry out accelerated corrosion tests: (a) schematic of specimen; (b) electrical connection made between DC supply and specimen; and (c) wetting of specimen during wet cycle. (Note: 1 mm = 0.039 in.)*

**Table 1—Input variables from experiments used for validation of numerical results**

| Parameter | Value |
|---|---|
| Concrete cover | 30 mm (1.18 in.) |
| Steel bar diameter | 8 mm (0.315 in.) |
| Tensile strength | 3.83 MPa (555.5 psi) |
| Modulus of elasticity | 10.67 GPa (1547.5 psi) |
| Poisson's ratio | 0.18 |
| Fracture energy | 50 N/m (0.285 lb/in.) |

function of time. The corrosion loading was then determined using the procedure outlined by Liu and Weyers,[23] with the total mass of rust ($W_{rust}$) obtained from Eq. (16).

$$W_{rust}(t) = \sqrt{2\int_0^t 0.105(1/\alpha_{rust})\pi\phi i_{corr}(t)\,dt} \tag{16}$$

Here, $i_{corr}$ (μA/cm$^2$) is the current density obtained from the accelerated corrosion test for steel bars varying with time $t$ (years).

Based on the elliptical distribution, radial displacements of the steel bars were calculated following Yang et al.[20] using Eq. (17) and (18).

$$d_\theta = \frac{(\phi + 2d_o + 2d_m)(\phi + 2d_o)}{\sqrt{(2\phi + 4d_o)^2 + 16d_m(\phi + 2d_o + d_m)\cos^2\theta}} \tag{17}$$

where

$$d_m = \frac{4W_{rust}}{\pi\phi}\left(\frac{1}{\rho_{rust}} - \frac{\alpha_{rust}}{\rho_{st}}\right) - 2d_o \tag{18}$$

where $\rho_{rust}$ and $\rho_{st}$ are the density (mg/mm$^3$) of corrosion products and steel, respectively; $\alpha_{rust}$ is the ratio of molecular weight of steel and corrosion products; $\phi$ is the diameter of the steel bar (mm); and $d_o$ is the thickness (mm) of the interfacial transition zone (ITZ).

The temperature field required to simulate rust expansion was obtained from Eq. (15) by substituting the calculated radial displacements. Input parameters used in the FE analysis of the RC specimen are provided in Table 1, with the tensile strength and modulus of elasticity of concrete determined according to IS 456:2000.[24]

Results are presented in terms of damage patterns obtained from both the numerical model and experimental observations, as shown in Fig. 5. In the simulations, damage developed predominantly around the corner bars, whereas only limited propagation was captured for the middle bar as the solution failed to converge beyond this point. It is also important to note that in the present model, the maximum crack width is constrained by the stress-displacement relationship, which typically corresponds to a hairline crack; therefore, direct comparison of crack width values between simulation and experiments was not possible, and the analysis was limited to comparing overall damage patterns. Importantly, nonuniform corrosion modeling was carried out during the validation process, enabling meaningful comparison of the numerical results with the experimentally observed damage. In the simulations, concrete was assumed to be homogeneous, and with the section being symmetric in geometry and loading, similar damage patterns were obtained around the left and right corner bars. By contrast, the experimental results revealed variations in crack inclination and propagation between the two corners. Along

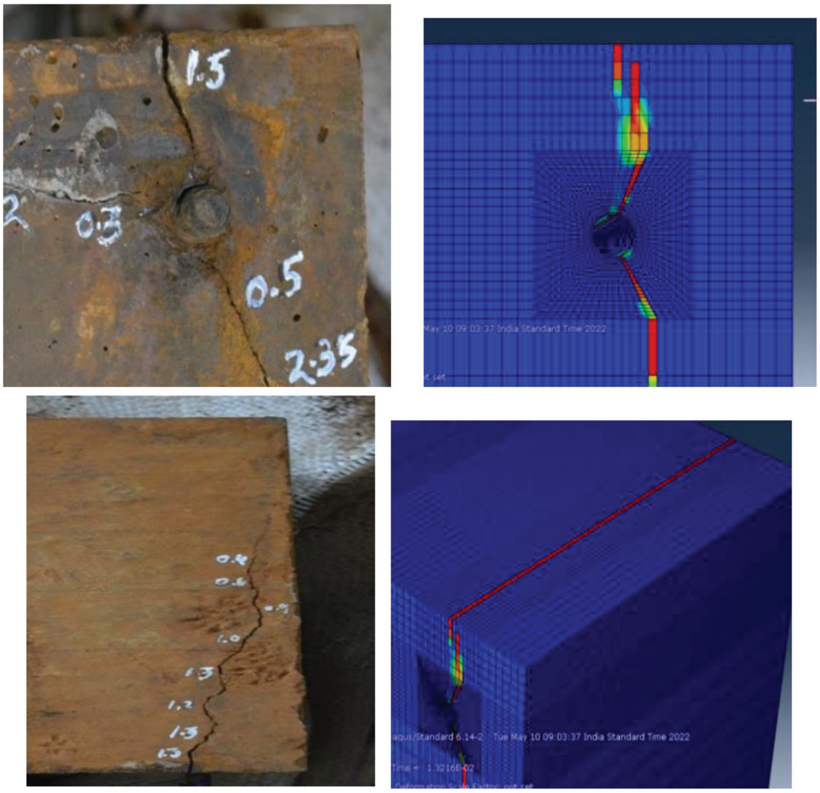

*Fig. 5—Damage patterns observed in test specimen from experiment and numerical results.*

the specimen length, simulated damage propagated nearly straight, whereas cracks in the experimental specimens were inclined. These differences arise from the neglect of aggregates in the model, as crack propagation in actual concrete is influenced by aggregate boundaries, often causing deviations in crack paths. Despite these limitations, the present model can capture the essential features of deterioration, including the overall distribution of damage within the cover zone, the critical locations of cracking (top and side cover), and the source of crack initiation, whether from the steel surface or the concrete surface.

## NUMERICAL SIMULATION

Numerical simulation of 2-D plane-strain and 3-D RC models is conducted to compare solutions for stresses, strains, and damage patterns/propagation under nonuniform corrosion loading. A concrete section reinforced with four steel bars of diameter $d = 16$ mm is considered. The multi-bar RC system chosen for this study is shown in Fig. 6.

Meshing of the 2-D and 3-D models are also shown in the figure. The 3-D model was chosen such that the length-to-breadth ratio of the section is 6. The aspect ratio of 6 ensures that the section's breadth is significantly smaller than its length dimensions. The chosen section is a multi-bar system that can capture the damage in the concrete cover adjoining corner bars and middle bars. Corner bars are more susceptible to nonuniform corrosion, and therefore the focus of the present analysis will be on this bar. As part of this ongoing research, studies are also being conducted to investigate damage assessment in relation to corrosion of the middle bars. Location around the corner bars is shown as angular values starting from 0 degrees.

The nonuniform corrosion of the steel bar is simulated as its radial thermal expansion, as explained in the preceding section. Thermal field around the steel bar is obtained from Eq. (15) and applied as thermal loading in the radial direction of the steel bar. The detailed nonuniform corrosion analysis of the 2-D plane-strain and 3-D FE is presented in the following subsections.

### Corrosion rate

To effectively simulate damage resulting from nonuniform corrosion, it is essential to first obtain corrosion rate fluctuations across both spatial and temporal dimensions. The current study also aims to comprehend the impact of real environmental relative humidity and temperature on damage caused by chloride-induced corrosion. Hence, actual variations in corrosion rate were obtained. Actual fluctuations in environmental relative humidity and temperature were collected for the tropical climate of Chennai, India. Daily average temperature and relative humidity variations were obtained over a span of 20 years, from 1997 to 2017. The same fluctuations in corrosion rate were used for 2-D as well as 3-D models, for meaningful comparative analysis. The fluctuation in temperature and relative humidity is shown in Fig. 7. Input parameters to solve for nonuniform corrosion rate in the present study are given in Table 2.[25] Corrosion rate variations for the corner bar in space and time are obtained from the numerical model outlined in the flowchart given in Fig. 1. The analysis reveals that corrosion propagated initially at $\Theta = 90$, 135, and 180 degrees—that is, the locations where chlorides exceeded the threshold in the beginning. These locations acted as anodes, while the remaining areas functioned as cathodes during the initial stages of

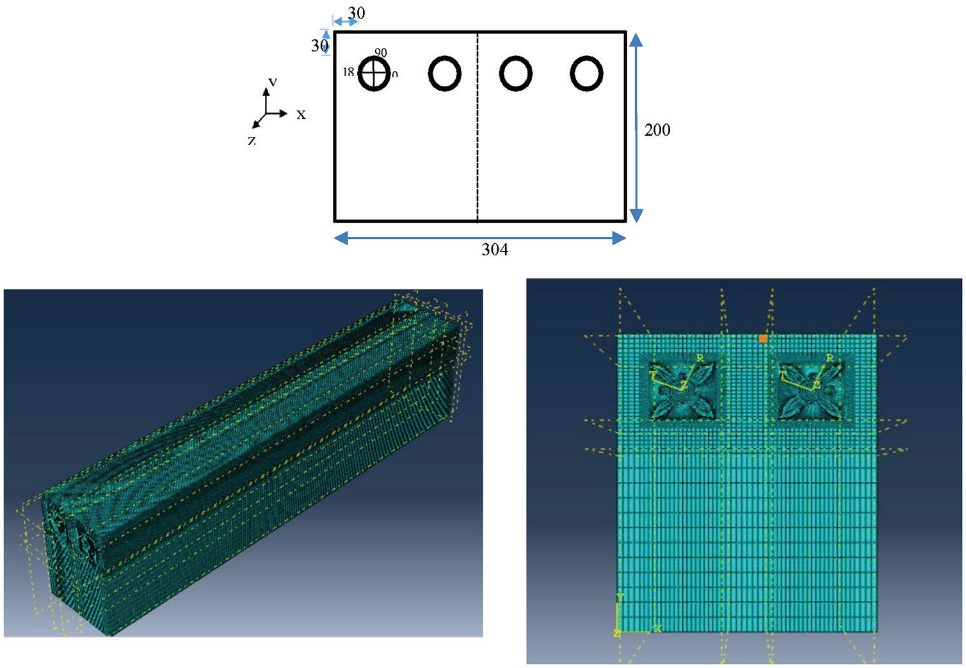

*Fig. 6—Multi-reinforcing bar RC section chosen for study. 3-D and 2-D model meshing chosen for numerical simulation.*

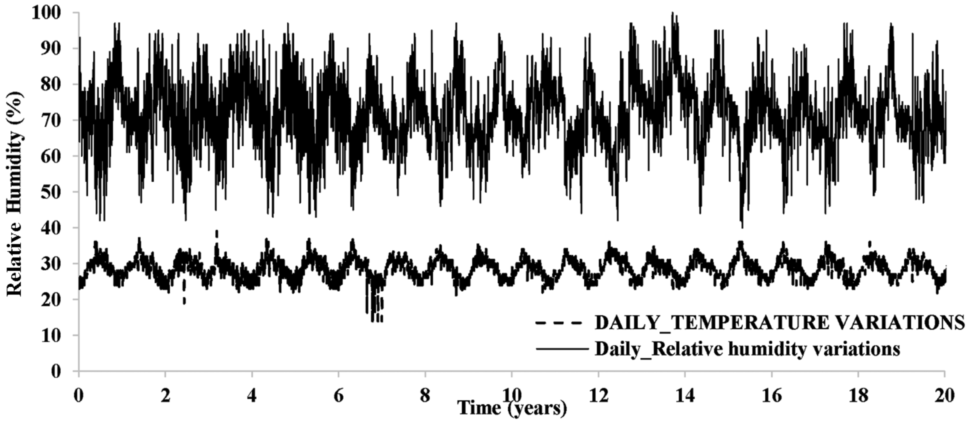

*Fig. 7—Daily variations in temperature and relative humidity for Chennai.*

**Table 2—Input parameters to obtain nonuniform corrosion rate in reinforced concrete[25]**

| Parameter | Value |
|---|---|
| Anodic Tafel coefficient ($\beta_a$) | 0.10 V/dec |
| Cathodic Tafel coefficient ($\beta_c$) | –0.20 V/dec |
| Exchange current density at anode ($i_{oa}$) | $10 \times 10^{-6}$ A/m$^2$<br>($1.078 \times 10^{-4}$ A/ft$^2$) |
| Exchange current density at cathode ($i_{oc}$) | $500 \times 10^{-6}$ A/m$^2$<br>(0.00542 A/ft$^2$) |
| Equilibrium potential at anode versus SCE ($\phi_a$) | –0.70 V |
| Equilibrium potential at cathode versus SCE ($\phi_c$) | 0 V |
| Thermal expansion coefficient of steel ($\alpha$) | $1.17 \times 10^{-5}$ |

Note: SCE is saturated calomel electrode.

corrosion. Among the anodic zones, the maximum corrosion rate of 6 μA/cm$^2$ was recorded at $\Theta$ = 135 degrees, followed by 5 μA/cm$^2$ at $\Theta$ = 90 and 180 degrees. As time progressed, chloride ingress reached additional circumferential positions, and previously passive cathodic regions (for example, at $\Theta$ = 225 and 45 degrees) also transformed into anodic sites after approximately 21 years. Consequently, the distribution of anodic and cathodic areas evolved with time, leading to a dynamic change in the anode-to-cathode surface area ratio, which directly influenced the rate and pattern of corrosion propagation. These observations are shown in Fig. 8. In addition to the observed delay in corrosion initiation at varying positions along the circumference, distinct variations in corrosion rate profiles were identified that can be related to the concrete microenvironment characterized by varying relative humidity and temperature in the real Chennai climate. Evidently, the corrosion propagation model effectively captured the nonuniform nature of corrosion rate patterns within spatial coordinates and their dynamic responses to climatic changes over time. These variations subsequently served as input for deriving corrosion loading to be used for both 2-D and 3-D models. In both the 2-D and 3-D models, the surface area of anode and cathode varies in a similar manner along the circumference,

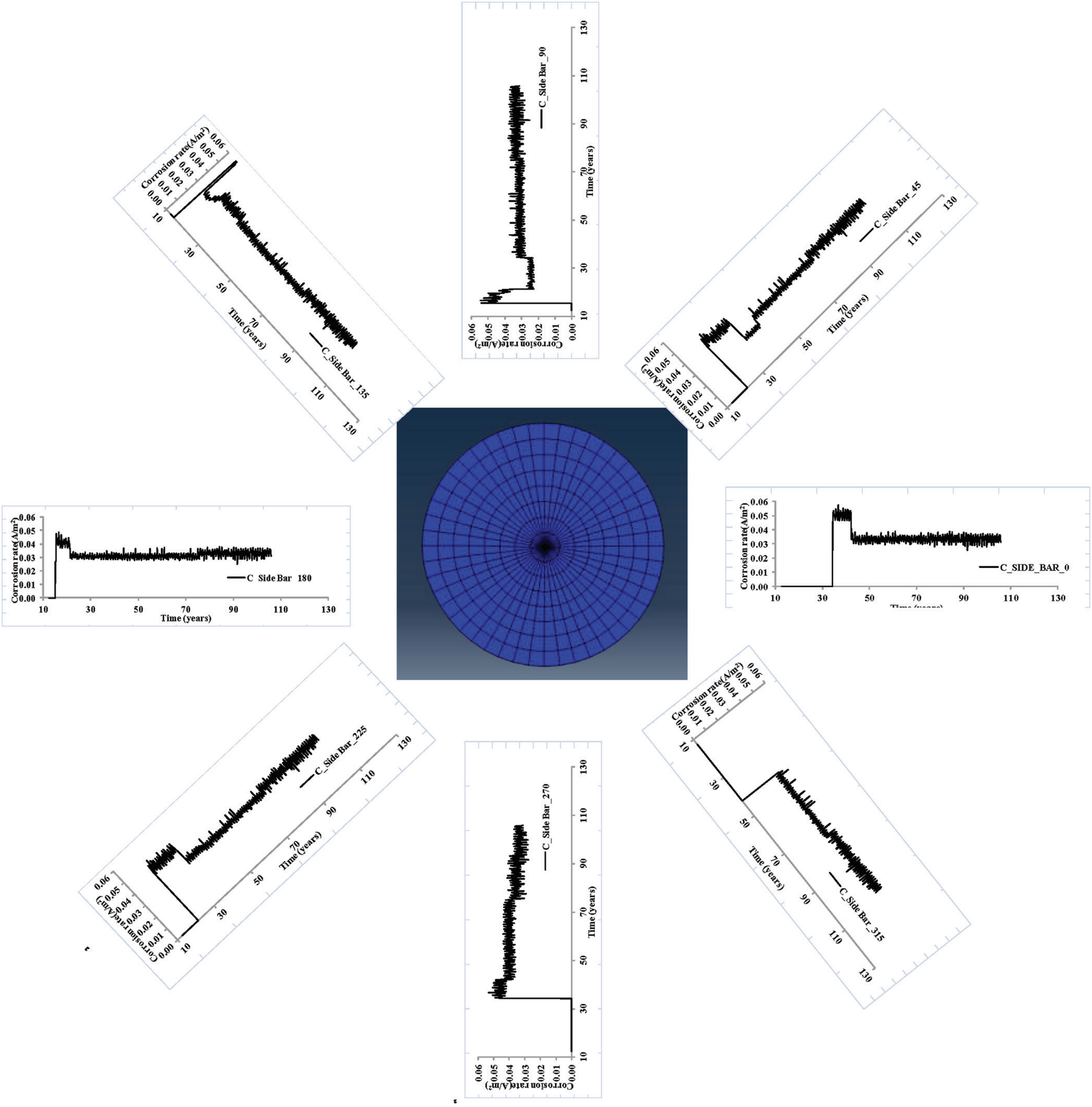

*Fig. 8—Temporal and spatial variations in corrosion rate around corner bar.*[2]

as the anode-cathode ratio changes dynamically with time due to chloride ingress. However, the anodic regions of reinforcing steel were assumed to be continuous along the longitudinal axis, primarily to facilitate direct comparison between 2-D and 3-D cases. However, in real structures, alternating anodic and cathodic regions interact electrochemically, which may influence the kinetics of corrosion propagation and strain development. Consideration of such localized anodic-cathodic distributions will be taken up in future models to better capture these practical effects.

## 2-D FE modeling

The 2-D nonlinear FE analysis was carried out to analyze elastic-plastic stresses, strains, and damage to the RC caused by nonuniform rust expansion using Abaqus. For analysis purposes, symmetric boundary conditions are specified along the x- and z-axis, as shown in Fig. 6. Plane-strain elements available in the Abaqus library, denoted as CPE4R, are used to mesh the 2-D model. The CPE4R element is a standard four-node quadrilateral plane-strain element that is suitable for modeling 2-D plane-strain problems, where deformation occurs only within the X-Y plane. This element is well-suited for capturing the behavior of structures in plane-strain conditions, such as the RC section being analyzed in this study.

## 3-D FE modeling

A 3-D FE model chosen in this study caters to the condition that dimension in the z-axis is sufficiently larger than those in the other two directions (x- and y-axis). The ratio of length to width of the reinforced section is chosen to be six, such that for a width of 300 mm, length is 1800 mm in this study. The three-dimensional FE model is meshed using the eight-node brick element (C3D8R), available in the Abaqus element library. Reduced integration is used for these elements in the analysis, where symmetric boundary conditions are specified along the x- and z-axis. Translation in the z-axis is restrained at the ends, to achieve corresponding zero strain in the z-direction. Nonuniform corrosion-induced expansion of the steel bar is applied in the radial direction and any expansion in the longitudinal direction is ignored in the present case. The input parameters selected for conducting the 2-D and 3-D simulations are listed in Table 3.

## RESULTS AND DISCUSSION

The numerical analysis of 2-D plane-strain and 3-D RC models subject to damage under nonuniform corrosion was conducted using Abaqus. In this section, the results are specifically presented for the corner bar of the selected RC section. This corner bar is more susceptible to experiencing higher degrees of corrosion due to nonuniform chloride ingress from the top and side faces. The comparison between the two models focuses on the corrosion propagation phase. This phase occurs when the chloride levels have already exceeded the threshold on the steel surface, leading to corrosion initiation and propagation with rust expansion. Analyzing this phase gives valuable insights into how the 2-D and 3-D models differ in predicting the extent of corrosion-induced concrete damage. This section is divided into two parts: the damage-initiation phase and the damage-propagation phase. Each phase will be examined separately to assess how the 2-D and 3-D models handle the corrosion-induced damage and how they differ in their predictions.

**Table 3—Input parameters adopted to carry out 2-D and 3-D damage studies on RC**

| Parameter | Value |
|---|---|
| Reinforcing bar diameter | 16 mm (0.630 in.) |
| RC section length in 3-D model | 1800 mm (70.87 in.) |
| Concrete tensile strength ($\sigma_t$) | 3 MPa (435.11 psi) |
| Concrete modulus of elasticity[24] | 18.82 GPa (2,731,488 psi) |
| Concrete Poisson's ratio[24] | 0.18 |
| Concrete fracture energy[24] | 50 N/m (29.63 lb/ft) |

### Damage initiation

The parameter tensile equivalent plastic strain (PEEQT) is used as a measure of damage initiation in the present FE model in Abaqus. It gives a measure of bulk strain output, and damage initiates at points when PEEQT is greater than zero. Damage in the present case is found to be initiated from the steel surface for both 2-D and 3-D models, as shown from the PEEQT contour plots in Fig. 9. Time to damage initiation for both the models is also the same—that is, 2.24 years. This happens as soon as the rust expands and exerts pressure on the concrete surface. It can be observed from the figure that damage initiates at the same location in both the models—that is, at a diagonally located point between the top and side faces of the RC section. This consistent pattern of damage initiation between the two models indicates that both models capture the same nonuniform corrosion-induced damage initiation location. It is to be noted here that the results for the 3-D model are presented for the cross-sectional area situated at the middle length of the RC.

### Damage propagation

After the initiation of damage, the damage patterns and crack width values are used to determine how the crack spreads over space and evolves over time. In the present analysis, the CDP model employed in Abaqus relies on identifying the propagation of damage in the concrete cover through PEEQT. As the corrosion progresses with more and more steel surface getting corroded, larger areas of concrete get strained and result in damage patterns in the concrete cover, as shown in Fig. 10. These damage patterns are compared between the 2-D and 3-D models to assess how the models predict and differ in simulating the crack propagation and damage evolution in the concrete cover over time. From the figure, it is evident that the overall damage patterns obtained from both the 2-D plane-strain and 3-D models exhibit similarities. The initial crack originates from the steel surface and propagates toward the concrete surface in the top cover for both models. However, there exists a slight disparity in the orientation of the top crack between the two models. In the 3-D model, the top crack appears to

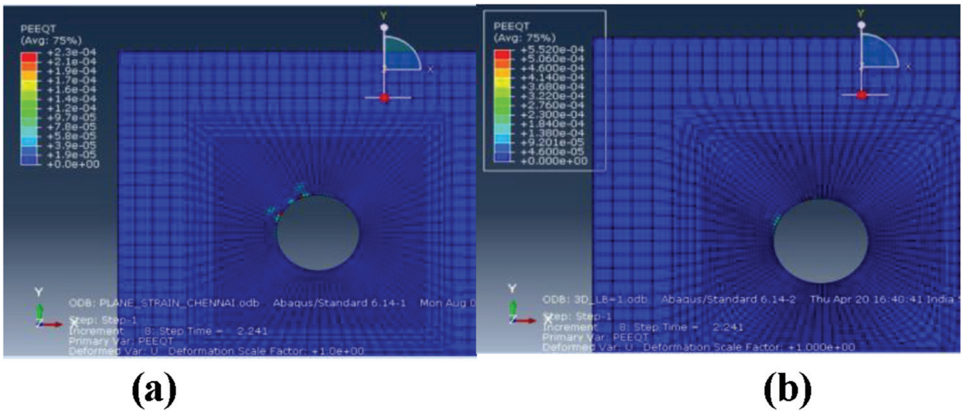

*Fig. 9—PEEQT contour plots showing location of damage initiation for: (a) 2-D; and (b) 3-D models.*

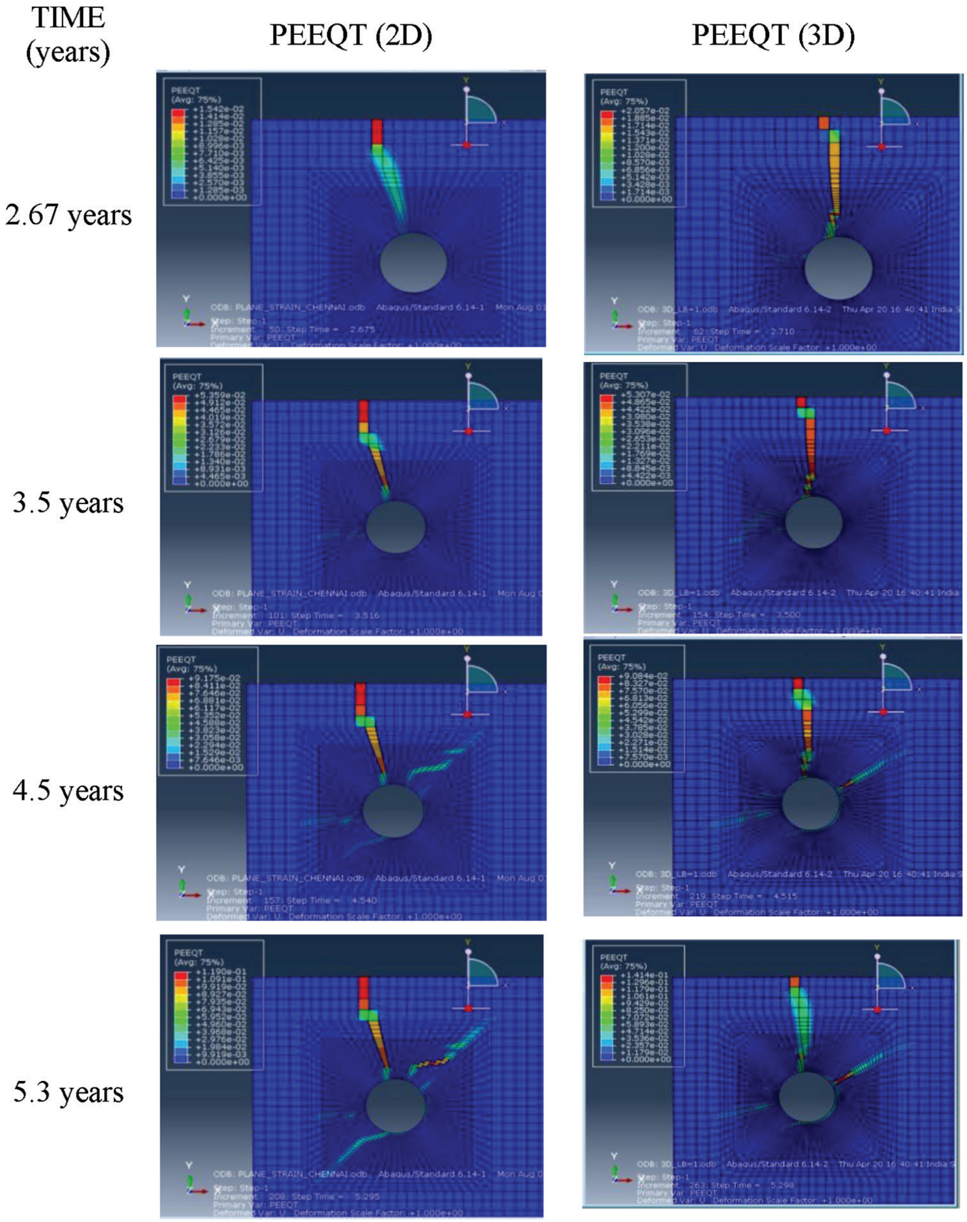

*Fig. 10—Damage contour plots represented by PEEQT for 2-D and 3-D models.*

be almost straight, while in the 2-D model, it exhibits a slight inclination. As the corrosion progresses, additional cracks develop in the side cover for both the 2-D and 3-D models. Nevertheless, the orientation of these cracks again did not differ much between the two models. Based on the observed similarities in the damage patterns between the 2-D plane-strain and 3-D models, it can be inferred that using a 2-D plane-strain FE model is a viable approach to obtain crack patterns under nonuniform chloride-induced corrosion. This choice offers the advantage of reducing computational effort compared to employing a full 3-D model. As observed from Fig. 10, a superficial crack is observed to be propagating on the top surface of concrete in both cases, and the variation in the crack width as a function of time is obtained for both the models. This is shown in Fig. 11, which indicates similar crack width values for both models.

As the employed CDP model primarily relies on stress-based criteria to predict cracking, it may not accurately capture the behavior of concrete beyond the hairline crack regime. Despite this limitation, the study's initial phase suggests that the present CDP model can effectively predict hairline crack widths on the concrete surface for both 2-D and 3-D models, with similar results. Therefore, using 2-D plane-strain models appears to be a viable alternative for predicting the time to damage initiation or hairline cracks on the concrete surface, avoiding the need to employ actual full-scale 3-D models in the analysis.

Further, to understand the variations in results under 2-D and 3-D models, various stress and strain components are plotted and thoroughly investigated for different times and at different locations around the steel bar and in the concrete cover. These locations are marked in Fig. 12 in red color. One location is adjacent to the steel bar, while the other is located at approximately equidistant positions from both the concrete and steel surfaces. These specific locations were chosen to capture the damage around the steel bar, which

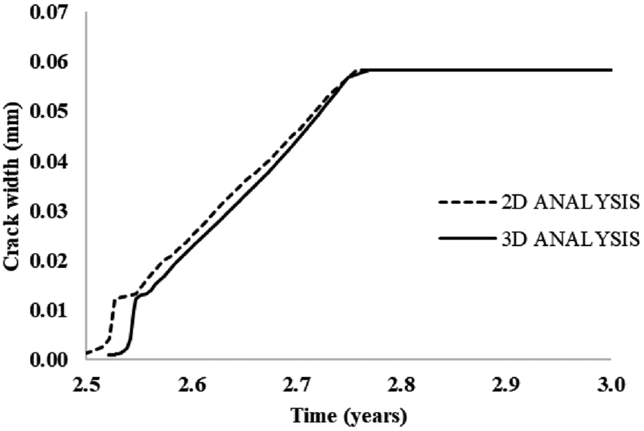

*Fig. 11—Crack width variation on concrete surface for 2-D and 3-D models. (Note: 1 mm = 0.039 in.)*

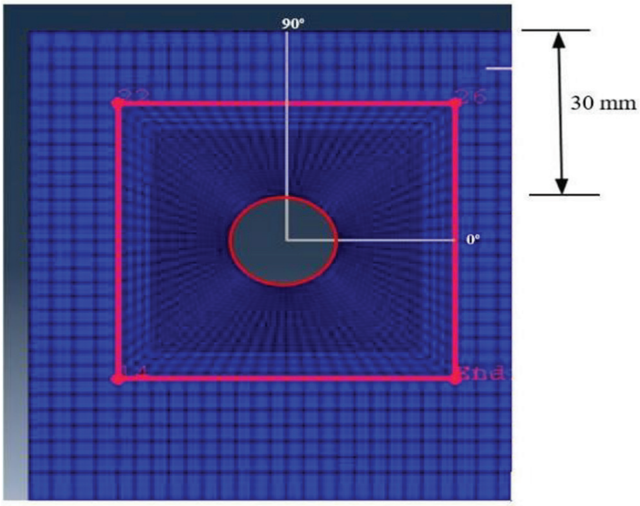

*Fig. 12—Model showing location around corner bar where hoop stress-strain plots obtained as function of time and circumferential angle. (Note: 1 mm = 0.039 in.; full-color PDF is available at www.concrete.org.)*

might originate from either the steel or concrete surface and subsequently propagate into the concrete cover. Examining stress-strain data at these chosen locations allows for a comprehensive understanding of the RC response to nonuniform corrosion.

Table 4 shows hoop stress and hoop plastic strain variations in the concrete adjacent to the steel bar as a function of circumferential angle around the steel bar. The stress and strain in this direction are chosen because they give a direct indication of concrete damage under tension, while being subjected to nonuniform rust expansion. By comparing stress and strain distributions at different locations and times, the study aimed to identify any significant differences between the two models, thus contributing to a more comprehensive assessment of the concrete's response to nonuniform corrosion and its resulting damage patterns. It can be observed from the figures in Table 4 that hoop stress values are comparable for both 2-D and 3-D models in the initial years of nonuniform corrosion—that is, at 2.67 and 3.5 years. The maximum values of the hoop stress obtained around the steel bar are approximately 3 N/mm$^2$ (435.11 psi), which is equal to the tensile strength of concrete assumed in the present study. The hoop stress plots for the initial years also show that there exist elastic-plastic regions in the concrete adjacent to the steel surface. In the analysis, the elastic regions are defined as areas where the hoop stresses remain well below the tensile strength of the concrete—that is, 3 N/mm$^2$ (435.11 psi). On the other hand, the plastic regions are characterized by hoop stresses that have reached the tensile strength of the concrete or decreased beyond the tensile strength value once damage has been initiated at those specific points. The position of these elastic and plastic regions can be determined from the corresponding hoop plastic strain plots and are found to vary spatially and temporally. The use of analytical models will be complicated in the present study; hence, numerical models provide a viable solution to solve such a complex phenomenon. As corrosion progresses, the hoop stress values decrease with a subsequent increase in the plastic hoop strains as a function of time. The values of hoop strains increased from a maximum value of approximately 0.0025 to 0.03 from 2.67 to 5.3 years. However, hoop strain values are observed to be different for both 2-D and 3-D models after an initial 2.67 years, even though the locations of the damage were the same. Plastic strains are observed to be higher for 3-D models compared to the 2-D plastic strain model at 3.5 and 4.5 years. At 5.3 years, maximum values of plastic strains are comparable between the models, signifying that damage in the 2-D model becomes equivalent to the 3-D model with time. Notably, significant differences are observed in the hoop stress values between the 2-D and 3-D models beyond 3.5 years. During these time periods, the tensile hoop stresses in the concrete adjacent to the steel become lower than the tensile strength of concrete, indicating extensive damage in these areas. The presence of extensive damage at the steel-concrete interface implies a potential degradation of the bond strength, which is a crucial parameter to monitor for the structural performance of RC. These observations are made for both 2-D and 3-D models. It demonstrates that the 2-D plane-strain model, when appropriately applied, can capture critical aspects of the stress distribution and damage patterns at the steel-concrete interface in a manner consistent with the more computationally intensive 3-D model.

To improve the prediction of damage variations in the cover concrete, stress-strain plots are generated for the concrete region lying in between the concrete cover depth. The hoop stress-versus-angle and hoop strain-versus-angle plots are obtained for both 2-D and 3-D models and are shown in Table 5. The abscissa in the plots refer to the circumferential angle measured with reference to the steel center and radially extending into the concrete. The results are shown for the corner bar as it is more susceptible to damage under nonuniform corrosion. The hoop strains plotted in the figure are plastic hoop strains, a positive finite value of which indicates permanent damage in the concrete. A higher value of these strains indicates a higher value of crack opening at the location results are obtained. From the figure, it is evident that hoop stress variation in the concrete is observed to be almost the same for both 2-D and 3-D

**Table 4—Hoop stress and hoop plastic strain variations as function of time for 2-D and 3-D models, determined at locations adjacent to steel bar**

| Time | Hoop stresses, N/mm$^2$ | Hoop plastic strains |
|---|---|---|
| 2.67 years | 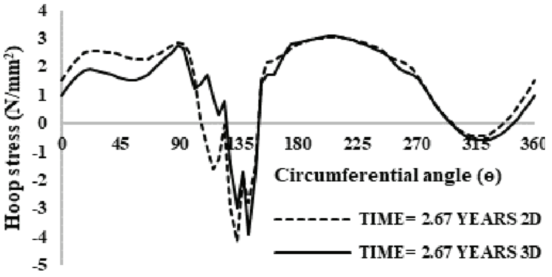 | 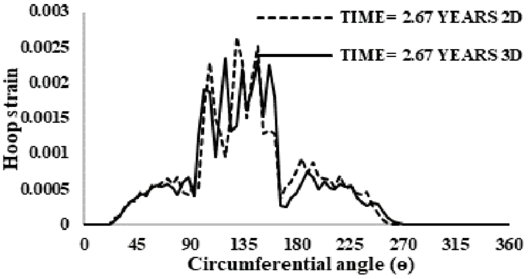 |
| 3.5 years | 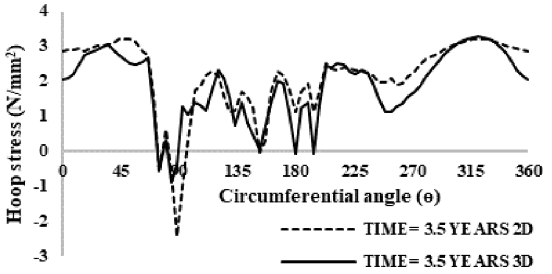 | 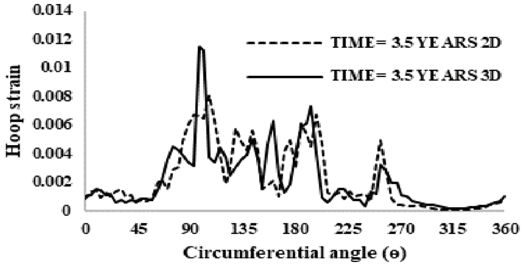 |
| 4.5 years | 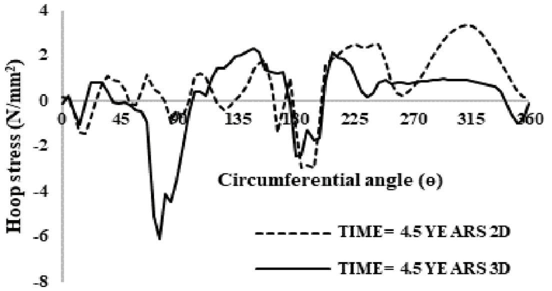 | 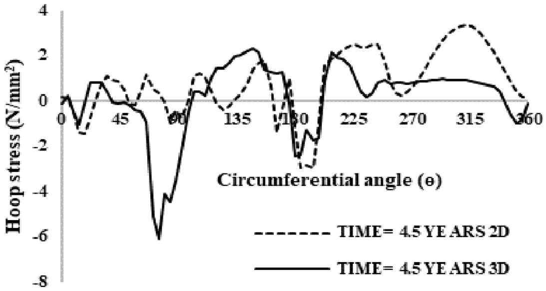 |
| 5.3 years | 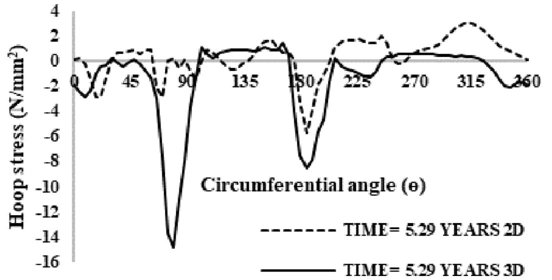 | 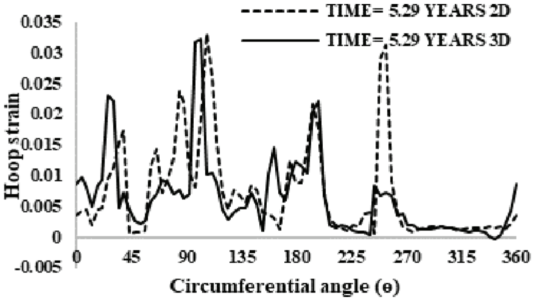 |

models until 4.5 years, after which there exists considerable difference in the variations at 5.3 years. This is similar to the trend that was observed in the concrete adjacent to the steel bar, where similar variations in hoop stresses were observed up to 3.5 years for both 2-D and 3-D models, and at later stages, considerable differences were observed in the stress values for both the models. On the contrary, observations from the hoop plastic strain plots shown in Table 5 suggest that considerable damage occurred in the region enclosed between 90 degrees to approximately 135 degrees in the concrete cover for the 3-D model, while it is lower for the 2-D model, even though the damage location is the same for both models. As corrosion progresses, plastic strains obtained from the 2-D model also increase and become comparable to 3-D model strains at 5.3 years. These findings state that the 3-D model can predict higher damage in the concrete cover as compared to the 2-D plane-strain model. But as corrosion progresses, the magnitude of damage, as observed from the plastic strain values, is observed to be the same for 2-D and 3-D models. This sheds light on the suitability of using a 2-D plane-strain model to predict damage under nonuniform corrosion considering its computational advantages compared to the 3-D model. However, it is crucial to consider the observed stress and strain variations at different stages of corrosion when choosing the appropriate modeling approach for a comprehensive and accurate representation of the RC's behavior over time. To further compare the models, components of elastic-plastic stresses generated in the concrete cover in radial, hoop, and axial directions are obtained along the radial path at location ϴ = 90 degrees and shown in Fig. 13. As is observed from the figure, radial and axial stresses in both the models are compressive along the radial path. While the hoop stresses are mostly tensile in nature, the magnitude of hoop stress is smaller than the

**Table 5—Hoop stress and hoop plastic strain variations as function of time for 2-D and 3-D models, determined at concrete region located within concrete cover**

| Time | Hoop stresses, N/mm$^2$ | Hoop plastic strains |
|---|---|---|
| 2.67 years | 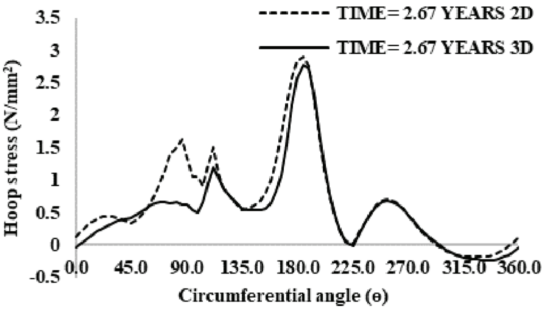 | 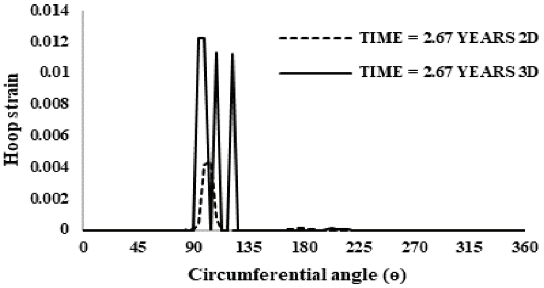 |
| 3.5 years | 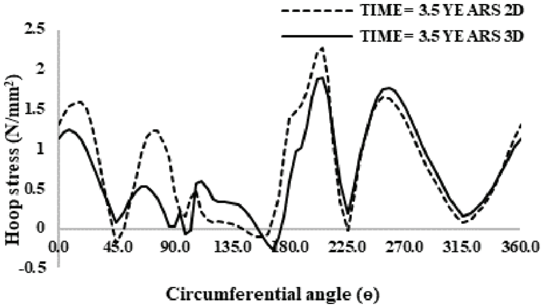 | 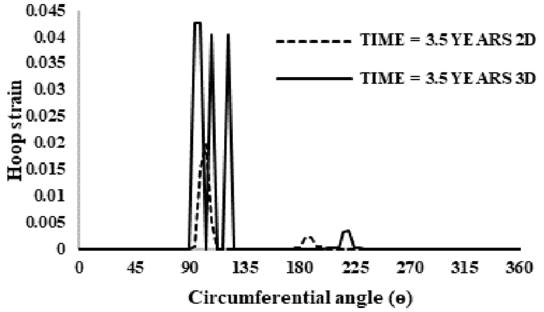 |
| 4.5 years | 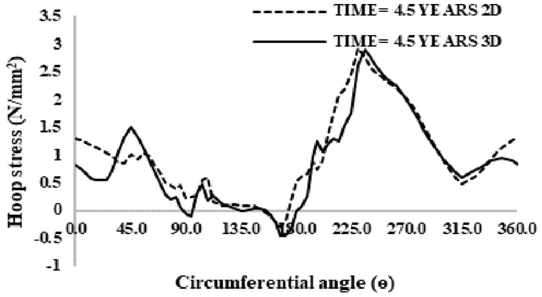 | 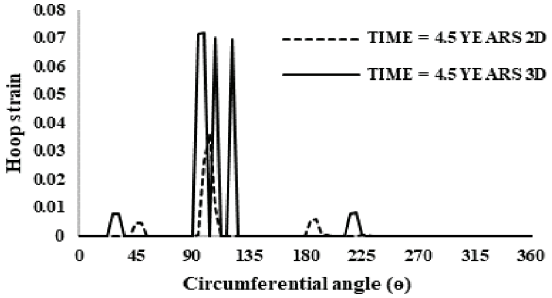 |
| 5.3 years | 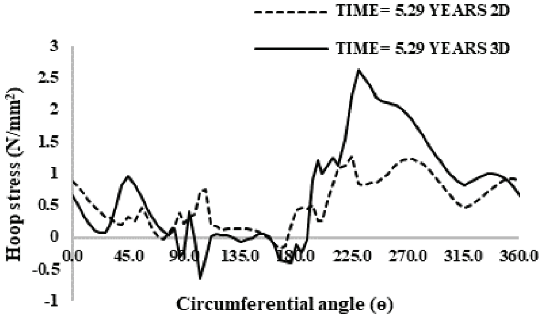 | 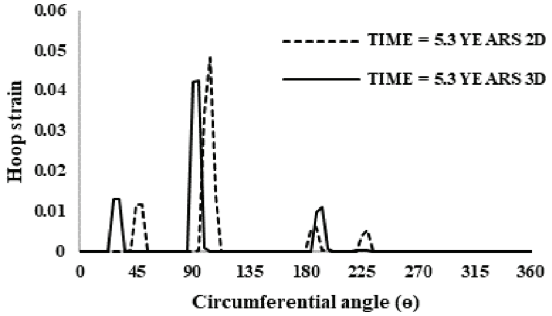 |

radial and axial stresses. This is true for stresses under both 2-D and 3-D models. At the 3.5-year mark, there is a minor difference between the stress values for the 2-D and 3-D models. However, as time progresses to 4.5 years, a more significant difference becomes apparent between the stress values—whether they are radial, hoop, or axial stresses—between the two models. Indeed, the same observation holds true for the earlier analysis as well. During the previous analysis, it was noted that the hoop stress values exhibited variations near the steel surface and within the concrete cover as time passed and more concrete damage occurred. These variations in stress values are likely a consequence of the evolving crack propagation and damage patterns within the concrete, leading to changes in the stress distribution over time for 2-D and 3-D models. However, the damage patterns and extent of damage measured by plastic strains incurred under both the models become comparable as corrosion progresses, as discussed in the previous sections.

## CONCLUSIONS

The main objective of the present work was to compare the commonly assumed two-dimensional (2-D) plane-strain formulation with the actual three-dimensional (3-D) model employed to predict damage under nonuniform corrosion in reinforced concrete (RC). For the analysis, a nonuniform corrosion rate model was used to carry out damage simulation. The simulation results were compared at different stages, starting from damage initiation to damage propagation defined by crack patterns and extent of damage in the concrete cover, as given by plastic strain values. The models were simulated under real temperature and relative humidity conditions to include this natural effect in the simulation. The comparison between the models suggests that:

1. Time to damage initiation and origin of damage around the corner bar are the same for 2-D plane-strain and 3-D RC models subject to chloride-induced nonuniform corrosion.
2. The state of stresses and strains are the same for 2-D and 3-D models in the beginning years of corrosion-induced damage.
3. With the passage of time, stress-strain behavior changes in space for both the models, and higher damage in the concrete cover is observed for the 3-D model.
4. At later stages of corrosion, damage in the 2-D plane-strain model becomes equivalent to damage in the 3-D model, justifying the applicability of the plane-strain condition to simulate damage in RC caused by chloride-induced nonuniform corrosion.
5. During the modeling process, it is essential to consider the observed stress and strain variations at different stages of corrosion to achieve an accurate representation of the RC behavior over time.
6. The present study demonstrates similar values of surface crack widths for both the 2-D and 3-D models obtained based on stress criteria, which are primarily limited to predicting hairline crack widths.

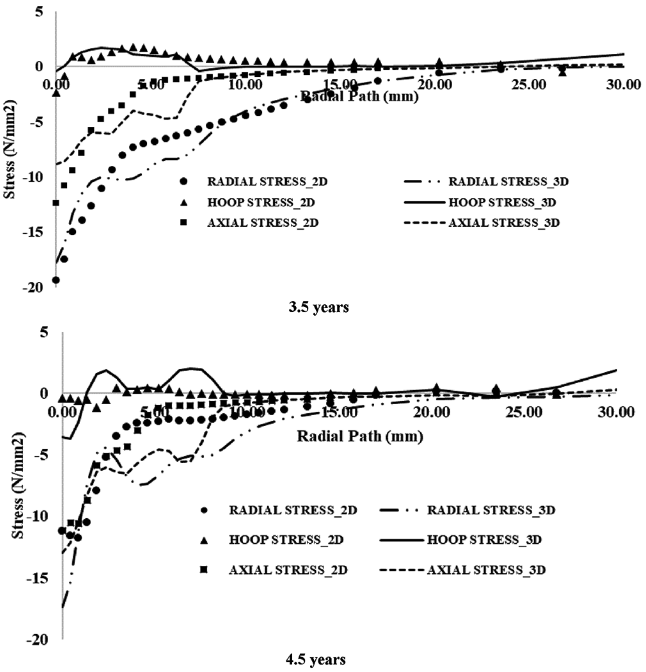

*Fig. 13—Stress distribution along radial path at Θ = 90 degrees. (Note: 1 mm = 0.039 in.; 1 N/mm$^2$ = 145.04 psi.)*

## AUTHOR BIOS

**Aditi Chauhan** *is an Assistant Professor in the Department of Civil Engineering at National Institute of Technology (NIT) Hamirpur, Harmipur, India. She received her PhD in structural engineering from the Indian Institute of Technology (IIT) Roorkee, Roorkee, India, and pursued a postdoctorate at IIT Bombay, Mumbai, India. Her research interests include the durability and service life of reinforced concrete structures, and advanced finite element modeling techniques.*

**Yogesh M. Desai** *is a Professor of structural engineering in the Department of Civil Engineering, IIT Bombay. His research interests include computational mechanics, finite element analysis, structural dynamics, and wind-induced vibrations.*

**Sauvik Banerjee** *is a Professor of structural engineering in the Department of Civil Engineering, IIT Bombay. He received his PhD from the University of California, Los Angeles, Los Angeles, CA. His research interests include structural health monitoring, ultrasonic nondestructive evaluation, guided wave propagation, the assessment of structures, fiber-reinforced polymer retrofitting, and impact response.*

**Umesh Kumar Sharma** *is a Professor of structural engineering in the Department of Civil Engineering, IIT Roorkee. His research interests include durability and service life of reinforced concrete, corrosion's impact on structural performance, structural fire engineering, repair and retrofitting of structures, and testing concrete at elevated temperatures.*

## ACKNOWLEDGMENTS

The authors express their sincere gratitude to the Centre for Computational Engineering and Science (CCES), Civil Engineering Department at IIT Bombay, for their invaluable support. The High-Performance Computing (HPC) facility effectively enabled the successful execution of the finite element analysis.

## REFERENCES

1. Chauhan, A., and Sharma, U. K., "Crack Propagation in Reinforced Concrete Exposed to Non-Uniform Corrosion under Real Climate," *Engineering Fracture Mechanics*, V. 248, Mar, 2021, p. 107719. doi: 10.1016/j.engfracmech.2021.107719

2. Chauhan, A., and Sharma, U. K., "Effect of Real Climate on Non-Uniform Corrosion in Reinforced Concrete," *ACI Materials Journal*, V. 116, No. 5, Sept. 2019, pp. 77-90. doi: 10.14359/51716829

3. Chauhan, A., and Sharma, U. K., "Influence of Temperature and Relative Humidity Variations on Non-Uniform Corrosion of Reinforced Concrete," *Structures*, V. 19, Jan. 2019, pp. 296-308. doi: 10.1016/j.istruc.2019.01.016

4. Cheng, X.; Su, Q.; Ma, F.; Liu, X.; and Liang, X., "Investigation on Crack Propagation of Concrete Cover Induced by Non-Uniform Corrosion of Multiple Rebars," *Engineering Fracture Mechanics*, V. 201, June 2018, pp. 366-384. doi: 10.1016/j.engfracmech.2018.07.037

5. Molina, F. J.; Alonso, C.; and Andrade, C., "Cover Cracking as a Function of Rebar Corrosion: Part 2-Numerical Model," *Materials and Structures*, V. 26, No. 9, 1993, pp. 532-548. doi: 10.1007/BF02472864

6. Yang, S. T.; Li, K. F.; and Li, C. Q., "Numerical Determination of Concrete Crack Width for Corrosion-Affected Concrete Structures," *Computers & Structures*, V. 207, 2018, pp. 75-82. doi: 10.1016/j.compstruc.2017.07.016

7. Zhang, J.; Ling, X.; and Guan, Z., "Finite Element Modeling of Concrete Cover Crack Propagation Due to Non-Uniform Corrosion of Reinforcement," *Construction and Building Materials*, V. 132, 2017, pp. 487-499. doi: 10.1016/j.conbuildmat.2016.12.019

8. Li, F.; Qu, Y.; Zhao, Y.; and Lu, R., "Numerical Simulation Method for Fracture Effect of Corroded Steel Strand under Tension," *Proceedings of the 4th International Conference on the Durability of Concrete Structures*, West Lafayette, IN, Apr. 2014, pp. 109-115. doi: 10.5703/1288284315390

9. Hingorani, R.; Pérez, F.; Sánchez, J.; Fullea, J.; Andrade, C.; and Tanner, P., "Loss of Ductility and Strength of Reinforcing Steel Due to Pitting Corrosion," *Proceedings of the 8th International Conference on Fracture Mechanics of Concrete and Concrete Structures: FraMCoS-8*, J. G. M. Van Mier, G. Ruiz, C. Andrade, R. C. Yu, and X. X. Zhang, eds., Toledo, Spain, 2013, pp. 2009-2018.

10. Cui, Z., and Alipour, A., "Concrete Cover Cracking and Service Life Prediction of Reinforced Concrete Structures in Corrosive Environments," *Construction and Building Materials*, V. 159, 2018, pp. 652-671. doi: 10.1016/j.conbuildmat.2017.03.224

11. Ožbolt, J.; Balabanić, G.; and Sola, E., "Determination of Critical Anodic and Cathodic Areas in Corrosion Processes of Steel Reinforcement in Concrete," *Materials and Corrosion*, V. 68, No. 6, 2017, pp. 622-631. doi: 10.1002/maco.201609295

12. Ožbolt, J.; Oršanić, F.; and Balabanić, G., "Modeling Corrosion-Induced Damage of Reinforced Concrete Elements with Multiple-Arranged Reinforcement Bars," *Materials and Corrosion*, V. 67, No. 5, 2016, pp. 542-552. doi: 10.1002/maco.201508569

13. Castorena-González, J. H.; Martin, U.; Gaona-Tiburcio, C.; Núñez-Jáquez, R. E.; Almeraya-Calderón, F. M.; Bastidas, J. M.; and Bastidas,

D. M., “Modeling Steel Corrosion Failure in Reinforced Concrete by Cover Crack Width 3D FEM Analysis,” *Frontiers in Materials*, V. 7, Feb. 2020, pp. 1-10. doi: 10.3389/fmats.2020.00041

14. Zaghian, S.; Martín-Pérez, B.; and Almansour, H., “Nonlinear Finite Element Modeling of the Impact of Reinforcement Corrosion on Bridge Piers under Concentric Loads,” *Structural Concrete*, V. 23, No. 1, 2022, pp. 138-153. doi: 10.1002/suco.202100254

15. Ožbolt, J.; Balabanić, G.; and Kušter, M., “3D Numerical Modelling of Steel Corrosion in Concrete Structures,” *Corrosion Science*, V. 53, No. 12, 2011, pp. 4166-4177. doi: 10.1016/j.corsci.2011.08.026

16. Chauhan, A.; Desai, Y. M.; Banerjee, S.; and Sharma, U. K., “3D Simulation of Non-Uniform Corrosion Induced Damage in Reinforced Concrete Exposed to Real Climate,” *Structures*, V. 56, 2023, p. 104852. doi: 10.1016/j.istruc.2023.07.042

17. Pedrosa, F., and Andrade, C., “Corrosion Induced Cracking: Effect of Different Corrosion Rates on Crack Width Evolution,” *Construction and Building Materials*, V. 133, 2017, pp. 525-533. doi: 10.1016/j.conbuildmat.2016.12.030

18. Ye, H.; Jin, N.; Fu, C.; and Jin, X., “Rust Distribution and Corrosion-Induced Cracking Patterns of Corner-Located Rebar in Concrete Cover,” *Construction and Building Materials*, V. 156, 2017, pp. 684-691. doi: 10.1016/j.conbuildmat.2017.09.033

19. Vidal, T.; Castel, A.; and François, R., “Analyzing Crack Width to Predict Corrosion in Reinforced Concrete,” *Cement and Concrete Research*, V. 34, No. 1, 2004, pp. 165-174. doi: 10.1016/S0008-8846(03)00246-1

20. Yang, S.; Xi, X.; Li, K.; and Li, C.-Q., “Numerical Modeling of Nonuniform Corrosion-Induced Concrete Crack Width,” *Journal of Structural Engineering*, ASCE, V. 144, No. 8, 2018, p. 04018120. doi: 10.1061/(ASCE)ST.1943-541X.0002108

21. Hillerborg, A., “The Theoretical Basis of a Method to Determine the Fracture Energy GF of Concrete,” *Materials and Structures*, V. 18, No. 4, 1985, pp. 291-296. doi: 10.1007/BF02472919

22. Jin, L.; Zhang, R.; Du, X.; and Li, Y., “Investigation on the Cracking Behavior of Concrete Cover Induced by Corner Located Rebar Corrosion,” *Engineering Failure Analysis*, V. 52, 2015, pp. 129-143. doi: 10.1016/j.engfailanal.2015.03.019

23. Liu, Y., and Weyers, R. E., “Modeling the Time-to-Corrosion Cracking in Chloride Contaminated Reinforced Concrete Structures,” *ACI Materials Journal*, V. 95, No. 6, Nov.-Dec. 1998, pp. 675-681.

24. IS 456:2000, “Plain and Reinforced Concrete—Code of Practice,” Bureau of Indian Standards, New Delhi, India, 2000.

25. Warkus, J.; Brem, M.; and Raupach, M., “BEM-Models for the Propagation Period of Chloride Induced Reinforcement Corrosion,” *Materials and Corrosion*, V. 57, No. 8, 2006, pp. 636-641. doi: 10.1002/maco.200603995

# NOTES:

ACI MATERIALS JOURNAL TECHNICAL PAPER

Title No. 123-M19

# Surface Treatment for Recycled Plastic Aggregate in Concrete: A Review

by Seongho Han, Nima Mahmoudzadeh Vaziri, and Kamal H. Khayat

*The use of recycled plastic aggregate in cement-based materials has emerged as a promising strategy to reduce plastic waste and promote sustainable construction. However, the inherent hydrophobicity of plastic surfaces poses a significant challenge by limiting their bonding with the cement matrix. This review critically examines five major surface treatment methods—coating, oxidation, silane, plasma, and radiation—to enhance the compatibility of recycled plastic aggregates in cementitious composites. Coating with materials such as water glass, slag powder, or acrylic resins improved compressive strength by up to 78%, depending on the coating type. Oxidation using hydrogen peroxide or calcium hypochlorite increased hydrophilicity and improved strength by approximately 10 to 30%, while excessive treatment with NaOH-hypochlorite mixtures reduced strength by up to 60%. Silane treatment significantly enhanced surface bonding, resulting in improved mechanical properties. Plasma treatment demonstrated high efficiency, reducing contact angles from ~108 to 44.0 degrees within 30 seconds. Radiation treatment using gamma rays and microwaves increased surface roughness and strength, with gamma irradiation at 100 to 200 kGy leading to substantial improvements in compressive strength and surface morphology. To the authors' knowledge, this is the first review to systematically compare the effectiveness, mechanisms, and limitations of these surface treatments specifically for recycled plastic aggregates in cement-based materials. This review also highlights the practical challenges of scaling such treatments, including energy demand, chemical handling, and cost, and identifies future directions, such as bio-based coatings and nanomaterial functionalization. The findings provide critical insight into optimizing surface treatments to improve the mechanical performance, durability, and sustainability of concrete incorporating plastic aggregates, supporting their broader adoption in sustainable construction practices.*

**Keywords:** hydrophilicity; plastic aggregate concrete; plastic waste; surface treatment.

## INTRODUCTION

The global consumption of plastics has surged dramatically over the past few decades, largely driven by rapid industrialization and economic growth in emerging markets. By 2019, global plastic production reached approximately 460 million tons, doubling since 2000, leading to a significant rise in plastic waste generation, which reached an estimated 353 million tons in 2019, more than twice the amount generated in 2000.[1,2] A significant portion of this waste is attributed to packaging materials, which alone account for 40% of the total plastic waste.[3] Additionally, consumer goods and clothing/textiles contribute 12% and 11%, respectively.[4] The widespread use of non-biodegradable conventional plastics has resulted in severe environmental pollution, posing serious threats to ecosystems, human health, and overall quality of life on a global scale.

Plastic waste has become a major component of global waste streams, accounting for 40% or more of total waste generated worldwide.[5] The accumulation of plastics in various environments, particularly in aquatic and ocean ecosystems, is an escalating concern.[6] The management of plastic waste has become a pressing global issue, with traditional methods, such as landfilling, incineration, and recycling, being the primary strategies used.[7] Currently, landfilling accounts for 50% of total plastic waste management, while incineration and recycling represent 19% and 9%, respectively. However, a significant 22% of plastic waste remains unmanaged, often ending up in uncontrolled dumpsites or leaking into aquatic environments.[8] The reliance on landfilling has severe environmental implications, including soil contamination, reduced soil water permeability, and adverse effects on soil fertility.[9] Additionally, the obstruction of drainage systems by plastic waste exacerbates environmental challenges. Incineration, while effective at reducing the volume of waste, introduces harmful toxins into the atmosphere, posing serious health risks and contributing to air pollution.[10] The environmental impact of plastic pollution is profound, disrupting ecosystems and hindering their ability to adapt to climate change. Given these environmental challenges, there is an urgent need to shift toward more sustainable plastic waste management practices, with a particular emphasis on recycling as a crucial element of sustainable development.

Recycling represents a critical solution in the effort to mitigate the environmental impact of plastic waste. By enhancing recycling efforts, reliance on landfilling and incineration can be reduced, thereby lessening the ecological footprint of plastic waste management. The transition from traditional waste management methods to the recycling of post-consumer plastics is essential to achieving sustainable development goals. Recycling processes are generally categorized into three primary types: primary, secondary, and tertiary.[11,12] Primary recycling, also known as closed-loop recycling, involves the direct conversion of uncontaminated discarded plastic into the same product without compromising its inherent properties. This method is highly

---

*ACI Materials Journal*, V. 123, No. 2, March 2026.

MS No. M-2024-431.R2, doi: 10.14359/51749270, received August 12, 2025, and reviewed under Institute publication policies. Pertinent discussion including author's closure, if any, will be published ten months from this journal's date if the discussion is received within four months of the paper's print publication.

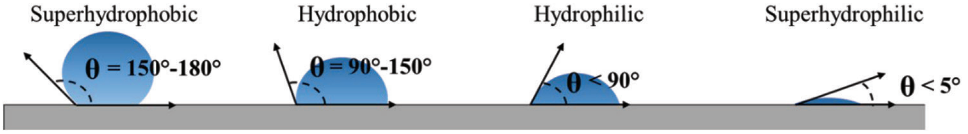

*Fig. 1—Contact angle of water droplets on surfaces with varying degrees of wettability.*

efficient and sustainable, as it preserves the material's original quality and functionality. Secondary recycling, or mechanical recycling, retains the polymer's chemical identity but reprocesses the material physically for different applications. This method is commonly used for plastics that have been contaminated or mixed with other materials, as it allows for the recovery of the polymer's value through physical reformation. Tertiary recycling, also known as chemical recycling, involves breaking down polymers into their basic chemical components using processes such as hydrolysis, pyrolysis, and depolymerization. These processes convert plastic into valuable raw materials that can be used to produce new plastic products or other industrial commodities, thus closing the loop in the plastic life cycle.

Despite advancements in recycling technology, the global rate of post-consumer plastic waste recycling or reuse remains low, with the rate in the United States standing at approximately 5 to 6%.[13,14] Even by 2050, projections suggest that only one-third of plastic waste will be recycled or reused.[15] This limited progress is largely due to several persistent challenges, including the diversity of polymer resins, mechanical incompatibility between different types of plastics, and high levels of impurities in the waste stream.[16,17] These factors necessitate extensive sorting, cleaning, and upgrading processes to ensure the quality and viability of recycled plastics. The complexities associated with these processes highlight the need for continued innovation and investment in recycling technologies to improve efficiency and increase recycling rates.

Despite ongoing challenges, the push toward more sustainable and circular practices in material use has led researchers to explore a broader range of waste-derived resources for construction applications. In particular, various industrial and agricultural wastes have been incorporated into cementitious composites as alternative binders or aggregates. These include fly ash, ground-granulated blast-furnace slag, waste glass, ceramic powder, and organic residues such as date palm kernels and pistachio shells. These materials are often used as partial replacements for cement or natural aggregates and have been shown to enhance durability, improve thermal performance, reduce production costs, and lower carbon emissions. For instance, fly ash can improve workability and long-term strength, while lightweight agricultural wastes serve effectively as fine aggregate substitutes.[18-21] Building on this foundation, recycled plastics have recently attracted considerable attention as a promising alternative aggregate, given their wide availability and potential environmental benefits. However, their incorporation presents unique technical challenges, especially related to interfacial bonding within cement-based matrixes due to the inherently hydrophobic nature of plastic surfaces.

In the construction engineering sector, there has been a growing interest in expanding the use of recycled plastics as construction materials. Numerous studies have explored the potential of incorporating recycled plastics as aggregate,[22,23] filler,[24,25] and fiber[26,27] in concrete and other building materials. Recycled plastic aggregate, in particular, has collected significant attention as both fine and coarse aggregates in concrete production.[28-30] The plastic aggregate is typically derived from various sources of recycled plastic, including post-consumer waste and industrial by-products. The process of preparing this aggregate often involves grinding the plastic to achieve the desired particle size, followed by sieving and washing to remove impurities. In some cases, additional grinding steps using specialized equipment, such as a propeller crusher, are used to further reduce the size of the plastic pieces, thereby enhancing their adhesion with the cementitious matrix in concrete. The types of plastics commonly used in construction applications include polyethylene (PE), which can be classified as high-density polyethylene (HDPE) and low-density polyethylene (LDPE), polypropylene (PP), polyethylene terephthalate (PET), polystyrene (PS), polycarbonate (PC), acrylonitrile butadiene styrene (ABS), polyoxymethylene (POM), and polyvinyl chloride (PVC).[31-33] These plastics are selected for their availability, durability, and recyclability. For instance, PET is frequently used in the production of concrete aggregate due to its relatively high strength, chemical resistance, and ability to withstand the harsh conditions of the construction environment.

By replacing natural aggregate with plastic aggregate, the construction industry can reduce its reliance on natural resources, decrease the environmental impact of aggregate extraction, and contribute to the overall sustainability of construction practices. However, the incorporation of plastic aggregate into concrete poses several challenges, primarily due to the inherent hydrophobic nature of plastic surfaces. The hydrophobic nature of plastic aggregate can hinder their interaction with the cement matrix, leading to weak spots within the concrete and potentially compromising the structural integrity and durability of the final product.[23] Hydrophobicity, a physical property of materials characterized by their repulsion of water, can significantly disrupt the bonding process between plastic aggregate and the cementitious matrix in concrete.[34,35] The degree of hydrophobicity or hydrophilicity of a material is typically measured by the contact angle of a water droplet on its surface. As illustrated in Fig. 1, the contact angle forms at the intersection of the liquid-solid and liquid-vapor interfaces. Materials with a contact angle of less than 5 degrees are classified as superhydrophilic, while those with a contact angle of 90 degrees are considered hydrophilic. Materials with a contact angle between 90 and 150 degrees are regarded as hydrophobic,

**Table 1—Surface treatment for enhancing plastic aggregate performance**

| Method | | Type of plastic | Description of method | Reference |
|---|---|---|---|---|
| Surface coating | | PET | Blast-furnace slag | Choi et al.[36] |
| | | Mixed<br>(PS + ABS + EP + PE) | 1) Water glass; 2) silicate paint;<br>3) water glass + blast-furnace slag;<br>4) water glass + quartz sand; 5) cement paste | Bágeľ and Matiašovský[37] |
| | | PP | Sand | Purnomo et al.[46] |
| | | PET | Ceramic waste | Ramakrishnan and Jegan[47] |
| | | Unsorted plastic film | Acrylic binder resin | Lee and Hong[48] |
| | | PP | 1) 0.1 or 0.2 wt. % nonionic surfactant; 2) 0.1 or 0.2 wt. % active component/anionic surfactant | Correa et al.[49] |
| | | PET | 5 wt. % PS resin + 5 wt. % phenoxy resin | El-Nadoury[50] |
| | | Mixed (PE + PP + PET + EVA + PVC) | 1) Liquid silicone amine resin; 2) liquid acrylic colorant resin; 3) 10 wt. % ethyl acrylate binder resin | Kim and Cho[51] |
| Oxidation | Hypochlorite treatment | HDPE | 1) 5 wt. % HOCl solution;<br>2) 5 wt. % HOCl + 4 wt. % NaOH solution | Naik et al.[52] |
| | | PET | 1) 5 wt. % NaOCl + 4 wt. % NaOH solution;<br>2) 5 wt. % NaOCl + 4 wt. % NaOH solution with washing | Thorneycroft et al.[53] |
| | | PET | 1) 2.5 wt. % $H_2O_2$ solution;<br>2) 5 wt. % $Ca(ClO)_2$ solution | Lee et al.[38] |
| | | PC, POM, PET, ABS, ABS/PC blend | 1) 5 wt. % NaOCl + 4 wt. % NaOH solution;<br>2) 5 wt. % NaOCl + 4 wt. % NaOH solution with washing | Kaur and Pavia[39] |
| | UV-ozone | Unsorted plastic film | UV intensity of 28 $mW/cm^3$ for 0 to 1200 seconds under $N_2$ purging | Lee and Hong[48] |
| Silane | | Unsorted plastic film | Silane coupling agent ((3-aminopropyl) triethoxysilane) | Lee and Hong[48] |
| | | PVC | Methacryl-functional silane coupling agent | Pan et al.[40] |
| Plasma | Oxygen plasma | Unsorted plastic film | Injecting $O_2$ and Ar gases at flow rates of 15 and 4 sccm, respectively, using RF power of 100 W under atmospheric pressure, while varying processing time from 0 to 30 seconds | Lee and Hong[48] |
| Radiation | Gamma | PET, PC | Irradiating at 100 and 200 kGy of gamma dose | Martínez-Barrera et al.[41] |
| | Microwave | PET, HDPE, PP, mixed (PET + HDPE + PE) | Exposed to 1100 W for 210 minutes | Abu-Saleem et al.[42] |

Note: EP is ethylene propylene; EVA is ethylene vinyl acetate.

and those with a contact angle greater than 150 degrees are categorized as superhydrophobic. A higher contact angle indicates a stronger liquid-liquid interaction strength, leading to increased hydrophobicity of the material.

To address these challenges, surface treatment of plastic aggregate is a process to enhance its performance and compatibility when used as a replacement for natural aggregate in concrete. The surface treatment is to modify the hydrophobic properties of the plastic aggregate, making it more hydrophilic. This modification improves the bonding between the cement matrix and plastic aggregate, leading to better mechanical performance and durability of the concrete. Various surface treatment methods have been reported in the literature for both concrete and construction products,[36-53] as well as for other applications,[54-56] each with its unique advantages and mechanisms. Proper treatment of plastic aggregate before use in building materials can enhance sustainability without compromising the quality or longevity of structures. Table 1 provides a comprehensive summary of these treatment methods, such as surface coating, oxidation using hypochlorite and ultraviolet (UV) ozone, plasma (that is, oxygen plasma), and radiation treatments. However, to date, no comprehensive review has systematically synthesized and evaluated the diverse surface treatment methods applied specifically to plastic aggregates in cementitious composites. While numerous individual studies have reported on treatment effects, there remains a lack of integrated understanding regarding their comparative effectiveness, underlying mechanisms, and influence on the fresh and hardened properties of cement-based materials. This gap limits the ability of researchers and engineers to make informed decisions regarding the most appropriate and effective surface treatments for different plastic types and construction applications.

Therefore, this review aims to fill this critical gap by providing an in-depth and structured assessment of existing surface treatment techniques for recycled plastic aggregates. The analysis will also explore how the use of treated plastic aggregate impacts the performance of plastic aggregate cement-based materials.

## RESEARCH SIGNIFICANCE

The significance of research on enhancing the performance of recycled plastic aggregate in concrete lies in addressing key environmental and engineering challenges. With the rising environmental burden of plastic waste, this research contributes to sustainable development by exploring ways to effectively use recycled plastic as aggregate in construction, reducing reliance on natural resources. The study's focus on surface treatments, such as coating, oxidation, silane, plasma, and radiation, aims to overcome the hydrophobicity of plastic, which hinders bonding with cement, thus improving material compatibility and mechanical performance in concrete applications.

## METHODOLOGY

This review was conducted through a structured literature survey to ensure comprehensive and unbiased coverage of studies related to the surface treatment of recycled plastic aggregates for cement-based materials. Peer-reviewed publications were collected from major scientific databases, including Scopus, Web of Science, and Google Scholar. The search strategy employed combinations of keywords, such as "plastic aggregate," "recycled plastic in concrete," "surface treatment," "coating," "plasma," "oxidation," "silane," and "radiation." The literature search covered all relevant publications up to the year 2024, with no language or regional restrictions, to provide a global and inclusive perspective on the topic. Studies were included if they involved cement-based composites incorporating recycled plastic aggregates and presented experimental or quantitative data regarding the effect of surface treatments on fresh, mechanical, or durability-related properties. To ensure scientific rigor, non-cementitious applications, conceptual reviews lacking original data, and non-peer-reviewed materials such as patents, editorials, and industrial white papers were excluded from the analysis. As most of these studies did not report statistical parameters such as standard deviation or confidence intervals, error bars were not included in the figures. This methodology ensures that the review captures the current state of knowledge based on validated scientific evidence, providing a reliable foundation for assessing the performance and applicability of surface-treated plastic aggregates in cement-based materials.

## SURFACE TREATMENT METHOD

### Surface coating

The surface coating method is a widely adopted approach for treating plastic aggregate due to its ease of application and effectiveness in mixing with other materials, as shown in Fig. 2. This process involves applying a thin layer of hydrophilic materials to the surface of plastic aggregate to convert its hydrophobic characteristics. Common coating materials include blast-furnace slag, sand, and cement paste, which are typically used in concrete applications.[36,37,46,47] Additionally, synthetic materials, such as paint, surfactant (nonionic and anionic), and resin, are used for surface coating.[37,48-51]

*Fig. 2—Surface coating methods for plastic aggregate with different coating materials: (a) blast-furnace slag powder[36]; (b) cement paste[37]; (c) volcanic sand[46]; (d) acrylic-based resin[48]; and (e) silicone amine resin.[51]*

The solid state of coating materials cannot efficiently coat plastic aggregate. Therefore, a heating process is needed to enhance the bonding of the coating material onto the plastic aggregate. This method is particularly effective for thermoplastics such as PET and PP, which easily deform when heated. The heat softens the plastic surface, allowing for better adhesion between the coating material and the plastic aggregate. For instance, in one study, the surfaces of recycled PET aggregate were enhanced by applying a blast-furnace slag powder coating.[36] PET bottle fragments were placed in a mixer maintained at 250 ± 10°C (482 ± 50°F) and rotated at speeds of 30 to 50 rpm for 20 seconds before introducing the slag for surface coating to improve bond to the PET aggregate. Similarly, Purnomo et al.[46] focused on coating PP aggregate with volcanic sand. Their approach involved placing uncoated plastic aggregate in a rotating cylinder and applying hot volcanic sand for coating.

Alternatively, using liquid materials offers a method to enhance coating efficiency for plastic aggregate without the need for heating equipment. Liquid coatings can be applied through simpler techniques, such as spraying or dipping, streamlining the process.[46,48-51] Bágeľ and Matiašovský[37] explored the effectiveness of improving the mechanical properties of concrete by using surface-coated plastic aggregate sourced from electric and electronic equipment, including PS, ABS, and PE. Various coating materials, such as water glass, silicate paint, and cement paste, were used. The process involved mixing plastic aggregate with an equal volume of the treating solution, forming a well-distributed liquid layer on the aggregate surface, with a weight ratio of 0.3. Additional coatings using ground blast-furnace slag powder and quartz sand were applied after treating the plastic aggregate with water glass, and the treated aggregate was subsequently air-dried. In other studies, acrylic-based resin was used as the coating material.[46,48-51] The acrylic binders were water-soluble resins with hydrophilic properties due to their polar carboxyl groups.[48,51] The coating process involved adjusting the thickness of the coating layer by varying the wetting time, which ranged from 0 to 300 seconds. Kim and Cho[51] used silicone amine resin, a modified silicone resin containing an amine group, for the surface coating. The amine group reduces surface tension and enhances hydrophilicity on the plastic aggregate. All these coating materials were in liquid form, simplifying the coating process and aligning with sustainability goals by reducing energy consumption.

## Oxidation treatment

To treat the surface of plastic aggregate chemically, oxidizing agents are commonly used, including hypochlorous acid (HOCl), sodium hypochlorite (NaOCl), calcium hypochlorite ($Ca(ClO)_2$), and hydrogen peroxide ($H_2O_2$) solutions.[39,52,53] The oxidation mechanism between the oxidizing agent and the plastic involves the breaking of the carbon-to-carbon bonds in the polymer chains, leading to the formation of hydroxyl (–OH), carbonyl groups (C=O), and other oxidized species.[57,58] The oxidation of plastic consists of three steps: initiation, propagation, and termination.[59,60] For example, the oxidation process of plastic using HOCl solution involves a chemical reaction between HOCl and the plastic surface, primarily aiming to enhance the surface's hydrophilicity and thereby improve its bonding capabilities when used as aggregate in concrete. The reaction mechanism begins with the HOCl solution reacting with unsaturated or reactive sites on the plastic surface, initiating the oxidation process through the formation of reactive oxygen species. These reactive oxygen species then attack the polymer chains, introducing oxygen-containing functional groups such as hydroxyl (–OH), carbonyl (–C=O), or carboxyl (–COOH) on the plastic surface, increasing its polarity and making it more hydrophilic.[61-63]

A high-alkaline solution can enhance the stability and effectiveness of hypochlorite.[64] Hypochlorite solutions, particularly NaOCl, can decompose over time, losing their effectiveness.[65-67] Sodium hydroxide (NaOH) is often used with hypochlorite solutions in various applications due to its ability to stabilize the hypochlorite by maintaining an alkaline pH during the surface treatment of plastic aggregate.[39,52,53] This prevents hypochlorite from decomposing into chlorine gas and other by-products, ensuring that the solution remains effective for a longer period. In an alkaline environment, hypochlorite ions ($OCl^–$) are more prevalent than hypochlorous acid (HOCl). These hypochlorite ions are strong oxidizing agents capable of effectively breaking down various organic and inorganic materials, including those found in plastics. This makes the combination of NaOH and hypochlorite particularly effective in degrading contaminants and residues on plastic surfaces. The addition of NaOH to hypochlorite helps maintain the solution's pH in the alkaline range, where the $OCl^–$ ions are the dominant species: $NaOCl + H_2O \leftrightarrow HOCl + NaOH$. However, in an alkaline environment: $HOCl + NaOH \rightarrow NaOCl + NaOH + H_2O$. This equilibrium favors the formation of $OCl^–$ ions, which are more stable and effective as oxidizing agents.

Researchers used hypochlorite solution with NaOH to provide a stable, effective, and efficient treatment for the surface of plastic aggregate. Naik et al.[52] explored three treatment methods for HDPE aggregate: immersion in water, a 5% HOCl solution, and a combined 5% HOCl and 4% NaOH solution. Thorneycroft et al.[53] studied different PET aggregates, with one set treated using an NaOCl and NaOH solution and another set undergoing additional washing. For the initial treatment, the PET aggregate was immersed in the solution for 1 hour, then drained and thoroughly dried with heaters to retain the surface solution. Furthermore, Kaur and Pavia[39] examined two distinct chemical treatment approaches presented by previous studies. Various types of plastic, such as PC, ABS, POM, and PET, were used as fine aggregate replacements at levels ranging from 5 to 15%. The initial approach, as introduced by Naik et al.,[52] involved immersing plastic aggregate in a solution comprising 5% NaOCl and 4% NaOH for 6 days, followed by 12 hours of air-drying at room temperature. Post-treatment, the plastic aggregate was integrated into the mortar preparation process. The second treatment method, as employed by Thorneycroft et al.,[53] showed a slight variation. In this approach, the plastic aggregate was washed using a solution containing 5% NaOCl and 4% NaOH. This treatment enhances the compressive strength of concrete by improving the interaction between the plastic aggregate and the cementitious matrix. However, the effectiveness of the treatment is highly dependent on thorough post-treatment washing to remove residual chemicals. Without proper washing, the treated plastic can lead to the formation of voids in the concrete, negatively impacting its strength. It shows promise for enhancing the performance of concrete containing recycled plastic aggregate, provided that careful attention is given to the washing process.

Another method for oxidizing and treating the surface of plastic aggregate is to expose the plastic to ozone ($O_3$) using a UV lamp.[48] This process uses the strong oxidative properties of $O_3$ to modify the surface characteristics of plastic aggregate. $O_3$ is a powerful oxidant that can react with double bonds in reactive sites within saturated polymers, leading to the formation of polar functional groups.[68,69] The fundamental principle of UV-$O_3$ treatment involves a series of reactions. The process begins with the generation of ozone using UV light. Specifically, UV lamps that emit light at a wavelength of 185 nm are used. When this UV light interacts with oxygen molecules in the air, it splits them into individual oxygen atoms. These oxygen atoms then react with other oxygen molecules to form $O_3$. Once the ozone is formed, it is exposed to UV light with a different wavelength, specifically 254 nm. This wavelength causes the ozone to decompose into molecular oxygen and highly reactive oxygen species (such as atomic oxygen). These reactive oxygen species then interact with the surface of the plastic aggregate, leading to the formation of an oxide layer containing various oxygen-functional groups, such as carbonyl (C=O) and carboxyl (COOH) groups. The introduction of these polar functional groups on the surface increases the overall polarity of the plastic aggregate, enhancing its interaction with water and improving wettability. Furthermore, the formation of polar functional groups improves the adhesion properties of the plastic, which is particularly beneficial in composite materials where strong adhesion between different components is crucial for mechanical strength and durability.

## Silane treatment

Silane coupling agents are versatile chemicals that can be used to modify surfaces, particularly to enhance hydrophilicity. These agents typically feature two distinct functional groups: one that reacts with a specific matrix and another that interacts with the surface of a filler material.[48,70] The general structure of silane coupling agents is $X_3SiR$, where X represents a chlorine atom or an alkoxy group, and R is an organic functional group.[40,71,72] Upon exposure to moisture, the X group undergoes hydrolysis to form a silanol (Si-OH) group, which subsequently reacts with hydroxyl groups on the filler surface, leading to the formation of siloxane or hydrogen bonds. This reaction sequence results in the modification of the filler's surface properties, while the R group facilitates chemical bonding or compatibility with the matrix.

In practical applications, the surface modification of recycled plastic aggregate using silane coupling agents has shown significant benefits. For instance, Lee and Hong[48] enhanced the hydrophilicity of a waste composite film-based aggregate by treating it with (3-aminopropyl)triethoxysilane. This silane coupling agent is notable for its hydrophilic amine functional group, which, through hydrolysis and condensation, successfully introduces hydrophilic properties to the surface of the recycled plastic aggregate. By adjusting the treatment duration, the degree of functional group incorporation can be controlled, thereby tailoring the surface characteristics for specific applications. Silane coupling agents also improve the interfacial strength between recycled PVC particles and cementitious materials.[40] Following hydrolysis, the inorganic and organic functional groups of the silane agents cover the surface of the recycled PVC particles, strengthening the chemical bonds between the particles and the cement matrix, as shown in Fig. 3. This modification significantly improves the compressive properties of recycled PVC concrete and mortar. The enhanced hydrophilicity of treated plastic aggregate is particularly beneficial in contexts where improved water interaction is essential. In concrete mixtures, for example, hydrophilic aggregates can ensure better bonding with the cement matrix, leading to enhanced mechanical properties and durability.

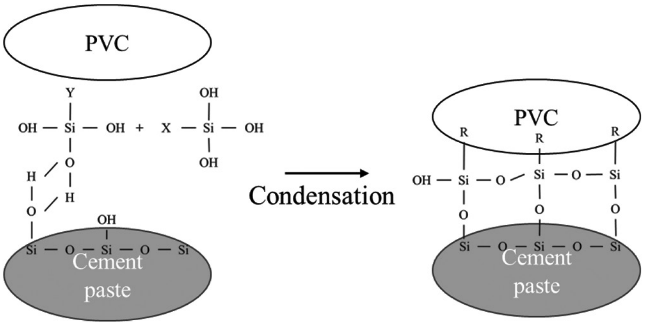

*Fig. 3—Reaction mechanism of silane coupling agent modification on PVC.*[40]

## Plasma treatment

Plasma treatment is a surface modification technique that enhances the properties of materials by introducing new functional groups without affecting their bulk characteristics.[48] This method uses ionized gas containing active species such as ions, radicals, electrons, and neutral particles. When a material is exposed to plasma, these species interact with the surface, leading to the formation of functional groups that improve wettability, adhesion, and compatibility with other materials. Atmospheric pressure plasma treatment, a specific type of plasma treatment performed at atmospheric pressure, is simpler and more cost-effective than vacuum plasma methods. It involves generating plasma using a combination of gases, typically oxygen ($O_2$) and argon (Ar), which are ionized by a power source. The reactive oxygen species generated in the plasma interact with the material's surface, forming new functional groups, such as hydroxyl (–OH) and carbonyl (–C=O) groups. This increases the surface energy and hydrophilicity of the material.

Atmospheric pressure plasma treatment is a highly efficient, versatile, and cost-effective technique for modifying the surface properties of various materials. It improves hydrophilicity and adhesion, making it suitable for applications that require better interaction with aqueous environments and stronger bonding in cement composite materials. This method's adaptability and efficiency are particularly valuable for industrial applications, such as the treatment of recycled plastic aggregate used in concrete mixtures. Lee and Hong[48] conducted studies on recycled plastic film-based aggregate that demonstrated the effectiveness of oxygen atmospheric pressure plasma treatment. The process involved injecting $O_2$ and Ar gases at flow rates of 15 and 4 sccm, respectively, with a radio frequency (RF) power of 100 W. The processing time varied from 0 to 30 seconds. The treatment significantly reduced the contact angle of the recycled plastic film-based aggregate, indicating improved hydrophilicity. The initial hydrophobic contact angle of approximately 108 degrees decreased to 44.0 degrees after plasma treatment, hence demonstrating the method's efficiency in enhancing surface properties.

### Radiation treatment

Radiation treatment is a method used to modify the properties of plastic through the application of ionizing or non-ionizing radiation. This treatment can alter the chemical structure and physical properties of materials, leading to improved performance in various applications. Different types of radiation treatments are discussed as follows, with each having unique mechanisms and effects on materials.

Gamma radiation treatment, a type of ionizing radiation, involves subjecting plastic aggregate to gamma rays. This process typically takes place in a radiation chamber or irradiation facility, where the plastic aggregate is exposed to a specified type and dose of radiation. Gamma radiation treatment eliminates the need for catalysts or additives to initiate chemical reactions. At lower radiation doses, polymer chains can undergo fragmentation, while higher doses prompt the formation of free radicals within these chains, leading to cross-linking. The interaction between ionizing radiation and the polymer structure of plastic aggregate induces a range of chemical and physical modifications at the molecular level. Martínez-Barrera et al.[41] documented substantial improvements in the mechanical properties of concrete incorporating PET aggregate subjected to gamma radiation at doses of 100 and 200 kGy, particularly at replacement levels ranging from 1 to 3% by weight. A significant transition is observed from a smooth surface in non-irradiated plastic aggregate to a textured surface with specific cavities and roughness at 100 kGy. At a higher dose of 200 kGy, the surface becomes even rougher, revealing detached particles and cracks. These morphological changes result from the cleavage of polymer chains within the plastic material, creating more contact points and a larger surface area on the plastic aggregate. These modified particles engage more effectively with the cement paste matrix, significantly enhancing the compressive strength of the concrete. However, despite the improvements in mechanical properties, handling gamma radiation poses significant challenges, including its inherent biological hazards, making this approach more complex and demanding.[73]

Microwave radiation treatment provides a safer alternative to gamma radiation. Microwave radiation interacts with materials through their dielectric permittivity, resulting in rapid heating. This occurs due to the interaction between microwave radiation and dielectric materials containing polar molecules, leading to dipole interactions and consequent heat generation.[42] Microwave radiation, part of the electromagnetic spectrum, has wavelengths ranging from 1 mm to 1 m and frequencies spanning 300 MHz to 300 GHz. Classified as non-ionizing radiation due to its limited penetration capability, microwave heating relies on the dielectric properties of plastic, allowing them to absorb and convert microwave energy into heat. Abu-Saleem et al.[42] explored the effects of microwave treatment on three types of recycled plastic aggregate—PET, HDPE, and PP—and their impact on the physical and mechanical properties, as well as the water absorption, of concrete. The study involved incorporating 15% PET and a combination of different recycled plastics (5% of each plastic) as partial replacements for coarse aggregate by volume. The results revealed intriguing insights into how microwave treatment alters the behavior of these plastic aggregates. For treated PET aggregate, a reduction in contact angle measurements indicated decreased hydrophobicity, thereby enhancing the surface wettability of the plastic. This increased wettability is crucial for improving the bond between the plastic aggregate and the cement matrix. In contrast, treated HDPE and PP aggregates exhibited increased contact angle values, suggesting that their surface wettability did not substantially improve. The microwave treatment caused micro-swelling on the surface of the PET aggregate, while HDPE and PP aggregates displayed a smoothing effect from the closing of microcracks. These surface modifications had a direct influence on the bond strength at the interfacial transition zone (ITZ), which positively impacted the mechanical properties of the concrete. Specifically, concrete incorporating treated PET aggregate demonstrated enhanced compressive, splitting tensile, and flexural strengths, as well as an improved modulus of elasticity, compared to concrete using untreated PET aggregate.[42] These findings underscore the multifaceted impact of microwave radiation treatment on recycled plastic aggregate and its potential benefits when incorporated into concrete, highlighting the importance of surface modification techniques in improving the performance of plastic aggregate cement-based materials.

## PERFORMANCE OF TREATED PLASTIC AGGREGATE IN CEMENT-BASED MATERIALS

### Wettability of treated plastic aggregate

After surface treatment, the contact angle of water droplets on treated plastic surfaces decreased, as shown in Table 2. Various surface modification methods, including UV-$O_3$ treatment, silane coupling agents, plasma, and acrylic binder coating, can change the contact angles of recycled plastic aggregate.[48] Among these, the plasma treatment was shown to be the most effective, reducing the contact angle to as low as 44.0 degrees within 30 seconds, indicating a significant increase in hydrophilicity. Moreover, different coating agents applied to treated plastic aggregate showed varying effects on surface wettability.[51] Certain coating agents were particularly effective in making the surface hydrophilic by reducing the contact angle to 61.3 degrees. It also highlights that PP plastic is naturally hydrophobic, but the use of surfactants can enhance its surface energy, thereby improving adhesion between PP and cementitious materials by making the surface more hydrophilic.[49] Microwave treatment had a significant impact on the surface modification of the PET aggregate, making it more hydrophilic.[42] The contact angle of water droplets on the surface of PET, HDPE, and PP before and

**Table 2—Contact angle of water droplets on treated plastic surfaces**

| Treatment method | Before treatment | After treatment |
|---|---|---|
| UV-ozone[48] | 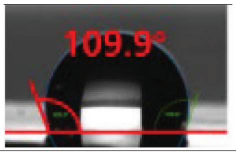 |  |
| Silane treatment[48] | 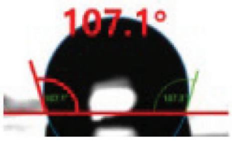 | 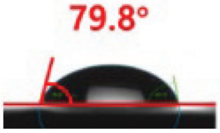 |
| Plasma treatment[48] | 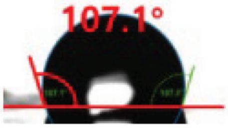 |  |
| Coating with acrylic binder[48] | 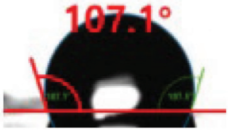 |  |
| Coating with resin[51] |  | 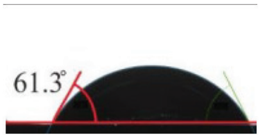 |
| Coating with surfactant[49] | 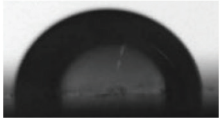 | 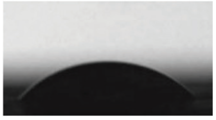 |
| Microwave treatment[42] | 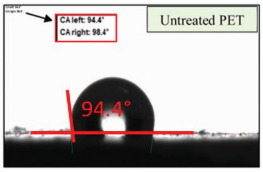 <br>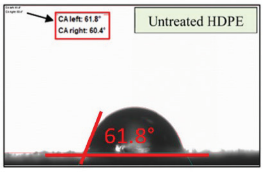 <br>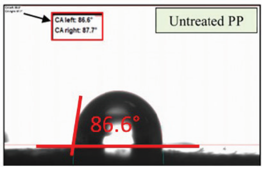 | 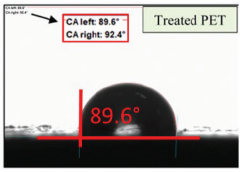 <br>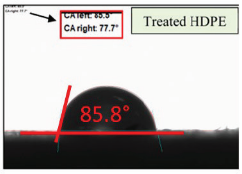 <br>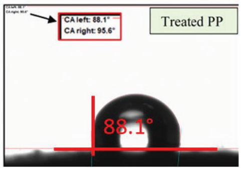 |

after treatment was investigated. The PET's contact angle decreased by 5.9%, indicating improved wettability, while HDPE and PP showed an increase in contact angles, indicating increased hydrophobicity.

In addition to changes in wettability, surface treatments significantly alter the physical properties of plastic aggregates. For instance, oxidation, plasma, and UV-$O_3$ treatments increase the surface roughness by introducing micropits or etching marks, while some coatings can smooth the surface. These modifications influence the mechanical interlocking between aggregate and cement paste. Moreover, certain treatments, such as silane coupling agents or surfactant coatings, enhance the surface energy of plastics, promoting chemical bonding with the cement hydrates. In some cases, thermal or microwave treatment can also change surface porosity by inducing microcracks or melting, thereby affecting water transport and interface compatibility.

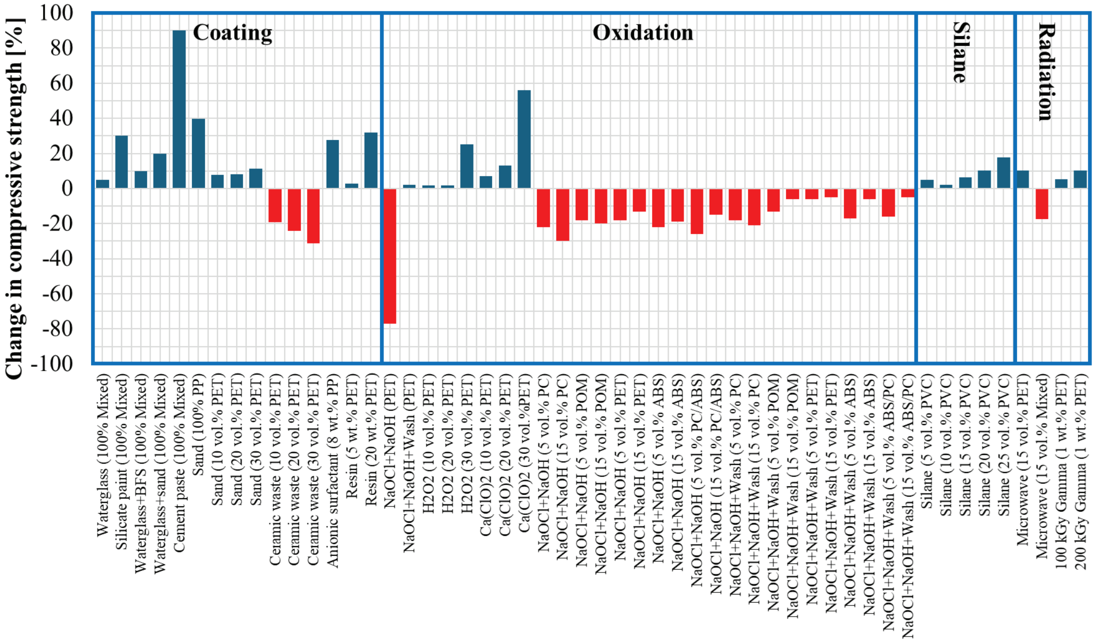

*Fig. 4—Change in compressive strength of cement-based materials made with treated plastic aggregate compared to untreated plastic aggregate.*

These changes collectively contribute to improved adhesion and overall performance of cementitious composites.

## Fresh properties of cement-based materials made with treated plastic aggregate

The difference in fresh density between cement-based materials using untreated and treated plastic aggregates is negligible.[36,39,42,46,74] Although chemical surface treatments such as oxidation, silane, and radiation can alter the chemical polymeric chains on the plastic surface and potentially reduce the density of the plastic aggregate, the overall effect on the density of the cement-based materials remains minimal. This is because the treated surface area of the plastic aggregate is relatively small compared to the total replacement ratio of natural aggregate. Additionally, the density of cement-based materials incorporating surface-coated plastic aggregate can vary depending on the type of coating materials used. However, these changes in density are typically too minor to significantly impact the overall density, especially when compared to the more substantial effect of increasing the proportion of plastic aggregate in the cement-based materials.

The workability of cement-based materials made with plastic aggregate, measured by slump or slump flow tests, is primarily influenced by the surface texture and shape of the plastic aggregate used. A smooth surface generally enhances the workability of plastic aggregate, regardless of the treatment method. However, certain surface treatment methods, such as oxidation and radiation, can roughen the surface texture of plastic aggregate, leading to decreased workability compared to untreated aggregate.[36,38,39,42,46,47,74] Additionally, the shape of the plastic aggregate affects the workability due to the interlocking action between the plastic and natural aggregates. Assuming the shape and texture of the plastic aggregate remain constant, surface-treated plastic aggregate can improve workability compared to untreated plastic aggregate. This improvement is also attributed to increased surface energy after treatment, which facilitates better wetting of the aggregates and reduces interparticle friction in the fresh state. Hydrophilic surfaces enhance lubrication within the mixture, leading to better flowability.

## Hardened properties of cement-based materials made with treated plastic aggregate

Figures 4 to 6 summarize the change ratio after surface treatment of compressive, flexural, and splitting tensile strengths of cement-based materials, respectively.[37-42,46,47,49,50,53] The mechanical performance varied significantly depending on the surface treatment method and the type of plastic aggregate used.

Coating, silane, and radiation treatment methods generally improved the mechanical properties of cement-based materials made with treated plastic aggregate. For example, water glass coating improved compressive strength by approximately 78% and sand coating by 40%, while resin coating showed a moderate enhancement (~10%), as seen in Fig. 4. However, plastic aggregate coated with ceramic waste showed a ~20 to 30% decrease in compressive and flexural strengths compared to those made with untreated plastic aggregate.[47] This reduction is likely due to the hydrophobic nature of the ceramic waste coating, which hindered proper bonding between the aggregate and the cement paste. Moreover, the modification of the surface of plastic aggregate with a water glass solution was generally ineffective and caused a ~30% decrease in flexural strength compared to the reference composite.[37] Additionally, cement-based materials made with microwave-treated plastic aggregate that included a mixture of different plastic types (PET, HDPE, and PP) had lower compressive, flexural, and splitting tensile strengths than those made with untreated plastic aggregate.[42] In the

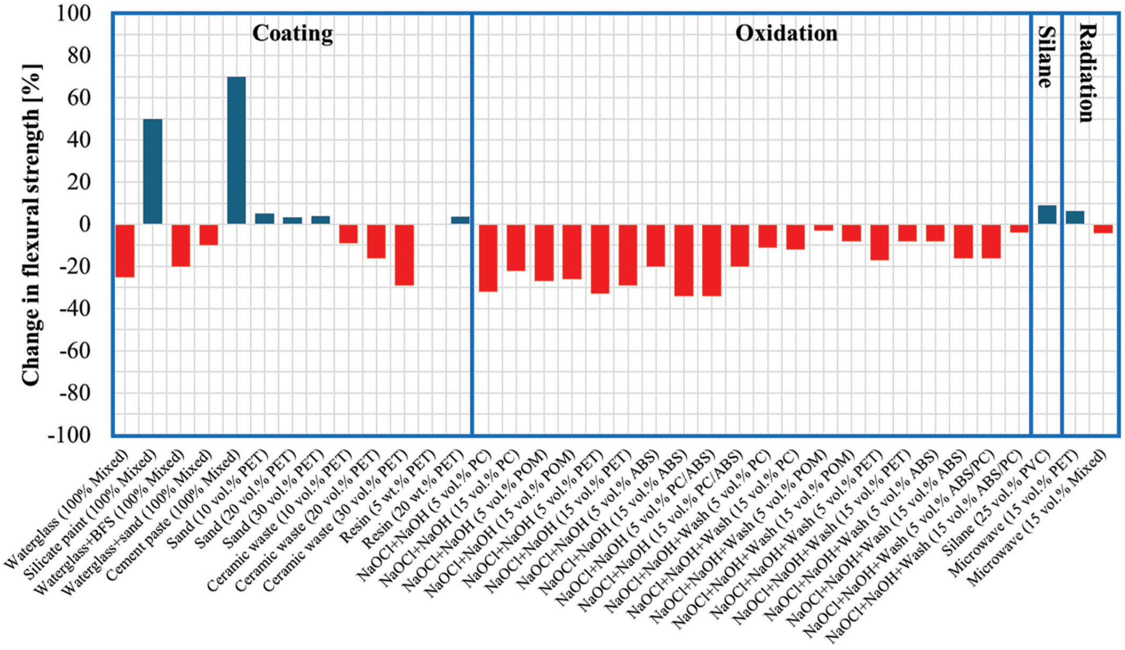

*Fig. 5—Change in flexural strength of cement-based materials made with treated plastic aggregate compared to untreated plastic aggregate.*

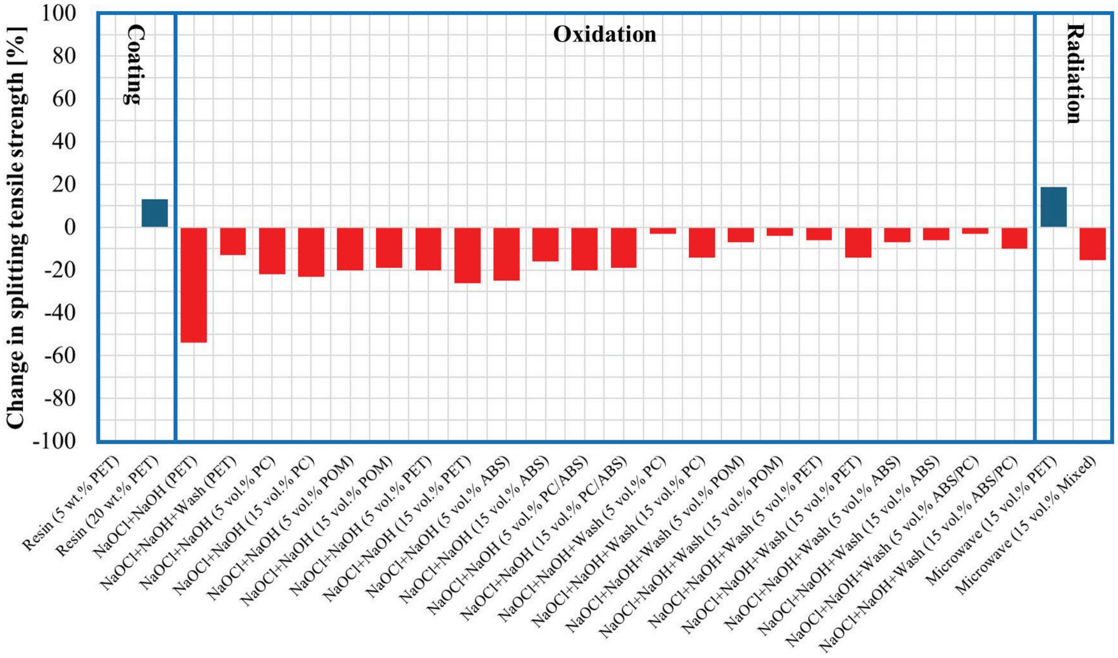

*Fig. 6—Change in splitting tensile strength of cement-based materials made with treated plastic aggregate compared to untreated plastic aggregate.*

case of mixed plastic concrete, the treatment of HDPE and PP increased the contact angle and smoothness of the plastic surface, as observed in scanning electron microscope (SEM) images, leading to poorer adhesion between the aggregate and the cement paste. This decline in performance may be attributed to the nonhomogeneous physical characteristics of the mixed plastic types within the concrete, which negatively affected the overall bonding and strength of the material.

While the use of coating, silane, and radiation treatment methods generally enhanced the compressive strength of cement-based materials made with treated plastic aggregate, oxidation treatment yielded different results. Specifically, using NaOH for the chemical stabilization of hypochlorous acid solution in modifying the surface of plastic aggregate contributed to a reduction of up to 60% in the compressive, flexural, and splitting tensile strengths of cement-based materials, even after a washing process was applied.[39,53] The aggressive nature of oxidation treatment, particularly with NaOH solution, can excessively alter the surface of the plastic aggregate, leading to degradation that negatively impacts strength. However, when $H_2O_2$ or $Ca(ClO)_2$ solutions were used without NaOH solution, the treated plastic aggregate exhibited improved compressive strength of ~10 to 30%, depending on the plastic type.[38] These oxidation treatments, without the addition of NaOH solution, were less harsh on the plastic aggregate surface, leading to improved bonding with the cement matrix and better overall material performance. These results emphasize that not only the chemical reactivity of surface treatments but also their effect on surface roughness, porosity, and surface energy directly impact ITZ development, which is a key determinant of the hardened mechanical performance.

### Water absorption and durability of cement-based materials made with treated plastic aggregate

Among various durability-related parameters, water absorption is often used as an indirect indicator of a material's permeability and resistance to fluid ingress. As shown in prior studies, the incorporation of surface-treated plastic aggregates has been associated with a reduction in water absorption of cement-based materials.[42,49] This reduction is primarily attributed to improvements in the interfacial bond between the treated plastic and the cement matrix, as well as modifications in surface characteristics such as wettability, roughness, and energy.

For instance, microwave treatment of PET aggregates led to a 5.4% reduction in water absorption, likely due to enhanced hydrophilicity and interfacial adhesion.[42] Similarly, oxidation and plasma treatments have been reported to increase surface roughness and energy, thereby reducing voids at the paste-aggregate interface and promoting better moisture resistance. In contrast, the treatment of HDPE and PP aggregates showed negligible effects on water absorption, largely due to thermal coalescence during treatment, which limited reductions in entrapped air. Nevertheless, when PET was present in the mixture, its hydrophilic nature partially compensated for the hydrophobicity of HDPE and PP, resulting in stabilized absorption levels. In the case of surfactant-coated PP, the 17% reduction in internal voids translated to a 25% decrease in overall water absorption.[49] These findings suggest that surface modification strategies that enhance roughness, surface energy, and reduce porosity may improve the moisture resistance of concrete composites.

While the influence on water absorption is noteworthy, it represents only one facet of durability. Other critical indicators, such as freezing-and-thawing resistance, drying shrinkage, creep, alkali-silica reaction (ASR), and sulfate attack, have received limited attention in the context of treated plastic aggregates. Improvements in the ITZ due to increased surface energy and adhesion may offer potential benefits for freezing-and-thawing resistance and sulfate durability; however, comprehensive experimental data remain scarce. Similarly, the effect of surface treatments on shrinkage and creep behavior is not well understood and may vary depending on the plastic type and treatment method. Because most plastic aggregates are nonreactive, they are unlikely to participate in ASR, although their influence on internal moisture transport could indirectly affect its kinetics.

In summary, while current research has primarily focused on water absorption, a more holistic evaluation encompassing a broader range of durability metrics is necessary to determine the long-term performance of treated plastic aggregates in structural concrete applications.

## PRACTICAL CHALLENGES AND FUTURE RESEARCH DIRECTIONS

Despite the promising results associated with various surface treatment techniques for plastic aggregates, the practicality of implementing these methods at commercial or infrastructure scale remains a significant concern. While improvements in interfacial bonding, mechanical strength, and durability have been demonstrated at the laboratory scale, several treatments present clear limitations in terms of cost-effectiveness, operational complexity, and scalability.

Among the widely studied methods, plasma treatment and UV-$O_3$ oxidation have shown excellent efficacy in enhancing surface wettability and energy. However, these approaches typically require specialized equipment, controlled environments, and high energy input, making them difficult to scale for large-volume processing of plastic waste. The short treatment durations reported in laboratory studies do not account for the logistical demands of handling and reintegrating treated aggregates into full-scale concrete production. Chemical approaches such as silane coupling agents and surfactant coatings are also effective in improving chemical compatibility with cementitious matrixes. Nevertheless, the cost of reagents, the need for solvent-based processes, and limited long-term stability under harsh environmental conditions constrain their practical use. Additionally, the disposal of chemical waste and safety concerns further limit field applicability. Thermal-based methods, such as microwave irradiation, offer a more straightforward process but can result in nonuniform treatment or even partial melting, particularly in mixed plastic streams, leading to inconsistent concrete performance. Wet chemical oxidation using agents such as NaOH or $Ca(ClO)_2$ can be more amenable to batch-scale processing; however, their corrosive nature and associated safety risks necessitate careful infrastructure and environmental controls.

Given these constraints, the selection of treatment methods for practical application must be guided by a holistic cost-benefit framework that considers not only the improvements in material performance but also the environmental impact, energy demand, worker safety, and integration feasibility within existing production systems. In this context, the development of low-cost, scalable, and environmentally benign treatment technologies, such as bio-based coatings or simple mechanical surface roughening, represents a promising research direction. In addition, emerging approaches such as enzymatic treatments and nanomaterial-based surface functionalization have theoretical advantages in terms of reaction selectivity, environmental benignity, and advanced surface engineering. However, to date, no peer-reviewed studies have reported the application of these techniques to plastic aggregates for cement-based materials. These methods remain an open area for future investigation and may offer innovative solutions to current limitations.

Beyond these practical challenges, several other areas merit further investigation. While most studies have focused on short-term mechanical improvements, long-term durability under multifactorial environmental exposures remains underexplored. The behavior of treated plastic aggregates in concrete exposed to freezing-and-thawing cycles, sulfate attack, carbonation, or chloride ingress is not yet well understood. These conditions are particularly critical for real-world infrastructure applications and should be addressed through long-term aging studies and accelerated durability testing. Furthermore, there is a need for standardized methodologies to evaluate the effectiveness of surface treatments across various plastic types. Establishing consistent protocols for contact angle measurement, interfacial bond strength, and durability performance will enhance the reliability and comparability of research outcomes. Environmental and economic sustainability should also be assessed through life-cycle analysis (LCA) and environmental impact studies. The true value of any surface treatment method must be supported by quantitative data on energy input, emissions, chemical use, and end-of-life recyclability. Finally, the transition from laboratory-scale experimentation to real-world implementation requires pilot studies and field trials. Demonstrating the feasibility of these treatments in ready mixed plants or precast facilities, alongside detailed techno-economic evaluations, will be essential for moving from research to practice.

In summary, while surface treatment of plastic aggregates shows significant promise for improving the performance of cement-based materials, its advancement will depend on resolving current limitations and aligning research efforts with the practical demands of large-scale, sustainable construction.

## SUMMARY AND CONCLUSIONS

The incorporation of these recycled plastics into concrete not only provides an alternative use for plastic waste but also offers several environmental benefits. The comprehensive review explored various surface treatment methods for plastic aggregate to improve their performance in cement-based materials. These methods include surface coating, oxidation treatment, silane treatment, plasma treatment, and radiation treatment. All these methods aim to modify the hydrophobic nature of plastic aggregate to enhance its hydrophilicity and improve bonding with the cement matrix. Surface coating methods, such as using blast-furnace slag, water glass, and synthetic resins, showed varying degrees of success in improving the surface characteristics of plastic aggregate. Generally, these coatings enhanced the mechanical properties of the concrete, although some coatings, such as ceramic waste, negatively impacted performance due to their inherent hydrophobic nature. Oxidation treatments using agents such as hypochlorite, hydrogen peroxide, and ozone successfully increased the hydrophilicity of the plastic aggregate. However, the use of NaOH solution in combination with hypochlorite led to excessive degradation of the plastic surface, which in turn reduced the mechanical strength of the cement-based materials. Treatments without NaOH, such as those using hydrogen peroxide or calcium hypochlorite, proved more effective and less damaging. Silane coupling agents were found to be effective in modifying the surface of plastic aggregate, particularly in improving the bonding between recycled plastic particles and the cementitious matrix. This method was especially beneficial for enhancing hydrophilicity, leading to better mechanical performance in concrete incorporating treated plastic aggregate. Plasma treatment was effective in significantly reducing the contact angle of plastic aggregate, thus increasing its hydrophilicity. This method showed considerable promise for industrial applications due to its efficiency in enhancing the surface properties of recycled plastic aggregate. Radiation treatments, including both gamma and microwave radiation, demonstrated potential to improve the mechanical properties of cement-based materials incorporating plastic aggregate. Gamma radiation was particularly effective at higher doses, although it presented challenges related to biological hazards. Microwave treatment can offer a safer alternative, especially for polyethylene terephthalate (PET) aggregate, leading to improved mechanical properties and reduced water absorption.

In conclusion, the study highlights the critical role of surface treatment in enhancing the performance of plastic aggregate in cement-based materials. While each treatment method has its own advantages and limitations, the choice of an appropriate method depends on the specific type of plastic aggregate and the desired properties of the final concrete product. Further research and innovation in surface treatment techniques are essential to advancing the sustainable use of recycled plastics in construction, contributing both to environmental protection and material durability.

## AUTHOR BIOS

**Seongho Han** *is an Assistant Research Professor at Missouri University of Science and Technology (Missouri S&T), Rolla, MO. He received his PhD from Korea Advanced Institute of Science and Technology, Daejeon, South Korea. His research interests include carbon use for cement-based materials, rheology of cement-based materials, sustainable construction materials, and three-dimensional (3-D) printing of concrete.*

**Nima Mahmoudzadeh Vaziri** *is a Graduate Student in civil engineering at Missouri S&T.*

**Kamal H. Khayat**, *FACI, is a Professor of civil engineering at Missouri S&T. He is past Chair, past Secretary, and a current member of ACI Committee 237, Self-Consolidating Concrete, and a member of ACI Committees 234, Silica Fume in Concrete; 236, Material Science of Concrete; 238, Workability of Fresh Concrete; and 552, Cementitious Grouting. His research interests include rheology of cement-based materials, and self-consolidating, high-performance, and ultra-high-performance concrete.*

## ACKNOWLEDGMENTS

This research was supported by the Center for Infrastructure Engineering Studies (CIES), for which deep gratitude is expressed.

## REFERENCES

1. Xu, T.; Lv, Q.; Sheng, G.; Zhang, Y.; Liu, Y.; and Shi, L., "Evolving Patterns and Drivers of Waste Plastic Trade in Key Global Economies," *Resources, Conservation and Recycling*, V. 206, July 2024, Article No. 107606. doi: 10.1016/j.resconrec.2024.107606

2. Singh, A. P.; Devi, A. S.; and Sahoo, U. K., "Quantifying Plastic Waste Generation in Aizawl City, India: Waste Management and Its Impact on Human and Environmental Health," *Environmental Science and Pollution Research*, V. 30, No. 49, Oct. 2023, 107390-107402. doi: 10.1007/s11356-023-27513-0

3. Faraca, G., and Astrup, T., "Plastic Waste from Recycling Centres: Characterisation and Evaluation of Plastic Recyclability," *Waste Management*, V. 95, July 2019, pp. 388-398. doi: 10.1016/j.wasman.2019.06.038

4. Han, S. H.; Khayat, K. H.; Park, S.; and Yoon, J., "Machine Learning-Based Approach for Optimizing Mixture Proportion of Recycled Plastic Aggregate Concrete Considering Compressive Strength, Dry Density, and Production Cost," *Journal of Building Engineering*, V. 83, Apr. 2024, Article No. 108393. doi: 10.1016/j.jobe.2023.108393

5. The World Bank, "What a Waste 2.0: A Global Snapshot of Solid Waste Management to 2050: Trends in Solid Waste Management," World Bank Group, Washington, DC, https://datatopics.worldbank.org/what-a-waste/trends_in_solid_waste_management.html. (last accessed Feb. 13, 2026)

6. Vivekanand, A. C.; Mohapatra, S.; and Tyagi, V. K., "Microplastics in Aquatic Environment: Challenges and Perspectives," *Chemosphere*, V. 282, Nov. 2021, Article No. 131151. doi: 10.1016/j.chemosphere.2021.131151

7. Chen, H. L.; Nath, T. K.; Chong, S.; Foo, V.; Gibbins, C.; and Lechner, A. M., "The Plastic Waste Problem in Malaysia: Management, Recycling and Disposal of Local and Global Plastic Waste," *SN Applied Sciences*, V. 3, No. 4, Apr. 2021, Article No. 437. doi: 10.1007/s42452-021-04234-y

8. OECD, "Plastic Pollution Is Growing Relentlessly as Waste Management and Recycling Fall Short, Says OECD," Organisation for Economic Co-operation and Development, Paris, France, Feb. 22, 2022, https://www.oecd.org/en/about/news/press-releases/2022/02/plastic-pollution-is-growing-relentlessly-as-waste-management-and-recycling-fall-short.html. (last accessed Feb. 13, 2026)

9. Canopoli, L.; Fidalgo, B.; Coulon, F.; and Wagland, S. T., "Physico-Chemical Properties of Excavated Plastic from Landfill Mining and Current Recycling Routes," *Waste Management*, V. 76, June 2018, pp. 55-67. doi: 10.1016/j.wasman.2018.03.043

10. Kibria, M. G.; Masuk, N. I.; Safayet, R.; Nguyen, H. Q.; and Mourshed, M., "Plastic Waste: Challenges and Opportunities to Mitigate Pollution and Effective Management," *International Journal of Environmental Research*, V. 17, No. 1, Feb. 2023, Article No. 20. doi: 10.1007/s41742-023-00507-z

11. Al-Salem, S. M.; Lettieri, P.; and Baeyens, J., "Recycling and Recovery Routes of Plastic Solid Waste (PSW): A Review," *Waste Management*, V. 29, No. 10, Oct. 2009, pp. 2625-2643. doi: 10.1016/j.wasman.2009.06.004

12. Merrington, A., "Recycling of Plastics," *Applied Plastics Engineering Handbook: Processing, Sustainability, Materials, and Applications*, third edition, M. Kutz, ed., William Andrew, Oxford, UK, 2023, pp. 191-217.

13. Geyer, R.; Jambeck, J. R.; and Law, K. L., "Production, Use, and Fate of All Plastics Ever Made," *Science Advances*, V. 3, No. 7, July 2017, Article No. e1700782. doi: 10.1126/sciadv.1700782

14. Stina, "2019 Plastic Recycling Data," Stina Inc., Sonoma, CA, https://circularityinaction.com/2019PlasticRecyclingData. (last accessed Feb. 13, 2026)

15. Lebreton, L.; Egger, M.; and Slat, B., "A Global Mass Budget for Positively Buoyant Macroplastic Debris in the Ocean," *Scientific Reports*, V. 9, No. 1, 2019, Article No. 12922. doi: 10.1038/s41598-019-49413-5

16. Hopewell, J.; Dvorak, R.; and Kosior, E., "Plastics Recycling: Challenges and Opportunities," *Philosophical Transactions of the Royal Society B: Biological Sciences*, V. 364, No. 1526, July 2009, pp. 2115-2126. doi: 10.1098/rstb.2008.0311

17. Li, H.; Aguirre-Villegas, H. A.; Allen, R. D.; Bai, X.; Benson, C. H.; Beckham, G. T.; Bradshaw, S. L.; Brown, J. L.; Brown, R. C.; Cecon, V. S.; Curley, J. B.; Curtzwiler, G. W.; Dong, S.; Gaddameedi, S.; García, J. E.; Hermans, I.; Kim, M. S.; Ma, J.; Mark, L. O.; Mavrikakis, M.; Olafasakin, O. O.; Osswald, T. A.; Papanikolaou, K. G.; Radhakrishnan, H.; Sanchez Castillo, M. A.; Sánchez-Rivera, K. L.; Tumu, K. N.; Van Lehn, R. C.; Vorst, K. L.; Wright, M. M.; Wu, J.; Zavala, V. M.; Zhou, P.; and Huber, G. W., "Expanding Plastics Recycling Technologies: Chemical Aspects, Technology Status and Challenges," *Green Chemistry*, V. 24, No. 23, Dec. 2022, pp. 8899-9002. doi: 10.1039/D2GC02588D

18. Alsalami, Z. H. A.; Harith, I. K.; and Dhahir, M. K., "Utilization of Dates Palm Kernel in High Performance Concrete," *Journal of Building Engineering*, V. 20, Nov. 2018, pp. 166-172. doi: 10.1016/j.jobe.2018.07.015

19. Alsalami, Z. H. A., "Study the Effect of Partially Replacement Sand by Waste Pistachio Shells in Cement Mortar," *Applied Adhesion Science*, V. 5, No. 1, Dec. 2017, Article No. 19. doi: 10.1186/s40563-017-0099-3

20. Marshdi, Q. S. R.; Al-Sallami, Z. H. A.; and Zaichenko, N. M., "Effect of Multicomponent Modifier on the Properties of Cement Pastes Formulated from Self-Compacting Concrete," *Magazine of Civil Engineering*, V. 98, No. 6, Oct. 2020, Article No. 9805.

21. Alsalami, Z. H. A., "Curing High-Performance Green Concrete Under Hot Weather," *Iranian Journal of Science and Technology, Transactions of Civil Engineering*, V. 46, No. 1, Feb. 2022, pp. 91-99. doi: 10.1007/s40996-021-00758-w

22. Guo, Y.-C.; Li, X.-M.; Zhang, J.; and Lin, J.-X., "A Review on the Influence of Recycled Plastic Aggregate on the Engineering Properties of Concrete," *Journal of Building Engineering*, V. 79, Nov. 2023, Article No. 107787. doi: 10.1016/j.jobe.2023.107787

23. Hamada, H. M.; Al-Attar, A.; Abed, F.; Beddu, S.; Humada, A. M.; Majdi, A.; Yousif, S. T.; and Thomas, B. S., "Enhancing Sustainability in Concrete Construction: A Comprehensive Review of Plastic Waste as an Aggregate Material," *Sustainable Materials and Technologies*, V. 40, July 2024, Article No. e00877. doi: 10.1016/j.susmat.2024.e00877

24. Mulyadi, A.; Asrullah, A.; Anggrainy, R.; Irawan, I.; and Rizal, C., "Characteristics the Marshall Test Subsitutution of Polypropylene Plastic Pellets as Filler in Mixture Asphalt Concrete Binder Course (AC BC)," *International Journal of Islamic Education, Research and Multiculturalism*, V. 5, No. 2, 2023, pp. 356-375. doi: 10.47006/ijierm.v5i2.234

25. Bayiha, B. N.; Kenmogne, F.; Bahel, B.; A'Paglan Bidime, É. Y.; Bell, E. Y.; and Billong, N., "Development and Characterization of a Composite Material with Geopolymer Matrix Obtained by Incorporation of Microparticles from Plastic Bottles," *Heliyon*, V. 10, No. 10, May 2024, Article No. e30801. doi: 10.1016/j.heliyon.2024.e30801

26. Borg, R. P.; Baldacchino, O.; and Ferrara, L., "Early Age Performance and Mechanical Characteristics of Recycled PET Fibre Reinforced Concrete," *Construction and Building Materials*, V. 108, Apr. 2016, pp. 29-47. doi: 10.1016/j.conbuildmat.2016.01.029

27. Duan, Z.; Deng, Q.; Liang, C.; Ma, Z.; and Wu, H., "Upcycling of Recycled Plastic Fiber for Sustainable Cementitious Composites: A Critical Review and New Perspective," *Cement and Concrete Composites*, V. 142, Sept. 2023, Article No. 105192. doi: 10.1016/j.cemconcomp.2023.105192

28. Almeshal, I.; Tayeh, B. A.; Alyousef, R.; Alabduljabbar, H.; Mohamed, A. M.; and Alaskar, A., "Use of Recycled Plastic as Fine Aggregate in Cementitious Composites: A Review," *Construction and Building Materials*, V. 253, Aug. 2020, Article No. 119146. doi: 10.1016/j.conbuildmat.2020.119146

29. Alyousef, R.; Ahmad, W.; Ahmad, A.; Aslam, F.; Joyklad, P.; and Alabduljabbar, H., "Potential Use of Recycled Plastic and Rubber Aggregate in Cementitious Materials for Sustainable Construction: A Review," *Journal of Cleaner Production*, V. 329, Dec. 2021, Article No. 129736. doi: 10.1016/j.jclepro.2021.129736

30. Alqahtani, F. K.; Sherif, M. A.; and Ghanem, A. M., "Green Lightweight Concrete Utilizing Sustainable Processed Recycled Plastic Aggregates: Technical, Economic and Environmental Assessment," *Construction and Building Materials*, V. 393, Aug. 2023, Article No. 132027. doi: 10.1016/j.conbuildmat.2023.132027

31. Ogundairo, T. O.; Olukanni, D. O.; Akinwumi, I. I.; and Adegoke, D. D., "A Review on Plastic Waste as Sustainable Resource in Civil Engineering Applications," *IOP Conference Series. Materials Science and Engineering*, V. 1036, No. 1, 2021, Article No. 012019. doi: 10.1088/1757-899X/1036/1/012019

32. Nyika, J., and Dinka, M., "Recycling Plastic Waste Materials for Building and Construction Materials: A Minireview," *Materials Today: Proceedings*, V. 62, Part 6, 2022, pp. 3257-3262. doi: 10.1016/j.matpr.2022.04.226

33. Lamba, P.; Kaur, D. P.; Raj, S.; and Sorout, J., "Recycling/Reuse of Plastic Waste as Construction Material for Sustainable Development: A Review," *Environmental Science and Pollution Research*, V. 29, No. 57, Dec. 2022, pp. 86156-86179. doi: 10.1007/s11356-021-16980-y

34. Li, X.; Ling, T.-C.; and Mo, K. H., "Functions and Impacts of Plastic/Rubber Wastes as Eco-Friendly Aggregate in Concrete – A Review," *Construction and Building Materials*, V. 240, Apr. 2020, Article No. 117869. doi: 10.1016/j.conbuildmat.2019.117869

35. Barnat-Hunek, D.; Szafraniec, M.; and Pavlík, Z., "The Hydrophobization of High Strength Concretes with Plastic Waste," *AIP Conference Proceedings*, V. 2305, No. 1, Nov. 2020, Article No. 020001. doi: 10.1063/5.0034027

36. Choi, Y.-W.; Moon, D.-J.; Chung, J.-S.; and Cho, S.-K., "Effects of Waste PET Bottles Aggregate on the Properties of Concrete," *Cement and Concrete Research*, V. 35, No. 4, Apr. 2005, pp. 776-781. doi: 10.1016/j.cemconres.2004.05.014

37. Bágeľ, Ľ., and Matiašovský, P., "Surface Pretreatment – A Way to Effective Utilization of Waste Plastics as Concrete Aggregate. Review and First Experiences," *Proceedings of CESB10 Prague - Central Europe towards Sustainable Building: From Theory to Practice*, P. Hájek, J. Tywoniak, A. Lupíšek, J. Růžička, and K. Sojková, eds., Prague, Czech Republic, 2010, 10 pp.

38. Lee, Z. H.; Paul, S. C.; Kong, S. Y.; Susilawati, S.; and Yang, X., "Modification of Waste Aggregate PET for Improving the Concrete Properties," *Advances in Civil Engineering*, V. 2019, No. 1, 2019, Article No. 6942052.

39. Kaur, G., and Pavia, S., "Chemically Treated Plastic Aggregates for Eco-Friendly Cement Mortars," *Journal of Material Cycles and Waste Management*, V. 23, No. 4, July 2021, pp. 1531-1543. doi: 10.1007/s10163-021-01235-2

40. Pan, Z.; Chen, J.; Zhan, Q.; Wang, S.; Jin, R.; Shamass, R.; and Rossi, F., "Mechanical Properties of PVC Concrete and Mortar Modified with Silane Coupling Agents," *Construction and Building Materials*, V. 348, Sept. 2022, Article No. 128574. doi: 10.1016/j.conbuildmat.2022.128574

41. Martínez-Barrera, G.; Martínez-López, M.; del Coz-Díaz, J. J.; López-Gayarre, F.; and Varela-Guerrero, V., "Waste Polymers and Gamma Radiation on the Mechanical Improvement of Polymer Mortars: Experimental and Calculated Results," *Case Studies in Construction Materials*, V. 11, Dec. 2019, Article No. e00273. doi: 10.1016/j.cscm.2019.e00273

42. Abu-Saleem, M.; Zhuge, Y.; Hassanli, R.; Ellis, M.; Rahman, M. M.; and Levett, P., "Microwave Radiation Treatment to Improve the Strength of Recycled Plastic Aggregate Concrete," *Case Studies in Construction Materials*, V. 15, Dec. 2021, Article No. e00728. doi: 10.1016/j.cscm.2021.e00728

43. Lu, Z.; Yin, R.; Yao, J.; and Leung, C. K. Y., "Surface Modification of Polyethylene Fiber by Ozonation and Its Influence on the Mechanical Properties of Strain-Hardening Cementitious Composites," *Composites Part B: Engineering*, V. 177, Nov. 2019, Article No. 107446. doi: 10.1016/j.compositesb.2019.107446

44. Signorini, C., and Volpini, V., "Mechanical Performance of Fiber Reinforced Cement Composites Including Fully-Recycled Plastic Fibers," *Fibers*, V. 9, No. 3, Mar. 2021, Article No. 16. doi: 10.3390/fib9030016

45. Farzadnia, N., and Khayat, K. H., "Modification of Nanomaterials for Nanostructured Cement-Based Materials," *Nanotechnology for Civil Infrastructure: Innovation and Eco-efficiency of Nanostructured Cement-Based Materials*, K. H. Khayat and W. Meng, eds., Elsevier, Amsterdam, the Netherlands, 2023, pp. 5-37.

46. Purnomo, H.; Pamudji, G.; and Satim, M., "Influence of Uncoated and Coated Plastic Waste Coarse Aggregates to Concrete Compressive Strength," *MATEC Web of Conferences*, V. 101, 2017, Article No. 01016.

47. Ramakrishnan, A., and Jegan, J., "Surface Modified Synthetic Plastic Aggregate for Concrete – Experimental and Analytical Studies," *Materials Science (Medžiagotyra)*, V. 29, No. 1, 2023, pp. 104-110. doi: 10.5755/j02.ms.31124

48. Lee, J. U., and Hong, J.-Y., "Comparison of Surface Modification Methods for Improving the Compatibility of Recycled Plastic Film-Based Aggregates," *Polymers*, V. 13, No. 22, Nov. 2021, Article No. 3956. doi: 10.3390/polym13223956

49. Correa, P. M.; Santana, R. M. C.; Guimarães, D.; and Graeff, A. G., "Post-Consumer PP as Partial Substitute of Sand: Effect of Surface Treatment PP with Surfactant on Concrete Properties," *Composite Interfaces*, V. 27, No. 9, 2020, pp. 815-828. doi: 10.1080/09276440.2019.1702858

50. El-Nadoury, W. W., "Chemically Treated Plastic Replacing Fine Aggregate in Structural Concrete," *Frontiers in Materials*, V. 9, July 2022, Article No. 948117. doi: 10.3389/fmats.2022.948117

51. Kim, K.-M., and Cho, Y.-K., "Effect of Surface Hydrophilized Plastic Waste Aggregates Made by Mixing Various Kinds of Plastic on Mechanical Properties of Mortar," *Materials*, V. 17, No. 1, Jan. 2024, Article No. 247. doi: 10.3390/ma17010247

52. Naik, T. R.; Singh, S. S.; Huber, C. O.; and Brodersen, B. S., "Use of Post-Consumer Waste Plastics in Cement-Based Composites," *Cement and Concrete Research*, V. 26, No. 10, Oct. 1996, pp. 1489-1492. doi: 10.1016/0008-8846(96)00135-4

53. Thorneycroft, J.; Orr, J.; Savoikar, P.; and Ball, R. J., "Performance of Structural Concrete with Recycled Plastic Waste as a Partial Replacement for Sand," *Construction and Building Materials*, V. 161, Feb. 2018, pp. 63-69. doi: 10.1016/j.conbuildmat.2017.11.127

54. Zhang, Y.; Jiang, H.; Wang, H.; and Wang, C., "Separation of Hazardous Polyvinyl Chloride from Waste Plastics by Flotation Assisted with Surface Modification of Ammonium Persulfate: Process and Mechanism," *Journal of Hazardous Materials*, V. 389, May 2020, Article No. 121918. doi: 10.1016/j.jhazmat.2019.121918

55. Zhang, Y.; Li, C.; Wang, L.; and Wang, H., "Application of Froth Flotation in the Separation of Polyvinyl Chloride and Polycarbonate for Recycling of Waste Plastic Based on a Novel Surface Modification," *Waste Management*, V. 110, June 2020, pp. 43-52. doi: 10.1016/j.wasman.2020.05.009

56. Jiang, H.; Zhang, Y.; and Wang, H., "Surface Reactions in Selective Modification: The Prerequisite for Plastic Flotation," *Environmental Science & Technology*, V. 54, No. 16, Aug. 2020, pp. 9742-9756. doi: 10.1021/acs.est.9b07861

57. Rabek, J. F., *Polymer Photodegradation: Mechanisms and Experimental Methods*, Springer Science+Business Media, Dordrecht, the Netherlands, 2012.

58. Liu, L.; Xu, M.; Ye, Y.; and Zhang, B., "On the Degradation of (Micro)Plastics: Degradation Methods, Influencing Factors, Environmental Impacts," *Science of the Total Environment*, V. 806, Part 3, Feb. 2022, Article No. 151312. doi: 10.1016/j.scitotenv.2021.151312

59. Singh, N.; Hui, D.; Singh, R.; Ahuja, I. P. S.; Feo, L.; and Fraternali, F., "Recycling of Plastic Solid Waste: A State of Art Review and Future Applications," *Composites Part B: Engineering*, V. 115, Apr. 2017, pp. 409-422. doi: 10.1016/j.compositesb.2016.09.013

60. Gewert, B.; Plassmann, M. M.; and MacLeod, M., "Pathways for Degradation of Plastic Polymers Floating in the Marine Environment," *Environmental Science: Processes & Impacts*, V. 17, No. 9, Sept. 2015, pp. 1513-1521. doi: 10.1039/C5EM00207A

61. Ebnesajjad, S., and Ebnesajjad, C. F., *Surface Treatment of Materials for Adhesion Bonding*, first edition, William Andrew Publishing, Norwich, NY, 2006, 276 pp.

62. Morris, J. C., "The Acid Ionization Constant of HOCl from 5 to 35°," *The Journal of Physical Chemistry*, V. 70, No. 12, Dec. 1966, pp. 3798-3805. doi: 10.1021/j100884a007

63. Held, A. M.; Halko, D. J.; and Hurst, J. K., "Mechanisms of Chlorine Oxidation of Hydrogen Peroxide," *Journal of the American Chemical Society*, V. 100, No. 18, Aug. 1978, pp. 5732-5740. doi: 10.1021/ja00486a025

64. Pişkin, B., and Türkün, M., "Stability of Various Sodium Hypochlorite Solutions," *Journal of Endodontics*, V. 21, No. 5, May 1995, pp. 253-255. doi: 10.1016/S0099-2399(06)80991-X

65. Gambarini, G.; De Luca, M.; and Gerosa, R., "Chemical Stability of Heated Sodium Hypochlorite Endodontic Irrigants," *Journal of Endodontics*, V. 24, No. 6, June 1998, pp. 432-434. doi: 10.1016/S0099-2399(98)80027-7

66. Marion, J. J. C.; Manhães, F. C.; Bajo, H.; and Duque, T. M., "Efficiency of Different Concentrations of Sodium Hypochlorite During Endodontic Treatment. Literature Review," *Dental Press Endodontics*, V. 2, No. 4, Oct.-Dec. 2012, pp. 32-37.

67. Wright, P. P.; Kahler, B.; and Walsh, L. J., "Alkaline Sodium Hypochlorite Irrigant and Its Chemical Interactions," *Materials*, V. 10, No. 10, Oct. 2017, Article No. 1147.

68. Umeda, K.; Miyasako, T.; Sugiyama, A.; Tanaka, A.; Suzuki, M.; Tokumitsu, E.; and Shimoda, T., "Impact of UV/$O_3$ Treatment on Solution-Processed Amorphous $InGaZnO_4$ Thin-Film Transistors," *Journal of Applied Physics*, V. 113, No. 18, May 2013, Article No. 184509. doi: 10.1063/1.4804667

69. Le-The, H.; Tiggelaar, R. M.; Berenschot, E.; van den Berg, A.; Tas, N.; and Eijkel, J. C. T., "Postdeposition UV-Ozone Treatment: An Enabling Technique to Enhance the Direct Adhesion of Gold Thin Films to Oxidized Silicon," *ACS Nano*, V. 13, No. 6, June 2019, pp. 6782-6789. doi: 10.1021/acsnano.9b01403

70. Cauich-Cupul, J. I.; Herrera-Franco, P. J.; García-Hernández, E.; Moreno-Chulim, V.; and Valadez-González, A., "Factorial Design Approach to Assess the Effect of Fiber–Matrix Adhesion on the IFSS and Work of Adhesion of Carbon Fiber/Polysulfone-Modified Epoxy Composites," *Carbon Letters*, V. 29, No. 4, Aug. 2019, pp. 345-358. doi: 10.1007/s42823-019-00039-7

71. Pritchard, G., "Coupling Agents," *Plastics Additives: An A-Z Reference*, G. Pritchard, ed., Springer, Dordrecht, the Netherlands, 1998, pp. 189-196.

72. Helmy, R., "Reaction of Organosilicon Hydrides with Inorganic Surfaces: An Example of Surface Catalyzed Self-Assembly and Water Porosimetry: A New Technique to Characterize Hydrophobic Porous Surfaces and Wetting in Nano-Confinement," PhD dissertation, Seton Hall University, South Orange, NJ, 2005, 161 pp.

73. Tyagi, G.; Singhal, A.; Routroy, S.; Bhunia, D.; and Lahoti, M., "Radiation Shielding Concrete with Alternate Constituents: An Approach to Address Multiple Hazards," *Journal of Hazardous Materials*, V. 404, Part B, Feb. 2021, Article No. 124201. doi: 10.1016/j.jhazmat.2020.124201

74. Choi, Y. W.; Moon, D. J.; Kim, Y. J.; and Lachemi, M., "Characteristics of Mortar and Concrete Containing Fine Aggregate Manufactured from Recycled Waste Polyethylene Terephthalate Bottles," *Construction and Building Materials*, V. 23, No. 8, Aug. 2009, pp. 2829-2835. doi: 10.1016/j.conbuildmat.2009.02.036

ACI MATERIALS JOURNAL TECHNICAL PAPER

Title No. 123-M20

# Sulfoaluminate Cement: Gypsum-Quicklime Impact on Grouting Material

by Nathan S. Teah, Lin Liao, Yubing Zhao, Zhiling Liao, Wanwen Xue, and Ruiqing Hao

*This study investigates the impact of the quicklime and gypsum ratio on grouting material made of sulfoaluminate cement (SAC). Gypsum and quicklime were selected to verify that sulfoaluminate cement retained ettringite (AFt). SAC’s efficiency as a grouting material was evaluated using gypsum and quicklime. SAC with varying gypsum-quicklime ratios was subjected to tests for compressive strength, pH, setting time, expansion rate, X-ray diffraction (XRD), and scanning electron microscopy (SEM). The microstructure was investigated with XRD at 1 and 28 days. The result obtained points to two key findings: the retention of AFt was excellent (≥99%) regardless of the gypsum-quicklime ratio, and the retention of AFt without gypsum and quicklime depended on the SAC; in this case, the setting time was prolonged, leading to expansion strain.*

**Keywords:** compressive strength; grouting material; gypsum; hydration product; quicklime; sulfoaluminate cement (SAC).

## INTRODUCTION

Many coal mine roadways are situated in extremely complicated environments, which can result in waterlogging, softening, deformation, and even failure of the roadway. Because of this, grouting reinforcement material has been widely used in coal mine empty lanes and roadways for support, as shown in Fig. 1.[1] Figure 1 shows the structure of the double liquid mold pumping pillar in four stages: Fig. 1(a) shows the double liquid mold pumping pillar grouting material being injected into flexure bags, taking on the shape of the bags; Fig. 1(b) shows the pillar supporting the empty lane roof; Fig. 1(c) shows the pillar during the mining operation; and Fig. 1(d) shows the stability and condition of the pillar after the mining operation.

Sulfoaluminate cement (SAC) is an inorganic substance and a hydraulic cement that originated in the 1970s and has been used and industrialized in the underground industry for more than a century. SAC has impressive engineering characteristics that make it suitable for grouting and can also be consumed as an environmentally friendly substitute for portland cement (PC) because of its quick setting time, high early strength, low $CO_2$ emissions, low clinker sintering temperature, low limestone consumption, and strong chemical corrosion resistance. In this study, belite ($C_2S$) and ye’elimite ($C_4A_3S$) make up the majority of the SAC. Also, as Table 1 and Eq. (1) and (2) illustrate, it contains trace minerals, including graphite fluoride ($C_2F$) and iron(III) oxide ($Fe_2O_3$), and its material system relies heavily on ye’elimite ($C_4A_3S$) for the synthesis of ettringite ($C_6AS_3H_{32}$).

$$C_4A_3S + 2CSH_2 + 38H \longrightarrow C_3A \cdot 3CS \cdot 32H + 2AH_3 \quad (1)$$

$$C_4A_3S + 18H \longrightarrow C_3A \cdot CS \cdot 12H + 2AH_3 \quad (2)$$

Although SAC has superior material performance, its weak alkalinity and high cost restrict its engineering application. Researchers have looked into the use of supplemental cementitious materials (SCMs) and mixed materials to enhance the engineering performance of SAC. According to research by Péra and Ambroise,[2] due to the tricalcium sulfoaluminate that hydrates in the form of ettringite (AFt) and alumina ferric oxide (AFm) after hydration, SAC is good for special engineering applications such as shrinkage resistance, self-stressing, and self-leveling. This is because AFt possesses expansion properties that can counteract the natural shrinkage that happens when the SAC paste dries. This results in a material that is more dimensionally stable and enhances the ability to form a denser microstructure, both of which are advantageous for applications involving self-stressing. Furthermore, the expanding character and quick strength development of ettringite contribute to its self-leveling qualities. AFt and AFm’s swift early strength growth also helps stabilize the material so that it does not sag or slump before setting, which makes it perfect for self-leveling applications. SAC can be used in applications that need shrinkage compensation because of the expansion brought on by the crystal development and water adsorption of AFt, which reduces volume, causes shrinkage, and creates compressive stresses in the surrounding concrete. In addition, other research stated that SAC is feasible in terms of workability and strength, but it needs retarding agents to regulate its setting time and avoid low pH after the hydration process.[3] In a recent study, Jia et al.[4] used SAC clinker, gypsum, and quicklime to create grouting material. The study shows that gypsum plays an important role in the fast generation of AFt in the hydration process of SAC. The gypsum promotes early hydration and allows a proper hydration mechanism and reaction formation (Eq. (3)).

$$C_4A_3S + 2CS + 38H \longrightarrow C_6AS_3H_{32} + 2AH_3 \quad (3)$$

---

*ACI Materials Journal*, V. 123, No. 2, March 2026.

MS No. M-2024-439.R4, doi: 10.14359/51749382, received August 24, 2025, and reviewed under Institute publication policies. Pertinent discussion including author’s closure, if any, will be published ten months from this journal’s date if the discussion is received within four months of the paper’s print publication.

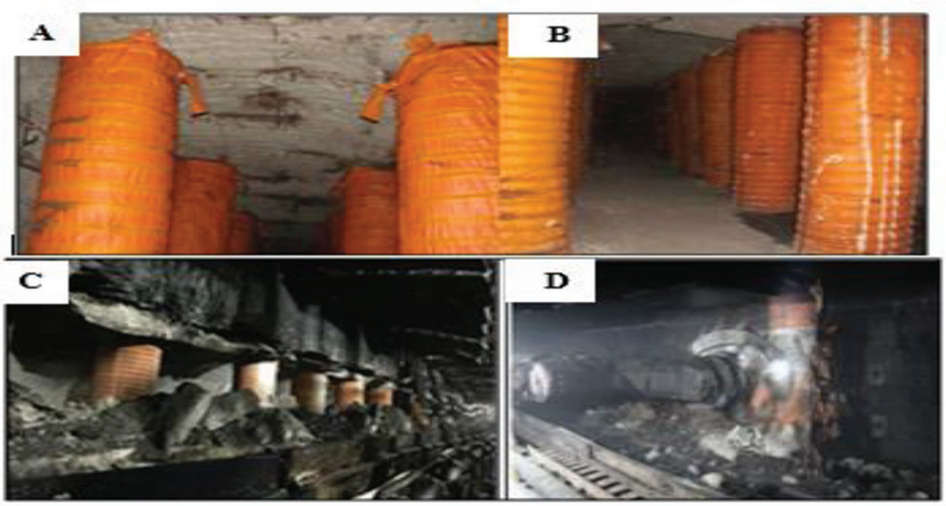

*Fig. 1—Different stages of SAC double liquid mold pumping in empty lane roadway.*

**Table 1—Chemical and mineral composition of SAC and gypsum, wt. %**

| | Chemical composition | | Mineral composition | |
|---|---|---|---|---|
| Chemical | SAC, wt. % | Gypsum, wt. % | Mineral | SAC, wt. % |
| $SiO_2$ | 9.52 | 4.24 | $C_2F$ | 6.54 |
| $Al_2O$ | 29.55 | 2.42 | $\beta$-$X_2S$ | 24.74 |
| CaO | 45.26 | 37.64 | $C_4A_3\check{S}$ | 58.47 |
| $Fe_2O_3$ | 2.95 | 0.95 | f-$SO_3$ | 1.93 |
| MgO | 0.95 | 2.05 | — | — |
| $TiO_2$ | 1.50 | — | — | — |
| $SO_3$ | 9.44 | 46.14 | — | — |
| Loss | 0.44 | 3.34 | — | — |

Moreover, following the stoichiometry reaction of Eq. (3), the hydration characteristic of the amount of gypsum represents approximately half of the ettringite weight (ettringite weight = 0.45), which had a significant impact on the rapid hardening and early strength, while quicklime had a significant impact on the micro-expansion as a cement-based grouting material.

Quicklime substance incorporation can result in an alkali that strengthens SAC. However, excess may result in the grouting material's vital expansibility feature. With the aid of gypsum, quicklime can accelerate the anhydrous sulfoaluminate hydration process. However, when the incorporation ratio of quicklime is significantly higher than that of gypsum, it causes expansion and slows the high strength of the material. The strength would decrease as the material expands and self-destructs, but in a later stage, the expansion value increases while the strength stays constant. Moreover, when the quicklime content is too low or high, its pH inhibits the production of ettringite. This indicates that the ratio of quicklime should be thoroughly studied before incorporating it into the mixture.

Additionally, in ternary blends of quicklime, gypsum, and SAC, gypsum is more reactive with sulfoaluminate clinker than quicklime. The incorporation of a proper dosage of gypsum will make the cement mortar more durable and stable enough to sustain pressure and stress during the construction phase as a grouting material.[5] The research also reported that, due to the retardation mechanism and increase in gypsum content, the SAC reacts with gypsum and hydrates quickly and produces more AFt, which deposits and forms a protective film against the tricalcium aluminate ($C_3A$) SAC particles to improve the hydration. An increase in gypsum and quicklime content also increases the production of ettringite and monocarbonate, decreases the monosulfoaluminate, and delays the setting time of SAC.[6]

The previous research findings have significantly contributed to the extensive and comprehensive application of SAC as a cement-based grouting material. However, there is limited research on how the mechanical qualities and performance of SAC-based grouting materials are impacted by gypsum and quicklime. To meet the practical application requirements, this research explores methods to enhance the early and later performance and characteristics of grouting materials by incorporating gypsum and quicklime into the SAC, thereby creating a novel cement-based grouting material. Additionally, quicklime and gypsum are added to influence the hydration reactions of the grouting materials and due to their impact on the compressive strength, expansion, pH, and setting time. The hydration process and the microlevel effects of gypsum on the novel SAC-based grouting materials are investigated using X-ray diffraction (XRD) and scanning electron microscopy (SEM). The results of this research can offer valuable insights into the application of SAC-gypsum and quicklime-based grouting material.

## RESEARCH SIGNIFICANCE

The majority of the published studies on gypsum studied the behavior of the pastes. This study lays the foundation for future experimental research on the impact of the gypsum-quicklime ratio on the physical properties and characteristics of SAC-based grouting material and its optimal proportions. The data presented in this study are also useful for understanding the behavior of sulfoaluminate cement grouting material (SACGM).

## EXPERIMENTAL PROGRAM

### Raw materials

The cement used in this study is a commercial SAC. Based on factory performance statistics, it has a measured density of 2.89 g/cm$^3$ and a specific surface area of 450 m$^2$/kg. Table 1 displays the mineral and chemical composition of SAC as determined by XRD.

The gypsum employed in this study is off-white and its density is 2.85 g/cm$^3$. It originated by dissolving calcium sulfate crystals in an aqueous solution, which was then deposited as gypsum. Its chemical composition was identified through X-ray fluorescence (XRF), as indicated in Table 1. When added to SAC, gypsum acts as a regulator to limit the rate at which $C_3A$ hydrates, decreasing the amount of ettringite produced. The quicklime used in this investigation is a white, alkaline, caustic, crystalline solid at room temperature. It has a density of 3.1 g/cm$^3$ and a chemical formula of calcium oxide (CaO). It has an effective CaO level above 90%. The quicklime rapidly reacts with water to produce calcium hydroxide.

### Test methods

The SACGM was mixed into two components (slurry A and B), as shown in Table 2. The mass ratio of the sulfoaluminate clinker to (gypsum + quicklime) is 1:1, and the water-cement ratio (*w*/*c*) is 0.5.

### Setting time

After the blending of the slurry, it was placed into a Vicat apparatus mold. The Vicat apparatus was used to measure the initial and final setting times of the blended cement paste by complying with the GB/T 1346-2011 standard.[7] The penetration of the Vicat needle determined the initial and final setting times of the blended cement paste at 26 ± 4 and 0.5 ± 0.5 mm, respectively.

### pH test

In this study, a precision pH tester was used to measure the slurry's pH.[8] The calibrated pH meter test pen was placed into four separate samples of a single proportion of the slurry, and the sample readings that had stabilized were taken as the pH value.

### Compressive strength test

The specimen's compressive strength was tested following the GB/T 50081-2002 test standard for testing the method of mechanical properties of ordinary concrete.[9] The mixed paste slurry was made using the mixture proportions indicated in Table 2 and placed into a 50 x 50 x 50 mm mold, as illustrated in Fig. 2. Compression testing equipment was used to assess the paste test block's compressive strength at a loading rate of 0.3 MPa/s for 1, 7, 14, and 28 days. The sample per series for each ratio is 1:1 (one percentage ratio—four test series). Based on the experimental proportions, the experimental value was determined by averaging the values of the four replicate test series.

**Table 2—Mixture proportions with SAC and gypsum-quicklime ratio**

| | Slurry A | Slurry B | | *w*/*c* |
|---|---|---|---|---|
| Mixture series | SAC, wt. % | Gypsum, wt. % | Quicklime, wt. % | Slurry A & B |
| 1_A:B | 100 | — | — | 0.5 |
| 2_A:B | — | 100 | 0 | — |
| 3_A:B | | 90 | 10 | |
| 4_A:B | | 80 | 20 | |
| 5_A:B | | 70 | 30 | 0.5 |
| 6_A:B | | 60 | 40 | — |
| 7_A:B | | 50 | 50 | |

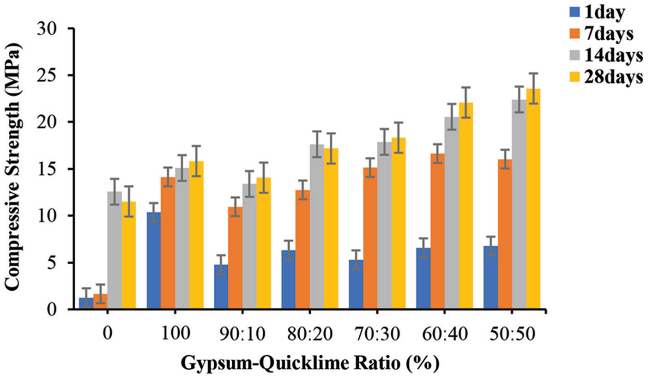

*Fig. 2—Strength curve of gypsum-quicklime ratio with different ages.*

### Expansion rate

Thermomechanical techniques on solid materials were used to investigate the expansion stability of the specimen paste. After blending the slurry mixture for 2 minutes, it was put into a 50 x 50 x 50 mm mold. The specimens' starting lengths ($L_0$) were measured after demolding, and they were then cured in water at 80°C for 1 day. Changes in the specimens were noted at 1, 7, 14, and 28 days, beginning on the day the original lengths were measured using the triple steel sheet with dimensions of 280 mm in length, 25 mm in width, and 25 mm in height, to determine the expansion of the specimen following the JC/T 313-2009 standard.[10] The formula for calculating the expansion rates ($E_X$) of the specimens is provided in Eq. (4), and the average of the expansion rates of the four curing ages was considered the outcome for each group of specimens

$$E_X = \frac{L_1 - L_2}{L_0 - (\Delta_1 - \Delta_2)} \times 100 \qquad (4)$$

where $E_X$ is the expansion rate of a specimen at the observed day (%); $L_1$ is the length of a specimen at the observed day (mm); $L_0$ is the initial length of a specimen (mm); and $\Delta_1$ and $\Delta_2$ are the lengths of the measuring heads at the left and right ends of the specimen (mm).

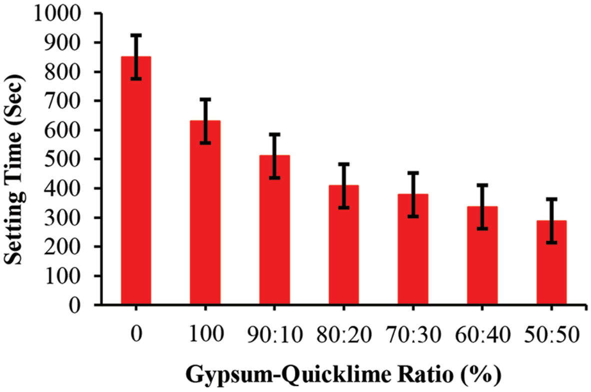

*Fig. 3—Change curve of setting time with different gypsum-quicklime ratios.*

## XRD

To stop the hydration, the hydrated samples were immersed in anhydrous ethanol for 2 days. A vacuum-drying oven was used to dry the hydrated specimens. The vacuum degree was 0.08 MPa, and the temperature was 40°C. The hydrated specimens were heated and then manually ground into a powder that was smaller than 0.025 mm and sieved through a 200-mesh screen. The hydrated specimens' mineralogical makeup of 1- and 28-day samples was performed using Rietveld refinement.[11] The test range was set from 5 to 30 degrees, with a scanning rate of 0.04 deg/s.

## SEM

The samples were taken from the same hydrated samples that were immersed in anhydrous ethanol for 2 days. The hydrated samples were ground flat to a size of less than 1 cm. Then, the ground specimen was examined by SEM using a secondary-electron image and energy-dispersive X-ray (Rietveld refinement) analysis.

## ANALYSIS OF EXPERIMENTAL RESULTS

### Impact of gypsum-quicklime content on SACGM

*Impact of gypsum-quicklime ratio on setting time*—Figure 3 displays the setting time of the SACGM. When SAC was mixed alone, the slurry experienced an 850-second setting time due to the increase in the production of $C_3A$ during the hydration process. However, as gypsum and SAC were incorporated, the slurry setting time was 630 seconds.[3] This is in line with the suggestion of Jia et al.,[4] who stated that SAC cannot play an important role in the setting time when it is mixed alone. Following the incorporation of the gypsum and quicklime with the SAC, the slurry setting time varied as the gypsum-quicklime ratio varied. When the gypsum-quicklime ratios were 90:10, 80:20, and 70:30, the slurry setting time decreased as the quicklime ratio increased, accumulating 510, 408, and 378 seconds, respectively. The ratios of 60:40 and 50:50 have the lowest setting time, accumulating 336 and 288 seconds, respectively. However, based on the numerical value, the ratio 50:50 is the best. This shows that gypsum has a significant impact on the setting time of the grouting slurry; however, when it is mixed with quicklime, it becomes more efficient regardless of the ratios.[12]

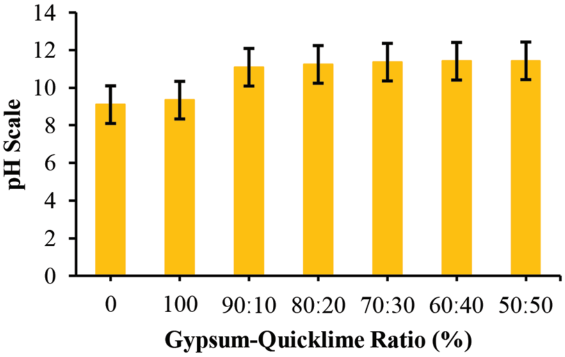

*Fig. 4—Change curve of pH with different gypsum-quicklime ratios.*

*Impact of gypsum-quicklime ratio on pH*—Figure 4 displays the impact of different gypsum-quicklime ratios on the pH of SAC slurry. As shown in Fig. 4, when SAC was mixed alone, the slurry experienced a pH of 9.1. Following the incorporation of gypsum and SAC alone, the pH increased to 9.34. This shows a little variation on the pH curve and agrees with previous research on gypsum and SAC pH after hydration.[3] When gypsum and quicklime were introduced in the slurry over a different range, the pH varied to a certain extent and rose steadily between 11.09 and 11.43.[13] This means the dissolver of quicklime could release a significant amount of hydroxide, which can reduce the slurry alkalinity, decelerate the coagulation, and affect the mechanical performance of the SACGM.[14]

*Impact of gypsum-quicklime ratio on compressive strength*—Figure 2 shows that when only SAC was incorporated, the overall trend of the strength change curve fluctuated. The 1-, 7-, 14-, and 28-day strengths were 1.25, 1.65, 12.56, and 11.52 MPa, respectively. Following the incorporation of gypsum and SAC alone, the compressive strength of the SACGM at 1, 7, 14, and 28 days increases at all ages, with 10.35 and 15.85 MPa being the compressive strength of 1 day and 28 days, respectively. Following the incorporation of different gypsum-quicklime ratios, the compressive strength curve exhibits different characteristics according to the dosage mixed. When the 90:10 ratio was incorporated, the strength curve experienced fluctuation; the early strength of SACGM was low due to the delay in hydration conditions, ensuring a substantial increase in its late strength. The 1- and 28-day compressive strengths reached 4.78 and 14.06 MPa, which were 6.2% and 20.3% higher than those in the control group with only SAC. The gypsum-quicklime ratio effects on the deterioration of the 1-day compressive strength of the SACGM were not obvious, because as the age of the SACGM increased, the compressive strength increased. Following the continuous incorporation of gypsum and quicklime, ratios of 70:30, 60:40, and 50:50 exhibited similar curve patterns; however, the 50:50 ratio was identified as the optimal proportion of SACGM, with compressive strengths reaching 6.76 and 23.58 MPa at 1 and 28 days, respectively, representing increases of 14.2% and 32%, as indicated by the strength trend curve. At this ratio, the 7-day strength reached 85% of the 28-day strength of the 80:20 ratio, and the 14-day strength increased continuously.

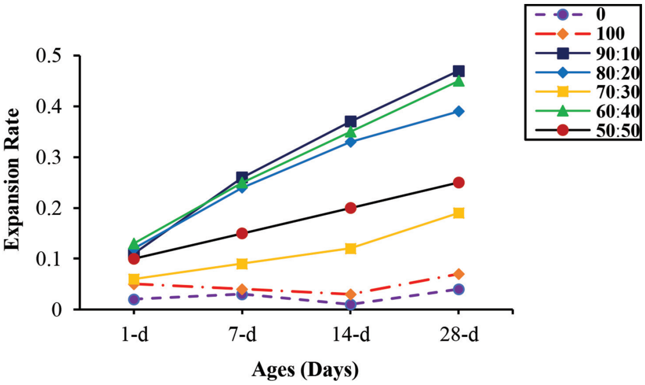

*Fig. 5—Change curve of expansion rate with different gypsum-quicklime ratios.*

This shows that although the incorporation of gypsum alone has a positive impact on the strength of the SACGM, its efficiency improves greatly when combined with quicklime.[15]

*Impact of gypsum-quicklime ratio on expansion rate*—Figure 5 shows the impact of the gypsum-quicklime ratio on the expansion rate. When the slurry material is SAC alone, there is a shrinkage of ≤0.04 on the test block of the specimen due to the improper and fast hydration process of the SAC clinker. With the incorporation of gypsum and SAC alone, there is little shrinkage strain of ≤0.07 due to the delay during the hydration process. This is because the incorporated gypsum ratio was too large. Following the incorporation of gypsum and quicklime at ratios from 90:10 to 50:50, the SACGM showed no level of shrinkage at all ages. As the gypsum-quicklime ratio changed, the specimen test blocks maintained non-shrinkage texture but exhibited slow hydration at an early age, which affected the early strength.[16] However, following the increase in age, at 7, 14, and 28 days, the hydration of the SACGM was rapid. This gives the SACGM the characteristics of fast mechanical strength development, which proves that the preparation of SACGM using gypsum and quicklime is feasible.[17]

*Impact of gypsum-quicklime content on hydration products*—

**XRD hydration products of SACGM:**

Figures 6(a) to (d) display the XRD pattern of the SACGM hydrated for 1 and 28 days under the effect of different gypsum-quicklime ratios. As can be seen from Fig. 6(a) to (d), compared with the blank group (SAC alone), the incorporation of only gypsum with SAC increased the intensity of the diffraction peaks of the hydrated minerals, such as ye'elimite ($Ca_4A_{l6}O_{12}SO_4$), calcium sulfate ($CaSO_4$), and magnesium oxide (MgO)[16] in the material, and slightly decreased and weakened the intensity of the diffraction peaks of the hydrated minerals, such as AFt and AFm in the material, which was attributed to the adsorption-permeation effect of gypsum regulating the early hydration rate of SACGM.[5] On the other hand, SAC and gypsum increased the sulfoaluminate hydration in the later phase, and the adsorption of sulfoaluminate promoted ye'elimite ($Ca_4A_{l6}O_{12}SO_4$) and increased the intensity peak of $CaSO_4$.

The XRD patterns in Fig. 6(e) to (f) show that gypsum and quicklime incorporation accelerated the early hydration, dissolved the $CaSO_4$, and increased the intensity of the diffraction peaks of the hydrated minerals, such as AFt and AFm. As the gypsum-quicklime ratio changed from 90:10 to 70:30, the AFt diffraction peak intensities increased continuously at 1 and 28 days.[17] This is because the diffusion rate of gypsum and quicklime was much higher than that of sulfoaluminate and was able to penetrate the hydration layer of ye'elimite ($Ca_4A_{l6}O_{12}SO_4$) and $CaSO_4$, facilitating the dissolution of ye'elimite ($Ca_4A_{l6}O_{12}SO_4$) and $CaSO_4$.[18] The relative peak intensities of SACGM-hydrated minerals under the effect of gypsum and quicklime were strong compared with those of the blank and only gypsum group, in which the AFm peak was weak, the intensities of AFm and $Ca(OH)_2$ diffraction peaks were significantly reduced, and the intensity of the AFt diffraction peak increased.

**SEM phase microstructure of SACGM:**

As illustrated in Fig. 7, when the gypsum dosage was 100%, the pin-rods of AFt and numerous flakes of calcium-silicate-hydrate (C-S-H) and aluminum hydroxide ($AH_3$) were observed. This was consistent with the physical phase found in the XRD peaks because quicklime was absent. Following the incorporation of the gypsum-quicklime ratio at 90:10, 80:20, and 70:30, the production of the stacked AFm and $AH_3$ gel was reduced, and the pin-rods and cluster AFt production increased. However, as seen in Fig. 7, the hydration products were not well-developed and closely linked to the low quantity of quicklime that was incorporated. When the gypsum-quicklime ratio is 60:40, the XRD pattern in Fig. 7 displays long needle-like AFt staggered crosses and numerous flaky single $AH_3$ stacks. Due to the high quicklime content, the slurry's hydration reaction proceeds quickly and is made up of many AFt crystals, which pass through the gypsum and SAC clinker without having had a chance to participate in the reaction.

Following the incorporation of a 50:50 gypsum-quicklime ratio, the system has a lot of AFm gel and needle-like AFt crystals that are longer in size, larger in number, and exhibit higher strength. It also has a lot of radiating AFt crystal clusters that mechanically compress with one another to produce the structure. As a result of the overall structure being denser and filled inside the skeleton, it is denser and harder. Moreover, the sulfate ion ($SO_4^{2-}$) in the liquid phase becomes more concentrated when the concentrations of the ions in the solution surpass the saturation point of gypsum, which explains the appearance of rod-shaped gypsum inside the sulfoaluminate skeleton structure.

## CONCLUSIONS

This research examines the different ratios of gypsum-quicklime sulfoaluminate cement (SAC) grouting material. To investigate the impact of the gypsum-quicklime ratio on the SAC grouting material (SACGM), strength, expansion rate, pH, and setting time tests were conducted, and the X-ray diffraction (XRD) pattern was then used to examine variations in hydration products with gypsum-quicklime ratios, which helps to explain the impact on the SACGM. Following these experimental procedures, the subsequent conclusions are established:

1. Gypsum-quicklime ratios have a great impact on the efficiency of the SACGM setting time (≥99%), regardless

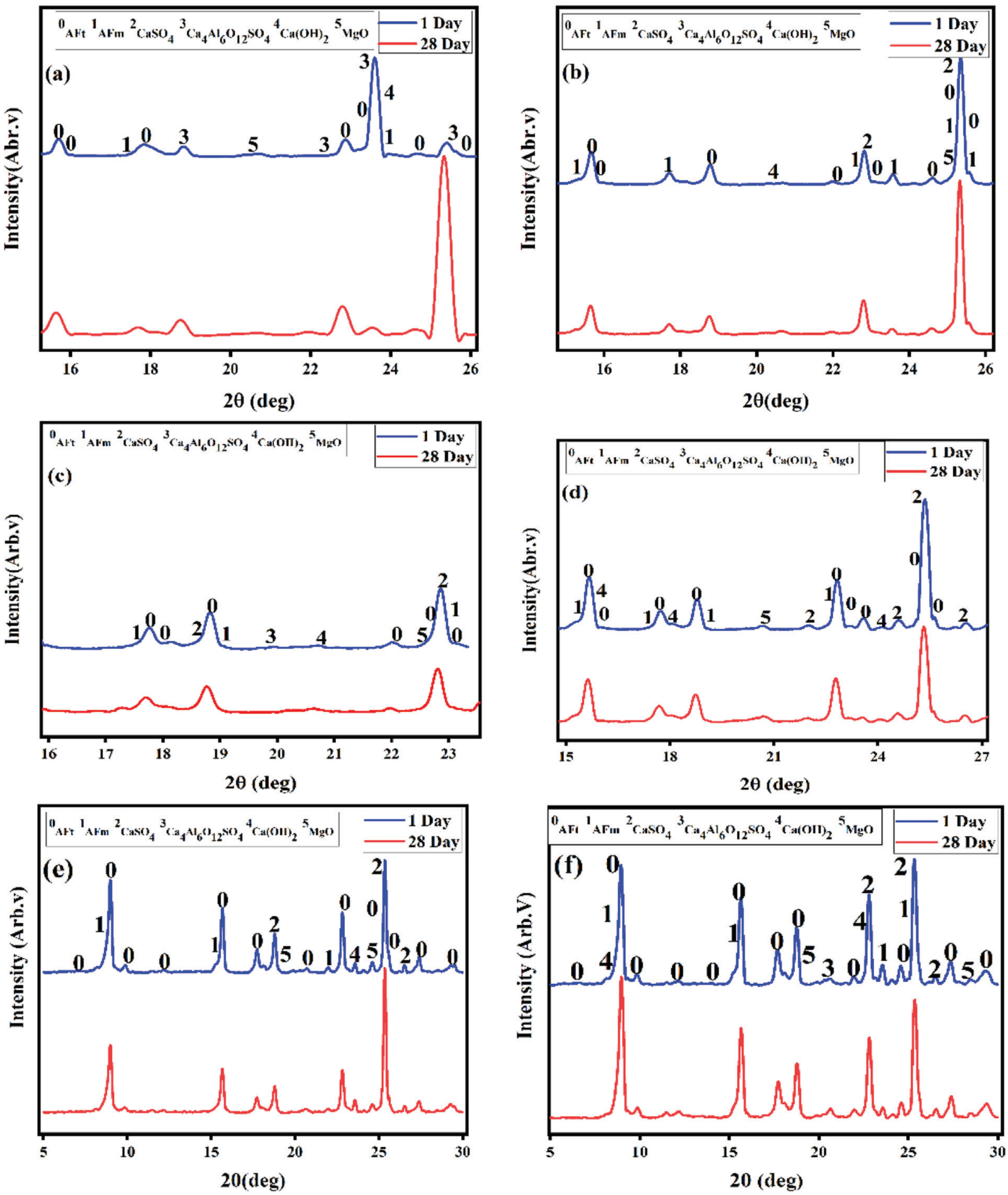

*Fig. 6—XRD pattern of gypsum and quicklime hydrated for 1 and 28 days: (a) 100:0; (b) 90:10; (c) 80:20; (d) 70:30; (e) 60:40; and (f) 50:50 (ye'elimite, MgO, AFt, AFm, $CaSO_4$, and $Ca(OH)_2$).*

of the ratio. The setting time was prolonged when the ratio changed from 100:0 to 90:10 because gypsum promotes the hydration of SACGM and the formation of more ettringite (AFt).[4] The pH of SACGM satisfied the requirements of the mixture proportions and was not significantly affected by the gypsum-quicklime ratio.

2. The effect of the gypsum-quicklime ratio on the deterioration of the 1-day compressive strength was not obvious, because as the ratio and age increased, the compressive strength increased. The best ratio of gypsum to quicklime in the SACGM was 50:50. It accumulated 14.2% and 32% of the 1- and 28-day compressive strength, respectively. The gypsum-quicklime ratio barely affects the grouting material expansions. There was no expansion rate with each gypsum-quicklime ratio used (Fig. 5), but with SAC alone, and gypsum with SAC, there was expansion strain at an early stage of hydration (Fig. 5).

3. The incorporation of gypsum and quicklime accelerated the early hydration, dissolved the $CaSO_4$, and increased the intensity of the diffraction peaks of the hydrated minerals, such as AFt and alumina ferric oxide (AFm). Under the condition of a high gypsum-quicklime ratio, gypsum and quicklime penetrate the hydration layer of ye'elimite ($Ca_4A_{l6}O_{12}SO_4$) and $CaSO_4$, facilitating their dissolution, weakening the peaks of AFm, significantly reducing the

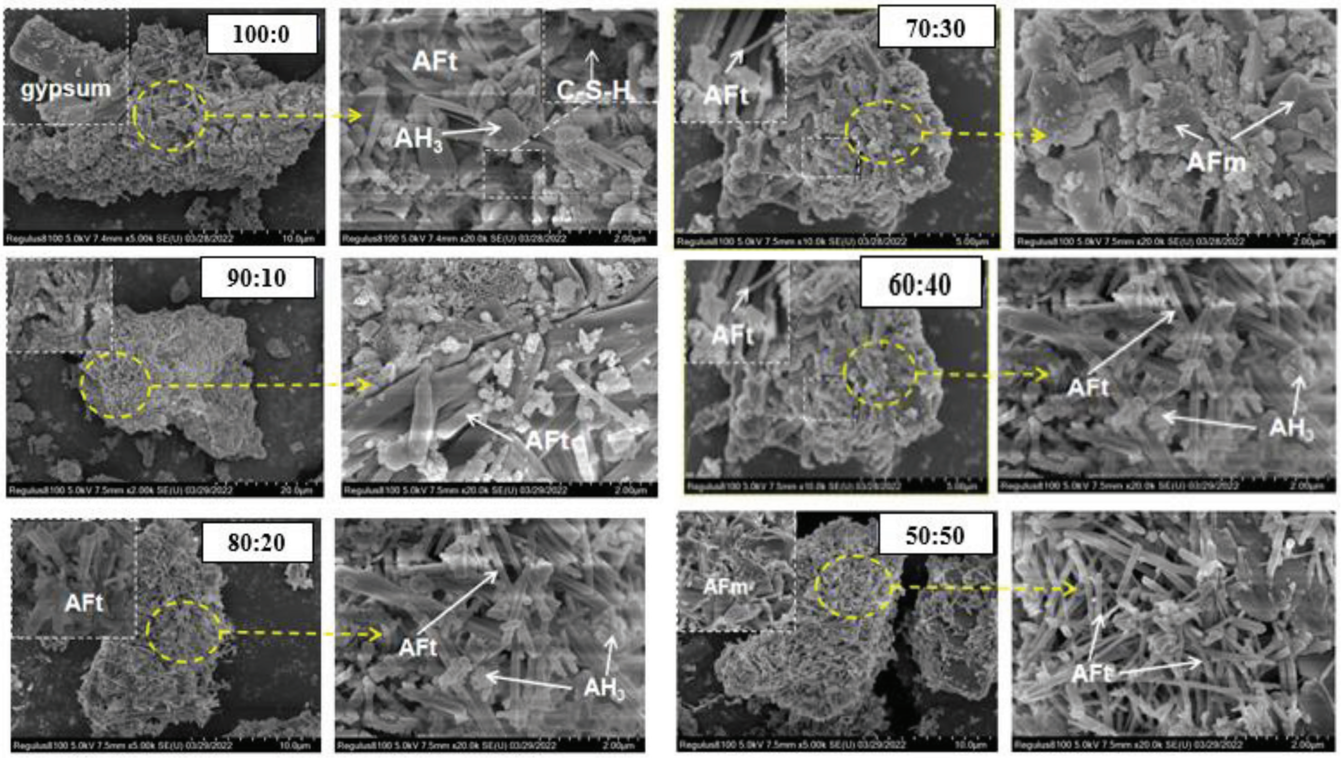

*Fig. 7—SEM at 1 and 28 days with different gypsum-quicklime ratios.*

intensities of AFm and $Ca(OH)_2$, and increasing the AFt diffraction peak.

4. The SACGM is significantly improved by the inclusion of the gypsum and quicklime. The scanning electron microscopy (SEM) characterizations confirmed that the hydration products of the SACGM system are rich in needle-like AFt crystals, stacked AFm, and flaky single aluminum hydroxide ($AH_3$), which contribute to strength enhancement. Moreover, the hydration of aluminum silicate ($Al_2SiO_5$) prevents the formation of calcium-silicate-hydrate (C-S-H), which dissolves into sulfoaluminate hydroxide and yields trace amounts of AFt as the hydration product.

## AUTHOR BIOS

**Nathan S. Teah** *is a Graduate Student at Taiyuan University of Technology, Taiyuan, Shanxi, China. He received his BS in mining engineering from the China University of Mining and Technology, Xuzhou, Jiangsu, China, in 2022.*

**Lin Liao** *is an Associate Professor in the Underground Engineering Department at Taiyuan University of Technology, where he received his BS and MS in civil and mechanical engineering in 2010 and 2012. He received his PhD in construction engineering from Universitat Politècnica de Catalunya, Barcelona, Spain, in 2015. His research interests include urban underground engineering, concrete structure design, and durability.*

**Yubing Zhao** *is a Graduate Student at Taiyuan University of Technology, where he received his BS in mining engineering in 2022.*

**Zhiling Liao** *is a Graduate Student at Taiyuan University of Technology. He received his BS in civil engineering from Shijiazhuang Tiedao University, Shijiazhuang, Hebei, China, in 2021.*

**Wanwen Xue** *is a Graduate Student at Taiyuan University of Technology, where she received her BS in underground engineering in 2022.*

**Ruiqing Hao** *is an Associate Professor in the Mining Engineering Department at Taiyuan University of Technology. She received her BS, MS, and PhD in mining engineering from Central South University, Changsha, Hunan, China, in 2011, 2013, and 2017, respectively. Her research interests include rock mechanics and underground engineering.*

## ACKNOWLEDGMENTS

First and foremost, the authors thank God Almighty for providing them with the wisdom and expertise necessary to finish this research. The authors would also like to express their gratitude to Shanxi Transportation Holdings Group Co., Ltd., for providing financial support for this study, and to Shanxi Zhongbao Construction and Building Materials Co., Ltd., for the supplies that helped with the execution of the experimental operations.

## REFERENCES

1. Krishnamoorthy, T. S.; Gopalakrishnan, S.; Balasubramanian, K.; Bharatkumar, B. H.; and Rama Mohan Rao, P., "Investigations on the Cementitious Grouts Containing Supplementary Cementitious Materials," *Cement and Concrete Research*, V. 32, No. 9, 2002, pp. 1395-1405. doi: 10.1016/S0008-8846(02)00799-8

2. Péra, J., and Ambroise, J., "New Applications of Calcium Sulfoaluminate Cement," *Cement and Concrete Research*, V. 34, No. 4, 2004, pp. 671-676. doi: 10.1016/j.cemconres.2003.10.019

3. Burris, L. E., and Kurtis, K. E., "Influence of Set Retarding Admixtures on Calcium Sulfoaluminate Cement Hydration and Property Development," *Cement and Concrete Research*, V. 104, 2018, pp. 105-113. doi: 10.1016/j.cemconres.2017.11.005

4. Jia, F.; Sun, H.; Yu, L.; Lu, X.; Zhou, Y.; Elchalakani, M.; and Du, P., "Effects of Different Gypsum Varieties on the Hydration and Mechanical Properties of Red Mud-Based Ferrite-Rich Sulfoaluminate Cement," *Journal of Materials Research and Technology*, V. 24, 2023, pp. 3086-3097. doi: 10.1016/j.jmrt.2023.03.197

5. Aimin, X., and Sarkar, S. L., "Microstructural Study of Gypsum-Activated Fly Ash Hydration in Cement Paste," *Cement and Concrete Research*, V. 21, No. 6, 1991, pp. 1137-1147. doi: 10.1016/0008-8846(91)90074-R

6. Pommersheim, J., and Chang, J., "Kinetics of Hydration of Tricalcium Aluminate in the Presence of Gypsum," *Cement and Concrete Research*, V. 18, No. 6, 1988, pp. 911-922. doi: 10.1016/0008-8846(88)90027-0

7. Zhu, Y.; Ma, B.; Li, X.; and Hu, D., "Ultra-High Early-Strength Self-Compacting Mortar Based on Sulfoaluminate Cement and Silica Fume," *Journal of Wuhan University of Technology-Materials Science Edition*, V. 28, No. 5, 2013, pp. 973-979. doi: 10.1007/s11595-013-0803-5

8. Xu, X.; Bi, H.; Yu, Y.; Fu, X.; Wang, S.; Liu, Y.; Hou, P.; and Cheng, X., "Low Leaching Characteristics and Encapsulation Mechanism of $Cs^+$ and

$Sr2^+$ from the SAC Matrix with Radioactive IER," *Journal of Nuclear Materials*, V. 544, 2021, p. 152701. doi: 10.1016/j.jnucmat.2020.152701

9. Yan, J.; Liu, K.; Zou, C.; Mo, Y.; and Ou, J., "Comparison of Evaluation Tests for Compressive Strength of Structural Concrete," *Periodica Polytechnica Civil Engineering*, V. 64, 2020, pp. 387-395. doi: 10.3311/PPci.12545

10. Chen, X.; Gao, J.; Yan, Y.; and Liu, Y., "Investigation of Expansion Properties of Cement Paste with Circulating Fluidized Bed Fly Ash," *Construction and Building Materials*, V. 157, 2017, pp. 1154-1162. doi: 10.1016/j.conbuildmat.2017.08.159

11. Jansen, D.; Wolf, J. J.; and Fobbe, N., "The Hydration of Nearly Pure Ye'elimite with a Sulfate Carrier in A Stoichiometric Ettringite Binder System. Implications for the Hydration Process Based on In-Situ XRD, 1H-TD-NMR, Pore Solution Analysis, and Thermodynamic Modeling," *Cement and Concrete Research*, V. 127, 2020, p. 105923. doi: 10.1016/j.cemconres.2019.105923

12. Chen, X.; Wang, J.; Jiao, H.; Yang, Z.; Zheng, D.; and Sun, J., "Study on Early Hydration Mechanism of Double-Liquid Grouting Material Modified by Composite Early Strength Agent," *Materials*, V. 16, No. 19, 2023, p. 6475. doi: 10.3390/ma16196475

13. Seo, J.; Kim, S.; Park, S.; Yoon, H. N.; and Lee, H. K., "Carbonation of Calcium Sulfoaluminate Cement Blended with Blast Furnace Slag," *Cement and Concrete Composites*, V. 118, 2021, p. 103918. doi: 10.1016/j.cemconcomp.2020.103918

14. Manocha, S., and Ponchon, F., "Management of Lime in Steel," *Metals*, V. 8, No. 9, 2018, p. 686. doi: 10.3390/met8090686

15. Li, Z.; Luo, J.; Yuan, S.; Gao, Y.; Zhang, J.; Gao, S.; and Zhu, M., "Mix Ratio Optimization and Comprehensive Performances of Novel High-Early Strength Non-Shrinkage Sleeve Grouting Material," *Structures*, V. 61, 2024, p. 106048.

16. Wei, X.; Liu, X.; Duan, Y.; and Feng, J., "Property Transformation of a Modified Sulfoaluminate Grouting Material Under Pressure Circulation for a Water-Sealed Underground Oil Cavern," *Construction and Building Materials*, V. 140, 2017, pp. 210-220. doi: 10.1016/j.conbuildmat.2017.02.137

17. Bi, R.; Cheng, W.; and Chen, X., "Effect of Calcium Sulfate Variety and Content on Hydration Mechanism of Grout Sealants for Coal-Bed Methane Drainage Boreholes," *Construction and Building Materials*, V. 203, 2019, pp. 443-455. doi: 10.1016/j.conbuildmat.2019.01.046

18. Pimraksa, K., and Chindaprasirt, P., "Sulfoaluminate Cement-Based Concrete," *Eco-Efficient Repair and Rehabilitation of Concrete Infrastructures*, F. Pacheco-Torgal, R. E. Melchers, X. Shi, N. De Belie, K. Van Tittelboom, and A. Sáez, eds., Woodhead Publishing, Sawston, UK, 2018, pp. 355-385.

ACI MATERIALS JOURNAL TECHNICAL PAPER

Title No. 123-M21

# Development of Wet-Mix Shotcrete with Portland-Limestone Cement

by Lihe (John) Zhang, Matthew Zhang, Dudley R. (Rusty) Morgan, and Sidney Mindess

*Portland-limestone cement (PLC) is being more and more specified and used in wet-mix shotcrete construction for ground support in tunnels and mines across the United States and Canada. The most widely used cement of Type GU (general use) in Canada and Type I in the United States is being replaced by Type GUL (general-use limestone) in Canada and Type IL in the United States. There is no significant research being conducted on the performance of shotcrete made using PLC, including plastic properties, early-age strength development, compressive strength development, and, when fibers are added, flexural toughness and residual tensile strength development. This paper presents studies on the properties of wet-mix shotcrete produced with PLC. Results show that PLC requires a higher dosage of alkali-free accelerator (AFA) to achieve similar development of early-age compressive strength compared to shotcrete made with portland cement (PC). Development of compressive strength at 7 and 28 days for shotcrete made with PLC is similar to shotcrete made with PC. When both steel and macrosynthetic fibers are used in wet-mix shotcrete made with PLC, development of residual tensile strength with notched beams and flexural toughness for round determinate panels is also similar to that for wet-mix shotcrete produced with PC. Future research on wet-mix shotcrete with Type GUL cement is also discussed.*

**Keywords:** alkali-free accelerator (AFA); early-age compressive strength development; flexural toughness; ground support; portland-limestone cement (PLC); residual tensile strength; shotcrete; Type GUL; Type IL.

## INTRODUCTION

The global movement for sustainability requires reduction of carbon emissions. In the cement and concrete industry, reducing greenhouse gas emissions during cement production and reducing the use of cement by the use of supplementary cementitious materials (SCMs) such as calcined clay, fly ash, silica fume, and ground-granulated blast-furnace slag have been used. In addition, performance-based design and proper curing and protection to improve service life of concrete structures are being studied, implemented, and promoted around the world to foster sustainability. One of the most practical techniques is to reduce the clinker content by adding limestone powder to produce Type IL cement in the United States or Type GUL (general-use limestone) cement in Canada. Type GUL cement refers to Type GU (general use) cement with addition of up to 15% limestone. Limestone is interground with the clinker during the cement production process. In the United States, Type IL cement refers to Type I cement with up to 15% limestone addition. Cement with up to 15% limestone content was introduced into concrete construction in the United States and Canada approximately a decade ago; CSA A23.1:24/CSA A23.2:24 has listed Type GUL cement since 2014.[1] Adding up to 15% limestone into the cement reduced the use and production of cement, and as a result, reduced energy consumption and greenhouse gas emissions.

Since 2023, major cement suppliers in North America have minimized the production of Type GU cement, and only Type GUL cement is now commercially available in most of the provinces in Canada and the states of the United States. The changes in the type of cement production and supply were rapid and left no choice for the construction industry. For the civil tunnel industry, this change caused many challenges, as contractors did not have much experience in working with Type GUL cement in concrete and shotcrete. Although suppliers have conducted research and provided some project experience for concrete using Type GUL cement, project experience for the use of Type GUL cement in wet-mix shotcrete for ground support—in particular, with the addition of accelerators and fibers—is relatively new to the tunnel construction industry. This paper discusses the properties of shotcrete made with Type GUL cement when used in wet-mix shotcrete. Most importantly, it provides testing data related to early- and later-age compressive strength development, residual tensile strength, and experience with shotcrete application during construction.

### Code development

Since the early 2010s, CSA Group, the American Concrete Institute (ACI), ASTM International, the American Cement Association (ACA), and other authorities have started to require limestone to be added into the cement to reduce the use of portland cement (PC). Limestone is added into the clinker and ground to a fineness that is suitable for optimal cement hydration. Since 2016, CSA A3000:23[2] and CSA A23.1/A23.2[1] have added a requirement that Type GUL cement should include up to 15% limestone. ASTM C150/C150M-24[3] also requires that Type IL cement include 15% limestone. Type IL cement is already listed as an approved material for use in ACI 301-16[4] and ACI 318-19.[5] Type GUL and Type IL are very similar in chemical composition except that Type GUL is based on Canadian standards and Type IL is based on U.S. standards. For discussion purposes, Type GUL cement is used in this paper for both Type GUL and Type IL cement.

---

*ACI Materials Journal*, V. 123, No. 2, March 2026.

MS No. M-2024-451.R2, doi: 10.14359/51749444, received September 3, 2025, and reviewed under Institute publication policies. Pertinent discussion including author's closure, if any, will be published ten months from this journal's date if the discussion is received within four months of the paper's print publication.

## Table 1—Blaine fineness for Type GU and Type GUL cement

| Finess of cement | Type GU cement | CSA A3000:18 for Type GU cement | Type GUL cement | CSA A3000:23 for Type GUL cement |
|---|---|---|---|---|
| Blaine fineness, $m^3$/kg | 410 | None | 455 | None |
| Retained 45 μm, % | 1.4 | 28 minutes | 99 | 72 minutes |

## Blaine fineness

When limestone was originally introduced into Type GU cement at a replacement rate of up to 15%, it was found that concrete made with Type GUL cement took a longer time to set, early-age compressive strength development was slower, and the heat of hydration was reduced. These changes received mixed feedback from the industry. The delayed setting time and early-age compressive strength development extended the construction schedule, while the reduced heat of hydration was beneficial for thermal control for structural elements, such as walls and, in particular, mass concrete/shotcrete structures. Type GUL cement is typically ground slightly finer than conventional PC (450 to 500 $m^2$/kg Blaine fineness versus 350 to 420 $m^2$/kg), as shown in Table 1.

## Impact on compressive strength

Type GUL cement was reported to have a slightly lower early-age compressive strength but improved later-age compressive strength, such as at 56 and 91 days. This may not be beneficial for wet-mix shotcrete used for ground support as this requires higher early-age compressive strength. Later-age compressive strength is generally satisfactory, as the 28-day compressive strength can usually meet the specified compressive strength requirements. It is worth testing compressive strength at later ages to see if shotcrete made with Type GUL cement meets the later-age compressive strength requirement, particularly when used with an alkali-free accelerator (AFA).

## RESEARCH SIGNIFICANCE

Type GUL cement is being increasingly used in wet-mix shotcrete for ground support. Type GUL cement has a slower setting time compared to Type GU cement, and early-age compressive strength development between 1 and 24 hours can be affected and is expected to negatively affect performance requirements for ground support. The performance of wet-mix shotcrete with Type GUL cement has not been systematically studied and reported. To address this issue, trial shooting and testing were carried out in several civil tunnel construction projects to study the plastic properties, pumpability, setting time, early-age compressive strength development, compressive strength development at 7 and 28 days, residual tensile strength for beams, and flexural toughness for round determinate panels (RDPs).

This paper provides general guidance for design and performance of wet-mix shotcrete with Type GUL cement, including:

- Use of Type GUL cement wet-mix mixture that is suitable for shotcrete batching, pumping, shooting, and finishing;
- Effect of Type GUL cement on early- and later-age compressive strength development; and
- Residual tensile strength and flexural toughness for Type GUL wet-mix shotcrete with both macrosynthetic and steel-fiber shotcrete.

## Table 2—Wet-mix shotcrete design for ground support

| Material | Mass SSD aggregate, kg/$m^3$ |
|---|---|
| Type GUL cement | 410 |
| Silica fume | 40 |
| Coarse aggregate (14 to 5 mm, SSD) | 430 |
| Fine aggregate (SSD) | 1320 |
| Estimated water, L | 180 |
| Fiber* | |
| HRWRA, L | 1 |
| Accelerator† | 25 to 33 |
| Air content (as-batched 5 to 8%) | 2.5 to 5.5% (as-shot) |

*Either steel fiber or macrosynthetic fiber is added into wet-mix shotcrete.

†Accelerator dosage is adjusted to meet early-age compressive strength requirements.

Note: SSD is saturated surface-dry.

## EXPERIMENTAL PROGRAM

### Mixture design

Table 2 shows a wet-mix shotcrete mixture design with Type GUL cement that includes fibers and an accelerator.[6] The total cementitious materials content of cement plus silica fume is 450 kg/$m^3$. Sometimes, the total cementitious materials content is increased to facilitate pumping and increase both the early- and later-age compressive strength development. Silica fume is commonly used as an SCM for wet-mix shotcrete in tunnels. Silica fume is normally added at 5 to 10% by mass of total cementitious materials, with 8% being a common percentage. Fly ash, when used, is added at up to 15% by mass of the total cementitious materials. Slag, when used, is commonly added at up to 25% by mass of the total cementitious materials,[6] although it may be added at up to 70% by mass of cementitious materials for shotcrete structures.[7]

For wet-mix shotcrete application, an AFA is typically used to accelerate the cement hydration process and achieve early-age compressive strength development.[6] The reaction between the cementitious materials and AFA is critical for early-age compressive strength development, and this is tested in the present testing program.

Fibers are widely used in wet-mix shotcrete mixtures for ground support in underground construction.[6,8-11] Either steel or macrosynthetic fibers are mixed into the wet-mix shotcrete to provide post-crack strengthening and meet the flexural toughness requirement. In the present study, macrosynthetic fibers were added into wet-mix shotcrete with various dosages of AFA. The optimized AFA dosage was determined to develop the proper early-age compressive strength.

This dosage of AFA was used for the steel fiber-reinforced wet-mix shotcrete trial shoot and test program discussed in the paper.

### Water-cementitious materials ratio

The water-cementitious materials ratio (*w*/*cm*) is the ratio of the mass of water versus the mass of total cementitious materials, including cement and silica fume used in the mixture. The *w*/*cm* of wet-mix shotcrete with Type GUL cement is 0.40 for the present study. This is within the most widely used range of 0.38 to 0.42 for wet-mix shotcrete used in ground support, structural elements, repair, and other applications.[6,12,13] A higher *w*/*cm* can increase the slump and reduce the dosage of water-reducing admixture, but will reduce the compressive strength.

### Batching, mixing, and production

Wet-mix shotcrete was batched and supplied by a local ready mixed supplier. An ACI-certified wet-mix shotcreter sprayed the test panels with dimensions of 600 x 600 x 200 mm. The AFA was added at the nozzle during shooting. The wet-mix shotcrete pump was typical of that used in the shotcrete industry and conformed to ACI 506 requirements.[12,13] Overall, the shotcrete trial shoot met ACI 506 requirements[12,13] and was representative of proper application. The mixing and shooting were conducted at the first author's laboratory in Vancouver, BC, Canada. On-site monitoring of shotcrete batching, mixing, and test panel production was provided by the first author. Testing for plastic properties of the shotcrete was provided by an ACI-certified concrete testing technician.

## TEST RESULTS AND DISCUSSION

### Plastic properties

Wet-mix shotcrete made with Type GUL cement is expected to exhibit similar workability during pumping to wet-mix shotcrete made with Type GU cement. However, it was observed that mixtures made with Type GUL cement tend to bleed at higher slumps—that is, above 190 to 200 mm.[6,7] This becomes more prominent when no silica fume is added. With silica fume added, the mixture tends to be more cohesive and shows no signs of bleeding even at slumps of up to 220 mm.

### Dosage of high-range water-reducing admixture

For wet-mix shotcrete mixtures with Type GU cement, high-range water-reducing admixtures (HRWRAs) are generally added at a dosage of approximately 0.8 to 1.0 L/m$^3$ of HRWRA, or full-range water-reducing admixture including HRWRA to achieve the optimized slump of 150 to 200 mm during underground construction.[6] The dosage of HRWRA is generally higher in wet-mix shotcrete using Type GUL cement and is approximately 1.2 L/m$^3$ to achieve similar slump and workability. This is likely due to the fact that the Type GUL cement particles are ground finer with an increased surface area, which subsequently requires more free water to coat the surface of the cement particles. It should also be noted that the slight increase in the HRWRA dosage is intended to meet the workability and pumpability requirements, and will not cause significant changes in early- and later-age compressive strength development.

### Pumpability

Shotcrete pumpability refers to good workability for delivery/transport, and pumping.[6,7,14] Wet-mix shotcrete for ground support is required to be pumped under high pressure of 13.8 MPa and above. During the pumping process the mixture needs to maintain suitable consistency, cohesion, and workability.

When fibers are added into wet-mix shotcrete, pumpability will be affected depending on the fiber type and dosage. The present study trial batched and shot wet-mix shotcrete with macrosynthetic fibers and steel fibers separately. Factors including fiber dosage, type, and distribution were found to affect pumpability. High fiber dosage requires more paste to coat the fiber surface and therefore requires higher slump and workability for pumping. This can be achieved by increasing the dosage of HRWRA slightly to reach the desired slump for pumping. The number of fibers added into the wet-mix shotcrete also affects pumpability. When added at the same volume percent into wet-mix shotcrete, macrosynthetic fibers, with a density of 920 kg/m$^3$, will result in a much higher number of fibers compared to steel fiber with a density of 7800 kg/m$^3$. A higher number of fibers requires more paste content to coat the fiber and therefore requires slightly higher slump to facilitate pumping. Distribution of fibers is of great importance to pumping during wet-mix shotcrete application. Fibers require a proper batching and addition sequence and a robust mixing process for fibers to be distributed into the shotcrete materials properly. This is controlled by the batching, mixing, discharge, and transport processes, all of which require proper quality control.

When Type GUL cement is added, pumpability is generally not impacted significantly other than for the finer particle sizes of cement. However, wet-mix shotcrete generally has a sand ratio—that is, percent sand of the total aggregates—of 65 to 75%, compared to that of cast-in-place concrete of 40 to 50%, and therefore has a higher fine aggregate content. It should be noted that with a Blaine fineness of 450 to 500 m$^2$/kg for Type GUL cement, adding larger particles such as fly ash or slag can be beneficial to fill the gap of size distribution between the fine aggregate and the Type GUL cement powder.

### Early-age compressive strength development

Early-age compressive strength is one of the most important performance requirements for shotcrete used in ground support in tunnels and mines.[6,7,14,15] Early age, when used in ground support for underground construction, refers to 1 to 24 hours after accelerator is added at the nozzle into the shotcrete.[6,15] Generally, an early-age compressive strength of minimum 1.0 to 2.0 MPa is required for the applied shotcrete to facilitate construction activities.[6,15] For wet-mix shotcrete, AFA is commonly added at the nozzle at dosages required to achieve suitable early-age compressive strength development. AFA was developed in the late 1990s and early 2000s. AFA contains primarily aluminum sulfate and is non-alkaline, with a pH value of 2 to 4. Since

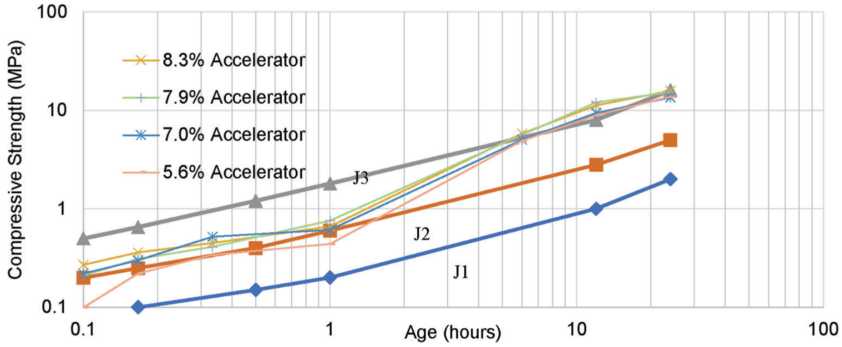

*Fig. 1—Early-age compressive strength development for macrosynthetic fiber-reinforced wet-mix shotcrete.*

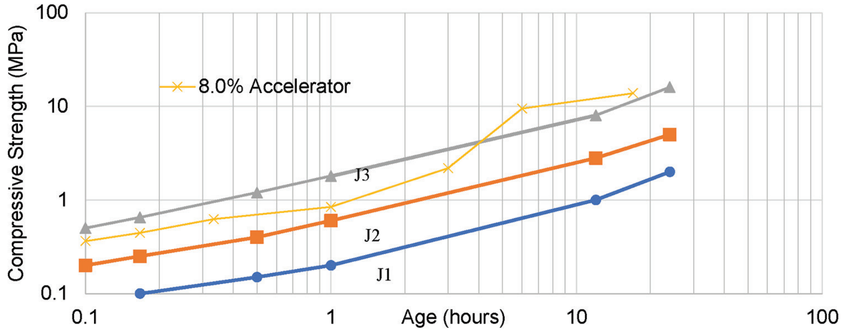

*Fig. 2—Early-age compressive strength development for steel fiber-reinforced wet-mix shotcrete.*

AFA was introduced into North America, it has been found that it generally takes an AFA dosage of approximately 6% by mass of cement to reach the required strength in 1 to 3 hours.[6] Variations in the early-age compressive strength development are dependent on the shotcrete mixture design, including the type of cement and chemical admixtures used, accelerator brand and performance, shotcrete temperature, ambient temperatures, proper handling and dispensing of accelerator, and shooting skills of the shotcreter.[6,8-11]

When Type GUL cement is used to replace Type GU cement, the early-age compressive strength development is affected. During recent projects, the authors tested early-age compressive strength with a needle penetrometer and end-beam tester. Figures 1 and 2 show typical early-age compressive strength development with AFA dosage when plotted against the J1-J2-J3 curve template developed by the Austrian Concrete Society.[15] J2 is generally regarded as the minimum performance requirement for shotcrete early-age compressive strength development for most ground support projects. For some ground conditions, including soft ground, a modified J2 is specified to allow a slightly higher early-age compressive strength to provide sufficient ground support.

Figure 1 shows the early-age compressive strength development of a wet-mix shotcrete with macrosynthetic fiber. The early-age compressive strength with 5.6% accelerator appeared not to meet the J2 requirement. At a dosage of 7.0% AFA, the early-age compressive strength marginally exceeded the J2 requirement. The early-age compressive strength increases with increasing accelerator dosages of 7.9% and 8.3%. This shows that a minimum of 7.0% AFA is needed to achieve the J2 requirement for the early-age compressive strength development.

Figure 2 shows the early-age compressive strength development of wet-mix shotcrete with steel fiber. The early-age compressive strength with 8.0% accelerator appeared to exceed the J2 requirement with a good margin of safety. These are very positive results for using Type GUL cement in wet-mix shotcrete for underground structures. The tunneling schedule is largely dependent on how fast the ground can be stabilized after wet-mix shotcrete is applied. The J2 curve is accepted in the tunneling industry as the most widely accepted criteria for early-age compressive strength development. With 8% AFA, which is higher than approximately 6% for wet-mix with Type GU cement,[6] the early-age compressive strength, which follows the J2 curve, develops fast and can sufficiently provide the required ground support for most ground conditions.

Early-age compressive strength development, shown in both Fig. 1 and 2, increases at a similar slope as the J2 curve for up to 3 to 4 hours, and then increases at a much faster rate than the J2 curve after 6 hours, and actually meets/exceeds the J3 curve. This shows that the compressive strength develops faster after 4 to 6 hours. The early-age strength development for steel fiber-reinforced wet-mix shotcrete and the macrosynthetic fiber-reinforced wet-mix shotcrete are similar.

In summary, the trial batch shooting and testing results for both macrosynthetic fiber and steel-fiber mixtures showed that the wet-mix shotcrete with Type GUL cement can meet the J2 curve requirement with dosages of 7.0% AFA by mass of cement. This appears to be slightly higher than the 6.0% AFA commonly used in wet-mix shotcrete made with Type GU cement.[6,8-11] The increased dosage of AFA was likely due to the reduced reactivity of Type GUL cement with 15% limestone and the increased fineness of the Type GUL cement particles, which requires more liquid to coat to initiate the cement hydration process in the first several hours.

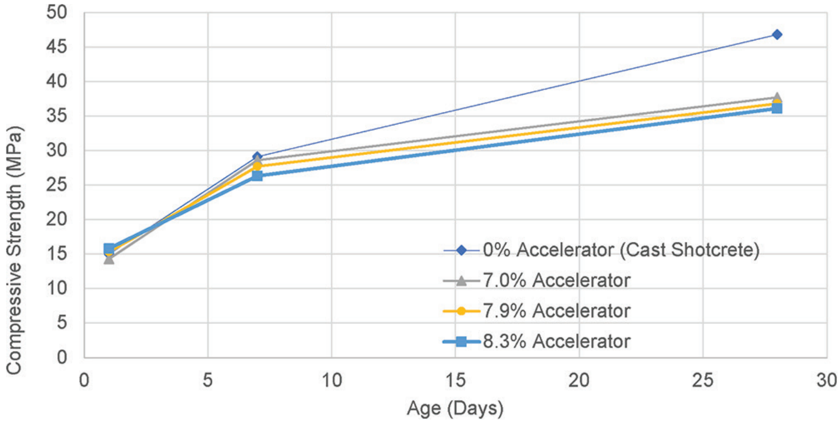

*Fig. 3—Compressive strength development for macrosynthetic fiber-reinforced wet-mix shotcrete.*

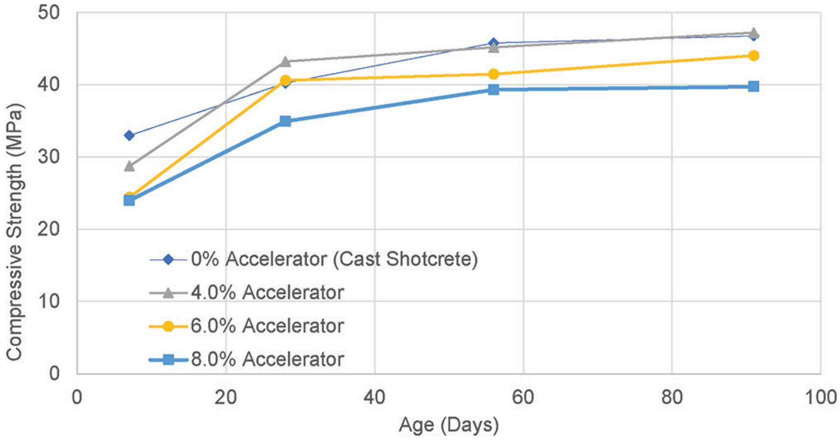

*Fig. 4—Compressive strength development for steel fiber-reinforced wet-mix shotcrete.*

## Compressive strength development

Compressive strength for wet-mix shotcrete is normally specified at 3, 7, and 28 days. Shotcrete test panels were produced and cured for 2 days. Cores were extracted from the test panels and delivered to the testing laboratory, where they were stored at standard laboratory curing conditions with 100% moisture and 23 ± 2°C temperature. Compressive strength testing for shotcrete cores is specified in ASTM C1604/C1604M-05(2019).[16]

Compressive strength development for wet-mix shotcrete is dependent on factors such as *w/cm*, cementitious materials type and content, as-shot air content, age of testing, consolidation of shotcrete, curing and handling of test panels, and most importantly, the dosage of AFA.[6]

Figure 3 shows that compressive strength for macrosynthetic fiber-reinforced wet-mix shotcrete increases with age but reduces with dosages of AFA. Compressive strength increases with age from 1 day to 7 and 28 days. At each age, compressive strength decreases with increasing dosages of AFA. Without accelerator—that is, in a cast shotcrete mixture—compressive strength can reach 47 MPa at 28 days, but will reduce to 36 MPa with an AFA of 8.3% by mass of cement. This is an approximately 23% reduction in compressive strength at 28 days for wet-mix shotcrete without AFA compared to wet-mix shotcrete with up to 8.3% accelerator. It should be noted that the cast shotcrete has an as-batched air content of 6.6%, while the shot shotcrete has an as-shot air content of 4.3%. The reduction in the air content generally increases the compressive strength. Therefore, the increase in the compressive strength due to air content reduction is offset by the addition of the accelerator.

Figure 4 shows the compressive strength development for steel fiber-reinforced wet-mix shotcrete at 7, 28, 56, and 91 days. The compressive strength reached 41 MPa for cast shotcrete without AFA. With 4% AFA, the 28-day compressive strength is close to 43 MPa. Compressive strength results for both cast shotcrete and shotcrete with 4% AFA are close at ages of 56 and 91 days. The as-batched air content was 8.6% and the as-shot air content was 4.9%. Typically, reduction in air content during shooting increases the compressive strength,[14] and this results in higher compressive strength for the shot wet-mix shotcrete mixture than that for the cast wet-mix shotcrete mixture. When the AFA is added into the wet-mix shotcrete through the shooting process, compressive strength will reduce with increasing AFA dosages at 91 days, as shown in Fig. 4. Compressive strength reduces by 2 to 3 MPa for wet-mix shotcrete with 4% AFA compared to that with 6% AFA, and reduces by another 2 to 3 MPa compared to that with 8% AFA. It is noted that shotcrete with 4% AFA has a higher compressive strength than cast shotcrete at 28 days, but similar compressive strength at both 56 and 91 days. The variation in compressive strength may be caused by testing variations, including compressive strength results from different core samples, as observed for wet-mix shotcrete with Type GU cement.[17]

Figure 4 shows that the compressive strength increases significantly from 7 to 28 days, but much less from 28 to 56 days, and just slightly increases from 56 to 91 days. This shows that although compressive strength results at 91 days are expected to be higher than those at 28 days, the increase is minimal. Therefore, regardless of the contribution of the later-age compressive strength by the Type GUL cement, 28-day compressive strength should be specified for the wet-mix shotcrete with AFA.

Figure 4 also shows that compressive strength reduces with increasing AFA dosages up to 8.0%.

Reduction in compressive strength with increasing AFA dosage is commonly seen in Type GU wet-mix shotcrete with AFA. The authors tested Type GU wet-mix shotcrete with various AFAs and observed a 25 to 35% reduction in compressive strength from 0 to 8% AFA.[6-11,14,16,17] The addition of AFA on compressive strength for wet-mix shotcrete with Type GUL cement is observed to reduce the compressive strength of wet-mix shotcrete with Type GU cement. It should be noted that reductions in compressive strength in the present research are approximately 23% for nonaccelerator compared to that with 8.3% accelerator for wet-mix with macrosynthetic fiber, and approximately 2 to 3 MPa for wet-mix shotcrete with steel fiber with AFA dosages from 4 to 6% and to 8%. This is not as significant as those reported for wet-mix shotcrete with Type GU cement. However, this needs to be further studied to establish the general trend of impact on compressive strength with increasing dosages of AFA for wet-mix shotcrete with Type GUL cement.

*Fig. 5—Fiber-reinforced wet-mix shotcrete notched beam tested according to EN 14651.*

## Fiber-reinforced wet-mix shotcrete

Nowadays, macrofibers, including the most commonly used macrosynthetic fiber and steel fibers, are added into the wet-mix shotcrete for ground support. Fiber-reinforced wet-mix shotcrete, when used with rock bolts, has become the predominant method of ground support in tunnels and mines across the United States and Canada.[6,8-11] When added into shotcrete, fibers contribute to crack resistance after shotcrete cracks—that is, they minimize cracks from widening by fiber deformation and elongation, fiber pullout, and fiber fracture. Due to the addition of fibers, shotcrete is able to bear the load after shotcrete cracks and absorb energy as cracks propagate. The performance of fiber-reinforced wet-mix is characterized by the energy absorbed, also called flexural toughness or residual tensile strength during the post-crack period.

## Residual tensile strength development

Residual tensile strength testing according to the EN 14651:2005[18] and EN 14488-3:2023 standards[19] is gradually being used more frequently in the civil tunnel industry in the United States and Canada.[6] The residual tensile strength test is conducted for beams with dimensions of 150 x 150 x 550 mm. A notch, at a depth of 25 mm, is cut in the center of the tension face of the beam, as indicated in Fig. 5. The beam is therefore precracked and then loaded in three-point bending. The deformation of the beam is recorded as the opening of the crack at the bottom notch—that is, crack mouth opening displacement (CMOD). The test sample is loaded with a closed-loop testing machine, and the load-versus-CMOD curve is recorded during the test (Fig. 6).

Wet-mix shotcrete with macrosynthetic and steel fibers was shot and tested. Residual tensile strength tests were conducted according to EN 14651—the notched-beam test method. Figure 7 shows the residual tensile strength results

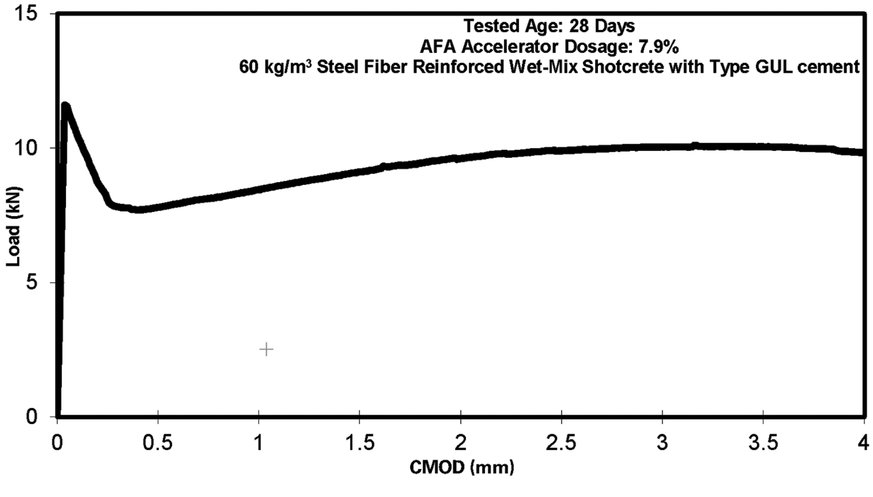

*Fig. 6—Load versus CMOD for fiber-reinforced wet-mix shotcrete notched beam tested according to EN 14651.*

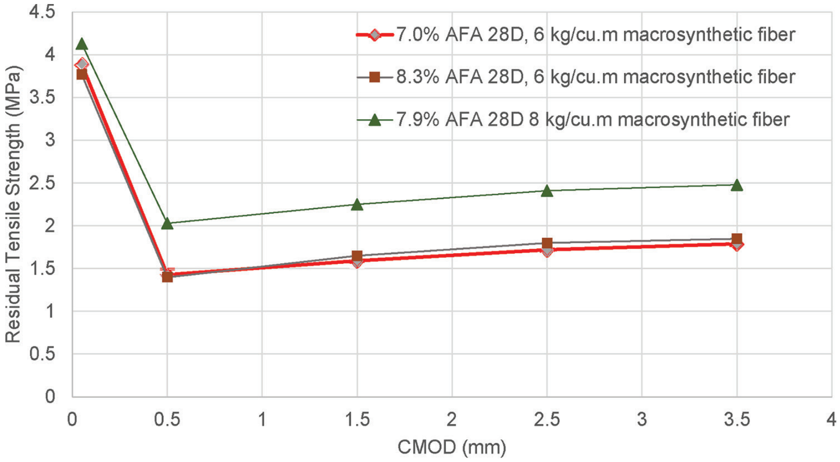

*Fig. 7—Residual tensile strength for macrosynthetic fiber-reinforced wet-mix shotcrete tested according to EN 14651.*

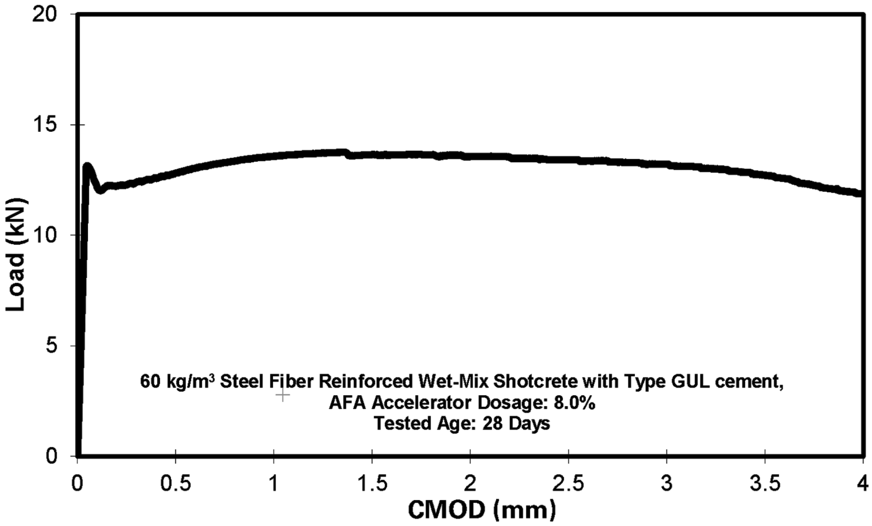

*Fig. 8—Load versus CMOD for steel fiber-reinforced wet-mix shotcrete notched beam tested according to EN 14651.*

for macrosynthetic fiber-reinforced wet-mix shotcrete, and Fig. 8 shows the residual tensile strength results for steel fiber-reinforced wet-mix shotcrete.

Figure 7 shows the results of residual tensile strength for macrosynthetic fiber at a dosage of 8 kg/m$^3$ with an AFA dosage of 7.9% and 6 kg/m$^3$ macrosynthetic fiber dosage with an AFA dosage of 8.3% and 7.0%, respectively. Results of the limit of proportionality (LOP)—that is, the peak tensile strength at CMOD < 0.05 mm—and residual tensile strength at CMOD of 0.5, 1.5, 2.5, and 3.5 mm are plotted in Fig. 7. Each data point is the average of nine beams tested at 28 days. Therefore, these results are statistically representative of a large sample population.

Figure 7 shows that wet-mix shotcrete with a higher macrosynthetic fiber dosage of 8.0 kg/m$^3$ resulted in higher residual tensile strength, including 2.5 MPa at CMOD of 3.5 mm, while it exhibited lower residual tensile strength of approximately 1.8 MPa with a macrosynthetic fiber dosage of 6.0 kg/m$^3$. The ratio of residual tensile strength versus dosage of fiber is approximately 0.3 for the wet-mix shotcrete for both fiber dosages. The most commonly specified residual tensile strength value for ground support is approximately 2.0 to 2.4 MPa at CMOD of 3.5 mm. Therefore, a macrosynthetic fiber dosage of 8 kg/m$^3$ is generally recommended for wet-mix shotcrete with AFA for ground support purposes. This has been consistently observed by the authors in several hundred beam residual tensile strength tests on wet-mix shotcrete with several high-performance macrosynthetic fibers in major tunnel projects across the United States and Canada.[6]

Figure 7 also shows that wet-mix shotcrete with a fiber content of 6.0 kg/m$^3$ but with two dosages of AFA exhibited close performance of residual tensile strength. This shows that although dosages of AFA affect the early-age compressive strength and compressive strength at 7 and 28 days, it has a minimal impact on residual tensile strength.

Wet-mix shotcrete with macrosynthetic fibers tends to have a lower load-bearing capacity at lower CMOD, such as 0.5 to 1.0 mm, but then increases at larger CMOD of up to 3.5 mm. This shows that macrosynthetic fibers tend to bear higher loads at larger CMOD—that is, larger deformations. This makes the macrosynthetic fiber beneficial for higher deformations related to larger ground movement.

Steel fibers were shot and tested at dosages of 40, 50, and 60 kg/m$^3$ and an AFA dosage of 8.0%. Results of LOP (the peak tensile strength at CMOD < 0.05 mm) and residual tensile strength at CMOD of 0.5, 1.5, 2.5, and 3.5 mm are plotted in Fig. 9. Each data point is the average of nine beams

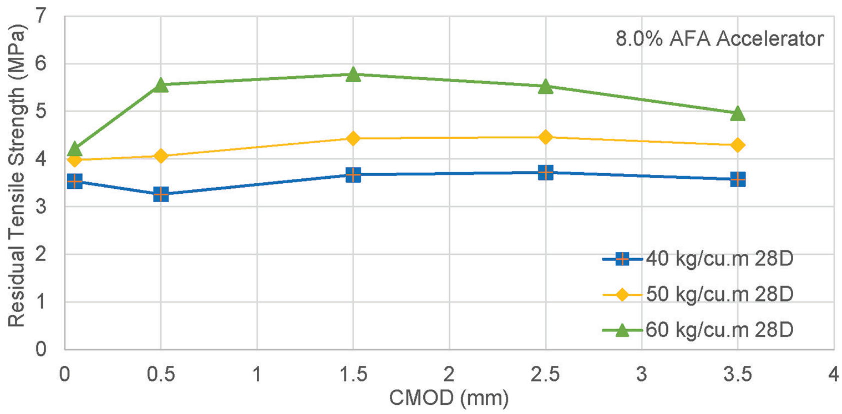

*Fig. 9—Residual tensile strength test for steel fiber-reinforced wet-mix shotcrete.*

*Fig. 10—Shooting and production of RDP (left); testing (middle); and failure pattern (right).*

tested at age 28 days. Therefore, these results are statistically representative of a large sample population.

A typical load-versus-CMOD curve is plotted in Fig. 8. It shows that the load-bearing capacity decreases slightly after the LOP, but increases at low CMOD, such as less than 0.5 mm. The load-bearing capacity then increases to the peak value at a larger CMOD, such as at approximately 1.0 mm, as shown in Fig. 8. This peak load value is higher than the load of LOP. This is also called a strain-hardening effect—that is, the post-peak load-bearing capacity (residual tensile strength) exceeds the load when the beam first cracks (LOP). This strain-hardening behavior in fiber-reinforced wet-mix shotcrete is very beneficial for ground support as it provides confidence for using fiber-reinforced wet-mix shotcrete to provide sufficient ground support even when shotcrete cracks occur. The strain-hardening behavior occurs with high-performance steel fibers. It is dependent on fiber dosages, strength, types, and bond with the shotcrete. It is also related to the shotcrete mixture design and process, including equipment, and most importantly, the shotcreter's shooting skill.[6]

Figure 9 shows the results of LOP and residual tensile strength for wet-mix shotcrete with steel fibers at dosages of 40, 50, and 60 kg/m$^3$. It clearly shows that the residual tensile strength increases with increasing fiber dosages. Figure 9 also shows that the load-bearing capacity at first crack (LOP) increases with increasing fiber dosages from 40 to 50 and 60 kg/m$^3$.

Figure 9 shows that wet-mix shotcrete with steel fiber at dosages of 50 and 60 kg/m$^3$ exhibits strain-hardening behavior—the post-crack residual tensile strength is higher than the tensile strength at first crack (LOP). Wet-mix shotcrete with steel fiber at a dosage of 40 kg/m$^3$, however, does not have a significant strain-hardening behavior.

Wet-mix shotcrete with steel fibers tends to have higher load-bearing capacity (residual tensile strength) at lower deformations (small CMOD). The residual tensile strength increases to a peak value with increasing CMOD of 1 mm, and then decreases at larger CMOD of up to 3.5 mm. This shows that steel fiber is beneficial for lower deformations—that is, small ground movement.

The residual tensile strength behavior of wet-mix shotcrete using Type GUL cement is consistent with observations of wet-mix shotcrete with Type GU cement. Characteristics of wet-mix shotcrete with both steel fibers and macrosynthetic fibers are consistent with what has been observed by the authors.[6,8-11]

## Flexural toughness development with round determinate panels according to ASTM C1550

Flexural toughness performance of fiber-reinforced shotcrete can also be evaluated by conducting the RDP test according to ASTM C1550-20.[20] A round panel with a diameter of 800 mm and thickness of 75 mm was centrally loaded on the top and supported with three rotary supports 120 degrees apart (Fig. 10). Deflection was measured with a linear variable displacement transducer (LVDT). Provided the fibers are distributed uniformly across the panel, there will be three radius cracks between each support point.

The energy absorption is defined as the area underneath the load-versus-deflection curve, as shown in Fig. 11 and 12.

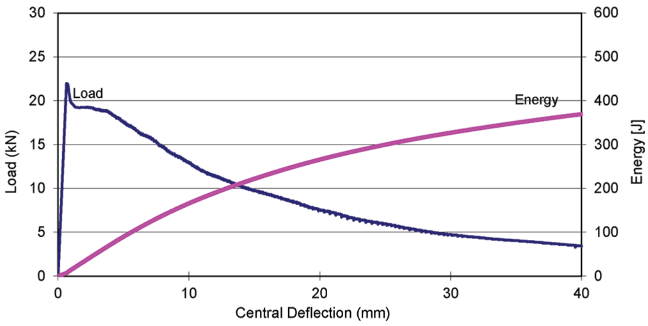

*Fig. 11—Load-versus-deflection curve for steel fiber-reinforced wet-mix shotcrete.*

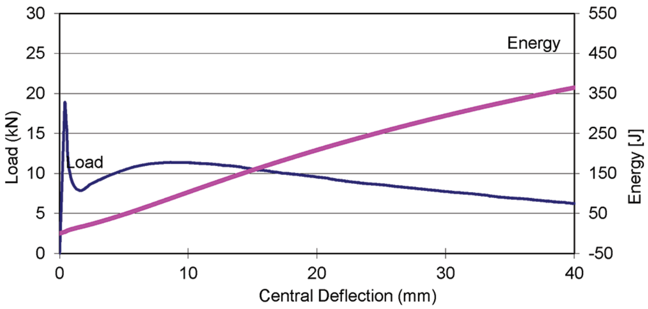

*Fig. 12—Load-versus-deflection curve for macrosynthetic fiber-reinforced wet-mix shotcrete.*

**Table 3—Summary and comparison of flexural toughness of steel-fiber and macrosynthetic fiber-reinforced wet-mix shotcrete**

| Steel-fiber shotcrete | At center point deflection of | | | | | |
|---|---|---|---|---|---|---|
| 35 kg/m$^3$ | Peak load | 7 mm | 10 mm | 20 mm | 30 mm | 40 mm |
| Corrected load, kN | 22.0 | 15.8 | 13.0 | 7.5 | 4.8 | 3.4 |
| Load versus first peak load | 100% | 72% | 59% | 34% | 22% | 16% |
| Corrected energy, J | 7.11 | 123 | 166 | 266 | 327 | 370 |
| Macrosynthetic fiber | At center point deflection of | | | | | |
| 6 kg/m$^3$ | Peak load | 7 mm | 10 mm | 20 mm | 30 mm | 40 mm |
| Corrected load, kN | 19.9 | 11.2 | 11.4 | 9.6 | 7.7 | 6.2 |
| Load versus first peak load | 100% | 56% | 57% | 48% | 39% | 31% |
| Corrected energy, J | 3.76 | 69 | 103 | 209 | 295 | 365 |

Figure 11 shows the load-versus-deflection curve for steel fiber-reinforced wet-mix shotcrete with Type GUL cement. It shows that the load reached a peak of approximately 22.7 kN at <1.0 mm deflection and this is where crack initiation started to propagate. At lower deflections of up to 3 mm, the load reduced to 18 to 19 kN and is 79 to 84% of the peak load. It then gradually decreased with increasing deflection. The load reduced to approximately 3.4 kN at a deflection of 40 mm.

Figure 12 shows the load-versus-deflection curve for macrosynthetic fiber-reinforced shotcrete. It shows that the load reached a peak of 18.9 kN at a deflection of <1.0 mm and immediately dropped to approximately 8 kN at a deflection of 1.5 mm. Then load then started to ascend to 11 kN at a deflection of 8 to 10 mm, and then reduced, at a much slower rate, to approximately 6.2 kN at a deflection of 40 mm.

Table 3 summarizes the peak load, residual load, and flexural toughness at various deflections. Both steel and macrosynthetic fiber-reinforced wet-mix shotcrete achieved similar flexural toughness (approximately 370 J) at a deflection of 40 mm. However, RDP with steel-fiber wet-mix shotcrete tends to retain a higher percentage of load-bearing capacity at smaller deflections—of <5.0 mm—while macrosynthetic fiber has a much lower load-bearing capacity at the same range of deflection, as detailed in Fig. 11 and 12. At larger deflections, such as 30 and 40 mm, the load-bearing capacity of steel fiber-reinforced wet-mix shotcrete is approximately 22% and 16% of the peak load, while it is approximately 39% and 31% for macrosynthetic fiber-reinforced wet-mix shotcrete. This indicates that the macrosynthetic fiber is able to withstand a higher load-bearing capacity at much larger deflections, such as 30 to 40 mm deflection, and this makes the macrosynthetic fiber-reinforced wet-mix shotcrete a good material for large ground movement, or deformation or convergence often called for in the mining industry. Steel fiber, on the other hand, is found to be able to withstand a higher load-bearing capacity at smaller deflections, and this makes steel fiber-reinforced wet-mix shotcrete a good material for smaller ground movement criteria, such as in the civil tunnel industry. All of these mechanical behaviors discussed herein are found to be consistent with that generally observed and reported in the industry with fiber-reinforced wet-mix shotcrete using Type GU cement.[6,8-11] Using Type GUL cement as a replacement for Type GU cement is not expected to significantly change mechanical behavior for fiber-reinforced shotcretes.

## FUTURE RESEARCH

The reactivity of AFA with Type GUL cement needs further study and investigation—in particular, Type GUL cement from different suppliers with different limestone content (less than 15%) and therefore different chemical components is worth studying.

The compressive strength reduction of wet-mix shotcrete Type GUL cement with increasing dosages of AFA needs to be further studied. The general trend of the reduction needs to be studied and established to provide a guideline for designers to refer to.

The strength of concrete and shotcrete with Type GUL cement still remains a challenge, as limestone hydration leads to excessive $Ca(OH)_2$, which remains a weaker link, and concrete will behave poorly if exposed to fire and high-temperature hazards. This aspect was not studied and will be studied in the future.

In addition, the addition of mineral pozzolans has been discussed and found to have a positive impact on workability and compressive strength development in concrete, but their effects are not known in wet-mix shotcrete. This will also be considered for future research.

## CONCLUSIONS

With proper mixture design, wet-mix shotcrete with Type GUL cement can be pumped properly. Slightly higher slump is required when silica fume and fibers are added.

When used in wet-mix shotcrete, Type GUL cement requires a slightly higher dosage of alkali-free accelerator (AFA) compared to that with Type GU cement to achieve the desired early-age compressive strength for ground support—that is, meeting the Austrian Concrete Society J2 curve.

Compressive strength for wet-mix shotcrete with Type GUL cement generally reduces with increasing AFA dosages, except that the wet-mix shotcrete mixture with 4% AFA has slightly higher strength than the cast shotcrete mixture with 0% AFA at both 28 and 56 days. The reduction in compressive strength in wet-mix shotcrete using Type GUL cement appears not to be as significant as the reduction with wet-mix shotcrete using Type GU cement. Further studies need to be conducted to establish the general trend of impact on compressive strength with increasing dosages of AFA for wet-mix shotcrete with Type GUL cement.

Wet-mix shotcrete with Type GUL cement exhibited similar behavior to shotcrete made with Type GU cement for residual tensile strength development with the notched-beam test and flexural toughness with the round determinate panel (RDP) test for both steel and macrosynthetic fibers.

In summary, Type GUL cement is rapidly becoming the most widely used cement in wet-mix shotcrete for ground support in North America. Wet-mix shotcrete with Type GUL cement appears to require increased dosages of AFA to develop the proper early-age compressive strength. Wet-mix shotcrete with Type GUL cement appears to develop compressive and residual tensile strengths similar to those reported for wet-mix shotcrete made with Type GU cement.[6-11,14,17] As more and more project experience becomes available, Type GUL cement will become the most commonly used cement in wet-mix shotcrete projects in North America. More testing results from future research as well as industrial projects will provide further details on the performance of wet-mix shotcrete with Type GUL cement.

## AUTHOR BIOS

**Lihe (John) Zhang**, *FACI, is a Principal Engineer at LZhang Consulting & Testing Ltd. He received his PhD in civil engineering from The University of British Columbia, Vancouver, BC, Canada. He is Chair of ACI Subcommittee 506-F, Shotcreting-Underground, and a member of ACI Committees 506, Shotcreting, and 544, Fiber-Reinforced Concrete. He is an ACI C660-approved Shotcreter Examiner. His research interests include fiber-reinforced concrete, concrete and shotcrete technology, and the evaluation and rehabilitation of infrastructure.*

**Matthew Zhang** *is a Grade 12 Student at St. Georges Senior School, Vancouver, BC, Canada. His research interests include engineering and materials testing, and he is involved in laboratory testing for beams and round panels, data analysis for the present results, and preparation of this paper.*

**Dudley R. (Rusty) Morgan**, *FACI, is a Civil Engineer with over 50 years of experience in the concrete and shotcrete industries. He served as a member and Secretary of ACI Committee 506, Shotcreting, for over 25 years.*

**Sidney Mindess**, *FACI, is a Professor Emeritus in the Department of Civil Engineering at The University of British Columbia. His research interests include cement and concrete technology, with a particular interest in fiber-reinforced concrete and the behavior of concrete under impact loading.*

## REFERENCES

1. CSA A23.1:24/A23.2:24, "Concrete Making Materials and Methods of Concrete Construction/Test Methods and Standard Practice for Concrete," CSA Group, Toronto, ON, Canada, 2024.

2. CSA A3000:23, "Cementitious Materials Compendium," CSA Group, Toronto, ON, Canada, 2023.

3. ASTM C150/C150M-24, "Standard Specification for Portland Cement," ASTM International, West Conshohocken, PA, 2024, 9 pp.

4. ACI Committee 301, "Specifications for Structural Concrete (ACI 301-16)," American Concrete Institute, Farmington Hills, MI, 2016, 64 pp.

5. ACI Committee 318, "Building Code Requirements for Structural Concrete (ACI 318-19) and Commentary (ACI 318R-19) (Reapproved 2022)," American Concrete Institute, Farmington Hills, MI, 2019, 624 pp.

6. Zhang, L., and Morgan, D. R., "Advances in Shotcrete Technology for Ground Support in Tunnels and Mines in North America," Tunnelling Association of Canada (TAC 2021), Toronto, ON, Canada, Oct. 21-24, 2021.

7. Zhang, L.; Morgan, D. R.; Kirk, I.; Rolland, A.; and Karchewski, R., "Mass Shotcrete Wall Construction and Thermal Control Plan," *ACI Materials Journal*, V. 118, No. 3, May 2021, pp. 71-82.

8. Zhang, L.; Morgan, D. R.; Moalli, S.; Gagnon, D.; and Dugas, D., "Tunnel Shotcrete Lining for Hydroelectric Projects in British Columbia, Canada," *Shotcrete*, Summer 2019, pp. 40-48.

9. Zhang, L., and Morgan, D. R., "Fiber Reinforced Shotcrete Tunnel Lining Quality Control and Testing in North America," 10th World Tunnel Congress, Vancouver, BC, Canada, May 2009.

10. Zhang, L., and Morgan, D. R., "Quality Control for Wet-Mix Fiber Reinforced Shotcrete in Ground Support," *Proceedings of Shotcrete for Underground Support XII*, M. Lu, O. Sigl, and G. Li, eds., Singapore, Oct. 11-13, 2015, 13 pp.

11. Zhang, L., and Morgan, D. R., "Recent Development of Shotcrete in Western Canada," Proceedings of the 7th International Symposium on Sprayed Concrete Modern Use of Wet Mix Sprayed Concrete for Underground Support, Sandefjord, Norway, June 16-19, 2014.

12. ACI Committee 506, "Shotcrete—Guide (ACI PRC-506-22)," American Concrete Institute, Farmington Hills, MI, 2022, 52 pp.

13. ACI Committee 506, "Specifying Underground Shotcrete—Guide (ACI PRC-506.5-22)," American Concrete Institute, Farmington Hills, MI, 2022, 61 pp.

14. Zhang, L.; Morgan, D. R.; and Mindess, S., "Comparative Study on Transport Properties of Shotcrete versus Cast-in-Place Concrete," *ACI Materials Journal*, V. 113, No. 3, May-June 2016, pp. 373-384.

15. Austrian Concrete Society, "Guideline: Sprayed Concrete," third edition, Vienna, Austria, 2013.

16. ASTM C1604/C1604M-05(2019), "Standard Test Method for Obtaining and Testing Drilled Cores of Shotcrete," ASTM International, West Conshohocken, PA, 2019, 6 pp.

17. Zhang, L., and Morgan, D. R., "Variability of Compressive Strength for Shotcrete," Proceedings of the 7th International Symposium on Sprayed Concrete Modern Use of Wet Mix Sprayed Concrete for Underground Support, Sandefjord, Norway, June 16-19, 2014.

18. EN 14651:2005, "Test Method for Metallic Fibered Concrete," European Committee for Standardization, Brussels, Belgium, 2005, 21 pp.

19. EN 14488-3:2023, "Testing Sprayed Concrete – Part 3: Flexural Strengths (First Peak, Ultimate and Residual) of Fibre Reinforced Beam Specimens," European Committee for Standardization, Brussels, Belgium, 2023, 24 pp.

20. ASTM C1550-20, "Standard Test Method for Flexural Toughness of Fiber Reinforced Concrete (Using Centrally Loaded Round Panel)," ASTM International, West Conshohocken, PA, 2020, 14 pp.

ACI MATERIALS JOURNAL TECHNICAL PAPER

Title No. 123-M23

# Mitigating Chloride-Ion Ingress in Cement Composite Using Nanosilica

by Fulin Qu, Hanbing Zhao, Qiao Wang, Kejin Wang, and Wengui Li

*Building resilient infrastructure in chloride-rich environments presents significant challenges. This study examines the impact of nanosilica (NS) and ground-granulated blast-furnace slag (GGBFS) on chloride ingress in cement composites exposed to seawater, NaCl solution, and a combined NaCl-$Na_2SO_4$ solution. Analysis using microcharacterization, backscattered electron energy-dispersive spectroscopy (BSE-EDS) hypermaps, and thermodynamic modeling reveals that GGBFS enhances chloride binding by forming Friedel's salt (FSS) across all environments, effectively immobilizing chloride ions. NS further refines the cement matrix by densifying the calcium-silicate-hydrate (C-S-H) structure and generating additional C-S-H gels, improving physical chloride binding. This combined effect reduces porosity and strengthens resistance to chloride diffusion. Sulfate ions significantly influence hydration products and chloride binding, with excessive sulfate-reducing FSS formation, thereby weakening chloride resistance. Sulfate may also convert FSS into monosulfate (AFm) and ettringite (AFt), altering chloride immobilization. Cement composites containing both GGBFS and NS demonstrated superior resistance to chloride and sulfate exposure, as confirmed by thermodynamic modeling. These findings provide insights into sulfate-chloride interactions and offer guidance for developing durable cementitious materials in aggressive environments.*

**Keywords:** chloride ingress; durability; nanosilica (NS); pozzolanic activity; quantified hypermaps; sulfate-chloride dynamics.

## INTRODUCTION

Cementitious composites are essential for marine infrastructure, including ports, offshore platforms, and coastal defenses, due to their adaptability and cost-efficiency.[1-4] However, their vulnerability to chloride-induced degradation threatens long-term durability and structural integrity.[5,6] Chloride ingress occurs through multiple pathways, such as deicing salts, seawater exposure, and the use of chloride-contaminated aggregates or mixing water.[7-9] This infiltration compromises the passive film protecting steel reinforcements, accelerating corrosion.

In cementitious matrixes, chloride ions exist in two forms: free and bound.[10,11] Free chlorides move freely through the matrix, posing a corrosion risk to steel reinforcement. In contrast, bound chlorides are immobilized within calcium chloroaluminate hydrates such as Friedel's salt (FSS) or Kuzel's salt, or adsorbed into calcium-silicate-hydrate (C-S-H) phases, preventing further penetration.[12,13] Converting free chlorides to a bound state significantly reduces their corrosive potential, protecting embedded steel from corrosion.[14,15] Factors influencing chloride binding include the presence of $C_3A$ in the cement matrix and the use of supplementary cementitious materials (SCMs) or nanomaterials.[16-19]

Replacing ordinary portland cement (OPC) with ground-granulated blast-furnace slag (GGBFS), a common SCM, enhances chloride binding and improves resistance to chloride ingress.[20-22] Otieno et al.[23] found that GGBFS particle fineness and chemical composition significantly affect its chloride resistance. In related studies, Ogirigbo et al.[24-26] further demonstrated that elevated temperatures improve chloride binding in GGBFS-blended cements due to increased hydration. This improved resistance is largely attributed to GGBFS's higher alumina content, which promotes FSS formation.[27] GGBFS-blended cements also exhibit increased C-S-H formation, which binds approximately two-thirds of the chloride ions. However, GGBFS composition varies between manufacturing plants, complicating efforts to establish a clear correlation between its chemical makeup and chloride resistance.[28]

Nanosilica (NS), known for its strong pozzolanic reactivity, can enhance the chloride resistance of SCM-augmented cement composites.[29,30] Liu et al.[31] reported that adding 0.5 wt. % colloidal NS to fly ash-based cement composites improved chloride binding by promoting hydrated gel formation. However, research into the impact of NS on the chloride ingress resistance of GGBFS-based cement composites remains limited. Sulfate ions can also affect the stability of bound chlorides, sometimes exacerbate chloride ingress, and increase corrosion risks. Recent research indicates that sulfate interactions with composite components can alter hydration products, potentially worsening chloride penetration.[32,33] This study investigates the combined effects of GGBFS, NS, and sulfates, focusing on their roles in enhancing the microstructural integrity and density of hydration products to reduce chloride ingress. The study evaluates GGBFS and NS's ability to mitigate sulfate-induced deterioration and improve chloride immobilization, thereby reducing corrosion risks for reinforcing steel.

Therefore, this study employs various analytical techniques to examine interactions within the system. Powdered samples were first dried under controlled conditions, followed by tests to assess chloride-binding properties and phase assemblages. Using microstructural analysis and

---

*ACI Materials Journal*, V. 123, No. 2, March 2026.

MS No. M-2024-473.R4, doi: 10.14359/51749257, received August 10, 2025, and reviewed under Institute publication policies. Pertinent discussion including author's closure, if any, will be published ten months from this journal's date if the discussion is received within four months of the paper's print publication.

**Table 1—LOI and chemical compositions of OPC and GGBFS, %**

| Material | $SiO_2$ | $Al_2O_3$ | $Fe_2O_3$ | CaO | MgO | $K_2O$ | $Na_2O$ | $P_2O_5$ | $SO_3$ | Others | LOI |
|---|---|---|---|---|---|---|---|---|---|---|---|
| GGBFS | 35.3 | 15.4 | 0.31 | 38.3 | 6.19 | 0.85 | 0.00 | 0.00 | 2.37 | 1.28 | 1.64 |
| OPC | 18.99 | 4.79 | 3.10 | 65.72 | 1.38 | 0.79 | 0.17 | 0.08 | 4.53 | 0.45 | 2.35 |

**Table 2—Mineral composition of OPC determined by XRD-Rietveld**

| Minerals | % |
|---|---|
| $C_3S$ | 55.7 |
| $C_2S$ | 15.4 |
| $C_3A$ | 5.7 |
| $C_4AF$ | 10.9 |

characterizations, this investigation explores how GGBFS, NS, and sulfate interactions influence material stability, aiming to improve resistance to environmental challenges. The findings are expected to support the development of durable cementitious composites for chloride-rich marine environments, advancing civil and coastal engineering practices.

## RESEARCH SIGNIFICANCE

This study presents a targeted approach to enhancing the durability of cementitious composites in chloride- and sulfate-rich environments by incorporating NS and GGBFS. The combined use of these supplementary materials promotes the formation of additional C-S-H, reduces capillary porosity, and enhances chemical binding with chloride ions. This synergistic effect not only limits chloride transport but also increases resistance to chemical deterioration. Furthermore, the interaction between sulfate ions and hydration products is evaluated to better understand the competitive binding mechanisms affecting long-term performance. The findings provide new insights into the chloride-binding behavior of blended systems and support the design of more durable cementitious materials for use in marine and sulfate-laden environments.

## EXPERIMENTAL PROGRAM

### Raw materials

This study used CEM I 42.5N OPC, GGBFS, and laboratory-grade powdered NS. The Blaine fineness values for OPC and GGBFS were 347 and 418 $m^2$/kg, with specific gravities of 3.15 and 2.92, respectively. NS, with a mean particle size of 20 nm, contained 99% $SiO_2$. The loss on ignition (LOI) and chemical compositions of OPC and GGBFS were determined using X-ray fluorescence (XRF), as shown in Table 1. The mineral composition of OPC was analyzed using X-ray diffraction (XRD)-Rietveld analysis (Table 2). Chloride solutions were prepared using laboratory-grade NaCl and $Na_2SO_4$ salts.

### Mixture proportions and cement mortar preparation

Table 3 presents the cementitious mortar mixture compositions used in this study. Three formulations were prepared: PC (100 wt. % OPC), PCG (30 wt. % OPC replaced with GGBFS), and PCGN (30 wt. % GGBFS and 1.0 wt. % NS). Both GGBFS and NS partially replaced cement. All mixtures maintained a water-binder ratio (*w*/*b*) of 0.5 and a binder-sand ratio (*B*/*S*) of 1:2 to ensure consistency.

All binder and sand components were mixed using a high-shear mixer.[34] The dry materials were blended at 500 rpm for 2 minutes to achieve uniformity. Deionized water or NS-infused deionized water (sonicated for 2 hours at 20 kHz and 600 W) was then added. Mixing continued at 500 rpm for 3 minutes, followed by a 2-minute pause, then an additional 2 minutes at 2000 rpm to ensure a homogeneous paste. The mixture was cast into sealed cylindrical molds (50 mm diameter x 100 mm height) and cured in a standard chamber for 24 days.

### Exposure conditions and sample preparation

Figure 1(a) illustrates the exposure methodology used in this study. After 24 days of standard conditioning, the cement specimens were demolded and dried at 40°C for 2 hours to remove residual moisture. Selected surfaces were then coated twice with epoxy to block moisture and ion penetration. Two days later, the specimens were resized to 50 mm in diameter and 80 mm in height to minimize property changes caused by atmospheric carbon dioxide exposure.[35] The processed specimens were submerged in deionized water for 48 hours to fully saturate their internal pore structure, simulating natural moisture exposure. After saturation, they were placed with the freshly cut surface facing downward and immersed in aggressive environments: natural seawater, a 5% saline solution, and a mixed solution of 5% sodium chloride and 5% sodium sulfate, maintained at 38°C.[32,35] A minimal gap between the specimen surface and the liquid ensured realistic chloride-exposure conditions. To maintain stable conditions, immersion solutions were replaced monthly throughout the 2-year study.[36]

After 2 years of immersion, the specimens were retrieved for analysis. The epoxy resin applied during immersion was carefully removed to prevent interference with subsequent tests. Specimens were then milled and drilled layer by layer using a milling and drilling machine (Fig. 2) to extract powder samples from various depths, assessing corrosion effects and penetration depth. Samples were collected at 0 to 3, 3 to 6, 6 to 9, 9 to 12, 12 to 15, 15 to 20, and 20 to 25 mm intervals. Each sample was assigned a project number for organized analysis (Table 4) and categorized based on exposure conditions: "SW" (seawater), "NC" (NaCl solution), and "NCS" (NaCl + $Na_2SO_4$ solution).

### Methodologies

As shown in Fig. 1(b), powdered samples were dried in a vacuum oven at 40°C for 48 hours to remove residual moisture, ensuring optimal conditions for analysis. After drying, samples were divided for further testing. Some were

## Table 3—Mixture proportions for cementitious composites, g

| Group | OPC | GGBFS | NS | Deionized water | *w*/*b* |
|---|---|---|---|---|---|
| PC | 1000 | — | — | 500 | 0.5 |
| PCG | 700 | 300 (30%) | — | 500 | 0.5 |
| PCGN | 686 | 297 (30%) | 10 (1%) | 500 | 0.5 |

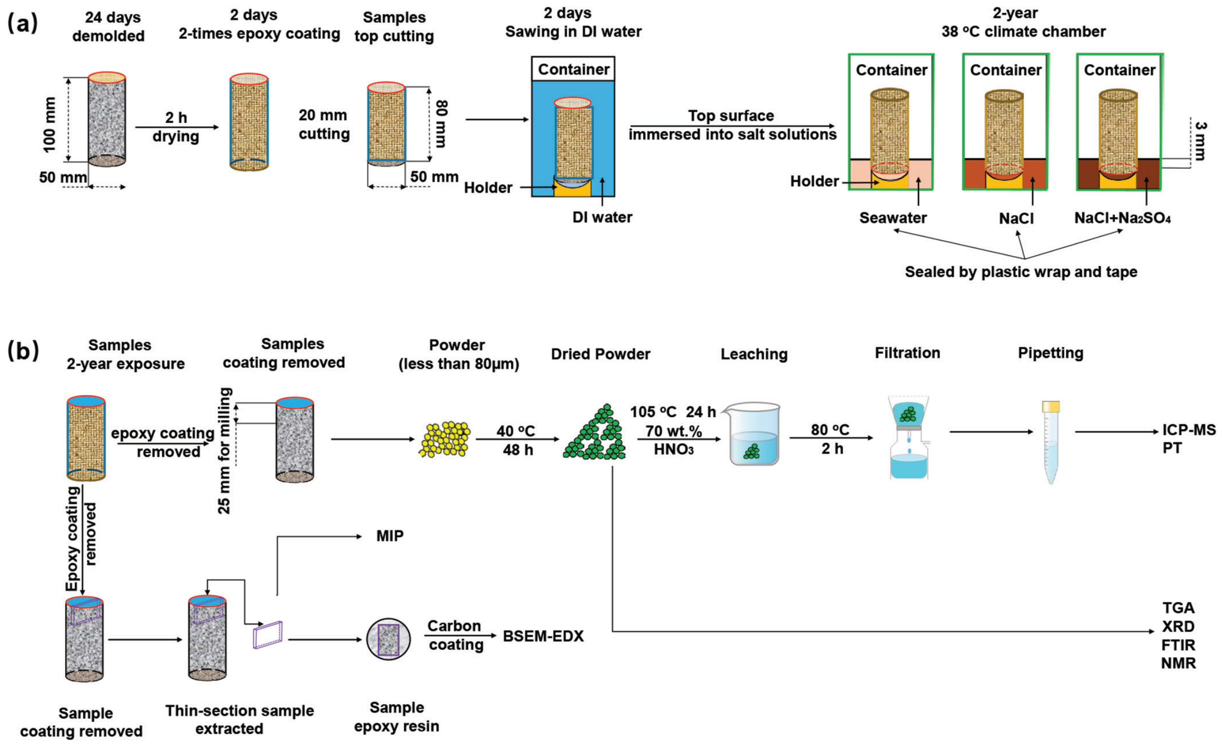

*Fig. 1—Experimental methods for: (a) exposure conditions; and (b) sample preparations.*

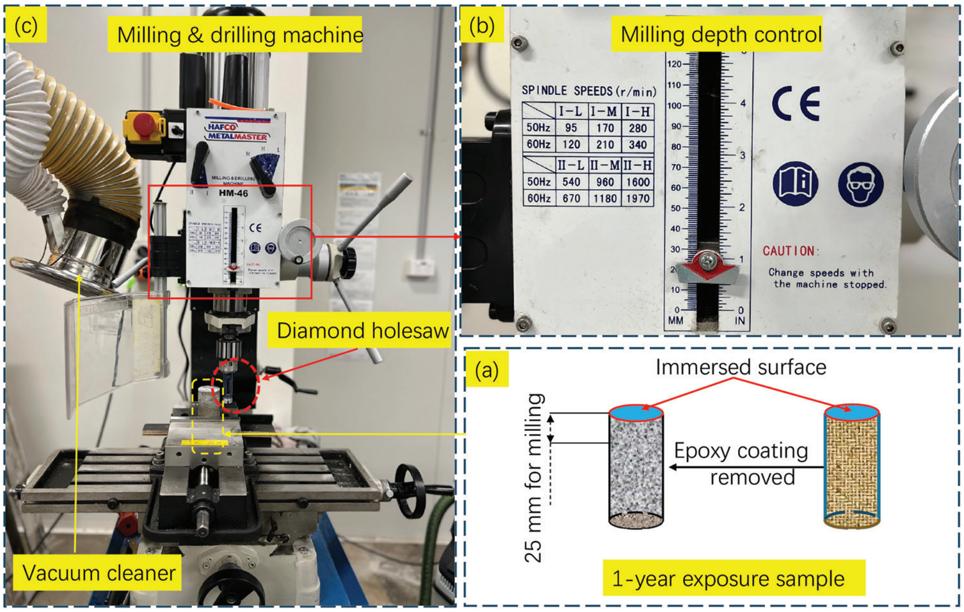

*Fig. 2—Sample milling along with depth.*

analyzed using inductively coupled plasma mass spectrometry (ICP-MS) for its sensitivity in detecting trace metals and other elements. Potentiometric titration (PT) was used to measure chloride concentrations, providing insights into chemical interactions. The remaining samples were analyzed using thermogravimetric analysis (TGA), XRD, Fourier-transform infrared spectroscopy (FTIR), and nuclear magnetic resonance (NMR). TGA assessed thermal stability and compositional changes, XRD identified crystalline structures and phase transitions, FTIR examined chemical

**Table 4—Types of samples exposed to different chloride solutions**

| Types | Depth, mm | | | | | | |
|---|---|---|---|---|---|---|---|
| | 0 to 3 | 3 to 6 | 6 to 9 | 9 to 12 | 12 to 15 | 15 to 20 | 20 to 25 |
| X-i-1 | O | — | — | — | — | — | — |
| X-i-2 | — | O | — | — | — | — | — |
| X-i-3 | — | — | O | — | — | — | — |
| X-i-4 | — | — | — | O | — | — | — |
| X-i-5 | — | — | — | — | O | — | — |
| X-i-6 | — | — | — | — | — | O | — |
| X-i-7 | — | — | — | — | — | — | O |

Note: X is PC, PCG, and PCGN, representing different mixtures; i is S, NC, and NCS, representing different salt solutions.

bonds and functional groups, and NMR investigated molecular structures. Together, these techniques provided a comprehensive understanding of the samples' compositions and properties.

Moreover, samples near the erosion surface, particularly those from the NCS environment, were analyzed using backscattered electron energy-dispersive spectroscopy (BSE-EDS) hypermaps to map elemental distributions and assess the penetration of corrosive agents. Thermodynamic modeling with GEM-Selektor 3 (GEM3) based on Gibbs energy minimization further supported the analysis. This combined approach provided valuable insights into the effects of corrosive environments on cementitious materials.

*Chloride content and pore solutions determination*—To assess chloride penetration and ion distribution, approximately 10 g of dried powder samples (dried at 105°C for 24 hours) were dissolved in 100 mL of acidified deionized water containing 70 wt. % $HNO_3$. The mixture was rotated for 2 hours to ensure complete dissolution, then heated to 80°C for 2 hours before cooling to room temperature. A 20 mL portion of the solution was agitated for 2 hours and filtered through a 4 μm cellulose filter.[37] The filtered solution was analyzed for chloride content using PT, while ICP-MS was used to determine aluminum, calcium, and other element concentrations. Chloride and element concentrations were recalculated relative to the samples' dry mass.[38]

*Phase assemblage analysis*—Dried powder samples, heated at 105°C for 24 hours, were analyzed for phase assemblages using TGA and XRD. Approximately 10 mg of each sample was placed in a corundum crucible and heated from 40 to 1000°C under a nitrogen atmosphere to obtain thermogravimetry (TG) and differential thermogravimetry (DTG) data. XRD analysis, performed with a $2\theta$ scanning range of 5 to 70 degrees and a step size of 0.02 degrees, provided detailed insights into compositional changes and mineralogical development in the GGBFS-NS cement composites.

In this study, semi-quantitative XRD analysis using the reference intensity ratio (RIR) method was employed to estimate the approximate quantities of FSS and calcium hydroxide (CH) within the powdered samples.[39,40] This method facilitates the calculation of the relative mass proportions of various minerals, specifically FSS and CH, present in the samples. The calculations are performed using the equations provided as follows

$$W_i = \frac{I_i/RIR_i}{\sum_{i=1}^{N}\left(\frac{I_i}{RIR_i}\right)} \tag{1}$$

$$W_1 + W_2 + W_3 + \cdot + W_i = 1 \tag{2}$$

where $W_i$ is the relative mass of mineral $i$; $RIR_i$ is the RIR for mineral $i$; $I_i$ is the integral intensity of the highest peak of mineral $i$; and $N$ is the total number of minerals present in the sample. This methodology allows for a structured approach to quantifying the distribution of minerals within the cementitious matrix, aiding in the comprehensive analysis of the sample's phase composition.

The quantity of CH can be quantitatively determined using DTG. The quantity of FSS is calculated by solving the following algebraic equations. The quantity of CH can be quantitatively determined using DTG analysis. To calculate the quantity of FSS, the following algebraic equations are employed

$$m_{FS}: m_{CH} = T_1 \tag{3}$$

$$m_{FS}: (m_{CH} + m_{FS}) = T_2 \tag{4}$$

$$m_{CH}: (m_{CH} + m_{FS}) = T_3 \tag{5}$$

where $m_{FS}$ and $m_{CH}$ are the masses of FSS and CH, respectively; and $T_1$, $T_2$, and $T_3$ are mass ratios derived from experimental data, facilitating a precise calculation of the respective proportions of FSS and CH in the sample. These ratios are critical for understanding the chemical stability and phase dynamics within the cementitious materials.

FTIR analysis was conducted to investigate the molecular alterations within the GGBFS-NS enhanced cement composites. The spectra were acquired using a spectrometer over a wavenumber range of 500 to 4000 $cm^{-1}$ with a precision of 8 $cm^{-1}$.

*$^{29}Si$ NMR measurement*—For the NMR analysis, samples were collected from the outermost region of the specimen, specifically within the 0 to 3 mm depth beneath the exposed surface. The silicate tetrahedral structures in GGBFS-NS cement composites were analyzed using a 500 MHz solid-state magic-angle spinning (MAS) NMR spectrometer. Spectra were recorded at 99.3 MHz with an 8 mm cross-polarization (CP)/MAS probe. To ensure complete relaxation

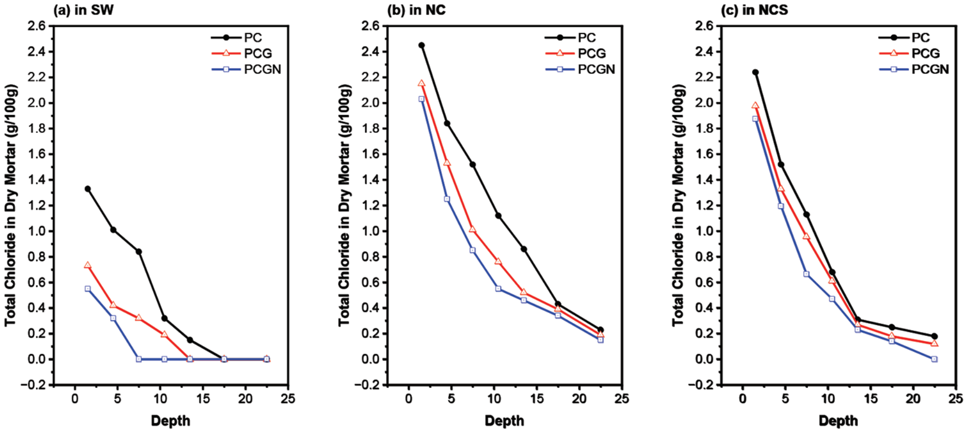

Fig. 3—*Total chloride profile determined by PT of ground mortar samples after 2 years of exposure to: (a) SW; (b) NC; and (c) NCS solutions.*

of silicate tetrahedra with varying connectivity, a 30-second relaxation delay and a 4000 Hz rotation rate were applied. Overlapping peaks in the $^{29}$Si MAS NMR spectra were deconvoluted using the Gaussian model in Origin software. The hydrated paste spectra featured three primary peaks: $Q^0$ (Si-O tetrahedra in unhydrated cement minerals), $Q^1$ (chain-end groups), and $Q^2$ (middle-chain groups in hydration products). For simplicity, $Q^2$(Al), linked to an Al-tetrahedra, was classified as $Q^2$.[41,42] Data analysis involved solid-state NMR software for phase adjustment, baseline correction, and other refinements.

*Microstructure characterization*—As shown in Fig. 1(b), a cross-sectional slice was prepared perpendicular to the exposed surface along the direction of maximum erosion depth and centered on the specimen. The surface was subsequently polished with diamond paste to achieve a final finish of 1 μm. Scanning electron microscopy (SEM) analysis was performed with an instrument, using BSE imaging and EDS for elemental hypermapping. The instrument was operated at an accelerating voltage of 15.0 kV and a working distance of 12.5 mm. Hypermap data were analyzed using ESPRIT 1.9 software, calibrated with element-specific standards. Paste samples were examined over an 860 x 645 μm area (500× magnification) with a resolution of 1000 x 750 pixels. Mortar samples were analyzed over a doubled area while maintaining the same resolution. Elemental composition and distribution were assessed using the edxia method developed by Georget et al.[43,44]

*Thermodynamic modeling*—Thermodynamic modeling was conducted using GEM3 through Gibbs energy minimization to predict equilibrium phase assemblages based on the total bulk elemental composition.[45,46] The modeling incorporated default PSI-GEMS databases supplemented with Cemdata14. This approach predicted phase transitions in GGBFS-NS cement composites exposed to various salt solutions. The model assumed constant water content throughout the study and that 80% of the cement participated in hydration. The following sections present the phase changes resulting from different salt concentrations and their effects on the structural integrity and chemical stability of the composites.

## RESULTS AND DISCUSSION

### Change in chloride content with depth

Figure 3 presents the total chloride profiles for all mortar samples exposed to various solutions over 2 years. The corrosive environment significantly influenced chloride penetration. Specimens exposed to seawater generally exhibited the lowest chloride content due to its lower chloride concentration compared to other environments. The PC group consistently recorded the highest chloride levels, particularly in the NaCl solution, indicating greater susceptibility to chloride ingress. In contrast, GGBFS-containing specimens (PCG) showed improved resistance, maintaining lower chloride levels across all environments. Notably, specimens incorporating both GGBFS and NS (PCGN) demonstrated superior chloride resistance, with consistently low chloride levels at all depths. This effect was most pronounced in the NaCl solution, highlighting the combined effectiveness of GGBFS[22] and NS in mitigating chloride penetration.[12]

While the NaCl solution accelerated chloride ingress near the surface, the presence of sulfate in the NCS solution appeared to moderate this effect in PCGN samples, suggesting sulfate may influence chloride mobility or its interactions with the cement matrix. Across all samples, chloride concentrations decreased rapidly just beneath the surface and gradually declined with depth, reflecting a typical diffusion pattern. These findings highlight the vulnerability of conventional cement formulations to chloride ingress, whereas composites containing GGBFS and NS demonstrated enhanced resistance. This improved performance underscores their potential for developing more durable materials in chloride-rich environments.

### Change in leaching behavior determined by ICP-MS

Figures 4(a) and (b) present the elemental composition of ground mortar samples, with calcium and aluminum contents measured by ICP-MS. The samples were exposed for 2 years to SW, NC, and NCS solutions, and the results are expressed as a percentage of dry mass (dried at 105°C). Calcium concentrations were highest near the exposed surface and progressively declined with depth. In the SW environment, PC samples exhibited the most pronounced surface calcium content but also showed significant depletion at depth. In

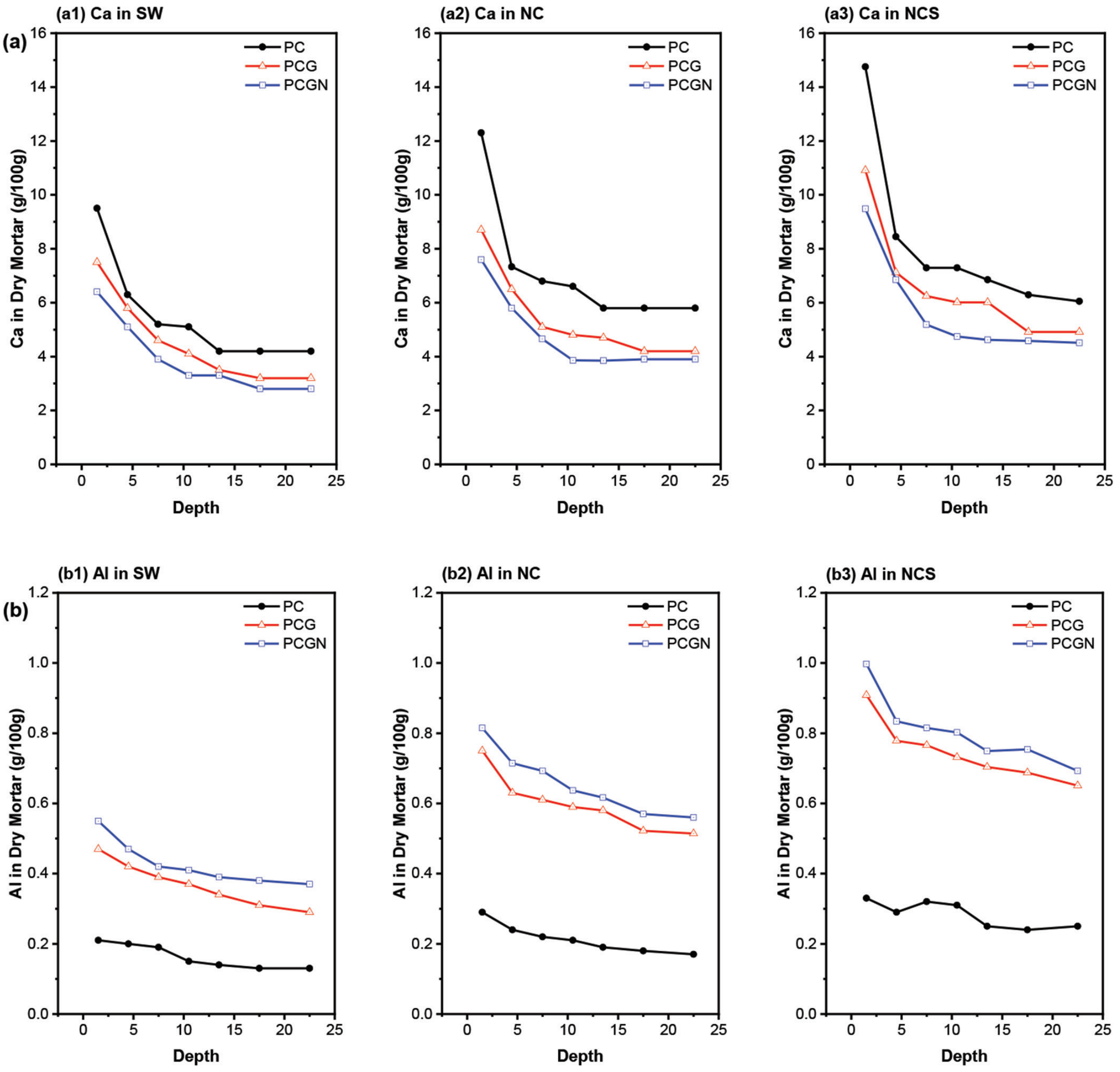

*Fig. 4—(a) Total Ca profile; and (b) total Al profile determined by ICP-MS for ground mortar samples after 2 years of exposure to SW, NC, and NCS solutions.*

contrast, PCG and PCGN samples demonstrated more uniform calcium retention, suggesting that GGBFS and NS effectively reduce calcium leaching. Similar trends were observed under NC exposure. PCGN samples displayed minimal calcium loss across the profile, indicating enhanced resistance to chloride-induced leaching, likely due to the pozzolanic activity and pore refinement provided by NS.[47] In the NCS environment, calcium depletion was initially observed in all mixtures but was subsequently stabilized in GGBFS- and NS-modified mortars. This behavior suggests that combined chloride and sulfate exposure may result in ion interactions that contribute to the retention of calcium within the matrix.

Aluminum concentrations declined slightly with the depth in all environments, reflecting its relative stability under leaching conditions. In the SW and NC exposures, PC samples showed a steady decline, while PCG and PCGN samples, particularly the latter, maintained higher aluminum levels. This stability is attributed to the protective role of GGBFS and NS. In the NCS condition, PC samples retained more aluminum than in the NC condition, implying that sulfate ions may contribute to aluminum stabilization.[32,48] These findings emphasize the role of supplementary materials in improving elemental retention and overall durability. GGBFS and NS significantly mitigated calcium and aluminum loss, particularly in chloride-rich environments, while the presence of sulfate in NCS solutions may further influence ion solubility and matrix stability.

## Change in phase assemblage

*TGA and semi-quantitative XRD analysis*—The DTG curves in Fig. 5 illustrate the thermal decomposition behavior of PC, PCG, and PCGN composites after 2 years of exposure to SW, NC, and NCS solutions. The curves highlight variations in hydration products and their thermal stability, marked by peaks corresponding to phases such as ettringite (AFt), monosulfate (AFm), and C-S-H, along with distinct portlandite (CH) peaks.[20,22,49] In PC composites, CH peaks appear consistently across all environments, with varying intensities influenced by the corrosive solution. Samples exposed to SW exhibited fluctuating CH peak intensities, suggesting portlandite content variations linked to differing

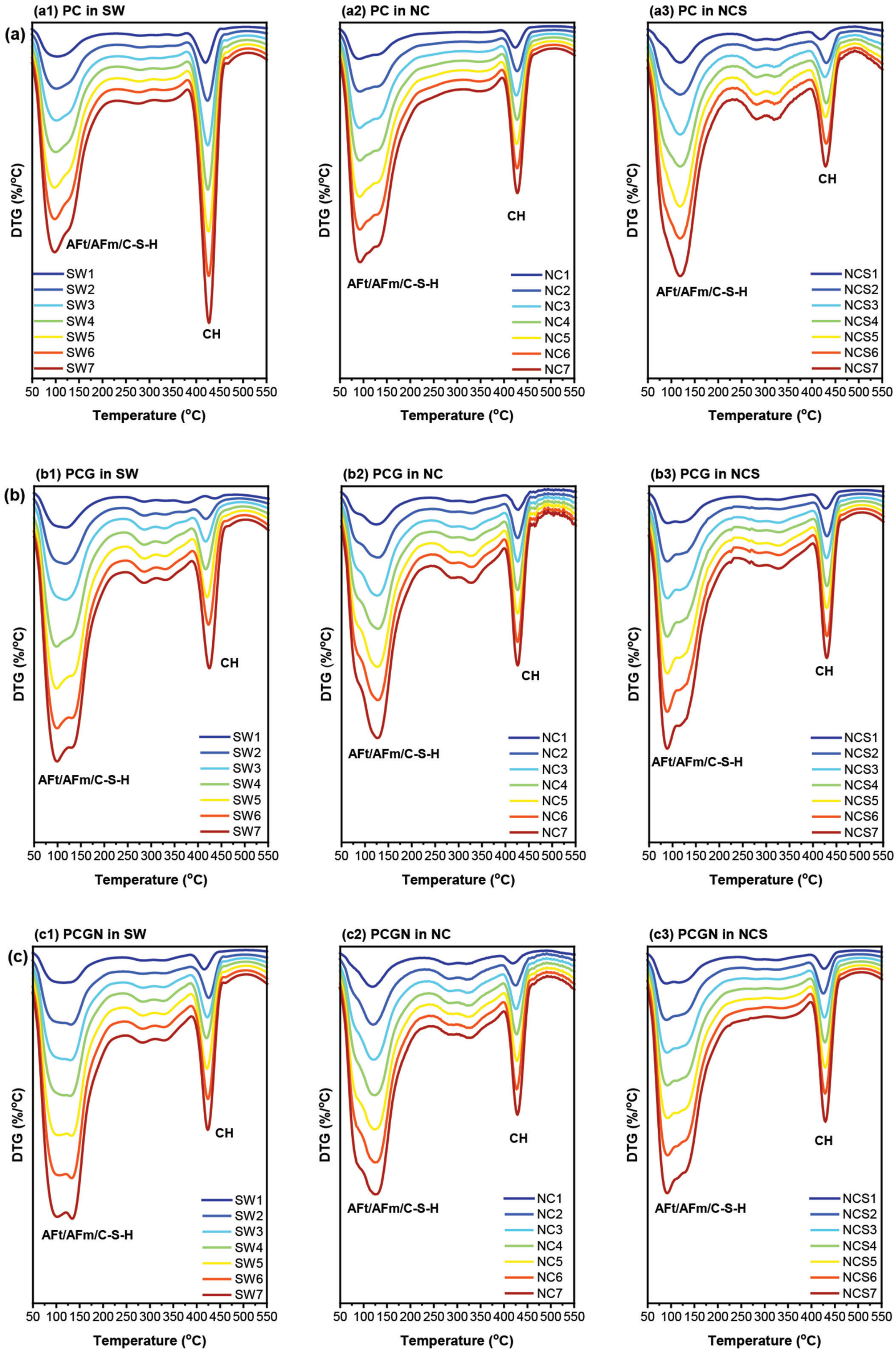

*Fig. 5—DTG curves of ground: (a) PC; (b) PCG; and (c) PCGN mortar samples after 2 years of exposure to SW, NC, and NCS solutions.*

salt concentrations. In the NC solution, peak shifts indicate possible changes in hydration phases due to chloride exposure. Samples exposed to the NCS solution further demonstrate that the combined presence of chloride and sulfate ions significantly affects the stability and distribution of hydration products, as reflected in the altered CH peak profiles.[33] These findings emphasize the complex environmental interactions that influence the structural and chemical stability of cement-based composites.

Furthermore, the DTG profiles of PCG composites in the SW environment highlight the influence of GGBFS on hydration product stability. The reduced CH peak intensity compared to PC samples suggests that GGBFS promotes the formation of more stable hydration products with improved thermal resistance. This trend persists in NC and NCS environments. In the NC solution, variations in the monosulfate (AFm)-to-ettringite (AFt) ratio and C-S-H peak intensities suggest chloride-induced phase changes or degradation. In the NCS environment, similar patterns emerge, with fluctuations likely reflecting complex sulfate-chloride interactions. The PCGN composites exhibited a distinct thermal decomposition profile. In the SW environment, the reduced CH peak intensity compared to PC and PCG samples indicates NS's role in modifying hydration products. This effect is more pronounced in the NC environment, where NS appears to enhance thermal stability and alter hydration phases. In the NCS environment, NS and sulfate-chloride interactions further stabilize hydration products, reflected in pronounced peak shifts and intensity variations.

The XRD spectra in Fig. 6 provides a semi-quantitative assessment of crystalline phases in PC, PCG, and PCGN composites after 2 years of exposure to different solutions. Identified phases include AFt, FSS, AFm, CH, and calcite.[32] In the SW environment, a distinct CH peak is observed in the PC sample, indicating that portlandite remained largely unaffected by marine exposure. No significant reduction in CH intensity is evident, suggesting minimal leaching or transformation of this phase in the surface region. Under NC exposure, the CH peak remains comparable in intensity, with only slight changes in the AFt peak, implying that chloride ingress did not substantially alter the quantity of crystalline portlandite, though minor interactions with sulfate phases may have occurred. In the NCS environment, the CH peak remains present, alongside intensified peaks corresponding to sulfate-containing phases (AFt and AFm). These results indicate that the combined presence of chloride and sulfate did not lead to notable CH depletion, although a moderate redistribution of sulfate-related phases was observed, reflecting ionic interactions influencing the crystalline phase composition.

The PCGN group exhibits distinct crystalline characteristics in the XRD patterns. Notably, the incorporation of NS alters the hydration products: for example, the CH peak intensity in PCGN is lower than in PC and PCG, indicating that additional pozzolanic reaction has consumed more portlandite to form secondary C-S-H. This change is most pronounced in the NC environment, suggesting that chloride interactions with the NS-modified matrix promote further consumption of CH. In the NCS environment, the combined presence of GGBFS and NS appears to enhance the stability of hydration products; the XRD peaks for CH and other crystalline hydrates (for example, AFt and FSS) remain evident, indicating that the matrix retains its crystalline phases despite exposure to both chloride and sulfate.

The profiles in Fig. 7 show the distribution of FSS across mortar depths after 2 years of immersion in SW, NC, and NCS solutions, determined through TGA-XRD analysis. FSS concentration reflects the cementitious matrix's chloride-binding capacity; however, higher FSS levels may also indicate increased chloride penetration and subsequent FSS formation, a key factor in assessing mortar resistance to chloride-induced corrosion. In the SW environment, FSS concentrations in all mortar types (PC, PCG, and PCGN) decline sharply near the surface before stabilizing at greater depths, indicating rapid initial chloride binding followed by equilibrium. The PC group exhibits an advanced leaching zone, marked by a significant FSS decrease beyond a certain depth, indicating extensive chloride penetration and subsequent leaching. In this zone, severe leaching compromises FSS stability, reducing its content near the surface.

In the NC environment, FSS content decreases near the surface and gradually declines with depth. The FSS profiles for the PCG and PCGN groups are closely aligned, indicating that GGBFS and NS have a comparable effect on chloride binding in a chloride-only environment. This similarity suggests both additives improve chloride binding compared to the PC group. In the NCS environment, FSS concentrations remain higher at greater depths in the PCGN group than in the PC and PCG groups. This highlights the synergistic effect of GGBFS and NS in enhancing chloride binding, even in the presence of competing sulfate ions. Sulfate may compete with chloride for available aluminum, potentially reducing FSS formation, yet the combined effect of GGBFS and NS in PCGN appears to mitigate this impact, improving chloride resistance.

Comparative analysis across the three environments reveals that while chloride presence significantly affects FSS distribution, mortar composition is critical in determining chloride-binding depth and extent. The PC group shows greater chloride penetration and leaching, reflected in the pronounced decrease in FSS content with depth, particularly in the SW environment. In contrast, GGBFS and NS in the PCG and PCGN groups improve chloride resistance by enhancing chloride binding. This protective effect was consistent across all solutions, indicating that modifying the cement matrix with GGBFS and NS not only improves chloride binding but also strengthens resistance to aggressive ions. The PCGN group's ability to retain higher FSS levels at greater depths, particularly in sulfate-rich conditions, highlights its enhanced durability. This characteristic is especially beneficial in environments requiring long-term resistance to chloride-induced corrosion, demonstrating the potential of these composites to extend structural lifespan in harsh conditions.

*Fourier-transform infrared (FTIR)*—The FTIR spectra in Fig. 8 provide insights into the chemical transformations and phase developments in PC, PCG, and PCGN composites after 2 years of exposure to SW, NC, and NCS

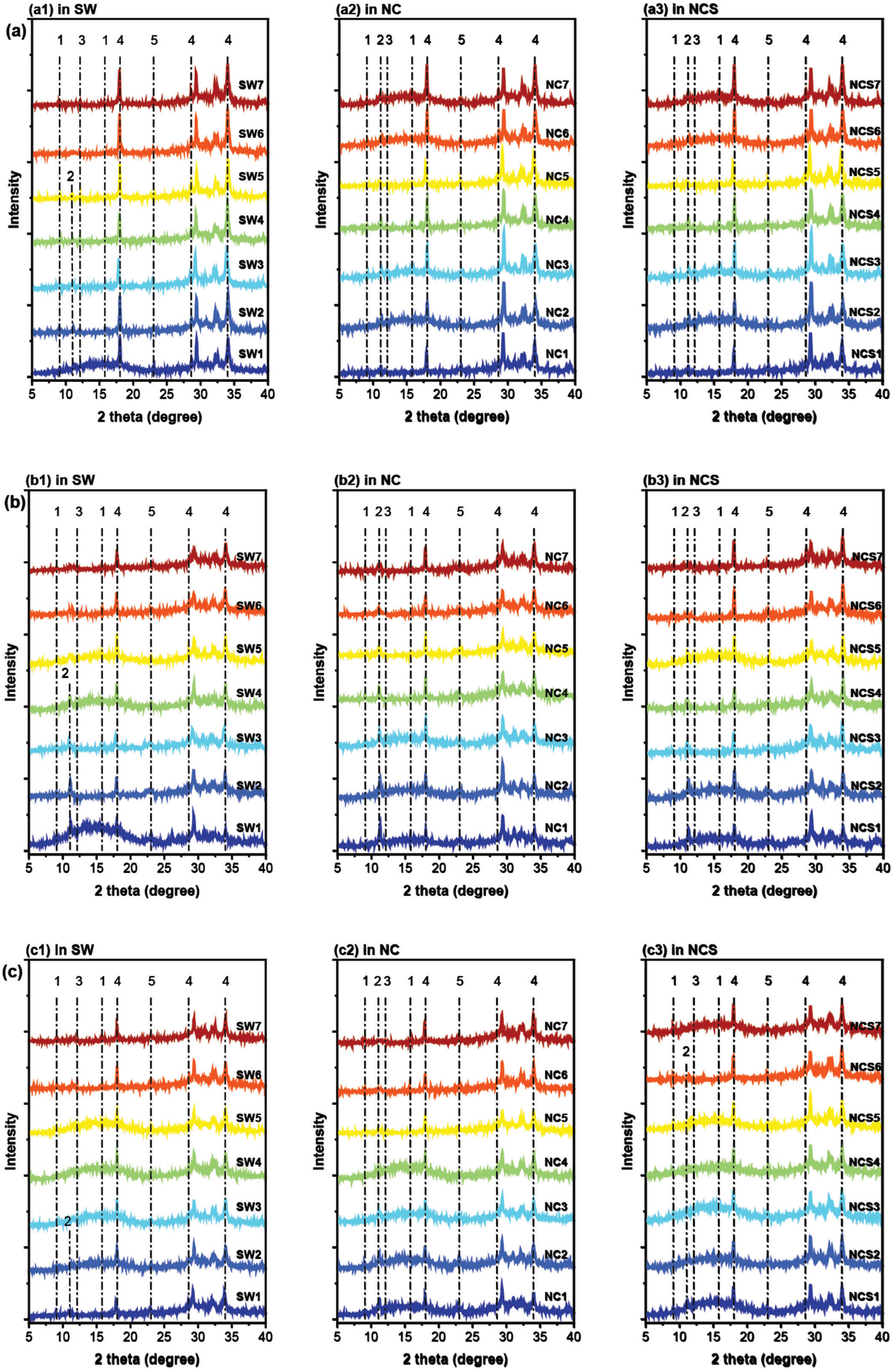

*Fig. 6—XRD curves of ground specimens: (a) PC; (b) PCG; and (c) PCGN mortar samples after 2 years of exposure to SW, NC, and NCS solutions (1-ettringite, 2-Friedel's salt, 3-monosulfate, 4-portlandite, and 5-calcite).*

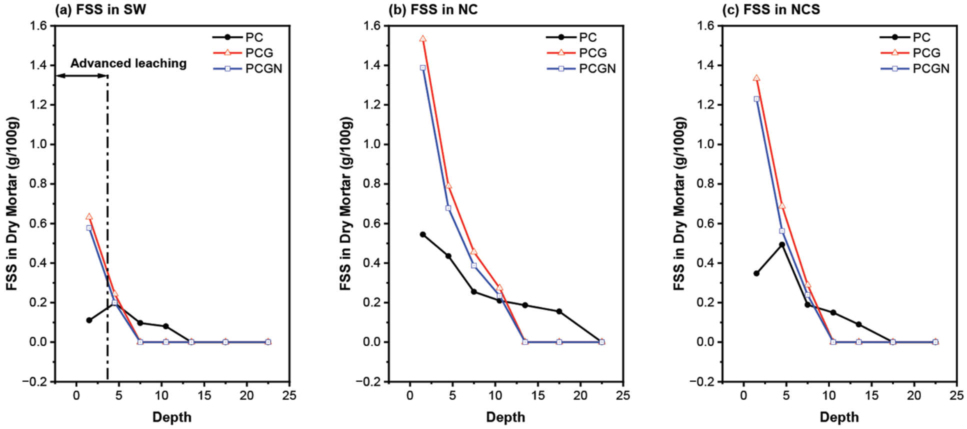

*Fig. 7—FSS profiles measured by TGA-XRD for ground mortar samples after 2 years of exposure to (a) SW; (b) NC; and (c) NCS solutions.*

solutions. The spectra reveal changes in key chemical bonds and functional groups, including S=O stretches associated with sulfate species in AFt/AFm phases and Si-O stretches characteristic of silicate structures in the cement matrix.[32] The FTIR spectra of the PC samples exposed to SW exhibit pronounced intensity increases in the sulfate-related bands near 1120 $cm^{-1}$ and shifts in the Si-O stretching region approximately 970 to 980 $cm^{-1}$. These changes are attributed to the formation or stabilization of sulfate-bearing hydration products, such as ettringite or monosulfate, facilitated by the availability of $SO_4^{2-}$ in the external environment. Under NC exposure, the enhancement of sulfate-associated peaks may result from chloride-induced transformations. Specifically, the formation of FSS could displace preexisting sulfate phases, triggering partial reprecipitation or structural adjustment of sulfate-containing compounds. In the NCS environment, more complex spectral modifications are observed, including overlapping and shifting of both sulfate and silicate bands. These features suggest simultaneous interaction of $Cl^-$ and $SO_4^{2-}$ ions with the cement matrix, leading to competitive ionic exchange. This co-presence appears to affect the polymerization of silicate chains in the C-S-H phase and the distribution of sulfate phases, resulting in dynamic alterations in matrix composition and structure.[50,51]

In the PCG group, the FTIR spectra show consistent sulfate-related peaks across all solutions, likely reflecting the stabilizing effect of GGBFS. The stable silicate-related peaks further suggest that GGBFS contributes to a more uniform C-S-H structure, promoting consistent chemical behavior in varied environments. This stability highlights GGBFS's protective role in mitigating chemical changes within the cement matrix. In the PCGN group, NS incorporation refines the spectral profiles, marked by distinct peak patterns across the three environments. The uniformity in S=O and Si-O peak intensities indicates improved chemical stability, enhancing resistance to ionic interactions in SW, NC, and NCS solutions. Notably, in the NCS environment, the spectra suggest that NS effectively regulates the balance between sulfate and chloride interactions, further stabilizing the cement matrix. FTIR analysis highlights the role of additives in enhancing chemical stability and reducing ion-induced degradation. The data indicate that the combined presence of GGBFS and NS in the PCGN group significantly improves chemical durability, particularly in aggressive chloride and sulfate environments. These findings underscore the benefits of incorporating such additives to enhance the longevity of cementitious materials in ion-rich conditions.

*$^{29}$Si NMR analysis*—The deconvolution of the $^{29}$Si MAS NMR spectra (Fig. 9) reveals the silicate environments in PC, PCG, and PCGN composites after 2 years of exposure to the NCS solution. This analysis provides insights into polymerization processes and the characteristics of silicate species within the cementitious matrix.

In the PC group, the NMR spectra show peaks corresponding to $Q^1$ and $Q^2$ species, indicating a less polymerized silicate network. This structure aligns with typical C-S-H in hydrated portland cement, where calcium availability reduces silicate crosslinking.[20,42] In the PCG group, a shift toward higher-order silicate species such as $Q^2$ is observed, reflecting the influence of GGBFS. GGBFS's inherently polymerized silicate chains promote a more complex silicate network, contributing to improved mechanical strength and durability. The PCGN group shows a further increase in highly polymerized silicate species, with a pronounced presence of $Q^2$. This indicates a denser, more interconnected C-S-H structure, likely enhanced by NS. The high reactivity of NS appears to promote nucleation, accelerating C-S-H formation and supporting extensive silicate polymerization.

The NMR spectra reveal how GGBFS and NS modify the cement matrix. The shift from lower- to higher-order silicate species in PC, PCG, and PCGN highlights the impact of these additives on the hydrated cement paste. GGBFS and NS promote C-S-H gel formation and extend C-S-H chains, enhancing the silica network. The incorporation of SCMs, particularly NS, refines the silica environment, improving chemical stability and resistance to ionic degradation in the NCS solution. These spectral trends demonstrate how $^{29}$Si NMR spectroscopy can guide cementitious material improvements for greater durability in corrosive environments. The findings emphasize SCMs' potential to enhance the silica network, improving resistance to ionic penetration and reducing degradation risks. This molecular-scale understanding supports the development of cementitious

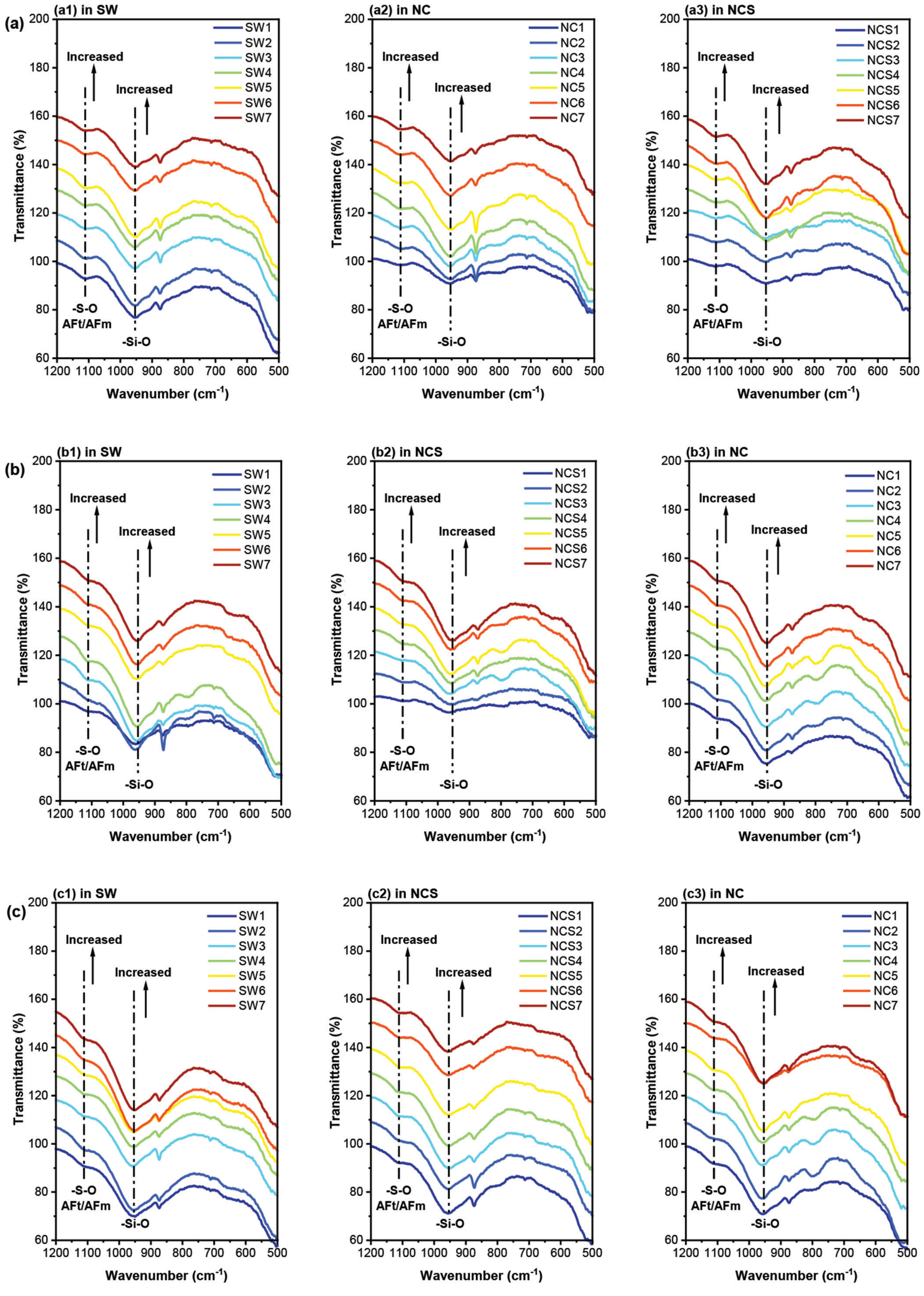

*Fig. 8—FTIR curves of specimens: (a) PC; (b) PCG; and (c) PCGN composites after 2 years of exposure to SW, NC, and NCS solutions.*

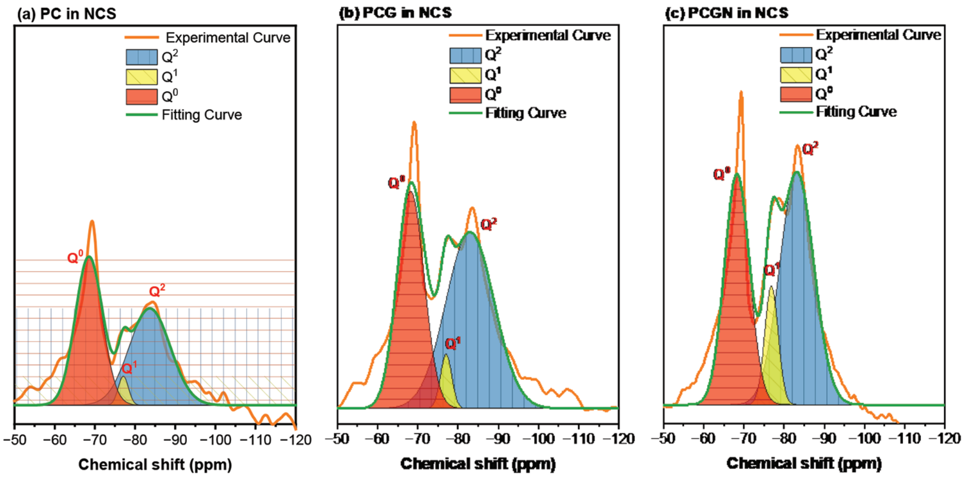

*Fig. 9—Deconvolution of $^{29}$Si MAS NMR spectra of: (a) PC; (b) PCG; and (c) PCGN composites after 2 years of exposure to NCS solution.*

composites designed for enhanced longevity in aggressive conditions.

## Change in microstructural properties

*BSE-EDS elemental maps*—The BSE-EDS elemental maps in Fig. 10 illustrate the elemental composition and distribution in PC, PCG, and PCGN composites after 2 years of exposure to the NCS solution. The elemental maps in Fig. 10 illustrate the concentration and spatial distribution of key elements within the cementitious matrix. This detailed visualization is essential for assessing the durability and stability of cementitious composites under prolonged corrosive conditions.[52,53]

The elemental map for the PC group shows a prominent calcium presence, reflecting the cementitious matrix. Silicon and aluminum distributions appear uniform, corresponding to the silicate and aluminate phases. Chlorine and sulfur, likely from the NCS solution, indicate some penetration and interaction with cement phases. The chlorine map highlights potential chloride accumulation sites, suggesting areas prone to chemical degradation or FSS formation. In the PCG group, chlorine levels are notably reduced, indicating improved chloride-binding capacity due to GGBFS, which enhances resistance to chloride-induced degradation. Sulfur distribution is more uniform, suggesting GGBFS's interaction with sulfate ions and the formation of secondary sulfate-bearing phases, further improving chemical stability and durability.

The elemental map for the PCGN group shows a distinct shift in composition, with NS integration notably enhancing silicon distribution, resulting in a more uniform and pronounced silicon map. Chlorine presence is significantly reduced compared to both PC and PCG, indicating improved resistance to chloride penetration. This enhancement is likely due to the pozzolanic reaction of GGBFS, which densifies the matrix and increases chloride-binding capacity. Across all groups, the maps reveal a progressive trend toward greater homogeneity and reduced chlorine content, from PC to PCG and ultimately PCGN, highlighting the role of material composition in enhancing resistance to ionic ingress. These SEM-EDS maps illustrate the microstructural improvements achieved with GGBFS and NS, offering valuable insights into developing durable cementitious materials for harsh environments. The reduced chlorine content in PCG, and particularly PCGN, underscores their suitability for conditions requiring resistance to both chloride and sulfate attack.

*Quantified BSE-EDS hypermaps*—The BSE-EDS hypermaps in Fig. 11 provide a detailed quantitative analysis of microstructural changes in PC, PCG, and PCGN composites after 2 years of exposure to the NCS solution. These maps highlight the impact of SCMs and NS on phase distributions and stoichiometric compositions. In the PC composite, elemental mapping and stoichiometric assessment reveal a relatively simple phase composition, dominated by FSS. This is evident in the Ca/Al versus Si/Ca and Al/Ca versus Si/Ca ratio plots, where data points cluster around regions typical of simpler C-S-H phases and elevated Al/Ca ratios, indicating AFt phases.[54,55] These findings suggest that without additives, the matrix is more susceptible to chloride and sulfate exposure, reflecting a basic chemical structure that offers limited resistance to ionic ingress.

In the PCG group, the incorporation of GGBFS diversifies the phase composition. The broader scatter in the ratio plots indicates a variety of hydration products, covering both internal and external C-S-H layers. The increased presence of AFt and AFm phases, resulting from GGBFS interactions with sulfate and chloride ions in the NCS solution, reflects improved stability and enhanced resistance to external ionic ingress. In the PCGN group, combining GGBFS and NS introduces greater microstructural complexity. The ratio plots show a notable increase in highly polymerized silicate phases, with data shifting toward higher Si/Ca ratios. This suggests advanced silicate polymerization, likely driven by NS's pozzolanic reaction, which promotes denser, interconnected C-S-H structures. The balanced presence of AFt and AFm phases further indicates improved sulfate and chloride regulation, enhancing the composite's structural stability and chemical durability in aggressive environments.

In conclusion, the progression from PC to PCG and PCGN groups reveals increased complexity and stability in the cementitious matrix. This trend highlights the effectiveness of incorporating GGBFS and NS, which not only

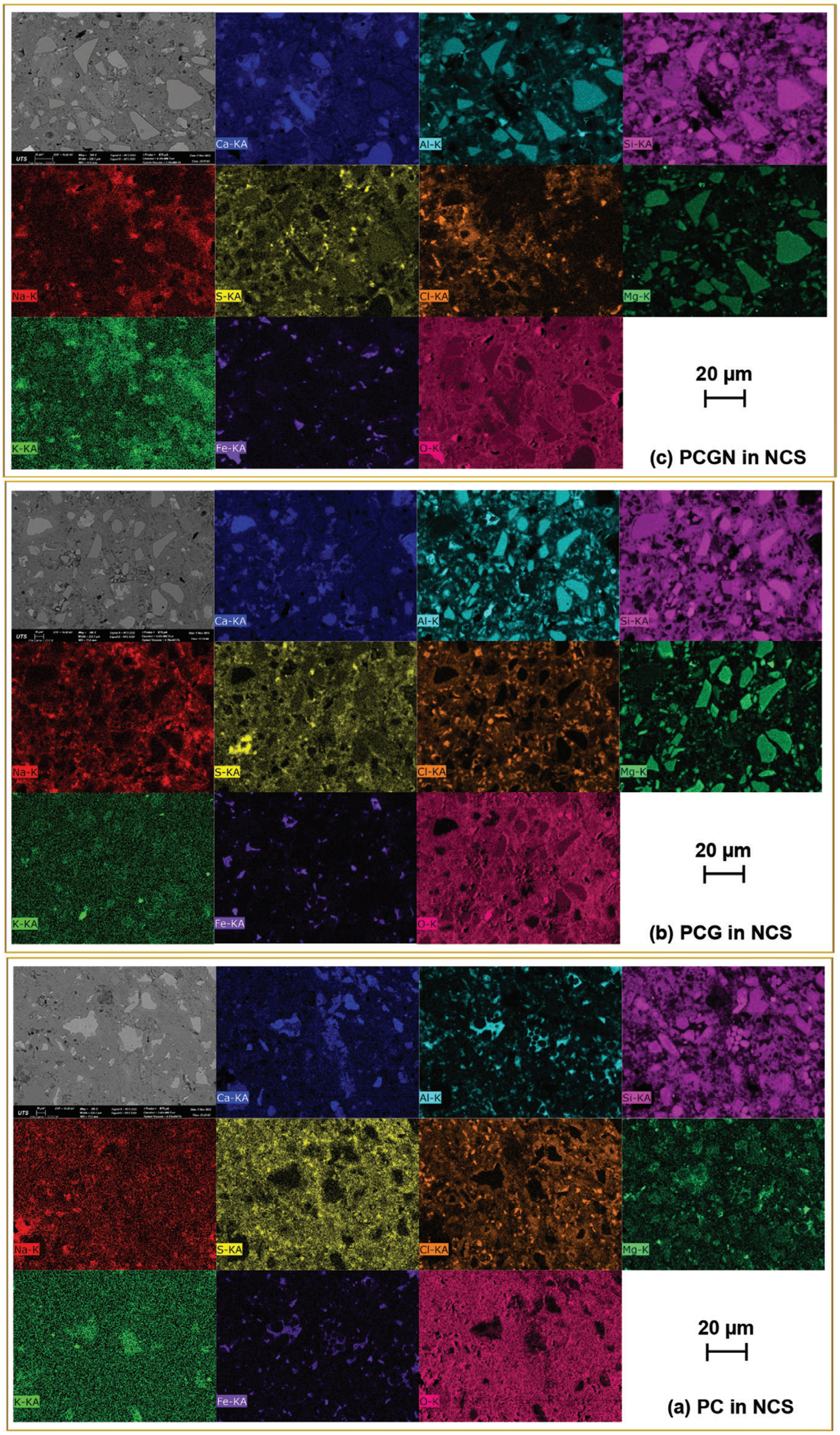

*Fig. 10—BSE-EDS elemental maps of PC, PCG, and PCGN mortars after 2 years of exposure to NCS solution.*

enriches the phase assemblage but also enhances durability and resistance to aggressive ionic environments, as shown in the NCS solution trials. The BSE-EDS hypermaps clearly demonstrate the positive impact of these additives on microstructural integrity and chemical stability, emphasizing their role in improving composite robustness.

## Effect of GGBFS-NS or sulfate on chloride ingress

Figure 12 illustrates the phase assemblages of PC, PCG, and PCGN composites exposed to NC and NCS solutions with varying salt concentrations, highlighting the complex interactions between cementitious components and the salt environment. Phase volumes change with increasing salt content, reflecting the dynamic chemical processes within the cement matrix. In the PC composite (Fig. 12(a) and (b)), phase development progresses from unhydrated components to hydrated phases such as C-S-H, CH, and AFm, alongside notable concentrations of FSS and AFt. As salt content increases, the formation of AFt and FSS becomes more pronounced, indicating that chloride and sulfate ions

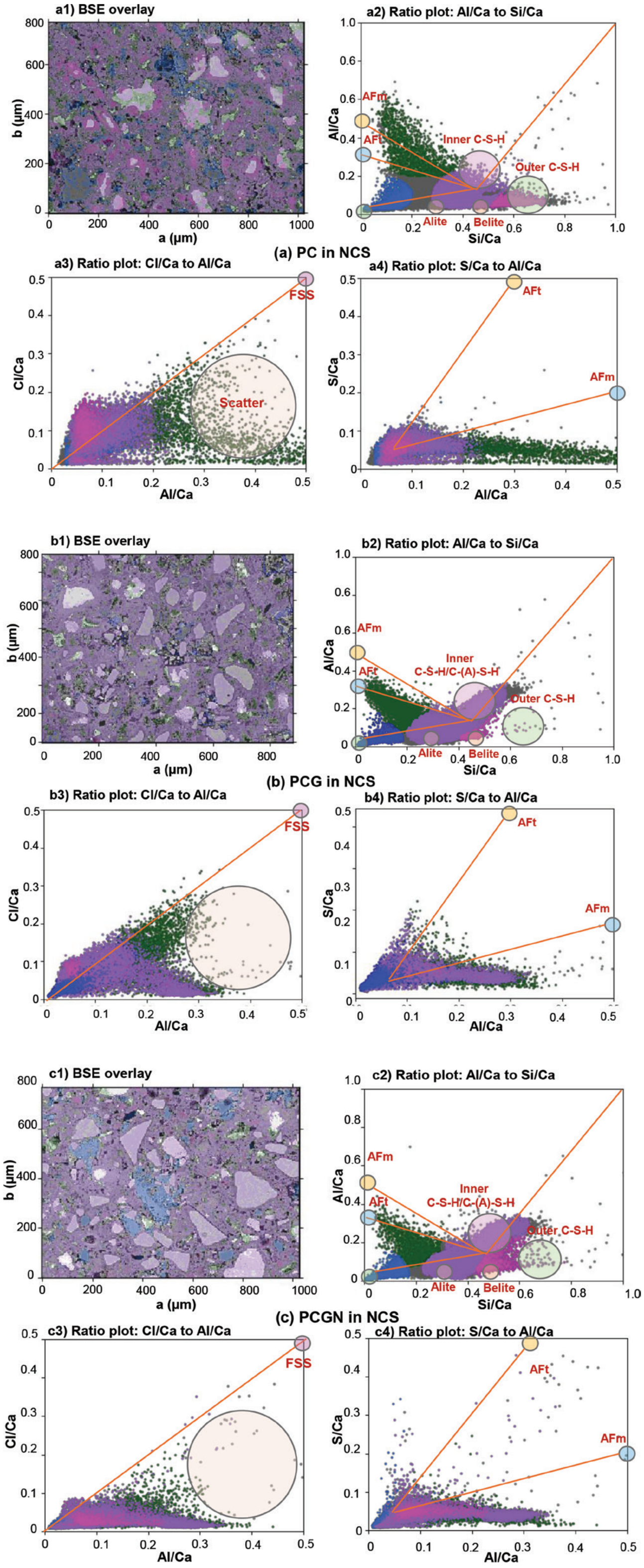

(a) PC in NCS

(b) PCG in NCS

(c) PCGN in NCS

*Fig. 11—Boundary definitions for specific phases and identified phases by stoichiometry as overlays of phase masks of PC, PCG, and PCGN composites after 2 years of exposure to NCS solution.*

promote these phases, which play a key role in the matrix's response to ionic exposure.[56]

In the PCG composite exposed to NC and NCS environments (Fig. 12(c) and (d)), the incorporation of GGBFS broadens the phase distribution, promoting a wider range of hydrated phases. The presence of calcium aluminosilicate hydrate (C-(A)-S-H) alongside C-S-H indicates a more complex hydration process. Ratio plots show that GGBFS not only alters initial hydration products but also stabilizes calcium and aluminum hydrates across a broader range of salt concentrations.[57] The increased presence of AFm and AFt phases suggests that GGBFS enhances the composite's ability to manage sulfate and chloride ions effectively. In the PCGN composite (Fig. 12(e) and (f)), the combined effects of GGBFS and NS further increase microstructural complexity. NS amplifies the stabilization of highly polymerized silicate phases, reflected in extended regions of C-S-H and C-(A)-S-H, indicating a denser, crosslinked matrix. Ratio plots show retention of critical phases, such as AFt and FSS, along with balanced chloride and sulfate management. This improvement is attributed to the pozzolanic and cementitious effects of the additives, enhancing resistance to ionic degradation.

Based on experimental results and thermodynamic modeling, Fig. 13 illustrates the impact of GGBFS, NS, and sulfate on chloride ingress in GGBFS-NS cement composites, providing insights into their environmental resilience in chloride-rich conditions. The schematic outlines the progressive chemical reactions that occur when GGBFS and NS are introduced into the cement matrix. It depicts the transformation of $C_3A$ to AFt, followed by the formation of AFm and FSS, highlighting the chemical pathways influenced by GGBFS and NS. The transition from AFt to AFm and eventually to FSS in chloride-rich environments underscores a key mechanism that can be controlled through GGBFS and NS incorporation to improve material durability.

The schematic for the PC group illustrates chloride ions freely penetrating the cement matrix, shown by the widespread distribution of yellow dots. This highlights the vulnerability of traditional cement composites to chloride ingress, which can weaken structural integrity over time. In the PCG group, GGBFS promotes the formation of complex silicate structures with abundant AFt and AFm phases, which play a key role in binding chloride ions and limiting their penetration into reinforcing steel. This increased phase presence reflects GGBFS's contribution to improving resistance against chloride attack.[20,27] The addition of NS further refines the matrix by enhancing hydration, resulting in denser C-S-H formations that appear as tightly bound clusters. This denser structure reduces chloride penetration, evidenced by fewer and less-dispersed yellow dots. Overall, the progressive incorporation of GGBFS and NS from PC to PCG and PCGN composites enhances the cementitious matrix's resistance to chloride and sulfate exposure.

## CONCLUSIONS

In this study, the enhanced chloride-binding capacity and improved performance of ground-granulated blast-furnace slag (GGBFS)-nanosilica (NS) composites in saline environments yielded several key conclusions:

1. The incorporation of GGBFS in cementitious composites leads to enhanced chemical and physical binding of chloride ions, as evidenced by the formation of Friedel's salt

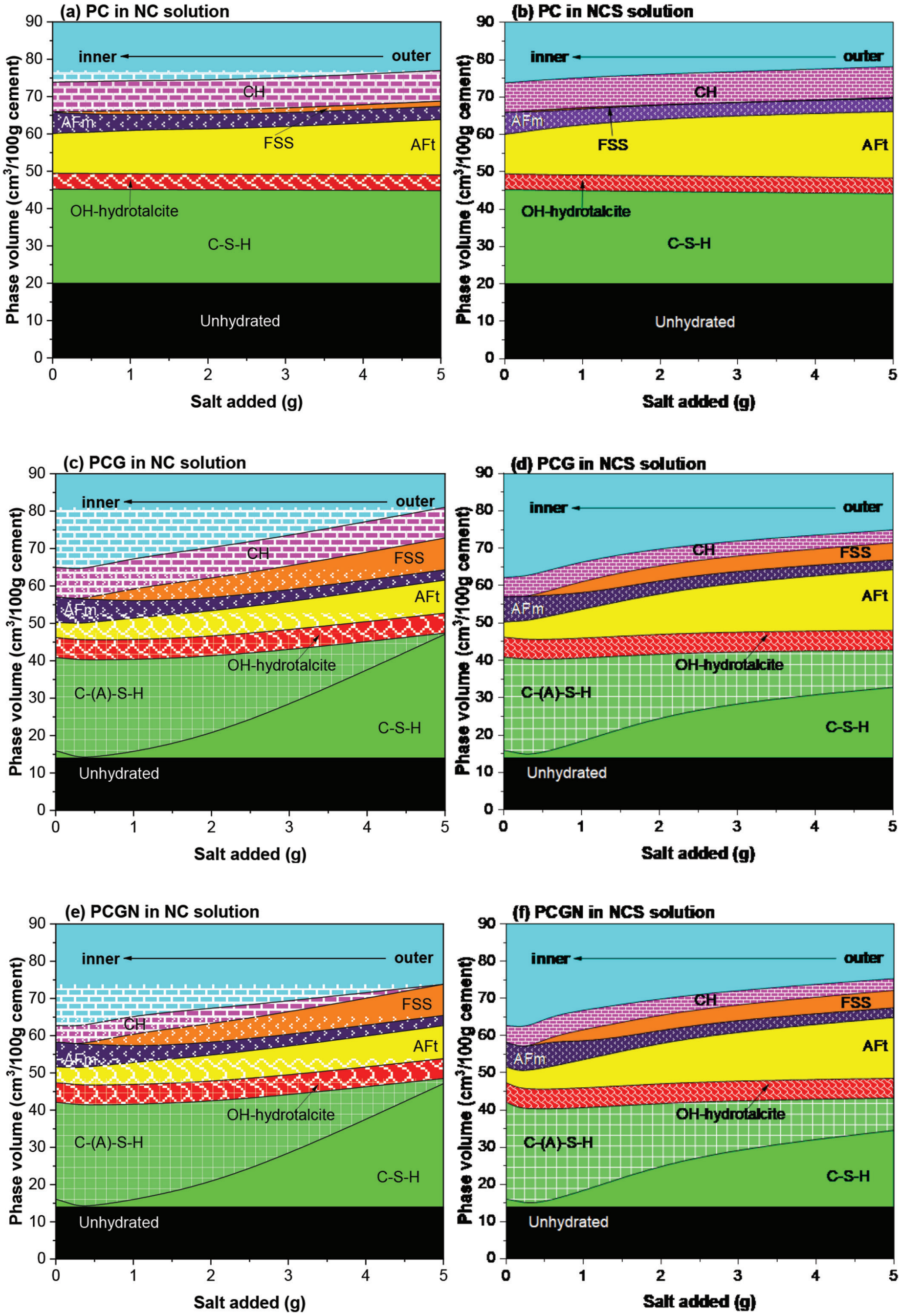

*Fig. 12—Phase assemblages for PC, PCG, and PCGN composites exposed to NC and NCS solutions.*

(FSS) and increased calcium-silicate-hydrate (C-S-H) gels, respectively.

2. The addition of NS to the cement-GGBFS matrix significantly refines the composite's microstructure. NS particles contribute to the densification of the C-S-H matrix, which increases the physical binding of chloride ions.

3. Sulfate ions initially participate in the formation of stable hydration products such as ettringite (AFt) and monosulfate (AFm). However, when sulfate ions are limited, excess chlorides may lead to the preferential formation of FSS. This competitive interaction between sulfate and chloride ions influences the extent of chloride sequestration.

4. The synergetic effect of GGBFS and NS is most pronounced in the PCGN composite. This synergy manifests in improved microstructural characteristics and chloride-binding capacity. The evidence suggests the potential of designing cementitious composites with targeted additives that can withstand specific chemical stresses encountered in chloride- and sulfate-rich conditions.

5. The chloride ingress of GGBFS-NS-enhanced cement composites is significantly affected by the addition of GGBFS and NS, along with sulfates. The presence of NS refines the matrix by enhancing the hydration process, leading to denser C-S-H formations.

## AUTHOR BIOS

**Fulin Qu** *is a Professor at the MOE Key Laboratory of High-Speed Railway Engineering, School of Civil Engineering, Southwest Jiaotong University, Chengdu, China. His research interests include concrete curability and low-carbon construction materials.*

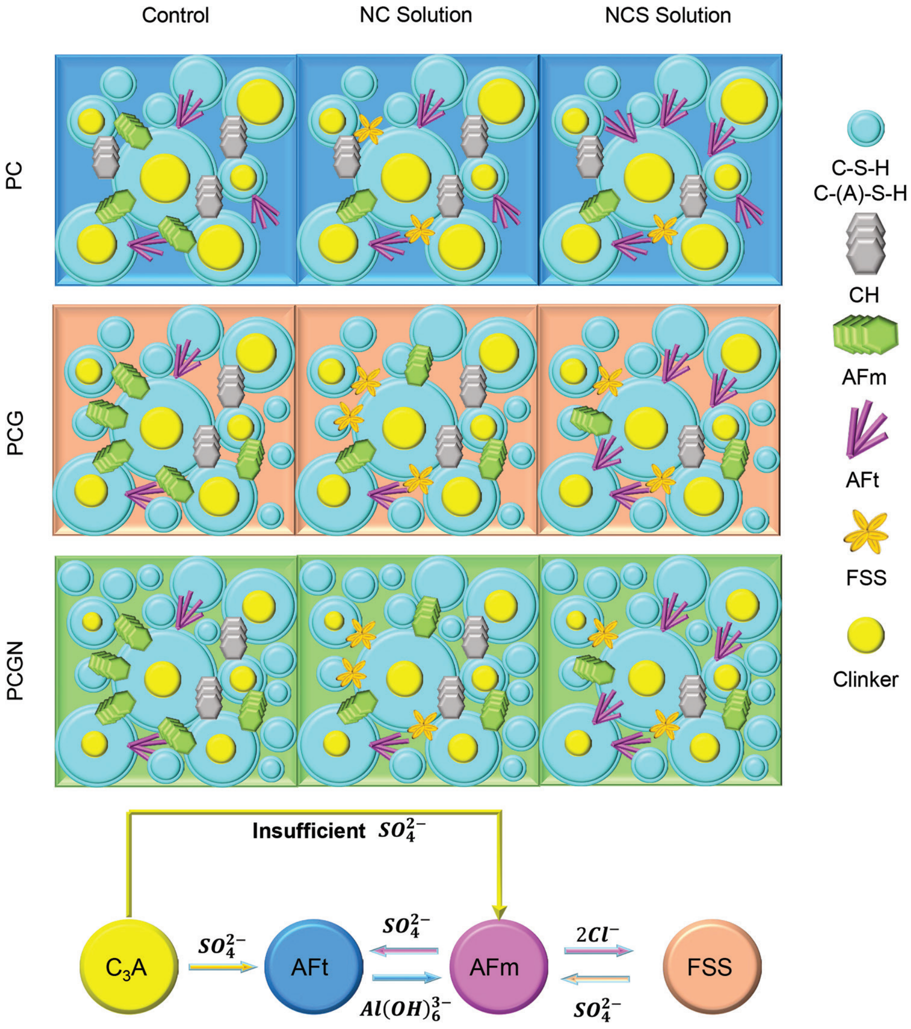

*Fig. 13—GGBFS-NS or sulfate affecting chloride ingress of GGBFS-NS cement composites within chloride-rich environment.*

**Hanbing Zhao** *is a Research Associate in the Centre for Infrastructure Engineering and Safety and the School of Civil and Environmental Engineering at the University of New South Wales, Sydney, NSW, Australia. His research interests include recycled concrete and concrete nanotechnology.*

**Qiao Wang** *is a Postdoctoral Research Fellow at the Institute of Building Materials Research at RWTH Aachen University, Aachen, Germany. His research interests include cement-based composites and limestone calcium clay concrete.*

**Kejin Wang**, *FACI, is a Professor in the Department of Civil, Construction and Environmental Engineering, Iowa State University, Ames, IA. Her research interests include chemistry, microstructure, characterization, and nanoparticle-modified concrete.*

**Wengui Li** *is a Scientia Associate Professor in the Centre for Infrastructure Engineering and Safety and the School of Civil and Environmental Engineering at the University of New South Wales. His research interests include concrete nanotechnology and multifunctional concrete.*

## ACKNOWLEDGMENTS

The authors appreciate the financial support from the Australian Research Council (ARC), Australia (FT220100177, LP240200692, LP230100288, DP220101051, DP220100036, and IH200100010).

## REFERENCES

1. Trejo, D., and Vasudevan, G. D., "Chlorides in Concrete: Science-Based Exposure Classifications and Allowable Limits," *ACI Materials Journal*, V. 121, No. 1, Jan. 2024, pp. 5-16.

2. Hayek, M.; Salgues, M.; Habouzit, F.; Bayle, S.; Souche, J.; De Weerdt, K.; and Pioch, S., "In Vitro and in Situ Tests to Evaluate the Bacterial Colonization of Cementitious Materials in the Marine Environment," *Cement and Concrete Composites*, V. 113, 2020, p. 103748. doi: 10.1016/j.cemconcomp.2020.103748

3. Yi, Y.; Zhu, D.; Guo, S.; Li, S.; Feng, G.; Liu, Z.; Zhou, L.; and Shi, C., "Development of a Low-Alkalinity Seawater Sea Sand Concrete for Enhanced Compatibility with BFRP Bar in the Marine Environment," *Cement and Concrete Composites*, V. 134, 2022, p. 104778. doi: 10.1016/j.cemconcomp.2022.104778

4. Qu, F.; Li, W.; Dong, W.; Tam, V. W.; and Yu, T., "Durability Deterioration of Concrete Under Marine Environment from Material to Structure: A Critical Review," *Journal of Building Engineering*, V. 35, 2021, p. 102074. doi: 10.1016/j.jobe.2020.102074

5. Hayek, M.; Salgues, M.; Souche, J.; De Weerdt, K.; and Pioch, S., "How to Improve the Bioreceptivity of Concrete Infrastructure Used in Marine Ecosystems? Literature Review for Mechanisms, Key Factors, and Colonization Effects," *Journal of Coastal Research*, V. 39, No. 3, 2023, pp. 553-568. doi: 10.2112/JCOASTRES-D-21-00158.1

6. De Weerdt, K.; Bernard, E.; Kunther, W.; Pedersen, M. T.; and Lothenbach, B., "Phase Changes in Cementitious Materials Exposed to Saline Solutions," *Cement and Concrete Research*, V. 165, 2023, p. 107071. doi: 10.1016/j.cemconres.2022.107071

7. Qu, F.; Li, W.; Wang, K.; Tam, V. W.; and Zhang, S., "Effects of Seawater and Undesalted Sea Sand on the Hydration Products, Mechanical Properties and Microstructures of Cement Mortar," *Construction and Building Materials*, V. 310, 2021, p. 125229. doi: 10.1016/j.conbuildmat.2021.125229

8. Du, T.; Li, C.; Wang, X.; Ma, L.; Qu, F.; Wang, B.; Peng, J.; and Li, W., "Effects of Pipe Diameter, Curing Age and Exposure Temperature on Chloride Diffusion of Concrete with Embedded PVC Pipe," *Journal of Building Engineering*, V. 57, 2022, p. 104957. doi: 10.1016/j.jobe.2022.104957

9. De Weerdt, K.; Lothenbach, B.; and Geiker, M. R., "Comparing Chloride Ingress From Seawater and NaCl Solution in Portland Cement Mortar," *Cement and Concrete Research*, V. 115, 2019, pp. 80-89. doi: 10.1016/j.cemconres.2018.09.014

10. Chen, Z., and Ye, H., "Understanding the Impact of Main Seawater Ions and Leaching on the Chloride Transport in Alkali-Activated Slag and Portland Cement," *Cement and Concrete Research*, V. 164, 2023, p. 107063. doi: 10.1016/j.cemconres.2022.107063

11. Liu, Q.; Shen, X.; Šavija, B.; Meng, Z.; Tsang, D. C.; Sepasgozar, S.; and Schlangen, E., "Numerical Study of Interactive Ingress of Calcium Leaching, Chloride Transport and Multi-Ions Coupling in Concrete," *Cement and Concrete Research*, V. 165, 2023, p. 107072. doi: 10.1016/j.cemconres.2022.107072

12. Qu, F.; Li, W.; Guo, Y.; Zhang, S.; Zhou, J. L.; and Wang, K., "Chloride-Binding Capacity of Cement-GGBFS-Nanosilica Composites Under Seawater Chloride-Rich Environment," *Construction and Building Materials*, V. 342, 2022, p. 127890. doi: 10.1016/j.conbuildmat.2022.127890

13. Xu, W.; Zhang, Y.; Li, M.; Qu, F.; Poon, C. S.; Zhu, X.; and Tsang, D. C., "Durability and Micromechanical Properties of Biochar in Biochar-Cement Composites Under Marine Environment," *Journal of Cleaner Production*, V. 450, 2024, p. 141842. doi: 10.1016/j.jclepro.2024.141842

14. Sui, S.; Wilson, W.; Georget, F.; Maraghechi, H.; Kazemi-Kamyab, H.; Sun, W.; and Scrivener, K., "Quantification Methods for Chloride Binding in Portland Cement and Limestone Systems," *Cement and Concrete Research*, V. 125, 2019, p. 105864. doi: 10.1016/j.cemconres.2019.105864

15. He, H.; Qiao, H.; Sun, T.; Yang, H.; and He, C., "Research Progress in Mechanisms, Influence Factors and Improvement Routes of Chloride Binding for Cement Composites," *Journal of Building Engineering*, V. 86, 2024, p. 108978. doi: 10.1016/j.jobe.2024.108978

16. Ojha, P.; Singh, A.; Singh, B.; Sen, S.; Kumar, R.; and Patra, B. M., "Studies on Portland Slag Cement Made Using Blast-Furnace and Linz-Donawitz Slag," *ACI Materials Journal*, V. 120, No. 1, Jan. 2023, pp. 143-154.

17. Yi, Y.; Zhu, D.; Guo, S.; Zhang, Z.; and Shi, C., "A Review on the Deterioration and Approaches to Enhance the Durability of Concrete in the Marine Environment," *Cement and Concrete Composites*, V. 113, 2020, p. 103695. doi: 10.1016/j.cemconcomp.2020.103695

18. Li, H.; Farzadnia, N.; Zhao, Y.; Hu, X.; and Shi, C., "Effects of SCMs on Chloride Binding Capacity of Ultra-Low Water-to-Binder Ratio Cement Paste with Internally Introduced Chloride," *Construction and Building Materials*, V. 413, 2024, p. 134725. doi: 10.1016/j.conbuildmat.2023.134725

19. De Weerdt, K., "Chloride Binding in Concrete: Recent Investigations and Recognised Knowledge Gaps: RILEM Robert L'Hermite Medal Paper 2021," *Materials and Structures*, V. 54, No. 6, 2021, p. 214. doi: 10.1617/s11527-021-01793-9

20. Qu, F.; Zhang, Y.; Zhu, X.; Xu, W.; Poon, C. S.; Li, W.; and Tsang, D. C., "Roles of Wood Waste Biochar for Chloride Immobilization in GGBS-Blended Cement Composites," *Construction and Building Materials*, V. 411, 2024, p. 134389. doi: 10.1016/j.conbuildmat.2023.134389

21. Song, B.; Hu, X.; Liu, S.; and Shi, C., "Chloride Binding of Early $CO_2$-Cured Portland Cement-Fly Ash-GGBS Ternary Pastes," *Cement and Concrete Composites*, V. 134, 2022, p. 104793. doi: 10.1016/j.cemconcomp.2022.104793

22. Bondar, D.; Basheer, M.; and Nanukuttan, S., "Suitability of Alkali Activated Slag/Fly Ash (AA-GGBS/FA) Concretes for Chloride Environments: Characterisation Based on Mix Design and Compliance Testing," *Construction and Building Materials*, V. 216, 2019, pp. 612-621. doi: 10.1016/j.conbuildmat.2019.05.043

23. Otieno, M.; Beushausen, H.; and Alexander, M., "Effect of Chemical Composition of Slag on Chloride Penetration Resistance of Concrete," *Cement and Concrete Composites*, V. 46, 2014, pp. 56-64. doi: 10.1016/j.cemconcomp.2013.11.003

24. Ogirigbo, O. R., and Black, L., "Chloride Binding and Diffusion in Slag Blends: Influence of Slag Composition and Temperature," *Construction and Building Materials*, V. 149, 2017, pp. 816-825. doi: 10.1016/j.conbuildmat.2017.05.184

25. Ogirigbo, O. R., and Black, L., "Influence of Slag Composition and Temperature on the Hydration and Microstructure of Slag Blended Cements," *Construction and Building Materials*, V. 126, 2016, pp. 496-507. doi: 10.1016/j.conbuildmat.2016.09.057

26. Ogirigbo, O. R., and Ukpata, J., "Effect of Chlorides and Curing Duration on the Hydration and Strength Development of Plain and Slag Blended Cements," *Journal of Civil Engineering Research*, V. 7, No. 1, 2017, pp. 9-16.

27. Ogirigbo, O. R., and Black, L., "The Effect of Slag Composition and Curing Duration on the Chloride Ingress Resistance of Slag-Blended Cements," *Advances in Cement Research*, V. 31, No. 5, 2019, pp. 243-250. doi: 10.1680/jadcr.17.00152

28. Babaee, M., and Castel, A., "Chloride Diffusivity, Chloride Threshold, and Corrosion Initiation in Reinforced Alkali-Activated Mortars: Role of Calcium, Alkali, and Silicate Content," *Cement and Concrete Research*, V. 111, 2018, pp. 56-71. doi: 10.1016/j.cemconres.2018.06.009

29. Niu, X.; Feng, G.; Han, Y.; Liu, Q.; Xue, G.; Cui, J.; and Song, C., "Synergistic Effect of Surfactant and Chlorine Salt on Dispersion of Nano-SiO2 and Performance of Cement-Based Grout Containing a Large Amount of Bentonite," *Cement and Concrete Composites*, V. 131, 2022, p. 104587. doi: 10.1016/j.cemconcomp.2022.104587

30. Li, Y.; Liu, Q.; Liu, Y.; Wang, D.; Song, W.; Chen, Y.; and Liu, J., "Calcium Chloride Hexahydrate/Nano-$SiO_2$ Composites as Form-Stable Phase Change Materials for Building Energy Conversation: The Influence of Pore Size of Nano-$SiO_2$," *Energy and Building*, V. 208, 2020, p. 109672. doi: 10.1016/j.enbuild.2019.109672

31. Liu, X.; Ma, B.; Tan, H.; Zhang, T.; Mei, J.; Qi, H.; Chen, P.; and Wang, J., "Effects of Colloidal Nano-SiO2 on the Immobilization of Chloride Ions in Cement-Fly Ash System," *Cement and Concrete Composites*, V. 110, 2020, p. 103596. doi: 10.1016/j.cemconcomp.2020.103596

32. Geng, J.; Easterbrook, D.; Li, L.; and Mo, L., "The Stability of Bound Chlorides in Cement Paste with Sulfate Attack," *Cement and Concrete Research*, V. 68, 2015, pp. 211-222. doi: 10.1016/j.cemconres.2014.11.010

33. Hemstad, P.; Lothenbach, B.; and De Weerdt, K., "Distribution of Sulphate and Aluminum in Hydrated Cement Pastes," *Cement and Concrete Research*, V. 180, 2024, p. 107467. doi: 10.1016/j.cemconres.2024.107467

34. Hogancamp, J., and Grasley, Z., "The Use of Microfine Cement to Enhance the Efficacy of Carbon Nanofibers with Respect to Drying Shrinkage Crack Resistance of Portland Cement Mortars," *Cement and Concrete Composites*, V. 83, 2017, pp. 405-414. doi: 10.1016/j.cemconcomp.2017.08.006

35. Babaahmadi, A.; Machner, A.; Kunther, W.; Figueira, J.; Hemstad, P.; and De Weerdt, K., "Chloride Binding in Portland Composite Cements Containing Metakaolin and Silica Fume," *Cement and Concrete Research*, V. 161, 2022, p. 106924. doi: 10.1016/j.cemconres.2022.106924

36. Figueiredo, F.; Figueiredo, G.; Botero, E.; Figueiredo, N.; and Maia, L., "Analysis of Partial Substitution of Cement with Marble and Granite Powders in Concrete Production," *ACI Materials Journal*, V. 119, No. 6, Nov. 2022, pp. 211-219.

37. De Weerdt, K.; Lothenbach, B.; Krüger, M. E.; Ranger, M.; and Leemann, A., "Impact of SCMs on Alkali Concentration in Pore Solution," *Proceedings of the 17th International Conference on Alkali-Aggregate Reaction in Concrete: ICAAR 2024 – Volume 1*, L. F. M. Sanchez and C. Trottier, eds., Springer, Cham, Switzerland, 2024, pp. 3-10.

38. De Weerdt, K.; Wilson, W.; Machner, A.; and Georget, F., "Chloride Profiles–What Do They Tell Us and How Should They Be Used?" *Cement and Concrete Research*, V. 173, 2023, p. 107287. doi: 10.1016/j.cemconres.2023.107287

39. Tabet, W. E.; Cerato, A. B.; Elwood Madden, A. S.; and Jentoft, R. E., "Characterization of Hydration Products' Formation and Strength Development in Cement-Stabilized Kaolinite Using TG and XRD," *Journal of Materials in Civil Engineering*, ASCE, V. 30, No. 10, 2018, p. 04018261. doi: 10.1061/(ASCE)MT.1943-5533.0002454

40. De Matos, P. R.; Neto, J. S. A.; Jansen, D.; Angeles, G.; Kirchheim, A. P.; and Campos, C. E., "In-Situ Laboratory X-Ray Diffraction Applied to Assess Cement Hydration," *Cement and Concrete Research*, V. 162, 2022, p. 106988. doi: 10.1016/j.cemconres.2022.106988

41. Sevelsted, T. F., and Skibsted, J., "Carbonation of C-S-H and C-A-S-H Samples Studied By $^{13}$C, $^{27}$Al and $^{29}$Si MAS NMR Spectroscopy," *Cement and Concrete Research*, V. 71, 2015, pp. 56-65. doi: 10.1016/j.cemconres.2015.01.019

42. Jamsheer, A. F.; Kupwade-Patil, K.; Büyüköztürk, O.; and Bumajdad, A., "Analysis of Engineered Cement Paste Using Silica Nanoparticles and Metakaolin Using $^{29}$Si NMR, Water Adsorption and Synchrotron X-Ray Diffraction," *Construction and Building Materials*, V. 180, 2018, pp. 698-709. doi: 10.1016/j.conbuildmat.2018.05.272

43. Georget, F.; Wilson, W.; and Scrivener, K. L., "Edxia: Microstructure Characterisation From Quantified SEM-EDS Hypermaps," *Cement and Concrete Research*, V. 141, 2021, p. 106327. doi: 10.1016/j.cemconres.2020.106327

44. Wilson, W.; Gonthier, J. N.; Georget, F.; and Scrivener, K. L., "Insights on Chemical and Physical Chloride Binding in Blended Cement Pastes," *Cement and Concrete Research*, V. 156, 2022, p. 106747. doi: 10.1016/j.cemconres.2022.106747

45. Kunther, W.; Dai, Z.; and Skibsted, J., "Thermodynamic Modeling of Hydrated White Portland Cement–Metakaolin–Limestone Blends Utilizing Hydration Kinetics From $^{29}$Si MAS NMR Spectroscopy," *Cement and Concrete Research*, V. 86, 2016, pp. 29-41. doi: 10.1016/j.cemconres.2016.04.012

46. Shi, Z.; Lothenbach, B.; Geiker, M. R.; Kaufmann, J.; Leemann, A.; Ferreiro, S.; and Skibsted, J., "Experimental Studies and Thermodynamic Modeling of the Carbonation of Portland Cement, Metakaolin and Limestone Mortars," *Cement and Concrete Research*, V. 88, 2016, pp. 60-72. doi: 10.1016/j.cemconres.2016.06.006

47. Huber, B.; Hilbig, H.; Mago, M. M.; Drewes, J. E.; and Müller, E., "Comparative Analysis of Biogenic and Chemical Sulfuric Acid Attack on Hardened Cement Paste Using Laser Ablation-ICP-MS," *Cement and Concrete Research*, V. 87, 2016, pp. 14-21. doi: 10.1016/j.cemconres.2016.05.003

48. Xu, J.; Zhang, C.; Jiang, L.; Tang, L.; Gao, G.; and Xu, Y., "Releases of Bound Chlorides From Chloride-Admixed Plain and Blended Cement Pastes Subjected to Sulfate Attacks," *Construction and Building Materials*, V. 45, 2013, pp. 53-59. doi: 10.1016/j.conbuildmat.2013.03.068

49. Shi, Z.; Geiker, M. R.; Lothenbach, B.; De Weerdt, K.; Garzón, S. F.; Enemark-Rasmussen, K.; and Skibsted, J., "Friedel's Salt Profiles From Thermogravimetric Analysis and Thermodynamic Modelling of Portland Cement-Based Mortars Exposed to Sodium Chloride Solution," *Cement and Concrete Composites*, V. 78, 2017, pp. 73-83. doi: 10.1016/j.cemconcomp.2017.01.002

50. Torréns-Martín, D., and Fernández-Carrasco, L., "Effect of Sulfate Content on Cement Mixtures," *Construction and Building Materials*, V. 48, 2013, pp. 144-150. doi: 10.1016/j.conbuildmat.2013.05.106

51. Nasrazadani, S.; Eghtesad, R.; Sudoi, E.; Vupputuri, S.; Ramsey, J.; and Ley, M., "Application of Fourier Transform Infrared Spectroscopy to Study Concrete Degradation Induced by Biogenic Sulfuric Acid," *Materials and Structures*, V. 49, No. 5, 2016, pp. 2025-2034. doi: 10.1617/s11527-015-0631-5

52. Trdan, U., and Grum, J., "SEM/EDS Characterization of Laser Shock Peening Effect on Localized Corrosion of Al Alloy in a Near Natural Chloride Environment," *Corrosion Science*, V. 82, 2014, pp. 328-338. doi: 10.1016/j.corsci.2014.01.032

53. Ansberque, C.; Mark, C.; Caulfield, J. T.; and Chew, D. M., "Combined In-Situ Determination of Halogen (F, Cl) Content in Igneous and Detrital Apatite by SEM-EDS and LA-Q-ICPMS: A Potential New Provenance Tool," *Chemical Geology*, V. 524, 2019, pp. 406-420. doi: 10.1016/j.chemgeo.2019.07.012

54. Wang, Q.; Wilson, W.; and Scrivener, K., "Unidirectional Penetration Approach for Characterizing Sulfate Attack Mechanisms on Cement Mortars and Pastes," *Cement and Concrete Research*, V. 169, 2023, p. 107166. doi: 10.1016/j.cemconres.2023.107166

55. Wang, Q.; Wilson, W.; and Scrivener, K., "A Novel Uniaxial Penetration Approach to Investigate External Sulfate Attack on Blended Cement Pastes," *International RILEM Conference on Synergising Expertise Towards Sustainability and Robustness of Cement-based Materials and Concrete Structures: SynerCrete'23 – Volume 1*, A. Jędrzejewska, F. Kanavaris, M. Azenha, F. Benboudjema, and D. Schlicke, eds., Springer, Cham, Switzerland, 2023, pp. 625-634.

56. Huang, Q.; Liu, H.; Wang, Q.; Shan, Y.; Tang, D.; Zhang, Z.; and Zhu, X., "Electric Field-Induced Deterioration of Cement Mortars Owing to Calcium Leaching," *Developments in the Built Environment*, V. 17, 2024, p. 100303. doi: 10.1016/j.dibe.2023.100303

57. Ukpata, J. O.; Basheer, P.; and Black, L., "Slag Hydration and Chloride Binding in Slag Cements Exposed to a Combined Chloride-Sulphate Solution," *Construction and Building Materials*, V. 195, 2019, pp. 238-248. doi: 10.1016/j.conbuildmat.2018.11.055

ACI MATERIALS JOURNAL TECHNICAL PAPER

Title No. 123-M24

# Enhancing Concrete Sustainability through $CO_2$ Mineralization: A Cost-Effective Solution

by Md Athar Kazmi and Lakshmi Vara Prasad Meesaraganda

*Carbon dioxide ($CO_2$) mineralization in concrete enhances cement hydration by reacting with calcium-rich materials, forming nanoscale calcium carbonate that fills micropores. This study explores $CO_2$-mineralized concrete performance produced using a two-step mineralization process. Concrete with 0.2% $CO_2$ by cement weight exhibited significantly higher compressive strength, increasing by 18.78%, 19.27%, and 20.63% at 7, 28, and 56 days, respectively. Isothermal calorimetric analysis confirmed increased heat evolution in $CO_2$-mineralized cement paste, while X-ray diffraction and scanning electron microscopy revealed calcium carbonate formation and more ettringite volume. The higher strength gain due to $CO_2$ mineralization is used to leverage the cement content. A comparative study reveals that $CO_2$-mineralized concrete with 7.5% reduced cement content achieves equivalent strength and durability to conventional concrete, reducing carbon emissions by 8% while significantly lowering cost per unit strength and enhancing sustainability and performance.*

**Keywords:** calcium carbonate; carbon dioxide ($CO_2$) mineralization; carbon reduction; concrete durability; concrete strength; hydration of cement; sustainability.

## INTRODUCTION

Approximately 0.6 metric tons of carbon dioxide ($CO_2$) are released while manufacturing one metric ton of ordinary portland cement (OPC).[1] $CO_2$ capture and beneficial use can minimize anthropogenic greenhouse gas emissions.[2,3] Carbon storage in cementitious materials is one of the preeminent solutions to the issue of rising anthropogenic $CO_2$ emissions.[4,5] Furthermore, this practice makes the construction sector more environmentally friendly and sustainable when industrial waste is used.[6] This process offers a dual benefit: first, it reduces $CO_2$ emissions and permanently sequestrates it; second, it is used as a raw material in the manufacturing of new construction materials.[7,8]

Concrete carbonation is a durability concern due to the diminished passivity of concrete, causing reinforcement corrosion. Instead of having the same effect, early-age carbonation combines with the hydrating stage to produce micro-level calcium carbonate ($CaCO_3$) and more hydration products that fill the concrete's minute pores,[9] densifying the concrete and enhancing its strength and durability.[10,11] In the 1970s, the University of Illinois started research to explore the carbonation process of OPC.[12] The calcium phases in hydrating OPC, such as dicalcium silicate ($C_2S$) and tricalcium silicate ($C_3S$), react with $CO_2$ and water to form $CaCO_3$ and calcium silicate hydrate (C-S-H) gel, as presented in Eq. (1) and (2)[13]

$$2(3CaO \cdot SiO_2) + 3CO_2 + 3H_2O \rightarrow 3CaO \cdot 2SiO_2 \cdot 3H_2O + 3CaCO_3 \quad (1)$$

$$2(2CaO \cdot SiO_2) + CO_2 + 3H_2O \rightarrow 3CaO \cdot 2SiO_2 \cdot 3H_2O + CaCO_3 \quad (2)$$

Furthermore, the calcium hydroxide (CH) in cement paste reacts with $CO_2$, as stated in Eq. (3)[14]

$$Ca(OH)_2 + CO_2 \rightarrow +CaCO_3 + H_2O \quad (3)$$

The reaction of $CO_2$ with the hydrating phase of OPC is exothermic and water-starving, so an optimal dose of $CO_2$ mineralization gives the best result.[15] The mineralization of small doses of $CO_2$ improved concrete strength and durability through a complication noticed in the mineralization process.[16,17] $CO_2$ is widely used in the concrete industry in three ways: carbon-based curing, carbon conditioning, and direct mineralization of $CO_2$ during mixing.[16,18,19] Carbonation curing has many limitations, such as the requirement of a closed chamber for curing, slow diffusion rate, low efficiency, application in precast concrete elements only, and overall high process expenditure.[14,20] Similarly, carbon conditioning is improving the characteristics of old adhered mortars of recycled aggregate.[21,22] Hence, carbon conditioning has similar limitations to carbon curing, such as the requirement of a closed chamber for carbon conditioning, slow diffusion rate, low efficiency, application in recycled aggregate concrete only, and overall high process expenditure.[23,24] Whereas the direct mineralization of $CO_2$ during mixing can be carried out conveniently, with a fast reaction rate and high efficiency, it does not require any chamber for long-term curing or conditioning. Also, it is a cost-effective approach.[25]

In current practices of $CO_2$ mineralization in concrete, the $CO_2$ is introduced with the concrete during the mixing process in the concrete mixer.[26] $CO_2$ mineralization during mixing requires an airtight closed mixing drum; furthermore, the efficiency of $CO_2$ use is approximately 60%. The present work followed a simplified two-step mineralization process, improving efficiency and cost-effectiveness. In the current work, $CO_2$ was first added to a slurry of OPC in a closed cylindrical container. Then, $CO_2$-mineralized OPC is mixed with the remaining ingredients to produce $CO_2$-mineralized concrete. While incorporating $CO_2$ into concrete during mixing improves its performance, the reaction between $CO_2$ and the hydration products of OPC also leads to water

---

*ACI Materials Journal*, V. 123, No. 2, March 2026.

MS No. M-2025-024.R4, doi: 10.14359/51749258, received September 5, 2025, and reviewed under Institute publication policies. Pertinent discussion including author's closure, if any, will be published ten months from this journal's date if the discussion is received within four months of the paper's print publication.

extraction, resulting in a marginal reduction in workability. However, the workability reduction scale is small, which can be deemed acceptable. This paper examines the concrete prepared with two-step $CO_2$ mineralization; the strength increment due to the $CO_2$ mineralization is used to design concrete mixtures with leveraged cement content. Further investigation was done to compare the durability of conventional concrete with $CO_2$-mineralized concrete with leveraged cement content. To find the optimal amount of $CO_2$ for the strength of concrete, different concrete mixtures were treated with varying doses of $CO_2$, and a conventional mixture that did not include any $CO_2$ mineralization was examined. Compared to conventional concrete, a relative strength change was observed, with increased compressive strength, enabling concrete design with reduced OPC. In the present investigation, $CO_2$ is captured from the emitting source, compressed and stored in liquefied form, and then transported to where it is used. Workability was assessed using slump value testing, while calorimetric analysis determined the total heat of hydration. Mechanical parameters were evaluated through compressive strength, flexural strength, and splitting tensile strength tests. The durability of concrete was assessed by the depth of water penetration test and carbonation resistance test; additionally, scanning electron microscopy and X-ray diffraction were used to examine the effects of $CO_2$ mineralization on the microstructural characteristics of concrete. Hence, the current work presents an innovative procedure for improving concrete performance through using $CO_2$ as an admixture and leveraging the OPC content, which provides a promising pathway for the valuable application of captured $CO_2$ in the construction industry, giving double-fold benefits.

## RESEARCH SIGNIFICANCE

Enhancing the sustainability of concrete has become a critical priority, driven by demands and performance targets from both within and outside the industry. Addressing this challenge necessitates innovative solutions, including new materials, processes, and ideas. Successfully scaling such innovations requires careful evaluation of their value and potential impacts. Introducing $CO_2$ into fresh concrete can promote mineralization, enhancing its compressive strength. This study aims to bring together key factors essential for adopting cleaner concrete technologies, including performance demonstration, durability assurance, and validation of environmental benefits.

## MATERIALS AND EXPERIMENTAL PROGRAM

### Materials

Commercially available OPC conforming to ASTM C150/C150M-16[27] was used for making concrete. The physical characteristics of OPC and fly ash are presented in Table 1, and their chemical characteristics are summarized in Table 2. The OPC has a fineness and specific gravity of 304 $m^2/kg$ and 3.14, respectively. Class F fly ash was used, according to ASTM C618-12a,[28] obtained from a nearby thermal power plant, located in the Bongaigaon district of the Indian state of Assam, with a specific gravity of 2.21. The coarse aggregate used was local crushed stone aggregate with a nominal maximum size of 20 mm. The coarse aggregate used had a fineness modulus of 7.084 and a specific gravity of 2.84. This project used Zone II River sand, readily available locally as fine aggregate. The fine aggregate has a specific gravity of 2.63 and a fineness modulus 2.51. Concrete specimens were mixed and allowed to cure in potable water. Ninety-nine-percent purified $CO_2$ from an ethanol factory was mineralized into concrete.

**Table 1—Physical characteristics of OPC**

| Properties | | Result |
|---|---|---|
| Fineness, $m^2/kg$ | | 304 |
| Residue on 75 μm, % | | 4.4 |
| Specific gravity | | 3.14 |
| Consistency, % | | 32 |
| Setting time, minutes | Initial | 52 |
| | Final | 320 |
| Compressive strength, MPa | 7 days | 34.5 |
| | 28 days | 53.8 |

**Table 2—Chemical compositions of OPC, % by weight**

| Contents | OPC | Fly ash |
|---|---|---|
| CaO | 63.46 | 4.78 |
| MgO | 0.92 | 2.53 |
| $SiO_2$ | 21.57 | 45.56 |
| $Al_2O_3$ | 4.73 | 32.54 |
| $SO_3$ | 2.54 | 0.65 |
| $Na_2O$ | 0.17 | 0.64 |
| $Fe_2O_3$ | 2.83 | 3.58 |
| $K_2O$ | 0.53 | 1.52 |
| Loss on ignition | 3.25 | 8.2 |

The fine aggregate used in this study was sourced from riverbeds due to its abundant local availability. The particle-size distribution exhibited a smooth S-shaped curve, indicating that the fine aggregate was well-graded. Additionally, it was confirmed that the sample met the Zone II requirements outlined in ASTM C33/C33M-24a.[29] Key properties of the river sand, such as water absorption, specific gravity, and fineness modulus, were recorded as 0.8%, 2.48, and 2.56, respectively. For coarse aggregate, 20 mm nominal size crushed stone was used, which adhered to the specifications of ASTM C33/C33M.[29] The coarse aggregate had a specific gravity of 2.74, water absorption of 1.04%, and a fineness modulus of 7.02. The particle-size distribution of both fine and coarse aggregates was determined through sieve analysis as per ASTM C33/C33M.[29]

### Mixture proportioning

Following the recommendations of ACI 211.1-91,[30] concrete mixture proportioning was done to meet the requirements as recommended in the ACI 301-20[31] specification. The concrete mixture was designed for a target compressive strength of 40 MPa at 28 days of testing. The

**Table 3—Mixture proportions of $CO_2$-mineralized concrete mixtures, kg/m$^3$**

| Ingredients | CM-0 | CM-1 | CM-2 | CM-3 |
|---|---|---|---|---|
| OPC | 400 | 400 | 400 | 400 |
| Fly ash | 100 | 100 | 100 | 100 |
| Water | 192 | 192 | 192 | 192 |
| Water-binder ratio (*w*/*b*) | 0.4 | 0.4 | 0.4 | 0.4 |
| Fine aggregate | 620 | 620 | 620 | 620 |
| Coarse aggregate | 1070 | 1070 | 1070 | 1070 |
| High-range water-reducing admixture | 1.00 | 1.05 | 1.10 | 1.15 |
| $CO_2$ | — | 0.400 | 0.800 | 1.200 |

**Table 4—Mixture proportions of $CO_2$-mineralized concrete mixtures with reduced OPC, kg/m$^3$**

| Ingredients | CM-2 | CM-21 | CM-22 | CM-23 | CM-24 |
|---|---|---|---|---|---|
| OPC | 400 | 390 | 380 | 370 | 360 |
| Fly ash | 100 | 108 | 116 | 124 | 132 |
| Water | 192 | 192 | 192 | 192 | 192 |
| Water-binder ratio (*w*/*b*) | 0.4 | 0.4 | 0.4 | 0.4 | 0.4 |
| Fine aggregate | 620 | 620 | 620 | 620 | 620 |
| Coarse aggregate | 1070 | 1070 | 1070 | 1070 | 1070 |
| High-range water-reducing admixture | 1.10 | 1.10 | 1.10 | 1.10 | 1.10 |
| $CO_2$ | 0.800 | 0.780 | 0.760 | 0.740 | 0.720 |

experimental program was conducted in two phases; in the first phase, the optimum dose of $CO_2$ to be mineralized was determined. To find the optimum dose of $CO_2$ in the concrete, four mixture designations were considered: CM-0, CM-1, CM-2, and CM-3, having $CO_2$ doses of 0, 0.1,0.2, and 0.3% respectively, by weight of OPC. Table 3 presents the weight of ingredients per unit volume of concrete with varying doses of $CO_2$. The compressive strength results in stage one indicate that the CM-2 mixture with 0.2% $CO_2$ performs better. In the second phase, cement was leveraged with the increment of compressive strength due to $CO_2$ mineralization without compromising its strength. A 2.5% reduction in OPC was implemented in CM-2, and to balance the mixture design, 5 kg of fly ash was added to each step of the OPC reduction. For the second phase, the mixture designations CM-21, CM-22, CM-32, and CM-34 had 2.5, 5, 7.5, and 10% lower OPC than CM-2. The mixture proportions for $CO_2$-mineralized concrete mixtures and $CO_2$-mineralized concrete mixtures with reduced OPC are presented in Tables 3 and 4, respectively.

## $CO_2$ mineralization into concrete

The process of mineralizing $CO_2$ into concrete was done in two steps; initially, the $CO_2$ was sequestrated in the OPC slurry, simplifying the process and raising the $CO_2$ sequestration efficiency to approximately 99%. Subsequently, it was integrated with the remaining ingredients to produce $CO_2$-mineralized concrete. The OPC slurry was prepared in a cylindrical container; after that, the cylindrical container was tightly packed with bolts. A flexible pipe was then connected between the $CO_2$ and slurry cylinders, and the slurry cylinder was placed on a weighing balance. After that, the required amount of $CO_2$ was added to the slurry cylinder, and then the slurry cylinder's valve was closed. To achieve a thorough reaction between $CO_2$ and OPC slurry, the cylinder was vigorously stirred for 1 minute. After that, the $CO_2$-sequestered OPC slurry was combined with the remaining components in the second stage to produce $CO_2$-mineralized concrete. The extent of $CO_2$ uptake was verified by monitoring the weight gain of the slurry cylinder placed on a digital balance, which stabilized once the injected gas was fully absorbed. Given the high alkalinity of the OPC slurry, the added $CO_2$ rapidly reacted to form stable carbonates. The sealed setup and vigorous stirring minimized leakage, ensuring nearly complete sequestration. Any trace unreacted $CO_2$ would remain dissolved in the pore solution and progressively mineralize during hydration, preventing its escape from the concrete.

## Experimental program

The calorimetric analysis was carried out as per ASTM C1702-23[32] on OPC slurry; entering the heat sink through the sensor, the heat of hydration emitted by the cementitious sample is measured by the calorimeter, which outputs the difference in thermal power, or heat flow, between the reference and sample cells. Data acquisition units and commercial calorimeters use the calibration equation to present the raw output data in units of J/g cement. Fourier-transform infrared spectroscopy (FTIR) was used to detect the hydration products after 24 hours, using a spectrometer on the OPC slurry, within a wavenumber range of 550 to 4000 cm$^{-1}$. Potassium bromide (KBr) powder was added to the samples at 1:100. The experimental test has a resolution of 2.0 cm$^{-1}$.

As per IS 1199 (Part-2),[33] equivalent to ASTM C143/C143M-20,[34] concrete workability was assessed by the slump test. The fresh density was calculated as the net weight of the container filled with concrete (in kg) ($M_c$) minus the net weight of the empty container (in kg) ($M_m$) divided by the total volume of the container (in m$^3$) ($V_m$), as given in Eq. (4), per IS 1199 (Part-3):2018[35] equivalent to ASTM C642-21.[36]

$$\text{Density (kg/m}^3\text{)} = \frac{M_c - M_m}{V_m} \tag{4}$$

The compressive strength, splitting tensile strength, and flexural strength tests were evaluated after 7, 28, and 56 days of water curing. The strength tests were conducted in accordance with IS 516 (Part 1/Sec 1):2021,[37] corresponding to ASTM C39/C39M-01[38] for compressive strength, ASTM C496/C496M-17[39] for splitting tensile strength, and ASTM C78/C78M-21[40] for flexural strength. Strength assessments were conducted on the cured concrete, and the load was applied steadily and without shock, maintaining a constant rate. For the compressive strength test, a compression testing machine with a capacity of 3000 kN was used to apply a load of 14 N/mm$^2$/min on a 150 mm cube. The splitting tensile strength test was conducted using a universal testing machine with a capacity of 2000 kN, applying a load of 0.7 N/mm$^2$/min on a cylindrical specimen measuring 300 mm in height and 150 mm in diameter. The flexural strength test was performed on a 100 x 500 mm beam, applying a 0.7 N/mm$^2$/min load. The test report, under the results and conclusions section, shows the average of the three samples examined for each day of testing.

The depth of water penetration test assesses concrete's resistance to water ingress under pressure, as per IS 516 (Part 2/Sec 1):2018[41] and EN 12390 (Part-8):2019.[42] A water pressure of 10 bars is applied to one face of a water-saturated concrete specimen for 72 hours. The specimen is then split longitudinally to expose the cross section. The water penetration depth is measured at various points to determine the maximum and average depths. This test helps evaluate concrete's impermeability and durability, with lower penetration depths indicating better performance in resisting water ingress.

The carbonation test was conducted following IS 516 (Part-2/Sec-4):2021,[43] which corresponds to RILEM CPC-18 (1988).[44] Prisms were water-cured for 28 days, then air-conditioned for another 28 days before sealing all but two opposite faces with paraffin wax. They were then placed in an accelerated carbonation chamber with controlled $CO_2$ concentration (3.0 ± 0.5% by volume), temperature (27 ± 2°C), and humidity (65 ± 5%) for 70, 120, and 180 days. After each period, a 50 mm thick slice was cut using a hammer and chisel, and phenolphthalein indicator was sprayed to identify carbonated and non-carbonated zones. Carbonation depth was measured at 10 points per prism, with necessary corrections made for aggregate density and air voids as per IS 516 (Part-5/Sec-3):2021,[45] which is equivalent to ASTM C642-21.[36]

X-ray diffraction (XRD) analysis was used to obtain diffraction patterns of the materials, aiding in determining their composition. Mineralogical studies were carried out using an XRD instrument equipped with a Cu-K$\alpha$ X-ray radiation source, as per ASTM C1365-18.[46] The analysis employed a step size of 0.026 degrees $\alpha$, covering a $2\theta$ angle range from 10 to 90 degrees at an acceleration voltage of 40 kV. Samples for XRD were prepared after completing compressive strength tests by halting hydration in anhydrous ethanol, drying the specimens in a 60°C oven for 24 hours, and grinding them into fine powder using a mortar. The powdered samples, mixed with anhydrous ethanol and passed through a 0.075 mm sieve, were then ready for XRD testing. Additionally, scanning electron microscopy (SEM) analysis was conducted following ASTM C1723-10[47] to examine the distinct morphological features of the various concrete mixtures.

## RESULTS AND DISCUSSION

### Calorimetric analysis

Isothermal calorimetric analysis was employed to investigate the hydration kinetics of cement paste, enabling real-time observation of the hydration reaction. The test was conducted as per ASTM C1702-23[32] on cement pastes having varying doses of $CO_2$—the cement paste designations C0, C1, C2, and C3 having 0, 0.1, 0.2, and 0.3% of $CO_2$ by weight of OPC, respectively. Figures 1(a) and (b) illustrate the rate of heat evolution and cumulative heat flow for cement pastes with and without $CO_2$. Samples treated with $CO_2$ showed higher peak heat flow than the conventional control batch. Figure 1(a) shows that the hydration onset after the induction period occurred earlier in all $CO_2$-treated samples than in the control, with subsequent hydration rates comparable to the reference. Notably, while the impact of $CO_2$ on hydration onset was consistent across dosages, the peak energy release decreased for $CO_2$ doses above 0.2%. The 0.2% $CO_2$ cement paste exhibited the highest peak energy release relative to the control. Additionally, the onset of heat evolution in $CO_2$-mineralized batches was earlier than in the control batch.

The heat energy curves provide insights into hydration behavior; in the carbonated samples,[48] the energy release for the central silicate hydration peak exceeded the subsequent aluminate activity peak, indicating modifications in $C_3S$ hydration. Conversely, in the non-$CO_2$-injected batch, the aluminate peak was more prominent than the leading hydration peak, highlighting a distinct hydration pattern. The cumulative heat of hydration, derived from integrating the power curves, is presented in Table 5. It presents that $CO_2$ mineralization increased total hydration, with the 0.2% $CO_2$ sample showing the maximum enhancement. However, at higher $CO_2$ dosages, a slight reduction in total hydration was observed at 40 hours. Nucleation sites are essential for the formation of hydration products. To enhance the hydration reaction, nuclei of hydration products begin forming on the surface of clinker particles shortly after initial mixing.[49]

The $CaCO_3$ generated in the $CO_2$-mixed pastes directly facilitates additional cement hydration. $CO_2$ accelerates the nucleation and growth of CH and C-S-H gel.[50] In the early

**Table 5—Heat of hydration and heat relative to reference at 24 and 40 hours of hydration**

| Batch | Energy at 24 hours, J/g | Relative to reference at 24 hours, % | Energy at 40 hours, J/g | Relative to reference at 40 hours, % |
|---|---|---|---|---|
| C0 | 208 | — | 267 | — |
| C1 | 225 | 8.17 | 284 | 6.37 |
| C2 | 236 | 13.46 | 292 | 9.36 |
| C3 | 231 | 11.06 | 291 | 8.99 |

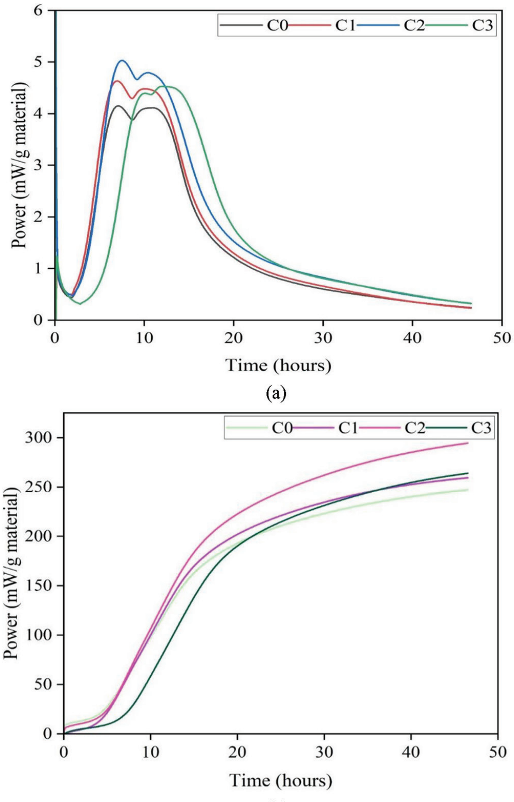

(a)

(b)

*Fig. 1—(a) Rate of heat of hydration; and (b) total heat of hydration.*

stages, $CaCO_3$ was deposited sporadically on the surface of anhydrous clinker particles, filling the matrix and serving as nucleation sites to increase the hydration reaction. However, later on, the residual $CO_3^{2-}$ in the sample solution, linked to the excess $CO_2$ supplied,[51] preferentially mixed with the $Ca^{2+}$ near the active dissolution sites rather than those away. Consequently, a thick layer of $CaCO_3$ formed on the clinker surface, preventing more thorough cement hydration. Sample C2 had a cumulative heat of hydration that is 13% to 9% greater than that of C0, which also sped up the early hydration of less than 8 hours, as shown in Fig. 1(a) and (b).

## Determination of optimal amounts of $CO_2$ to be mineralized

To determine the optimal $CO_2$ content for concrete to be mineralized, workability, fresh density and compressive strength tests were conducted for varying doses of $CO_2$. Mixtures CM-0, CM-1, CM-2, and CM-3 had 113, 112, 110, and 109 mm slump values, respectively. CM-0 had the maximum slump; adding $CO_2$ caused a marginal decline in the slump. Mixture CM-3's slump value was 5 mm lower than CM-0, with the CM-0 slump value of 113 mm and CM-3 of 109 mm. Compared to CM-0, the observed decrease indicates that $CO_2$-mineralized concrete has a sufficient slump value. The change in slump was minimal, suggesting that $CO_2$-mineralized concrete behaves similarly to CM-0. The marginal decrease in a slump can be attributed to the water consumed from the freshly mixed concrete when $CO_2$ and OPC's hydration phases interact.[52] The addition of $CO_2$ into concrete marginally increased the fresh density; densities of 2412.43, 2413.43, 2412.67, and 2412.79 kg/m$^3$ were found in CM-0, CM-1, CM-2, and CM-3, respectively. The fresh density increased as the $CO_2$ content increased due to the microscale formation of the $CaCO_3$ compound filling the minute pores.[53] The increase in the fresh density of $CO_2$-mineralized concrete further indicated that the $CO_2$ is completely sequestrated into the cementitious material and does not exist separately.

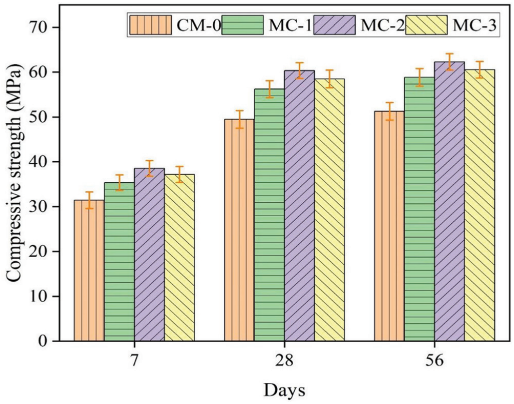

*Fig. 2—Compressive strength of concrete at different $CO_2$ doses.*

Figure 2 depicts the compressive strength values for conventional and $CO_2$-mineralized concrete. Mixture CM-2 exhibited the most significant improvement, showing that the modest amount of $CO_2$ mineralization enhanced the concrete's compressive strength. Mixtures CM-1, CM-2, and CM-3 exhibited significantly higher compressive strength than CM-0; a 12.44, 19.27, and 18.29% higher compressive strength was found, respectively. The compressive strength of CM-2 was 38.53, 60.35, and 62.29 MPa at 7, 28, and 56 days of testing, respectively. The compressive strength of CM-2 was 18.78, 19.27, and 20.63% higher than that of CM-0 at 7, 28, and 56 days of testing, respectively. This enhancement can be attributed to the formation of $CaCO_3$ microcrystals, which leads to a densification of the concrete matrix and the sealing of micro-pores. Compressive strength increased due to a higher amount of cement hydration product created by $CO_2$ mineralization. The nucleation effect plays a crucial role in hydration by increasing compressive strength by filling in the tiny voids left by hydration products.[54] A $CO_2$ dose larger

**Table 6—Economy index analysis**

| Mixture ID<br>Ingredients | Region | Ingredients cost per kg/m$^3$, USD | | | |
|---|---|---|---|---|---|
| | | CM-0 | CM-1 | CM-2 | CM-3 |
| OPC | India | 47.61 | 47.61 | 47.61 | 47.61 |
| | United States | 70.00 | 70.00 | 70.00 | 70.00 |
| Fly ash | India | 2.20 | 2.20 | 2.20 | 2.20 |
| | United States | 3.00 | 3.00 | 3.00 | 3.00 |
| Coarse aggregate | India | 6.5 | 6.5 | 6.5 | 6.5 |
| | United States | 4.00 | 4.00 | 4.00 | 4.00 |
| Fine aggregate | India | 4.0 | 4.0 | 4.0 | 4.0 |
| | United States | 2.5 | 2.5 | 2.5 | 2.5 |
| $CO_2$ | India | 0.50 | 0.48 | 0.46 | 0.44 |
| | United States | 2.5 | 2.35 | 2.2 | 2.10 |
| Total cost | India | 60.81 | 60.79 | 60.77 | 60.75 |
| | United States | 82.00 | 81.85 | 81.70 | 81.60 |
| Compressive strength at 28 days, MPa | — | 49.46 | 56.21 | 58.75 | 57.48 |
| Economy index (strength/cost) | India | 0.81 | 0.93 | 0.97 | 0.95 |
| | United States | 0.61 | 0.69 | 0.72 | 0.71 |

than 0.2 may cause insufficient water for continuous cement hydration, resulting in incomplete hydration.

## Cost analysis

Calculating the economy index involves dividing the overall expense of raw materials by the compressive strength attained after 28 days.[55] Table 6 presents a detailed economic index and ingredient prices analysis. To address regional variability in material and $CO_2$ handling costs, a separate economic analysis was conducted using approximate U.S. market prices. While the absolute costs in the United States are higher than in India, the relative trend remains consistent: $CO_2$-mineralized concretes, particularly CM-2, achieve the most favorable economy index. This consistency across two regions demonstrates that the proposed approach is not limited to a specific market but has broader global feasibility, subject to local cost adjustments. Because fly ash is a by-product obtained from an industry such as a thermal power plant or a waste material, only the transportation cost for fly ash was considered. Similarly, the cost of capturing and transporting $CO_2$ from the emission source to the site of use was evaluated. $CO_2$-mineralized concrete mixtures have a higher economy index. Hence, the highest 28-day compressive strength per unit cost is found in $CO_2$-mineralized concrete. The fact that CM-0 had the lowest economy index indicates that its compressive strength is at least 28 days for every unit of concrete price, while CM-2 has a maximum economy index of 0.97, in Indian context. In the American context, CM-0 exhibited the lowest economy index, reflecting the least strength gain per unit cost, whereas CM-2 achieved the maximum economy index of 0.89, demonstrating the most cost-effective balance between strength and material expense

Damineli et al.[56] discussed the importance of analyzing $CO_2$ emissions control to understand the environmental impact. It includes capturing the emitted $CO_2$, minimizing the $CO_2$ emission, and using materials that emit less $CO_2$.[2] The environmental benefit of using $CO_2$ in concrete is due to its mineralization, which reduces $CO_2$ emissions, and further OPC is leveraged. The environmental benefit is mainly driven by the reduction of cement in concrete compositions. The carbon intensity of concrete performance can be assessed based on the adjusted $CO_2$ mixtures, with CM-2 showing a reduction of OPC by 7.5% and, overall, approximately 8% reduction of carbon emissions.

## OPC reduction in ideal amount of $CO_2$-mineralized mixture

Strength gains due to the mineralization of $CO_2$ were used to leverage OPC content, thereby minimizing OPC consumption. Subsequently, a 0.2% dose of $CO_2$ was found to give maximum compressive strength, and the CM-2 was further examined with reduced OPC to determine the highest OPC decrease that does not compromise compressive strength compared to CM-0.

The slump values for CM-2, CM-21, CM-22, CM-33, and CM-24 were 113, 117, 119, 122, and 125 mm, respectively. Notably, the slump value of $CO_2$-mineralized concrete tended to increase when OPC content was reduced, possibly due to the fly ash addition in these mixtures. The fresh density decreased as the OPC reduction increased due to the lower specific gravity of fly ash than OPC; additionally, the decrease in the density was minimal, deemed acceptable. Mixtures CM-2, CM-21, CM-22, CM-33, and CM-24 had fresh densities of 2412.43, 2409.65, 2407.23, 2405.87, and 2403.54 kg/m$^3$, respectively. Figure 3 presents the compressive strength result of $CO_2$-mineralized concrete with reduced cement content; CM-23 exhibited compressive strength similar to that of the corresponding standard mixture without $CO_2$. Mixture CM-23 exhibited compressive strengths of 30.53, 49.32, and 54.29 MPa at 7, 28, and 56 days, respectively. The compressive strength of CM-23 was marginally

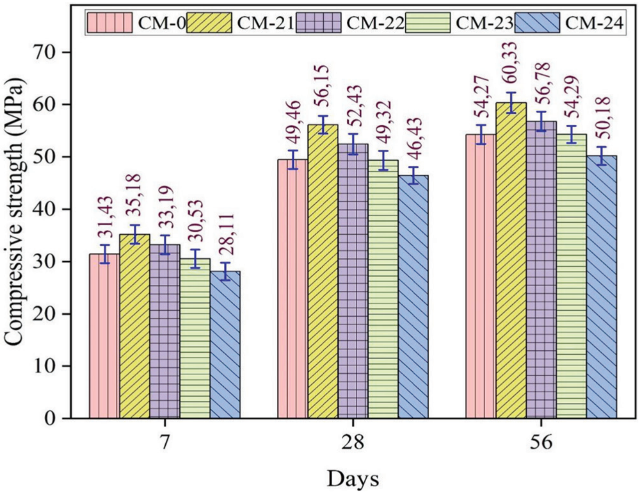

*Fig. 3—Compressive strength of 0.2% $CO_2$-mineralized concrete with decreased OPC.*

higher than that of CM-2. Therefore, through $CO_2$ mineralization, a 7.5% reduction in OPC content can be achieved without decreasing the concrete compressive strength.

### Splitting tensile strength

The splitting tensile strength values of CM-23 were equivalent to CM-0, marginally higher, tested at 7, 28 and 56 days of water curing; the splitting tensile strength result is presented in Fig. 4. The test result shows that a 0.25% addition of $CO_2$ by the weight of OPC can allow for an OPC reduction of 7.5% without any decrease in tensile strength. The higher volume of ettringite and C-S-H gel formation led to higher bond strength among the concrete ingredients, improving the splitting tensile strength at lower OPC content.[57] It can be observed from Fig. 4 that the splitting tensile strength of CM-23 is equivalent to that of CC. At 7, 28, and 56 days, the splitting tensile strengths of CM-23 were 3.12, 4.58, and 5.45 MPa, which closely resembled the splitting tensile strength of the CM-0 at the respective testing days. Further, it can be deduced that up to a 7.5% reduction of OPC can be achieved by adding $CO_2$ as an admixture. The equivalent splitting tensile strength of $CO_2$-mineralized concrete with reduced OPC compared to conventional concrete was due to the development of $CaCO_3$ microcrystals. It caused the concrete matrix to densify and fill micropores. The increase in splitting tensile was due to a higher amount of cement hydration product produced by $CO_2$ mineralization. Furthermore, adding $CaCO_3$ to C-S-H could result in a more powerful C-S-H phase.[49]

### Flexural strength

At 7, 28, and 56 days of water curing, the flexural strength values of CM-23 were equivalent to those of CM-2, with a marginal increase; the results of the flexural strength test are shown in Fig. 5. It can be noticed that approximately 7.5% reduction in cement and marginal increment of fly ash in $CO_2$-mineralized concrete does not affect flexural strength. The flexural strengths for CM-0 and CM-23 were 3.53 and 3.57 MPa at 7 days of testing, 5.76 and 5.82 MPa at 28 days, and 6.67 and 6.84 MPa at 56 days, respectively. The flexural strength deviation was very close; the conventional and $CO_2$-mineralized concrete with leveraged cement had equivalent flexural strength to the corresponding mixture without $CO_2$. This is due to nano- to microscale $CaCO_3$ forming, filling the micropores and densifying the concrete matrix.[58] The proposed optimum $CO_2$-mineralized M23 had a 7.5% lower cement content than the corresponding conventional concrete; hence, it can be concluded that a 7.5% reduction of cement content is possible in $CO_2$-mineralized concrete without affecting flexural strength.

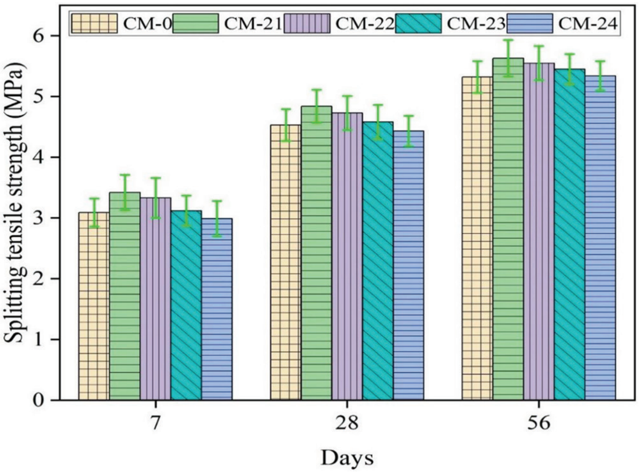

*Fig. 4—Splitting tensile strength test result of conventional and $CO_2$-mineralized concrete.*

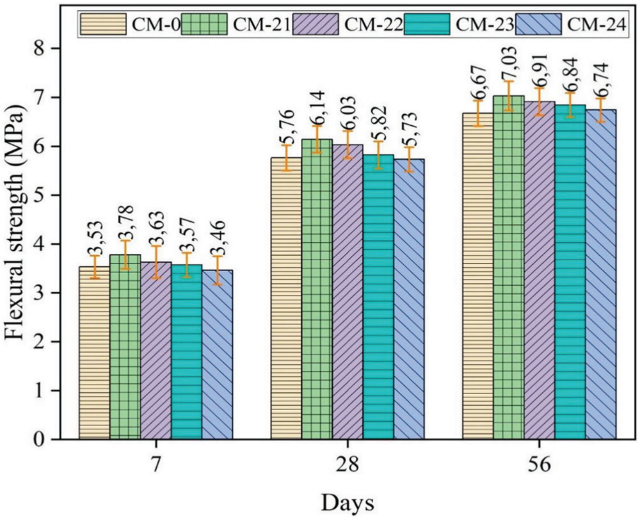

*Fig. 5—Flexural strength test results of control and $CO_2$-mineralized concrete.*

The flexural strength of $CO_2$-mineralized concrete with reduced cement was equivalent to conventional concrete due to the formation of $CaCO_3$ microcrystals, which caused the filling of micropores and densified the concrete matrix. An enormous volume of the cement hydration product, which was brought on by the mineralization of $CO_2$, was the cause of improvement in flexural strength. Additionally, adding $CaCO_3$ to C-S-H may have created a more substantial calcium-silicate-hydrate binding phase.[50]

### Carbonation depth

Table 7 presents the results of the carbonation test; it can be observed that the $CO_2$-mineralized concrete performs superior to conventional concrete. This is due to the formation of $CaCO_3$ nanoparticles and more C-S-H gel upon $CO_2$ mineralization into concrete.[58] The carbonation depth of all the concrete mixtures at 180 days of testing was well lower than the minimum nominal cover requirement to meet the durability requirement in a mild exposure condition, with a value of 20 mm.[59] Carbonation depths of 9.8, 14.3, and 18.2 mm were found in CM-23 at 70, 120, and 180 days of accelerated carbonation curing, respectively, which was marginally lower than that of CM-0. Figures 6(a) to (c) show the carbonated specimens of CM-0 and CM-23 at 70, 120, and 180 days of testing, respectively, sprayed with 1% phenolphthalein solution. The formation of $CaCO_3$ nanoparticles and more C-S-H gel upon $CO_2$ mineralization into concrete results in lower carbonation depth. Therefore, the higher the C-S-H gel and the denser the concrete, the less vulnerable it is to environmental effects. The resistance developed to the ingress of the external agent into the concrete matrix is also the reason behind the best performance of $CO_2$-mineralized concrete under carbonation conditions.

$CO_2$-mineralized concrete with leveraged OPC performs equivalently to the conventional concrete; the reasons behind this could be the dose of $CO_2$ mineralized in this mixture, optimizing the C-S-H gel from both the reactions—namely, the fresh carbonation reaction between cementitious materials and $CO_2$ and the hydration of the cementitious materials. Therefore, the more C-S-H gel and the denser the concrete, the less vulnerable to environmental effects. The resistance to the ingress of the external agent into the concrete matrix is also the reason behind the best performance of CM23 under carbonation conditions.

The improved carbonation resistance of $CO_2$-mineralized concrete can be attributed to its modified pore structure. The precipitation of finely distributed $CaCO_3$ nanoparticles during mineralization fills capillary pores and refines the pore size distribution, thereby reducing the diffusivity of $CO_2$ through the concrete matrix. Simultaneously, the additional formation of C-S-H gel densifies the microstructure, further restricting the pathways for gas ingress. The dual effect of pore refinement and gel densification explains the lower carbonation depths observed in mineralized mixtures as compared to the control. Consequently, $CO_2$ mineralization consumes part of the free $Ca(OH)_2$ and also optimizes the pore network, enhancing resistance against further carbonation and ensuring sustained durability.

**Table 7—Depth of carbonation at 70, 120, and 180 days of accelerated carbonation, mm**

| Days | CM-0 | CM-21 | CM-22 | CM-23 | CM-24 |
|---|---|---|---|---|---|
| 70 days | 10.2 | 8 | 8.6 | 9.8 | 11.1 |
| 120 days | 14.7 | 12.1 | 13.5 | 14.3 | 15.4 |
| 180 days | 18.6 | 15.7 | 16.9 | 18.2 | 19.6 |

## Depth of water penetration

The water permeability was determined after 56, 120, and 180 days of water curing. The specimen was placed in the water permeability apparatus, and a water pressure of 5 kg/cm$^2$ was applied for 72 hours. After that, the specimen was split into two halves, the maximum water penetration was noted, and three specimens were tested for each mixture; the average values are reported in Fig. 7. The water permeability test results indicated that a minor percentage mineralization of $CO_2$ by weight of cement in concrete gives the best result; it shows that $CO_2$-mineralized concrete performs quite well compared to conventional concrete. Mixture CM-23 was found to be the least permeable; the permeability slowly rose as the cement content decreased. Hence, the present results indicate that a 6 to 7.5% OPC reduction followed by $CO_2$ mineralization does not alter the durability of concrete in terms of ingress of exposure conditions.

The water penetration depth of CM-23 was 15.72, 13.46, and 12.94 mm at 56, 120, and 180 days of testing, respectively; of CM-0 was 16.42, 13.74, and 13.02 mm at 56, 120,

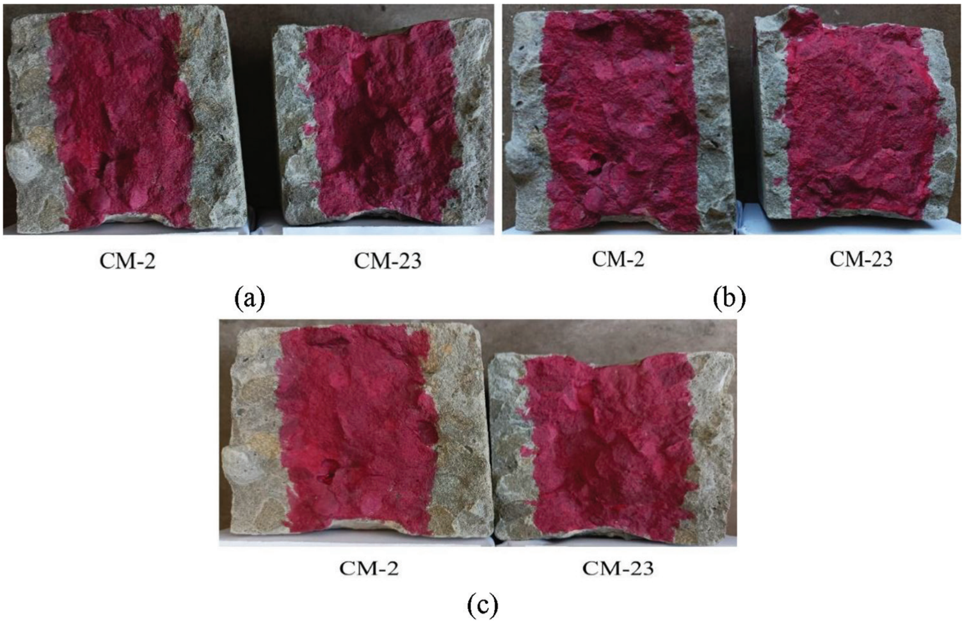

*Fig. 6—Depth of carbonation at: (a) 70 days; (a) 120 days; and (a) 180 days of acceleration carbonation.*

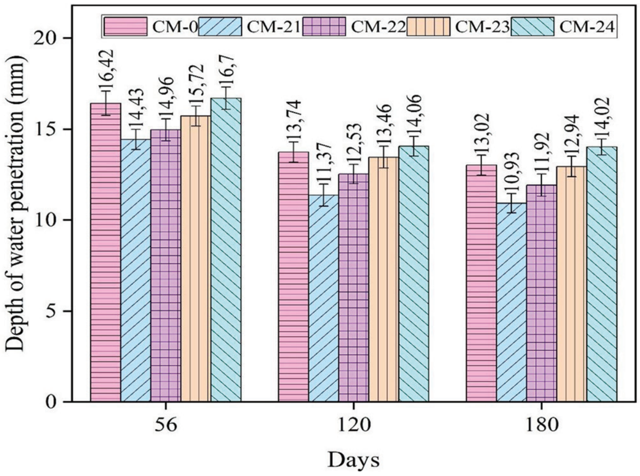

*Fig. 7—Depth of water penetration test result of conventional and $CO_2$-mineralized concrete.*

and 180 days of testing, respectively; and of CM-23 was equivalent to that of CM-0. The water penetration depth of CM-24 was higher than that of CM-0. Hence, $CO_2$ mineralization can reduce cement content by 7.5% in M40-grade concrete without affecting its durability. The formation of minute-scale $CaCO_3$ that fills the pores is the leading cause of lower water penetration in $CO_2$-mineralized concrete.[52]

## XRD analysis

Introducing $CO_2$ into OPC-based concrete through pre-carbonation alters the hydration process of $C_3A$. The resulting reaction products are predominantly influenced by the molar ratios of $CO_2/Al_2O_3$ and $C_3A/SO_3$, as demonstrated by thermodynamic simulations.[60] For instance, when the molar $C_3A/SO_3$ ratio of the cement approaches 1, $CO_2$ modifies the hydration of $C_3A$, leading to distinct reaction pathways and products.[61]

Increasing the amount of $CO_2$ added to concrete results in the partial or complete replacement of hemicarbonate with monocarbonate in the hydration process. The adjustment in mineralogy leads to several beneficial changes in the hydrated cement: 1) increased production and stabilization of ettringite; 2) better formation of monocarbonate; and 3) a reduction or elimination of monosulfate. These changes collectively enhance the strength and durability of concrete.

The ettringite formation contributes to strength improvement by generating more solid products and reducing porosity due to its significant volume expansion, as seen in Fig. 8. Additionally, monocarbonate, with its high bulk modulus of 54 GPa, contributes to increased stiffness and strength in the concrete. Eliminating or minimizing monosulfate further improves durability, as monosulfate can transform into ettringite under high humidity or $CO_2$ exposure. This transformation can lead to expansion, microcracking in the matrix, and gaps around aggregates, ultimately causing delayed ettringite formation. By mitigating these issues, the overall structural integrity of the concrete is preserved.

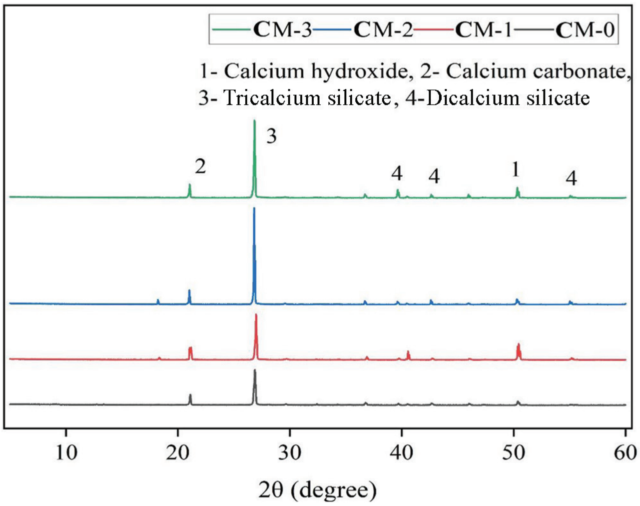

*Fig. 8—XRD result of conventional and $CO_2$-mineralized concrete.*

## Scanning electron microscopy (SEM) analysis

Figures 9(a) to (e) demonstrate SEM images of conventional and $CO_2$-mineralized concrete. The concrete microstructure densified due to a small amount of $CO_2$ mineralization, as seen by the SEM images. The surface of CM-0 concrete was porous and loose in contrast to the $CO_2$-mineralized concrete. $CO_2$-infused concrete exhibited more needlelike and clumped hydration products such as ettringite and C-S-H gel. This is due to the surface of $CO_2$-mineralized concrete having $CaCO_3$, which calcified due to the hydration products' carbonation, formation, precipitation, and convergence.[62] Compared to all other mixtures, the denser morphology of CM-2 produced the best results, as a small quantity of $CO_2$ optimizes the two reactions that occur in $CO_2$-mineralized concrete due to the hydration of cementitious ingredients and the initial carbonation process.

Nano- to sub-micron-scale $CaCO_3$ contributed to pore refinement by filling capillary voids, which reduces permeability and improves resistance against the ingress of aggressive agents. Additionally, the increased volume of ettringite enhances mechanical properties by generating expansive solid products that reduce porosity and densify the matrix, thereby improving compressive strength and durability. These mechanisms collectively explain the superior performance of $CO_2$-mineralized concrete compared to the control mixtures.

While this study primarily focused on OPC and Class F fly ash, the effectiveness of $CO_2$ mineralization may vary with other cementitious systems. For instance, binders with higher calcium content, such as Class C fly ash or ground-granulated blast-furnace slag, may accelerate $CaCO_3$ precipitation and enhance early-age densification, whereas highly pozzolanic materials such as silica fume or metakaolin could contribute to additional pore refinement through secondary C-S-H formation. These variations highlight that the balance between carbonation reactions and hydration products is binder-specific, and future studies can be carried out for the applicability of $CO_2$ mineralization across diverse blended cement systems. Furthermore, this method is applicable for precast construction, where controlled curing conditions can facilitate efficient $CO_2$ use, accelerate strength gain, and improve durability. These aspects suggest that

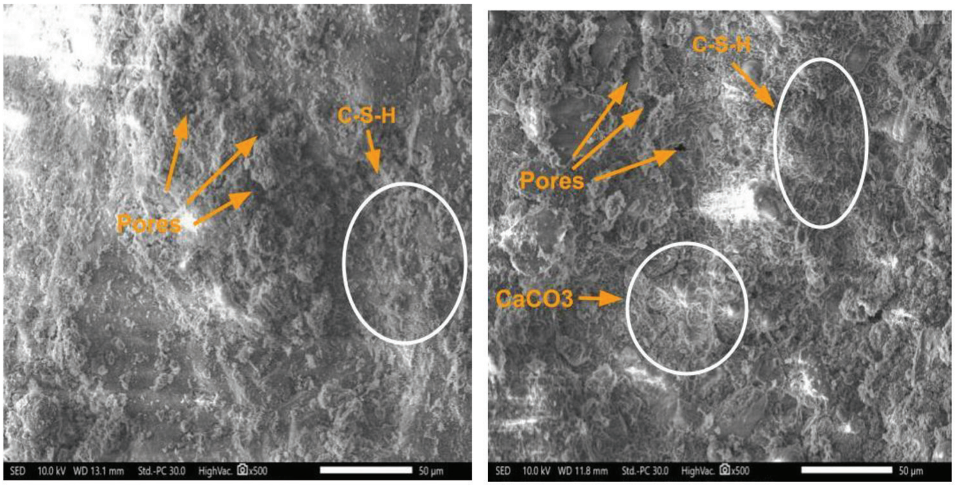

(a) CM-0 (b) CM-1

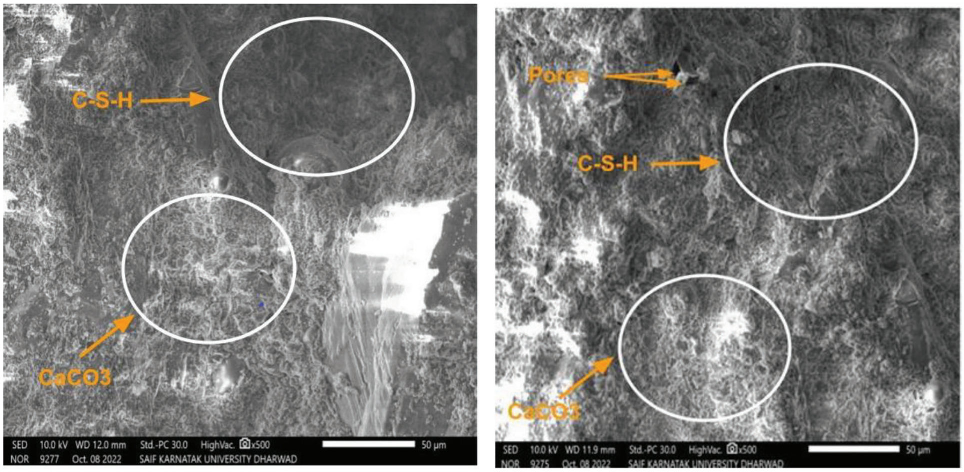

(c) CM-2 (d) CM-3

*Fig. 9—SEM images of conventional and $CO_2$-mineralized concrete.*

$CO_2$ mineralization has vast potential across diverse binder systems and industrial practices.

## CONCLUSIONS

This study investigates the performance of carbon dioxide ($CO_2$)-mineralized concrete; it was noted that an ideal level of $CO_2$ mineralization enhances concrete performance. The procedure for $CO_2$ mineralization into concrete used in this study consists of two stages: first, $CO_2$ is sequestrated into OPC, and then the $CO_2$-sequestered ordinary portland cement (OPC) is combined with the remaining ingredients to produce $CO_2$-mineralized concrete. The current method overcomes the limitation of using $CO_2$ for early-age concrete carbonation by carbonation curing only. From the research, the following conclusions emerge:

- Experimental results reveal that the best strength is achieved with a 0.20% $CO_2$ dose by weight of OPC. Mixtures CM-1, CM-2, and CM-3 exhibit significantly higher compressive strength than CM-0; 12.44, 19.27, and 18.29% higher compressive strengths were found, respectively. Isothermal calorimetric analysis reveals that $CO_2$-mineralized cement paste yields a higher heat of hydration than cement pastes without $CO_2$.
- Concrete mixture design can be optimized to achieve the target strength with lower OPC content by leveraging the strength gain from $CO_2$ mineralization. The study demonstrates that cement content can be reduced by up to 7.5% without compromising performance, corresponding to nearly an 8% reduction in carbon emissions. This approach uses $CO_2$ effectively and also decreases the environmental footprint of concrete production, offering a cost-efficient and sustainable pathway for developing eco-friendly construction materials.
- The slump value decreases as the $CO_2$ content increases in the concrete. However, there was a marginal rise in the slump of $CO_2$-mineralized concrete with lower OPC and a higher volume of fly ash than conventional concrete. The fresh density increases due to the $CO_2$ mineralization into concrete.
- The $CO_2$-mineralized concrete with leveraged OPC has equivalent durability properties to conventional concrete, as tested by the depth of water penetration and resistance to carbonation test. The optimized mixture CM-23 showed water penetration depths of 15.72, 13.46, and 12.94 mm at 56, 120, and 180 days, respectively, and carbonation depths of 9.8, 14.3, and 18.2 mm at 70, 120, and 180 days, respectively, comparable to or lower than the control mixture and well within durability limits. The improved resistance is attributed to pore refinement from in-place calcium carbonate ($CaCO_3$)

and enhanced calcium-silicate-hydrate (C-S-H) gel formation.

- X-ray diffraction (XRD) confirmed that the $CO_2$ mineralization promotes monocarbonate formation, stabilizes ettringite, and suppresses monosulfate, thereby enhancing stiffness and durability while reducing risks of delayed ettringite formation. Scanning electron microscopy (SEM) observations showed that $CO_2$-mineralized mixtures, particularly CM-2, developed a denser microstructure with refined C-S-H gel, ettringite, and $CaCO_3$ filling pores compared to the porous control mixture.

## AUTHOR BIOS

*ACI member* **Md Athar Kazmi** *is a Research Associate in the Corrosion and Material Protection Division at the Central Electrochemical Research Institute (CSIR), Karaikudi, Tamil Nadu, India. He received his PhD in civil engineering from the National Institute of Technology Silchar, Silchar, Assam, India. His research interests include $CO_2$ mineralization in cementitious materials, the rheology of novel cement and concrete, the performance of cement-based materials, and innovative low-carbon cementitious materials.*

**Lakshmi Vara Prasad Meesaraganda** *is an Associate Professor of the Civil Engineering Department at the National Institute of Technology Silchar. He received his PhD in civil engineering from the National Institute of Technology Warangal, Warangal, Telangana, India. His research interests include carbon-cured concrete, $CO_2$ mineralization into concrete, limestone calcined clay cement, waste management in construction, fiber-reinforced concrete, self-consolidating concrete, geopolymer concrete, low-cost housing, recycled aggregate concrete, eco-friendly materials, and sustainability concepts.*

## ACKNOWLEDGMENTS

The authors thank the Council of Scientific and Industrial Research (CSIR) and the Government of India, New Delhi, for financial assistance through a senior research fellowship (141-115-4861/2K23/1). The authors thank the Director of the National Institute of Technology Silchar, Assam, India, for providing the necessary research facilities to conduct this work.

## REFERENCES

1. Barcelo, L.; Kline, J.; Walenta, G.; and Gartner, E., "Cement and Carbon Emissions," *Materials and Structures*, V. 47, No. 6, 2014, pp. 1055-1065. doi: 10.1617/s11527-013-0114-5

2. Rosa, L.; Becattini, V.; Gabrielli, P.; Andreotti, A.; and Mazzotti, M., "Carbon Dioxide Mineralization in Recycled Concrete Aggregates can Contribute Immediately to Carbon-Neutrality," *Resources, Conservation and Recycling*, V. 184, 2022, p. 106436. doi: 10.1016/j.resconrec.2022.106436

3. Wang, X. Y., "Evaluation of $CO_2$ Uptake of Fly-Ash-Blended High-Strength Concrete Due to Carbonation," *ACI Materials Journal*, V. 117, No. 6, Nov. 2020, pp. 231-241. doi: 10.14359/51725982

4. Cheng, X.; Tian, W.; Yuan, Q.; Chen, W.; Guo, J.; Yi, G.; and Cai, J., "Synergistic Effect of $CO_2$-Mixing and Steel Slag Addition on Performance and Microstructure of Concrete," *Construction and Building Materials*, V. 439, 2024, p. 137324. doi: 10.1016/j.conbuildmat.2024.137324

5. Monkman, S.; Cialdella, R.; and Pacheco, J., "Performance, Durability, and Life Cycle Impacts of Concrete Produced with $CO_2$ as Admixture," *ACI Materials Journal*, V. 120, No. 1, Jan. 2023, pp. 53-62. doi: 10.14359/51734732

6. Meesaraganda, L. V. P., and Kazmi, M. A., "Performance Enhancement of Concrete Produced with Two-Step $CO_2$ Mineralization," *Civil Engineering*, V. 47, 2024. doi: 10.1007/s40996-024-01492-9

7. Yi, Z.; Wang, T.; and Guo, R., "Sustainable Building Material from $CO_2$ Mineralization slag: Aggregate for Concretes and Effect of $CO_2$ Curing," *Journal of $CO_2$ Utilization*, V. 40, 2020, p. 101196. doi: 10.1016/j.jcou.2020.101196

8. Zhang, D., and Li, V. C., "$CO_2$-Sequestered Cast-in-Place Engineered Cementitious Composites," *ACI Materials Journal*, V. 120, No. 1, Jan. 2023, pp. 29-40. doi: 10.14359/51737331

9. Monkman, S., and Shao, Y., "Assessing the Carbonation Behavior of Cementitious Materials," *Journal of Materials in Civil Engineering*, ASCE, V. 18, No. 6, 2006, pp. 768-776. doi: 10.1061/(ASCE)0899-1561(2006)18:6(768)

10. Kazmi, M. A.; Vara Prasad Meesaraganda, L.; and Suresh Chandra Babu, P., "Durability Performance of Self-Compacting Concrete Produced Using $CO_2$ as an Admixture," *Materials Today: Proceedings*, 2023. doi: 10.1016/j.matpr.2023.04.453

11. MacMaster, D., and Tavares, O., "Carbon Sequestration of Concrete Masonry Units," *ACI Materials Journal*, V. 112, No. 6, Nov.-Dec. 2015, pp. 775-780. doi: 10.14359/51688069

12. Wang, Y.; Tian, Y.; and Wang, J., "Effects of Carbide Slag and $CO_2$ Curing on Physical Properties of Gypsum Plaster," *ACI Materials Journal*, V. 117, No. 5, Sept. 2020, pp. 170-178. doi: 10.14359/51725977

13. Mahoutian, M.; Ghouleh, Z.; and Shao, Y., "Carbon Dioxide Activated Ladle Slag Binder," *Construction and Building Materials*, V. 66, 2014, pp. 214-221. doi: 10.1016/j.conbuildmat.2014.05.063

14. Gupta, S.; Kashani, A.; and Mahmood, A. H., "Carbon Sequestration in Engineered Lightweight Foamed Mortar – Effect on Rheology, Mechanical and Durability Properties," *Construction and Building Materials*, V. 322, 2022, p. 126383. doi: 10.1016/j.conbuildmat.2022.126383

15. Monkman, S., and MacDonald, M., "Carbon Dioxide Upcycling into Industrially Produced Concrete Blocks," *Construction and Building Materials*, V. 124, 2016, pp. 127-132. doi: 10.1016/j.conbuildmat.2016.07.046

16. Dixit, A.; Du, H.; and Pang, S. D., "Carbon Capture in Ultra-High-Performance Concrete Using Pressurized $CO_2$ Curing," *Construction and Building Materials*, V. 288, 2021, p. 123076. doi: 10.1016/j.conbuildmat.2021.123076

17. Monkman, S.; Sargam, Y.; Naboka, O.; and Lothenbach, B., "Early Age Impacts of $CO_2$ Activation on the Tricalcium Silicate and Cement Systems," *Journal of $CO_2$ Utilization*, V. 65, 2022, p. 102254. doi: 10.1016/j.jcou.2022.102254

18. Yu, Z.; Meng, Y.; Mo, K. H.; Liu, H.; and Ling, T. C., "Influences of w/c and $CO_2$ Curing Duration on the High Temperature Properties of Cement Pastes," *Journal of Building Engineering*, V. 69, 2023, p. 106293. doi: 10.1016/j.jobe.2023.106293

19. Pan, G.; Zhan, M.; Fu, M.; Wang, Y.; and Lu, X., "Effect of $CO_2$ Curing on Demolition Recycled Fine Aggregates Enhanced by Calcium Hydroxide Pre-Soaking," *Construction and Building Materials*, V. 154, 2017, pp. 810-818. doi: 10.1016/j.conbuildmat.2017.07.079

20. Ruan, S., and Unluer, C., "Influence of Mix Design on the Carbonation, Mechanical Properties and Microstructure of Reactive MgO Cement-Based Concrete," *Cement and Concrete Composites*, V. 80, 2017, pp. 104-114. doi: 10.1016/j.cemconcomp.2017.03.004

21. Ben Ghacham, A.; Pasquier, L.-C.; Cecchi, E.; Blais, J.-F.; and Mercier, G., "Valorization of Waste Concrete through $CO_2$ Mineral Carbonation: Optimizing Parameters and Improving Reactivity Using Concrete Separation," *Journal of Cleaner Production*, V. 166, 2017, pp. 869-878. doi: 10.1016/j.jclepro.2017.08.015

22. Liang, C.; Lu, N.; Ma, H.; Ma, Z.; and Duan, Z., "Carbonation Behavior of Recycled Concrete with CO2-Curing Recycled Aggregate under Various Environments," *Journal of $CO_2$ Utilization*, V. 39, 2020, pp. 1-13.

23. Kou, S. C.; Zhan, B. J.; and Poon, C. S., "Use of a $CO_2$ Curing Step to Improve the Properties of Concrete Prepared with Recycled Aggregates," *Cement and Concrete Composites*, V. 45, 2014, pp. 22-28. doi: 10.1016/j.cemconcomp.2013.09.008

24. Hosseini, Z. A.; Mamirov, M.; Kim, S.; and Hu, J., "$CO_2$-Treatment of Recycled Concrete Aggregates to Improve Mechanical and Environmental Properties for Unbound Applications," *Construction and Building Materials*, V. 275, 2021, p. 122180. doi: 10.1016/j.conbuildmat.2020.122180

25. Rahmani, O., "$CO_2$ Sequestration by Indirect Mineral Carbonation of Industrial Waste Red Gypsum," *Journal of $CO_2$ Utilization*, V. 27, 2018, pp. 374-380.

26. Monkman, S., and MacDonald, M., "On Carbon Dioxide Utilization as a Means to Improve the Sustainability of Ready-Mixed Concrete," *Journal of Cleaner Production*, V. 167, 2017, pp. 365-375. doi: 10.1016/j.jclepro.2017.08.194

27. ASTM C150/C150M-16, "Standard Specification for Portland Cement," ASTM International, West Conshohocken, PA, 2016, 10 pp.

28. ASTM C618-12a, "Standard Specification for Coal Fly Ash and Raw or Calcined Natural Pozzolan for Use in Concrete," ASTM International, West Conshohocken, PA, 2012, 5 pp.

29. ASTM C33/C33M-24a, "Standard Specification for Concrete Aggregates," ASTM International, West Conshohocken, PA, 2024, 7 pp.

30. ACI Committee 211, "Standard Practice for Selecting Proportions for Normal, Heavyweight, and Mass Concrete (ACI 211.1-91) (Reapproved 2016)," American Concrete Institute, Farmington Hills, MI, 1991, 38 pp.

31. ACI Committee 301, "Specifications for Concrete Construction (ACI 301-20)," American Concrete Institute, Farmington Hills, MI, 2020, 69 pp.

32. ASTM C1702-23, “Standard Test Method for Measurement of Heat of Hydration of Hydraulic Cementitious Materials Using Isothermal Conduction Calorimetry,” ASTM International, West Conshohocken, PA, 2023, 8 pp.

33. IS 1199 (Part-2):2018, “Fresh Concrete — Methods of Sampling, Testing and Analysis, Part- 2; Determination of Consistency of Fresh Concrete,” Bureau of Indian Standards, New Delhi, India, 2018.

34. ASTM C143/C143M-20, “Standard Test Method for Slump of Hydraulic-Cement Concrete,” ASTM International, West Conshohocken, PA, 2020, 4 pp.

35. IS 1199 (Part 3):2018, “Fresh Concrete — Methods of Sampling, Testing and Analysis Part 3 Determination of Density of Fresh Concrete,” Bureau of Indian Standards, New Delhi, India, 2018.

36. ASTM C642-21, “Standard Test Method for Density, Absorption, and Voids in Hardened Concrete,” ASTM International, West Conshohocken, PA, 2021, 3 pp.

37. IS 516: Part I (Sec-1), “Hardened Concrete — Methods of Test - Testing of Strength of Hardened Concrete,” Bureau of Indian Standards, New Delhi, India, 2021.

38. ASTM C39/C39M-01, “Standard Test Method for Compressive Strength of Cylindrical Concrete Specimens,” ASTM International, West Conshohocken, PA, 2001, 8 pp.

39. ASTM C496/C496M-17, “Standard Test Method for Splitting Tensile Strength of Cylindrical Concrete Specimens,” ASTM International, West Conshohocken, PA, 2017, 5 pp.

40. ASTM C78/C78M-18, “Standard Test Method for Flexural Strength of Concrete (Using Simple Beam with Third-Point Loading),” ASTM International, West Conshohocken, PA, 2018, 5 pp.

41. IS 516 (Part 2/Sec 1):2018, “Properties of Hardened Concrete Other Than Strength- Density of Hardened Concrete and Depth of Water Penetration Under Pressure,” Bureau of Indian Standards, New Delhi, India, 2018.

42. EN 12390-8:2019 (Part 8), “Testing Hardened Concrete: Depth of Penetration of Water under Pressure,” European Committee for Standardization, Brussels, Belgium, 2019.

43. IS 516 (Part-2/Sec-4):2021, “Properties of Hardened Concrete Other Than Strength -Determination of the Carbonation Resistance by Accelerated Carbonation Method,” Bureau of Indian Standards, New Delhi, India, 2021.

44. RILEM CPC-18. “Measurement of Hardened Concrete Carbonation Depth,” *Materials and Structures*, V. 21, No. 6, 1988, pp. 453-455. doi: 10.1007/BF02472327

45. IS 516 (Part-5/Sec-3):2021, “Non-Destructive Testing of Concrete, Carbonation Depth Test,” Bureau of Indian Standards, New Delhi, India, 2021.

46. ASTM C1365-18, “Test Method for Determination of the Proportion of Phases in Portland Cement and Portland-Cement Clinker Using X-Ray Powder Diffraction Analysis,” ASTM International, West Conshohocken, PA, 2018, 11 pp.

47. ASTM C1723-10, “Standard Guide for Examination of Hardened Concrete Using Scanning Electron Microscopy,” ASTM International, West Conshohocken, PA, 2010, 9 pp.

48. Han, F.; Liu, R.; Wang, D.; and Yan, P., “Characteristics of the Hydration Heat Evolution of Composite Binder at Different Hydrating Temperature,” *Thermochimica Acta*, V. 586, 2014, pp. 52-57. doi: 10.1016/j.tca.2014.04.010

49. Monkman, S.; Lee, B. E. J.; Grandfield, K.; MacDonald, M.; and Raki, L., “The Impacts of In-Situ Carbonate Seeding on the Early Hydration of Tricalcium Silicate,” *Cement and Concrete Research*, V. 136, 2020, p. 106179. doi: 10.1016/j.cemconres.2020.106179

50. Fang, Y., and Chang, J., “Microstructure Changes of Waste Hydrated Cement Paste Induced by Accelerated Carbonation,” *Construction and Building Materials*, V. 76, 2015, pp. 360-365. doi: 10.1016/j.conbuildmat.2014.12.017

51. Wu, Y.; Mehdizadeh, H.; Mo, K. H.; and Ling, T.-C., “High-Temperature $CO_2$ for Accelerating the Carbonation of Recycled Concrete Fines,” *Journal of Building Engineering*, V. 52, 2022, p. 104526. doi: 10.1016/j.jobe.2022.104526

52. Li, L.; Hao, L.; Li, X.; Xiao, J.; Zhang, S.; and Poon, C.-S., “Development of $CO_2$-Integrated 3D Printing Concrete,” *Construction and Building Materials*, V. 409, 2023, p. 134233. doi: 10.1016/j.conbuildmat.2023.134233

53. Vara Prasad Meesaraganda, L., and Kazmi, M. A., “Carbonation Behavior of Concrete Produced Using $CO_2$ as an Admixture,” *Cement, Wapno, Beton*, V. 28, No. 6, 2024, pp. 364-374. doi: 10.32047/CWB.2023.28.6.1

54. Skocek, J.; Zajac, M.; and Ben Haha, M., “Carbon Capture and Utilization by Mineralization of Cement Pastes Derived from Recycled Concrete,” *Scientific Reports*, V. 10, No. 1, 2020, p. 5614. doi: 10.1038/s41598-020-62503-z

55. Thomas, B. S.; Gupta, R. C.; Mehra, P.; and Kumar, S., “Performance of High Strength Rubberized Concrete in Aggressive Environment,” *Construction and Building Materials*, V. 83, 2015, pp. 320-326. doi: 10.1016/j.conbuildmat.2015.03.012

56. Damineli, B. L.; Kemeid, F. M.; Aguiar, P. S.; and John, V. M., “Measuring the Eco-Efficiency of Cement Use,” *Cement and Concrete Composites*, V. 32, No. 8, 2010, pp. 555-562. doi: 10.1016/j.cemconcomp.2010.07.009

57. Wang, X. Y., “$CO_2$-Optimal Design of Fly Ash Marine Concrete with Global Warming and Stress Types,” *ACI Materials Journal*, V. 119, No. 3, May 2022, pp. 91-102. doi: 10.14359/51734604

58. Zajac, M.; Skocek, J.; Skibsted, J.; and Ben Haha, M., “$CO_2$ Mineralization of Demolished Concrete Wastes into a Supplementary Cementitious Material – A New CCU Approach for the Cement Industry,” *RILEM Technical Letters*, V. 6, 2021, pp. 53-60. doi: 10.21809/rilemtechlett.2021.141

59. Kazmi, M. A., and Prasad, M. L. V., “Experimental Study on the Potential Use of $CO_2$ as an Admixture in Concrete,” *Innovative Infrastructure Solutions*, V. 8, No. 3, 2023, p. 95. doi: 10.1007/s41062-023-01062-4

60. Guo, B.; Chu, G.; Yu, R.; Wang, Y.; Yu, Q.; and Niu, D., “Effects of Sufficient Carbonation on the Strength and Microstructure of $CO_2$-Cured Concrete,” *Journal of Building Engineering*, V. 76, 2023, p. 107311. doi: 10.1016/j.jobe.2023.107311

61. Sahoo, P.; Dwivedi, A.; Tuppad, S. M.; and Gupta, S., “Sequestration and Utilization of Carbon Dioxide to Improve Engineering Properties of Cement-Based Construction Materials with Recycled Brick Powder: A Pathway for Cleaner Construction,” *Construction and Building Materials*, V. 395, 2023, p. 132268. doi: 10.1016/j.conbuildmat.2023.132268

62. Lin, R. S., and Wang, X. Y., “Carbon Dioxide Conversion and Use as Admixture for Calcined Clay Blended Pastes,” *ACI Materials Journal*, V. 120, No. 5, Sept. 2023, pp. 31-41. doi: 10.14359/51738889

ACI MATERIALS JOURNAL TECHNICAL PAPER

Title No. 123-M25

# Performance Prediction of Multi-Generation Recycled Fine Aggregate Concrete

by Chunhong Chen, Yunchun Chen, Jiang Yu, Pinghua Zhu, Ronggui Liu, and Xinjie Wang

*The concept of multi-generation concrete recycling is increasingly relevant as many existing recycled concrete structures near the end of their service lives. This study examines the performance variation and recyclability of multi-generation concrete subjected to chloride salt drying-and-wetting cycling. After 30 drying-and-wetting cycles, natural aggregate concrete, designed with three different strength grades, was crushed to produce the first generation of recycled fine aggregate, which was then used to prepare the second generation of concrete. This second generation was subjected to the same drying-and-wetting cycling and subsequently crushed to yield a second generation of recycled fine aggregate. The results demonstrate a significant decline in the performance of the second generation of concrete, with an average compressive strength reaching only 89.52% of the first generation. Notably, the performance deterioration was more pronounced in lower-strength mixtures, which exhibited increased porosity, greater mass loss, and deeper chloride penetration. Both generations of recycled fine aggregate met the standards for Class III aggregate; however, some properties of the recycled fine aggregate derived from higher-strength concrete qualified for Class II aggregate status. Additionally, a regression analysis model was developed to predict the attenuation coefficients for the third generation of concrete with design strengths of 30, 45, and 60 MPa, yielding coefficients of 56.84%, 67.75%, and 71.72%, respectively. This study underscores the potential for multi-generational use of recycled fine aggregates and highlights the importance of selecting appropriate design strengths to enhance durability and recyclability in chloride-rich environments.*

**Keywords:** chloride-ion erosion; drying-and-wetting cycles; multi-generation concrete; recyclability; recycled fine aggregate (RFA).

## INTRODUCTION

With the growing global demand for construction materials, the construction industry is increasingly focusing on sustainable and eco-friendly practices.[1-4] As natural sand resources become increasingly scarce, efficiently using and recycling concrete resources has become an urgent issue.[5,6] Recycled fine aggregate (RFA) has emerged as a promising solution, helping to reduce construction waste and decrease dependence on natural resources.[7-9] However, RFA concrete (RC) faces a number of challenges in practical applications compared to natural aggregate concrete (NC), especially in terms of durability in the marine environment.[10-13]

RC first saw practical application in the 1970s, and since then, the practice has evolved to include RFA.[14] However, as structures built with the first generation of RC approach the end of their life cycle, the question arises: can concrete be recycled again? Thus, the concept of multi-generation concrete recycling has emerged.[7,15,16] The idea is not only to recycle concrete once but to create a sustainable cycle where concrete is repeatedly reused across generations. This approach aligns with the principles of resource conservation, sustainability, and environmental protection by reducing the need for virgin materials and minimizing waste. The idea of recycling recycled concrete drives the study of multi-generation concrete, where the long-term sustainability of recycling practices is tested, particularly under harsh environmental conditions such as those found in marine environments.

In marine environments, concrete structures frequently undergo drying-and-wetting cycling, which accelerates chloride-ion erosion and leads to performance degradation of the internal structure of concrete. Chen et al. and other scholars[17,18] have detailed the process of chloride-ion erosion in concrete under the combined effects of drying-and-wetting cycling and loading, but few studies address multi-generation concrete. Thomas et al.[19] assessed the performance of three generations of concrete using various methods but did not consider the deterioration of concrete during service. Dadd et al.[7] discussed the physical and mechanical properties of 45 mixture designs in the production of four generations of concrete, yet did not account for the service conditions of the concrete. Other scholars have developed systems for multi-generation concrete recycling. Wang et al.[15] established a comprehensive experimental and theoretical analysis system for multi-generation concrete recycling under freezing-and-thawing conditions.

Although many studies have demonstrated the feasibility of multi-generation recycling, the mechanisms of performance degradation remain debated. Some researchers attribute the deterioration mainly to the increasing content of residual mortar and microcracks generated during crushing, which elevate porosity and water absorption, thereby weakening the mechanical interlocking between the old and new mortar phases. Others emphasize the critical role of the interfacial transition zone (ITZ), where microstructural defects and uneven stress distribution accelerate the propagation of cracks and chloride ingress. Tam et al.,[20] Xiao et al.,[21] and Kou and Poon[22] showed that the ITZ in recycled aggregate concrete exhibits higher porosity and weaker calcium-silicon ratios (Ca/Si) compared to NC, significantly affecting strength and durability. Such divergent interpretations

---

*ACI Materials Journal*, V. 123, No. 2, March 2026.

MS No. M-2025-042.R2, doi: 10.14359/51749500, received October 27, 2025, and reviewed under Institute publication policies. Pertinent discussion including author's closure, if any, will be published ten months from this journal's date if the discussion is received within four months of the paper's print publication.

**Table 1—Mixture proportions of concrete, kg/m$^3$**

| Design strength | Coarse aggregate | Fine aggregate | OPC | FA | SF | Water | *w/b* |
|---|---|---|---|---|---|---|---|
| 30 MPa | 1062.33 | 674.34 | 308.93 | 57.93 | 19.31 | 180.85 | 0.47 |
| 45 MPa | 1115.67 | 621.42 | 356.55 | 66.85 | 22.28 | 160.94 | 0.36 |
| 60 MPa | 1132.93 | 604.30 | 371.95 | 69.74 | 23.25 | 154.50 | 0.33 |

highlight that the performance degradation of recycled aggregates is a multi-factor process involving both physical damage and chemical-structural changes.

Therefore, this study focuses on how chloride salt drying-and-wetting cycling exacerbates ITZ deterioration and aggregate degradation across generations. While some research has explored multi-generation recycling, studies under chloride salt drying-and-wetting cycling remain lacking. As this process not only weakens mechanical and durability performance but also affects recyclability, understanding degradation patterns under such conditions is crucial for improving the practical application of recycled aggregates.

## RESEARCH SIGNIFICANCE

This study explores the performance variations of two generations of RC subjected to chloride salt drying-and-wetting cycling through experimental analysis. Concrete specimens with varying design strengths were used, and RFAs were produced by crushing to prepare second-generation RC. Over the course of 60 drying-and-wetting cycles, the physical and mechanical properties, durability, and recyclability of the concrete were systematically evaluated. The research focuses on determining the attenuation coefficient of concrete strength during these cycles and predicting the performance of subsequent generations of concrete. The results offer valuable insights for optimizing concrete mixture design and improving the durability of RC in practical engineering applications.

## EXPERIMENTAL INVESTIGATION

### Materials

In this study, concrete with design strengths of 30, 45, and 60 MPa was prepared. The first-generation concrete—that is, NC—was made using basalt as the coarse aggregate, river sand as the fine aggregate, and a combination of cementitious materials consisting of ordinary portland cement (OPC) (P.O 42.5) with 15 wt. % fly ash (FA) and 10 wt. % silica fume (SF) replacing part of the cement. After 60 drying-and-wetting cycles, the NC was crushed using a two-stage crushing ratio method to produce first-generation RFA. The second-generation concrete was then prepared using basalt as the coarse aggregate, the first-generation RFA as the fine aggregate, and the same cementitious materials as in the NC.

The concrete mixture ratios, aggregate properties, and cementitious material compositions are provided in Tables 1 to 3. All aggregates and cementitious materials used in this study were obtained from qualified commercial suppliers and conform to Chinese national standards (GB/T 14684-2022 for natural sand, GB/T 14685-2022 for crushed stone, and GB/T 25177-2023 for RFAs).

The key physical and mechanical properties of the aggregates—including apparent density, water absorption, and crushing index—are summarized in Table 2. These values are consistent with those required by the corresponding standards. Other parameters, such as oven-dry and saturated surface-dry density, mud content, and needle-like content, were within the permissible limits and are therefore not tabulated separately.

**Table 2—Physical and mechanical properties of natural aggregates**

| Physical properties | Apparent density, kg/m$^3$ | Water absorption, % | Crushing index, % |
|---|---|---|---|
| Basalt | 2720 | 0.4 | 8.8 |
| Sand | 2634 | 0.2 | 10.5 |

**Table 3—Chemical composition of cementitious materials, wt. %**

| Component | OPC | FA | SF |
|---|---|---|---|
| CaO | 61.02 | 3.82 | 0.22 |
| $SiO_2$ | 20.39 | 52.5 | 86.2 |
| $Al_2O_3$ | 7.42 | 28.32 | 1.08 |
| $Fe_2O_3$ | 3.75 | 3.66 | 0.92 |
| MgO | 1.26 | 1.13 | 0.79 |
| MnO | 0.16 | 0.21 | 0.12 |
| $K_2O$ | 0.75 | 1.69 | 0 |
| $TiO_2$ | 0.27 | 0.97 | 0 |
| $SO_3$ | 2.08 | 1.75 | 0.83 |
| Loss on ignition | 2.57 | 1.83 | 1.79 |
| Specific surface area, m$^2$/kg | 369 | 430 | 23,000 |
| Apparent density, kg/m$^3$ | 3152 | 2524 | 2721 |

It should be noted that the RFAs were produced by crushing laboratory-prepared parent concrete under controlled conditions to ensure uniformity. Although this study did not include detailed microstructural or compositional analyses (such as X-ray diffraction [XRD], scanning electron microscopy [SEM], or quantification of adhered old mortar), these investigations will be incorporated into subsequent research to establish a quantitative relationship between the old mortar characteristics, hydration degree, and aggregate performance.

Because the density of RFA is lower than that of natural river sand, adjustments were made to the mixture proportions based on the bulk density of RFA to match the volume of river sand used in the NC mixture. The grading curves for all aggregates indicated good particle distribution.

### Specimens

The dimensions of specimens for the two generations of concrete were 100 x 100 x 400 mm. All the specimens were demolded 24 hours after casting and cured for a standard

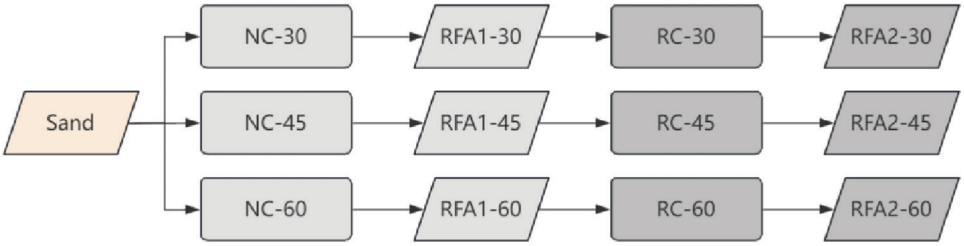

*Fig. 1—Multi-generation preparation process of concrete specimens.*

period of 28 days (in a curing room maintained at 20 ± 2°C and relative humidity ≥95% in accordance with GB/T 50082-2009). After curing, epoxy resin was applied to four consecutive surfaces of the specimens to simulate one-dimensional chloride attack; two opposite surfaces were left uncoated and used for applying loads. A four-point bending loading device was used to apply bending loads to the specimens, and the applied stresses were 25% of the flexural strength of the specimens.

The preparation process of the specimens in this study, involving two generations of fine aggregates and two generations of concrete, is illustrated in Fig. 1. NC-30 refers to the first-generation concrete with a design strength of 30 MPa. RC-30 indicates the second-generation concrete with a design strength of 30 MPa. RFA1-30 denotes the RFA produced by crushing the NC with a design strength of 30 MPa. RFA2-30 represents the RFA obtained by crushing the second-generation concrete with a design strength of 30 MPa. This notation applies similarly to concrete specimens and RFA with design strengths of 45 and 60 MPa.

## Drying-and-wetting cycling process

To simulate the typical service conditions of multi-generation concrete in real-world projects, a drying-and-wetting cycling experiment was designed based on the theory of environmental similarity. This experiment aimed to replicate the intertidal environment of Zhoushan, Zhejiang Province, China. The Nernst-Einstein equation (Eq. (1))[23] was used to calculate the experimental temperature in the indoor accelerated environment, which was 24°C, based on the average air temperature in the coastal area of Zhoushan.[24]

In the drying stage, a temperature of 60°C was adopted to accelerate the moisture evaporation and chloride migration processes while maintaining microstructural integrity. This temperature was selected according to the Arrhenius-type temperature acceleration principle. Several previous studies[17,18] recommend 60°C as an equivalent accelerated condition for simulating marine exposure and chloride ingress in laboratory settings. Therefore, 60°C was used as a reasonable accelerated aging temperature, providing a consistent activation energy response without causing unrealistic thermal damage to the cementitious matrix.

In the drying-and-wetting cycling test, the specimens together with the loading device were first immersed in a thermostatic water bath containing a 5% NaCl solution for 12 hours, and then placed in a blower drying oven at 60°C for 36 hours. A total of 60 drying-and-wetting cycles were conducted in the test period for a total of 120 days, and the performance of the concrete was examined once every 12 cycles

$$D_{CL} = D_0 \frac{T}{T_0} e^{q\left(\frac{1}{T_0}-\frac{1}{T}\right)} \tag{1}$$

where $D_{CL}$ and $D_0$ are chloride diffusion coefficients at temperature $T$ and $T_0$ (K), respectively; and $q$ is the activation coefficient, which is related to the water-binder ratio ($w/b$). When the $w/b$ are 0.33, 0.36, and 0.40, the values of $q$ are 6100, 6050, and 6000 K, respectively. Figure 2 shows the flow of the whole experiment, involving drying-and-wetting cycling of NC and RC, and the preparation and testing of two generations of RFA.

## Items of investigation

The physical and mechanical properties of basalt, sand, RFA1, and RFA2 were evaluated according to GB/T 14684-2022 and GB/T 14685-2022, including grading curves, water absorption, apparent density, bulk density, crushing value, and soundness.

The porosity and compressive strength of both concrete generations were tested following GB/T 50081-2019, using 100 x 100 x 100 mm cubic specimens. Porosity, defined as the ratio of pore volume to total volume, was determined indirectly from water absorption after immersion. The sample preparation process is shown in Fig. 3.

Using a silicon carbide saw, three 100 mm cuts were made on the 100 x 100 x 400 mm prismatic specimens—one at the center and one on each side—to obtain two cubes, one of which was used for compressive strength testing. All strength tests were performed with a universal testing machine.

Following GB/T 50082-2009, the durability of both concrete generations against chloride erosion was evaluated by mass change, relative dynamic elastic modulus (RDEM), chloride penetration depth, and free chloride content. Three prismatic specimens from each group were tested per drying-and-wetting cycle. Each specimen was numbered, tracked, and weighed to record mass change.

The chloride penetration depth and free chloride-ion content were measured according to GB/T 50082-2009 and JGJ/T 322-2013. After each drying-and-wetting cycle, specimens were split perpendicular to the chloride ingress direction. A 0.1 mol/L $AgNO_3$ solution was sprayed on the freshly exposed surface; after ~15 minutes, the chloride-contaminated region turned white (AgCl), while the unaffected area remained brown. The chloride front was defined as the average distance between the color-change boundary and surface, measured at multiple points with a Vernier

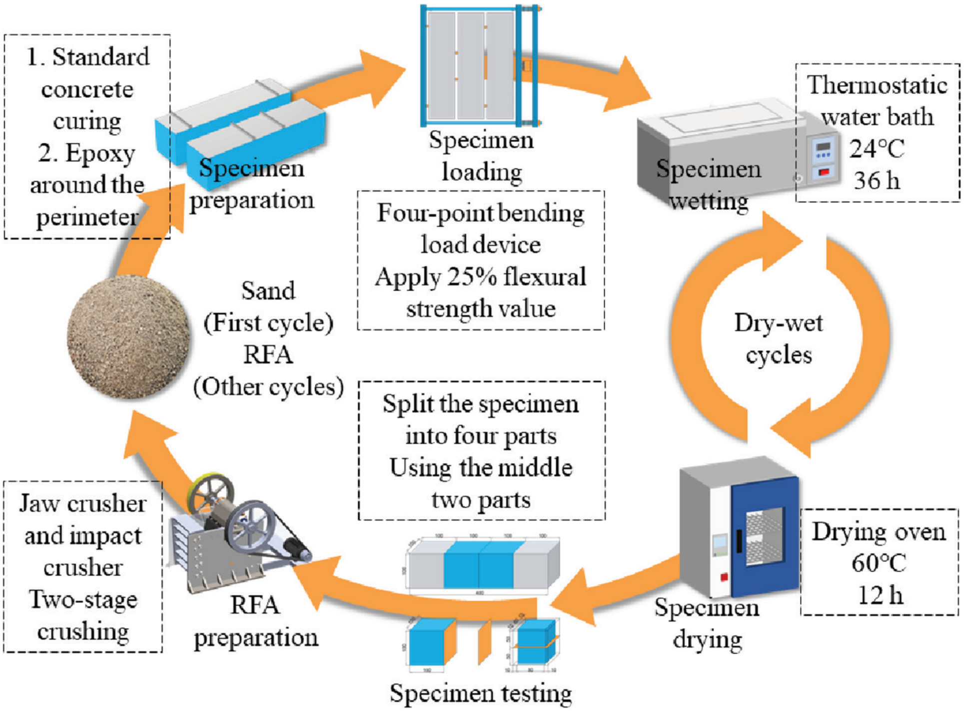

*Fig. 2—Flow of multi-generation concrete drying-and-wetting cycling experiment.*

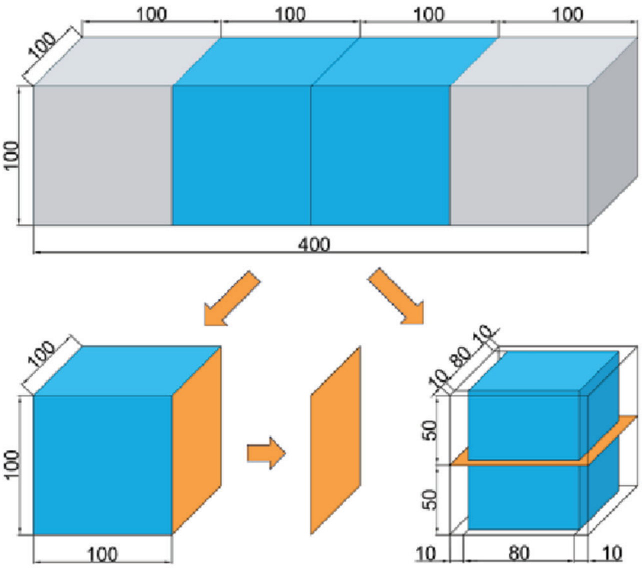

*Fig. 3—Preparation of compressive strength specimens.*

caliper (±0.02 mm). The average of three specimens was taken as the representative penetration depth.

For free chloride-ion content, powdered samples were drilled at 4 mm intervals (2 to 10 mm depth) and 5 mm intervals (10 to 30 mm depth) from the exposed surface. Samples were oven-dried at 50°C, sieved through a 0.315 mm mesh, and analyzed using a rapid chloride-ion content tester per JGJ/T 322-2013. The chloride concentration was expressed as the mass ratio of chloride ions to binder mass, and each data point represents the mean of three replicates.

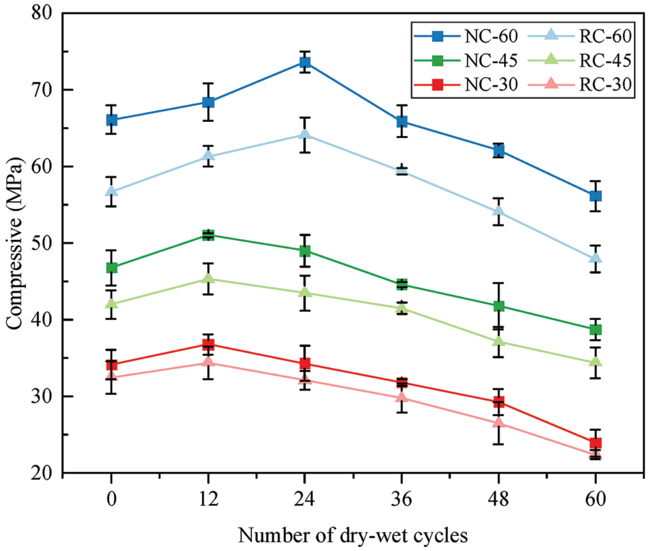

*Fig. 4—Compressive strength of concretes during drying-and-wetting cycling.*

## EXPERIMENTAL RESULTS AND DISCUSSION

### Compressive strength

As shown in Fig. 4, during the drying-and-wetting cycling, the compressive strength of specimens with different design strengths (different color lines) first increased and then decreased. The maximum increase for NC-30, NC-45, NC-60, RC-30, RC-45, and RC-60 was 7.51%, 9.04%, 11.35%, 5.85%, 7.86%, and 13.05% of the initial strength, respectively, and the maximum decrease was 30.00%, 17.20%, 15.07%, 31.08%, 18.10%, and 15.52% of the initial strength, respectively. The increase in concrete strength is due to the occurrence of internal secondary hydration reactions.[25,26] The decrease in strength is due to the coupled effects of loading and chloride erosion, leading to pore damage, crack development, and the formation of multiple crack interconnections. As the drying-and-wetting cycling continues, the damage accumulates, resulting in a decrease in the compressive strength of the concrete.[27-30]

The compressive strength of the two generations of concrete with the same design strength showed similar trends, but the compressive strength of the NC (dark lines) was higher than that of the RC (light lines), with the average compressive strength of RC being 89.52% of that of NC. This is attributed to the fact that RFA, made by crushing NC, contains a large proportion of adhered mortar, resulting in RC made with RFA having lower compressive strength than NC.[31,32]

Additionally, after 60 drying-and-wetting cycles, the compressive strength loss rates of RC-30, RC-45, and RC-60 were 1.08%, 0.89%, and 0.45%, respectively, compared to NC-30, NC-45, and NC-60. This indicates that the lower the design strength of the first-generation concrete (NC), the smaller the compressive strength loss in the second-generation concrete (RC). This trend can be attributed to the higher design strength of NC, resulting in stronger mortar adhering to the RFA. The enhanced physical and mechanical properties of the RFA lead to a reduction in the compressive strength loss of RC. Therefore, the high-strength mortar attached to the RFA improves the corrosion resistance of concrete under chloride-ion erosion conditions.[33-35]

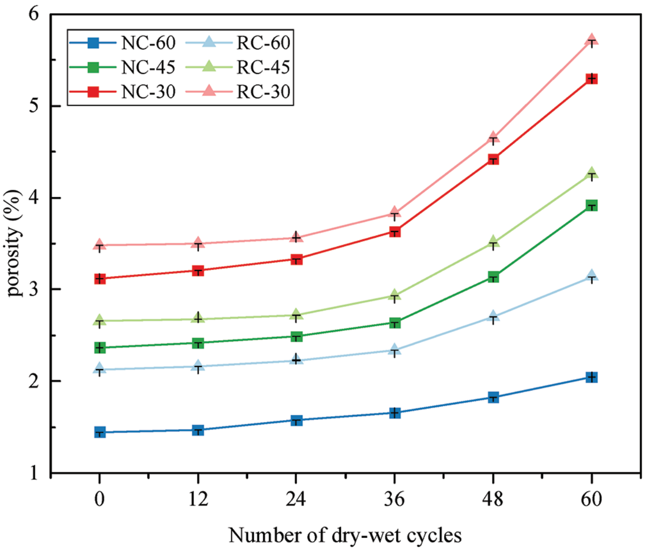

*Fig. 5—Porosity of concretes during drying-and-wetting cycles.*

Furthermore, the superior performance of RC-60 can be explained by the microstructural densification of the ITZ in high-strength concrete. This topic will be discussed later in the text.

## Porosity

As shown in Fig. 5, the porosity of the concrete shows an increasing trend. The final increase in porosity for NC-30, NC-45, NC-60, RC-30, RC-45, and RC-60 was 2.18%, 1.55%, 0.60%, 2.23%, 1.60%, and 1.01%, respectively. The average porosity of NC during the drying-and-wetting cycles is 85.98% of that of RC. This is because RFA has a loose and porous nature, making the porosity of RC higher. Additionally, compared with NC, the higher initial porosity of RC leads to more chloride erosion, causing RC to deteriorate faster,[36] which leads to greater increase in its porosity as the drying-and-wetting cycle progresses.[35,36]

## Mass change, RDEM, and chloride erosion depth

As illustrated in Fig. 6(a) and (b), during the initial 0 to 12 cycles of drying-and-wetting cycling, the mass and RDEM of the concrete exhibited a slight increase before experiencing a significant decline. This initial rise, akin to the observed increase in compressive strength, can be attributed to the narrowing of pores and cracks caused by load compression, the formation of secondary hydration products, and the filling of voids with chlorides. However, as the cycles progressed, cumulative damage ensued from repeated deformation due to water loss and shrinkage during the drying phase, followed by water absorption and expansion during the wetting phase. This led to the expansion of internal cracks and an increase in pore volume within the concrete.[30,37] Furthermore, the internal stresses caused by salt crystallization from chloride erosion,[18,38] combined with the accumulated shrinkage and expansion strains from drying-and-wetting cycling, resulted in surface spalling of the concrete specimens, contributing to mass loss and a decrease in RDEM.[39]

The final average mass change rate of RC for the three design strengths is 2.61 times that of NC, while the final average RDEM for RC is 91.30% that of NC. Furthermore,

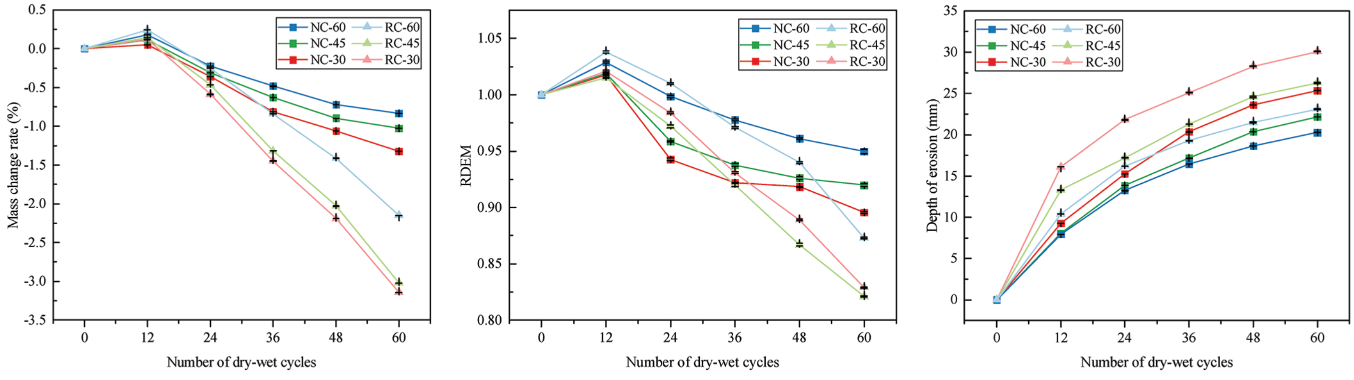

(a) (b) (c)

*Fig. 6—(a) Mass change; (b) RDEM; and (c) chloride erosion depth of concretes during drying-and-wetting cycles.*

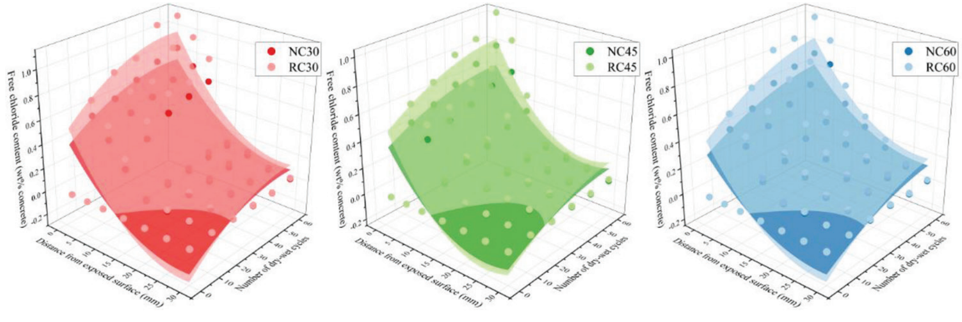

**(a)** **(b)** **(c)**

*Fig. 7—Free chloride content at different erosion depths of concretes during drying-and-wetting cycles: design strength of: (a) 30; (b) 45; and (c) 60 MPa.*

**Table 4—Fitted equations for free chloride-ion content of concrete at different depths during drying-and-wetting cycles**

| Concrete | Model type | Parameter value | $R^2$ |
|---|---|---|---|
| NC-30 | Parabola<br>$z = z_0 + a \times x + b \times y + c \times x^2 + d \times y^2$ | $z_0 = 0.68742$; $a = -0.0687$; $b = 0.01557$; $c = 0.00122$; $d = -1.41568 \times 10^{-4}$ | 0.79625 |
| RC-30 | | $z_0 = 0.52415$; $a = -0.05223$; $b = 0.01204$; $c = 9.27815 \times 10^{-4}$; $d = -1.12139 \times 10^{-4}$ | 0.79841 |
| NC-45 | | $z_0 = 0.47821$; $a = -0.05206$; $b = 0.00875$; $c = 0.00106$; $d = -7.36607 \times 10^{-5}$ | 0.81563 |
| RC-45 | | $z_0 = 0.62401$; $a = -0.06808$; $b = 0.0109$; $c = 0.00139$; $d = -8.50849 \times 10^{-5}$ | 0.81365 |
| NC-60 | | $z_0 = 0.39839$; $a = -0.0397$; $b = 0.00942$; $c = 6.94241 \times 10^{-4}$; $d = -6.82752 \times 10^{-5}$ | 0.83759 |
| RC-60 | | $z_0 = 0.52615$; $a = -0.05316$; $b = 0.01248$; $c = 9.40025 \times 10^{-4}$; $d = -8.95452 \times 10^{-5}$ | 0.83745 |

as shown in Fig. 6(c), the average chloride penetration depth in NC was 22.60 mm, compared to 26.50 mm in RC. The impact of different design strengths on the performance of NC and RC also showed distinct variations. Higher design strength in NC led to improved durability and resistance to chloride penetration, resulting in slower mass loss and RDEM degradation.

Compared to NC with the same design strength, RC demonstrated greater mass loss and deeper chloride penetration, attributed to the inferior quality of adhesion in the RFA. This difference was more pronounced at lower design strengths. For example, the mass loss of RC with a design strength of 30 MPa was 42.17% greater than that of NC, while for 45 and 60 MPa, the mass loss of RC was 33.95% and 38.81% greater than NC, respectively. In terms of RDEM, NC showed smaller reductions compared to RC, with NC-30 retaining 92.56% of the RDEM of RC-30, NC-45 retaining 89.26% of RC-45, and NC-60 retaining 91.91% of RC-60. Regarding chloride penetration, the depth in RC-30 was 84.22% of that in NC-30, 84.30% for RC-45 compared to NC-45, and 87.75% for RC-60 compared to NC-60. These differences can be attributed to the fact that lower-design-strength concrete tends to produce RFA with more adhered mortar,[40,41] while higher-strength concrete produces RFA that accumulates more damage during production, leading to increased deterioration in RC. Despite these differences, all three types of NC exhibited consistent trends in mass change, RDEM variation, and chloride penetration depth throughout the cycling process, and similar patterns were observed in the corresponding RC specimens.

Although an increase in porosity contributes to higher chloride penetration, it is not the sole determining factor. As supported by SEM observations, the formation of interconnected microcracks and deterioration of the ITZ structure play a more dominant role in facilitating chloride transport. During drying-and-wetting cycling, repeated expansion and shrinkage stresses induce crack coalescence, enhancing pore connectivity and forming continuous diffusion pathways. Therefore, the observed increase in chloride penetration depth in Fig. 6(c) results from the combined effects of increased porosity and microcrack connectivity, rather than porosity alone. In particular, RC specimens, owing to their weaker ITZ and higher initial defect density, exhibit more rapid development of connected cracks, which accelerates chloride ingress even when the total porosity increase is relatively modest.

## Free chloride-ion content

Figure 7 shows the free chloride-ion content at different depths of concrete during drying-and-wetting cycling (dark color for NC, light color for RC), and the fitting surface information is shown in Table 4. During the drying-and-wetting cycling, the average free chloride-ion content in the depth range of 0 to 30 mm from the exposed surface of NC-30, NC-45, NC-60, RC-30, RC-45, and RC-60 was 0.255 wt. %, 0.199 wt. %, 0.190 wt. %, 0.330 wt. %, 0.259 wt. %, and 0.251 wt. %, respectively. At the same depth from the exposed surface, the free chloride-ion content increased as the number of drying-and-wetting cycles progressed. Additionally, at the same number of cycles, the free chloride-ion content decreased with increasing depth from the exposed surface. After 60 drying-and-wetting cycles, the average free chloride-ion content at a depth of 2 mm in NC was 96.67% of that in RC.

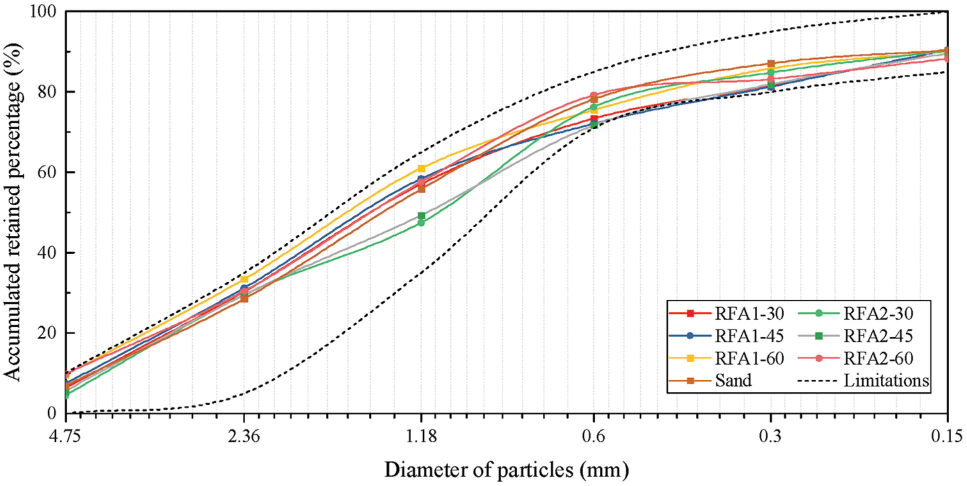

*Fig. 8—Grading curves of virgin aggregate and two generations of recycled aggregate.*

The free chloride-ion content in both NC and RC with different design strengths can be fitted using polynomial functions (Table 4), with a high correlation coefficient ($R^2$). This indicates that NC and RC with varying strengths exhibit similar patterns of chloride salt erosion throughout the entire drying-and-wetting cycling process.

Moreover, SEM coupled with energy-dispersive X-ray spectroscopy (SEM-EDS) analyses revealed that chloride ions accumulated predominantly within the ITZ and nearby hydration products after cyclic exposure. The elevated Cl signals corresponded to the presence of Friedel's salt and Kuzel's salt, formed through the reaction of chloride with calcium aluminate hydrates. This transformation locally consumed portlandite and disturbed the calcium-silicate-hydrate (C-S-H) network, thereby weakening microstructural compactness. Such interactions contribute to increased microcracking and accelerated chloride transport in subsequent cycles.[42,43] These findings confirm that chloride ions play a dual role—both chemically and physically—in deteriorating the concrete microstructure under repeated drying-and-wetting exposure.

## Grading curve

As shown in Fig. 8, the grading curves for the sand, RFA1, and RFA2 all meet the standard requirements. However, the residual mass of RFA2-60 on the 4.75 mm sieve is close to the upper limit specified by GB/T 25176-2010. This may be due to the higher design strength of the concrete, making it difficult to break the material into finer particles under mechanical force and particle collisions during the crushing and screening processes, resulting in a lower fine content and coarser particles.[35,44] Similarly, the retained mass of RFA2-30 between the 0.3 and 0.6 mm sieve sizes is slightly below the lower limit specified by the standards. This may be due to the lower design strength of concrete, which makes it easier to form RFAs with finer particles during secondary crushing, resulting in a higher fine content in the RFA produced. Additionally, the gradation of RFA2 is notably inferior compared to that of sand and RFA1. These observations indicate that the gradation curves of RFA from lower-strength concrete are relatively poor, and the gradation tends to further deteriorate with increased cycles of reuse. However, the gradation remains within the acceptable range.

## Physical properties

Figure 9 shows the physical properties of RFA1 and RFA2 obtained from NC and RC after 60 cycles of drying-and-wetting cycling, compared to the physical properties of sand. As illustrated in Fig. 9, as the design strength decreases, the apparent density and bulk density of RFA gradually increase, while the crushing value and soundness gradually decrease. The average apparent density, bulk density, crushing value, and soundness of RFA1 are 92.33%, 89.79%, 222.54%, and 156.86% of those of sand, respectively. Additionally, at the same design strength, the average apparent density of RFA2 is 95.07% of RFA1, the average bulk density is 96.30%, the average crushing value is 112.97%, and the soundness is 106.37%.

The data suggest that the attenuation rates of RFA in terms of apparent density, bulk density, crushing index, and soundness are influenced by the design strength of the original concrete. Specifically, RFAs from both higher- and lower-strength concrete show higher attenuation rates. For instance, RFAs produced from higher-strength concrete (for example, RFA-60) exhibit modest increases in attenuation rates for apparent density (0.9581) and bulk density (0.9634), while the crushing index (1.1634) and soundness (1.0792) increase more substantially. This is likely due to the harder mortar adhering to the RFA, which accumulates internal damage during crushing, leading to greater degradation in mechanical properties.[45,46] Conversely, RFA from lower-strength concrete (for example, RFA-30) also experiences notable attenuation in the crushing index (1.1023) and soundness (1.0263), attributed to the weaker mortar in the original concrete, resulting in greater performance degradation during the recycling process.

According to Chinese standard GB/T 25176-2010, the performance indicators of RFA1-60 meet the Class II standard, while those of RFA1-45, RFA2-30, RFA2-45, and RFA2-60 meet the Class III standard. This again demonstrates the potential for multi-generational use of RFAs. Furthermore, a comprehensive comparison of aggregate quality reveals

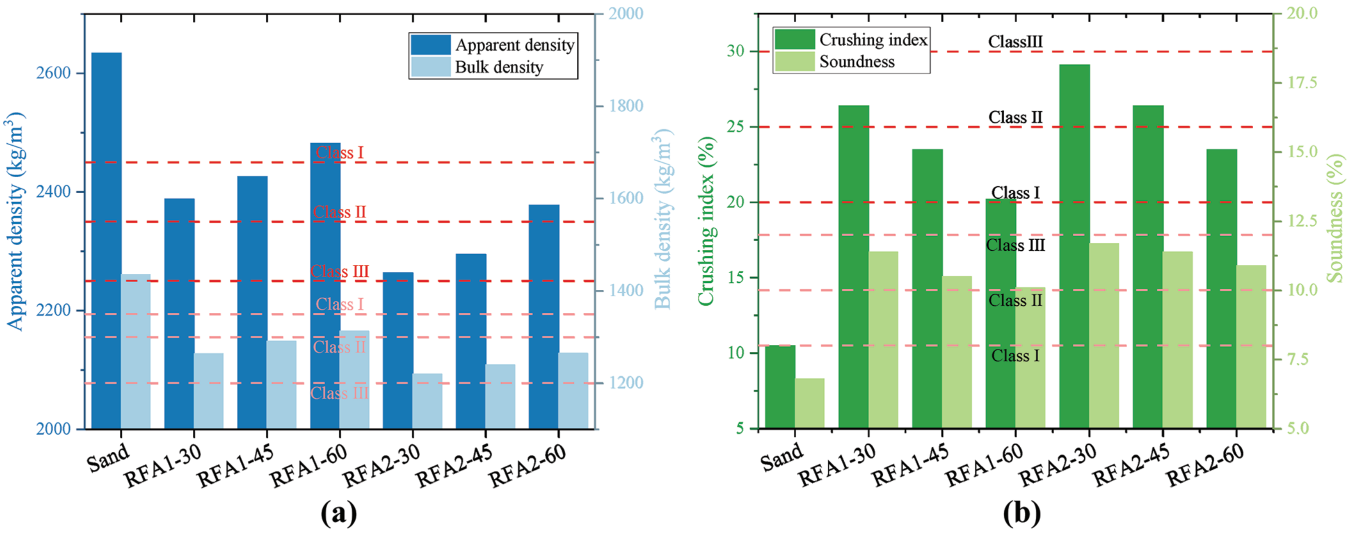

*Fig. 9—(a) Apparent density and bulk density; and (b) crushing value and water absorption of recycled aggregates.*

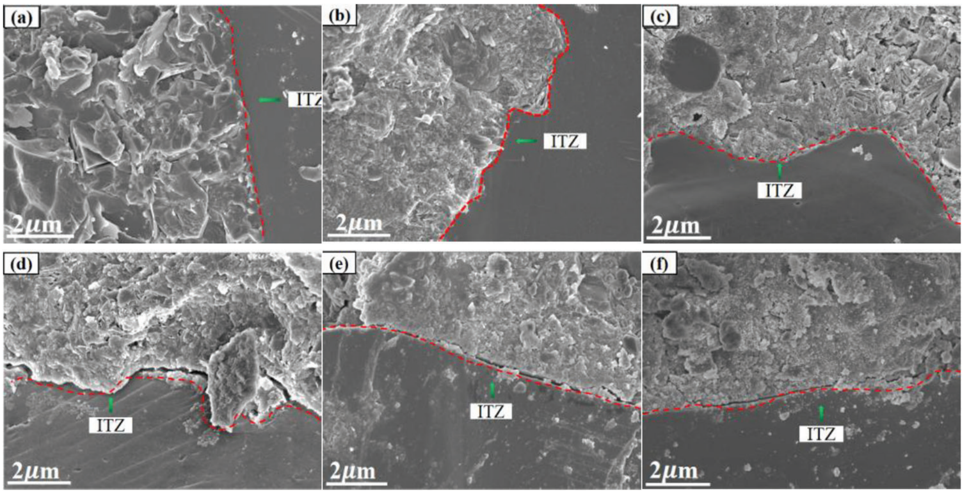

*Fig. 10—SEM images of ITZ after 60 drying-and-wetting cycles: (a) NC-30; (b) NC-45; (c) NC-60; (d) RC-30; (e) RC-45; and (f) RC-60.*

that the regeneration potential of RFA, ranked from largest to smallest, was: RFA1-60, RFA1-45, RFA2-60, RFA1-30, RFA2-45, and RFA2-30. This is because the adhered mortar strength in RFAs from higher-design-strength concrete is greater, leading to less internal damage under the same crushing conditions; therefore, these aggregates maintain higher quality despite the relatively high attenuation rates of RFA-60.[47]

## SEM-EDS analysis

After 30 drying-and-wetting cycles, SEM analysis was conducted on the two generations of concrete specimens (Fig. 10). The results indicate that the concrete with a design strength of 30 MPa has a rougher mortar surface. This roughness is likely due to the higher *w*/*b* in lower-strength concrete, which creates a less-dense cement paste, resulting in more pores and unhydrated particles on the surface. Moreover, the ITZ in RC is noticeably wider than that in NC.

In this study, the ITZ was identified in SEM micrographs based on both morphological and compositional characteristics, following established approaches in the literature.[48-50] Morphologically, the ITZ region was distinguished by a visibly porous texture and the presence of microcracks along the aggregate-paste interface under secondary electron imaging. Compositionally, EDS line scans revealed a gradual decrease in the Ca/Si and an increase in Al and O contents across the transition region, which is consistent with the typical hydration heterogeneity at the ITZ.

This observation is consistent with prior studies, which reported quantitative ITZ widths of approximately 120 μm in RC versus 60 μm in NC under comparable conditions.[51] This could be attributed to the higher water absorption rate of the RFA, which draws in more water during mixing, reducing the effective water content in the cement paste and hindering complete hydration of the mortar, thereby widening the ITZ region. However, in the present study, the authors did not perform a full statistical analysis of ITZ width (mean, standard deviation, and distribution) across different strength grades; this is a limitation of this work due to the limited number of SEM images and measurement points collected. The authors plan to include such a quantitative microstructural characterization in follow-up research, where the data

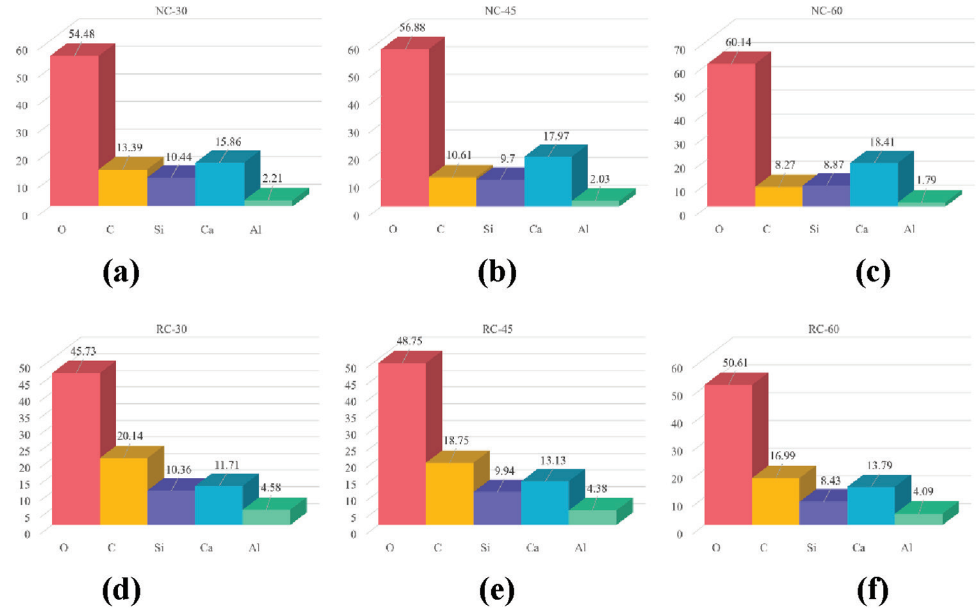

*Fig. 11—Elemental mass distribution in ITZ of samples after 60 drying-and-wetting cycles: (a) NC-30; (b) NC-45; (c) NC-60; (d) RC-30; (e) RC-45; and (f) RC-60.*

set will be expanded, image-processing algorithms will be applied, and ITZ width will be correlated statistically with strength grade and durability metrics.

As shown in Fig. 11, SEM-EDS surface scans of the ITZ for different concrete samples reveal notable variations in elemental composition. The Ca/Si increases with the design strength of the concrete. For instance, NC-30 exhibits a Ca/Si of approximately 1.52, which rises to 1.85 in NC-60, indicating a denser and more hydrated matrix in higher-strength concrete. In contrast, RC samples show a less pronounced increase in Ca/Si, with RC-30 at 1.13 and RC-60 at 1.63. Additionally, RC samples have higher aluminum content, such as 4.58% in RC-30 compared to 2.21% in NC-30, likely due to the mixing of alumina-rich materials during the recycling process. The overall elemental distribution in the ITZ suggests that RC samples have a more porous and less homogeneously hydrated ITZ compared to NC samples, contributing to the observed wider ITZ region in RC.

SEM-EDS analysis (Fig. 10 and 11) shows that the Ca/Si in the ITZ increases from 1.52 in NC-30 to 1.85 in NC-60, and from 1.13 in RC-30 to 1.63 in RC-60, reflecting the formation of a denser C-S-H gel network with fewer capillary pores. The refined ITZ structure effectively restricts chloride transport and reduces microcrack connectivity, resulting in a slower rate of mechanical degradation under drying-and-wetting cycling. In addition, the adhered mortar from the high-strength parent concrete (NC-60) contributes to a more compact ITZ in RC-60, which enhances the chloride resistance and delays the onset of microstructural damage.

## Multi-generation recyclability analysis

As shown in Fig. 12, the study evaluated four key aspects of concrete performance: a) mechanical properties, including compressive strength; b) physical characteristics, such as initial porosity; c) durability, covering changes in porosity, mass variation, RDEM changes, chloride penetration depth, and free chloride content during the drying-and-wetting cycling; and d) the physical properties of aggregates derived from crushed concrete, including apparent density, bulk density, crushing value, and soundness.

The performance indicators in Fig. 12 for two generations of concrete in the study before drying-and-wetting cycling were normalized to facilitate comparison and weighting in the calculations. Strength attenuation during the drying-and-wetting cycling was selected as the attenuation coefficient for each generation of concrete based on a comprehensive comparison. Subsequently, a multivariate regression analysis was conducted using a Python program to train the regression model, which calculated the weights of each performance indicator and established a model capable of predicting the performance attenuation rate of the next generation of concrete. The regression model assumes that the attenuation coefficient ($\lambda$) is a linear combination of various performance indicators

$$\lambda = P_0 + w_1 \times P_1 + w_2 \times P_2 + \ldots + w_n \times P_n \qquad (2)$$

where $P_0$ is the intercept; $P_1$, $P_2$, …, $P_n$ are the coefficients of the performance indicators; and $w_1$, $w_2$, …, $w_n$ are their corresponding weights. Multivariate regression analysis was performed using Python, determining the contribution of each performance indicator to the overall attenuation coefficient. By standardizing the regression coefficients, the relative importance of each indicator was calculated, as shown in Table 5.

It can be observed that the weights of porosity (0.333) and mass change (0.417) are notably higher than those of the other parameters. Physically, this indicates that these two factors dominate the degradation process under chloride drying-and-wetting cycling. Porosity governs the ease of chloride-ion and moisture transport within the concrete, determining the rate of internal damage evolution. Mass change reflects the cumulative effects of physical

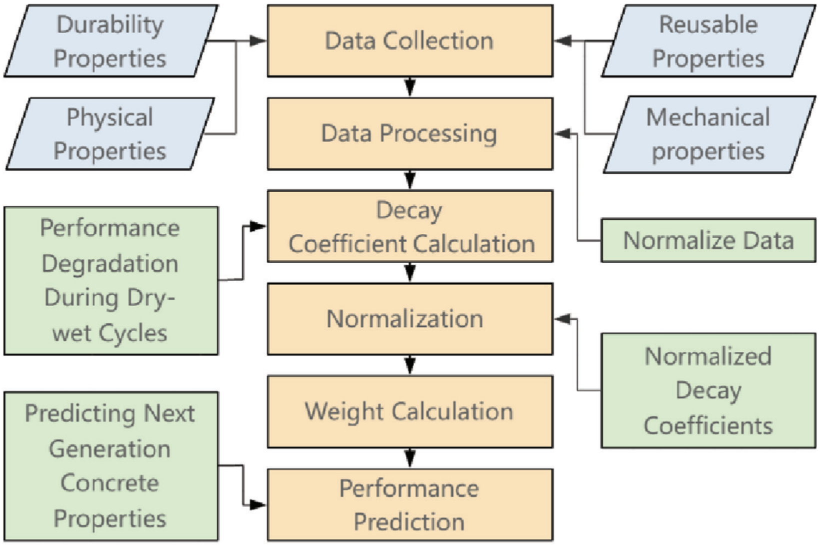

*Fig. 12—Multi-generation concrete recyclability analysis process.*

**Table 5—Corresponding weights of indicators in multiple linear regression model**

| Indicator | Regression coefficient | Weights |
|---|---|---|
| Compressive strength | $5.07 \times 10^{-6}$ | $2.38 \times 10^{-6}$ |
| Porosity | $-7.09 \times 10^{-1}$ | $3.33 \times 10^{-1}$ |
| Mass change | $8.86 \times 10^{-1}$ | $4.17 \times 10^{-1}$ |
| RDEM | $5.60 \times 10^{-2}$ | $2.63 \times 10^{-2}$ |
| Chloride erosion depth | $-5.74 \times 10^{-2}$ | $2.70 \times 10^{-2}$ |
| Free chloride-ion content | $1.03 \times 10^{-1}$ | $4.82 \times 10^{-2}$ |
| Apparent density | $2.33 \times 10^{-2}$ | $1.10 \times 10^{-2}$ |
| Bulk density | $-7.02 \times 10^{-2}$ | $3.30 \times 10^{-2}$ |
| Crushing index | $-1.30 \times 10^{-1}$ | $6.13 \times 10^{-2}$ |
| Soundness | $-9.27 \times 10^{-2}$ | $9.27 \times 10^{-2}$ |

deterioration (spalling, salt crystallization) and chemical alteration (loss of hydration products). In recycled concrete, the adhered mortar on RFAs exhibits higher porosity and a weaker microstructure compared to natural aggregates, which enhances the permeability and accelerates deterioration. Consequently, variations in porosity and mass have a more pronounced influence on the degradation coefficient. Similar conclusions regarding the critical role of porosity in chloride transport and durability loss of recycled aggregate concrete have been reported by Zhu et al.[52] and Wang et al.[53]

According to the regression model predictions, the compressive strength decay coefficients for concrete with parent concrete strengths of 30, 45, and 60 MPa are 0.5684, 0.6775, and 0.7172, respectively. This indicates that, after 60 drying-and-wetting cycles, the compressive strength of third-generation recycled concrete from these parent concretes will decrease to 56.84%, 67.75%, and 71.72% of their initial values. Specifically, under the same mixture proportions, the compressive strength of RFA2-30, RFA2-45, and RFA2-60 concretes drops to 17.05, 30.49, and 43.03 MPa, respectively, which is significantly lower than their original design strengths.

According to GB 50010-2010 and EN 1992-1-1 (Eurocode 2), the minimum compressive strength requirement for marine structural concrete typically exceeds 30 MPa to ensure adequate durability and chloride resistance. Hence, the predicted strength of RFA2-30 concrete (17.05 MPa) falls below the threshold for both structural and durability performance, making it unsuitable for marine or load-bearing use. In contrast, RFA2-45 and RFA2-60 concretes (30.49 and 43.03 MPa, respectively) may marginally satisfy serviceability requirements for secondary structural components or inland exposure environments but remain vulnerable to chloride-induced degradation. These findings suggest that, without further enhancement measures, third-generation recycled concrete cannot fully meet practical engineering demands, particularly in aggressive environments such as marine exposure.

However, it should be noted that the main limitation of third-generation recycled concrete lies in the performance degradation of RFAs caused by multiple recycling cycles. Previous studies have shown that technical interventions such as surface modification,[54] nanosilica[55] or pozzolanic slurry coating,[56] and optimized mixture proportioning can effectively strengthen the recycled aggregates and improve the ITZ, thereby enhancing the mechanical and durability performance of multi-generation recycled concrete. Therefore, future research should focus on aggregate modification and mixture optimization to extend the applicability of third-generation recycled concrete in engineering practice.

This finding is consistent with the research by Thomas et al.,[19,57] who also observed that without additional interventions, the recycling potential of multi-generation recycled coarse aggregate concrete is limited to three generations.[58]

## CONCLUSIONS

Based on the results of this experimental investigation under tidal conditions, the following conclusions are drawn:

1. Concrete with design strengths of 30, 45, and 60 MPa, whether natural aggregate concrete (NC) or recycled fine aggregate (RFA) concrete (RC), showed similar degradation

patterns under chloride salt drying-and-wetting cycling. Compressive strength, mass change, and relative dynamic elastic modulus (RDEM) first increased and then decreased, while porosity and chloride penetration depth continuously increased. Higher design strengths enhanced durability against chloride erosion during multi-generation recycling.

2. The chloride resistance of RC was lower than that of NC. After 60 cycles, the average compressive strength of RC was 42.50 MPa (89.52% of NC), with higher porosity (25%), greater mass loss (6%), and deeper chloride penetration (25 mm). The difference between RC and NC was more pronounced at lower design strengths: RC-30 had 42.17% more mass loss than NC-30, RC-45 33.95%, and RC-60 38.81%. Regarding RDEM, NC-30 retained 92.56% of RC-30's RDEM, NC-45 89.26%, and NC-60 91.91%. Similarly, chloride penetration was deeper in RC, with RC-30, RC-45, and RC-60 showing 84.22%, 84.30%, and 87.75% of NC's penetration depth after 60 cycles.

3. The grading curves of sand, RFA1, and RFA2 met standard requirements. However, RFA from higher-strength concrete contained coarser particles, while that from lower-strength concrete was finer. The apparent density, bulk density, crushing value, and soundness of RFA degraded more in lower-strength concrete. For instance, the apparent density of RFA1 was 92.33% of sand, and RFA2 was 95.07% that of RFA1. The crushing value and soundness of RFA1 were 222.54% and 156.86% that of sand, while for RFA2 they were 112.97% and 106.37% that of RFA1, respectively. Despite these declines, all RFAs remained within acceptable limits.

4. Scanning electron microscopy (SEM)-energy-dispersive X-ray spectroscopy (EDS) analysis after 30 cycles revealed that RC had a wider interfacial transition zone (ITZ) and lower Ca/Si ratios than NC. The Ca/Si increased from 1.52 (NC-30) to 1.85 (NC-60), and from 1.13 (RC-30) to 1.63 (RC-60). RC also showed higher Al content (4.58% in RC-30 versus 2.21% in NC-30). These results indicate that higher porosity and Al content in RC's ITZ lead to less uniform hydration, explaining its reduced performance.

5. The regression model predicted strength attenuation coefficients for third-generation concrete as 0.5684 (30 MPa), 0.6775 (45 MPa), and 0.7172 (60 MPa). After 60 cycles, the compressive strengths of RFA2-30, RFA2-45, and RFA2-60 were predicted to decrease to 17.05, 30.49, and 43.03 MPa, respectively. Given the minimum strength requirement for marine and structural concrete (≥30 MPa), RFA2-30 concrete fails to meet standards, while RFA2-45 and RFA2-60 only partially satisfy functional demands. These findings underscore the need for technical interventions (for example, surface modification or nanosilica treatment) to maintain performance across generations and ensure sustainable use of third-generation recycled concrete.

This study highlights the potential for multi-generational use of RFA in concrete, but also the necessity of optimized mixture designs to ensure durability in chloride-rich environments. Future work should optimize mixture designs under various exposure and load conditions and explore the long-term recyclability of RFAs to promote sustainable concrete practices.

## AUTHOR BIOS

**Chunhong Chen** *is a PhD Candidate at the Faculty of Civil Engineering and Mechanics, Jiangsu University, Zhenjiang, China, and an Associate Professor at the School of Urban Construction, Changzhou University, Changzhou, China. She received her BS from Nanchang University, Nanchang, China, and her MS from Southeast University, Nanjing, China. Her research interests include the durability of recycled aggregate concrete in various environments.*

**Yunchun Chen** *is a Master's Candidate at the School of Urban Construction, Changzhou University. He received his BS from Shenyang Agricultural University, Shenyang, China. His research interests include the performance of recycled aggregate concrete under drying-and-wetting cycles.*

**Jiang Yu** *is a Master's Candidate at the School of Urban Construction, Changzhou University. He received his BS from Jinling Institute of Technology, Nanjing, China. His research interests include the durability of recycled concrete structures subjected to chloride-ion erosion.*

**Pinghua Zhu** *is a Professor and Doctoral Supervisor at Changzhou University. He received his BS, MS, and PhD from Wuhan University of Technology, Wuhan, China. His research interests include the durability of concrete structures, the performance of recycled concrete, and building energy efficiency technology.*

**Ronggui Liu** *is a Professor and Doctoral Supervisor at the Faculty of Civil Engineering and Mechanics, Jiangsu University. He received his BS and MS from Lanzhou Jiaotong University, Lanzhou, China, and his PhD from Southeast University. His research interests include the durability of modern prestressed structures, nonlinear behavior and control of long-span prestressed structures with carbon fiber cables, and key technologies for the complete preparation and promotion of eco-concrete.*

**Xinjie Wang** *is a Professor and Doctoral Supervisor at Changzhou University. He received his BS from Anhui Jianzhu University, Hefei, China; his MS from Guizhou University, Guiyang, China; and his PhD from Hohai University, Nanjing, China. His research interests include the durability of concrete structures, the performance of recycled concrete, and building energy efficiency technology.*

## ACKNOWLEDGMENTS

This research was funded by the National Natural Science Foundation of China (No. 52108190, No. 51778272, and No. 52078068).

## REFERENCES

1. Chakradhara Rao, M., "Influence of Brick Dust, Stone Dust, and Recycled Fine Aggregate on Properties of Natural and Recycled Aggregate Concrete," *Structural Concrete*, V. 22, No. S1, 2021, pp. E105-E120. doi: 10.1002/suco.202000103

2. Mohamad Bohari, A. A.; Skitmore, M.; Xia, B.; Teo, M.; Zhang, X.; and Adham, K. N., "The Path towards Greening the Malaysian Construction Industry," *Renewable and Sustainable Energy Reviews*, V. 52, 2015, pp. 1742-1748. doi: 10.1016/j.rser.2015.07.148

3. Sev, A., "How Can the Construction Industry Contribute to Sustainable Development? A Conceptual Framework," *Sustainable Development*, V. 17, No. 3, 2009, pp. 161-173. doi: 10.1002/sd.373

4. Ortiz, O.; Castells, F.; and Sonnemann, G., "Sustainability in the Construction Industry: A Review of Recent Developments Based on LCA," *Construction and Building Materials*, V. 23, No. 1, 2009, pp. 28-39. doi: 10.1016/j.conbuildmat.2007.11.012

5. Torres, A.; Simoni, M. U.; Keiding, J. K.; Müller, D. B.; zu Ermgassen, S. O. S. E.; Liu, J.; Jaeger, J. A. G.; Winter, M.; and Lambin, E. F., "Sustainability of the Global Sand System in the Anthropocene," *One Earth*, V. 4, No. 5, 2021, pp. 639-650. doi: 10.1016/j.oneear.2021.04.011

6. Siddique, R., and Noumowe, A., "Utilization of Spent Foundry Sand in Controlled Low-Strength Materials and Concrete," *Resources, Conservation and Recycling*, V. 53, No. 1-2, 2008, pp. 27-35. doi: 10.1016/j.resconrec.2008.09.007

7. Dadd, L.; Xie, T.; Bennett, B.; and Visintin, P., "Exploring the Physical and Mechanical Characteristics of Multi-Generation Recycled Aggregate Concrete at Equivalent Compressive Strengths," *Journal of Cleaner Production*, V. 451, 2024, Article No. 141965. doi: 10.1016/j.jclepro.2024.141965

8. Tošić, N.; Peralta Martínez, D.; Hafez, H.; Reynvart, I.; Ahmad, M.; Liu, G.; and de la Fuente, A., "Multi-Recycling of Polypropylene Fibre Reinforced Concrete: Influence of Recycled Aggregate Properties on New Concrete," *Construction and Building Materials*, V. 346, 2022, Article No. 128458. doi: 10.1016/j.conbuildmat.2022.128458

9. Rahimzadeh Oskooei, P.; Mohammadinia, A.; Arulrajah, A.; Horpibulsuk, S.; and Emam, S., "Crushing Behavior of Recycled Waste Materials: Experimental Analysis and DEM Simulation," *Construction and Building Materials*, V. 299, 2021, Article No. 124226. doi: 10.1016/j.conbuildmat.2021.124226

10. Cao, Y.; Bao, J.; Zhang, P.; Sun, Y.; and Cui, Y., "A State-of-the-Art Review on the Durability of Seawater Coral Aggregate Concrete Exposed to Marine Environment," *Journal of Building Engineering*, V. 60, 2022, Article No. 105199. doi: 10.1016/j.jobe.2022.105199

11. Qu, F.; Li, W.; Dong, W.; Tam, V. W. Y.; and Yu, T., "Durability Deterioration of Concrete under Marine Environment from Material to Structure: A Critical Review," *Journal of Building Engineering*, V. 35, 2021, Article No. 102074. doi: 10.1016/j.jobe.2020.102074

12. Yi, Y.; Zhu, D.; Guo, S.; Zhang, Z.; and Shi, C., "A Review on the Deterioration and Approaches to Enhance the Durability of Concrete in the Marine Environment," *Cement and Concrete Composites*, V. 113, 2020, Article No. 103695. doi: 10.1016/j.cemconcomp.2020.103695

13. Li, K.; Zhang, D.; Li, Q.; and Fan, Z., "Durability for Concrete Structures in Marine Environments of HZM Project: Design, Assessment and Beyond," *Cement and Concrete Research*, V. 115, 2019, pp. 545-558. doi: 10.1016/j.cemconres.2018.08.006

14. Tam, V. W. Y.; Soomro, M.; and Evangelista, A. C. J., "A Review of Recycled Aggregate in Concrete Applications (2000-2017)," *Construction and Building Materials*, V. 172, 2018, pp. 272-292. doi: 10.1016/j.conbuildmat.2018.03.240

15. Wang, Z.; Zhu, P.; Liu, H.; Wang, X.; and Chen, C., "An Innovative and Efficient Multi-Generation Recycling System for Waste Concrete Subjected to Freeze-Thaw Environment: A Theory Model and Case Study," *Journal of Cleaner Production*, V. 363, 2022, Article No. 132135. doi: 10.1016/j.jclepro.2022.132135

16. Visintin, P.; Dadd, L.; Ul Alam, M.; Xie, T.; and Bennett, B., "Flexural Performance and Life-Cycle Assessment of Multi-Generation Recycled Aggregate Concrete Beams," *Journal of Cleaner Production*, V. 360, 2022, Article No. 132214. doi: 10.1016/j.jclepro.2022.132214

17. Chen, F.; Gao, J.; Qi, B.; Shen, D.; and Li, L., "Degradation Progress of Concrete Subject to Combined Sulfate-Chloride Attack under Drying-Wetting Cycles and Flexural Loading," *Construction and Building Materials*, V. 151, 2017, pp. 164-171. doi: 10.1016/j.conbuildmat.2017.06.074

18. Chen, C.; Wang, L.; Liu, R.; Zhu, P.; Liu, H.; Wang, X.; Yu, J.; and Chen, Y., "Chloride Penetration of Concrete Exposed to Dry-Wet Cycle with Various Dry-Wet Ratios and Temperature," *Construction and Building Materials*, V. 400, 2023, Article No. 132883. doi: 10.1016/j.conbuildmat.2023.132883

19. Thomas, C.; de Brito, J.; Cimentada, A.; and Sainz-Aja, J. A., "Macro- and Micro- Properties of Multi-Recycled Aggregate Concrete," *Journal of Cleaner Production*, V. 245, 2020, Article No. 118843. doi: 10.1016/j.jclepro.2019.118843

20. Tam, V. W. Y.; Gao, X. F.; and Tam, C. M., "Microstructural Analysis of Recycled Aggregate Concrete Produced from Two-Stage Mixing Approach," *Cement and Concrete Research*, V. 35, No. 6, 2005, pp. 1195-1203. doi: 10.1016/j.cemconres.2004.10.025

21. Xiao, J.; Li, W.; Sun, Z.; Lange, D. A.; and Shah, S. P., "Properties of Interfacial Transition Zones in Recycled Aggregate Concrete Tested by Nanoindentation," *Cement and Concrete Composites*, V. 37, 2013, pp. 276-292. doi: 10.1016/j.cemconcomp.2013.01.006

22. Kou, S. C., and Poon, C. S., "Enhancing the Durability Properties of Concrete Prepared with Coarse Recycled Aggregate," *Construction and Building Materials*, V. 35, 2012, pp. 69-76. doi: 10.1016/j.conbuildmat.2012.02.032

23. Amey, S. L.; Johnson, D. A.; Miltenberger, M. A.; and Farzam, H., "Predicting the Service Life of Concrete Marine Structures: An Environmental Methodology," *ACI Structural Journal*, V. 95, No. 2, Mar.-Apr. 1998, pp. 205-214.

24. Gao, Y.-H.; Zhang, J.-Z.; Zhang, S.; and Zhang, Y.-R., "Probability Distribution of Convection Zone Depth of Chloride in Concrete in a Marine Tidal Environment," *Construction and Building Materials*, V. 140, 2017, pp. 485-495. doi: 10.1016/j.conbuildmat.2017.02.134

25. Zheng, Q.; Li, C.; Song, F.; He, B.; Li, W.; and Jiang, Z., "Autogenous Self-Healing of Ultra-High-Performance Fiber-Reinforced Concrete with Varying Silica Fume Dosages: Secondary Hydration and Structural Regeneration," *Cement and Concrete Composites*, V. 137, 2023, Article No. 104905. doi: 10.1016/j.cemconcomp.2022.104905

26. Wang, D.; Shi, C.; Wu, Z.; Xiao, J.; Huang, Z.; and Fang, Z., "A Review on Ultra High Performance Concrete: Part II. Hydration, Microstructure and Properties," *Construction and Building Materials*, V. 96, 2015, pp. 368-377. doi: 10.1016/j.conbuildmat.2015.08.095

27. Ting, M. Z. Y.; Wong, K. S.; Rahman, M. E.; and Meheron, S. J., "Deterioration of Marine Concrete Exposed to Wetting-Drying Action," *Journal of Cleaner Production*, V. 278, 2021, Article No. 123383. doi: 10.1016/j.jclepro.2020.123383

28. Wu, Z.; Wong, H. S.; and Buenfeld, N. R., "Transport Properties of Concrete after Drying-Wetting Regimes to Elucidate the Effects of Moisture Content, Hysteresis and Microcracking," *Cement and Concrete Research*, V. 98, 2017, pp. 136-154. doi: 10.1016/j.cemconres.2017.04.006

29. Gao, Y.; Zhang, J.; and Luosun, Y., "Shrinkage Stress in Concrete under Dry–Wet Cycles: An Example with Concrete Column," *Mechanics of Time-Dependent Materials*, V. 18, No. 1, 2014, pp. 229-252. doi: 10.1007/s11043-013-9225-1

30. Zhang, J.; Gao, Y.; Han, Y.; and Sun, W., "Shrinkage and Interior Humidity of Concrete under Dry–Wet Cycles," *Drying Technology*, V. 30, No. 6, 2012, pp. 583-596. doi: 10.1080/07373937.2011.653614

31. Muhammad, F.; Harun, M.; Ahmed, A.; Kabir, N.; Khalid, H. R.; and Hanif, A., "Influence of Bonded Mortar on Recycled Aggregate Concrete Properties: A Review," *Construction and Building Materials*, V. 432, 2024, Article No. 136564. doi: 10.1016/j.conbuildmat.2024.136564

32. Wang, Y.; Liu, J.; Zhu, P.; Liu, H.; Wu, C.; and Zhao, J., "Investigation of Adhered Mortar Content on Recycled Aggregate Using Image Analysis Method," *Journal of Materials in Civil Engineering*, ASCE, V. 33, No. 9, 2021, p. 04021225. doi: 10.1061/(ASCE)MT.1943-5533.0003864

33. Sainz-Aja, J.; Carrascal, I.; Polanco, J.; Cimentada, A.; Thomas, C.; and Brito, J., "Aging of Recycled Aggregates Mortars by Drying-Wetting Cycles," *Construction and Building Materials*, V. 307, 2021, Article No. 124934. doi: 10.1016/j.conbuildmat.2021.124934

34. Andreu, G., and Miren, E., "Experimental Analysis of Properties of High Performance Recycled Aggregate Concrete," *Construction and Building Materials*, V. 52, 2014, pp. 227-235. doi: 10.1016/j.conbuildmat.2013.11.054

35. Akbarnezhad, A.; Ong, K. C. G.; Tam, C. T.; and Zhang, M. H., "Effects of the Parent Concrete Properties and Crushing Procedure on the Properties of Coarse Recycled Concrete Aggregates," *Journal of Materials in Civil Engineering*, ASCE, V. 25, No. 12, 2013, pp. 1795-1802. doi: 10.1061/(ASCE)MT.1943-5533.0000789

36. Ben, X.; Jiang, L.; Guo, M.-Z.; Meng, Y.; Chen, L.; Jin, W.; and Wang, F., "Chloride Erosion Resistance of Calcium Formate Incorporated Cement Mortar under Chloride Attack," *Construction and Building Materials*, V. 314, Part A, 2022, Article No. 125611. doi: 10.1016/j.conbuildmat.2021.125611

37. Xie, Y.; Zhang, B.; Liu, B.; Zeng, Z.; Zhang, Y.; and Zheng, Y., "Shrinkage Cracking and Strength Deterioration of Red Clay under Cyclic Drying and Wetting," *Alexandria Engineering Journal*, V. 61, No. 3, 2022, pp. 2574-2588. doi: 10.1016/j.aej.2021.08.011

38. Zhang, M.; Xu, R.; Liu, K.; and Sun, S., "Research Progress on Durability of Marine Concrete under the Combined Action of $Cl^-$ Erosion, Carbonation, and Dry–Wet Cycles," *Reviews on Advanced Materials Science*, V. 61, No. 1, 2022, pp. 622-637. doi: 10.1515/rams-2022-0049

39. Cheng, S.; Shui, Z.; Gao, X.; Lu, J.; Sun, T.; and Yu, R., "Degradation Progress of Portland Cement Mortar under the Coupled Effects of Multiple Corrosive Ions and Drying-Wetting Cycles," *Cement and Concrete Composites*, V. 111, 2020, Article No. 103629. doi: 10.1016/j.cemconcomp.2020.103629

40. Ma, J.; Wang, Y.; Zhang, L.; Zeng, L.; Wang, X.; and Dang, J., "Influence of Geometric Shape, Pore Structure and Surface Modification of Recycled Fine Aggregate on the Rheology Behaviour and Strength Development of Mortar," *Journal of Building Engineering*, V. 91, 2024, Article No. 109604. doi: 10.1016/j.jobe.2024.109604

41. Yaragal, S. C., and Muhammad, R. A. K., "Usage Potential of Recycled Aggregates in Mortar and Concrete," *Advances in Concrete Construction*, V. 5, No. 3, 2017, pp. 201-219.

42. Long, W.-J.; Zhang, X.; Feng, G.-L.; Xie, J.; Xing, F.; Dong, B.; Zhang, J.; and Khayat, K. H., "Investigation on Chloride Binding Capacity and Stability of Friedel's Salt in Graphene Oxide Reinforced Cement Paste," *Cement and Concrete Composites*, V. 132, 2022, Article No. 104603. doi: 10.1016/j.cemconcomp.2022.104603

43. Li, X.; Xu, F.; Chen, B.; Li, B.; Chen, Z.; Zhu, J.; Peng, C.; and Lin, J., "Investigation on the Chloride Ion Erosion Mechanism of Cement Mortar in Coastal Areas: From Experiments to Molecular Dynamics Simulation," *Construction and Building Materials*, V. 350, 2022, Article No. 128810. doi: 10.1016/j.conbuildmat.2022.128810

44. Fang, H.-Y.; Liu, F.-L.; and Yang, J.-H., "High-Quality Coarse Aggregate Recycling from Waste Concrete by Impact Crushing," *Journal of Material Cycles and Waste Management*, V. 22, No. 3, 2020, pp. 887-896. doi: 10.1007/s10163-020-00984-w

45. Lei, B.; Yu, L.; Chen, T.; Lv, Z.; Zaland, S.; and Tang, Z., "Experimental Study on the Initial Damage and Mechanical Property Evolution of Recycled Coarse Aggregates under Freeze–Thaw Cycles and Repeated Loads," *Construction and Building Materials*, V. 375, 2023, Article No. 130972. doi: 10.1016/j.conbuildmat.2023.130972

46. Wei, D.; Zhu, P.; Yan, X.; Liu, H.; Chen, C.; and Wang, Z., "Potential Evaluation of Waste Recycled Aggregate Concrete for Structural Concrete Aggregate from Freeze-Thaw Environment," *Construction and Building Materials*, V. 321, 2022, Article No. 126291. doi: 10.1016/j.conbuildmat.2021.126291

47. Zhang, Z.; Zhang, Y.; Yan, C.; and Liu, Y., "Influence of Crushing Index on Properties of Recycled Aggregates Pervious Concrete," *Construction and Building Materials*, V. 135, 2017, pp. 112-118. doi: 10.1016/j.conbuildmat.2016.12.203

48. Liu, Y.; Ren, P.; Garcia-Troncoso, N.; Mo, K. H.; and Ling, T.-C., "Roles of Enhanced ITZ in Improving the Mechanical Properties of Concrete Prepared with Different Types of Recycled Aggregates," *Journal of Building Engineering*, V. 60, 2022, Article No. 105197. doi: 10.1016/j.jobe.2022.105197

49. Liu, J.; Ma, K.; Shen, J.; Zhu, J.; Long, G.; Xie, Y.; and Liu, B., "Influence of Recycled Concrete Aggregate Enhancement Methods on the Change of Microstructure of ITZs in Recycled Aggregate Concrete," *Construction and Building Materials*, V. 371, 2023, Article No. 130772. doi: 10.1016/j.conbuildmat.2023.130772

50. Xu, L.; Wang, J.; Huang, R.; Li, B.; Ran, B.; and Hu, X., "Investigations on Micro-Mechanical Properties of the ITZs between Recycled Aggregates and Recycled Cement Paste," *Construction and Building Materials*, V. 450, 2024, Article No. 138640. doi: 10.1016/j.conbuildmat.2024.138640

51. Sun, D.; Huang, W.; Liu, K.; Ma, R.; Wang, A.; Guan, Y.; and Shen, S., "Effect of the Moisture Content of Recycled Aggregate on the Mechanical Performance and Durability of Concrete," *Materials*, V. 15, No. 18, 2022, Article No. 6299. doi: 10.3390/ma15186299

52. Zhu, C.; Liu, X.; Liu, C.; Yu, W.; and Bai, G., "Study on the Chloride Ion Transport Mechanism of Recycled Mixed Aggregate Concrete Based on Evolution Characteristics of Pore Structure," *Construction and Building Materials*, V. 353, 2022, Article No. 129101. doi: 10.1016/j.conbuildmat.2022.129101

53. Wang, J.; Zhang, J.; and Cao, D., "Pore Characteristics of Recycled Aggregate Concrete and Its Relationship with Durability under Complex Environmental Factors," *Construction and Building Materials*, V. 272, 2021, Article No. 121642. doi: 10.1016/j.conbuildmat.2020.121642

54. Geng, W.; Li, C.; Zeng, D.; Chen, J.; Wang, H.; Liu, Z.; and Liu, L., "Effect of Epoxy Resin Surface-Modified Techniques on Recycled Coarse Aggregate and Recycled Aggregate Concrete," *Journal of Building Engineering*, V. 76, 2023, Article No. 107081. doi: 10.1016/j.jobe.2023.107081

55. Li, L.; Xuan, D.; Sojobi, A. O.; Liu, S.; Chu, S. H.; and Poon, C. S., "Development of Nano-Silica Treatment Methods to Enhance Recycled Aggregate Concrete," *Cement and Concrete Composites*, V. 118, 2021, Article No. 103963. doi: 10.1016/j.cemconcomp.2021.103963

56. Siletani, A. H.; Asayesh, S.; Shirzadi Javid, A. A.; Korayem, A. H.; and Ghanbari, M. A., "Influence of Coating Recycled Aggregate Surface with Different Pozzolanic Slurries on Mechanical Performance, Durability, and Micro-Structure Properties of Recycled Aggregate Concrete," *Journal of Building Engineering*, V. 83, 2024, Article No. 108457. doi: 10.1016/j.jobe.2024.108457

57. Thomas, C.; de Brito, J.; Gil, V.; Sainz-Aja, J. A.; and Cimentada, A., "Multiple Recycled Aggregate Properties Analysed by X-Ray Microtomography," *Construction and Building Materials*, V. 166, 2018, pp. 171-180. doi: 10.1016/j.conbuildmat.2018.01.130

58. Zhu, P.; Liu, W.; Niu, Z.; Wei, D.; and Hu, K., "Strength and Chloride Diffusion Behaviour of Three Generations of Repeated Recycled Fine Aggregate Concrete," *Journal of Wuhan University of Technology-Materials Science Edition*, V. 33, No. 5, 2018, pp. 1113-1120. doi: 10.1007/s11595-018-1943-4

## NOTES:

ACI MATERIALS JOURNAL TECHNICAL PAPER

Title No. 123-M26

# Effect of Synergistic Activation on Properties of Recycled Concrete Powder

by Shuiping Li, Chengxiao Yu, Jincheng Jiang, Bin Yuan, Jian Cheng, and Qing Lin

*The amount of recycled concrete powder (RCP) experiences an exponential increase due to the construction and demolition activities associated with buildings and infrastructure. To enhance the reactivity and use of RCP, this study investigated the effect of thermal (calcination), inorganic (calcium hydroxide [CH]), organic (diethanolisopropanolamine [DEIPA]), and synergistic activation on the strength development of RCP-cement (RCP-C) pastes. The microstructure of hardened pastes was characterized by X-ray diffraction (XRD), Fourier-transform infrared spectroscopy (FT-IR), thermogravimetric (TG) analysis, and scanning electron microscopy (SEM). The results indicated that the optimal compressive and flexural strengths were achieved when pastes were activated by calcination at 700°C for 30 minutes, followed by inorganic and organic activation using CH and DEIPA as activators successively. The compressive (flexural) strength at 1, 3, and 28 days increased by 42% (26.9%), 27.0% (18.6%), and 25.5% (16.3%), respectively, compared to the control group. The microstructure analysis revealed that the enhancement mechanism can be attributed to a thermal-inorganic-organic synergistic activation.*

**Keywords:** cement paste; microstructure; recycled concrete powder (RCP); strength development; synergistic activation.

## INTRODUCTION

Cement-based materials, such as mortar, concrete, slabs, concrete blocks, and so on, are widely used in the construction industry as building materials. It is well known that these building materials are generally produced using ordinary portland cement (OPC) as the cementitious material and natural granular materials as fine and coarse aggregates. However, the production of OPC and aggregate not only consumes a significant amount of energy, but also leads to a large volume of $CO_2$ emissions.[1-3] For example, the cement industry represents approximately 5% of global $CO_2$ emissions,[2] which may contribute to rising sea levels.[3] So, the development of alternative materials for OPC is necessary and urgent.

In the past two decades, the rapid development of urbanization has led to a significant increase in construction and demolition waste (CDW) worldwide.[4] The use of CDW is crucial for the building industry because simply disposing of it in landfills can occupy a significant amount of land space and has a profound impact on the environment.[5,6] More and more scholars have focused on the preparation of recycled aggregate from CDW.[7-11] During the process of preparing recycled aggregate from CDW through crushing, screening, and shaping,[12] a significant quantity of recycled concrete powder (RCP), which accounts for 20 to 30% volume of CDW, with particle size <75 μm,[13] is generated. RCP, which consists of hydration products, finely ground sands, and unhydrated cement and/or other cementitious materials,[14] is rich in silicon and aluminum components and exhibits certain reactivity. In addition, the preparation process of RCP, such as calcination and grinding, requires a certain amount of energy. However, the replacement of 1 ton of portland cement with RCP can achieve a significant carbon reduction of approximately 617 kg. Therefore, RCP may be a high-value, low-cost, eco-friendly, and low-carbon supplementary cementitious material due to these previous active compositions.[15,16]

However, the use of RCP is challenging, which may be attributed to its low reactivity.[17,18] Therefore, various activation methods, such as mechanical, alkali, and thermal activations, have been employed to boost the reactivity of RCP.[19-25] Mechanical activation can refine particle sizes and distribution and optimize shape and surface cracks.[26,27] Nevertheless, special attention should be paid to the significant energy consumption and noise emissions associated with mechanical activation. Alkali activation, such as NaOH, KOH, and water glass, can break the Si-O or Al-O bonds present in RCP and form new gel products through polycondensation reactions.[21-25] However, the mechanical properties are significantly lower than those of cement due to the presence of numerous low-reactivity crystalline minerals.[17]

When RCP is thermally activated at 600 to 800°C, several hydration products, including calcium hydroxide ($Ca(OH)_2$ [CH]), calcium-silicate-hydrate (C-S-H), ettringite (AFt), and calcite, are sequentially decomposed, along with a change in quartz structure.[27] New active components, such as calcium oxide (CaO) and calcium silicate, are generated,[28] which can re-react with $H_2O$ and form new hydration products. After thermal activation at 800 to 1200°C, active metakaolin and amorphous components (active $SiO_2$) are generated in RCP.[29] Zhang et al.[30] found that the strength activity index of RCP increased when heat treatment temperature increased from 600 to 800°C. Kim and Kim[31] also suggested that the proper temperature required to improve the reactivity of waste cementitious powder was 600 to 800°C. Chen et al.[32] found that recycled fine powder, which was activated by thermally activated systems at 700°C, exhibited excellent mechanical properties. Hence,

---

*ACI Materials Journal*, V. 123, No. 2, March 2026.
MS No. M-2025-057.R4, doi: 10.14359/51749295, received August 21, 2025, and reviewed under Institute publication policies. Pertinent discussion including author's closure, if any, will be published ten months from this journal's date if the discussion is received within four months of the paper's print publication.

**Table 1—Chemical composition of RCP and cement, wt. %**

| Composition | CaO | $Al_2O_3$ | $SiO_2$ | MgO | $Fe_2O_3$ | $Na_2O$ | $TiO_2$ | $SO_3$ | Loss |
|---|---|---|---|---|---|---|---|---|---|
| RCP | 40.48 | 7.6 | 42.56 | 2.4 | 4.4 | 0.38 | 0.76 | — | 1.42 |
| Cement | 63.71 | 5.0 | 20.35 | 1.37 | 3.3 | 0.39 | — | 2.48 | 2.6 |

thermal activation in the range of 600 to 800°C may have a significant impact on the activation of RCP.

As a common grinding aid in cement mills, alkanolamine can significantly reduce energy consumption and enhance cement properties. When alkanolamine is used as a cement chemical additive, it can change the hydration and hardening properties of the cement bond.[33] Moreover, the complexation of alkanolamine with $Ca^{2+}$, $Al^{3+}$, and $Fe^{3+}$ in portland cement contributes to the accelerated dissolution and hydration of cement minerals.[34] As a new type of alkanolamine, diethanolisopropanolamine (DEIPA), has a strong complexation capability with $Fe^{3+}$ and $Al^{3+}$ ions,[35,36] which may result in accelerating $C_4AF$ dissolution[37] and hydration reaction.[38] Furthermore, the presence of DEIPA may enhance hydration of ferrite and lead to the formation of denser hydration products.[39] Besides, DEIPA can promote the formation of the AFt phase, the transformation of AFt into monosulfoaluminate hydrates (AFm) phase, and the formation of microcrystalline portlandite (CH) at early age.[40] DEIPA may also accelerate alite hydration and reduce the pore size and porosity of hardened pastes.[38] Therefore, the application of DEIPA in the activation of RCP may be beneficial to the hydration and improve the chemical effect of the pastes.

Recently, many scholars have focused on the effect of synergistic activation modes on the properties of RCP.[19,25,28,30] Xu et al.[41] found that the compressive strength of geopolymers prepared by RCP treated with mechanical and thermal activation can be enhanced to varying degrees. Zhang et al.[25] found that both calcination and carbonation pretreatment enhanced the properties of RCP, thereby improving the mechanical properties of recycled alkali-activated cement. Zhang et al.[30] suggested that the most feasible and effective activation method of RCP is thermal activation, followed by chemical activation and grinding activation. However, Sasui et al.[27] found that the highest strength obtained after alkali activation of thermally activated RCP was less than 10 MPa.

CH, as an inorganic material, has always played a significant role in the pozzolanic reaction of supplementary cementitious materials. Generally, the products of hydration reaction between RCP-cement (RCP-C) and CH are mainly C-S-H and calcium aluminate silicate hydrate (C-A-S-H) gels, which are similar to those of OPC.[32] However, the hydration of active compositions in supplementary cementitious material-cement systems is influenced by many factors, such as temperature, particle size, sulfates, alkalies, and so on.[42-44] This hydration is also significantly influenced by the availability of CH, which originates from the hydration of tricalcium silicate.[45,46] There are numerous works on the hydration process and the pozzolanic reactivity of RCP in cement systems.[47,48] However, there may be a major limitation: all of these works focused on hydration with limited availability of CH in the RCP-C system.[46] Actually, the content of RCP as a supplementary cementitious material has been 30 wt. %, or even exceeded 40 wt. %,[9,12,16,21] resulting in a lack of sufficient CH to react with all available pozzolans.[44] So, it is necessary to study the addition of CH, which may lead to a complete understanding of RCP-C systems.

The novelty of this work is to investigate the synergistic effect of thermal-inorganic-organic activation on the strength development of RCP-C pastes. Moreover, microstructure changes and the enhancement mechanism of RCP-C pastes were analyzed using X-ray diffraction (XRD), Fourier-transform infrared spectroscopy (FT-IR), thermogravimetric (TG) analysis, and scanning electron microscopy (SEM). This study proposes a useful and effective synergistic activation mode for the high-value use of RCP.

## RESEARCH SIGNIFICANCE

The amount of RCP experiences an exponential increase due to the construction and demolition activities associated with buildings and infrastructure. To increase the use of RCP, this study provides a novel route to enhance its reactivity.

## MATERIALS AND EXPERIMENTS

### Materials

The raw materials for preparing RCP were collected from waste concrete during the demolition of a reinforced concrete building and ground using a ball mill for 30 minutes. The resulting powder exhibited a density and Blaine fineness of 2.42 g/cm$^3$ and 378 m$^2$/kg, which were obtained by the displacement method and nitrogen adsorption method, respectively. Moreover, P·I 52.5 portland cement was used following GB 175-2020. The chemical compositions of RCP and P·I 52.5 portland cement were determined by X-ray fluorescence (XRF) and are listed in Table 1. The particle-size distributions of RCP and portland cement, which were determined by a laser particle-size analyzer, are shown in Fig. 1 and 2. Analytical-grade CH purchased was used as the inorganic activator. Commercial-grade DEIPA was used as the organic activator.

### Sample preparation

The activation diagram of RCP is shown in Fig. 3, illustrating thermal, inorganic, organic, and thermal-inorganic-organic synergistic activation. Inorganic and organic activators were added to water in advance to form a solution. RCP replaced 40% of the cement with equal mass content. The water-binder ratio of the RCP-C pastes was set at 0.35:1. The RCP mixture proportions are listed in Table 2. The paste containing unactivated RCP was named as the control group. The contents of CH were set to 0.5, 1, 1.5, 2, and 2.5% of the RCP content, and those of DEIPA were 0.02, 0.03, 0.04, 0.05, and 0.06%. For thermal activation, the RCP was placed in a muffle furnace for calcination in advance. The target temperatures (600, 700, and 800°C) were achieved at a heating rate of 10°C/min, and each temperature was maintained for 30 minutes to fully activate the RCP. For synergistic activation, the RCP was first calcined at 700°C for 30 minutes, followed by the addition of 1% of CH and 0.04% of DEIPA successively. A 20 x 20 x 80 mm paste test piece was fabricated. The samples were removed from the mold after 24 hours and placed in a standard curing box with a relative humidity of 98% and temperature of 20 ± 2°C. Strength testing at 1, 3, and 28 days was performed according to GB/T 17671-2021 and measured using a microcomputer-controlled universal testing machine. Each sample consisted of three strength test pieces, and the average results were obtained from at least three samples for compressive strength and six samples for flexural strength.

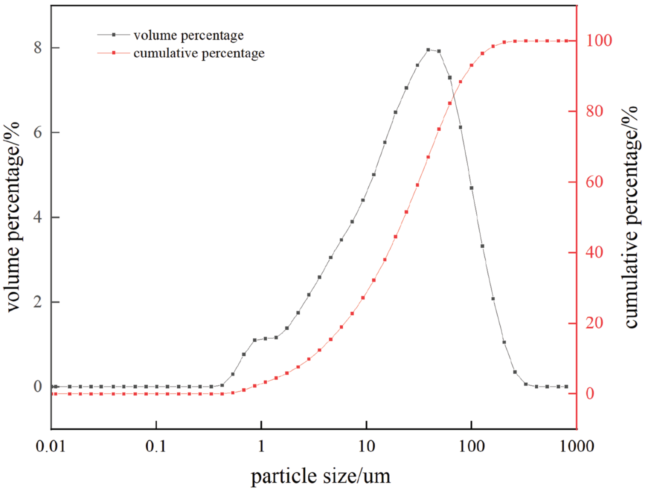

*Fig. 1—Particle-size distribution of RCP.*

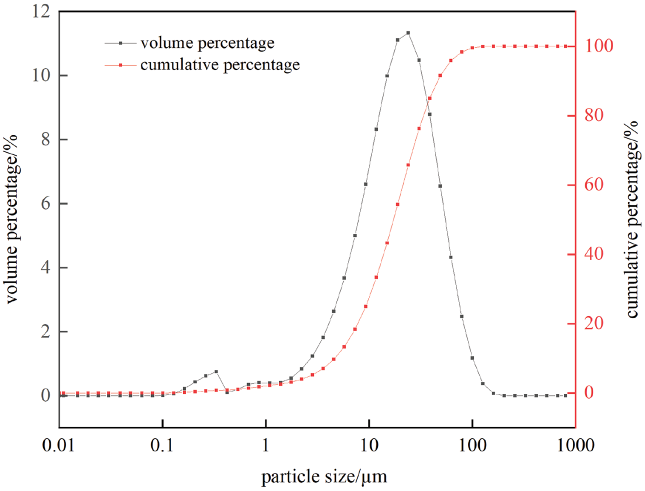

*Fig. 2—Particle-size distribution of portland cement.*

### Characterization

XRD was used to identify mineral compositions (an X-ray diffractometer with Cu Kα radiation and $2\theta$ from 5 to 75 degrees).

FT-IR spectra were obtained on a Fourier-transform infrared spectroscope with a resolution of 4 cm$^{-1}$ and scanned within the range of 400 to 4000 cm$^{-1}$.

The TG curves of paste were detected by a simultaneous measuring instrument in a nitrogen atmosphere from 40 to 1000°C with a temperature rate of 10°C/min.

The morphology analysis was observed after compressive testing with SEM. Before experimenting, all the samples were sputter-coated with gold.

## RESULTS AND DISCUSSION

### Strength development

*Thermal activation*—Figure 4 shows the strength development of the RCP-C pastes activated at different temperatures. The 3- and 28-day compressive strengths of thermally activated pastes, as shown in Fig. 4(a), were higher than those of the control sample. For instance, the 3- and 28-day compressive strength of thermally activated pastes at 800°C was 46.7 and 58.2 MPa, respectively. This was 20.4% and 29.3% higher than that of the control sample. The decrease in the 1-day compressive strength of the thermally activated paste at 800°C may be attributed to the loss of free water and part of the bound water in RCP, leading to a delay in the initial hydration of RCP-C pastes.[49] However, it should be noted that there was no obvious improvement in flexural strength at any age for thermally activated RCP-C paste compared to the control sample (Fig. 4(b)). This result suggests that thermal activation may greatly improve the compressive strength of RCP-C pastes while showing no significant enhancement in the flexural strength.

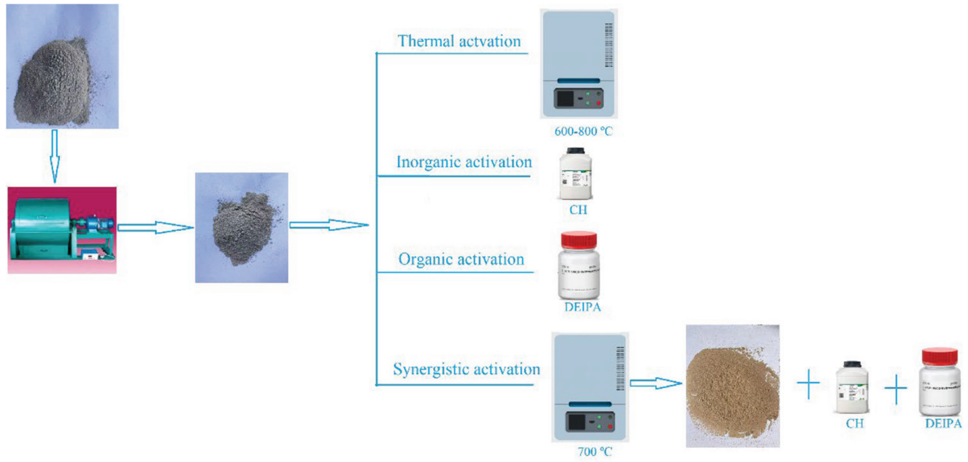

*Fig. 3—Schematic of different activation processes.*

## Table 2—RCP mixture proportions

| Sample | Cement, g | RCP, g | CH, % | DEIPA, % |
|---|---|---|---|---|
| P1 (control) | 300 | 200 (unactivated) | — | — |
| S1 | 300 | 200 (600°C) | — | — |
| S2 | 300 | 200 (700°C) | — | — |
| S3 | 300 | 200 (800°C) | — | — |
| S4 | 300 | 200 (700°C) | 0.5 | — |
| S5 | 300 | 200 (700°C) | 1.0 | — |
| S6 | 300 | 200 (700°C) | 1.5 | — |
| S7 | 300 | 200 (700°C) | 2.0 | — |
| S8 | 300 | 200 (700°C) | 2.5 | — |
| S9 | 300 | 200 (700°C) | — | 0.02 |
| S10 | 300 | 200 (700°C) | — | 0.03 |
| S11 | 300 | 200 (700°C) | — | 0.04 |
| S12 | 300 | 200 (700°C) | — | 0.05 |
| S13 (synergistic) | 300 | 200 (700°C) | 1.0 | 0.04 |

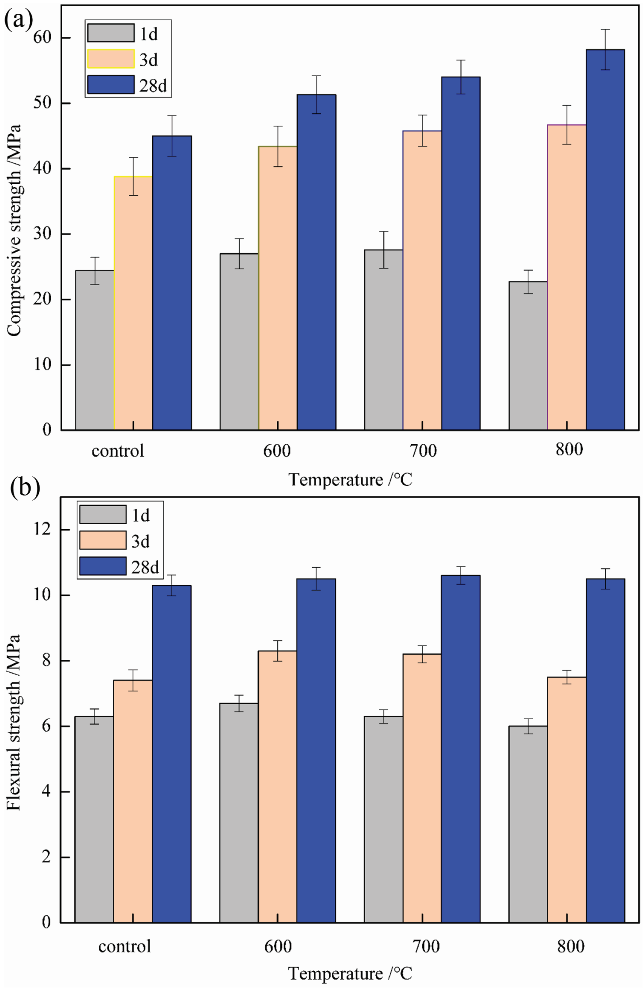

*Fig. 4—Impact of thermal activation on RCP-C pastes: (a) compressive strength; and (b) flexural strength.*

During the calcination process, C-S-H gel decomposed to form polycrystalline dicalcium silicate, including incompletely crystallized $\beta$-$C_2S$.[50] Moreover, calcite decomposed to form CaO. Besides, a certain RCP reactivity can be achieved owing to the formation of $\beta$-$C_2S$ and CaO during thermal activation,[51] which can both react with $H_2O$ and form hydration products. However, Chen et al.[32] determined that the decomposition of calcite at 600°C is incomplete, which may lead to weak reactivity. Besides, the 1- and 3-day flexural strengths of thermally activated samples at 800°C were close to the control sample. Therefore, it can be concluded that thermal activation of RCP at 700°C has significant potential for improving strength, particularly compressive strength.

*Inorganic activation*—The influence of CH content on the strength development of RCP-C pastes is shown in Fig. 5. The 1-, 3-, and 28-day compressive strengths of the control sample were 18.9, 31.6, and 56.3 MPa, respectively (Fig. 5(a)). The 1-day compressive strength of the 0.5 to 2.5% CH-activated sample was close to the control sample. The 3- and 28-day compressive strengths of the CH-activated sample increased slightly with the increase in the dosage of CH and then decreased. Furthermore, the highest 28-day strength (62.8 MPa) of the samples increased by 11.3% compared to the control sample. In addition, when the CH content was in the range of 0.5 to 1%, the 1-, 3-, and 28-day flexural strengths all increased slightly, but the increasing trend diminished thereafter (Fig. 5(b)). However, it is worth noting that the flexural strengths at all ages for RCP-C pastes with more than 1.5% CH were consistently lower than the control sample.

The previous results show that inorganic activator (CH) improved the later-stage (28-day) strength of the samples, and the early (1- and 3-day) strength development showed a poor activation effect. This could be attributed to the fact that CH activator can provide a certain amount of $OH^-$ ions to the liquid phase in the early stage of the samples.[32] The unreacted $Ca^{2+}$ and $OH^-$ ions would crystallize and precipitate on the surface and restrain the dissolution of RCP and cement grains.[52] Additionally, the addition of appropriate amounts of CH may benefit the formation of AFt.[53] However, excessive CH may be adsorbed onto the surfaces of unhydrated particles, inhibiting subsequent hydration processes in the

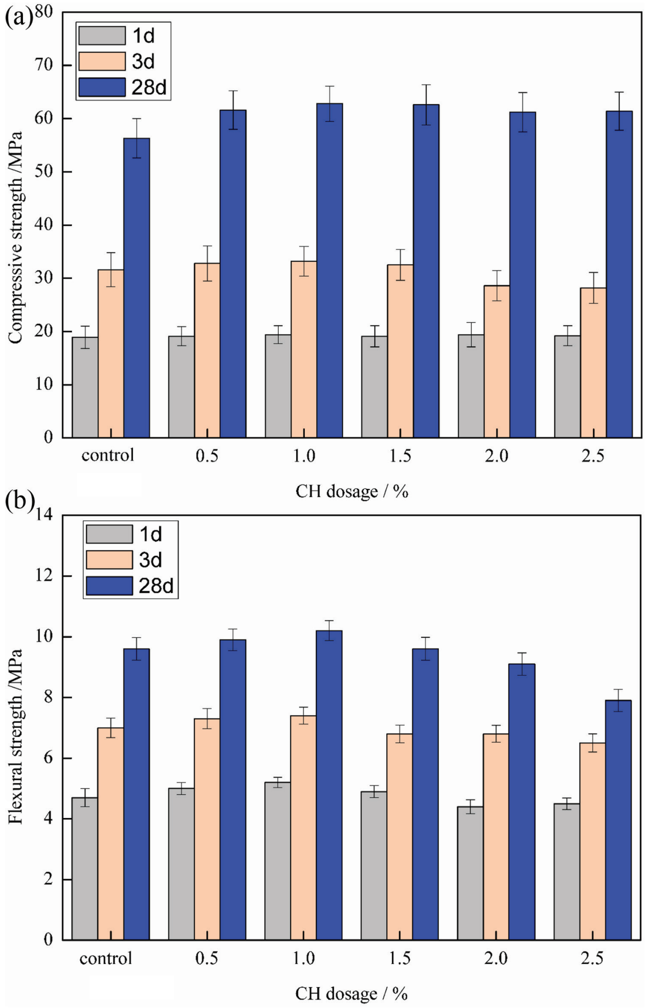

*Fig. 5—Influence of inorganic activator on RCP-C pastes: (a) compressive strength; and (b) flexural strength.*

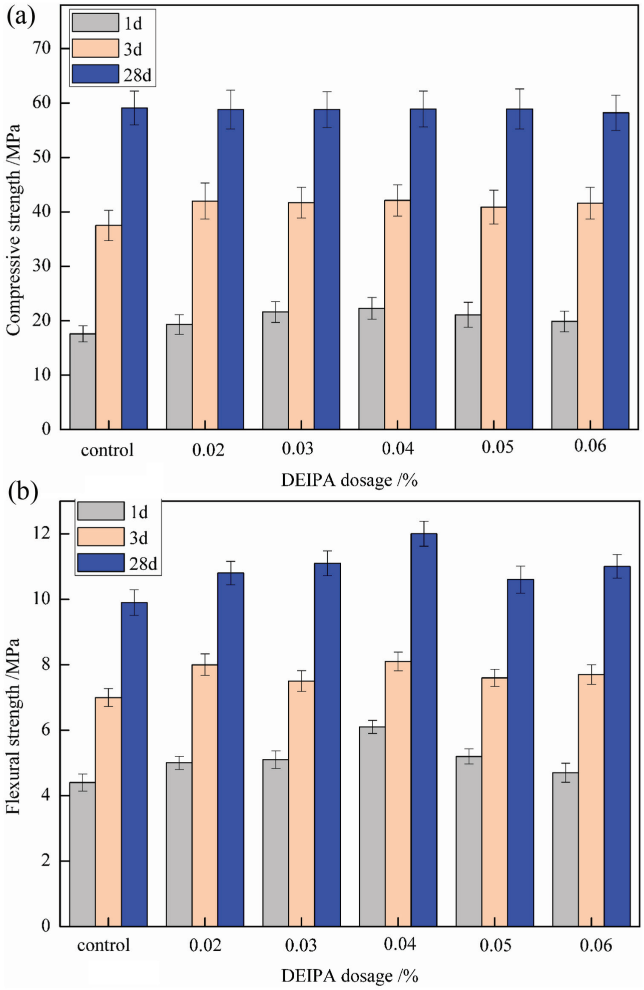

*Fig. 6—Influence of organic activator on RCP-C pastes: (a) compressive strength; and (b) flexural strength.*

system and leading to a reduction in strength. Besides, an excess of $OH^-$ ions in the liquid phase may hinder the hydration of $C_3S$, whose hydration products are C-S-H gel and CH.[45,46] Moreover, the pozzolanic reaction between calcium hydroxide and amorphous $SiO_2$, which originated from the fine RCP, was slow.[46] After the transformation of AFt to AFm, the strength of samples reduced, which may be attributed to the fact that AFm could not compensate for the structural defects caused by the expansion of AFt.[54]

*Organic activation*—Figure 6 illustrates the compressive and flexural strengths of DEIPA-activated RCP-C pastes at different ages. On the first day, the compressive strength increased with the increase in DEIPA content, but the increasing trend reduced thereafter (Fig. 6(a)). For instance, the compressive strength of 0.04% DEIPA-activated RCP-C paste was 22.3 MPa, which was 26.8% higher than that of the control sample. On the third day, a similar enhancement was observed, but this enhancement weakened over time. The increased compressive strength could be related to the complexation effect of DEIPA on the accelerating aluminates and silicates hydration to form a much denser microstructure.[55,56] It has been reported that a cement-fly ash-limestone ternary blend with the activation of DEIPA exhibited higher 28-day compressive strength than the reference sample.[50] However, ignoring the influence of error, the 28-day compressive strength of DEIPA-activated RCP-C paste was close to the control sample in this study. On one hand, the AFm, which is thermodynamically stable and coated on the surface of unhydrated particles, will reduce the subsequent dissolution and hydration of the particles. On the other hand, the presence of DEIPA may affect the formation of $Ca(OH)_2$ and C-S-H gels. Therefore, ignoring the influence of error, the 28-day compressive strength of DEIPA-activated RCP-C pastes was close to the control sample in this study, indicating that DEIPA activation may not affect the later compressive strength development of RCP-C paste. It can be concluded that DEIPA contributed to higher early compressive strength.

It was interesting to observe that the appropriate content of DEIPA can obviously enhance the flexural strength of RCP-C pastes at all ages (Fig. 6(b)). For instance, the 1-, 3-, and 28-day flexural strength of 0.04% DEIPA-activated RCP-C paste was 6.1, 8.1, and 12.0 MPa, respectively. This was 40.3%, 17.1%, and 21.4% higher than that of the control RCP-C paste. This improvement may be related to accelerating hydration of ferrite ($C_4AF$),[37] which contributes to flexural strength development in cement-based materials. It has been reported that the flexural strength of cement using DEIPA as the grinding aid decreased.[57] However, a small amount of DEIPA significantly enhances the flexural strength of RCP-C paste in this work.

*Thermal-inorganic-organic synergistic activation*—Figure 7 illustrates the influence of various activation modes on the strength development of RCP-C pastes. Synergistic activation demonstrated superior promotion from 1 to 28 days. In detail, the 1-, 3-, and 28-day compressive strengths of the synergia-activated group improved by 41.5%, 26.8%, and 25.6% compared to the unactivated control group, respectively (Fig. 7(a)). Furthermore, the 1-, 3-, and 28-day flexural strengths of the synergia-activated group improved by 26.9%, 18.6%, and 16.3% compared to the control group (Fig. 7(b)). Moreover, the strength of the synergia-activated group was also higher than that of the other three activated groups. The improvement demonstrated that the reactivity of RCP-C was greatly enhanced by the synergistic activation mode of inorganic, organic, and thermal activation. A probable explanation for this is that first, the hydration products in RCP decomposed under thermal activation, which could enhance the content of reactive components, including CaO, $SiO_2$, and $Al_2O_3$, and expedite the breakdown of Si-O and Al-O bonds.[27,28,31,32] Therefore, a portion of unactive $SiO_2$ may transform into metastable $SiO_2$.[32] Second, it has been reported that alkanolamine accelerated the dissolution of cement particles due to its high surface activity, which could accelerate the silicate reaction.[58] The presence and complexation of DEIPA could improve the alkalinity of the slurry, prolong the hydration process, and enhance the compressive strength of pastes.[40,57] DEIPA showed an excellent accelerated effect in the early and late ages of the paste, likely due to its high steric hindrance, resulting in a higher hydration rate of $C_3S$ and $C_2S$ in the later stages than in the reference paste.[39] Meanwhile, metastable $SiO_2$ may participate in the hydration reaction, forming more C-S-H gels and accelerating the formation of AFt and transformation to AFm.[51,59] Lastly, CH could ensure the alkalinity in the pores, reduce the decomposition of C-S-H gels,[59] and enhance long-term strength due to its cementation effect.[60]

It can be concluded that DEIPA contributes to higher early strength, while calcium hydroxide contributes to higher later strength of the RCP-C pastes. Thermal activation contributes to the development of compressive strength at all stages.

## XRD analysis

Figure 8 shows the XRD patterns of the control, inorganic, organic, thermally, and synergistic activated RCP-C pastes. The main crystalline hydrates identified were portlandite, calcite, unhydrated tricalcium silicate ($C_3S$) and dicalcium silicate ($C_2S$), AFt and AFm (Fig. 9), and quartz ($SiO_2$). Low reactivity of RCP hindered the phase transformations of monocarboaluminate (Mc) and hemicarboaluminate (Hc).

After 1 day (Fig. 8(a)), the inorganic activator may restrain the hydration of $C_3S$, which may be attributed to the increase in the concentration of $Ca^{2+}$ and $OH^-$ ions. In contrast, the organic activator could accelerate the hydration of belite and alite,[38] contributing to the decrease in peak intensity of $C_2S$ and $C_3S$. Additionally, DEIPA activation may facilitate the generation of AFt and accelerate the transformation of AFt into AFm.[56,62] The intensity of quartz in the thermally activated sample was lower than in the organic activated sample, which may be attributed to the fact that a portion of stabilized $SiO_2$ converted to reactive $SiO_2$ during this process. The peak intensity of $SiO_2$ in the pattern of synergistic activated paste was lower than that of the other three pastes. This decrease may be attributed to the depolymerization of the silica tetrahedron under thermal activation, facilitating the reaction between alkalies and metastable $SiO_2$.[33]

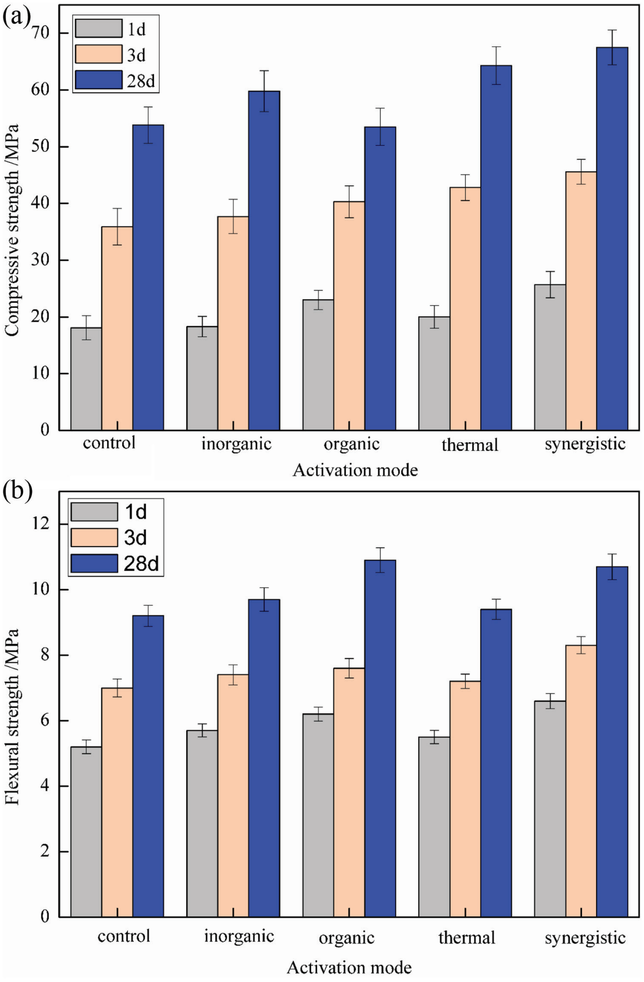

*Fig. 7—Comparative study for different activation modes: (a) compressive strength; and (b) flexural strength.*

After 28 days, the peak intensity of portlandite and $SiO_2$ in the activated samples decreased (Fig. 8(b)). This change indicated that external CH could facilitate the pozzolanic reaction of reactive $SiO_2$ in RCP, contributing to the formation of additional C-S-H gels. Additionally, the presence of DEIPA may restrain the nucleation of CH crystals, leading to a decrease in CH peak intensity. Moreover, the saturability of $Ca^{2+}$ ions in the pore solution decreased, probably due to the chelation of DEIPA,[35] as well as hindering the nucleation and growth of CH.[62]

## FT-IR analysis

The FT-IR spectra of the control, inorganic, organic, thermally, and synergistic activated RCP-C pastes are illustrated in Fig. 10. The band at 3645 $cm^{-1}$ was related to the stretching vibration of O-H from CH, with the band position

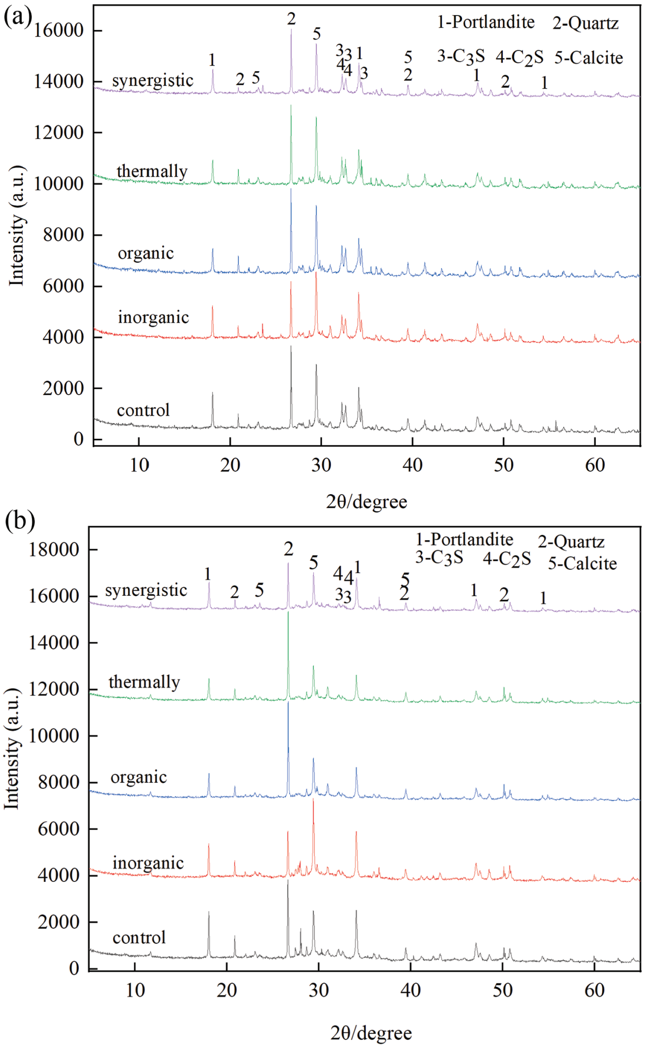

*Fig. 8—XRD patterns of different groups: (a) on first day; and (b) on 28th day.*

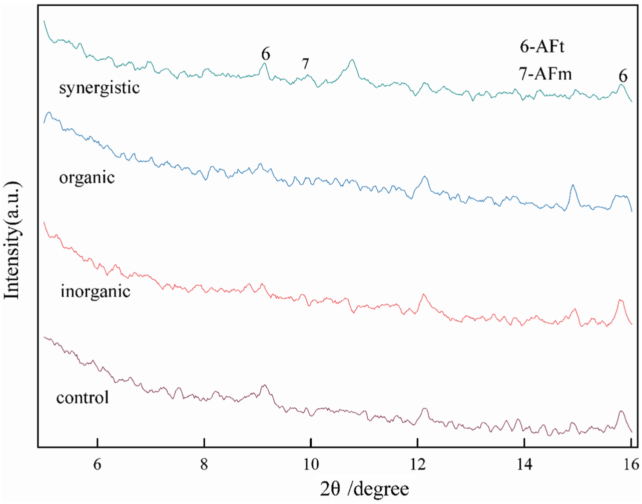

*Fig. 9—XRD patterns of control, inorganic, organic, and synergistic activated RCP-C pastes for low angles.*

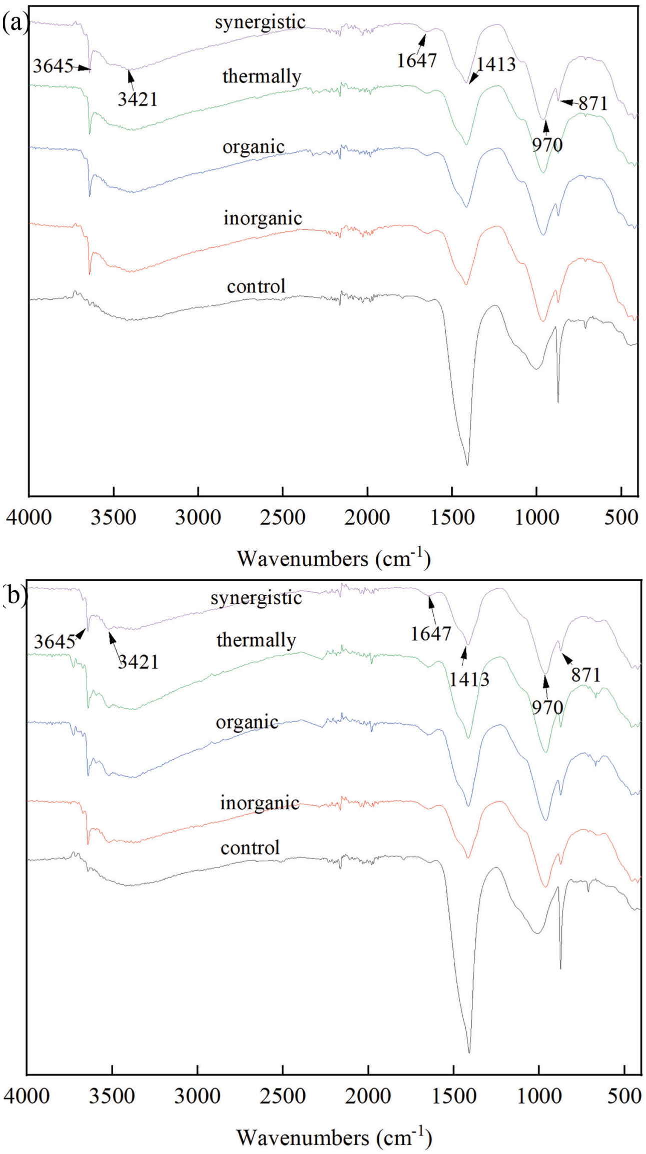

*Fig. 10—FT-IR spectra of different groups: (a) on first day; and (b) on 28th day.*

approaching 3639 $cm^{-1}$, as reported by Li et al.[57] The peaks at 3421 and 1647 $cm^{-1}$ may correspond to the tensile vibration of H-OH and bending vibration of O-H, respectively, which were related to the structural and interlayer water of chemical phases.[63] The absorption peak at 996 $cm^{-1}$ could be related to Si-O stretching vibrations of C-S-H gel,[56] which enhanced as hydration continued to 28 days. This peak shifted to 970 $cm^{-1}$ in the FT-IR curve of the synergistic sample, suggesting an increase in the depolymerization of Si-O-Si(Al). The absorption peaks at 875 and 1409 $cm^{-1}$ could be related to the O-C-O asymmetric stretching vibration of $CO_3^{2-}$ in hydration products and calcite ($CaCO_3$),[64,65] which may be due to the carbonation of CH and other hydration products.

According to other researchers' reports,[56,66,67] C-S-H gel mainly appears from 800 to 1200 $cm^{-1}$, including 850 to 900 $cm^{-1}$, 970 to 1040 $cm^{-1}$, approximately 1100 $cm^{-1}$, and approximately 1150 $cm^{-1}$. With the increase in wavenumber, C-S-H gel exhibits decreased Ca/Si ratios from calcium-rich gel to silica-rich gel.[68] It has been reported that the addition of DEIPA could contribute to forming less silica-rich gel.[62] However, synergistic activation may contribute to forming a calcium-rich gel, which may be attributed to the promotion

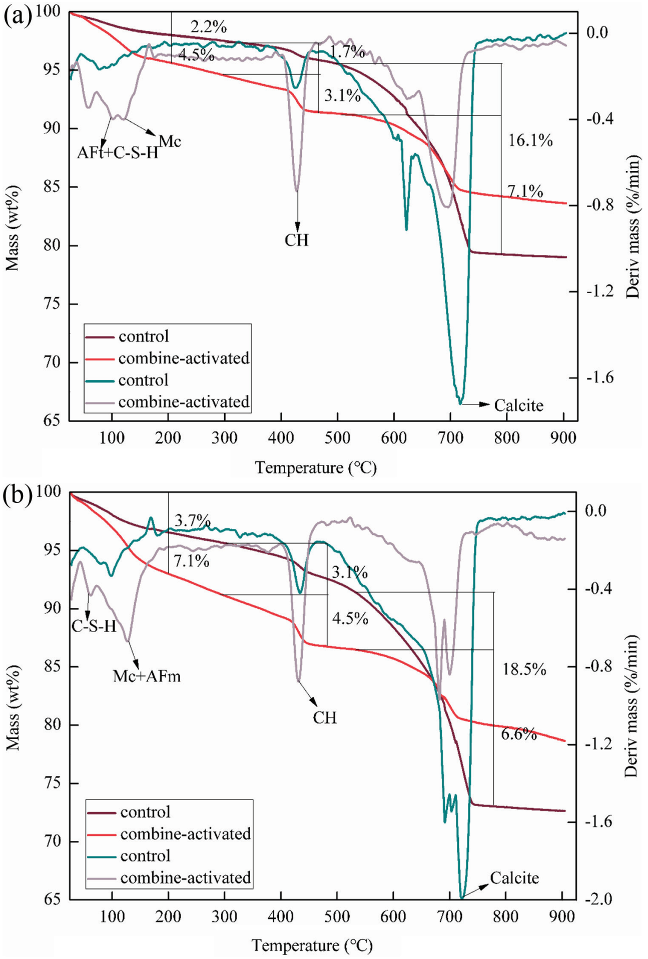

*Fig. 11—TG curve of synergistic group: (a) on first day; and (b) on 28th day.*

effect of DEIPA on dissolution of the system[62] and more $Ca^{2+}$ ions released from the additional CH. The FT-IR analysis demonstrates that synergistic activation could accelerate the hydration of silicate phases.

## TG analysis

Figure 11 presents the thermal analyses of synergia-activated pastes. The endothermic peak at approximately 100°C referred to the decomposition of AFt or C-S-H gel.[35] Meanwhile, the endothermal peak at approximately 130°C referred to the decomposition of Mc.[36] Wang et al.[55] also reported that this endothermal peak represented the decomposition of carboaluminates in ternary cement containing fly ash and limestone. Besides, the endothermic peaks at 430 and 690°C referred to the decomposition of CH and calcite, respectively. According to Fig. 11(a), there were no obvious endothermic peaks for AFm or aluminate other than AFt forms at 1 day. At 28 days, the endothermic peak of approximately 127°C (Fig. 11(b)) enhanced as hydration continued, with more Mc and AFm formed, as concluded by XRD results. Thus, the results validated that synergistic activation may be beneficial to the formation of AFm and Mc.

The corresponding mass loss observed in the TG curve at 1 day for the combine-activated (control) group was 4.5% (2.2%), 3.1% (1.7%), and 7.1% (16.1%), respectively. Additionally, the mass loss at 28 days for the combine-activated (control) group was 7.1% (3.7%), 4.5% (3.1%), and 6.6% (18.5), respectively. Obviously, the first and second corresponding mass losses in the TG curve of the combine-activated group at 1 and 28 days were higher than those of the control group, indicating that the hydration process of the RCP-C group was accelerated by combination activation. Meanwhile, the mass loss in the TG curve of the combine-activated group at 1 and 28 days was lower than that of the control group, which demonstrated that the combine-activated group formed a denser microstructure and facilitated resistance to carbonization.

## SEM morphology

The SEM images, which were applied to visualize the microstructures of the hydration products activated in different modes on the first and 28th days, are presented in Fig. 12 and 13, respectively. On the first day, the microstructures of these four groups all exhibited low density, with a certain amount of micropores and voids, leading to a low strength. Additionally, the microstructure of the control group showed a small number of C-S-H gels and AFt crystals, as well as several cracks (Fig. 12(a)). As seen from the images, the microstructures of the hydration products activated by inorganic, organic, and synergistic activation exhibited different morphologies compared to those of the control group. For example, the microstructure of the hydration products in the CH-activated group presented many tetragonum portlandites, with several anchor-plate C-S-H and needle-like AFt (Fig. 12(b)). Meanwhile, the amount of C-S-H was inferior to that of the control group, which may be attributed to the restriction effect of excess CH for the hydration of $C_3S$. The needle-like AFt crystals in the DEIPA-activated group almost disappeared and were replaced by a large number of anchor-plate C-S-H and tetragonum CH (Fig. 12(c)). DEIPA activation not only accelerated the hydration of $C_3A$ and $C_4AF$ but also facilitated the complexation of $Ca^{2+}$ ions, resulting in a low supersaturation of calcium hydroxide.[40] Therefore, it was difficult for CH to form an ordered hexagonal plate shape. The microstructure of the hydration products in the synergia-activated group exhibited large amounts of anchor-plate C-S-H, continuous C-S-H gels (Fig. 12(d)), and hexagonal-plate CH (Fig. 14). These hydration products formed a denser microstructure, which may explain the superior strength of the group compared to other groups.

On the 28th day, the microstructure of the hydration products in the control group exhibited several large-sized prismatic belts of CH and more C-S-H gels (Fig. 13(a)), which may contribute to the formation of a dense microstructure. However, there are several cracks in the microstructure, resulting in low strength. The morphology of the CH-activated group showed significant quantities of well-crystallized prism CH, many continuous C-S-H gels, and several tufted AFm crystals (Fig. 13(b)). The microstructure of the hydration products in the DEIPA-activated group exhibited a large number of C-S-H gels, as well as a small amount of irregular flake-shaped CH and AFm (Fig. 13(c)). As concluded by the XRD, FT-IR, and TG results, the hydration products of the synergia-activated group mainly consisted of C-S-H gels,

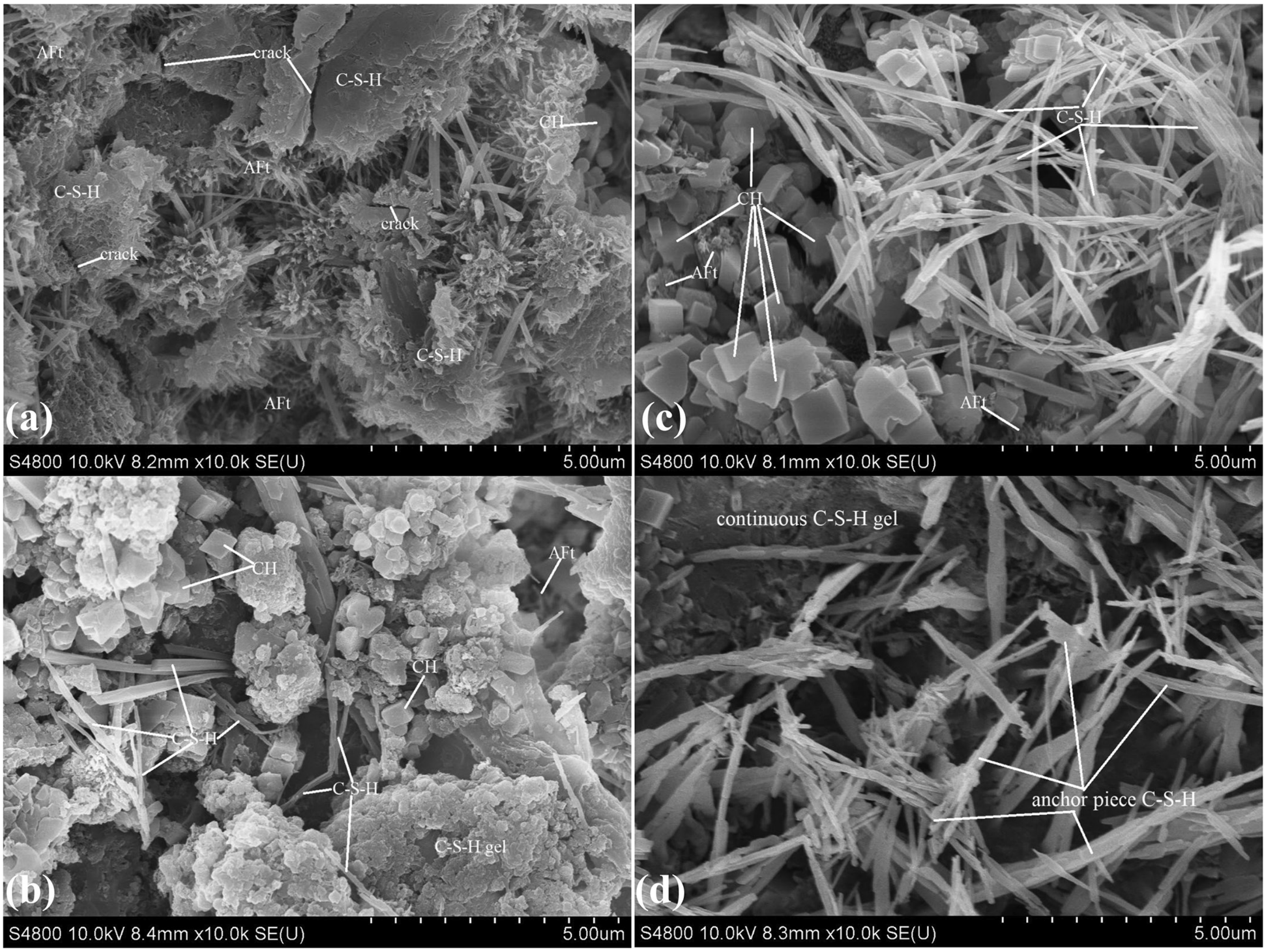

*Fig. 12—SEM images on first day: (a) hardened control group; (b) hardened inorganic group; (c) hardened organic group; and (d) hardened synergistic group.*

portlandites, CH, and AFm. However, the morphology of the synergia-activated group only exhibited a mass of C-S-H gels (Fig. 13(d)). Additionally, the morphology showed a highly dense microstructure, with minimal presence of micropores, which may be attributed to the filling effect of hydration products and partition effect of AFm with a steel-frame structure. Besides, porosity and pore size and number were significantly decreased for this group compared to the other three groups, which resulted in the increased strength of the former compared to the latter.

## CONCLUSIONS

For further enhancement of the reactivity of recycled concrete powder (RCP), herein, the strength development of the thermal, inorganic, organic, and synergistic activation of RCP-cement (RCP-C) pastes and their microstructure were investigated through strength tests, X-ray diffraction (XRD), Fourier-transform infrared spectroscopy (FT-IR), thermogravimetric (TG) analysis, and scanning electron microscopy (SEM) of paste. This study holds crucial theoretical and practical significance, as it is feasible to enhance the high-value use of RCP as a supplementary cementitious material by a synergistic activation route. The following conclusions can be drawn:

1. Thermal activation may greatly improve the compressive strength of RCP-C pastes, while showing inconspicuous enhancement in the flexural strength. The 3- and 28-day compressive strengths of the thermally activated group increased by 20.4% and 29.3%, respectively, compared to the control group.

2. Inorganic (calcium hydroxide [CH]) activation may contribute slightly to enhancing the later strength of RCP-C pastes. The 28-day compressive strength of the 1% CH-activated group was 62.6 MPa, which was 11.2% higher than that of the control group.

3. Organic (diethanolisopropanolamine [DEIPA]) activation can contribute to higher early compressive and flexural strengths. The 1-day compressive strength of the 0.04% DEIPA-activated group was 22.3 MPa, which represented an increase of 26.7% compared to the control group, while the flexural strength increased to 40.3%.

4. The effect of synergistic activation on the strength development of RCP-C pastes was superior to single inorganic, organic, and thermal activation. Furthermore, the synergistic activation could contribute to the compressive strength development at all stages. For example, the 1-, 3-, and 28-day compressive strengths were 42%, 27.02%, and 25.46% higher than those of the control group, respectively.

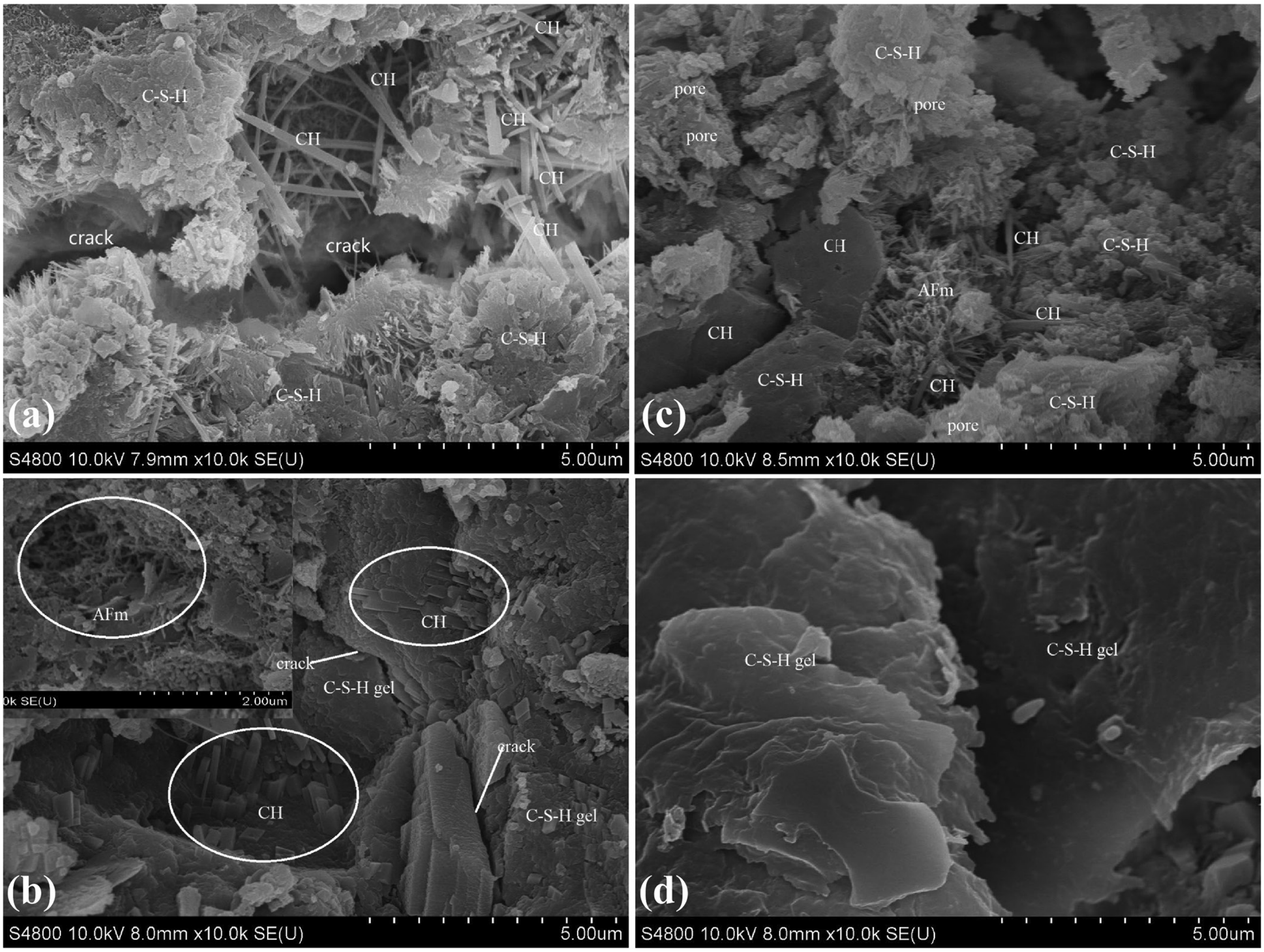

*Fig. 13—SEM images on 28th day: (a) hardened control group; (b) hardened inorganic group; (c) hardened organic group; and (d) hardened synergistic group.*

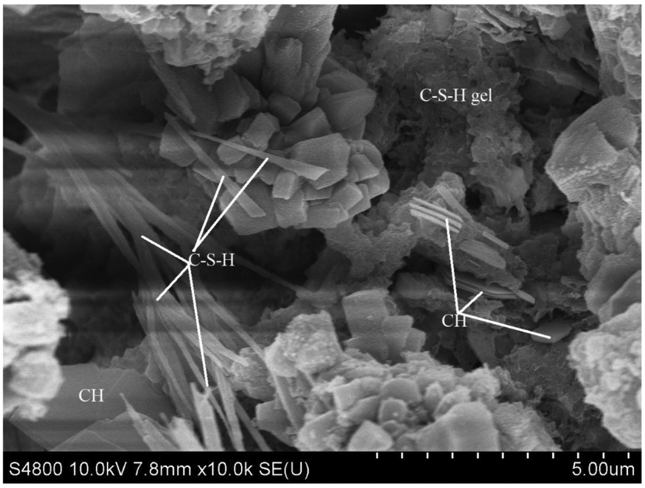

*Fig. 14—Supporting microstructure image of hydration products in synergia-activated group.*

5. The enhancement mechanism may be attributed to increasing the content of active compositions and breaking Si-O and Al-O bonds, reducing the decomposition of calcium-silicate-hydrate (C-S-H) gels, and accelerating the formation of ettringite (AFt) and more C-S-H gels through thermal, inorganic, and organic activation, respectively.

## AUTHOR BIOS

**Shuiping Li** *is an Associate Professor at Yangzhou University, Yangzhou, Jiangsu, China. He received his BS, MS, and PhD in materials science and engineering from Yancheng Institute of Technology, Yancheng, Jiangsu, China; Nanjing Tech University, Nanjing, Jiangsu, China; and Nanjing University of Science and Technology, Nanjing, Jiangsu, China, in 2006, 2009, and 2017, respectively. His research interests include low-carbon cementitious materials.*

**Chengxiao Yu** *is a Graduate Student at Yangzhou University. He received his BS in civil engineering from Changshu Institute of Technology, Suzhou, Jiangsu, China, in 2023. His research interests include the activation and application of recycled concrete powder.*

**Jincheng Jiang** *is a Graduate Student at Yangzhou University. He received his BS in civil engineering from Changshu Institute of Technology in 2023. His research interests include the activation and application of recycled concrete powder.*

**Bin Yuan** *is a Graduate Student at Yangzhou University. He received his BS in civil engineering from Liaoning Petrochemical University, Fushun, Liaoning, China, in 2022. His research interests include the activation and application of recycled concrete powder.*

**Jian Cheng** *is a Graduate Student at Yangzhou University. He received his BS in civil engineering from the University of South China, Hengyang, Hunan, China, in 2021. His research interests include the activation and application of recycled concrete powder.*

**Qing Lin** *is an Associate Professor at Jinling Institute of Technology, Nanjing, Jiangsu, China. He received his BS and PhD in materials science and engineering from Yancheng Institute of Technology and Nanjing Tech University in 2006 and 2011, respectively. His research interests include green building materials and biomaterials.*

## DATA AVAILABILITY STATEMENT

All data, models, or code that support the findings of this study are available from the corresponding author upon reasonable request.

## ACKNOWLEDGMENTS

This study was funded by Yangzhou Government-Yangzhou University Cooperative Platform Project for Science and Technology Innovation (YZ2020262).

## REFERENCES

1. Yao, Y.; Liu, C.; Liu, H.; Zhang, W.; and Hu, T., "Deterioration Mechanism Understanding of Recycled Powder Concrete Under Coupled Sulfate Attack and Freeze–Thaw Cycles," *Construction and Building Materials*, V. 388, 2023, p. 131718. doi: 10.1016/j.conbuildmat.2023.131718

2. Barcelo, L.; Kline, J.; Walenta, G.; and Gartner, E., "Cement and Carbon Emissions," *Materials and Structures*, V. 47, No. 6, 2014, pp. 1055-1065. doi: 10.1617/s11527-013-0114-5

3. Benhelal, E.; Zahedi, G.; Shamsaei, E.; and Bahadori, A., "Global Strategies and Potentials to Curb $CO_2$ Emissions in Cement Industry," *Journal of Cleaner Production*, V. 51, 2013, pp. 142-161. doi: 10.1016/j.jclepro.2012.10.049

4. Wu, H.; Liang, C.; Zhang, Z.; Yao, P.; Wang, C.; and Ma, Z., "Utilizing Heat Treatment for Making Low-Quality Recycled Aggregate Into Enhanced Recycled Aggregate, Recycled Cement and Their Fully Recycled Concrete," *Construction and Building Materials*, V. 394, 2023, p. 132126. doi: 10.1016/j.conbuildmat.2023.132126

5. Aquino Rocha, J. H., and Toledo Filho, R. D., "The Utilization of Recycled Concrete Powder as Supplementary Cementitious Material in Cement-Based Materials: A Systematic Literature Review," *Journal of Building Engineering*, V. 76, 2023, p. 107319. doi: 10.1016/j.jobe.2023.107319

6. Dal Poggetto, G.; Fortunato, M.; Cardinale, A. M.; and Leonelli, C., "Thermal, Chemical and Mechanical Characterization of Recycled Corundum Powder in Metakaolin-Based Geopolymer Binder," *Applied Clay Science*, V. 237, 2023, p. 106875. doi: 10.1016/j.clay.2023.106875

7. Du, J.; Zhang, T.; Chen, P.; Guo, Y.; Zhan, B.; Wei, J.; and Yu, Q., "Phase Separation of Recycled Concrete Powder During Grinding and Consequent Influences on its Hydration Behaviors in Cement Paste," *Cement and Concrete Composites*, V. 142, 2023, p. 105203. doi: 10.1016/j.cemconcomp.2023.105203

8. Zhu, H.; Shen, Z.; Li, Z.; Zhao, Z.; Liang, S.; Yang, S.; Ruan, Z.; and Ding, Y., "Properties Study of Artificial Aggregate with High-Content Recycled Concrete Powder," *Journal of Building Engineering*, V. 78, 2023, p. 107697. doi: 10.1016/j.jobe.2023.107697

9. Bian, Y.; Li, Z.; Zhao, J.; and Wang, Y., "Synergistic Enhancement Effect of Recycled Fine Powder (RFP) Cement Paste and Carbonation on Recycled Aggregates Performances and its Mechanism," *Journal of Cleaner Production*, V. 344, 2022, p. 130848. doi: 10.1016/j.jclepro.2022.130848

10. Ma, Z.; Hu, R.; Yao, P.; and Wang, C., "Utilizing Heat-Mechanical Synergistic Treatment for Separating Concrete Waste into High-Quality Recycled Aggregate, Active Recycled Powder and New Concrete," *Journal of Building Engineering*, V. 68, 2023, p. 106161. doi: 10.1016/j.jobe.2023.106161

11. Shen, Z.; Zhu, H.; Zhao, Z.; Pang, S.; Li, Z.; Yang, S.; Cao, P.; and Lin, S., "High-Performance Artificial Aggregate Prepared with Recycled Concrete Powder and its Impact on Concrete Properties," *Construction and Building Materials*, V. 404, 2023, p. 133151. doi: 10.1016/j.conbuildmat.2023.133151

12. Li, J.; Zhan, B.; Gao, P.; Hu, L.; Qiao, M.; Sha, H.; and Yu, Q., "Effects of Recycled Concrete Powders on the Rheology, Setting and Early Age Strength of Cement Paste," *Construction and Building Materials*, V. 401, 2023, p. 132899. doi: 10.1016/j.conbuildmat.2023.132899

13. Wang, C.; Yu, Q.; Zhan, B.; Gao, P.; Guo, B.; Chu, Y.; Chen, Y.; and Bian, P., "Activity Quantification and Assessment of Recycled Concrete Powder Based on the Contributions of the Dilution Effect, Physical Effect and Chemical Effect," *Journal of Cleaner Production*, V. 442, 2024, p. 140918. doi: 10.1016/j.jclepro.2024.140918

14. Xiao, J.; Ma, Z.; Sui, T.; Akbarnezhad, A.; and Duan, Z., "Mechanical Properties of Concrete Mixed with Recycled Powder Produced from Construction and Demolition Waste," *Journal of Cleaner Production*, V. 188, 2018, pp. 720-731. doi: 10.1016/j.jclepro.2018.03.277

15. Kim, J., and Jang, H., "Closed-Loop Recycling of C&D Waste: Mechanical Properties of Concrete with the Repeatedly Recycled C&D Powder as Partial Cement Replacement," *Journal of Cleaner Production*, V. 343, 2022, p. 130977. doi: 10.1016/j.jclepro.2022.130977

16. Sun, C.; Chen, L.; Xiao, J.; Singh, A.; and Zeng, J., "Compound Utilization of Construction and Industrial Waste as Cementitious Recycled Powder in Mortar," *Resources, Conservation and Recycling*, V. 170, 2021, p. 105561. doi: 10.1016/j.resconrec.2021.105561

17. Cheng, X.; Liu, S.; Wen, J.; Feng, T.; Chen, G.; and Tan, Y., "Effects of Recycled Mortar Powder on the Properties and Microstructure of Magnesium Potassium Phosphate Cement," *Construction and Building Materials*, V. 403, 2023, p. 133144. doi: 10.1016/j.conbuildmat.2023.133144

18. Yao, T.; Tian, Q.; Zhang, M.; Qi, S.; Wang, C.; Ruan, M.; Xu, G.; and Cai, J., "Experimental Research on the Preparation and Properties of Formed Concrete Using Recycled Waste Concrete Powder," *Construction and Building Materials*, V. 407, 2023, p. 133370. doi: 10.1016/j.conbuildmat.2023.133370

19. Deng, X.; Guo, H.; Tan, H.; He, X.; Zheng, Z.; Su, Y.; and Yang, J., "An Accelerator Prepared from Waste Concrete Recycled Powder and its Effect on Hydration of Cement-Based Materials," *Construction and Building Materials*, V. 296, 2021, p. 123767. doi: 10.1016/j.conbuildmat.2021.123767

20. Sharma, A.; Singh, P.; and Kapoor, K., "Utilization of Recycled Fine Powder as an Activator in Fly Ash Based Geopolymer Mortar," *Construction and Building Materials*, V. 323, 2022, p. 126581. doi: 10.1016/j.conbuildmat.2022.126581

21. Liu, M.; Yang, D.; Chen, L.; Chen, G.; and Ma, Z., "Effect of Silicate Modulus and Alkali Content on the Microstructure and Macroscopic Properties of Alkali-Activated Recycled Powder Mortar," *Construction and Building Materials*, V. 397, 2023, p. 132365. doi: 10.1016/j.conbuildmat.2023.132365

22. Liu, Y.; Lu, C.; Zhang, H.; and Li, J., "Experimental Study on Chemical Activation of Recycled Powder as a Cementitious Material in Mine Paste Backfilling," *Environmental Engineering Research*, V. 21, No. 4, 2016, pp. 341-349. doi: 10.4491/eer.2015.129

23. Gong, Y. F.; Fang, Y. H.; Yan, Y. R.; and Chen, L. Q., "Investigation on Alkali Activated Recycled Cement Mortar Powder Cementitious Material," *Materials Research Innovations*, V. 18, 2014, pp. 784-787. doi: 10.1179/1432891714Z.000000000477

24. Xiao, Y.; Wu, Z.; and Gong, Y., "Study on Alkali-Activated Prefabricated Building Recycled Concrete Powder for Foamed Lightweight Soils," *Materials*, V. 16, No. 11, 2023, p. 4167. doi: 10.3390/ma16114167

25. Zhang, B.; Feng, Y.; Xie, J.; Dai, J.; Chen, W.; Xue, Z.; Li, L.; Li, Y.; and Li, J., "Effects of Pretreated Recycled Powder Substitution on Mechanical Properties and Microstructures of Alkali-Activated Cement," *Construction and Building Materials*, V. 406, 2023, p. 133360. doi: 10.1016/j.conbuildmat.2023.133360

26. Meng, T.; Dai, D.; Jia, Y.; Ying, K.; Meng, R.; and Hong, Y., "Comparative Study of Nanomaterials Activated Recycled Powders from Demolition and Decoration Wastes as Supplementary Cementitious Material," *Case Studies in Construction Materials*, V. 19, 2023, p. e02543. doi: 10.1016/j.cscm.2023.e02543

27. Sasui, S.; Kim, G.; van Riessen, A.; Alam, S. F.; Nam, J.; Ishak, S.; and Eu, H., "Influence of Elevated Temperature on Waste Concrete Powder and its Application in Alkali Activated Materials," *Journal of Cleaner Production*, V. 434, 2024, p. 140423. doi: 10.1016/j.jclepro.2023.140423

28. Yu, R., and Shui, Z., "Influence of Agglomeration of a Recycled Cement Additive on the Hydration and Microstructure Development of Cement Based Materials," *Construction and Building Materials*, V. 49, 2013, pp. 841-851. doi: 10.1016/j.conbuildmat.2013.09.004

29. He, Z.; Hu, R.; Ma, Z.; Liu, X.; Wang, C.; and Wu, H., "Reusing Thermoactivated Construction Waste Spoil as Sustainable Binder for Durable Concrete: Microstructure and Chloride Transport," *Construction and Building Materials*, V. 398, 2023, p. 132553. doi: 10.1016/j.conbuildmat.2023.132553

30. Zhang, D.; Zhang, S.; Huang, B.; Yang, Q.; and Li, J., "Comparison of Mechanical, Chemical, and Thermal Activation Methods on the Utilization of Recycled Concrete Powder from Construction and Demolition Waste," *Journal of Building Engineering*, V. 61, 2022, p. 105295. doi: 10.1016/j.jobe.2022.105295

31. Kim, J., and Kim, N., "Exploring the Role of Thermal Activation of Cement Exposed to the External Environment on the Improvement of Concrete Properties," *Journal of Materials Research and Technology*, V. 24, 2023, pp. 2868-2878. doi: 10.1016/j.jmrt.2023.03.195

32. Chen, L.; Wei, M.; Lei, N.; and Li, H., "Effect of Chemical-Thermal Activation on the Properties of Recycled Fine Powder Cementitious Materials," *Case Studies in Construction Materials*, V. 20, 2024, p. e02956. doi: 10.1016/j.cscm.2024.e02956

33. Chen, J.; Jia, J.; Zhu, M.; and Zhang, L., "Advances of Alkanolamine in Hydration of Portland Cement," *Materials Today Communications*, V. 37, 2023, p. 107129. doi: 10.1016/j.mtcomm.2023.107129

34. Zou, F.; Tan, H.; He, X.; Ma, B.; Deng, X.; Zhang, T.; Mei, J.; Liu, X.; and Qi, H., "Effect of Triisopropanolamine on Compressive Strength and Hydration of Steaming-Cured Cement-Fly Ash Paste," *Construction and Building Materials*, V. 192, 2018, pp. 836-845. doi: 10.1016/j.conbuildmat.2018.10.087

35. Huang, H.; Li, X.; and Shen, X., "Hydration of Ternary Cement in the Presence of Triisopropanolamine," *Construction and Building Materials*, V. 111, 2016, pp. 513-521. doi: 10.1016/j.conbuildmat.2016.02.079

36. Zhou, R.; Jin, B.; Wu, S.; Fan, S.; Hang, F.; and Chen, H., "Study on Sustainable Application of Low-Carbon Supersulfated Cement with Alkanolamines," *Sustainability*, V. 16, No. 7, 2024, p. 3008. doi: 10.3390/su16073008

37. Zhai, Q.; Kurumisawa, K.; and Moon, J., "A Comparative Study of Alkanolamines and Inorganic Additives on the Microstructure Development of Blast Furnace Slag Blended Cement at Low Curing Temperature," *Construction and Building Materials*, V. 408, 2023, p. 133779. doi: 10.1016/j.conbuildmat.2023.133779

38. Riding, K.; Silva, D. A.; and Scrivener, K., "Early Age Strength Enhancement of Blended Cement Systems by Cacl2 and Diethanol-Isopropanolamine," *Cement and Concrete Research*, V. 40, No. 6, 2010, pp. 935-946. doi: 10.1016/j.cemconres.2010.01.008

39. Lee, J.; Lothenbach, B.; and Moon, J., "Performance Improvement of Portland-Limestone Cement by Mechanochemical Activation," *Cement and Concrete Research*, V. 176, 2024, p. 107411. doi: 10.1016/j.cemconres.2023.107411

40. Ma, S.; Li, W.; Zhang, S.; Hu, Y.; and Shen, X., "Study on the Hydration and Microstructure of Portland Cement Containing Diethanol-Isopropanolamine," *Cement and Concrete Research*, V. 67, 2015, pp. 122-130. doi: 10.1016/j.cemconres.2014.09.002

41. Xu, J.; Kang, A.; Wu, Z.; Gong, Y.; and Xiao, P., "The Effect of Mechanical-Thermal Synergistic Activation on the Mechanical Properties and Microstructure of Recycled Powder Geopolymer," *Journal of Cleaner Production*, V. 327, 2021, p. 129477. doi: 10.1016/j.jclepro.2021.129477

42. Mishra, G.; Emmanuel, A. C.; and Bishnoi, S., "Influence of Temperature on Hydration and Microstructure Properties of Limestone-Calcined Clay Blended Cement," *Materials and Structures*, V. 52, No. 5, 2019, p. 91. doi: 10.1617/s11527-019-1390-5

43. Mao, Y.; He, P.; Drissi, S.; Zhang, J.; Hu, X.; and Shi, C., "Effect of Conditions on Wet Carbonation Products of Recycled Cement Paste Powder," *Cement and Concrete Composites*, V. 144, 2023, p. 105307. doi: 10.1016/j.cemconcomp.2023.105307

44. Jia, L.; Jia, Z.; Zhang, Z.; Tang, Z.; Wang, W.; Cao, R.; and Zhang, Y., "Effect of Recycled Brick Powder with Various Particle Features on Early-Age Hydration, Water State, and Rheological Properties of Blended Cement Paste in the Context of 3D Printing," *Construction and Building Materials*, V. 418, 2024, p. 135428. doi: 10.1016/j.conbuildmat.2024.135428

45. de Azevedo Basta, P., and Estolano de Lima, V., "Effect of Curing Temperature in the Relative Decrease Peak Intensity of Calcium Hydroxide Pastes for Assessing Pozzolanicity of Supplementary Cementitious Materials," *Construction and Building Materials*, V. 325, 2022, p. 126767. doi: 10.1016/j.conbuildmat.2022.126767

46. Parashar, A., and Bishnoi, S., "Influence of the Availability of Calcium Hydroxide, Sulphates, and Alkalis on Hydration of Supplementary Cementitious Materials," *Cement and Concrete Research*, V. 175, 2024, p. 107388. doi: 10.1016/j.cemconres.2023.107388

47. Liu, Q.; Tong, T.; Liu, S.; Yang, D.; and Yu, Q., "Investigation of Using Hybrid Recycled Powder from Demolished Concrete Solids and Clay Bricks as a Pozzolanic Supplement for Cement," *Construction and Building Materials*, V. 73, 2014, pp. 754-763. doi: 10.1016/j.conbuildmat.2014.09.066

48. Wu, C.-H.; Wang, W.-C.; and Jung, C. H., "Potential Pozzolanic Reactivity of Recycled Aggregates and Waste Powders as Cement Mortar Component," *Journal of the Chinese Institute of Engineers*, V. 46, No. 4, 2023, pp. 399-408. doi: 10.1080/02533839.2023.2194920

49. Wu, H.; Yang, D.; and Ma, Z., "Micro-Structure, Mechanical and Transport Properties of Cementitious Materials with High-Volume Waste Concrete Powder and Thermal Modification," *Construction and Building Materials*, V. 313, 2021, p. 125477. doi: 10.1016/j.conbuildmat.2021.125477

50. Serpell, R., and Zunino, F., "Recycling of Hydrated Cement Pastes by Synthesis of $\alpha'_H$-$C_2S$," *Cement and Concrete Research*, V. 100, 2017, pp. 398-412. doi: 10.1016/j.cemconres.2017.08.001

51. Wu, H.; Xu, J.; Yang, D.; and Ma, Z., "Utilizing Thermal Activation Treatment to Improve the Properties of Waste Cementitious Powder and its Newmade Cementitious Materials," *Journal of Cleaner Production*, V. 322, 2021, p. 129074. doi: 10.1016/j.jclepro.2021.129074

52. Cho, Y.-K.; Yoo, S.-W.; Jung, S.-H.; Lee, K.-M.; and Kwon, S.-J., "Effect of Na2O Content, Sio2/Na2O Molar Ratio, and Curing Conditions on the Compressive Strength of FA-Based Geopolymer," *Construction and Building Materials*, V. 145, 2017, pp. 253-260. doi: 10.1016/j.conbuildmat.2017.04.004

53. Kafi, M. A.; Sadeghi-Nik, A.; Bahari, A.; Sadeghi-Nik, A.; and Mirshafiei, E., "Microstructural Characterization and Mechanical Properties of Cementitious Mortar Containing Montmorillonite Nanoparticles," *Journal of Materials in Civil Engineering*, ASCE, V. 28, No. 12, 2016, p. 04016155. doi: 10.1061/(ASCE)MT.1943-5533.0001671

54. Aguilar Rosero, I.; Soriano Somarriba, E.; and Farivar, B., "Effects of Mixture Design Parameters on the Properties of Belitic Calcium Sulfoaluminate Concrete," *Magazine of Concrete Research*, V. 76, No. 5, 2024, pp. 217-228. doi: 10.1680/jmacr.23.00067

55. Wang, Y.; Lei, L.; Hu, X.; Liu, Y.; and Shi, C., "Effect of Diethanolisopropanolamine and Ethyldiisopropylamine on Hydration and Strength Development of Portland Cement," *Cement and Concrete Research*, V. 162, 2022, p. 106999. doi: 10.1016/j.cemconres.2022.106999

56. Zunino, F., and Scrivener, K., "Assessing the Effect of Alkanolamine Grinding Aids in Limestone Calcined Clay Cements Hydration," *Construction and Building Materials*, V. 266, 2021, p. 121293. doi: 10.1016/j.conbuildmat.2020.121293

57. Li, W.; Ma, S.; Hu, Y.; and Shen, X., "The Mechanochemical Process and Properties of Portland Cement with the Addition of New Alkanolamines," *Powder Technology*, V. 286, 2015, pp. 750-756. doi: 10.1016/j.powtec.2015.09.024

58. Zhao, J.; Wang, D.; and Wang, X., "Characteristics and Mechanism of Modified Triethanolamine as Cement Grinding Aids," *Journal of Wuhan University of Technology-Materials Science Edition*, V. 30, 2015, pp. 134-141.

59. Bai, R.; Zhang, J.; Yan, C.; Liu, S.; Wang, X.; and Yang, Z., "Calcium Hydroxide Content and Hydration Degree of Cement in Cementitious Composites Containing Calcium Silicate Slag," *Chemosphere*, V. 280, 2021, p. 130918. doi: 10.1016/j.chemosphere.2021.130918

60. Shenbagam, V. K., and Chaunsali, P., "Influcence of Calcium Hydroxide and Calcium Sulfate on Early-Age Properties of Non-Expansive Calcium Sulfoaluminate Belite Cement," *Cement and Concrete Composites*, V. 128, 2022, p. 104444. doi: 10.1016/j.cemconcomp.2022.104444

61. Wang, Y.; Lei, L.; and Shi, C., "Effect of Diethanolisopropanolamine and Ethyldiisopropylamine on Hydration and Strength Development of Cement-Fly Ash-Limestone Ternary Blend," *Cement and Concrete Composites*, V. 145, 2024, p. 105354. doi: 10.1016/j.cemconcomp.2023.105354

62. Bakharev, T., "Durability of Geopolymer Materials in Sodium and Magnesium Sulfate Solutions," *Cement and Concrete Research*, V. 35, No. 6, 2005, pp. 1233-1246. doi: 10.1016/j.cemconres.2004.09.002

63. Dai, Y.; Qian, G.; Cao, Y.; Chi, Y.; Xu, Y.; Zhou, J.; Liu, Q.; Xu, Z. P.; and Qiao, S. Z., "Effective Removal and Fixation of Cr(VI) from Aqueous Solution with Friedel's Salt," *Journal of Hazardous Materials*, V. 170, No. 2-3, 2009, pp. 1086-1092. doi: 10.1016/j.jhazmat.2009.05.070

64. Lu, C.; Zhang, Z.; Hu, J.; Yu, Q.; and Shi, C., "Effects of Anionic Species of Activators on the Rheological Properties and Early Gel Characteristics of Alkali-Activated Slag Paste," *Cement and Concrete Research*, V. 162, 2022, p. 106968. doi: 10.1016/j.cemconres.2022.106968

65. García-Lodeiro, I., "FTIR Study of the Sol-Gel Synthesis of Cementitious Gels: C-S-H and N-A-S-H," *Journal of Sol-Gel Science and Technology*, V. 45, No. 1, 2008, pp. 63-72. doi: 10.1007/s10971-007-1643-6

66. Chen, J. J., "Solubility and Structure of Calcium Silicate Hydrate," *Cement and Concrete Research*, V. 34, No. 9, 2004, pp. 1499-1519. doi: 10.1016/j.cemconres.2004.04.034

67. Zhang, L.; Yamauchi, K.; Li, Z.; Zhang, X.; Ma, H.; and Ge, S., "Novel Understanding of Calcium Silicate Hydrate from Dilute Hydration," *Cement and Concrete Research*, V. 99, 2017, pp. 95-105. doi: 10.1016/j.cemconres.2017.04.016

68. Huang, H., and Shen, X., "Interaction Effect of Triisopropanolamine and Glucose on the Hydration of Portland Cement," *Construction and Building Materials*, V. 65, 2014, pp. 360-366. doi: 10.1016/j.conbuildmat.2014.04.077

ACI MATERIALS JOURNAL TECHNICAL PAPER

Title No. 123-M27

# Performance-Based Evaluation of Concrete Freezing-and-Thawing Considering Climate Change

by Jin-Su Kim, Woo-Ri Kwon, Norhazilan Md Noor, and Jang-Ho Jay Kim

*Due to global warming, the temperature of the Earth's surface increased by 0.95 to 1.20°C in the past four decades. The increase in temperature has significant effects on the concrete industry, causing alternations in concrete curing conditions and degradation in strength and durability properties. The understanding of changes in concrete properties due to variations in curing conditions from climate change is an imminent task that has to be resolved. Among the durability properties of concrete, freezing-and-thawing (FT) resistance is most directly affected by climate change. However, in all the studies conducted on the FT behavior of concrete, the dramatic changes in environmental conditions due to climate change were not considered. Therefore, the focus of this study is to understand the FT performance of concrete under extreme changes in temperature and relative humidity (RH) during curing. To find the relationship between the changes in curing conditions and FT resistance levels as a function of time, a three-dimensional (3-D) satisfaction surface graph was developed using the Bayesian probabilistic method. Then, an example of 3-D satisfaction surface diagrams for FT resistance based on the weather conditions in New York City between 2001 and 2100 was shown. Furthermore, considering the reduction rate of the average annual FT cycle due to climate change, this study confirmed that FT resistance performance increased. This approach contributes to a performance-based evaluation (PBE) strategy for concrete exposed to FT cycles under various environmental conditions. The study details and results are discussed in the paper.*

**Keywords:** climate change; freezing-and-thawing (FT) resistance life; performance-based evaluation (PBE).

## INTRODUCTION

The world has achieved industrialization using fossil fuels as an energy source. The use of fossil fuels emits greenhouse gases, which destroy the ozone layer. The destruction of the ozone layer has caused severe climate change in the twenty-first century due to global warming, resulting in phenomena such as heavily localized rainfall, snowfall, and typhoons. These abnormal weather patterns have induced critical global challenges that the world is facing presently.[1-3]

According to the Intergovernmental Panel on Climate Change (IPCC) Sixth Assessment Report (AR6), published in 2021, global warming has increased the average temperature of the Earth's surface by 1.09°C over the period of 1980 to 2020 (range between 0.95 and 1.20°C). The projected climate change is expected to have detrimental impacts on the environment and ecology, which will lead to economic and social challenges.[4]

Following this historical footstep, the cement and concrete industries have suffered from carbon emission reduction policies such as the net-zero policy. In addition, design and construction regulations have been strengthened to combat performance degradation that can occur during the casting and curing processes due to climate change. Therefore, it is important to understand the effect of temperature and relative humidity (RH) on the casting and curing processes of concrete used in construction projects. Changes in temperature and RH affect the moisture behavior within the concrete, leading to a reduction in entrained air content, slump, and hydration, which can lead to multiple cracking and internal pore formations that deteriorate the durability of concrete.[5-8]

Concrete durability performance is sensitive to changes in curing temperature and RH, which can significantly affect its freezing-and-thawing (FT) resistance. FT causes the free water inside the concrete to freeze, leading to volumetric expansion and ultimately leading to crack formations. Repeated FT leads to concrete quality degradation and durability degradation.[9] Additionally, during the curing process, concrete is particularly vulnerable to changes in temperature and RH. If the external temperature decreases and RH increases rapidly, the moisture inside the concrete may freeze prior to being fully hardened. Through repeated FT cycles, water can easily freeze and expand, potentially causing premature freeze damage.[10,11] Prolonged FT cycles can degrade the durability of concrete, thus causing serviceability problems in the structures.[12,13] Therefore, measures to overcome the abnormal deviations in the conditions in handling, mixing, transporting, and curing of concrete are required.[14-17]

In this study, the characteristics of concrete with severe fluctuations in curing conditions, namely temperature and RH, due to climate change, are studied. More specifically, concrete specimens were prepared according to ASTM C192/C192M-12[18] and cured under various temperature and RH conditions to understand the change in concrete properties. FT tests were conducted to measure the relative dynamic modulus of elasticity (RDME) after 100, 200, and 300 cycles according to ASTM C666/C666M-15.[17,19]

It is nearly impossible to evaluate the FT resistance life of concrete by only conducting tests due to changes in curing conditions of temperature and RH because the sufficient number of specimens that reflect all the changes occurring over 100 years is too large to consider. Therefore,

---

*ACI Materials Journal*, V. 123, No. 2, March 2026.

MS No. M-2025-062.R2, doi: 10.14359/51749445, received August 12, 2025, and reviewed under Institute publication policies. Pertinent discussion including author's closure, if any, will be published ten months from this journal's date if the discussion is received within four months of the paper's print publication.

**Table 1—Mixture proportions of concrete**

| Maximum coarse aggregate size, mm | Slump, mm | $w/b$, % | Percentage of fine aggregate ($s/a$), % | Air, % | kg/m$^3$<br>Water (W) | Cement (C) | Fine aggregate (S) | Coarse aggregate (G) | $f_{ck}$, MPa |
|---|---|---|---|---|---|---|---|---|---|
| 25 | 120.0 | 55.0 | 42.0 | 5.0 | 183.4 | 333.4 | 677.3 | 1013.0 | 27 |

Note: $f_{ck}$ is design compressive strength.

to investigate the climate change-altered FT behavior in concrete, probabilistic statistical methods should be used to identify trends that affect performance. The representative method using such probabilistic statistics is performance-based evaluation (PBE). The PBE method uses Bayesian probabilistic statistics to determine the satisfaction level of a target structure, where the x-, y-, and z-axes represent the FT resistance life, the curing condition, and the satisfaction level, respectively. An example of three-dimensional (3-D) satisfaction diagrams for FT resistance life of a target concrete structure located in New York City is shown. Additionally, to reflect the annual FT cycles due to climate change, the study results of the annual FT cycles obtained from the Federal Highway Administration (FHWA) report and the United States Environmental Protection Agency (U.S. EPA) reports[20,21] were used for the PBE of FT resistance life. The FT cycles over 100 years decreased from 5400 to 3519 cycles, which was induced by changes in the temperature and RH curing condition ranges: 35 to 40°C and 65 to 90%, respectively. Using these changes in temperature, RH, and FT cycles, the effect on FT resistance life was reanalyzed for comparison purposes.

## RESEARCH SIGNIFICANCE

This study proposes a method to evaluate the FT performance of concrete under various conditions by using Bayesian probability statistics to calculate the satisfaction curve (SC) for temperatures ranging from 8 to 45°C and RH levels ranging from 40 to 95%. The analysis results are presented as a 3-D satisfaction surface (SS) with a duration of 100 years to account for time dependency. Additionally, the FT resistance life was calculated considering the annual average FT cycles from the FHWA and the reduced annual average FT cycles projected by the U.S. EPA to account for climate change.

## EXPERIMENTAL INVESTIGATION

### Specimens

The mixture proportions used in this study are listed in Table 1. The water-binder ratio ($w/b$) was 55%, and only ordinary portland cement was used as the binder. The maximum size of the coarse aggregate was 25 mm, the slump was 120 mm, the fine aggregate ratio was 42%, the air content was 5%, and the 28-day compressive design strength was 27 MPa. Cylindrical concrete specimens (Φ100 x 200 mm) were prepared for compressive strength and FT tests in accordance with ASTM C192/C192M.[18] Five specimens were prepared for each test. To accurately represent the mean trend of the test results, the minimum and maximum values were excluded from the test data. Fresh concrete was cast in a laboratory environmental setting with a temperature of 23°C and RH of 65%. They were subsequently demolded 24 hours after casting. The curing conditions applied after demolding are described in the following section.

### Curing condition

Concrete is typically cured under standard temperature and RH conditions of approximately 23 ± 2°C and 95% or higher, respectively. These conditions do not account for variations in climate. In this study, ordinary portland cement was used to produce normal-strength concrete for investigating the relationship between temperature and RH curing conditions and concrete strength. Temperature gradients within the specimens were assumed to be negligible due to their small size (Φ100 x 200 mm) and the use of curing chambers with constant temperature and RH for each temperature and RH combination curing conditions.

The annual and monthly average temperatures and RHs over the past 10 years in the New York metropolitan area were obtained from the weather survey website, as shown in Fig. 1. It illustrates that the most suitable period for concrete casting is between April and October, as evident from Fig. 1(b) and (d). The appropriate curing temperature and RH range were 15 to 30°C and 50 to 90%, respectively.

To account for the changes in temperature and RH due to climate change, low-temperature curing conditions of 15°C or less—namely, 8 and 12°C—were selected for the study. With respect to high-temperature curing conditions, temperatures of 30°C or higher—namely, 35, 40, and 45°C—were selected. RH was selected based on the monthly average of 65% from April to October, with the extreme RH condition set at 95% or higher, and the low RH condition set at 40% or lower.

### Compressive strength test method

Concrete cylindrical specimens (Φ100 x 200 mm) were prepared according to ASTM C192/C192M.[18] Compressive strength of concrete is typically measured at 3, 7, and 28 days to evaluate early-, intermediate-, and standard-age strength according to ASTM C39/C39M-05,[22] respectively. The contact surfaces with the testing machine were ground flat, and rubber caps were used on the contact surfaces to prevent load eccentricity according to ASTM C1231/C1231M-09,[23] which permits the use of such caps provided that the rubber cap satisfies the specified hardness and thickness requirements. The specimen was applied with a load control rate of 0.6 ± 0.2 MPa/s. A universal testing machine with a maximum capacity of 1000 kN and an accuracy of 500 N was used for the test. All compressive strength tests were conducted after the specimens reached thermal equilibrium at room temperature. Therefore, eigen-stresses caused

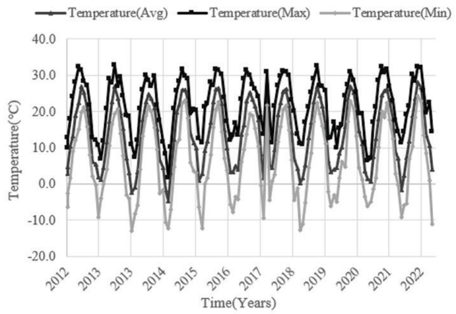

a) Temperatures in New York City from 2012 to 2022

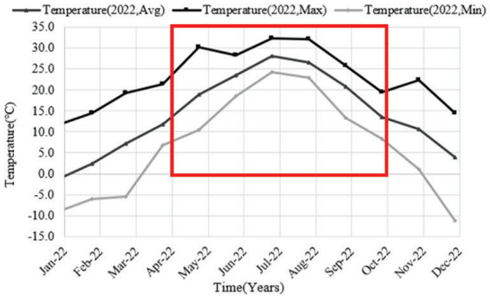

b) Temperatures in New York City, 2022

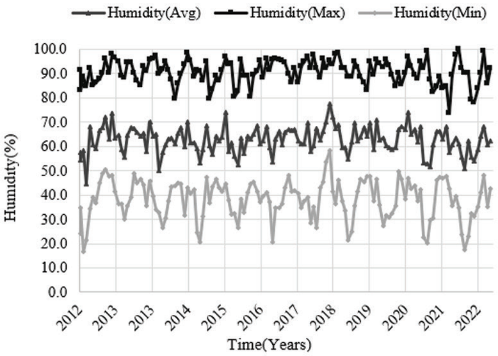

c) RH in New York City from 2012 to 2022

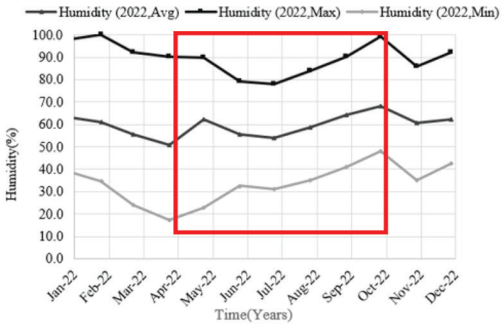

d) RH in New York City, 2022

*Fig. 1—New York City weather data for past 10 years, courtesy of U.S. Weather Underground.*

by differences between the zero-stress reference temperature and the actual temperature were not considered.

## Freezing-and-thawing test method

The FT tests were conducted in accordance with ASTM C666/C666M.[19] The central temperature of the concrete specimens was maintained at –18°C during freezing and +4°C during thawing in an FT chamber. Each FT cycle ensured that the maximum and minimum temperatures at the center of the specimen were within the range of 4 ± 2°C and –18 ± 2°C, respectively. More specifically, the temperature of the specimen should not fall below –20°C or rise above 6°C. The cycles consisted of 4 hours of freezing followed by 4 hours of thawing. The RDME of the specimen was obtained before and after 300 cycles, in accordance with ASTM C215-19.[24] Typically, FT tests are concluded after 300 cycles, but if the RDME drops below 60%, the test may be terminated instantly. In this study, measurements were taken at different cycles (0, 100, 200, and 300 cycles) under different curing conditions to calculate the RDME using Eq. (1) and Eq. (2)

$$P_c = \left(\frac{{n_c}^2}{{n_o}^2}\right) \times 100 \tag{1}$$

where $P_c$ is the RDME (%) after FT cycle $N_o$; ${n_c}^2$ is the primary resonance frequency (Hz) of deformation vibration in FT cycle $N_o$; and ${n_o}^2$ is the primary resonance frequency (Hz) of deformation vibration in FT cycle 0

$$DF = \frac{P_c N_o}{M} \tag{2}$$

where $DF$ is the durability index of the test specimen; $P_c$ is the RDME (%) in cycle $N_o$; $N_o$ is the number of cycles in which the RDME becomes 60% or the number of cycles at the end of the FT exposure; and $M$ is the cycle at the end of the FT exposure.

# ANALYTICAL INVESTIGATION

## Performance-based evaluation method

Designing structures to satisfy design requirements, standards, and specifications based on structural types and use is called performance-based design (PBD). According to the International Council for Building Research report, approaching structures from a performance perspective means emphasizing results over methods or processes.[25] In general, prescriptive design methods, such as the limit state, working stress, and ultimate strength design methods, use resistance coefficients by calculating stiffness and load-carrying capacity. These methods tend to be driven by satisfying design requirements of common goals and specifications. More specifically, the *fib* Model Code adopts a deemed-to-satisfy approach for FT deterioration, which assumes a service life of 50 or 100 years, provided that the concrete satisfies the minimum requirements for compressive strength, air content, water-cement ratio (*w*/*c*), cement content, and cover thickness according to the designated exposure grade or limit states. However, these design criteria and specifications limit designers' ability to achieve design solutions with multiple options for various environmental conditions.

The PBE method used in this study evaluates the material performance satisfaction of concrete using new design solutions, interpretation methods, and test results for

## Table 2—Compressive strength test results

| Case | Compressive strength, MPa | | |
|---|---|---|---|
| | 3 days | 7 days | 28 days |
| T8H40 | 11.20 ± 0.25 | 16.19 ± 0.56 | 21.23 ± 0.38 |
| T8H65 | 14.99 ± 0.46 | 18.25 ± 0.53 | 25.93 ± 1.56 |
| T8H95 | 15.71 ± 0.55 | 20.30 ± 0.57 | 28.90 ± 0.61 |
| T12H40 | 11.52 ± 0.33 | 16.56 ± 0.60 | 22.77 ± 0.55 |
| T12H65 | 15.23 ± 0.79 | 21.35 ± 0.90 | 25.93 ± 0.84 |
| T12H95 | 17.19 ± 0.36 | 24.52 ± 0.76 | 31.82 ± 0.93 |
| T35H40 | 15.12 ± 1.47 | 19.34 ± 0.88 | 26.53 ± 0.25 |
| T35H65 | 18.32 ± 1.59 | 23.83 ± 0.97 | 28.18 ± 1.13 |
| T35H95 | 20.27 ± 0.11 | 25.70 ± 0.92 | 30.23 ± 2.09 |
| T40H40 | 16.12 ± 2.78 | 19.34 ± 1.30 | 24.01 ± 0.32 |
| T40H65 | 18.32 ± 1.21 | 22.80 ± 1.04 | 27.62 ± 0.98 |
| T40H95 | 18.27 ± 1.52 | 23.70 ± 0.31 | 28.19 ± 1.29 |
| T45H40 | 18.35 ± 0.19 | 21.22 ± 1.02 | 25.81 ± 0.72 |
| T45H65 | 18.69 ± 1.81 | 20.68 ± 0.46 | 25.57 ± 0.59 |
| T45H95 | 19.26 ± 0.91 | 24.66 ± 1.54 | 28.83 ± 0.80 |

probabilistic statistical determination. A satisfaction diagram is created using the Bayesian probability method, which uses the information obtained from sampling data to evaluate the satisfaction probability. Specifically, the normal probability distribution function is used to generate virtual data to compensate for the insufficient number of available test data points, which can supplement the data points needed for the development of SCs.[24-27] Through this approach, PBDs that accommodate diverse requirements at construction sites can be developed.

The lognormal cumulative distribution method is used to determine the satisfaction probability. The method uses a probability function that requires three variables: material variable value, mean value, and standard deviation for calculation, as shown in Eq. (3). The Bayesian probabilistic method was used to create a fragility curve for seismic failure evaluation. In Eq. (3), the $a_i$ value is the material variable, which is the result value of RDME according to the FT test results for the temperature and RH curing conditions, and the $N$ value is the number of material variable data points.

In fragility analysis, 1 and 0 are assigned to a structure damaged or undamaged by an earthquake, respectively. In contrast, the PBE of the material performance property is assigned a value of 1 or 0 for satisfying or not satisfying the design requirement, respectively. If these three variable data are evaluated by the Bayesian probability method, the result would be in the form of an accrued curve of the assigned lognormal distribution. Then the average value and standard deviation are obtained to draw an SC[26-29]

$$L = \prod_{i=1}^{N} [F(a_i)]^{x_i} [1 - F(a_i)]^{1-x_i} \tag{3}$$

where $F(.)$ is the SC of a specific material requirement; $a_i$ is the design material requirement of variable I; $x_i$ is determined to be 0 or 1 depending on the satisfaction to the material performance value, such as $a_i$; and $N$ is determined by the total number of related material data obtained for material performance evaluation.

## Compressive strength results and discussion

The compressive strength was measured at 3, 7, and 28 days after concrete casting. For all temperature and RH combinations, three specimens were tested to obtain the average strengths. The denomination system for the concrete specimens is as follows: "T" represents the curing temperature (°C), and "H" denotes the curing RH (%). The test results are shown in Table 2 and Fig. 2. The results showed that, as the curing age increased from 3 to 28 days, the strengths increased for all curing conditions, as expected. As shown in Fig. 2(a) to (c), compressive strength generally increased as the curing temperature increased, with the highest compressive strength observed at a temperature of 35°C. However, at 40 and 45°C, the compressive strength slightly decreased due to the effects of high temperature, showing an irregular trend. For the 3-day strength results, the specimens cured at 8 and 12°C had lower strengths than those cured under 35, 40, and 45°C. More specifically, the 3-day strengths of 8 and 12°C with RH of 95% were 6 to 29% lower than the specimens cured under temperatures of 35, 40, and 45°C with RH of 95%. For 7-day strengths, the trend was similar to that of 3-day strengths. More specifically, the 7-day strengths of 8 and 12°C were 16 to 21% lower than the specimens cured under temperatures of 35, 40, and 45°C.

The 28-day strengths showed no clear trend. Meanwhile, for all temperature curing conditions with RH of 95%, the 28-day strengths satisfied the target strength of the mixture of 27 MPa. The specimens that satisfied the target strength of 27 MPa were T8H95, T12H95, T35H40, T35H65, T35H95, T40H65, T40H95, and T45H95. As shown in Fig. 2(d) to (h), the strength increased as RH increased. At temperatures of

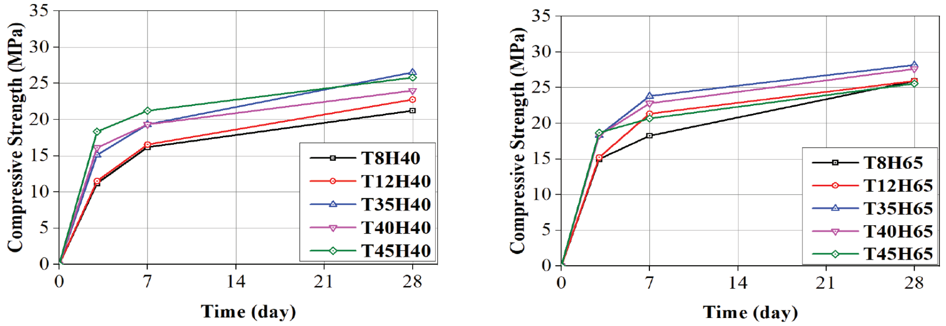

a) Various temperatures for 40% RH b) Various temperatures for 65% RH

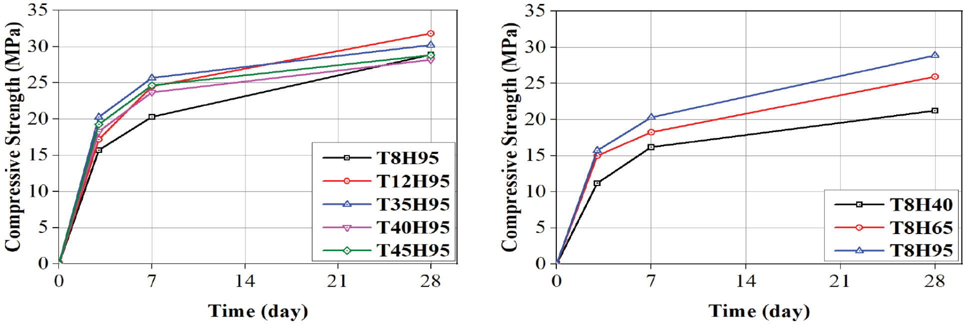

c) Various temperatures for 95% RH d) Various RHs for 8 °C Temperature

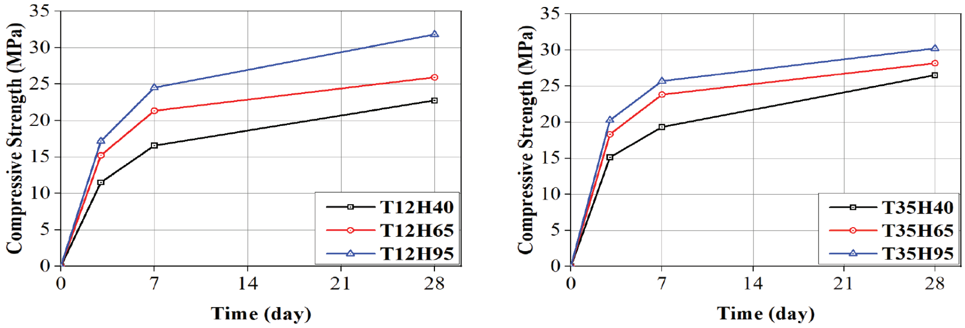

e) Various RHs for 12 °C Temperature f) Various RHs for 35 °C Temperature

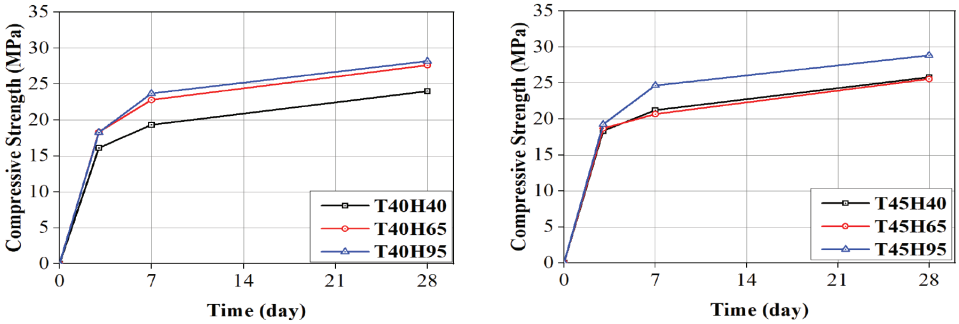

g) Various RHs for 40 °C Temperature h) Various RHs for 45 °C Temperature

*Fig. 2—Compressive strength results for various temperatures and RH curing conditions.*

8 and 12°C, the effect of RH on the strength increase was significant. However, the effect was minimal at temperatures of 35, 40, and 45°C. More specifically, when the RH increased from 40 to 95%, the 28-day strength increased by 40% at 12°C and by 12% at 45°C, respectively. The trend can be attributed to a high RH condition providing enough moisture for the hydration reaction. In the case of a curing temperature of 45°C, the number of pores and microcracks increased inside the concrete due to the nonuniform diffusion of hydration products and differences in the thermal expansion coefficients of concrete materials, resulting in an unexpected trend in compressive strength.[30,31] The specimens cured under relatively extreme conditions of 35 to 40°C and RH of 65 to 95% satisfied the target strength requirement of 27 MPa.

## Freezing-and-thawing test results and discussion

The FT test was conducted in accordance with ASTM C666/C666M. For all temperature and RH curing condition combinations, three specimens were tested to obtain the average RDME. The test results are shown in Table 3 and Fig. 3. The RDME of specimens was measured after 100, 200, and 300 FT cycles. The result showed that, as the FT increased from 100 to 300 cycles, the RDME decreased for all curing conditions, as expected. As shown in

**Table 3—FT test results**

| | RDME, % | | | |
|---|---|---|---|---|
| Case | 0 cycles, % | 100 cycles, % | 200 cycles, % | 300 cycles, % |
| T8H40 | 100.00 | 84.67 ± 0.45 | 73.60 ± 1.06 | 69.13 ± 1.04 |
| T8H65 | 100.00 | 84.36 ± 0.95 | 73.10 ± 0.79 | 66.70 ± 1.73 |
| T8H95 | 100.00 | 86.13 ± 1.23 | 71.60 ± 1.06 | 65.03 ± 1.42 |
| T12H40 | 100.00 | 89.43 ± 1.84 | 76.46 ± 1.17 | 69.60 ± 1.45 |
| T12H65 | 100.00 | 88.76 ± 0.40 | 76.83 ± 1.61 | 69.03 ± 1.17 |
| T12H95 | 100.00 | 87.76 ± 2.03 | 74.00 ± 0.75 | 67.60 ± 0.30 |
| T35H40 | 100.00 | 92.03 ± 1.86 | 85.06 ± 2.14 | 77.50 ± 3.64 |
| T35H65 | 100.00 | 94.00 ± 1.05 | 85.63 ± 1.07 | 75.23 ± 1.95 |
| T35H95 | 100.00 | 95.36 ± 0.85 | 90.60 ± 0.85 | 85.46 ± 1.11 |
| T40H40 | 100.00 | 91.90 ± 1.85 | 83.40 ± 2.03 | 77.63 ± 2.46 |
| T40H65 | 100.00 | 93.03 ± 2.40 | 83.86 ± 1.66 | 74.60 ± 2.21 |
| T40H95 | 100.00 | 92.49 ± 1.13 | 86.69 ± 0.35 | 83.30 ± 0.91 |
| T45H40 | 100.00 | 93.30 ± 1.44 | 83.20 ± 1.49 | 69.06 ± 1.80 |
| T45H65 | 100.00 | 90.26 ± 2.67 | 81.56 ± 1.18 | 68.33 ± 0.75 |
| T45H95 | 100.00 | 93.76 ± 2.93 | 80.03 ± 2.21 | 72.33 ± 2.06 |

Fig. 3(a) to (c), the RDME generally increased as the curing temperature increased, with the highest RDME observed at a temperature of 35°C. However, at 40 and 45°C, the RDME slightly decreased due to the effects of high temperature, similar to the trend in compressive strength results. For 100 cycles, the specimens cured at 8 and 12°C had lower RDME than those cured at 35, 40, and 45°C. More specifically, for the specimens cured at 8 and 12°C and 95% RH, the RDMEs after 100 FT cycles were 3 to 10% lower than those for the specimens cured at 35, 40, and 45°C and RH of 95%. For the 200-cycle results, the trend was similar to the 100-cycle results. More specifically, the RDME results of 8 and 12°C and 95% RH after 200 cycles were 6 to 26% lower than those from the specimens cured at 35, 40, and 45°C and 95% RH. For the 300-cycle results, the RDME results showed that they increased with increasing temperature at 95% RH. However, no clear trend can be observed in the results from the specimens cured under other RH conditions. More specifically, the 300-cycle RDME results from the specimens cured at 8 and 12°C were 8 to 31% lower than those from the specimens cured at 35 and 40°C. In the case of a curing temperature of 45°C, similar to the trend in compressive strength results, RDMEs decreased due to the formation of microcracks.[31]

In all curing conditions, the 300-cycle RDMEs satisfied the criterion of requiring greater than 60% of the RDME of the specimens without FT cycles, as specified in ASTM C666/C666M.[19] If the RDME requirement increases to 70%, the specimens cured at 35°C or higher can satisfy the requirement. In fact, the T35H95 and T40H95 specimens can satisfy the requirement even if the requirement is increased to 80%. Under low-temperature curing conditions, RDME decreases as RH increases. In contrast, under high-temperature curing conditions, RDME increases with an increase in RH. As shown in Fig. 3(d) and (e), for the low-temperature curing condition, RDME decreased by 3 to 6% as RH increased. The result trend can be attributed to hydration reactions being delayed due to the reduction in internal free water from the low-temperature condition of FT cycles. On the other hand, as shown in Fig. 3(g) and (h), for the high-temperature curing condition, RDME increased by 5 to 10% as curing RH increased. High-temperature curing conditions induce internal moisture movement, promoting greater hydration reactions and an increase in RDME. As FT cycles increased, the RDME reduction rate was approximately 10 to 15% for the specimens cured at 35 and 40°C, while the RDME increase rate was the highest as RH increased under the same temperature conditions. Therefore, the optimal curing condition was identified as a temperature of 35°C and an RH of 95%.

## ANALYTICAL RESULTS AND DISCUSSION

### Freezing-and-thawing resistance life evaluation considering climate change in New York City

Climate change is decreasing the average number of FT cycles occurring in a season due to gradually increasing temperatures. To predict the FT resistance life of a concrete structure, it is necessary to estimate the average FT cycle reduction in the region where the structure is located. For this study, the target location to consider climate change conditions was selected as New York City. According to the FHWA report,[20] the annual FT cycles occurring in and around New York City are approximately 54 cycles per year. Therefore, the FT cycles occurring in New York City over 1 to 100 years would be 54 to 5400 cycles. According to the U.S. EPA report,[21] the annual FT reduction was 0.38 days, as shown in Fig. 4. Applying this reduction as a base to incorporate the effect of climate change, the FT cycles occurring in New York City over 1 to 100 years would be 54 to 3519 cycles.

To evaluate the FT resistance life of a concrete structure in New York City, the prediction of RDME as a function of the

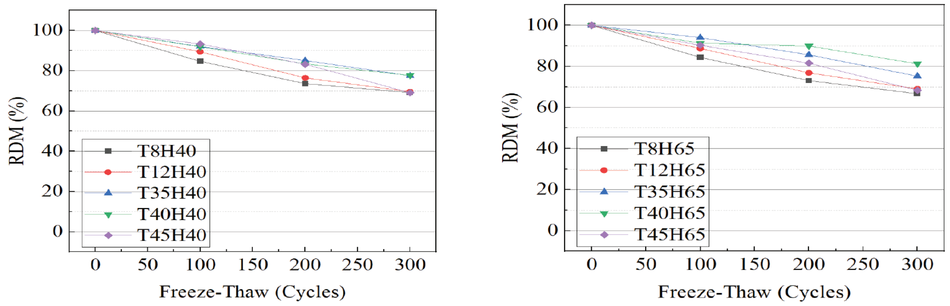

a) Various temperatures for 40% RH b) Various temperatures for 65% RH

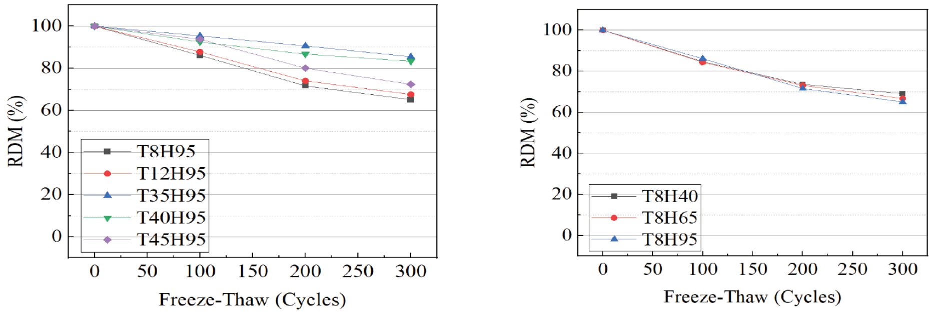

c) Various temperatures for 95% RH d) Various RHs for 8 °C Temperature

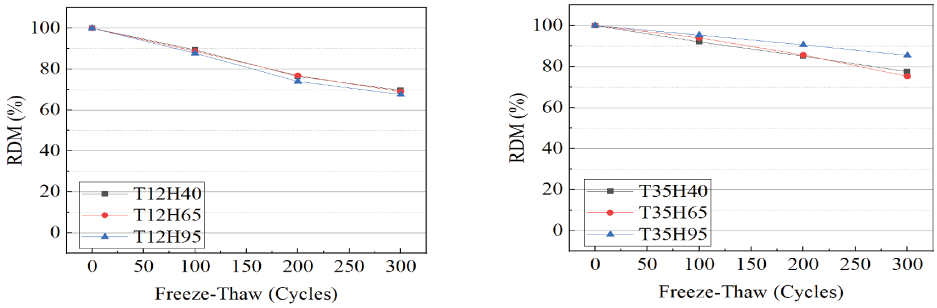

e) Various RHs for 12 °C Temperature f) Various RHs for 35 °C Temperature

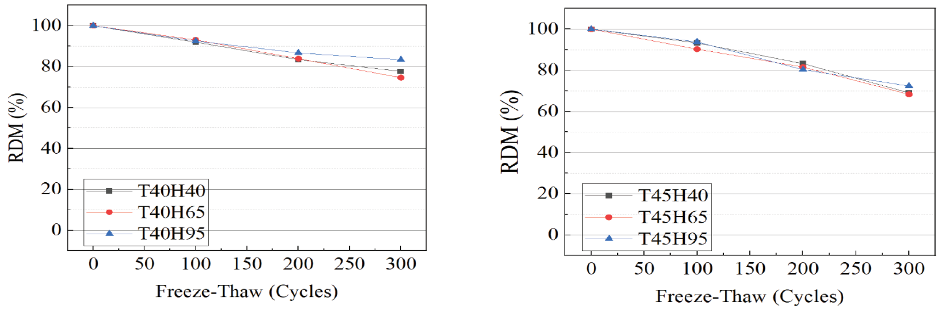

g) Various RHs for 40 °C Temperature h) Various RHs for 45 °C Temperature

*Fig. 3—RDME results after 300 FT cycles cured under various temperatures and RHs.*

number of FT cycles occurring annually is needed. Using the predicted RDMEs, the FT resistance of the concrete structure during its service life can be obtained through drawing satisfaction graphs. However, it is nearly impossible to obtain an RDME equation for an extended duration, such as 100 or 150 years, due to the time and cost required to perform FT cycle tests. Also, the RDME equations for various combinations of temperature and RH curing conditions are nearly impossible to obtain due to an insurmountable amount of work required to obtain a sufficient number of FT RDME data. Therefore, based on the RDME data obtained from the FT tests with a limited number of FT cycles in this study, the RDME equations were obtained for the curing conditions applied in this study. The base equation that was used to curve-fit the data was as follows

$$\mathrm{RDME} = c_1 \times \ln(N_{FT}) + c_2 \tag{4}$$

where RDME is the relative dynamic modulus of elasticity; $c_1$ and $c_2$ are the coefficients obtained from the curve fitting; and $N_{FT}$ is the number of FT cycles.

All the curve-fitted equations for the curing conditions considered in this study are shown in Table 4. The equations are derived based on the criterion of RDME equaling 60% of the RDME without FT damage. More specifically, for each curing condition, data-fitted equations were proposed

## Table 4—Number of years when RDME falls below 60%

| Case | RDME prediction formula | Coefficient of determination | Failure years | | Failure cycles |
|---|---|---|---|---|---|
| | | $R^2$ | FHWA standard | U.S. EPA standard | |
| T8H40 | RDME = $-14.34\ln(N) + 150.41$ | 0.99 | 11 | 11 | 549 |
| T8H65 | RDME = $-16.09\ln(N) + 158.44$ | 0.99 | 9 | 9 | 455 |
| T8H95 | RDME = $-19.4\ln(N) + 175.16$ | 0.99 | 8 | 8 | 379 |
| T12H40 | RDME = $-18.12\ln(N) + 172.77$ | 0.99 | 10 | 10 | 505 |
| T12H65 | RDME = $-17.88\ln(N) + 171.22$ | 0.99 | 10 | 10 | 504 |
| T12H95 | RDME = $-18.51\ln(N) + 172.76$ | 0.99 | 9 | 9 | 443 |
| T35H40 | RDME = $-12.88\ln(N) + 151.89$ | 0.97 | 23 | 25 | 1259 |
| T35H65 | RDME = $-16.55\ln(N) + 171.03$ | 0.96 | 15 | 17 | 822 |
| T35H95 | RDME = $-8.78\ln(N) + 136.15$ | 0.97 | 108 | None | 5877 |
| T40H40 | RDME = $-12.91\ln(N) + 151.48$ | 0.99 | 22 | 25 | 1199 |
| T40H65 | RDME = $-16.39\ln(N) + 169.12$ | 0.98 | 10 | 10 | 519 |
| T40H95 | RDME = $-8.37\ln(N) + 131.03$ | 0.99 | 89 | None | 4876 |
| T45H40 | RDME = $-18.6\ln(N) + 179.72$ | 0.94 | 10 | 10 | 508 |
| T45H65 | RDME = $-19.16\ln(N) + 179.75$ | 0.93 | 10 | 10 | 519 |
| T45H95 | RDME = $-22.19\ln(N) + 196.42$ | 0.99 | 11 | 11 | 562 |

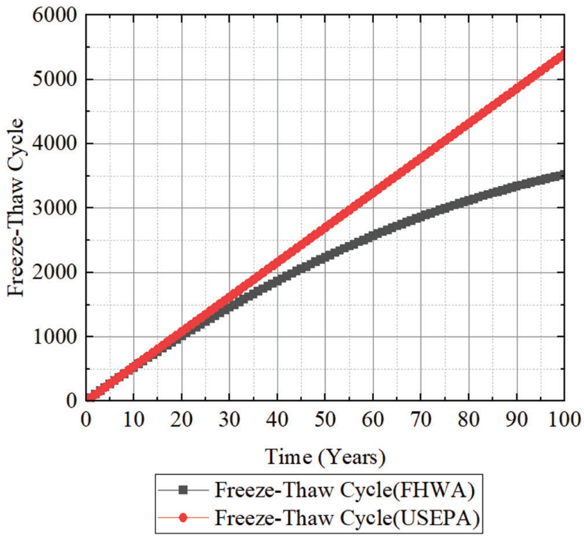

*Fig. 4—Changes in FT cycle due to climate change.*

to represent the relationship between RDME and 100, 200, and 300 FT cycles. It should be noted that the fitted RDME model (Eq. (4)) is extrapolated beyond 300 FT cycles to estimate the long-term FT resistance life. This extrapolation is based on the assumption that the RDME degradation trend observed up to 300 cycles continues in a similar pattern. The logarithmic nature of the model reflects the decelerating damage accumulation typically observed in concrete under FT conditions, as reported by Chen and Qiao[32] and Yan et al.[33] While this approach introduces uncertainty, it provides a rational basis for performance comparison under various temperature and RH combinations during curing. Table 4 also shows the number of years to reach the 60% RDME using both the FHWA and U.S. EPA standards. It should also be noted that the model does not explicitly consider strength development due to aging beyond 28 days. At this stage, additional strength development has minimal influence on FT resistance, as FT resistance is more critically influenced by internal pore structure and external exposure conditions.[13]

With respect to the FT resistance life prediction, the T8H95 specimen had the shortest FT resistance life of 9 years, whereas the T35H95 specimen had the longest FT resistance life of 108 years. Similar to the previous FT test results, the FT resistance life of specimens cured at lower temperatures of 8 and 12°C was two to 13 times shorter than that of specimens cured at higher temperatures of 35, 40, and 45°C. For 8 and 12°C curing temperatures, the FT resistance life decreased by 10 to 20% from increasing RH, whereas for 35 and 40°C curing temperatures, the FT resistance life increased four to five times from increasing RH. This indicates that the FT resistance life of concrete is directly influenced by the curing conditions, including temperature and RH.

## Performance-based evaluation development of freezing-and-thawing resistance life

To develop FT SCs, the yearly RDME is needed to predict the state of FT resistance of the concrete structure. In this study, the yearly RDME considering curing conditions was obtained from the curve-fitted RDME equations as a function of the number of FT cycles, shown in Table 4. The FT SCs were developed based on two parameters: temperature and RH curing conditions. The criterion used to determine the success/failure of the satisfaction was 60% RDME for a duration of 1 to 100 years. Using the Bayesian probabilistic method, the satisfaction graphs can be developed by considering the annual FT cycles proposed by the FHWA standard, as shown in Fig. 5. The two-dimensional (2-D) SCs are shown in Fig. 5(a) and (b), and the 3-D SSs are shown in Fig. 5(c) and (d). The difference between the 2-D and 3-D graphs comes from the time dependency of the durability performance of concrete. For example, the 2-D FT SC is drawn at a selected time of concrete life, such as the

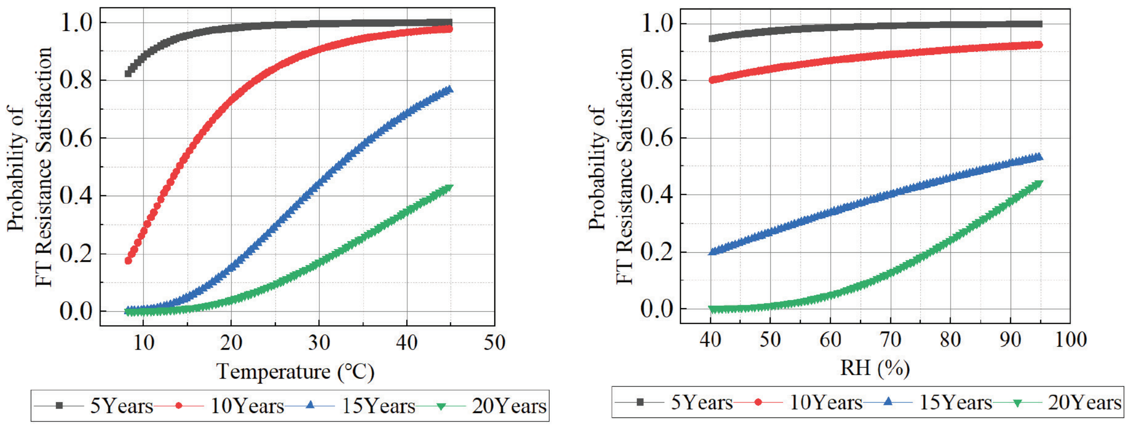

a) 2D SC for curing temperature

b) 2D SC for curing RH

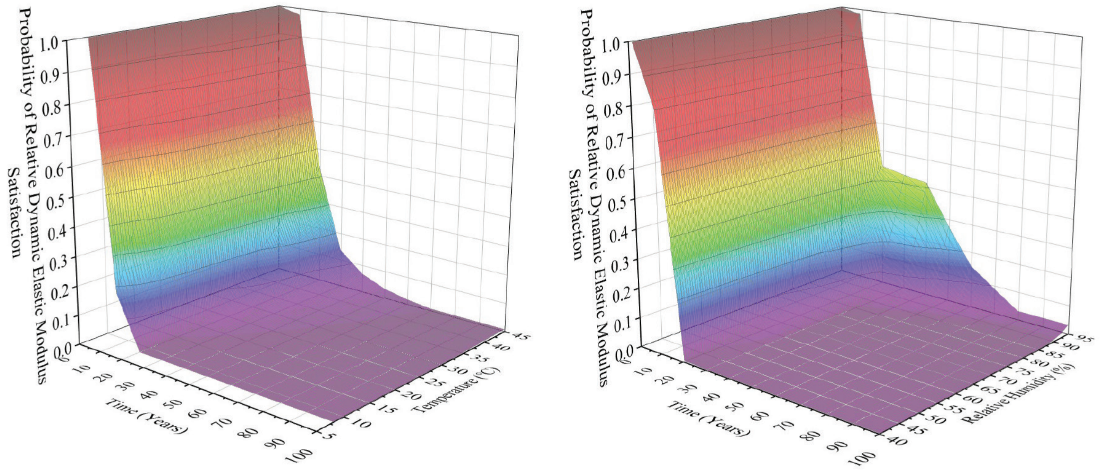

c) 3D SS for curing temperature

d) 3D SS for curing RH

*Fig. 5—FHWA FT resistance life satisfaction graphs according to temperature and RH.*

first, 20th, or 100th year. However, the 3-D FT SS is drawn for a duration of 100 years of service life. More specifically, 100 2-D SCs would be used to draw a 3-D SS.

As shown in Fig. 5(a), the satisfaction level decreased as the FT exposure time increased, as expected. As shown in Fig. 5(a), the satisfaction increase rate after 5 years of FT exposure was relatively similar for all the curing temperatures, while the satisfaction increase rate after 10, 15, and 20 years of FT exposure was significant as the curing temperature increased. For the 10-year FT resistance SC, the satisfaction percentage rapidly increased with curing temperature up to 20°C, then tapered off beyond 20°C. For 15- and 20-year FT resistance SCs, the satisfaction percentage increase is more gradual as the curing temperature increases.

The trend in RH results is similar to the temperature results, as shown in Fig. 5(b). As shown in Fig. 5(b), the satisfaction level decreased as the FT exposure time increased, as expected. Unlike the temperature results, the RH results show that the increase rate for all FT exposure durations (that is, 5, 10, 15, and 20 years) is more gradual as the RH increases. For the 5-, 10-, and 15-year FT exposures, the satisfaction results show almost linear relationships. Only for the 20-year FT exposure, the satisfaction level for the specimens cured at 50% RH is 0%, but it gradually increases beyond the RH. The overall results showed that high satisfaction levels are shown for the 5- and 10-year FT exposures, and relatively low satisfaction levels are shown for the 15- and 20-year FT exposures. The 3-D FT resistance SSs developed for a duration of 100 years are shown in Fig. 5(c) and (d). The comparison of the FT resistance life predictions from the developed satisfaction graphs and the test data curve-fitted RDME equations reveals that the FT resistance life sharply decreased by 9 to 11 years for the temperature conditions of 8 and 12°C and the RH conditions of 40 and 65%. The reasonable comparison results indicate that the 3-D graph generated through PBE is reliable for use in evaluations of real scenarios.

As an example of PBE, a scenario is examined in which a structure is required to achieve a satisfaction level of 0.5 or higher and a target FT resistance life of at least 15 years. As shown in Fig. 5(a), this performance could be achieved at curing temperatures of 33°C or higher. As shown in Fig. 5(b), the RH should be maintained at 86% or higher. In addition, a structure cured at a temperature of 30°C and an RH of 90% is estimated to have an FT resistance life of approximately 14 years. To overcome the limited number of test data points in this study, supplemental data points generated from the normal probability distribution function were obtained. These generated virtual data points are used to generalize the evaluation results. The proposed method is based on a probabilistic framework designed to demonstrate

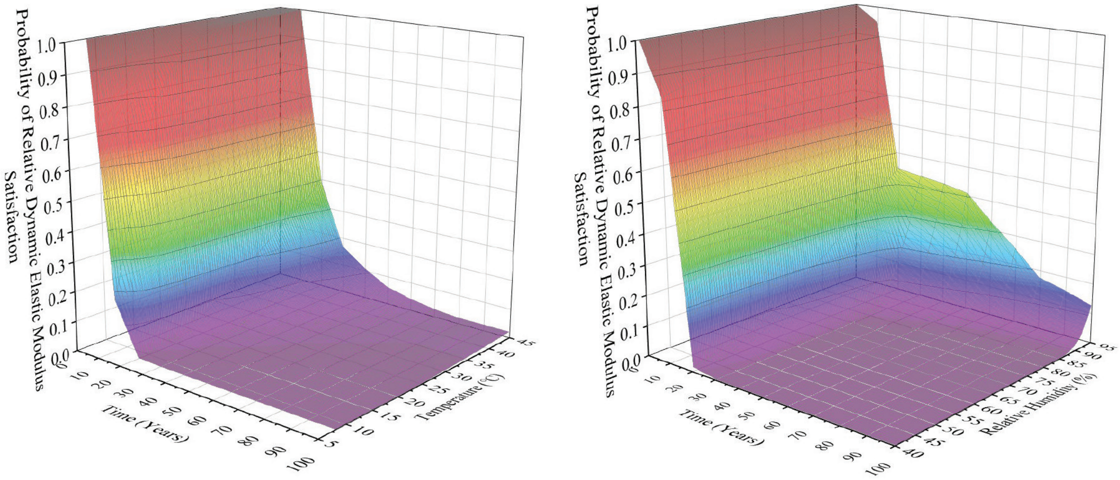

a) 3D SS for curing temperature

b) 3D SS for curing RH

*Fig. 6—U.S. EPA FT resistance life satisfaction graphs according to temperature and RH.*

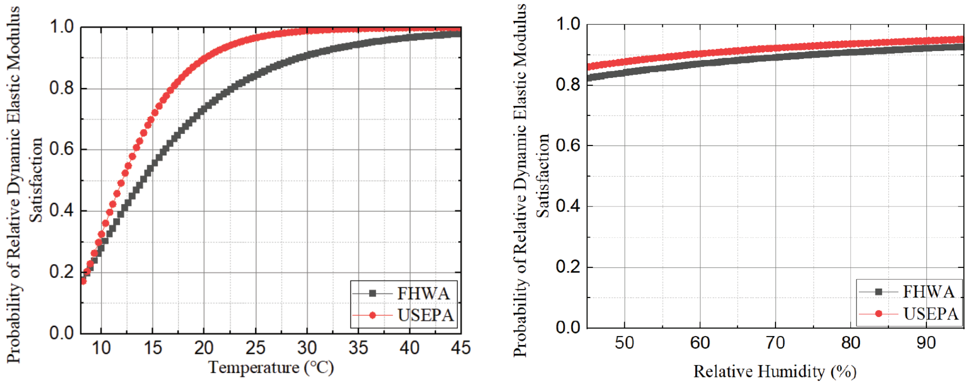

a) 2D SC for curing temperature

b) 2D SC for curing RH

*Fig. 7—Comparison of 10-year FT resistance SCs for FHWA and U.S. EPA.*

the applicability of PBE to FT resistance under various curing conditions. For further analysis, additional experimental investigations on aged or deteriorated concrete structures will be necessary in the future.

## Freezing-and-thawing performance-based evaluation considering climate change in New York City

To develop the SC considering climate change in the New York City area, the FT cycle reduction rate of the U.S. EPA, shown in Fig. 6, was used. The U.S. EPA SSs for curing temperature and RH are shown in Fig. 6(a) and (b), respectively. Comparisons of the 10-year FT resistance SCs for curing temperature and RH developed based on climate change predictions of the FHWA and U.S. EPA are shown in Fig. 7(a) and (b), respectively. In general, FT resistance life increases when climate change is considered, because the annual FT cycles are reduced due to global warming. More specifically, the FT resistance life based on the FHWA climate change prediction increases after 10 years. The T35H40, T35H65, T40H40, and T45H95 specimens showed 2 to 3 years longer FT resistance life. On the other hand, the FT resistance life for the T35H95 and T40H95 specimens could not be calculated, because for the duration of 150 years, the reduction in annual FT days exceeded the annual FT cycles, which theoretically eliminated the possibility of an FT event occurring. Moreover, no changes in FT resistance life were observed under other temperature and RH curing combinations.

The 10-year FT resistance life SCs for curing temperature, developed based on the FHWA and U.S. EPA climate change predictions, showed the largest difference, as shown in Fig. 7. As shown in Fig. 7(a), the FT resistance life showed a difference of approximately 25% satisfaction percentage within the temperature range of 13 to 25°C when climate change was considered. With respect to the FT resistance life for curing RH, approximately a 10% difference in satisfaction percentage occurred, as shown in Fig. 7(b). This trend can be attributed to the annual FT cycles decreasing by 0.38 days due to U.S. EPA climate change predictions, leading to an increase in FT resistance life and satisfaction percentage.

Additionally, because the number of FT cycles decreases each year due to global warming, the 100-year FT satisfaction percentage calculations are conducted to consider the long-term climate change predictions from various organizations, such as the FHWA and U.S. EPA. The comparative analysis revealed that the duration required to reach the 50% FT resistance satisfaction percentage is over 16 years, which is the same for both the FHWA and U.S. EPA predictions.

However, the duration required to reach the 30% satisfaction percentage for temperature curing conditions differed, with the FHWA prediction giving 22 years and the U.S. EPA prediction giving 24 years. For RH curing conditions, the FHWA predicted 48 years, and the U.S. EPA predicted 63 years. These differences can be attributed to the increase in temperature due to the global warming phenomenon from climate change, leading to reduced FT cycles and increased FT satisfaction levels.

## CONCLUSIONS

Based on the results of the study, the following conclusions are drawn:

1. In the freezing-and-thawing (FT) resistance tests under specific temperature and relative humidity (RH) curing conditions, relative dynamic modulus of elasticity (RDME) results from the specimens cured at 8 and 12°C were 8 to 31% lower than those from the specimens cured at 35 and 40°C. For the low-temperature curing condition, RDME decreased by 3 to 6% as RH increased, while for the high-temperature curing condition, RDME increased by 5 to 10% as RH increased.

2. Regarding the FT resistance prediction for New York City, the FT resistance lives of specimens cured at 8 and 12°C (considered as low curing temperatures) were two to 13 times shorter than those of specimens cured at 35, 40, and 45°C. At low temperatures of 8 and 12°C, the FT resistance life decreased by 10 to 20% as the RH curing condition increased. Conversely, at optimal temperatures of 35 and 40°C, the FT resistance life increased by four to five times as the RH curing condition increased.

3. The satisfaction increase rate after 5 years of FT exposure was relatively similar for all the curing temperatures, while the satisfaction increase rate after 10, 15, and 20 years of FT exposure was significant as the curing temperature increased. For 10-year FT resistance SC, the satisfaction percentage rapidly increased for the curing temperature up to 20°C, then tapered off beyond 20°C. The comparison of the FT resistance life predictions from the developed satisfaction graphs and the test data curve-fitted RDME equations revealed that the FT resistance life sharply decreased by 9 to 11 years for the temperature conditions of 8 and 12°C and the RH conditions of 40 and 65%.

4. The 10-year FT resistance life satisfaction curves (SCs) for curing temperature developed based on the Federal Highway Administration (FHWA) and United States Environmental Protection Agency (U.S. EPA) climate change predictions showed the largest difference. The FT resistance life showed a difference of approximately 25% satisfaction percentage within the temperature range of 13 to 25°C when climate change was considered. With respect to the FT resistance life for curing RH, approximately a 10% difference in satisfaction percentage occurred.

5. The proposed method offers a probabilistic framework for evaluating FT resistance based on satisfaction levels under various curing conditions, rather than relying on prescriptive life predictions. While the extrapolated RDME models provide useful insights into long-term performance, they are primarily intended for comparative purposes and require further validation. This study tried to overcome the limitations of test variability and curve fitting by performing the analysis using statistical averaging. This approach can be considered a performance-based evaluation (PBE) strategy for concrete exposed to FT cycles under various environmental conditions.

## FURTHER STUDY

Because the study has already been completed, FT data of other cement type mixture proportions are not available at this time. Therefore, in a future study, more quantitative data from additional mixture proportions using various cement types, fly ash, silica fume, ground-granulated blast-furnace slag, and ferro-nickel slag will be collected. In addition, the durability behavior with respect to chloride penetration resistance and carbonation tests will be quantified.

## AUTHOR BIOS

**Jin-Su Kim** *is a PhD Student in the Department of Civil and Environmental Engineering at Yonsei University, Sinchon, Seoul, South Korea. He received his BS from Induk University, Seoul, South Korea. His research interests include the durability of reinforced concrete structures in climatic environments.*

**Woo-Ri Kwon** *is an MS Student in the Department of Civil and Environmental Engineering at Yonsei University. She received her BS from Hanyang University's ERICA Campus, Ansan, Gyeonggi, South Korea. Her research interests include enhancing the durability of concrete with carbon fiber-reinforced polymer.*

**Norhazilan Md Noor** *is a Professor of structure and materials at Universiti Teknologi Malaysia, Skudai, Johor, Malaysia. He received his BS and MS from Universiti Teknologi Malaysia, and his PhD from Heriot-Watt University, Edinburgh, UK. His research interests include structural reliability and risk assessment, and probabilistic assessment and artificial intelligence (AI)-driven digital twin technologies for marine and oil and gas infrastructure.*

**Jang-Ho Jay Kim** *is a Professor of civil engineering and environmental engineering at Yonsei University. He received his BS from the University of California, Los Angeles, Los Angeles, CA; his MS from the University of California, Berkeley, Berkeley, CA; and his PhD from Northwestern University, Evanston, IL. His research interests include the performance-based evaluation of the durability of reinforced concrete structures.*

## ACKNOWLEDGMENTS

This work is supported by the Korea Agency for Infrastructure Technology Advancement (KAIA) grant funded by the Ministry of Land, Infrastructure and Transport (Grant RS-2021-KA163381).

## NOTATION

$a_i$ = design material requirement of variable I
$c_1, c_2$ = coefficients obtained from curve fitting
$DF$ = durability index of test specimen
$F(.)$ = SC of specific material requirement
$M$ = cycle at end of FT exposure
$N$ = determined by total number of related material data obtained for material performance evaluation
$N_{FT}$ = number of FT cycles
$N_o$ = number of cycles in which relative dynamic modulus of elasticity becomes 60% or number of cycles at end of freezing-and-thawing exposure
$n_c^2$ = primary resonance frequency (Hz) of deformation vibration in FT cycle $N_o$
$n_o^2$ = primary resonance frequency (Hz) of deformation vibration in FT cycle 0
$P_c$ = relative dynamic modulus of elasticity (%) after freezing-and-thawing cycle $N_o$
$x_i$ = determined to be 0 or 1 depending on satisfaction to material performance value such as $a_i$

## REFERENCES

1. Anderson, K., "What was the Industrial Revolution's Environmental Impact?" Greenly Leaf Media, Aug. 25, 2024, https://greenly.earth/en-us/blog/ecology-news/what-was-the-industrial-revolutions-environmental-impact. (last accessed Feb. 23, 2026)

2. Neale, P. J.; Hylander, S.; Banaszak, A. T.; Häder, D.-P.; Rose, K. C.; Vione, D.; Wängberg, S.-Å.; Jansen, M. A. K.; Busquets, R.; Andersen, M. P. S.; Madronich, S.; Hanson, M. L.; Schikowski, T.; Solomon, K. R.; Sulzberger, B.; Wallington, T. J.; Heikkilä, A. M.; Pandey, K. K.; Andrady, A. L.; Bruckman, L. S.; White, C. C.; Zhu, L.; Bernhard, G. H.; Bais, A.; Aucamp, P. J.; Chiodo, G.; Cordero, R. R.; Petropavlovskikh, I.; Neale, R. E.; Olsen, C. M.; Hales, S.; Lal, A.; Lingham, G.; Rhodes, L. E.; Young, A. R.; Robson, T. M.; Robinson, S. A.; Barnes, P. W.; Bornman, J. F.; Harper, A. B.; Lee, H.; Mackenzie Calderón, R.; Ossola, R.; Paul, N. D.; Revell, L. E.; Wang, Q.-W.; and Zepp, R. G., "Environmental Consequences of Interacting Effects of Changes in Stratospheric Ozone, Ultraviolet Radiation, and Climate: UNEP Environmental Effects Assessment Panel, Update 2024," *Photochemical & Photobiological Sciences*, V. 24, No. 3, Mar. 2025, pp. 357-392.

3. Leal Filho, W.; Azul, A. M.; Brandli, L.; Lange Salvia, A.; and Wall, T., eds., *Affordable and Clean Energy*, Springer, Cham, Switzerland, 2021, 1309 pp.

4. IPCC Working Group 1 Technical Support Unit, eds., "Climate Change 2021: The Physical Science Basis," Working Group I Contribution to the Sixth Assessment Report of the Intergovernmental Panel on Climate Change, Cambridge University Press, Cambridge, UK, 2021, 2409 pp.

5. Shen, D., *Early-age Cracking Control on Modern Concrete*, Springer, Singapore, 2024, 439 pp.

6. Alshammari, T. O.; Guadagnini, M.; and Pilakoutas, K., "The Effect of Harsh Environmental Conditions on Concrete Plastic Shrinkage Cracks: Case Study Saudi Arabia," *Materials*, V. 15, No. 23, Dec. 2022, Article No. 8622. doi: 10.3390/ma15238622

7. Xia, D.; Yu, S.; Yu, J.; Feng, C.; Li, B.; Zheng, Z.; and Wu, H., "Damage Characteristics of Hybrid Fiber Reinforced Concrete Under the Freeze-Thaw Cycles and Compound-Salt Attack," *Case Studies in Construction Materials*, V. 18, July 2023, Article No. e01814. doi: 10.1016/j.cscm.2022.e01814

8. Fülöp, L.; Ferreira, M.; Bohner, E.; Valokoski, J.; Vuotari, J.; and Tirkkonen, T., "Inspection of Bridges for Effects of Air-Entrainment on the Porosity and Compressive Strength of Concretes," *Case Studies in Construction Materials*, V. 17, Dec. 2022, Article No. e01211. doi: 10.1016/j.cscm.2022.e01211

9. Ma, Q.; Xiao, J.; Ding, T.; Duan, Z.; Song, M.; and Cao, X., "The Prediction of Compressive Strength for Recycled Coarse Aggregate Concrete in Cold Region," *Case Studies in Construction Materials*, V. 19, Dec. 2023, Article No. e02546. doi: 10.1016/j.cscm.2023.e02546

10. Ji, Y., and Wang, D., "Durability of Recycled Aggregate Concrete in Cold Regions," *Case Studies in Construction Materials*, V. 17, Dec. 2022, Article No. e01475.

11. Guo, J.; Zhou, Z.; Zhang, Z.; Tang, J.; Li, X.; and Zou, Y., "Effects of Alternating Positive and Negative Temperature Curing on the Mechanical Properties of Ultra-High Performance Concrete," *Case Studies in Construction Materials*, V. 20, July 2024, Article No. e02752. doi: 10.1016/j.cscm.2023.e02752

12. Guo, J.; Sun, W.; Xu, Y.; Lin, W.; and Jing, W., "Damage Mechanism and Modeling of Concrete in Freeze–Thaw Cycles: A Review," *Buildings*, V. 12, No. 9, Sept. 2022, Article No. 1317. doi: 10.3390/buildings12091317

13. Luo, S.; Bai, T.; Guo, M.; Wei, Y.; and Ma, W., "Impact of Freeze–Thaw Cycles on the Long-Term Performance of Concrete Pavement and Related Improvement Measures: A Review," *Materials*, V. 15, No. 13, July 2022, Article No. 4568. doi: 10.3390/ma15134568

14. Wang, R.; Hu, Z.; Li, Y.; Wang, K.; and Zhang, H., "Review on the Deterioration and Approaches to Enhance the Durability of Concrete in the Freeze–Thaw Environment," *Construction and Building Materials*, V. 321, Feb. 2022, Article No. 126371. doi: 10.1016/j.conbuildmat.2022.126371

15. Joshaghani, A.; Balapour, M.; and Ramezanianpour, A. A., "Effect of Controlled Environmental Conditions on Mechanical, Microstructural and Durability Properties of Cement Mortar," *Construction and Building Materials*, V. 164, Mar. 2018, pp. 134-149. doi: 10.1016/j.conbuildmat.2017.12.206

16. Shen, X.; Li, L.; Cui, W.; and Feng, Y., "Coupled Heat and Moisture Transfer in Building Material with Freezing and Thawing Process," *Journal of Building Engineering*, V. 20, Nov. 2018, pp. 609-615. doi: 10.1016/j.jobe.2018.07.026

17. Chen, J.; Li, Y.; Li, Y.; Wen, L.; and Guo, H., "Effects of Curing Conditions with Different Temperature and Humidity on Damage Evolution of Concrete During Freeze–Thaw Cycling," *Materials and Structures*, V. 55, No. 2, Mar. 2022, Article No. 80. doi: 10.1617/s11527-022-01921-z

18. ASTM C192/C192M-12, "Standard Practice for Making and Curing Concrete Test Specimens in the Laboratory," ASTM International, West Conshohocken, PA, 2012, 8 pp.

19. ASTM C666/C666M-15, "Standard Test Method for Resistance of Concrete to Rapid Freezing and Thawing (Withdrawn 2024)," ASTM International, West Conshohocken, PA, 2015, 6 pp.

20. Hansen, W.; Jensen, E. A.; and Mohr, P., "The Effects of Higher Strength and Associated Concrete Properties on Pavement Performance," Report No. FHWA-RD-006-161, Federal Highway Administration, McLean, VA, 2001, 255 pp.

21. EPA, "Technical Documentation: Freeze-Thaw Conditions," U.S. Environmental Protection Agency, Washington, DC, 2023, 10 pp.

22. ASTM C39/C39M-05, "Standard Test Method for Compressive Strength of Cylindrical Concrete Specimens," ASTM International, West Conshohocken, PA, 2005, 7 pp.

23. ASTM C1231/C1231M-09, "Standard Practice for Use of Unbonded Caps in Determination of Compressive Strength of Hardened Concrete Cylinders," ASTM International, West Conshohocken, PA, 2009, 5 pp.

24. ASTM C215-19, "Standard Test Method for Fundamental Transverse, Longitudinal, and Torsional Resonant Frequencies of Concrete Specimens," ASTM International, West Conshohocken, PA, 2019, 7 pp.

25. Abate, M. S.; Evangelista, A. C. J.; and Tam, V. W. Y., "Global Research Trends in Performance-Based Structural Design: A Comprehensive Bibliometric Analysis," *Buildings*, V. 15, No. 3, Feb. 2025, Article No. 363. doi: 10.3390/buildings15030363

26. Kim, J.-H. J.; Phan, H. D.; Yi, N.-H.; Kim, S.-B.; and Jeong, H.-S., "Application of the One-Parameter Bayesian Method as the PBMD for Concrete Mix Proportion Design," *Magazine of Concrete Research*, V. 63, No. 1, Jan. 2011, pp. 31-47. doi: 10.1680/macr.2011.63.1.31

27. Kim, J.-H. J.; Phan, H. D.; Kim, B.-Y.; Choi, J.-W.; and Han, T.-S., "Development of Satisfaction Curves to Evaluate Concrete Mix Design Performance Using a Bayesian Probabilistic Method," *Construction and Building Materials*, V. 27, No. 1, Feb. 2012, pp. 578-584. doi: 10.1016/j.conbuildmat.2011.07.005

28. Phan, H. D.; Kim, J.-H. J.; Yi, N.-H.; You, Y.-J.; and Kim, J.-W., "Strength Targeted PBMD of HSC based on One-parameter Bayesian Probabilistic Method," *Journal of Advanced Concrete Technology*, V. 10, No. 4, 2012, pp. 137-150. doi: 10.3151/jact.10.137

29. Kim, T.-K.; Choi, S.-J.; Choi, J.-H.; and Kim, J.-H. J., "Prediction of Chloride Penetration Depth Rate and Diffusion Coefficient Rate of Concrete from Curing Condition Variations due to Climate Change Effect," *International Journal of Concrete Structures and Materials*, V. 13, No. 1, Dec. 2019, Article No. 15. doi: 10.1186/s40069-019-0333-4

30. Kang, S.-H.; Lee, J.-H.; Hong, S.-G.; and Moon, J., "Microstructural Investigation of Heat-Treated Ultra-High Performance Concrete for Optimum Production," *Materials*, V. 10, No. 9, Sept. 2017, Article No. 1106. doi: 10.3390/ma10091106

31. Zhang, X.; Yang, J.; Li, K.; Pu, H.; Meng, X.; Zhang, H.; and Liu, K., "Effects of Steam on the Compressive Strength and Microstructure of Cement Paste Cured Under Alternating Ultrahigh Temperature," *Cement and Concrete Composites*, V. 112, Sept. 2020, Article No. 103681.

32. Chen, F., and Qiao, P., "Probabilistic Damage Modeling and Service-Life Prediction of Concrete Under Freeze–Thaw Action," *Materials and Structures*, V. 48, No. 8, Aug. 2015, pp. 2697-2711. doi: 10.1617/s11527-014-0347-y

33. Yan, W.; Wu, Z.; Niu, F.; Wan, T.; and Zheng, H., "Study on the Service Life Prediction of Freeze–Thaw Damaged Concrete with High Permeability and Inorganic Crystal Waterproof Agent Additions Based on Ultrasonic Velocity," *Construction and Building Materials*, V. 259, Oct. 2020, Article No. 120405. doi: 10.1016/j.conbuildmat.2020.120405

ACI MATERIALS JOURNAL TECHNICAL PAPER

Title No. 123-M27

# Effects of Limestone Powder on Chloride Concentration of Cement Paste

by X. Wang, W. Deng, Q. Zhang, X. Jia, R. Chen, M. Wang, R. Chen, L. Weng, and D. Wang

*The concentration of chloride ions involves both chemical binding and physical adsorption. This study investigated how limestone powder and supplementary cementitious materials (SCMs) synergistically affect chloride concentration in cement paste, using analyses of corrosion products, pore structure, and the chloride concentration coefficient. Cement pastes with 0 to 50% limestone powder and fly ash or slag were tested. Results showed that the synergy between limestone powder and fly ash or slag promoted carboaluminate formation, which completely converted to Friedel's salt in chloride environments. This enhanced chemical binding and increased physical adsorption of chloride ions, while reducing porosity and the most probable pore diameter. When limestone powder was 5 to 25% with fly ash less than 10%, or both limestone powder and slag were 20 to 30%, the chloride concentration coefficient reached its peak. Thus, proper limestone powder content improves chloride resistance by enhancing both chemical and physical chloride binding.*

**Keywords:** carboaluminate; chloride concentration; Friedel's salt; limestone powder (LP); supplementary cementitious materials (SCMs); synergistic effect.

## INTRODUCTION

The cement industry accounts for approximately 5 to 8% of global anthropogenic $CO_2$ emissions (Chang et al. 2022). Incorporating supplementary cementitious materials (SCMs) such as fly ash (FA) and slag can reduce emissions (Gartner 2004), but their limited availability restricts broader application and sustainability. Hence, low-carbon, abundant alternatives are in demand. Limestone powder (LP), a waste by-product of crushed limestone, contributes to pollution. Using LP as a cement substitute reduces both cost and $CO_2$ emissions (Wang et al. 2017). Studies show LP promotes early hydration by serving as nucleation sites (Kang et al. 2019). It reacts with $C_3A$ to form carboaluminates, which refine pore structure and enhance performance through their chemical and filling roles (Antoni et al. 2012; Li and Jiang 2020). However, excessive LP may cause substantial performance degradation due to dilution. Based on extensive research and practical applications, LP has been incorporated into national standards worldwide. The British standard allows up to 20%, with some cases permitting 35% (Elgalhud et al. 2016; Irassar 2009). European standard EN 197-1 permits 5% as an addition and defines four types of portland-limestone cement with 6 to 35% LP (Irassar 2009). The Chinese standard for limestone portland cement (JC/T 600-2010 [2010]) allows 10 to 25%, while that for common portland cement (GB 175-2007 [2007]) stipulates a maximum LP content of 5%. In alkali-activated systems, LP improves reaction kinetics, pore structure, strength, and shrinkage resistance (Marsh et al. 2022; Rashad et al. 2021), expanding its applicability across cementitious materials.

Chloride-induced reinforcing bar corrosion has caused serious economic losses (Elgalhud et al. 2016; Wang et al. 2018a, 2019a; Shi et al. 2017a). Scholars generally find that when chloride-ion concentration exceeds a threshold, it breaks down the passive film on steel (Wang et al. 2021b), initiating localized corrosion that degrades reinforcing bar mechanical performance and reduces structural reliability (Stewart and Al-Harthy 2008; Gu et al. 2018). Hornain et al. (1995) found the addition of LP can effectively reduce the chloride-ion diffusion coefficient. Wang et al. (2023) investigated chloride transport in alkali-activated slag-LP systems under various marine environments and found that 10% LP achieved the lowest diffusion coefficient, as small LP additions improved microstructure. However, excessive LP content had adverse effects. Li and Jiang (2022) showed that 8 wt. % LP reduced total porosity and increased the proportion of fine pores, indicating that the improved pore-size distribution may be responsible for the decreased chloride diffusion coefficient. Lollini et al. (2014) reported that 5 to 15% LP had minimal impact on $Cl^-$ penetration resistance. However, some studies have shown that excessive LP increases chloride ingress. Bonavetti et al. (2000) reported 43% and 114% increases in $Cl^-$ penetration depth with 10% and 20% LP, respectively. Hosseini and Eftekhari (2022) observed a significant rise in permeability coefficient under seawater curing at 30% LP. Elgalhud et al. (2018) reported that 35% LP increased chloride intrusion by approximately 60% compared to concrete without LP. Li and Jiang (2023) reported that the $Cl^-$ binding capacity decreased with increasing LP content in concrete due to reduced physical adsorption and chemical binding.

Due to variations in the physical and chemical properties of LP, its effect on chloride permeability remains inconsistent. Notably, the chloride permeability coefficient does not accurately reflect the free $Cl^-$ concentration in pore solution, which is a key factor in steel corrosion. Nagataki et al. (1993) reported that after 10 years of seawater exposure, the $Cl^-$ concentration in pore solution exceeded that of seawater by over four times, a phenomenon known as chloride

---

*ACI Materials Journal*, V. 123, No. 2, March 2026.

MS No. M-2025-071.R3, doi: 10.14359/51749271, received August 8, 2025, and reviewed under Institute publication policies. Pertinent discussion including author's closure, if any, will be published ten months from this journal's date if the discussion is received within four months of the paper's print publication.

**Table 1—Chemical components of cementitious materials, wt. %**

| No. | CaO | $SiO_2$ | $Al_2O_3$ | $Fe_2O_3$ | MgO | $SO_3$ | MnO | $Na_2O$ | $K_2O$ | $TiO_2$ | LOI |
|---|---|---|---|---|---|---|---|---|---|---|---|
| C | 63.93 | 20.78 | 5.01 | 3.50 | 2.01 | 2.21 | — | — | — | — | 1.80 |
| LP | 52.66 | 0.52 | 0.27 | 0.24 | 2.66 | — | — | — | — | — | 43.33 |
| FA | 3.32 | 51.34 | 34.82 | 5.33 | 0.605 | — | 0.053 | 0.371 | 1.23 | 1.85 | 1.081 |
| S | 41.20 | 30.70 | 14.00 | 0.40 | 9.90 | — | 0.3 | 0.5 | 0.40 | 1.40 | 0.95 |

Note: LOI is loss on ignition.

concentration, which involves both chemical binding and physical adsorption. The chloride concentration coefficient is commonly used to evaluate this. Glass et al. (1996) found that after immersing slices of cement paste in 0.135 mol/L NaCl solution, the free $Cl^-$ concentration in filtrate increased over time and exceeded the immersion solution by approximately 30% after 28 days. Similarly, Baroghel-Bouny et al. (2007) reported that after soaking in an 18.2 g/L chloride solution, the water-soluble $Cl^-$ content of samples eventually doubled that of the soaking solution. Therefore, it is essential to explore how LP influences the chloride concentration coefficient of cement-based materials under chloride exposure. The limited study found that pastes with 10%, 20%, and 30% LP had concentration coefficients 9.1%, 98.2%, and 94.2% higher than those without LP (Xiao et al. 2017). While existing studies primarily focus on the durability of concrete containing LP, including resistance to water and chloride penetration, carbonation, sulfate attack, and freezing-and-thawing cycles, the specific impact of LP on the chloride concentration coefficient remains underexplored.

The aluminate phase in SCMs or $C_3A$ in cement can chemically react with LP to form carboaluminate, demonstrating a synergistic effect. Alyousef et al. (2023) found that combining FA, LP, and ultrafine filler improves high-strength concrete porosity. Carboaluminates produced from reactions between LP and the aluminum phase in the SCMs or cement help fill pores and reduce porosity (Li and Jiang 2020; Lothenbach et al. 2008). Similarly, combining metakaolin with LP refines the pore structure, enhances strength, and improves chloride resistance (Zunino and Scrivener 2021). Moreover, calcium carbonate and calcium hydroxide can react with aluminum phases to form hemicarboaluminate (Hc) and monocarboaluminate (Mc) (Zolfagharnasab et al. 2021), which are thermodynamically more stable than Friedel's salt, resulting in a lower chloride binding capacity (Wang et al. 2019b). Therefore, it is essential to study how LP combined with FA or slag influences the chemical binding and physical adsorption of $Cl^-$ in cementitious materials, as well as the composition and chemical properties of corrosion products, pore structure, and chloride concentration.

Since the chloride concentration phenomenon in cement-based materials was first reported (Nagataki et al. 1993), various studies have explored factors influencing the chloride concentration coefficient. Xiao et al. (2017) examined the effects of the amount and particle size of LP on the chloride-ion concentration performance through the chloride-ion concentration coefficient, while Alyousef et al. (2023) focused on the influence of FA, LP, and fillers on the porosity of high-performance concrete under different curing conditions, without addressing the phenomenon of chloride concentration. However, research on the synergistic effects of LP and SCMs on this phenomenon remains limited. To address this, 15 mixture designs were prepared using the simplex-centroid method, immersed in 0.5 mol/L NaCl solution for 42 days, and tested for $Cl^-$ content in pore solutions extracted by press filtration to calculate the chloride concentration coefficient. Scanning electron microscopy (SEM) and mercury intrusion porosimetry (MIP) were used to examine microstructure and pore characteristics, while thermogravimetric analysis (TGA) and X-ray diffraction (XRD) characterized corrosion products. This study provides guidance for the safe application of concrete mixed with LP in chloride environments.

## RESEARCH SIGNIFICANCE

Chloride-ion erosion is a main reason of steel corrosion in concrete. However, limited research exists on the synergistic effect of LP and SCMs on the chloride concentration coefficient. This study addresses this gap by revealing their combined influence, offering a sustainable alternative to traditional SCMs and theoretical support for low-cost, low-carbon concrete design. The findings are significant for improving concrete durability and advancing green buildings.

## EXPERIMENTAL INVESTIGATION

### Materials

The chemical compositions of cement (C), LP, FA, and slag (S) (measured by X-ray fluorescence) used in this study are listed in Table 1. The P·I 42.5 cement meets GB 175-2007 specifications. LP has a specific surface area of 500 $m^2$/kg (2441.2 $ft^2$/lb) and a mean particle size of 32.42 μm (1.3 mil) (measured by laser diffraction particle-size analyzer). Both FA and slag conform to GB/T 51003-2014 (2014). Deionized water was used throughout the experiments.

### Experimental procedure

The relationship between concrete properties and material composition can be effectively established using a simplex-centroid design (Nagataki et al. 1993), which has been applied in previous studies to evaluate multicomponent cementitious systems (Shi and Day 1993; Wu et al. 2018; Shi et al. 2015, 2018; Wang and Zhang 2021). The main advantage of this design is its ability to relate concrete performance to mixture composition with minimal testing, enabling the construction of contour maps using mathematical models and software, providing a clear understanding of the effects of individual components. In this study, 15 mixture designs were prepared with a water-binder ratio of 0.4; the mixture proportions are presented in Fig. 1 and Table 2.

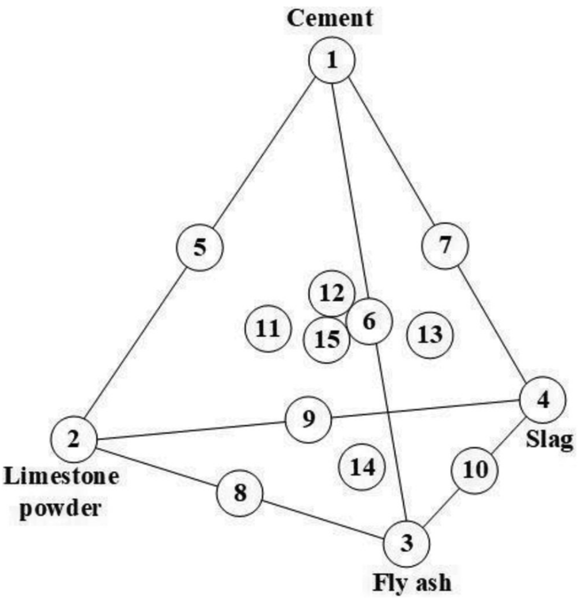

*Fig. 1—Cement-LP-FA-slag cementitious material composition design.*

Cement pastes were cast in polyvinyl chloride (PVC) tubes (50 mm [2.0 in.] diameter x 200 mm [7.9 in.] length), sealed with double-layer plastic film. After 24 hours of standard curing, the pastes were cut into 5 mm (0.2 in.) slices, then water-cured at 20 ± 2°C (68 ± 3.6°F) for 28 days and saturated in limewater for 24 hours. Specimens were immersed in 0.5 mol/L NaCl solution for 42 days (solution-to-paste volume ratio of 40:1, with solution renewed every 2 weeks). Chloride content was analyzed in 1 mm increments within the top 5 mm using a milling machine. Collected powders were stored for analysis. Results showed $Cl^-$ content stabilized at 2.0 to 2.3%, with minimal variation across depths, indicating uniform chloride distribution.

## Test method

*X-ray diffraction (XRD)*—The samples were crushed into smaller pieces, immersed in anhydrous ethanol for 24 hours to terminate hydration, and then ground. The ground powder was vacuum-dried at 40°C (104°F) until constant mass, followed by sieving through a 45 μm (1.8 mil) mesh. All procedures were conducted under vacuum to avoid carbonation.

XRD analysis was carried out using an X-ray diffractometer operating at 30 kV and 10 mA. Scanning was performed from 5 to 55 degrees at 2 deg/min with a test step size of 0.02 degrees. Phase identification was conducted using Jade software.

*Thermogravimetric analysis (TGA)*—Sample preparation followed the XRD procedure. Approximately 10 ± 0.1 mg of powder was tested in a simultaneous thermal analyzer under nitrogen ($N_2$) protection. Thermogravimetric (TG) and differential thermogravimetric analysis (DTG) curves were used to estimate Friedel's salt and $Ca(OH)_2$ contents. Because LP decomposes upon heating, releasing $CO_2$ and causing mass loss, the measured residue underestimates the true residual solid content. So the residual mass at 550°C (1022°F) was taken as the baseline (De Weerdt et al. 2011), as major carbonate decomposition occurs above this temperature. This correction ensures accurate quantification of phase components.

**Table 2—Design of cementitious materials composition of cement-LP-FA-slag binder, wt. %**

| No. | Mixture proportions | | | |
|---|---|---|---|---|
| | Cement | LP | FA | Slag |
| C100 | 100 | 0 | 0 | 0 |
| C50L50 | 50 | 50 | 0 | 0 |
| C50F50 | 50 | 0 | 50 | 0 |
| C50S50 | 50 | 0 | 0 | 50 |
| C75L25 | 75 | 25 | 0 | 0 |
| C75F25 | 75 | 0 | 25 | 0 |
| C75S25 | 75 | 0 | 0 | 25 |
| C50L25F25 | 50 | 25 | 25 | 0 |
| C50L25S25 | 50 | 25 | 0 | 25 |
| C50F25S25 | 50 | 0 | 25 | 25 |
| C66L17F17 | 67 | 17 | 17 | 0 |
| C66L17S17 | 67 | 17 | 0 | 17 |
| C66F17S17 | 67 | 0 | 17 | 17 |
| C50L17F17S17 | 50 | 17 | 17 | 17 |
| C62.5L12.5F12.5S12.5 | 62.5 | 12.5 | 12.5 | 12.5 |

Friedel's salt decomposes at approximately 325°C (617°F) (Shi et al. 2017b), and its decomposition equation is as follows (Eq. (1)). Friedel's salt content $\omega_F$ was calculated as Eq. (2)

$$C_3A \cdot CaCl_2 \cdot 10H_2O \xrightarrow{325°C} C_3A + CaCl_2 + 10H_2O \tag{1}$$

$$\omega_F = \frac{\omega_{mass\ loss} \times M_F \times 100\%}{10M_{H_2O} \times \omega_{residual\ mass}} \tag{2}$$

where $\omega_{mass\ loss}$ represents the mass loss at approximately 325°C (617°F) in the TG curve; $\omega_{residual\ mass}$ indicates the corresponding residual mass at approximately 550°C (1022°F); $M_{H2O}$ is the molar mass of $H_2O$; and $M_F$ is the molar mass of Friedel's salt.

$Ca(OH)_2$ decomposes at approximately 450°C (842°F), and its decomposition equation is as follows (Eq. (3)). $Ca(OH)_2$ content $\omega_{CH}$ was calculated as Eq. (4)

$$Ca(OH)_2 \xrightarrow{450°C} CaO + H_2O\uparrow \tag{3}$$

$$\omega_{CH} = \frac{\omega_{mass\ loss} \times M_{CH} \times 100\%}{M_{H_2O} \times \omega_{residual\ mass}} \tag{4}$$

where $M_{CH}$ is the molar mass of $Ca(OH)_2$.

*Scanning electron microscopy (SEM)*—Samples were immersed in anhydrous ethanol for 24 hours to stop hydration, dried in a vacuum oven at 40°C (104°F), gold-coated by vacuum sputtering, and examined for micromorphology

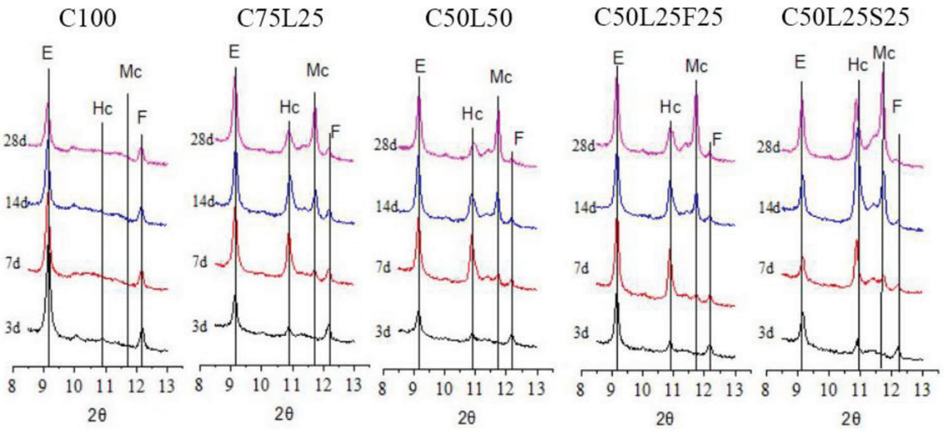

*Fig. 2—XRD patterns of samples before immersing in 0.5 mol/L NaCl solution for 42 days (Li and Jiang 2020). (Note: E is ettringite; Hc is hemicarbonate; Mc is monocarbonate; F is ferrite phase.)*

using a multifunctional tungsten filament scanning electron microscope.

*Mercury intrusion porosimetry (MIP)*—MIP was performed using a porosimeter with a pressure range of 7.10 to 344,738 kPa (1.03 to 50,000 psi), covering pore sizes from 3 to 1080 μm (0.1 to 42.5 mil). Pore structure data were obtained by combining low- and high-pressure intrusion curves.

*$Cl^-$ concentration coefficient*—Currently, two main methods are used to determine free chloride-ion concentration in cement paste. The first is high-pressure filtration, which may slightly overestimate chloride levels due to partial extraction of bound chlorides. The second is solvent extraction, which is less reliable due to chloride binding during immersion and variability from immersion and stirring times. High-pressure filtration is the most widely adopted due to its superior accuracy and lower margin of error (Glass et al. 1996). In this study, specimens were placed in an extrusion device under a 3000 kN (674,427 lb) press. The process involved two 180-second loading cycles, reaching up to 900 kN (202,328 lb). The expressed pore solution was collected immediately and sealed in plastic vials.

The pore solution obtained by pressure filtration was diluted 20 times. Then 1 mL of the dilution was transferred to a beaker, followed by the addition of deionized water and concentrated nitric acid. The $Cl^-$ concentration was determined using an automatic potentiometric titrator. The chloride concentration in the 1 mL diluted sample was recorded, and the chloride concentration coefficient ($N$) was calculated using Eq. (5)

$$N = \frac{c_k}{c_j} \tag{5}$$

where $c_j$ is the $Cl^-$ concentration of the soaking solution; and $c_k$ is the $Cl^-$ concentration of the pore solution.

## RESULTS AND DISCUSSION

### Phase identification of cement pastes by XRD

As demonstrated in the authors' previous publication (Wang et al. 2019a) (Fig. 2), no carboaluminate diffraction peaks were detected in cement pastes without LP. However, the synergistic effect of LP and SCMs promoted carboaluminate formation. After 42 days of NaCl solution immersion, no carboaluminate peaks were observed (Fig. 3), suggesting its complete transformation into Friedel's salt, likely due to the replacement of carbonate ions by chloride ions in carboaluminate ($C_4ACH_{11}$; $C_4AC_{0.5}H_{12}$) to form Friedel's salt ($C_4AClH_{10}$).

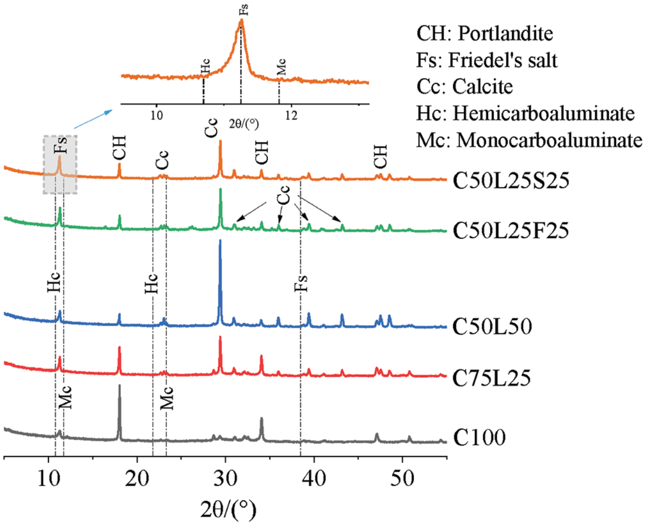

*Fig. 3—XRD patterns of samples after immersing in 0.5 mol/L NaCl solution for 42 days.*

As shown in Fig. 3, the Friedel's salt peak at $2\theta$ = 11.3 degrees is weaker in the C50L50 group than in C75L25, indicating that higher LP content reduces the availability of aluminum phases. This reduces the paste's ability to solidify the $Cl^-$. Similarly, Sui et al. (2019) reported that increasing LP content from 0 to 55% reduced physically adsorbed chloride and overall chloride binding capacity.

Furthermore, Friedel's salt peaks in the C50L25F25 group are stronger than in C50L50, indicating that FA enhances chloride binding. This is linked to the hydration of the aluminum phase, where higher aluminum phase content increases $Cl^-$ binding capacity (Luo et al. 2002). In chloride environments, carbonate ions in carboaluminate can be replaced by $Cl^-$, with Hc transforming into Friedel's salt (Mesbah et al.

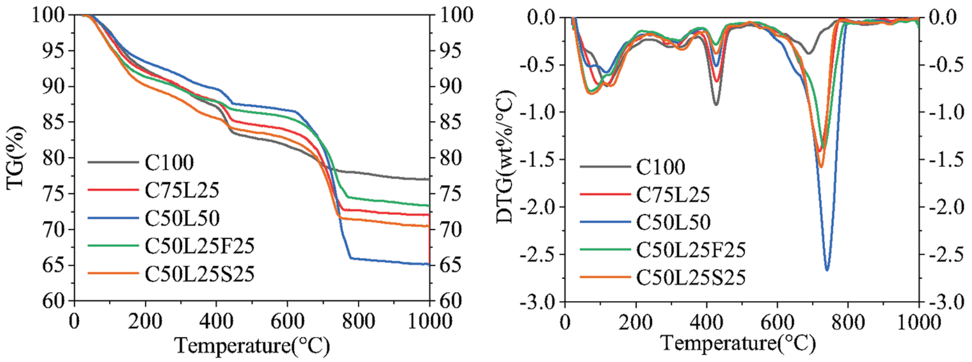

(a)

(b)

*Fig. 4—TG-DTG patterns of samples after immersing in 0.5 mol/L NaCl solution for 42 days: (a) TG curve; and (b) DTG curve. (Note: °F = [°C × 1.8] + 32.)*

**Table 3—Contents of $Ca(OH)_2$ and Friedel's salt in different samples after immersing in 0.5 mol/L NaCl solution for 42 days**

| No. | Mass loss at ~300°C (572°F), % | Friedel's salt content, % | Mass loss at ~450°C (842°F), % | $Ca(OH)_2$, % |
|---|---|---|---|---|
| C100 | 0.77 | 2.91 (1.12%) | 3.77 | 18.81 (2.46%) |
| C75L25 | 0.82 | 3.03 (1.67%) | 2.77 | 13.50 (1.53%) |
| C50L50 | 0.47 | 1.67 (2.08%) | 1.99 | 9.32 (2.37%) |
| C50L25F25 | 0.97 | 3.51 (2.36%) | 0.96 | 4.58 (2.61%) |
| C50L25S25 | 1.43 | 5.35 (2.28%) | 1.25 | 6.17 (2.31%) |

Note: Values in parentheses are relative standard deviations (RSD).

2011). FA promotes carboaluminate formation, which binds more chloride ions, yielding higher Friedel's salt peaks. Similarly, C50L25S25 shows stronger peaks than C50L50 due to slag's high active $Al_2O_3$ content, which promotes carboaluminate and calcium-aluminum-silicate-hydrate (C-(A)-S-H) formation, generating more Friedel's salt and increasing chloride binding capacity (Mapa et al. 2023). Zunino and Scrivener (2021) reported that LP and metakaolin in blended cement form hemicarboaluminate and monocarboaluminate (Hc/Mc), improving pore structure, though their study focused on porosity and mechanical performance without considering chloride exposure. In contrast, the authors' study shows that LP with FA or slag not only promotes carboaluminate formation but also facilitates its transformation into Friedel's salt in chloride-rich environments, enhancing chemical chloride binding and providing added durability benefits. Similarly, Li and Jiang (2023) found that in cement-LP binary systems, LP's dilution effect reduced Friedel's salt formation and chloride binding capacity. The authors' study shows that combining LP with FA or slag overcomes this limitation by promoting the transformation of carboaluminates into Friedel's salt, thereby improving chemical chloride binding.

## Quantitative analysis of hydration products by TG-DTG

Figure 4 shows the TG-DTG pattern of samples, with quantitative calculation results in Table 3. The Friedel's salt contents of the C100, C75L25, C50L50, and C50L25F25 were 2.91%, 3.03%, 1.67%, and 3.51%, respectively. The Friedel's salt contents of C100 and C75L25 are not much different. As the use of LP increased, the formation of Friedel's salt decreased, consistent with the XRD analysis results. Compared with the C75L25 group, the Friedel's salt content in the C50L50 group was reduced by 44.9%. This decline is not solely due to dilution. Ipavec et al. (2013) reported that LP reduces chloride binding in high-alkalinity systems. In addition, the substitution of $SO_4$-AFm by $CO_3$-AFm in the reaction products is another significant factor (Balonis et al. 2010). Compared with the C50L50 group, the Friedel's salt content of the C50L25F25 group increased by 110.18%. The content of $Al_2O_3$ in FA is high, and the LP reacts with $Al_2O_3$ to form carboaluminate, which could chemically bind chloride ions. In addition, the excess aluminum phase in FA can also solidify chloride ions.

As shown in Eq. (6) and (7), $Ca(OH)_2$ is involved in the process of $Cl^-$ solidification by carboaluminate, leading to the formation of Friedel's salt (Wang et al. 2019a). In Eq. (8) to (10), the ionization of ≡SiOH is also affected by alkaline conditions (Xiao et al. 2017; Hu et al. 2018). These will affect the adsorption of $Cl^-$. Therefore, the influence of $Ca(OH)_2$ should be considered

$$C_4ACH_{11} + 2Cl^- + Ca(OH)_2 \rightarrow C_4ACl_2H_{10} + CaCO_3 + 2OH^- + H_2O \quad (6)$$

$$C_4AC_{0.5}H_{12} + 2Cl^- + 0.5Ca(OH)_2 \rightarrow C_4ACl_2H_{10} + 0.5CaCO_3 + 2OH^- + 1.5H_2O \quad (7)$$

$$\equiv SiOH \Rightarrow \equiv SiO^- + H^+ \quad (8)$$

$$\equiv SiO^- + Ca^{2+} \Rightarrow \equiv SiOCa^+ \quad (9)$$

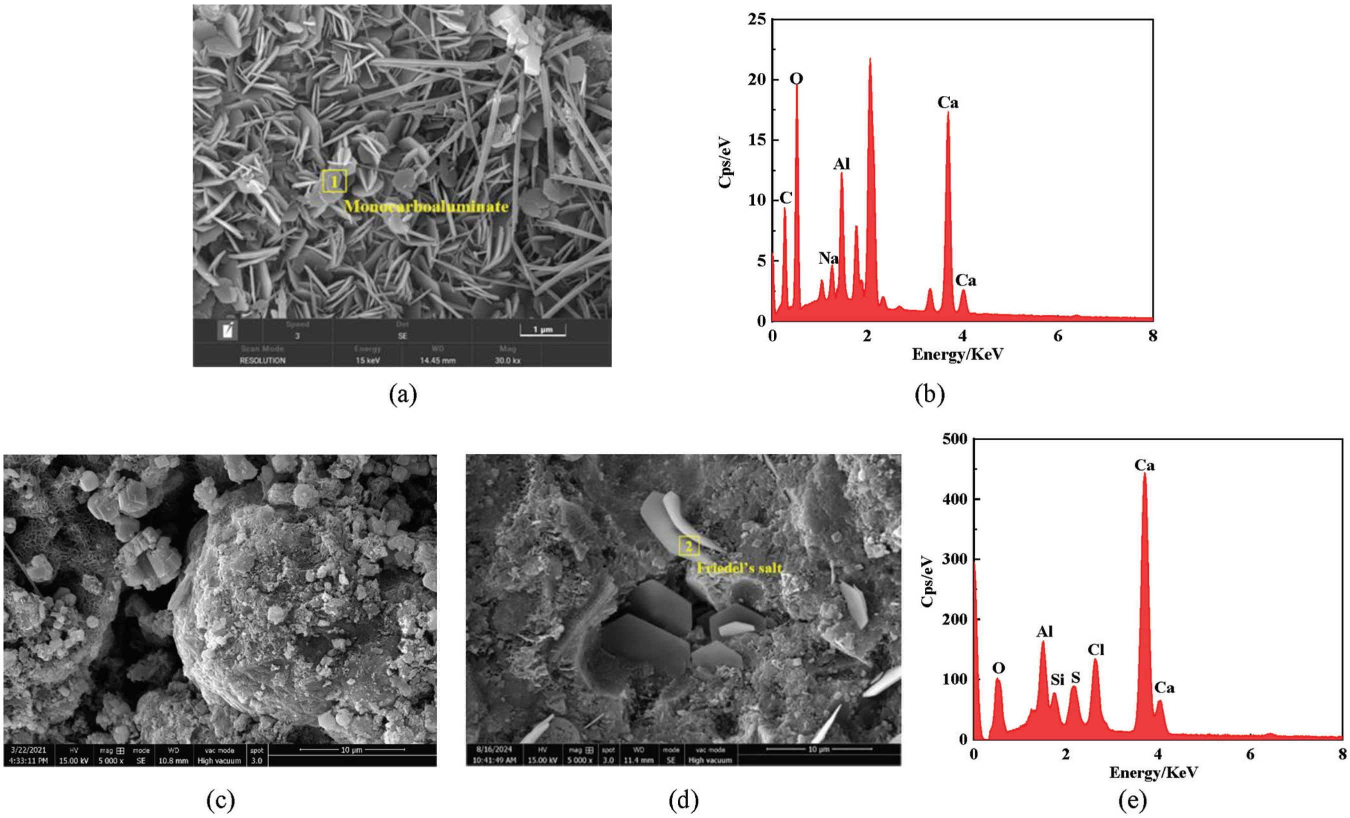

(a) (b)

(c) (d) (e)

*Fig. 5—SEM pictures of specimens before and after immersing in 0.5 mol/L NaCl solution for 42 days. Before immersing: (a) C50L50, ×30,000 times; and (b) EDX elemental analysis of point "1." After immersing: (c) C50L25F25, ×5000 times; (d) C50L25F25, ×5000 times; and (e) EDX elemental analysis of point "2."*

$$\equiv \mathrm{SiOCa^{+}} + \mathrm{Cl^{-}} \Rightarrow \equiv \mathrm{SiOCaCl} \quad (10)$$

Table 3 shows that the contents of $Ca(OH)_2$ in the C100, C75L25, C50L50, and C50L25F25 groups are 18.81%, 13.50%, 9.32%, and 4.58% respectively. This decreasing trend results from the reduction in cement clinker with increasing LP content. Compared to C50L50, the $Ca(OH)_2$ content in C50L25F25 decreases by 50.86%, mainly due to the pozzolanic reaction of FA and further cement dilution by LP. As shown in Fig. 4 and Table 3, compared with the C50L50 group, the Friedel's salt content in C50L25S25 increased by 220.36%, while $Ca(OH)_2$ decreased by 33.80%. This is attributed to the better chloride binding capacity of slag, which contains more active aluminum phases that react with $Cl^-$ to form Friedel's salt (Ukpata et al. 2019). Additionally, LP reacts with aluminum phases to form carboaluminate, further contributing to $Cl^-$ binding (Li et al. 2020). The pozzolanic reaction of slag also consumes significant amounts of $Ca(OH)_2$, explaining its lower content in C50L25S25.

The physical adsorption of $Cl^-$ is primarily attributed to calcium-silicate-hydrate (C-S-H) gel (Geng et al. 2015). To minimize interference from ettringite and adsorbed water within the 30 to 230°C (86 to 446°F) range, mass loss between 145 and 230°C (293 and 446°F) was used to estimate the relative C-S-H gel content (Chang and Fang 2015; Steiner et al. 2020). Although this method is not accurate enough, it allows for comparative analysis. As shown in Fig. 4, the C-S-H gel mass losses for C75L25, C50L50, C50L25F25, and C50L25S25 were 4.3%, 3.25%, 3.67%, and 4.32%, respectively. Compared to C50L50, the C-S-H gel content in C50L25S25 increased by 32.92%, due to the pozzolanic reaction of slag, which is rich in $Al_2O_3$ and $SiO_2$. In contrast, the C75L25 group produced more C-S-H gel, as excessive LP contributes little to hydration and instead exerts a dilution effect.

## Effects of synergistic effects of LP and SCMs on microscopic morphology of cement pastes

Figure 5 presents SEM images of hydration products in various cementitious systems before and after 42 days of immersion in 0.5 mol/L NaCl solution. In Fig. 5(a), hexagonal plate-like crystals with structural symmetry were observed. Elemental analysis in Fig. 5(b) identified these as Mc (Liu et al. 2024), consistent with Mc peaks in XRD. In Fig. 5(c), the surface of FA particles in the C50L25F25 group is uneven, indicating a notable pozzolanic reaction. Although FA shows low early reactivity, prolonged curing and chloride exposure promote secondary pozzolanic reactions that refine pore structure, reducing the volume of large pores and increasing the volume of small pores (Beaudoin et al. 1990). After immersion in NaCl solution, no carboaluminate was detected in any samples, but crystalline Friedel's salt was observed in the C50L25F25 group. As shown in Fig. 5(d), it exhibited a regular hexagonal plate-like morphology, consistent with previous findings (Xie 2020), and was confirmed by energy-dispersive X-ray spectroscopy (EDX) analysis (Fig. 5(e)). The high $Al_2O_3$ content in FA reacts with LP to form carboaluminate, which is then converted into Friedel's salt through ion exchange in chloride environments. The formation of Friedel's salt, with its larger volume, helps refine pore-size distribution and improve the compactness of the pore structure (Kim et al. 2019). Consequently, the C50L25F25 group shows a denser structure and higher chloride concentration coefficient than C50L50, consistent with Mao et al. (2022), who attributed the effect to the abundant alumina in FA, which promotes Friedel's salt formation.

### Effects of synergistic effects of LP and SCMs on pore structure of cement pastes

The pore structure results are presented in Fig. 6 and 7 and Table 4. Compared to the C50L50 group, the porosity of the C75L25 group decreased by 35.86%. In C50L50, the high LP content diluted the cementitious components, delaying hydration and increasing porosity. Studies have shown that when LP content exceeds 30 to 50%, both porosity and pore size tend to increase (Elgalhud et al. 2016; Li et al. 2018). He et al. (2019) also reported that LP additions above 50% elevated pore volume and reduced Archie's tortuosity coefficient.

The combination of LP and FA exhibited a strong synergistic effect, promoting carboaluminate formation, which subsequently converted into Friedel's salt and refined the pore structure. Compared to the C50L50 group, the most probable pore diameter and porosity of the C50L25F25 group decreased by 64.58% and 9.32%, respectively. The chemical reactivity of LP significantly affected the pore structure (He et al. 2019). Moreover, the additional alumina provided by FA enhanced carboaluminate formation, effectively filling voids in the interfacial transition zones and reducing overall porosity (Wang et al. 2018b).

The synergy between LP and slag also promoted carboaluminate formation, which converted into Friedel's salt and refined the pore structure. As shown in Table 4 and Fig. 6, the most probable pore diameter and porosity of the C50L25S25 group decreased by 83.35% and 40.53%, respectively, compared to the C50L50 group. This synergy reduced the proportion of larger pores, densified the microstructure, and refined the pore structure (Li and Jiang 2020). The resulting structure enhanced the influence of the electric double layer (EDL), improving Cl⁻ physical adsorption (Luo et al. 2002). Similar effects occur in systems with LP and metakaolin, where C-A-S-H formation replaces $CO_3$-AFm. Slag also contains abundant $Al^{3+}$, and through the interaction between aluminate and calcite, further enhances the synergistic effect in ternary blends (Dhandapani et al. 2021).

As shown in Table 4 and Fig. 7, harmful and multi-harmful pores (>50 nm [$>2.0 \times 10^{-6}$ in.]) accounted for 50.70% in the C50L50 group, 166.84% higher than in C75L25. Compared with the C50L50 group, C50L25F25 and C50L25S25 showed marked reductions, with the proportion of harmful and multi-harmful pores decreased by 62.35% and 77.18%,

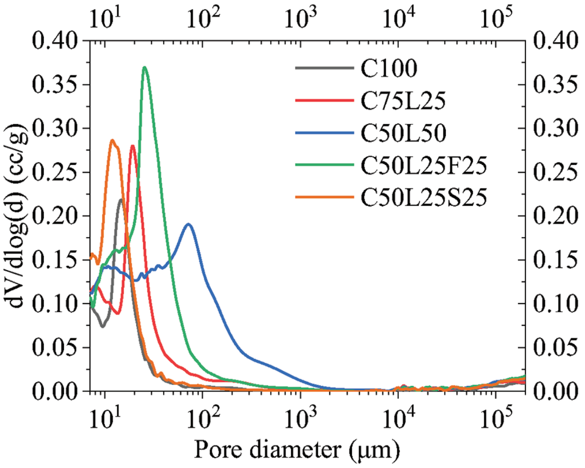

*Fig. 6—Pore structure of cement paste after immersing in 0.5 mol/L NaCl solution for 42 days. (Note: 1 μm = 3.937 × $10^{-5}$ in.)*

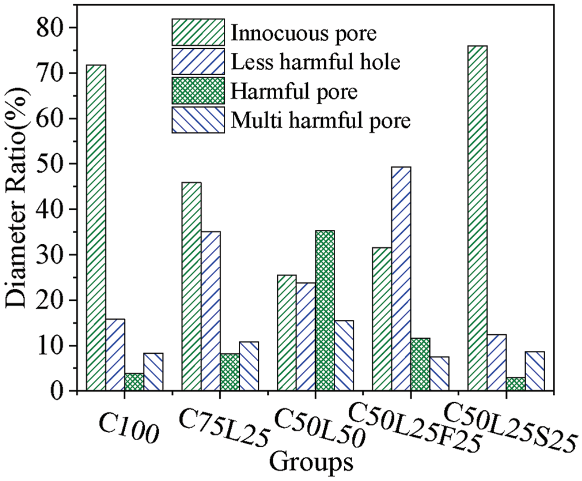

*Fig. 7—Pore-size distribution of samples.*

**Table 4—Pore structure characteristic parameters of samples after immersing in 0.5 mol/L NaCl solution for 42 days**

| No. | Total porosity, % | Most probable pore size, nm | Pore-size distribution, %<br>Innocuous pore (≤20 nm) | Less harmful hole (20 to 50 nm) | Harmful pore (50 to 200 nm) | Multi-harmful pore (≥200 nm) |
|---|---|---|---|---|---|---|
| C100 | 14.88 (2.11%) | 14.62 | 71.76 | 15.81 | 3.88 | 8.35 |
| C75L25 | 21.95 (1.37%) | 19.26 | 45.88 | 35.12 | 8.17 | 10.83 |
| C50L50 | 34.22 (2.54%) | 71.76 | 25.47 | 23.83 | 35.27 | 15.43 |
| C50L25F25 | 31.03 (2.42%) | 25.42 | 31.59 | 49.32 | 11.58 | 7.51 |
| C50L25S25 | 20.35 (1.39%) | 11.95 | 76.00 | 12.43 | 2.90 | 8.67 |

Note: Values in parentheses are RSD; 1 nm = 3.937 × $10^{-8}$ in.

**Table 5—Chloride concentration coefficient of different samples**

| No. | Curing time, days | Soaking time, days | Soaking solution concentration, mol/L | $c_k$, mol/L (RSD) | $N$ |
|---|---|---|---|---|---|
| C100 | 28 | 42 | 0.5 | 0.6862 (4.57%) | 1.3724 |
| C50L50 | 28 | 42 | 0.5 | 0.6428 (5.29%) | 1.2856 |
| C50F50 | 28 | 42 | 0.5 | 0.6562 (6.55%) | 1.3124 |
| C50S50 | 28 | 42 | 0.5 | 0.5086 (6.37%) | 1.0172 |
| C75L25 | 28 | 42 | 0.5 | 0.7383 (7.21%) | 1.4766 |
| C75F25 | 28 | 42 | 0.5 | 0.7010 (6.33%) | 1.4020 |
| C75S25 | 28 | 42 | 0.5 | 0.6563 (5.58%) | 1.3126 |
| C50L25F25 | 28 | 42 | 0.5 | 0.7026 (8.36%) | 1.4052 |
| C50L25S25 | 28 | 42 | 0.5 | 0.8926 (6.98%) | 1.7852 |
| C50F25S25 | 28 | 42 | 0.5 | 0.6030 (7.51%) | 1.2060 |
| C66L17F17 | 28 | 42 | 0.5 | 0.5888 (6.35%) | 1.1776 |
| C66L17S17 | 28 | 42 | 0.5 | 0.9236 (4.27%) | 1.8472 |
| C66F17S17 | 28 | 42 | 0.5 | 0.5996 (7.39%) | 1.1992 |
| C50L17F17S17 | 28 | 42 | 0.5 | 0.7841 (8.21%) | 1.5682 |
| C62.5L12.5F12.5S12.5 | 28 | 42 | 0.5 | 0.7437 (6.44%) | 1.4874 |

Note: $c_k$ is $Cl^-$ concentration of pore solution; $N$ is chloride concentration coefficient.

respectively, indicating that increased Friedel's salt formation effectively refined the pore structure.

The synergistic effects of FA or slag and LP refine the pores and increase the proportion of gel pores (<100 nm [<3.9 × $10^{-6}$ in.]) in cement paste. According to EDL theory, as the pore size decreases, the charge on the pore wall increases. In cement paste, the overlap of diffusion layers occurs in gel pores rather than in capillary pores (He et al. 2016). If the pores in cement paste become smaller, the transmission of $Cl^-$ will become more difficult due to the overlapping effect of the EDL, and the adsorption of the charge will also be enhanced (Hu et al. 2020; Wang et al. 2021a). Therefore, refining the pore size could enhance $Cl^-$ adsorption in cement pastes.

## Effects of synergistic effects of LP and SCMs on chloride concentration coefficient of cement pastes

After pressure filtration, the calculated results for chloride concentration coefficients are listed in Table 5. As shown in Fig. 8, these coefficients decreased with increasing LP content. Compared to C100 and C75L25, C50L50 exhibited reductions of 6.32% and 12.94%, respectively, mainly due to the dilution effect. LP reduced the contents of tricalcium silicate ($C_3S$) and dicalcium silicate ($C_2S$), leading to less C-S-H gel, which is primarily responsible for $Cl^-$ physical adsorption (Geng et al. 2015; Chang and Fang 2015). Liu et al. (2023) also reported improved chloride resistance using various SCMs at a 30% replacement level.

The chloride concentration coefficient of the C50L25F25 group is 1.4052, 9.30% higher than that of C50L50, indicating that FA enhances $Cl^-$ physical adsorption in cement pastes. The main active components in FA are $Al_2O_3$ and $SiO_2$. It has been demonstrated that $SiO_2$ can undergo a reaction with $Ca(OH)_2$ to form a secondary C-S-H gel, improving $Cl^-$ physical adsorption. Although FA has limited early pozzolanic activity (Steiner et al. 2020), it still increases chloride binding after 42 days of immersion in 0.5 mol/L NaCl solution. However, its coefficient is 4.84% lower than C75L25, likely because $OH^-$ consumption during hydration hinders Si-OH deprotonation in C-S-H, reducing $Cl^-$ adsorption. Additionally, a lower Ca/Si ratio from FA incorporation may weaken chloride binding (Guo et al. 2013). As shown in Fig. 8, when LP ranges between 5 and 25% and the FA is less than 10%, cement pastes show the highest coefficient and strongest free $Cl^-$ adsorption.

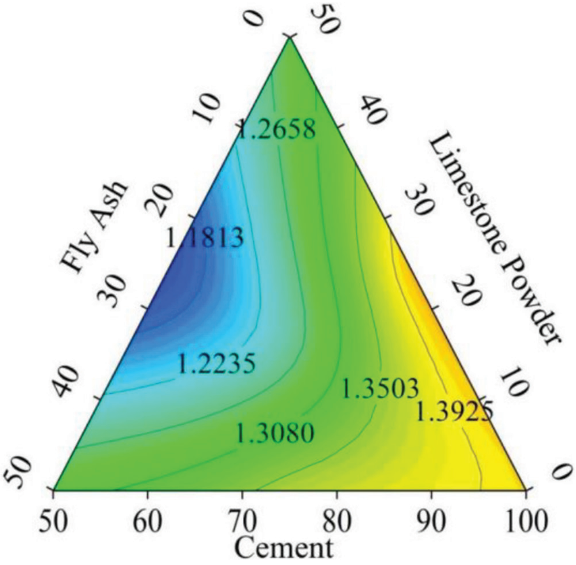

*Fig. 8—Triangular contour diagram of chloride concentration coefficient of cement-LP-FA cementitious material.*

The chloride concentration coefficient of the C50L25S25 group is 38.86% higher than that of C50L50, indicating that slag significantly enhances $Cl^-$ adsorption. This improvement is attributed to the high reactivity of slag within the first 28 days, during which $Ca(OH)_2$ reacts with slag to form additional C-S-H gel (Thomas et al. 2012), thereby increasing the physical adsorption capacity of $Cl^-$ and the chloride concentration coefficient. As shown in Fig. 9, when both LP and slag are in the range of 20 to 30%, the chloride concentration coefficient reaches its maximum, reflecting the strongest $Cl^-$ adsorption capacity.

A regression model was developed based on 15 uniformly designed mixtures to quantify the relationship between the chloride concentration coefficient and the contents of LP, FA, and slag. The model (Eq. (11) to (15)) captures not only the direct effect of LP but also its synergistic interactions with FA and slag, offering insights into the compositional dependence of chloride binding in blended systems

$$Y = \beta_1 x_1 + \beta_2 x_2 + \beta_3 x_3 + \beta_4 x_4 + \beta_{12} x_1 x_2 + \beta_{13} x_1 x_3 + \beta_{14} x_1 x_4 + \beta_{23} x_2 x_3 + \beta_{24} x_2 x_4 + \beta_{34} x_3 x_4 + \beta_{123} x_1 x_2 x_3 + \beta_{124} x_1 x_2 x_4 - \beta_{134} x_1 x_3 x_4 + \beta_{234} x_2 x_3 x_4 + \beta_{1234} x_1 x_2 x_3 x_4 \tag{11}$$

$$Y = 1.3724 x_1 + 0.018 x_2 + 0.7756 x_3 - 0.2804 x_4 + 2.3616 x_1 x_2 + 0.9536 x_1 x_3 + 1.8848 x_1 x_4 + 32.4267 x_2 x_3 - 13.2706 x_2 x_4 + 14.5311 x_2 x_4 - 61.4551 x_1 x_2 x_3 + 46.8228 x_1 x_2 x_4 - 27.7438 x_1 x_3 x_4 - 105.3127 x_2 x_3 x_4 + 206.7706 x_1 x_2 x_3 x_4 \tag{12}$$

$$\frac{\delta_Y}{\delta_{x_2}} = 0.018 + 2.3616 x_1 + 32.4267 x_2 - 13.2706 x_4 - 61.4551 x_1 x_3 + 46.8228 x_1 x_4 - 105.3127 x_3 x_4 + 206.7706 x_1 x_3 x_4 \tag{13}$$

$$\frac{\delta_Y}{\delta_{x_3}}\left(\frac{\delta_Y}{\delta_{x_2}}\right) = 32.4267 - 61.4551 x_1 - 105.3127 x_4 + 206.7706 x_1 x_4 \tag{14}$$

$$\frac{\delta_Y}{\delta_{x_4}}\left(\frac{\delta_Y}{\delta_{x_2}}\right) = -13.2706 + 46.8228 x_1 - 105.3127 x_3 + 206.7706 x_1 x_3 \tag{15}$$

where $Y$ is the chloride concentration coefficient; $x_1$, $x_2$, $x_3$, and $x_4$ represent the proportions of cement, LP, FA, and slag, respectively; and $\beta_i$ is the coefficient.

## CONCLUSIONS AND PERSPECTIVES

### Conclusions

To investigate the synergistic effects of limestone powder (LP) with fly ash (FA) or slag on chloride binding behavior—including chemical binding, physical adsorption, phase composition, corrosion product characteristics, pore structure, and chloride concentration coefficient of cement paste—15 sample groups were prepared using a simplex-centroid design. Thermogravimetric analysis (TGA), X-ray diffraction (XRD), scanning electron microscopy (SEM), mercury intrusion porosimetry (MIP), and chloride concentration coefficient tests were conducted. The main conclusions are as follows:

1. The synergy of LP with FA or slag promoted carboaluminate formation and its complete conversion to Friedel's salt, increasing its content by 110.18% and 220.36% in the C50L25F25 and C50L25S25 groups, respectively, compared with C50L50.

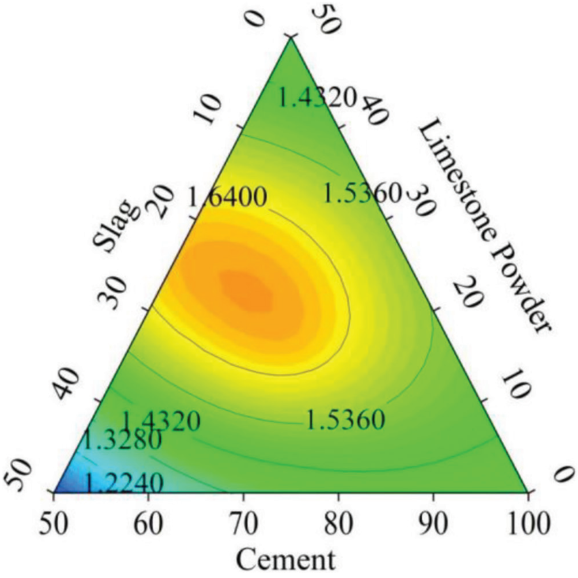

*Fig. 9—Triangular contour diagram of chloride concentration coefficient of cement-LP-slag cementitious material.*

2. LP combined with FA or slag enhanced chemical binding and physical adsorption of $Cl^-$, improving the pore-size distribution of the cement paste. Compared with C50L50, the most probable pore diameters in C50L25F25 and C50L25S25 decreased by 64.58% and 83.35%, and porosity by 9.32% and 40.53%, respectively.

3. The chloride concentration coefficient of cement paste is mainly determined by the composition and chemical properties of hydration products and pore structure. When LP was 5 to 25% and FA was less than 10%, the cement-LP-FA system showed the highest chloride concentration coefficient and strongest free $Cl^-$ adsorption. Similarly, with both LP and slag at 20 to 30%, the cement-LP-slag system achieved the highest coefficient and optimal $Cl^-$ adsorption performance.

4. This study advanced beyond the provisions of standards such as EN 197-1 and GB 175-2007 by providing systematic experimental evidence on the synergistic effects of LP with supplementary cementitious materials (SCMs) on chloride concentration and binding mechanisms. The results identified specific binder combinations and replacement ratios that maximize chloride binding and improve resistance to chloride ingress, thereby offering a scientific basis for optimizing LP use in reinforced concrete exposed to chloride environments.

### Perspectives

The study reveals that when LP is used at 5 to 25% and FA is less than 10%, or both LP and slag are at 20 to 30%, the cementitious systems exhibit the highest chloride concentration coefficient and strongest chloride binding capacity. However, the applicability of these optimal formulations under various exposure conditions (for example, atmospheric, splash, tidal, and immersion zones) remains unexplored, limiting their practical implementation. Future research should focus on evaluating the performance of these optimized binders in different environmental conditions to facilitate their broader application in concrete structures.

## AUTHOR BIOS

**Xuefang Wang** *is an Associate Researcher in the School of Civil Engineering at Fuzhou University, Fuzhou, China, where she received her MS and PhD. She received her BS from Sichuan Union University, Chengdu, China. Her research interests include the material science of concrete.*

**Wenhui Deng** *is a Graduate Student in the School of Civil Engineering at Fuzhou University. His research interests include the durability of cementitious materials.*

**Qizhi Zhang** *is a Graduate Student in the School of Civil Engineering at Fuzhou University. His research interests include the material science of concrete.*

**Xuxiu Jia** *is a Graduate Student in the School of Civil Engineering at Fuzhou University. Her research interests include the material science of concrete.*

**Rong Chen** *is an Engineer at Hengchao Construction Engineering Group Co., Ltd. His research interests include materials and durability.*

**Ming Wang** *is an Engineer at Hengchao Construction Engineering Group Co., Ltd. His research interests include chloride transport in concrete.*

**Ran Chen** *is an Engineer at Fujian Red Coral Construction Co., Ltd. His research interests include materials and durability.*

**Lincheng Weng** *is an Engineer at Haoyao Times (Fujian) Group Co., Ltd. His research interests include the durability of concrete.*

**Dehui Wang** *is an Associate Researcher in the School of Civil Engineering at Fuzhou University. His research interests include the material science of concrete.*

## ACKNOWLEDGMENTS

The authors sincerely acknowledge the support from the National Natural Science Foundation of China (51608187) and the Starting Research Fund from Fuzhou University (XRC-18016).

## REFERENCES

Alyousef, R.; Abbass, W.; Aslam, F.; and Gillani, S. A. A., 2023, "Characterization of High-Performance Concrete Using Limestone Powder and Supplementary Fillers in Binary and Ternary Blends under Different Curing Regimes," *Case Studies in Construction Materials*, V. 18, Article No. e02058. doi: 10.1016/j.cscm.2023.e02058

Antoni, M.; Rossen, J.; Martirena, F.; and Scrivener, K., 2012, "Cement Substitution by a Combination of Metakaolin and Limestone," *Cement and Concrete Research*, V. 42, No. 12, pp. 1579-1589. doi: 10.1016/j.cemconres.2012.09.006

Balonis, M.; Lothenbach, B.; Le Saout, G.; and Glasser, F. P., 2010, "Impact of Chloride on the Mineralogy of Hydrated Portland Cement Systems," *Cement and Concrete Research*, V. 40, No. 7, pp. 1009-1022. doi: 10.1016/j.cemconres.2010.03.002

Baroghel-Bouny, V.; Belin, P.; Maultzsch, M.; and Henry, D., 2007, "AgNO$_3$ Spray Tests: Advantages, Weaknesses, and Various Applications to Quantify Chloride Ingress into Concrete. Part 1: Non-Steady-State Diffusion Tests and Exposure to Natural Conditions," *Materials and Structures*, V. 40, No. 8, pp. 759-781. doi: 10.1617/s11527-007-9233-1

Beaudoin, J. J.; Ramachandran, V. S.; and Feldman, R. F., 1990, "Interaction of Chloride and C-S-H," *Cement and Concrete Research*, V. 20, No. 6, pp. 875-883. doi: 10.1016/0008-8846(90)90049-4

Bonavetti, V.; Donza, H.; Rahhal, V.; and Irassar, E., 2000, "Influence of Initial Curing on the Properties of Concrete Containing Limestone Blended Cement," *Cement and Concrete Research*, V. 30, No. 5, pp. 703-708. doi: 10.1016/S0008-8846(00)00217-9

Chang, J., and Fang, Y., 2015, "Quantitative Analysis of Accelerated Carbonation Products of the Synthetic Calcium Silicate Hydrate (C–S–H) by QXRD and TG/MS," *Journal of Thermal Analysis and Calorimetry*, V. 119, No. 1, pp. 57-62. doi: 10.1007/s10973-014-4093-8

Chang, Z.; Long, G.; Xie, Y.; and Zhou, J. L., 2022, "Recycling Sewage Sludge Ash and Limestone for Sustainable Cementitious Material Production," *Journal of Building Engineering*, V. 49, Article No. 104035. doi: 10.1016/j.jobe.2022.104035

De Weerdt, K.; Sellevold, E.; Kjellsen, K. O.; and Justnes, H., 2011, "Fly Ash–Limestone Ternary Cements: Effect of Component Fineness," *Advances in Cement Research*, V. 23, No. 4, pp. 203-214. doi: 10.1680/adcr.2011.23.4.203

Dhandapani, Y.; Santhanam, M.; Kaladharan, G.; and Ramanathan, S., 2021, "Towards Ternary Binders Involving Limestone Additions — A Review," *Cement and Concrete Research*, V. 143, Article No. 106396. doi: 10.1016/j.cemconres.2021.106396

Elgalhud, A. A.; Dhir, R. K.; and Ghataora, G., 2016, "Limestone Addition Effects on Concrete Porosity," *Cement and Concrete Composites*, V. 72, pp. 222-234. doi: 10.1016/j.cemconcomp.2016.06.006

Elgalhud, A. A.; Dhir, R. K.; and Ghataora, G., 2018, "Chloride Ingress in Concrete: Limestone Addition Effects," *Magazine of Concrete Research*, V. 70, No. 6, pp. 292-313. doi: 10.1680/jmacr.17.00177

Gartner, E., 2004, "Industrially Interesting Approaches to 'Low-CO$_2$' Cements," *Cement and Concrete Research*, V. 34, No. 9, pp. 1489-1498. doi: 10.1016/j.cemconres.2004.01.021

GB 175-2007, 2007, "Common Portland Cement," Standardization Administration of the People's Republic of China, Beijing, China.

GB/T 51003-2014, 2014, "Technical Code for Application of Mineral Admixture," Ministry of Housing and Urban-Rural Development of the People's Republic of China, Beijing, China.

Geng, J.; Easterbrook, D.; Li, L.; and Mo, L., 2015, "The Stability of Bound Chlorides in Cement Paste with Sulfate Attack," *Cement and Concrete Research*, V. 68, pp. 211-222. doi: 10.1016/j.cemconres.2014.11.010

Glass, G. K.; Wang, Y.; and Buenfeld, N. R., 1996, "An Investigation of Experimental Methods Used to Determine Free and Total Chloride Contents," *Cement and Concrete Research*, V. 26, No. 9, pp. 1443-1449. doi: 10.1016/0008-8846(96)00115-9

Gu, X.; Guo, H.; Zhou, B.; Zhang, W.; and Jiang, C., 2018, "Corrosion Non-Uniformity of Steel Bars and Reliability of Corroded RC Beams," *Engineering Structures*, V. 167, pp. 188-202. doi: 10.1016/j.engstruct.2018.04.020

Guo, M.; Guan, X.; and Zhang, H., 2013, "Study on Chloride Binding Ability of Ettringite," *Materials Reports*, V. 27, No. 10, pp. 136-139.

He, F.; Shi, C.; Hu, X.; Wang, R.; Shi, Z.; Li, Q.; Li, P.; and An, X., 2016, "Calculation of Chloride Ion Concentration in Expressed Pore Solution of Cement-Based Materials Exposed to a Chloride Salt Solution," *Cement and Concrete Research*, V. 89, pp. 168-176. doi: 10.1016/j.cemconres.2016.08.006

He, Z.; Cai, R.; Chen, E.; and Tang, S., 2019, "The Investigation of Early Hydration and Pore Structure for Limestone Powder Wastes Blended Cement Pastes," *Construction and Building Materials*, V. 229, Article No. 116923. doi: 10.1016/j.conbuildmat.2019.116923

Hornain, H.; Marchand, J.; Duhot, V.; and Moranville-Regourd, M., 1995, "Diffusion of Chloride Ions in Limestone Filler Blended Cement Pastes and Mortars," *Cement and Concrete Research*, V. 25, No. 8, pp. 1667-1678. doi: 10.1016/0008-8846(95)00163-8

Hosseini, S. A., and Eftekhari, N., 2022, "Permeability of Concrete Containing Limestone Powder in Marine Curing Conditions," *Iranian Journal of Science and Technology, Transactions of Civil Engineering*, V. 46, No. 3, pp. 1853-1861. doi: 10.1007/s40996-021-00720-w

Hu, X.; Shi, C.; Yuan, Q.; Zhang, J.; and De Schutter, G., 2018, "Influences of Chloride Immersion on Zeta Potential and Chloride Concentration Index of Cement-Based Materials," *Cement and Concrete Research*, V. 106, pp. 49-56. doi: 10.1016/j.cemconres.2018.01.015

Hu, X.; Shi, C.; Zhu, D.; and de Schutter, G., 2020, "Investigation on Influential Factors on Chloride Concentration Index of Cement-Based Materials by Pore Solution Expression Method," *Construction and Building Materials*, V. 231, Article No. 117135. doi: 10.1016/j.conbuildmat.2019.117135

Ipavec, A.; Vuk, T.; Gabrovšek, R.; and Kaučič, V., 2013, "Chloride Binding into Hydrated Blended Cements: The Influence of Limestone and Alkalinity," *Cement and Concrete Research*, V. 48, pp. 74-85. doi: 10.1016/j.cemconres.2013.02.010

Irassar, E. F., 2009, "Sulfate Attack on Cementitious Materials Containing Limestone Filler — A Review," *Cement and Concrete Research*, V. 39, No. 3, pp. 241-254. doi: 10.1016/j.cemconres.2008.11.007

JC/T 600-2010, 2010, "Limestone Portland Cement," Ministry of Industry and Information Technology of the People's Republic of China, Beijing, China.

Kang, S.-H.; Jeong, Y.; Tan, K. H.; and Moon, J., 2019, "High-Volume Use of Limestone in Ultra-High Performance Fiber-Reinforced Concrete for Reducing Cement Content and Autogenous Shrinkage," *Construction and Building Materials*, V. 213, pp. 292-305. doi: 10.1016/j.conbuildmat.2019.04.091

Kim, T.; Kim, I.-T.; Seo, K.-Y.; and Park, H.-J., 2019, "Strength and Pore Characteristics of OPC-Slag Cement Paste Mixed with Polyaluminum Chloride," *Construction and Building Materials*, V. 223, pp. 616-628. doi: 10.1016/j.conbuildmat.2019.07.009

Li, C., and Jiang, L., 2020, "Utilization of Limestone Powder as an Activator for Early-Age Strength Improvement of Slag Concrete," *Construction and Building Materials*, V. 253, Article No. 119257. doi: 10.1016/j.conbuildmat.2020.119257

Li, C., and Jiang, L., 2022, “Effect of Limestone Powder Addition on Corrosion Initiation Time of Reinforced Concrete,” *Journal of Building Engineering*, V. 59, Article No. 105132. doi: 10.1016/j.jobe.2022.105132

Li, C., and Jiang, L., 2023, “The Role of Chloride Binding Mechanism in the Interpretation of Chloride Profiles in Concrete Containing Limestone Powder,” *Journal of Sustainable Cement-Based Materials*, V. 12, No. 1, pp. 24-35. doi: 10.1080/21650373.2021.2010243

Li, C.; Jiang, L.; and Li, S., 2020, “Effect of Limestone Powder Addition on Threshold Chloride Concentration for Steel Corrosion in Reinforced Concrete,” *Cement and Concrete Research*, V. 131, Article No. 106018. doi: 10.1016/j.cemconres.2020.106018

Li, C.; Jiang, L.; Xu, N.; and Jiang, S., 2018, “Pore Structure and Permeability of Concrete with High Volume of Limestone Powder Addition,” *Powder Technology*, V. 338, pp. 416-424. doi: 10.1016/j.powtec.2018.07.054

Liu, J.-C.; Hossain, M. U.; Xuan, D.; Ali, H. A.; Ng, S. T.; and Ye, H., 2023, “Mechanical and Durability Performance of Sustainable Concretes Containing Conventional and Emerging Supplementary Cementitious Materials,” *Developments in the Built Environment*, V. 15, Article No. 100197. doi: 10.1016/j.dibe.2023.100197

Liu, Y.; Zhang, M.; Dong, B.; and Wang, Y., 2024, “Influence of Microcrystalline $AH_3$ Content on Properties of High Alkali Carboaluminate Cementitious Materials,” *Journal of Building Materials*, V. 27, No. 12, pp. 1135-1142.

Lollini, F.; Redaelli, E.; and Bertolini, L., 2014, “Effects of Portland Cement Replacement with Limestone on the Properties of Hardened Concrete,” *Cement and Concrete Composites*, V. 46, pp. 32-40. doi: 10.1016/j.cemconcomp.2013.10.016

Lothenbach, B.; Le Saout, G.; Gallucci, E.; and Scrivener, K., 2008, “Influence of Limestone on the Hydration of Portland Cements,” *Cement and Concrete Research*, V. 38, No. 6, pp. 848-860. doi: 10.1016/j.cemconres.2008.01.002

Luo, R.; Cai, Y.; Wang, C.; and Huang, X., 2002, “The Mechanism of Ground Granulated Blast Furnace Slag to Resist Chloride Corrosion,” *China Civil Engineering Journal*, No. 6, pp. 100-104.

Mao, M.; Ai, Q.; Zhang, D.; Li, S.; and Li, J., 2022, “Durability Performance of Concrete with Fly Ash as Fine Aggregate Eroded by Chloride Salt,” *Advances in Materials Science and Engineering*, V. 2022, No. 1, Article No. 6760385. doi: 10.1155/2022/6760385

Mapa, D. G.; Zhu, H.; Nosouhian, F.; Shanahan, N.; Riding, K. A.; and Zayed, A., 2023, “Chloride Binding and Diffusion of Slag Blended Concrete Mixtures,” *Construction and Building Materials*, V. 388, Article No. 131584. doi: 10.1016/j.conbuildmat.2023.131584

Marsh, A. T. M.; Yue, Z.; Dhandapani, Y.; Button, K.; Adu-Amankwah, S.; and Bernal, S. A., 2022, “Influence of Limestone Addition on Sodium Sulphate Activated Blast Furnace Slag Cements,” *Construction and Building Materials*, V. 360, Article No. 129527. doi: 10.1016/j.conbuildmat.2022.129527

Mesbah, A.; Rapin, J.-P.; François, M.; Cau-dit-Coumes, C.; Frizon, F.; Leroux, F.; and Renaudin, G., 2011, “Crystal Structures and Phase Transition Of Cementitious Bi-Anionic AFm-($Cl^-$, $CO_3^{2-}$) Compounds,” *Journal of the American Ceramic Society*, V. 94, No. 1, pp. 261-268. doi: 10.1111/j.1551-2916.2010.04050.x

Nagataki, S.; Otsuki, N.; Wee, T.-H.; and Nakashita, K., 1993, “Condensation of Chloride Ion in Hardened Cement Matrix Materials and on Embedded Steel Bars,” *ACI Materials Journal*, V. 90, No. 4, July-Aug., pp. 323-332.

Rashad, A. M.; Morsi, W. M.; and Khafaga, S. A., 2021, “Effect of Limestone Powder on Mechanical Strength, Durability and Drying Shrinkage of Alkali-Activated Slag Pastes,” *Innovative Infrastructure Solutions*, V. 6, No. 2, Article No. 127. doi: 10.1007/s41062-021-00496-y

Shi, C., and Day, R. L., 1993, “Acceleration of Strength Gain of Lime-Pozzolan Cements by Thermal Activation,” *Cement and Concrete Research*, V. 23, No. 4, pp. 824-832. doi: 10.1016/0008-8846(93)90036-9

Shi, C.; Wang, D.; An, X.; and Jiao, D., 2018, “Method for Mixture Design of Concrete with Multiple Performance Requirements,” *Journal of the Chinese Ceramic Society*, V. 46, No. 2, pp. 230-238.

Shi, C.; Wang, D.; Jia, H.; and Liu, J., 2017a, “Role of Limestone Powder and its Effect on Durability of Cement-Based Materials,” *Journal of the Chinese Ceramic Society*, V. 45, No. 11, pp. 1582-1593.

Shi, C.; Wang, D.; Wu, L.; and Wu, Z., 2015, “The Hydration and Microstructure of Ultra High-Strength Concrete with Cement–Silica Fume–Slag Binder,” *Cement and Concrete Composites*, V. 61, pp. 44-52. doi: 10.1016/j.cemconcomp.2015.04.013

Shi, Z.; Geiker, M. R.; Lothenbach, B.; De Weerdt, K.; Garzón, S. F.; Enemark-Rasmussen, K.; and Skibsted, J., 2017b, “Friedel’s Salt Profiles from Thermogravimetric Analysis and Thermodynamic Modelling of Portland Cement-Based Mortars Exposed to Sodium Chloride Solution,” *Cement and Concrete Composites*, V. 78, pp. 73-83. doi: 10.1016/j.cemconcomp.2017.01.002

Steiner, S.; Lothenbach, B.; Proske, T.; Borgschulte, A.; and Winnefeld, F., 2020, “Effect of Relative Humidity on the Carbonation Rate of Portlandite, Calcium Silicate Hydrates and Ettringite,” *Cement and Concrete Research*, V. 135, Article No. 106116. doi: 10.1016/j.cemconres.2020.106116

Stewart, M. G., and Al-Harthy, A., 2008, “Pitting Corrosion and Structural Reliability of Corroding RC Structures: Experimental Data and Probabilistic Analysis,” *Reliability Engineering & System Safety*, V. 93, No. 3, pp. 373-382. doi: 10.1016/j.ress.2006.12.013

Sui, S.; Wilson, W.; Georget, F.; Maraghechi, H.; Kazemi-Kamyab, H.; Sun, W.; and Scrivener, K., 2019, “Quantification Methods for Chloride Binding in Portland Cement and Limestone Systems,” *Cement and Concrete Research*, V. 125, Article No. 105864. doi: 10.1016/j.cemconres.2019.105864

Thomas, M. D. A.; Hooton, R. D.; Scott, A.; and Zibara, H., 2012, “The Effect of Supplementary Cementitious Materials on Chloride Binding in Hardened Cement Paste,” *Cement and Concrete Research*, V. 42, No. 1, pp. 1-7. doi: 10.1016/j.cemconres.2011.01.001

Ukpata, J. O.; Basheer, P. A. M.; and Black, L., 2019, “Slag Hydration and Chloride Binding in Slag Cements Exposed to a Combined Chloride-Sulphate Solution,” *Construction and Building Materials*, V. 195, pp. 238-248. doi: 10.1016/j.conbuildmat.2018.11.055

Wang, C.; Jin, Z.; Liu, G.; Dong, W.; Pang, B.; and Ding, X., 2023, “Mechanisms of Chloride Transport in Low Carbon Marine Concrete: An Alkali-Activated Slag System with High Limestone Powder,” *Journal of Building Engineering*, V. 72, Article No. 106539. doi: 10.1016/j.jobe.2023.106539

Wang, D., and Zhang, Z., 2021, “The Relationship between Cementitious Composition and Properties of Ultrahigh Strength Concrete,” *Advances in Civil Engineering*, V. 2021, No. 1, Article No. 5549161. doi: 10.1155/2021/5549161

Wang, D.; Shi, C.; Farzadnia, N.; Jia, H.; Zeng, R.; Wu, Y.; and Lao, L., 2019a, “A Quantitative Study on Physical and Chemical Effects of Limestone Powder on Properties of Cement Pastes,” *Construction and Building Materials*, V. 204, pp. 58-69. doi: 10.1016/j.conbuildmat.2019.01.154

Wang, D.; Shi, C.; Farzadnia, N.; Shi, Z.; Jia, H.; and Ou, Z., 2018a, “A Review on Use of Limestone Powder in Cement-Based Materials: Mechanism, Hydration and Microstructures,” *Construction and Building Materials*, V. 181, pp. 659-672. doi: 10.1016/j.conbuildmat.2018.06.075

Wang, Q.; Yang, J.; and Chen, H., 2017, “Long-Term Properties of Concrete Containing Limestone Powder,” *Materials and Structures*, V. 50, No. 3, Article No. 168. doi: 10.1617/s11527-017-1040-8

Wang, R.; He, F.; Chen, C.; and Dai, L., 2021a, “Coupling Effect of the Connected Pores and Pore Solution on Chloride Ion Migration in Cement-Based Materials,” *Construction and Building Materials*, V. 297, Article No. 123773. doi: 10.1016/j.conbuildmat.2021.123773

Wang, X.-P.; Shao, M.; Ye, C.-Q.; Dong, S.-G.; Du, R.-G.; and Lin, C.-J., 2021b, “Study on Effect of Chloride Ions on Corrosion Behavior of Reinforcing Steel in Simulated Polluted Concrete Pore Solutions by Scanning Micro-Reference Electrode Technique,” *Journal of Electroanalytical Chemistry*, V. 895, Article No. 115454. doi: 10.1016/j.jelechem.2021.115454

Wang, Y.; Shui, Z.; Gao, X.; Huang, Y.; Yu, R.; and Ling, G., 2019b, “Chloride Binding Behaviors of Metakaolin-Lime Hydrated Blends: Influence of Gypsum and Atmospheric Carbonation,” *Construction and Building Materials*, V. 201, pp. 380-390. doi: 10.1016/j.conbuildmat.2018.12.162

Wang, Y.; Shui, Z.; Yu, R.; and Huang, Y., 2018b, “Chloride Ingress and Binding of Coral Waste Filler-Coral Waste Sand Marine Mortar Incorporating Metakaolin,” *Construction and Building Materials*, V. 190, pp. 1069-1080. doi: 10.1016/j.conbuildmat.2018.09.189

Wu, M.; Zhang, Y.; Liu, G.; Wu, Z.; Yang, Y.; and Sun, W., 2018, “Experimental Study on the Performance of Lime-Based Low Carbon Cementitious Materials,” *Construction and Building Materials*, V. 168, pp. 780-793. doi: 10.1016/j.conbuildmat.2018.02.156

Xiao, J.; Wang, J.; Guo, M.; and Wang, D., 2017, “Performance of Chloride Ion Condensation of the Cement Pastes with Ground Limestone,” *Journal of the Chinese Ceramic Society*, V. 36, No. 8, pp. 2523-2529.

Xie, X., 2020, “Characterization of the Diffusion and Distribution Behaviors of Chloride Ions in Concrete and their Influencing Factors,” dissertation, Guangxi University, Nanning, China.

Zolfagharnasab, A.; Ramezanianpour, A. A.; and Bahman-Zadeh, F., 2021, “Investigating the Potential of Low-Grade Calcined Clays to Produce Durable $LC^3$ Binders against Chloride Ions Attack,” *Construction and Building Materials*, V. 303, Article No. 124541. doi: 10.1016/j.conbuildmat.2021.124541

Zunino, F., and Scrivener, K., 2021, “The Reaction between Metakaolin and Limestone and Its Effect in Porosity Refinement and Mechanical Properties,” *Cement and Concrete Research*, V. 140, Article No. 106307. doi: 10.1016/j.cemconres.2020.106307

# NOTES:

# REVIEWERS IN 2025

In 2025, the individuals listed on these pages served as technical reviewers of papers offered for publication in ACI periodicals. A special "thank you" to them for their voluntary assistance in helping ACI maintain the high quality of its publication program.

---

**£aźniewska-Piekarczyk, Beata**
Silesian University of Technology Faculty of Civil Enginering
*Gliwice, Poland*

**A, Rajprabhu**
Indian Institute of Technology Madras
*Chennai, Tamil Nadu, India*

**A, Suresh Kumar**
Kalasalingam Academy of Research and Education
*Krishnan Kovil, Tamil Nadu, India*

**A. Abbas, Waleed**
University of Technology
*Al-Sinaa Street, Baghdad, Iraq*

**Aaleti, Sriram**
University of Alabama
*Tuscaloosa, AL, United States*

**Abbadi, Abdulrahman**
University of Leeds
*Leeds, United Kingdom of Great Britain and Northern Ireland*

**Abbas Gillani, Syed Tafheem**
Henan University of Technology
*Zhengzhou, China*

**Abbas, Aamer**
*Baghdad, Iraq*

**Abbas, Abdelgadir**
Carleton University
*Ottawa, ON, Canada*

**Abbas, Yassir**
*Riyadh, Saudi Arabia*

**Abbas, Zainab**
*Babylon, Iraq*

**Abd El-Aleem, Saleh**
Fayoum University- Faculty of Science
*El-Fayoum, Egypt*

**Abd Elrahman, Mohamed**
TU Berlin
*Berlin, Germany*

**Abd Elrazek, Mostafa**
*Assiut, Egypt*

**Abdalla, Hany**
College of Technological Studies
*Shuwaikh, Kuwait*

**Abdallah, Amr**
University of Manitoba
*Winnipeg, MB, Canada*

**Abdel Shafy, Yasser**
El MIna High Technology Institute
*Beni Suef, Egypt*

**Abdelaleem, Tarek**
*Assiut, Assiut, Egypt*

**Abdeldjalil, Mhammed**
University of Science and Technology of Oran Mohamed Boudiaf
*El M'énouer, Algeria*

**Abdelgader, Hakim**
Tripoli University
*Tripoli, Libyan Arab Jamahiriya*

**Abdelkader, Ahmed**
Horus University
*Mansoura, Egypt*

**Abdellatef, Mohammed**
University of New Mexico
*Albuquerque, NM, United States*

**Abdelwahab, Louay**
Universiti Teknologi Petronas
*Tronoh, Perak, Malaysia*

**Abdul Baki, Ali**
University of Mosul
*Mosul, Iraq*

**Abdulazeez, Mohanad**
University of Missouri-Kansas City - Volker Campus
*Kansas City, MO, United States*

**Abdulhameed, Ali**
University of Baghdad
*Baghdad, Iraq*

**Abdulla, Nwzad**
University of Salahaddin
*Erbil, Iraq*

**Abdulla, Safaa**
*Sharjah, United Arab Emirates*

**Abdullah, Ahmad**
Aswan University
*Sahary City, Aswan, Egypt*

# REVIEWERS IN 2025

**Abdullah, Saman**
University of California, Los Angeles
*Los Angeles, CA, United States*

**Abdul-Razzaq, Khattab**
University of Diyala
*Diyala, Iraq*

**Abed, Farid**
American University of Sharjah
*Sharjah, United Arab Emirates*

**Abed, Ziyad**
University of Technology
*Baghdad, Baghdad, Iraq*

**Abellan-García, Joaquin**
Universidad del Norte
*Barranquilla, Colombia*

**Abi Farraj, Faten**
Laboratory of Materials and Durability of Constructions
*Toulouse, France*

**Abousnina, Rajab**
University of Southern Queensland
*Toowoomba, QLD, Australia*

**Abou-Zeid, Mohamed**
American University in Cairo
*Cairo, Egypt*

**Abu Obeidah, Adi**
*Piscataway, NJ, United States*

**Abu Taqa, Ala**
Qatar University
*Doha, Qatar*

**Abu Yosef, Ali**
Pivot Engineers
*Austin, TX, United States*

**Abu-Abaileh, Adham**
GSG Consultants Inc.
*Schaumburg, IL, United States*

**Abubakri, Shahriar**
Rowan University
*Glassboro, NJ, United States*

**Accornero, Federico**
Shantou University
*Shantou, China*

**Acun, Bora**
UBC Okanagan
*Kelowna, BC, Canada*

**Adak, Dibyendu**
National Institute of Technology Meghalaya
*Shillong, Meghalaya, India*

**Addai Boateng, Anthony**
The Ohio State University
*Columbus, OH, United States*

**Adekunle, Saheed**
King Fahd University of Petroleum and Minerals
*Dhahran, Saudi Arabia*

**Adinkrah-Appiah, Kwadwo**
Sunyani Polytechnic
*Sunyani, Ghana*

**Afif, Rahma**
Arab International University (AIU), Faculty of Civil Engineering
*Daraa Governorate, Syrian Arab Republic*

**Aghaee, Kamran**
Cornell University
*Ithaca, NY, United States*

**Agnihotri, Anamika**
MNIT
*Jaipur, Rajasthan, India*

**Agrawal, Unnati**
*Nagpur, Maharashtra, India*

**Agustiningtyas, Rudi**
Ministry of Public Works and Public Housing
*Bandung, Indonesia*

**Ahani, Elshan**
Sahand University of Technology
*Tabriz, Islamic Republic of Iran*

**Ahmad, Mohd Hilton**
Universiti Tun Hussein Onn Malaysia
*Batu Pahat, Johor, Malaysia*

**Ahmad, Seleem**
Zagazig University Faculty of Engineering
*Zagazig, Egypt*

**Ahmadi, Jamal**
University of Science of Technology
*Tehran, Tehran, Islamic Republic of Iran*

**Ahmed, Ahmed A.**
Oregon State University
*Corvallis, OR, United States*

**Ahmed, Anwar**
University of Nyala
*Nyala, Sudan*

# REVIEWERS IN 2025

**Ahmed, Doaa**
Women's College for Arts, Science and Education, Ain Shams University
*Cairo, Cairo, Egypt*

**Ahmed, Saddam**
Anna University
*Chennai, Tamil Nadu, India*

**Aire, Carlos**
National Autonomous University of Mexico
*Mexico, DF, Mexico*

**Akakin, Tumer**
Aggregate and Ready Mix Association of Minnesota
*Eagan, MN, United States*

**Akalin, Ozlem**
PLUSTECHNO Ltd
*İstanbul, Turkey*

**Akbarzadeh Bengar, Habib**
University of Mazandaran
*Babolsar, Islamic Republic of Iran*

**Akhlaghi, Alireza**
*Isfahan, Islamic Republic of Iran*

**Akhondi, Milad**
*Tehran, Islamic Republic of Iran*

**Akiyama, Hiroshi**
The Zenitaka Corporation
*Tokyo, Japan*

**Akkaya, Yildir**
Istanbul Teknik Universitesi
*Istanbul, Maslak, Sariyer, Turkey*

**Al Fahad, Abdullah**
Rajshahi University of Engineering and Technology
*Kazla, Rajshahi, Bangladesh*

**Al- Haddad, Diala**
*Dubai, United Arab Emirates*

**Al Obaidey, Shubbar**
University of Technology - Iraq
*Baghdad, Iraq*

**Alaluf, Rafael**
EQRM Interntaional Inc.
*Istanbul, Turkey*

**Alam, A. K. M. Jahangir**
Bangladesh University of Engineering and Technology (BUET)
*Dhaka, Bangladesh*

**Al-Ani, Moustafa**
*Auckland, New Zealand*

**Al-Attar, Tareq**
University of Technology
*Baghdad, Baghdad, Iraq*

**Al-Azzawi, Adel**
Al-Nahrain University
*Baghdad, Iraq*

**Al-Bahadli, Hussein**
*Najaf, Iraq*

**Albahttiti, Mohammed**
California State University, Chico
*Chico, CA, United States*

**Albuquerque, Albéria**
Federal Institute of Technological Education of Mato Grosso
*Cuiabá, Mato Grosso, Brazil*

**Alcocer, Sergio**
Institute of Engineering, UNAM
*Mexico City, DF, Mexico*

**Aldawsari, Salem**
Florida State University
*Tallahassee, FL, United States*

**Aldwaik, Mais**
*Russeifa, Zarqa, Jordan*

**Alghossoon, Abdullah**
The Hashemite University
*Shafa Badran/Amman, Amman, Jordan*

**Al-Hamd, Rwayda Kh. S.**
*Baghdad*

**Alhashmi, Abdalla**
Dalhousie University
*Halifax, NS, Canada*

**Alhassan, Mohammad**
Al Ain University
*Al Ain, United Arab Emirates*

**Ali, Aynoor**
University of Technology
*Baghdad, Iraq*

**Ali, Shehroze**
NFC Institute of Engineering and Fertilizer Research
*Faisalabad, Punjab, Pakistan*

**Ali, Yahia**
*Nanjing, Jiangsu, China*

**Al-Jabri, Khalifa**
Sultan Qaboos University College of Engineering
*Muscat, Oman*

# REVIEWERS IN 2025

**Alkerwei, Rana**
Mustansiriyah University
*Baghdad, Iraq*

**Alkhairi, Fadi**
Dar Omran
*Amman, Jordan*

**Alkhateb, Hunain**
University of Mississippi
*University, MS, United States*

**Alkhrissat, Tariq**
Al-Ahliyya Amman University
*Amman, Jordan*

**Allahdadi, Hamidreza**
*Bangalore, India*

**Al-Lebban, Yasir**
University of Central Florida
*Orlando, FL, United States*

**Allena, Srinivas**
Cleveland State University
*Cleveland, OH, United States*

**Almbaidheen, khalil**
Mapei SpA
*Dubai, Dubai, United Arab Emirates*

**Almeshal, Ibrahim**
Universiti Sains Malaysia - Engineering Campus Seri Ampangan
*Nibong Tebel, Pulau Pinang, Malaysia*

**Almuhsin, Bayrak**
University of Technology
*Karrada, Baghdad, Iraq*

**Al-Obaidey, Shubbar**
University of Technology
*Baghdad, Iraq*

**Alqam, Maha**
The University of Jordan
*Amman, Jordan*

**Al-Rubaye, Salam**
Tikrit University
*Tikrit, Iraq*

**Alsheltat, Mohamed**
Libyan Academy Misrata
*Misrata, Libya*

**Alsiwat, Jaber**
Saudi Consulting Services
*Riyadh, Saudi Arabia*

**Al-Sodani, Khaled**
University of Hafr Al Batin
*Hafr Al Batin, Eastern Province, Saudi Arabia*

**Alsomiri, Mujahed**
Southeast University
*Nanjing, China*

**Altabey, Wael**
Alexandria University
*Alexandria, Egypt*

**Al-Tarafany, Dhiaa**
Al-Nahrain University
*Baghdad, Baghdad, Iraq*

**Al-Thairy, Haitham**
University of Al-Qadisiyah College of Engineering
*Al Diwaniyah, Iraq*

**Al-Tikrite, Ahmed**
Tikrit University
*Tikrit, Iraq*

**Altlomate, Abdelmajeed**
College of Engineering Technology
*Houn, Libya*

**Al-Zuheriy, Ahmed**
University of Technology- Iraq
*Baghdad, Baghdad, Iraq*

**Ametefe, Timothy**
CSIR Building and Road Research Institute
*Kumasi, Ashanti, Ghana*

**Amir, Sana**
University of Wollongong in Dubai
*Dubai, United Arab Emirates*

**Anderson, Neal**
Simpson Gumpertz & Heger
*Chicago, IL, United States*

**Andersson, Ronny**
*Hollviken, Sweden*

**Andrade, Humberto**
Universidade Federal de Ouro Preto
*Ouro Preto, MG, Brazil*

**Andrade, Jairo**
Catholic University of Rio Grande do Sul
*Porto Alegre, RS, Brazil*

**Andriolo, Francisco**
Andriolo Ito Engenharia S/C Ltda
*Sao Carlos, Sao Paulo, Brazil*

# REVIEWERS IN 2025

**Ann, Ki Yong**
Hanyang University - ERICA Campus
*Ansan, Republic of Korea*

**Antommattei, Oscar**
*Austin, TX, United States*

**Antoni, Antoni**
Petra Christian University
*Surabaya, Indonesia*

**Antunes de Almeida, Jacinto Manuel**
UFRGS
*Porto Alegre, Brazil*

**Antunes, Rodrigo**
University of Florida
*Gainesville, FL, United States*

**Anwari, Qareeb Ullah**
Nust Institute of Civil Engineering
*Islamabad, Islamabad, Pakistan*

**Arabsarhangi, Reza**
Semnan University
*Semnan, Semnan, Islamic Republic of Iran*

**Arafa, Ahmed**
Universite de Sherbrooke
*Sherbrooke, QC, Canada*

**Araghi, Hassan**
Azad University of South Tehran
*Karaj, Tehran, Islamic Republic of Iran*

**Aras, Murat**
Bilecik Şeyh Edebali University
*Bilecik, Bilecik, Turkey*

**Araujo, Guilherme**
State University of Campinas Faculty of Technology
*Limeira, Brazil*

**Arce, Gabriel**
Virginia Transportation Research Council
*Charlottesville, VA, United States*

**Arcine, Maicon de Freitas**
Universidade Federal de São Carlos
*Sao Carlos, São Paulo, Brazil*

**Arito, Philemon**
University of Namibia
*Ongwediva, Oshana, Namibia*

**Asheghi Mehmandari, Tohid**
Morgan State University
*Baltimore, MD, United States*

**Assaad, Joseph**
University of Balamand
*Balamand, Lebanon*

**Athanasopoulou, Adamantia**
Metropolitan College
*Xalandri, Attiki, Greece*

**Attiogbe, Emmanuel**
*Discovery Bay, CA, United States*

**Attiyah, Ali**
University of Kufa
*Kufa, Iraq*

**Audenaert, Katrien**
Ghent University, Magnel Laboratory for Concrete Research
*Ghent, Belgium*

**Awida, Tarek**
SQC International Consultant
*Kuwait, Kuwait, Kuwait*

**Aydin, Ertug**
Lefke Avrupa Universitesi
*Lefke, Cyprus*

**Aykac, Sabahattin**
Gazi University, Faculty of Engineering and Architecture
*Ankara, Turkey*

**Ayothiraman, Ramanathan**
IIT Delhi
*New Delhi, India*

**Aziz, Omar**
Salahaddin University-Hawler
*Erbil, Kurdistan Region, Iraq*

**B, Parthiban**
Annamalai University
*Chidambaram, Tamil Nadu, India*

**Babatola, Oluwatosin**
*Akure, Ondo, Nigeria*

**Bae, Baek Il**
Hanyang Cyber University
*Seoul, Seoul, Republic of Korea*

**Bagerzadeh Karimi, Mohammad Reza**
*Tabriz, Islamic Republic of Iran*

**Bahhou, Abdelmoujib**
*Sherbrooke, QC, Canada*

**Bai, Yongtao**
Kyoto University
*Kyoto, Kyoto, Japan*

# REVIEWERS IN 2025

**Balakrishnan, Bijily**
Indian Institute of Technology Tirupati
*Tirupati, India*

**Banerjee, Debargha**
NIT-Durgapur
*Durgapur, India*

**Bansal, Sahil**
Indian Institute of Technology Delhi
*New Delhi, Delhi, India*

**Bao, Chao**
Ningxia University
*Yinchuan, China*

**Barbhuiya, Salim**
University of East London
*London, United Kingdom of Great Britain and Northern Ireland*

**Barbosa Lima, Nataniel**
University of Brasilia
*Brasilia, Brazil*

**Barman, Manik**
University of Minnesota Duluth
*Duluth, MN, United States*

**Baskar, Prabu**
Annapoorana Engineering College
*Salem, India*

**Bassim, Raymond**
University of Illinois Chicago
*Chicago, IL, United States*

**Baweja, Daksh**
BG&E Pty Ltd
*Sydney, NSW, Australia*

**Bawono, Ali Aryo**
TUM Create
*Singapore, Singapore*

**Beglarigale, Ahsanollah**
Okan Universitesi
*Istanbul, Turkey*

**Bektas, Fatih**
Minnesota State University, Mankato
*Mankato, MN, United States*

**Ben Abdelmalek, Jamel**
*Bizerte, Tunisia*

**Benouis, Abdelhalim**
Civil and Hydraulic Laboratory
*Guelma, Algeria*

**Bertero, Raul**
Universidad de Buenos Aires
*Buenos Aires, Argentina*

**Bertero, Santiago**
Universidad de Buenos Aires Facultad de Ingenería
*Buenos Aires, Argentina*

**Beyene, Mengesha**
Turner-Fairbank Highway Research Center
*McLean, VA, United States*

**Bhanja, Santanu**
National Institute of Technical Teachers' Training & Research, Kolkata
*Kolkata, West Bengal, India*

**Bhargava, Kapilesh**
Bhabha Atomic Research Centre
*Mumbai, Maharashtra, India*

**Bhojaraju, Chandrasekhar**
St Joseph Engineering College
*Mangalore, Karnataka, India*

**Bian, R. B.**
Jiangsu Research Institute of Building Science
*Nanjing, Jiangsu, China*

**Bidkar, Kisan**
*Nasik, India*

**Bilek, Vlastimil**
ZPSV a.s.
*Brno, Czech Republic*

**Bilir, Turhan**
İstanbul University-Cerrahpaşa
*İstanbul, Turkey*

**Bilisik, Kadir**
Erciyes University
*Kayseri, Central Anatolia, Turkey*

**Billah, AHM Muntasir**
University of Calgary
*Calgary, AB, Canada*

**Birely, Anna**
Texas A&M University
*College Station, TX, United States*

**Bischoff, Peter**
University of New Brunswick
*Fredericton, NB, Canada*

**Blandón Valencia, John**
National University of Colombia Medellin
*Medellin, Antioquia, Colombia*

# REVIEWERS IN 2025

**Bolander, John**
University of California, Davis
*Davis, CA, United States*

**Borzovič, Viktor**
Slovak University of Technology, Faculty of Civil Engineering
*Bratislava, Slovakia*

**Boulfiza, Moh**
University of Saskatchewan
*Saskatoon, SK, Canada*

**Boulifa, Ridha**
Mohamed Cherif Messaadia University Souk-Ahras
*Souk-Ahras, Algeria*

**Bouras, Rachid**
UMMTO
*Tiziouzou, Tiziouzou, Algeria*

**Bouzid, Haytham**
Universite Ibn Khaldoun Tiaret
*Tiaret, Algeria*

**Branco, Luiz**
Universidade FUMEC
*Belo Horizonte, MG, Brazil*

**Brandtner-Hafner, Martin**
Fracture Analytics
*Mörbisch am See, Austria*

**Brena, Sergio**
University of Massachusetts
*Amherst, MA, United States*

**Brewe, Jared**
*Palatine, IL, United States*

**Browning, JoAnn**
University of Kansas
*Lawrence, KS, United States*

**Bui, Linh**
Tokyo City University
*Setagaya-ku, Japan*

**Burak Bakir, Burcu**
Orta Dogu Teknik Universitesi
*Ankara, Turkey*

**Buttignol, Thomaz Eduardo**
Universidade Estadual de Campinas - Campus Cidade Universitaria Zeferino Vaz
*Campinas, SP, Brazil*

**Bzeni, Dallshad**
University of Salahaddin
*Erbil, Iraq, Iraq*

**C, Akin**
KCG College of Technology
*Chennai, India*

**Calderon, Victor**
Walter P Moore
*Washington, DC, United States*

**Camões, Aires**
University of Minho
*Guimarães, Portugal*

**Campos, Claudia**
Universidade Federal Fluminense
*Rio de Janeiro, Rio de Janeiro, Brazil*

**Cao, Jian**
Nanchang Institute of Technology
*Nanchang, Jiangxi, China*

**Cao, Qi**
Dalian University of Technology
*Dalian, Liaoning, China*

**Carloni, Christian**
Case Western Reserve University
*Cleveland, OH, United States*

**Carlos, Thiago**
University of Sao Paulo
*Sao Paulo, São Paulo, Brazil*

**Carpio, Víctor**
Escuela Politécnica Nacional
*Quito, Pichincha, Ecuador*

**Carrette, Jordan**
University of Manitoba
*Winnipeg, MB, Canada*

**Carrillo, Julian**
Universidad Militar Nueva Granada
*Bogota, Colombia*

**Castillo, Alberto**
Purdue University
*West Lafayette, IN, United States*

**Cavalline, Tara**
University of North Carolina at Charlotte
*Charlotte, NC, United States*

**Chang, Ta-Peng**
NTUST
*Taipei, Taiwan, China*

**Chanthabouala, Khatthanam**
Nanyang Technological University
*Singapore, Singapore*

# REVIEWERS IN 2025

**Chao, Shih-Ho**
The University of Texas at Arlington
*Arlington, TX, United States*

**Chao, Wang**
Northeastern University
*Shenyang, Liao Ning, China*

**Chapirom, Aphai**
Suranaree University of Technology Institute of Science
*Nakhon Ratchasima, Nakhon Ratchasima, Thailand*

**Charalambidi, Barbara**
Technical University of Crete
*Chania, Greece*

**Chaunsali, Piyush**
Indian Institute of Technology Madras
*Chennai, India*

**Chen, Chunhong**
*Zhenjiang, Jiangsu, China*

**Chen, Jiankang**
*Chengdu, China*

**Chen, Tao**
China Academy of Building Research
*Beijing, China*

**Chen, Xin**
*Shenyang, Liaoning, China*

**Chen, Zongping**
*Nanning, Guangxi, China*

**Cheng, Min-Yuan**
National Taiwan University of Science and Technology
*Taipei, Taiwan, China*

**Chhom, Amnoth**
Novosibirsk State University of Architecture and Civil Engineering
*Novosibirsk, Russian Federation*

**Chiker, Tarek**
Universite de Jijel
*Antony, France*

**Cho, Jae-Yeol**
Seoul National University
*Seoul, Republic of Korea*

**Cho, Seung**
Stellenbosch University
*Stellenbosch, Western Cape, South Africa*

**Cho, Soon-Ho**
Gwangju University
*Gwangju, Republic of Korea*

**Choi, Chang-Sik**
Hanyang University
*Seoul, Republic of Korea*

**Choi, Yoon Suk**
Korea Conformity Laboratories
*Seoul, Republic of Korea*

**Chotickai, Piya**
Kasetsart University Faculty of Engineering
*Bangkok, Thailand*

**Christen, Robert**
American Engineering Testing Inc.
*Port Charlotte, FL, United States*

**Chu, S. H.**
Columbia University
*New York, NY, United States*

**Chun, Sung-Chul**
Incheon National University
*Incheon, Republic of Korea*

**Cleland, Ned**
Blue Ridge Design Inc.
*Winchester, VA, United States*

**Conforti, Antonio**
University of Brescia
*Brescia, Brescia, Italy*

**Conway, Robert**
USDOT
*Baltimore, MD, United States*

**Cook, Dan**
Oklahoma State University
*Stillwater, OK, United States*

**Cordoba, Gisela**
Universidad Nacional del Centro de la Provincia de Buenos Aires
*Olavarría, Buenos Aires, Argentina*

**Costa Piccinini, Ângela**
Universidade Federal do Rio de Janeiro
*Rio de Janeiro, Brazil*

**Dang, Yudong**
Tongji University
*Shanghai, China*

**Dang, Yudong**
*Chongqing, China*

**Darvishvand, Hamid Reza**
Qazvin Islamic Azad University
*Qazvin, Qazvin, Islamic Republic of Iran*

**Das Adhikary, Satadru**
National University of Singapore
*Singapore, Singapore*

**Daugevičius, Mykolas**
Vilnius Gediminas Technical University
*Vilnius, Lithuania*

**Dauji, Saha**
Bhabha Atomic Research Centre
*Mumbai, Maharashtra, India*

**Dawood, Mohammad Sulaiman**
Clarkson University
*Potsdam, NY, United States*

**DC, Mitra**
College of Engineering Trivandrum
*Thiruvananthapuram, Kerala, India*

**De Brito, Jorge**
IST / TUL
*Lisbon, Portugal*

**de Oliveira, Gabriel**
UNICAMP
*Campinas, São Paulo, Brazil*

**DeFord, Harvey**
Florida Department of Transportation
*Gainesville, FL, United States*

**Degtyarev, Vitaliy**
*Lexington, SC, United States*

**Demis, Sotiris**
University of Patras
*Patra, Greece*

**Derogar, Shahram**
*Istanbul, Turkey*

**Desai, Vijay**
Central Water and Power Research Station
*Pune, Maharashtra, India*

**Deyu, Kong**
Zhejiang University of Technology
*Hangzhou, China*

**Dhole, Rajaram**
*Katy, TX, United States*

**Dhonde, Hemant**
University of Houston
*Houston, TX, United States*

**Diab, Amjad**
The University of Texas at Austin
*Austin, TX, United States*

**Diniz, Sofia Maria**
Federal University of Minas Gerais School of Engineering
*Belo Horizonte, Minas Gerais, Brazil*

**Dogan, Unal**
Istanbul Technical University
*Istanbul, Turkey*

**Dolan, Charles**
University of Wyoming
*Laramie, WY, United States*

**Dong-Qiu, Lan**
Beijing University of Technology
*Beijing, Beijing, China*

**Dragovich, Jeff**
*Shoreline, WA, United States*

**Du, Lianxiang**
The University of Alabama at Birmingham
*Birmingham, AL, United States*

**Du, Yingang**
Anglia Ruskin University, UK
*Chelmsford, United Kingdom of Great Britain and Northern Ireland*

**Duanmu, Xiangyong**
*Shanghai, Shanghai, China*

**Dugvekar, Mitali**
MANIT
*Bhopal, Madhya Pradesh, India*

**Dumeignil, Sacha**
City of Montreal
*Montreal, QC, Canada*

**Dutta, Debabrata**
Camellia Group Education
*Kolkata, West Bengal, India*

**Dwairi, Hazim**
The Hashemite University
*Zarqa, Zarqa, Jordan*

**Dyba, Marcin**
Tadeusz Kosciuszko Cracow University of Technology Faculty of Civil Engineering
*Krakow, Lesserpoland, Poland*

**Dymond, Ben**
Northern Arizona University
*Flagstaff, AZ, United States*

**Eid, Fatma**
Menoufia University
*Shebin El-Kom, Egypt*

# REVIEWERS IN 2025

**Ekinci, Cevdet**
Firat University
*Elazig, Turkey*

**El Nadoury, Wegdan**
Pharos University in Alexandria
*Alexandria, Egypt*

**El Sayed, Mohamed**
NTH Consultants Ltd.
*Northville, MI, United States*

**Elaqra, Hossam**
*Gaza, State of Palestine*

**Elbady, Ahmed**
Université de Sherbrooke
*Sherbrooke, QC, Canada*

**El-Gendy, Mohammed**
Lakehead University Faculty of Engineering
*Thunder Bay, ON, Canada*

**El-Hassan, Hilal**
United Arab Emirates University Faculty of Engineering
*Al Ain, United Arab Emirates*

**El-Hawary, Moetaz**
Kuwait University
*Kuwait, Kuwait*

**Elmenshawi, Abdelsamie**
University of Calgary
*Calgary, AB, Canada*

**El-Salakawy, Ehab**
University of Manitoba
*Winnipeg, MB, Canada*

**Elshina, Lyudmila**
NIC Stroitelstvo
*Moscow, Russian Federation*

**Eltahawy, Reham**
Ain Shams University
*Cairo, Egypt*

**Elyiğit, Belkıs**
Firat University
*Elazig, Turkey*

**Emamy Farvashany, Firooz**
Perthpolis Pty Ltd
*Perth, WA, Australia*

**Eng, Tian Zi**
Nanjing University of Aeronautics and Astronautics
*Nanjing, China*

**Erkmen, Emre**
Concordia University
*Montreal, QC, Canada*

**Esquivel, Hugo**
Estructuras del Norte
*Barranquilla, ATL, Colombia*

**Fan, Shengxin**
Nanyang Technological University
*Singapore, Singapore*

**Fantilli, Alessandro Pasquale**
Politecnico di Torino
*Torino, Italy*

**Faried, Ahmed**
Menoufia University
*Shebeen El-Kom, Menoufia, Egypt*

**Farivar, Behzad**
University of Arkansas Fayetteville
*Fayetteville, AR, United States*

**Farrag, Sharef**
Rutgers University
*Piscataway, NJ, United States*

**Farshadfar, Omid**
Thornton Tomasetti
*Lawrence, KS, United States*

**Fatemi, Hassan**
*Montreal, QC, Canada*

**Feng, Muzai**
Walter P Moore
*Dallas, TX, United States*

**Ferche, Anca-Cristina**
*Toronto, TX, United States*

**Fernandes, Fernando Antonio da Silva**
Federal University of Pará - Campus Salinópolis - Faculty of Engineering
*Salinópolis, Pará, Brazil*

**Fernandez Montes, David**
*Madrid, Madrid, Spain*

**Ferraro, Christopher**
University of Florida
*Gainesville, FL, United States*

**Fick, Damon**
*Bozeman, MT, United States*

**Fikry, Ahmed**
Helwan University
*Cairo, Saudi Arabia*

# REVIEWERS IN 2025

**Fitik, Birol**
Hochschule fur Technik Stuttgart
*Stuttgart, Germany*

**Folino, Paula**
University of Buenos Aires
*Buenos Aires, Argentina*

**Fraga, Yuri**
Universidade de Brasilia
*Brasilia, Federal District, Brazil*

**Franco-Lujan, Victor**
Tecnologico Nacional de Mexico
*Mexico City, Mexico City, Mexico*

**Gąćkowski, Roman**
Czestochowa University of Technology
*Czestochowa, Poland*

**Gali, Sahith**
Turner-Fairbank Highway Research Center
*McLean, VA, United States*

**Galić, Mirela**
University of Split Faculty of Civil Engineering Architecture and Geodesy
*Split, Dalmatia, Croatia*

**Gallandorm, Edith**
PCI
*Chicago, IL, United States*

**Gan, Dan**
*Chongqing, China*

**Ganesan, N.**
National Institute of Technology
*Calicut, India*

**Gao, Lubin**
Federal Highway Administration
*Washington, DC, United States*

**Gao, Peng**
Hefei University of Technology
*Hefei, China*

**Garcia, Sergio**
Universidade Estadual do Norte Fluminense Darcy Ribeiro
*Campos dos Goytacazes, Rio de Janeiro, Brazil*

**Gbadamosi, Aderemi**
University of Nevada, Las Vegas
*Las Vegas, NV, United States*

**Geevar, Indu**
Indian Institute of Technology Madras
*Chennai, Tamil Nadu, India*

**Genikomsou, Aikaterini**
Queen's University
*Kingston, ON, Canada*

**Georget, Fabien**
RWTH Aachen University
*Aachen, Germany*

**Ghahreman, Masoud**
The University of Texas at Arlington
*Arlington, TX, United States*

**Gheni, Ahmed**
Komar University of Science and Technology
*Sulaymania, Iraq*

**Ghezal, Aïcha**
Ecole de Technologie de Montreal
*Montreal, QC, Canada*

**Ghiami Azad, Amir Reza**
University of Tehran
*Boston, MA, United States*

**Ghimire, Krishna**
Kansas State University
*Manhattan, KS, United States*

**Ghoddousi, Parviz**
Iran University of Science and Technology
*Tehran, Tehran, Islamic Republic of Iran*

**Ghodke, Swapnil**
Indian Institute of Technology Roorkee
*Roorkee, India*

**Gholamhoseini, Ali**
*Auckland, Auckland, New Zealand*

**Giduquio, Marnie**
National Taiwan University of Science and Technology
*Taipei, Taiwan, China*

**Girgin, Canan**
Yildiz Technical University
*Istanbul, Turkey*

**Gongxun, Wang**
Hunan University of Science and Technology
*Xiangtan, China*

**González, Javier**
University of Basque Country
*Bilbao, Basque Country, Spain*

**Grandić, Davor**
University of Rijeka
*Rijeka, Croatia*

# REVIEWERS IN 2025

**Guades, Ernesto**
University of Guam
*Mangilao, Guam*

**Guan, Bowen**
*Xi'an, China*

**Gujar, Pratik**
Indian Institute of Technology Madras
*Chennai, Tamil Nadu, India*

**Guner, Serhan**
University of Toledo
*Toledo, OH, United States*

**Guo, Honglei**
Wuhan Polytechnic University
*Wu Han City, Hu Bei Province, China*

**Guo, Liping**
Southeast University
*Nanjing, Jiangsu Province, China*

**Gutierrez Moreno, Jose**
Universidad Autonoma de Baja California
*Mexicali, Baja California, Mexico*

**Ha, Thi**
University of Colorado Denver
*Denver, CO, United States*

**Haach, Vladimir**
University of Sao Paulo
*Sao Carlos, Sao Paulo, Brazil*

**Habel, Katrin**
*Edmonton, AB, Canada*

**Haber, Zachary**
University of South Florida
*Tampa, FL, United States*

**Haddadin, Laith**
United Nations
*New York, NY, United States*

**Hakuzweyezu, Theogene**
*Wuhan, Hubei, China*

**Halmen, Ceki**
Texas A&M University
*College Station, TX, United States*

**Han, Baoguo**
Dalian University of Technology
*Dalian, China*

**Haneefa Kolakkadan, Mohammed**
SSN College of Engineering
*Kalavakkam, Tamil Nadu, India*

**Hanifa, Mohd**
Central Building Research Institute
*Roorkee, Uttarakhand, India*

**Harajli, Mohamed**
American University of Beirut
*Beirut, Lebanon*

**Hassan, Maan**
University of Technology
*Baghdad, Baghdad, Iraq*

**Hassan, Mostafa**
University of Connecticut
*Storrs, CT, United States*

**Hassan, Wael**
University of Alaska Anchorage
*Anchorage, AK, United States*

**Hassani Esgandani, Mohammadreza**
University of Technology Sydney
*Ultimo, NSW, Australia*

**Hausfeld, John**
Construction Quality Consulting
*Liberty Twp, OH, United States*

**He, Zhiqi**
Southeast University
*Nanjing, Jiangsu, China*

**Heitmeyer, Keila**
*Phoenix, AZ, United States*

**Hentges, Tatiane**
Unisinos
*Sao Leopoldo, Rio Grande do Sul, Brazil*

**Hermawan, Fahmy**
Universitas Trisakti
*Kota Jakarta Barat, DKI Jakarta, Indonesia*

**Hernández-Montes, Enrique**
University of Granada
*Granada, Granada, Spain*

**Holly, Ivan**
Slovak University of Technology in Bratislava Faculty of Civil Engineering
*Bratislava, Slovakia*

**Homayoonmehr, Reza**
RWTH Aachen University
*Aachen, Germany*

**Hong, Seongwon**
Korea National University of Transportation
*Chungju, Chungbuk, Republic of Korea*

# REVIEWERS IN 2025

**Hosseini, Payam**
Genex Systems, LLC
*McLean, VA, United States*

**Hover, Kenneth**
Cornell University
*Ithaca, NY, United States*

**Hrynyk, Trevor**
The University of Texas at Austin
*Waterloo, ON, Canada*

**Hu, Jiong**
University of Nebraska–Lincoln
*Omaha, NE, United States*

**Hu, Nan**
South China University of Technology
*Guangzhou, Guangdong, China*

**Hu, Zhong-Wei**
*Nanjing, China*

**Huang, Bo-Tao**
The Hong Kong Polytechnic University
*Kowloon, Hong Kong, China*

**Huang, Jianwei**
Southern Illinois University Edwardsville
*Edwardsville, IL, United States*

**Huang, Jun**
*United States*

**Huang, Yuan**
Hunan University
*Changsha, Hunan, China*

**Huber, Patrick**
Vienna University of Technology
*Vienna, Austria*

**Husan, Md. Redoy**
Sylhet Engineering College
*Sylhet, Sylhet, Bangladesh*

**Hussein, Mohamed**
Helwan University Faculty of Engineering (Helwan)
*Cairo, Cairo, Egypt*

**Huts, Andriy**
Politechnika Rzeszowska im Ignacego Lukasiewicza
*Rzeszow, Poland*

**Hwang, Hyeon-Jong**
Seoul National University
*Seoul, Republic of Korea*

**Hwang, Shyh-Jiann**
National Taiwan University
*Taipei, Taiwan, China*

**Ilki, Alper**
Istanbul Technical University
*Istanbul, Turkey*

**Ioannou, Sokrates**
Higher Colleges of Technology
*Abu Dhabi, United Arab Emirates*

**Ippili, Adarsh Kumar**
KL Deemed to be University
*Guntur, Andhra Pradesh, India*

**Ishikawa, Yasuaki**
Meijo University
*Nagoya, Aichi, Japan*

**Ismail, Fouad**
Florida International University
*Miami, FL, United States*

**J, Jeyanthi**
Mepco Schlenk Engineering College Department of Civil Engineering
*Sivakasi, Tamil Nadu, India*

**Jafari, Alireza**
Sharif University of Technology
*Tehran, Islamic Republic of Iran*

**Jahami, Ali**
University of Balamand Faculty of Engineering
*El-Koura, Lebanon*

**Jaiswal, Ankit**
Visvesvaraya National Institute of Technology
*Nagpur, Maharastra, India*

**Jamshidi, Masoud**
Building and Housing Research Center (BHRC)
*Tehran, Tehran, Islamic Republic of Iran*

**Jang, Bong**
K-water
*Deajeon, Republic of Korea*

**Janssen, Donald**
*Seattle, WA, United States*

**Javid, Alireza**
Sharif University of Technology
*Tehran, Islamic Republic of Iran*

**Jędrzejewska, Agnieszka**
Silesian Technical University
*Gliwice, Poland*

# REVIEWERS IN 2025

**Jeng, Chyuan-Hwan**
National Chi Nan University-Taiwan
*Puli/Nantou, Taiwan, China*

**Jensen, Ole**
Technical University of Denmark
*Lyngby, Denmark*

**Jeyan Sudhakar, Alein**
SRM Institute of Science and Technology
*Kattankulathur, India*

**Jiang, Hua**
McDermott International Inc.
*Plainfield, IL, United States*

**Jiang, Jinyang**
Southeast University
*Nanjing, China*

**Jing, Gouqing**
Beijing Jiaotong University
*Beijing, China*

**Jo, Kwangwon**
Seoul National University
*Seoul, Republic of Korea*

**Jones, Christopher**
Kansas State University
*Manhattan, KS, United States*

**Joshi, Aayush**
Women Institute of Technology
*Dehradun, Uttarakhand, India*

**Joshi, Buddhi**
Pokhara University
*Lekhnath, Nepal*

**Jozić, Dražan**
Faculty of Chemical Technology
*Split, Croatia*

**Kan, Yu-Cheng**
Chaoyang University of Technology
*Taichung County, Taiwan, China*

**Kanaan, Dima**
The University of British Columbia
*Kelowna, BC, Canada*

**Kanagaraj, Balamurali**
Karunya Institute of Technology and Sciences
*Coimbatore, India*

**Kandasami, Sivakumar**
Larsen and Toubro Ltd.
*Chennai, Tamil Nadu, India*

**Kang, Thomas**
Seoul National University
*Seoul, Republic of Korea*

**Kankam, Charles**
Kwame Nkrumah University of Science & Technology
*Kumasi, Ghana*

**Kanta Rao, Velidandi**
Central Road Research Institute
*New Delhi, Delhi, India*

**Karade, Sukhdeo**
CSIR-Central Building Research Institute
*Roorkee, Uttarakhand, India*

**Karaki, Ghada**
University of the West of England - Frenchay Campus
*Bristol, United Kingdom of Great Britain and Northern Ireland*

**Kareem, Aseel**
University of Baghdad Al-Jaderyia Campus College of Science
*Baghdad, Iraq*

**Karimi, Hossein**
Eindhoven University of Technology
*Eindhoven, Netherlands*

**Kasaniya, Mahipal**
University of New Brunswick
*Fredericton, NB, Canada*

**Kassem, Moustafa**
*Nibong Tebal, Malaysia*

**Kaufmann, Christopher**
Dow Chemical Co.
*Midland, MI, United States*

**Kazmi, Md Athar**
National Institute of Technology Silchar
*Silchar, Assam, India*

**Ke, Guo-Ju**
Research Institute of Highway Ministry of Transport
*Beijing, China*

**Keskin, Süleyman**
Mugla Sitki Kocman Universitesi
*Mugla, Turkey*

**Khabaz, Amjad**
Hasan Kalyoncu University
*Gaziantep, Turkey*

**Khalil, Nariman**
University of Balamand
*Kelhat, Koura, Lebanon*

**Khaliq, Wasim**
National University of Sciences and Technology
*Islamabad, ICT, Pakistan*

**Khan, Sadaqat Ullah**
NED University of Engineering and Technology
*Karachi, Sindh, Pakistan*

**Khanzadeh Moradllo, Mehdi**
Temple University
*Philadelphia, PA, United States*

**Kim, Chulgoo**
Seoul National University
*Seoul, Republic of Korea*

**Kim, Tae-Hoon**
Korea Railroad Research Institute
*Uiwang, Republic of Korea*

**Kim, Taehwan**
University of New South Wales
*Sydney, NSW, Australia*

**Kim, Uksun**
California State University, Fullerton
*Fullerton, CA, United States*

**Klein, Gary**
Wiss, Janney, Elstner Associates, Inc.
*Northbrook, IL, United States*

**Kleinhans, Danielle**
Mateenbar Composite Reinforcements
*Concord, NC, United States*

**Klemencic, Ronald**
Magnusson Klemencic Associates
*Seattle, WA, United States*

**Kotecha, Payal**
The University of Texas at Arlington
*Daytona Beach, FL, United States*

**Kotsovos, Gerasimos**
Heriot-Watt University
*Edinburgh, United Kingdom of Great Britain and Northern Ireland*

**Krstulovic-Opara, Neven**
ExxonMobil Production Co
*Houston, TX, United States*

**Kumar, Dinesh**
Academy of Scientific and Innovative Research
*Ghaziabad, Uttar Pradesh, India*

**Kumar, Rakesh**
Central Road Research Institute
*Delhi, India*

**Kumbasaroglu, Atila**
Erzincan Universitesi
*Erzincan, Turkey*

**LaFave, James**
University of Illinois
*Champaign, IL, United States*

**Lakshmi, R.**
Kamaraj College of Engineering and Technology
*Virudhunagar, Tamil Nadu, India*

**Lan, Shuwei**
Kunming University
*Kunming, China*

**Larbi, Kacimi**
University of Sciences and Technology of Oran
*Oran, Oran, Algeria*

**Le, Chau**
UNC Charlotte
*Charlotte, NC, United States*

**Lee, Chang Hoon**
Cornell University
*Ithaca, NY, United States*

**Lee, Deuckhang**
Chungbuk National University
*Cheongju, Republic of Korea*

**Lee, Hung-Jen**
National Yunlin University of Science and Technology
*Douliou, China*

**Lee, Michael**
*Dallas, TX, United States*

**Lekshmi, Sreedevi**
Indian Institute of Technology Bombay
*Mumbai, India*

**Lequesne, Rémy**
University of Kansas
*Lawrence, KS, United States*

**Li, Fumin**
China University of Mining and Technology
*Xuzhou, Jiangsu, China*

**Li, Shuguang**
China Institute of Water Resources and Hydropower Research
*Beijing, China*

**Li, Yi-An**
National Chung Hsing University
*Taichung, Taiwan, China*

# REVIEWERS IN 2025

**Li, Zhengqi**
*Missouri City, TX, United States*

**Lima, Nathalia**
Universidade Federal de Pernambuco
*Recife, PE, Brazil*

**Lima, Thamara Tofeti**
Hanyang University
*Ansansi, Gyeonggido, Republic of Korea*

**Lin, Wei-Ting**
Dept. of Civil Engineering
*Ilan, Taiwan, China*

**Lines, Samuel**
*Tipp City, OH, United States*

**Ling, Tung Chai**
Hunan University
*Changsha, China*

**Ling, Yifeng**
Iowa State University
*Ames, IA, United States*

**Lipa Cusi, Leonel**
Pontificia Universidad Catolica del Peru
*Lima, Lima, Peru*

**Liu, Ci**
Hohai University
*Nanjing, Jiangsu, China*

**Liu, Kai-Wei (Victor)**
Prairie View A&M University
*Prairie View, TX, United States*

**Liu, Peng**
*Changsha, China*

**Liu, Qing-Feng**
Shanghai Jiao Tong University
*Shanghai, China*

**Liu, Xuejian**
The University of Texas at Arlington
*Arlington, TX, United States*

**Liu, Yanbo**
Harbin Engineering University
*Harbin, Heilongjiang, China*

**Liu, Zanqun**
School of Civil Engineering
*Changsha, China*

**Lizarazo Marriaga, Juan**
Universidad Nacional de Colombia - Sede Bogotá
*Bogota, Colombia*

**Lopes, Anne**
Furnas Centrais Eletricas SA
*Aparecida de Goiania, Goias, Brazil*

**Lotfy, Abdurrahmaan**
Lafarge Canada Inc.
*Toronto, ON, Canada*

**Lounis, Zoubir**
National Research Council
*Ottawa, ON, Canada*

**Lu, Yiqiu**
The University of Auckland
*Auckland, New Zealand*

**Luan, Yao**
Saitama University
*Saitama, Japan*

**Lubell, Adam**
Read Jones Christoffersen Ltd.
*Vancouver, BC, Canada*

**Lucero, Catherine**
US Bureau of Reclamation Denver Federal Center
*Denver, CO, United States*

**Luo, Da**
Chang'an University
*Xian, Shanxi, China*

**Luo, Dayou**
Iowa State University
*Ames, IA, United States*

**Ma, Dongpeng**
Guangdong University of Technology
*Guangzhou, China*

**Madera Sierra, Carlos**
Universidad del Valle
*Cali, Valle del Cauca, Colombia*

**Mahdy, Mohamed**
Faculty of Engineering, Masoura University
*Mansoura, Dakhlia, Egypt*

**Mahrenholtz, Christoph**
*Berlin, Germany*

**Majeed, Hozan**
Salahaddin University - Erbil
*Erbil, Iraq*

**Mander, John**
Texas A&M University
*College Station, TX, United States*

**Marikunte, Shashi**
Southern Illinois University
*Carbondale, IL, United States*

**Martin, Renaud-Pierre**
Université Gustave Eiffel - Campus de Marne-la-Vallée
*Champs-sur-Marne, France*

**Martinez Andino, Marcos**
Desimone Consulting Engneers
*Atlanta, GA, United States*

**Maruyama, Ippei**
The University of Tokyo
*Bunkyo, Japan*

**Masmoudi, Radhouane**
University of Sherbrooke
*Sherbrooke, QC, Canada*

**Mathew, George**
Cochin University of Science and Technology
*Cochin, Kerala, India*

**Matta, Fabio**
University of South Carolina
*Columbia, SC, United States*

**Maximos, Hany**
Maximos Engineering
*Mississauga, ON, Canada*

**McCall, W.**
Concrete Engineering Consultants
*Charlotte, NC, United States*

**Mechaala, Abdelmounaim**
University of Houston
*Houston, TX, United States*

**Megally, Sami**
PBS&J
*San Diego, CA, United States*

**Megid, Wael**
Tisec Inc.
*Morin Heights, QC, Canada*

**Mehany, Shehab**
University of Sherbrooke
*Sherbrooke, QC, Canada*

**Meinheit, Donald**
Wiss, Janney, Elstner Associates, Inc.
*Chicago, IL, United States*

**Melugiri Shankaramurthy, Bharath**

**Meng, Weina**
Missouri University of Science and Technology
*Rolla, MO, United States*

**Menu, Bruce**
Université Laval Faculté des Sciences et de Génie
*Quebec, QC, Canada*

**Miarka, Petr**
Institute of Physics of Materials Czech Academy of Sciences
*Brno, Czech Republic*

**Mirmiran, Amir**
The University of Texas at Tyler
*Tyler, TX, United States*

**Mirrashid, Masoomeh**
Abu Dhabi University
*Abu Dhabi, United Arab Emirates*

**Mishra, Dhanada**
KMBB College of Engg and Tech
*Khordha, Odisha, India*

**Mishra, Laxmi**
MNNIT
*Allahabad, UP, India*

**Mo, Shiguang**
Xiamen University
*Xiamen, Guangxi Province, China*

**Mo, Xiangyin**
Nanjing Normal University
*Nanjing, Jiangsu, China*

**Mobley, Sarah**
University of Tennessee Knoxville College of Engineering
*Knoxville, TN, United States*

**Mogili, Srinivas**
Indian Institute of Technology Delhi
*New Delhi, Delhi, India*

**Mohammed, Tarek**
Islamic University of Technology
*Gazipur, Dhaka, Bangladesh*

**Mohle, Jon**
*Sacramento, CA, United States*

**Moorthi, A Selva Ganesa**
IIT Madras
*Chennai, Tamil Nadu, India*

**Moradi, Mahdi**
Islamic Azad University of Qom
*Qom, Islamic Republic of Iran*

# REVIEWERS IN 2025

**Morais, Paulo**
University of Brasíli
*Brasilia, DF, Brazil*

**Moreno Rangel, Erick Daniel**
Oregon State University
*Corvallis, OR, United States*

**Moretti, Marina**
National Technical University of Athens
*Athens, Greece*

**Mosallam, Ayman**
University of California, Irvine
*Irvine, CA, United States*

**Mostafa, Mostafa M. A.**
Al-Azhar University - Assiut Branch
*Qena, Egypt*

**Mostofinejad, Davood**
Isfahan University of Technology
*Isfahan, Islamic Republic of Iran*

**Motter, Christopher**
Washington State University
*Pullman, WA, United States*

**MS, Sandeep**
Muthoot Institute of Technology and Science
*Cochin, Kerala, India*

**Muciaccia, Giovanni**
Politecnico di Milano
*Milan, Italy*

**Mukai, David**
University of Wyoming
*Laramie, WY, United States*

**Mukhopadhyay, Anol**
Texas A&M University Transportation Institute
*Bryan, TX, United States*

**Mullins, Gray**
University of South Florida
*Tampa, FL, United States*

**Murcia-Delso, Juan**
Universitat Politècnica de Catalunya - BarcelonaTech
*Barcelona, Spain*

**Murray, Cameron**
University of Arkansas
*Fayetteville, AR, United States*

**Muszynski, Larry**
University of Florida
*Gainseville, FL, United States*

**Mutsuddy, Rupak**
Bangladesh University of Engineering and Technology
*Dhaka, Bangladesh*

**Myers, John**
Missouri University of Science and Technology
*Rolla, MO, United States*

**N, Pannirselvam**
SRM Institute of Science and Technology
*Kanchipuram, Tamil Nadu, India*

**Nadertehrani, Bahare**
Isfahan University of Technology
*Isfahan, Esfahan, Islamic Republic of Iran*

**Nair, Sooraj**
United States Gypsum Corp.
*Libertyville, IL, United States*

**Najimi, Meysam**
Iowa State University
*Ames, IA, United States*

**Narayanan, Subramanian**
*Gaithersburg, MD, United States*

**Naser, M. Z.**
Clemson University
*Clemson, SC, United States*

**Nassiri, Somayeh**
University of California, Davis
*Davis, CA, United States*

**Nguyen, Hoang**
Northwestern University
*Evanston, IL, United States*

**Nguyen, Tan**
Ton Duc Thang University
*Ho Chi Minh City, Viet Nam*

**Nian, Tengfei**
*Lanzhou, China*

**Nicholas, Thomas**
Middle Tennessee State University
*Murfreesboro, TN, United States*

**Nili, Mahmoud**
Bu-Ali Sina University
*Hamedan, Islamic Republic of Iran*

**Nishiyama, Minehiro**
Kyoto University
*Kyoto, Japan*

**Noor, Munaz**
Bangladesh University of Engineering and Technology
*Dhaka, Bangladesh*

**Noviari Wibowo, Yosi**
Institut Teknologi Sepuluh Nopember
*Surabaya, East Java, Indonesia*

**Nzambi, Aaron**
Universidade Federal do Pará
*Belem, Pará, Brazil*

**Okeil, Ayman**
Louisiana State University
*Baton Rouge, LA, United States*

**Omran, Mohamed**
Nile University
*Sheikh Zayed City, Egypt*

**Onuoha, Ifeanyichukwu**
Temple University
*Philadelphia, PA, United States*

**O'Reilly, Matt**
University of Kansas
*Lawrence, KS, United States*

**Ospina, Carlos**
Simpson Gumpertz & Heger Inc.
*Houston, TX, United States*

**Othman, Nor Hazurina**
Universiti Tun Hussein Onn Malaysia
*Batu Pahat, Johor, Malaysia*

**Oukaili, Nazar**
University of Baghdad
*Baghdad, Iraq*

**Oundhakar, Abhijeet**
Invictus Consultancy Services
*Navi Mumbai, Maharashtra, India*

**Oyguc, Resat**
Istanbul Teknik Universitesi
*Istanbul, Turkey*

**Özdemir, Anıl**
Gazi Universitesi
*Ankara, Turkey*

**Ozturan, Turan**
Bogazici University
*Istanbul, Turkey*

**Ozturk, Baki**
*Ankara, Turkey*

**Ozturk, Onur**
Cornell University
*Ithaca, NY, United States*

**Ozyildirim, H. Celik**
Virginia Transportation Research Council
*Charlottesville, VA, United States*

**P V, Ponambala Moorthi**
University of Louisville
*Louisville, KY, United States*

**Pacheco, Alexandre**
Universidade Federal do Rio Grande do Sul (UFRGS)
*Porto Alegre, RS, Brazil*

**Pacheco, Jose**
MJ2 Consulting
*Chicago, IL, United States*

**Palieraki, Vasiliki**
National Technical University of Athens
*Athens, Zografou, Greece*

**Pan, Wang Fook**
SEGi University
*Petaling Jaya, Selangor, Malaysia*

**Panagiotou, Marios**
Nabih Youssef Associates
*Los Angeles, CA, United States*

**Panchmatia, Parth**
Kansas State University
*Manhattan, KS, United States*

**Pandit, Poornachandra**
Manipal Institute of Technology
*Manipal, India*

**Pantazopoulou, Stavroula**
York University - Keele Campus
*Toronto, ON, Canada*

**Pantelides, Chris**
University of Utah
*Salt Lake City, UT, United States*

**Park, Honggun**
Seoul National University
*Gwanak-gu, Republic of Korea*

**Parsekian, Guilherme**
UFSCar
*Sao Carlos, Brazil*

**Patel, Devansh**
Arizona State University
*Tempe, AZ, United States*

# REVIEWERS IN 2025

**Patrisia, Yulin**
RMIT University
*Melbourne, VIC, Australia*

**Paulson, Conrad**
Wiss, Janney, Elstner Associates, Inc.
*Pasadena, CA, United States*

**Persson, Bertil**
*Bara, Sweden*

**Pollalis, William**
Texas A&M University
*College Station, TX, United States*

**Potnoor, Naveen**
Adani Enterprises Ltd.
*Mumbai, India*

**Pourbaba, Masoud**
Islamic Azad University, Maragheh
*Maragheh, East Azarbayjan, Islamic Republic of Iran*

**Princigallo, Antonio**
Heidelberg Materials Italia Cementi S.p.A
*Peschiera Borromeo, Milano, Italy*

**Proestos, Giorgio**
North Carolina State University
*Raleigh, NC, United States*

**Pugliaro, Andrea**
Senior Materials and Laboratory Engineer (Civil and Geotechnical)
*Savona, Italy*

**PV, Premalatha**
CARE School of Engineering
*Tiruchirappalli, India*

**Qiao, Hongxia**
*Lanzhou, China*

**Qissab, Musab**
Al-Nahrain University
*Baghdad, Iraq*

**Quach, Phillip**
RJC Engineers
*Toronto, ON, Canada*

**Quintana Gallo, Patricio**
University of Rostock Faculty of Agricultural and Environmental Sciences
*Rostock, Germany*

**Quiroga, Pedro**
Escuela Colombiana de Ingenieria
*Bogota, Colombia*

**R, Kondalraj**
Indian Institute of Technology Madras
*Chennai, India*

**Rafi, Muhammad**
NED University of Engineering and Technology
*Karachi, Sindh, Pakistan*

**Ragheb, Wael**
Alexandria University
*Windsor, ON, Canada*

**Rahal, Khaldoun**
Kuwait University
*Safat, Kuwait*

**Ramaswamy, Nagesh**
University of Houston
*Houston, TX, United States*

**Ramirez Garcia, Alberto**
University of Arkansas
*Fayetteville, AR, United States*

**Rashad, Alaa**
Housing and Building National Research Center
*Giza, Egypt*

**Rasheed, Abdur**
Shaqra University
*Shaqra, Saudi Arabia*

**Razmara, Mehrdad**
Purdue University College of Engineering
*West Lafayette, IN, United States*

**Restrepo, Jose**
University of California, San Diego
*La Jolla, CA, United States*

**Ridha, Maha (Lianne)**
*Melbourne, VIC, Australia*

**Rizwan, Syed Ali**
National University of Computer and Emerging Sciences - Lahore Campus
*Lahore, Punjab, Pakistan*

**Rodriguez, Mario**
National Autonomous University of Mexico
*Ciudad de Mexico, Mexico*

**Rodriguez, Sofia**
Universidad de los Andes
*Bogotá, Cundinamarca, Colombia*

**Rojas Aguero, Rosangel**
Universidade Federal do Rio Grande
*Rio Grande, Rio Grande do Sul, Brazil*

# REVIEWERS IN 2025

**Rojas, Gullem**
University of Stavanger
*Stavanger, Norway*

**Ross, Brandon**
Clemson University
*Clemson, SC, United States*

**S, Kumaravel**
Annamalai University
*Cuddalore, Tamil Nadu, India*

**Saafan, Mohamed**
Menoufia University
*Shebeen El-Koom, Menoufia, Egypt*

**Saeed, Yasir**
Portland State University
*Portland, OR, United States*

**Sagaseta, Juan**
University of Surrey
*Guildford, Surrey, United Kingdom of Great Britain and Northern Ireland*

**Saleh Ahari, Reza**
Islamic Azad University Tabriz Branch
*Tabriz, Islamic Republic of Iran*

**Sánchez, Emil**
Fluminense Federal University
*Rio de Janeiro, Rio de Janeiro, Brazil*

**Santos, Daniel**
University of Sao Paulo Polytechnic School
*Sao Paulo, Sao Paulo, Brazil*

**Santos, Sérgio**
SBS Engineering Consultancy
*Goiânia, Goiás, Brazil*

**Sarkar, Manas**
Zhejiang University
*Hangzhou, Zhejiang, China*

**Sarkhosh, Reza**
*The Hague, South-Holland, Netherlands*

**Sato, Yuichi**
Kyoto University
*Kyoto, Kyoto, Japan*

**Sayed Ahmed, Mahmoud**
Toronto Metropolitan University
*Toronto, ON, Canada*

**Schokker, Andrea**
University of Minnesota Duluth
*Duluth, MN, United States*

**Segura, Christopher**
National Institute of Standards and Technology
*Gaithersburg, MD, United States*

**Seręga, Szymon**
Cracow University of Technology
*Kraków, Poland*

**Sezen, Halil**
Ohio State University
*Columbus, OH, United States*

**Shafigh, Payam**
Wenzhou University of Technology
*Wenzhou, Zhejiang, China*

**Shafiq, Nasir**
University Technology Petronas
*Tronoh, Perak, Malaysia*

**Shaheen, Ehab**
University of Calgary
*Calgary, AB, Canada*

**Shahmansouri, Amir Ali**
University of Miami
*Coral Gables, FL, United States*

**Shakouri, Mahmoud**
Boise State University
*Boise, ID, United States*

**Shang, Ziduan**
Shanghai Nuclear Engineering Research and Design Institute
*Shanghai, China*

**Sharifzad, Shayan**
The University of Texas at Arlington College of Engineering
*Arlington, TX, United States*

**Shariq, Mohd**
Civil Engg Section
*Aligarh, Uttarpradesh, India*

**Sharma, Akanshu**
Institute of Construction Materials
*Stuttgart, Germany*

**Sharma, Sumedh**
Texas A&M University
*College Station, TX, United States*

**Shen, Yin**
Tongji University
*Shanghai, China*

**Shi, Jie**
*Nanjing, China*

# REVIEWERS IN 2025

**Shi, JinJie**
Southeast University
*Nanjing, China*

**Shi, Jinyan**
Central South University
*Changsha, China*

**Shi, Tao**
Zhejiang University of Technology
*Hangzhou, Zhejiang, China*

**Shi, Xianming**
University of Miami
*Coral Gables, FL, United States*

**Shi, Xijun**
Texas State University
*San Marcos, TX, United States*

**Shivali, Ram**
Central Soil and Materials Research Station
*New Delhi, India*

**Shreshthi, Rohan**
Dr. D.Y. Patil College of Engineering and Technology, Kasaba Bawada, Kolhapur
*Kolhapur, Maharashtra, India*

**Shrestha, Samyog**
Purdue University
*West Lafayette, IN, United States*

**Shumuye, Eskinder Desta**
Shenzhen University College of Civil and Transportation Engineering
*Shenzhen, GD, China*

**Silfwerbrand, Johan**
KTH Royal Institute of Technology
*Stockholm, Sweden*

**Silva, Antonio**
LNEC
*Lisboa, Portugal*

**Singh, D D N**
*New Delhi, India*

**Singh, Surender**
Indian Institute of Technology Madras
*Chennai, Tamil Nadu, India*

**Sirico, Alice**
University of Parma
*Parma, Italy*

**Soares, Renan**
Universidade Federal de Pernambuco
*Recife, Pernambuco, Brazil*

**Sobuz, Md. Habibur Rahman**
Khulna University of Engineering and Technology
*Khulna, Bangladesh*

**Soliman, Ahmed**
Western University
*London, ON, Canada*

**Soltani, Masoud**
Tarbiat Modares University
*Tehran, Tehran, Islamic Republic of Iran*

**Soltani, Matthew**
Bradley University Caterpillar College of Engineering and Technology
*Peoria, IL, United States*

**Sonkusare, Hemantkumar**
G H Raisoni College of Engineering
*Nagpur, Maharashtra, India*

**Sonyal, Muhammad**
University of Engineering and Technology
*Lahore, Punjab, Pakistan*

**Sousa, Jedson**
Universidade Estadual do Norte Fluminense Darcy Ribeiro Centro de Ciência e Tecnologia
*Campos dos Goytacazes, Rio de Janeiro, Brazil*

**Souza, Wallace**
Universidade Federal do Maranhão
*São Luís, Maranhão, Brazil*

**Söylev, Altug**
Yeditepe University
*Istanbul, Turkey*

**Sreekala, R**
Structural Engineering Research Centre
*Chennai, Tamil Nadu, India*

**Sreekumaran, Sreenath**
SASTRA Deemed University
*Thanjavur, Tamil Nadu, India*

**Stanton, John**
University of Washington
*Seattle, WA, United States*

**Stella, Alberto**
Iuav University of Venice
*Venice, Italy*

**Stengel, Thorsten**
Hochschule für angewandte Wissenschaften München
*Munchen, Germany*

# REVIEWERS IN 2025

**Stojadinovic, Bozidar**
Swiss Federal Institute of Technology
*Zurich, Switzerland*

**Stonys, Rimvydas**
Vilnius Gediminas Technical University
*Vilnius, Lithuania*

**Su, Yu-Min**
National Kaohsiung University of Science and Technology
*Kaohsiung, Taiwan, China*

**Suraneni, Prannoy**
University of Miami
*Coral Gables, FL, United States*

**Surehali, Sahil**
Arizona State University
*Tempe, AZ, United States*

**Suryawanshi, Yogesh**
JSPM's Imperial College of Engineering and Research Wagholi
*Pune, Maharashtra, India*

**T., Hemalatha**
CSIR-Structural Engineering Research Centre
*Chennai, Tamil Nadu, India*

**Tabkhi Wayghan, Amir Reza**
Carleton University Faculty of Engineering and Design
*Ottawa, ON, Canada*

**Tabsh, Sami**
American University of Sharjah
*Sharjah, United Arab Emirates*

**Tajaddini, Abbas**
University of Bath Faculty of Engineering and Design
*Bath, United Kingdom of Great Britain and Northern Ireland*

**Taki, Amirmasoud**
Islamic Azad University, Science and Research Branch
*Tehran, Islamic Republic of Iran*

**Tang, Fujian**
Dalian University of Technology
*Dalian, Liaoning, China*

**Tang, Xiusheng**
Nanjing Hydraulic Research Institute
*Nanjing, China*

**Tastani, S. P.**
Demokritus University of Thrace
*Xanthi, Greece*

**Tatum, Garrett**
University of Wyoming College of Engineering and Applied Science
*Laramie, WY, United States*

**Tekin, Ilker**
Bayburt University
*Bayburt, Turkey*

**Tepke, David**
*State College, PA, United States*

**Thomas, Robert**
Clarkson University
*Potsdam, NY, United States*

**Thompson, Phillip**
*Palm Desert, CA, United States*

**Tian, Ying**
University of Nevada, Las Vegas
*Las Vegas, NV, United States*

**Tikalsky, Paul**
Oklahoma State University
*Stillwater, OK, United States*

**Tiwari, Ashish**
*Kalka, Haryana, India*

**Tobber, Lisa**
The University of British Columbia Okanagan
*Kelowna, BC, Canada*

**Tognonvi, Tohoue Monique**
Université de Sherbrooke
*Sherbrooke, QC, Canada*

**Tohidi, Mosleh**
University of West London
*London, United Kingdom of Great Britain and Northern Ireland*

**Tore, Erkan**
Balikesir University
*Balikesir, Balikesir, Turkey*

**Tran, Mien**
Ho Chi Minh City University of Technology
*Ho Chi Minh City, Viet Nam*

**Tripathi, Avinaya**
Arizona State University
*Tempe, AZ, United States*

**Tsai, Ren-Jie**
University of Auckland
*Auckland City, New Zealand*

**Tuchscherer, Robin**
Northern Arizona University
*Flagstaff, AZ, United States*

**Tunstall, Lori**
Colorado School of Mines
*Golden, CO, United States*

# REVIEWERS IN 2025

**Turgut, Paki**
Inonu Universitesi
*Malatya, Turkey*

**Umipig, Jorge**
Vistaland & Lifescapes Inc.
*Mandaluyong City, Metro Manila, Philippines*

**Vafaei, Babak**
University of Miami
*Coral Gables, FL, United States*

**Vandenberg, Aileen**
International Code Council - Evaluation Services
*Brea, CA, United States*

**Vanhove, Yannick**
Artois University - Tecnology Institute Béthune
*Bethune, France*

**Varney, Nancy**
Northeastern University
*Boston, MA, United States*

**Vasovic, Dejan**
University of Belgrade, Faculty of Architecture
*Belgrade, Serbia*

**Vasudevan, Gokul Dev**
*Corvallis, OR, United States*

**Vaughan, John**
*Louisville, KY, United States*

**Villacis, Eugenia de las**
Escuela Politecnica Nacional
*Quito, Pichincha, Ecuador*

**Vollum, Robert**
Dept of Civil and Env Engrg
*London, United Kingdom of Great Britain and Northern Ireland*

**Wang, Ben**
University of Houston
*Houston, TX, United States*

**Wang, Jiaduo**
*ZiBo, ShanDong, China*

**Wang, Kejin**
Iowa State University
*Ames, IA, United States*

**Wang, Penghui**
Lanzhou University of Technology
*Lanzhou, Gansu, China*

**Wang, Shuwei**
*Qinzhou, Guangxi, China*

**Wardhono, Arie**
The State University of Surabaya
*Surabaya, Jawa Timur, Indonesia*

**Wegner, Leon**
University of Saskatchewan College of Engineering
*Saskatoon, SK, Canada*

**Wei-Jian, Yi**
*Changsha, China*

**Werner, Anne**
SIUE
*Edwardsville, IL, United States*

**West, Jeffrey**
Wiss, Janney, Elstner Associates, Inc.
*Austin, TX, United States*

**Wietek, Bernhard**
Wietek ZT
*Sistrans, Tirol, Austria*

**Wigum, Børge**
Heidelberg Materials AG
*Reykjavik, Reykajvik, Iceland*

**Wilde, W. James**
Texas State University
*San Marcos, TX, United States*

**Williams, Christopher**
Purdue University System
*West Lafayette, IN, United States*

**Witwit, Jaafar**
*Baghdad, Iraq*

**Wong, Sook Fun**
Nanyang Technological University
*Singapore, Singapore*

**Worsfold, Benjamin**
University of Minnesota
*Minneapolis, MN, United States*

**Woyciechowski, Piotr**
Warsaw University of Technology
*Warsaw, Poland*

**Wu, Chao**
Wuhan University of Technology
*Wuhan, Hubei, China*

**Wu, Chenglin**
Missouri University of Science and Technology
*Rolla, MO, United States*

**Wu, Kai**
*Nanjing, Jiangsu, China*

**Wu, Teng**
University at Buffalo - The State University of New York
*Buffalo, NY, United States*

**Wu, Yu-You**
Foshan University
*Foshan, Guangdong, China*

**Xia, Zhi-Yu**
*United States*

**Xiangguo, Wu**
Harbin Institute of Technology
*Harbin, Heilongjiang, China*

**Xie, Guoshuai**
Wuhan University
*Wuhan, Hubei, China*

**Xie, Luqi**
Southeast University
*Nanjing, China*

**Xu, Aimin**
ARRB Group
*Melbourne, VIC, Australia*

**Yan, ChangWang**
Inner Mongolia University of Technology
*Hohhot, China*

**Yan, Peiyu**
Tsinghua University
*Beijing, China*

**Yang, Rick**
SNC-Lavalin Engineers and Constructors Inc
*Houston, TX, United States*

**Yang, Sung Chul**
Hongik University
*Mapo-gu, Republic of Korea*

**Yapa, Hiran**
University of Peradeniya Faculty of Engineering
*Peradeniya, Sri Lanka*

**Yassein, Mohamed**
*Abu Dhabi, Abu Dhabi, United Arab Emirates*

**Yasso, Samir**
University of Mosul
*Mosul-Bartella, Nineveh, Iraq*

**Yerramala, Amarnath**
Dundee University
*Dundee, United Kingdom of Great Britain and Northern Ireland*

**Yi, Kwanwoo**
Seoul National University
*Seoul, Republic of Korea*

**Yindeesuk, Sukit**
University of Illinois Urbana-Champaign
*Urbana, IL, United States*

**YK, Guru**
Indian Institute of Science
*Bangalore, India*

**Yoon, Hyeong Jae**
The Consulting Engineers Group, Inc.
*San Antonio, TX, United States*

**Yoon, Young-Soo**
Korea University
*Seoul, Republic of Korea*

**Yousefpour, Hossein**
Babol Noshirvani University of Technology
*Babol, Mazandaran, Islamic Republic of Iran*

**Yuen, Terry Yu Ping**
National Yang Ming Chiao Tung University
*Hsinchu, Taiwan, China*

**Zapata, Luis**
Universidad Industrial de Santander
*Bucaramanga, Santander, Colombia*

**Zarshin Zanoish, Romina**
*Rasht, Islamic Republic of Iran*

**Zhang, Feng**
Nanjing Hydraulic Research Institute
*Nanjing, China*

**Zhang, Qian**
*Nanjing, China*

**Zhang, Qin**
Dalian University of Technology, Dalian
*Dalian, Liaoning, China*

**Zhang, Wei**
Tsukuba Daigaku
*Tsukuba, Japan*

**Zhao, Haitao**
Hohai University
*Nanjing, China*

**Zhao, Jianjun**
*Harbin, China*

**Zhao, Xingzhuang**
University of Maryland
*College Park, MD, United States*

# REVIEWERS IN 2025

**Zhao, Xin-Yu**
South China University of Technology
*Guangzhou, China*

**Zhao, Zengfeng**
Tongji University
*Shanghai, China*

**Zheng, Herbert**
Gammon Construction Limited
*Hong Kong, Hong Kong, China*

**Zhu, Wenjun**
L'Institut National des Sciences Appliquées de Toulouse
*Toulouse, Toulouse, France*

**Zych, Mariusz**
Politechnika Krakowska im Tadeusza Kosciuszki
*Krakow, Poland*

# REGISTER TODAY

# ACI FOUNDATION
# CONCRETE INNOVATION FORUM

---

## AUGUST 18-20, 2026, COLUMBUS, OH, USA

Hyatt Regency Columbus 350 N. High St.

**The Concrete Innovation Forum is an innovation-focused educational and networking event for concrete professionals. The Forum is your opportunity to connect with representatives from material suppliers, architecture & engineering firms, contractors, academics, top-level executives, and regulatory agencies. You will learn from industry-experts about current trends, emerging technologies, and new product innovations. Build strategic relationships and expand your network.**

aci Foundation
Building the Future

# JOIN AN ACI Chapter!

The American Concrete Institute has Chapters and Student Chapters located throughout the world. Participation in a local chapter can be extremely rewarding in terms of gaining greater technical knowledge and networking with leaders in the concrete community.

Because chapters are distinct and independent legal entities, membership includes both ACI members and non-ACI members and is made up of a diverse blend of architects, engineers, consultants, contractors, educators, material suppliers, equipment suppliers, owners, and students—basically anyone interested in concrete. Many active ACI members initially became involved in ACI through their local chapter. In addition to technical programs and publications, many chapters sponsor ACI Certification programs, ACI educational seminars, project award recognition programs, and social events with the goal of advancing concrete knowledge.

To find a chapter near you, go to: https://www.concrete.org/getinvolved/chapters.aspx

---

## Student Chapters

Join or form an ACI Student Chapter to maximize your influence, knowledge sharing, and camaraderie! ACI has 240+ student chapters located throughout the world, each providing opportunities for students to:

- Connect with their peers and participate in concrete-related activities such as: student competitions, ACI Conventions, ACI Certification Programs, ACI Educational Seminars, local chapter meetings, social events, and community service projects;
- Network with members of local chapters, many of whom have been in the industry for decades and can help to develop professional relationships and offer career advice;
- Win recognition for their universities through the University Award; and
- Learn about the many scholarships and fellowships offered by the ACI Foundation and by ACI's local chapters.

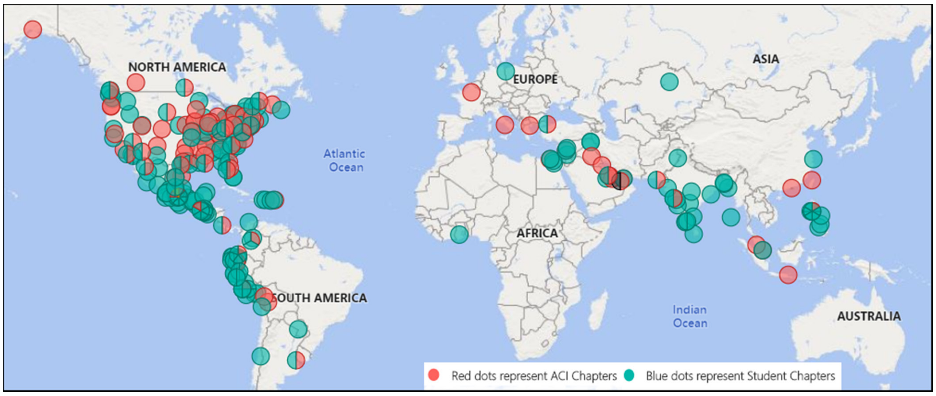

American Concrete Institute

www.concrete.org/getinvolved/chapters.aspx

# Become a Peer Reviewer for ACI Journals

Peer reviewers help ensure the quality, accuracy, and impact of published concrete research. Your expertise directly supports advancement in the field.

## Why Review?

- Shape research that informs codes and practice
- Stay current with new findings and technologies
- Strengthen your professional credentials
- Connect with editors, authors, and industry experts

## Areas of Expertise We Seek

- Structural analysis, design, and performance
- Concrete materials, durability, and behavior
- Repair, rehabilitation, and strengthening
- High-performance, sustainable, and low-carbon concrete
- Structural resilience and durability-related performance
- Alternative and non-metallic reinforcement
- Fiber-reinforced concrete
- UHPC and emerging materials
- Performance-based design
- Seismic design and retrofit
- Fire resistance of concrete and masonry
- Testing, evaluation, and condition assessment
- Nondestructive testing and sensing technologies
- Digital tools, modeling, and artificial intelligence

## Reviewer Expectations

Technical expertise • Clear, constructive feedback
Timely reviews • Professionalism & confidentiality

## How to Join

1. Create an account at **mc.manuscriptcentral.com/aci**
2. Select your areas of expertise
3. Email **journal.manuscripts@concrete.org** to request reviewer status

aci®

American Concrete Institute

*Always advancing*

# ARE YOU A RESEARCHER?

## SIGN UP FOR ORCID TODAY!

1. Register
2. Use your ORCID ID
3. Share

ORCID provides a digital identifier that distinguishes you from every other researcher and, through integration in key research workflows such as manuscript and grant submission, supports automated linkages between you and your professional activities, ensuring that your work is recognized.

ORCID services are FREE and it’s as easy as **1-2-3**.

**WWW.ORCID.ORG**

# WHY JOIN THE aci Faculty Network?

The Faculty Network is a free connection group for educators interested in ACI and the concrete industry.

## FREE DESK COPIES

Faculty Network members can request a complimentary print or PDF copy of:

- **ACI CODE-318-25:** Building Code for Structural Concrete—Code Requirements and Commentary (includes a free subscription to ACI 318 PLUS)
- **ACI/PCI CODE-319-25:** Structural Precast Concrete—Code Requirements and Commentary
- **ACI/PTI Code-320-25:** Post-Tensioned Structural Concrete—Code Requirements and Commentary
- **ACI CODE-323-24:** Low-Carbon Concrete—Code Requirements and Commentary
- **ACI CODE-562-25:** Assessment, Repair, and Rehabilitation of Existing Concrete Structures—Code Requirements and Commentary
- **ACI MNL-3(20):** Guide to the Code for Assessment, Repair, and Rehabilitation of Existing Concrete Structures
- **ACI MNL-5(19):** Contractor's Guide to Quality Concrete Construction, 4th Edition
- **Professors' Resources for ACI/ASCC Contractor's Guide to Quality Concrete Construction**, 4th Edition
- **ACI SP-4:** Formwork for Concrete

## NETWORKING

Exchange ideas and network at the Faculty Network Reception twice a year during the ACI Concrete Conventions.

aci 318PLUS

Faculty Network members receive a complimentary annual subscription to ACI 318 PLUS: a digital version of ACI CODE 318, which includes access to ACI CODE-318-25: Building Code for Structural Concrete; ACI MNL-17(21): ACI Reinforced Concrete Design Handbook; and MNL-66(20): ACI Detailing Manual. Professors can also create and share custom notes for students to view alongside the Code.

aci Professors' Workshop
Materials | Pavements | Structures
Sponsor: aci Foundation

Designed for current and aspiring concrete course instructors, this workshop helps professors strengthen course structure, boost student engagement, and better align learning outcomes, assessments, and instructional strategies.

aci Foundation
Building the Future

The Concrete Research Council (CRC) funds research that advances the knowledge and sustainability of concrete materials, construction, and structures in collaboration with ACI Committees. Proposals are accepted **annually** from August 1 to December 1.

## FREE 1-YEAR EDUCATOR MEMBERSHIP

ACI offers complimentary membership ($310 USD) to teaching professionals who have not been an ACI member within the past 5 years. Renewal membership rates are subject to change. The total value of ACI membership and Faculty Network resources is over $2,000 USD.

*Membership fees are subject to change.*

**ADVANCE YOUR CLASSROOM WITH aci**
**JOIN OR RENEW TODAY! concrete.org/educatorsandresearchers**

# aci in Your Classroom

## Integrate aci into your classroom!

To support future leaders, ACI has launched several initiatives to engage students in the Institute's activities and programs – select programs that may be of interest to Educators are:

- **Free student membership –** encourage students to sign up
- **Special student discounts on *ACI 318 Building Code Requirements for Structural Concrete*, *ACI 530 Building Code Requirements and Specification for Masonry Structure*, & *Formwork for Concrete* manual.**
- **Access to *Concrete International* –** free to all ACI student members
- **Access to *ACI Structural Journal* and *ACI Materials Journal* –** free to all ACI student members
- **Free sustainability resources –** free copies of Sustainable Concrete Guides provided to universities for use in the classroom
- **Student competitions –** participate in ACI's written and/or team-based competitions
- **Scholarships and fellowships –** students who win awards are provided up to $15,000 and may be offered internships and paid travel to attend ACI's conventions
- **ACI Award for University Student Activities –** receive local and international recognition for your University's participation in concrete-related activities
- **Free access to the *ACI Collection of Concrete Codes, Specifications, and Practices* –** in conjunction with ACI's chapters, students are provided free access to the online ACI Collection
- **ACI online recorded web sessions and continuing education programs –** online learning tools ideal for use as quizzes or in-class study material

https://www.concrete.org/educatorsandresearchers/aciinyourclassroom.aspx

# ACI MATERIALS JOURNAL

The American Concrete Institute (ACI) is a leading authority and resource worldwide for the development and distribution of consensus-based standards and technical resources, educational programs, and certifications for individuals and organizations involved in concrete design, construction, and materials, who share a commitment to pursuing the best use of concrete.

Individuals interested in the activities of ACI are encouraged to explore the ACI website for membership opportunities, committee activities, and a wide variety of concrete resources. As a volunteer member-driven organization, ACI invites partnerships and welcomes all concrete professionals who wish to be part of a respected, connected, social group that provides an opportunity for professional growth, networking, and enjoyment.

aci®

American Concrete Institute